Optimising Spin-Coated Titanium Dioxide Photocatalysts

Genevieve Ososki BSc ATCL

A thesis submitted in partial fulfilment of the requirements for the degree of Doctor of Philosophy

Cardiff University

School of Chemistry

March 2022

Abstract

Spin-coating was used to produce a multitude of mesoporous titanium dioxide thin films, using stearic acid as a model organic pollutant to assess their activity. Spin speeds between 500 and 8000 rpm were used to produce films of TiO_2, meso-TiO_2 and Cu-doped *meso*-TiO_2. Layering films was explored to determine its effect on the activity of the resulting surface coatings. An optimum was reached at four layers, after which subsequent layers proved detrimental to the activity. The activity of films with 0.1 to 5 wt% copper-doping was assessed, finding copper-doping above 1 wt% proved to be detrimental to the activity of the photocatalysts. The 0.5 and 0.1 wt% samples proved to be more active than undoped meso-TiO_2 films. Photocatalytic testing using a solid layer of stearic acid spin-coated directly on top of the photocatalyst film allowed for an effective mechanistic study. It was possible to decompose stearic acid on the surface in air, nitrogen, and under vacuum, revealing the Mars-van Krevelen mechanism by which the reactions on the surface progress. Accurate film depth measurements using optical profilometry exposed the non-Newtonian behaviour of the fluid used to produce the films. Comparing the spin speed, film depth, kinetics, and activity of the films showed that the spin-coating process has a greater impact than merely the film thickness. The critical shear rate of the fluids used to produce these films coincided with a change in the kinetics of the decomposition of stearic acid over the photocatalysts. The 5 wt% copper-doped meso-TiO_2 samples showed a clear increase in bandgap energy with increasing spin speed, beyond any changes in film depth. The photocatalysts also proved to be effective at decomposing polystyrene. Increasing the spin-speed improved the selectivity towards the phenyl ring, showing that these materials could be easily tailored to specific needs.

Acknowledgements

Two charities have helped me greatly over the course of my PhD. The Chemists' Community Fund and The Benevolent Society of Blues granted me money that allowed me to purchase a wheelchair without which I would not have been able to continue my career in chemistry. I am extremely grateful for the assistance they have provided.

I would especially like to thank my supervisor, Phil Davies. I am certain that his influence during my undergraduate and postgraduate studies has led me down my current path in life and I am grateful for all the support he has given me over the years.

Nothing that I have achieved since coming to Cardiff would have been possible without the love and support of my husband, Sam. He has been by my side for the last ten years and has helped me through some of the most difficult periods of my life.

Table of Contents

Table of Figures

Chapter 1. Introduction

1.1 Photocatalysis

Photocatalysis is a powerful tool as it can utilize the safe and clean energy of the sun for sustainable and economically viable technologies. It is being increasingly used and developed for the decomposition of industrial and environmental pollutants.[1,2] Photocatalysts can be used to decompose dyes, plastics, and many other types of pollutants.[3–7]

Typically, heterogeneous catalysis is used, where a solid photocatalyst is placed into solution with the target pollutant, but composite plastic-photocatalyst films and immobilized photocatalysts have also been successfully used.[3,8,9]

1.2 Titanium dioxide as a photocatalyst

Titanium dioxide is an ideal photocatalyst since it is photoactive whilst being chemically stable and non-toxic. Uses in development and production include purification of polluted air and water, self-cleaning glasses and tiles.[10]

Titanium dioxide is a semiconductor. When exposed to light where the photon energy, $h\nu$, exceeds the band gap of TiO_2, a photocatalyzed reaction can be initiated. The absorbed photon excites an electron from the valence band to the conduction band generating a positive hole in the valence band, and leaving an electron in the conduction band (the electron-hole pair).[11] The excited electron can undergo redox reactions in order to break down pollutants in contact with the surface of the material.[12] Oxidation of water or hydroxyl ions by the positive hole can produce hydroxyl radicals, which are powerful oxidants of organic compounds.[13]

The photo-excited electron in the conduction band can react with oxygen to produce a superoxide radical anion ($O_2^{\bullet -}$) which, when protonated, forms a hydroperoxide radical ($^{\bullet}OOH$). Equations 1-6 summarise the mechanism by which the reactive oxygen species are produced and Equations 7 and 8 demonstrate how the superoxide radical anion and hyperoxide radical can react with pollutants to give water and carbon dioxide as products.[14]

$$TiO_2 + h\nu \rightarrow e_{CB}^- + h_{VB}^+ \quad \textbf{1.1}$$

$$H_2O + h_{VB}^+ \rightarrow \bullet OH + H^+ \quad \textbf{1.2}$$

$$O_2 + e_{CB}^- \rightarrow O_2^{\bullet -} \quad \textbf{1.3}$$

$$O_2^{\bullet -} + H^+ \rightarrow {}^{\bullet}OOH \quad \textbf{1.4}$$

$${}^{\bullet}OOH + e_{CB}^- \rightarrow HOO^- \quad \textbf{1.5}$$

$$HOO^- + H^+ \rightarrow H_2O_2 \quad \textbf{1.6}$$

$$O_2^{\bullet -} + C_xH_y \rightarrow H_2O + CO_2 \quad \textbf{1.7}$$

$${}^{\bullet}OOH + \text{pollutant} \rightarrow H_2O + CO_2 \quad \textbf{1.8}$$

Typically, the mechanism of TiO_2 photocatalysis is studied using TiO_2 powders in a solution containing the reactant. This system involves three oxygen sources: the lattice oxygen from the photocatalyst itself, oxygen from the solvent, and the surrounding atmosphere. Experiments using $H_2{}^{18}O$ and ${}^{18}O_2$ have shown labelled oxygen incorporated into both intermediates and final reaction products.[15] As it is not possible to remove the solvent and atmospheric oxygen sources in these experiments, it is not possible to determine the source of oxygen incorporated into the products. It is possible that labelled oxygen is merely replacing lattice oxygen that has been lost during the reaction and is being incorporated into the products through a Mars-van Krevelen type mechanism. As the work undertaken here involves a solid photocatalyst, solid reactant and the atmosphere surrounding it, it offers a unique approach to the study of these reaction mechanisms. The atmosphere surrounding the samples can be replaced with nitrogen while under UV irradiation in order to eliminate all sources of oxygen except the lattice oxygen of the photocatalyst. Work by Ali et al. showed evidence for a Mars-van Krevelen type mechanism in zinc oxide thin film catalysts,[4] however, they were unable to remove the liquid and gaseous oxygen and instead, drew their conclusions from observing the morphology and rates of the reaction over the catalysts while flowing various rates of oxygen through the solution containing the catalyst and reactants.

1.3 Doped Titanium Dioxide

The main drawback of TiO_2 as a photocatalyst is the large bandgap of 3.2 eV. Doping TiO_2 photocatalysts has been explored as a method of reducing the bandgap, with coalloying,[16] doping,[17] and titanium-terminated anatase surfaces[18] providing promising results. Doping of TiO_2 can also increase its photocatalytic activity by forming new energy levels near the conduction band.[19]

There are a wide range of elements that have been used as dopants including aluminium, copper, molybdenum, tungsten and nitrogen.[19–21] A wide range of dopant inclusions have been reported with substitutional, metal oxide nanoparticles and single atom surface species reported.[19,22]

1.4 Methods for producing films

When deciding upon techniques to use in this work, the main issues to be addressed were the need for high quality, uniform porous films using techniques that allow facile, accurate reproducibility of samples. There are many techniques capable of depositing thin films onto substrates such as dip coating, spin coating, spray pyrolysis and pulsed laser deposition.

Dip coating produces films by immersing a substrate into a solution, resulting in a uniform film. The film thickness can be adjusted by altering the viscosity of the solution used to coat the substrate, however this does mean that a new solution is required for each thickness of film.[23] The process can be slow, and if small numbers of samples need to be produced at differing film thicknesses, then a lot of wastage will be encountered.

Spray pyrolysis creates films by spraying a solution onto a heated substrate.[24] The products other than the desired compounds should be volatile at the temperature of deposition in order to effectively deposit a film of the desired material.[25] Spray pyrolysis is a relatively cost-effective method for producing thin films, but the initial cost of equipment is relatively high. Uniformity across the film surface can be an issue, as proximity to heating elements will affect the deposition of the film.

Pulsed laser deposition is a method of producing thin films by ablating atoms or molecules from a surface using a laser source and depositing on a substrate.[26] Sputtering works in a similar way to PLD, instead using a physical, non-thermal sputtering process where surface atoms are ejected from a surface by momentum transfer from an atomic-sized bombarding particle, usually a gaseous ion.[27,28] The source to substrate distance is much shorter than for pulsed laser

deposition.[29] Both methods are expensive and producing large quantities of samples would be extremely time consuming. The control over film thickness is relatively easy, but compatibility with a templating polymer would be an issue.

Spin coating is a method for producing uniform thin coatings on a flat substrate. Altering the spin speed, viscosity of the solution used and number of layers of the solution being coated onto the substrate can be used to control the thickness of films. When compared to other techniques discussed in this section, spin coating is generally more versatile, effective and economical.[30]

There have been numerous papers where titanium (IV) oxide has been spin coated onto surfaces to explore various properties including the morhpology,[31] porous structure[32], photocatalytic activity,[33] optical properties[34] as well as a number of other studies investigating similar properties of mixed oxides.[31,35,36]

To be able to explore the effect that film thickness, doping and porosity have on the catalytic behaviour of the films, many samples will need to be produced. Spin-coating offers a cost-effective method of doing this, while producing high quality, repeatable surface coatings.

1.5 Mesoporous materials

A mesoporous material is defined by the International Union of Pure and Applied Chemistry as a material containing pores with diameters between 2 and 50 nm.[37] Mesoporous materials have a significantly increased surface area when compared to their non-porous counterparts. This can dramatically increase the number of surface sites available for photocatalytic activity.

A mesoporous structure can significantly alter the solid-state chemistry of crystalline inorganic materials by limiting the number of lattice units. This was demonstrated by Eftekhari et al. in their work on mesoporous materials for lithium-ion batteries.[38]

1.5.1 Templating methods

There are two templating methods for preparing mesoporous materials, known as hard and soft templating. Hard templating uses pre-existing porous materials to provide the desired structure in materials that do not normally form pores and has been widely used to produce porous TiO_2. Examples of materials that can be used include ZnO nanorods, commercial filter paper and butterfly wings.[39–41] Soft-templating uses polymers as a template for the pores. The aggregates

formed by these molecules have been exploited to give the regular porous structures desired in mesoporous materials.

Hard templating can be performed by either applying a coating to a material, or by creating a template, filling the pores with the desired material and removing the original template.[42] Mesoporous silica have diverse pore size, distribution and architecture, so are often used for the preparation of mesoporous materials.[43] Mesoporous carbon can also be used as a template.

Whilst hard templating works extremely well for powders and other large-scale materials, it is not always appropriate to use for thin surface coatings because the best results for these are often achieved by coating with a liquid and the porosity of the material would be lost when dissolved. Spin-coating can be performed with a suspension; however the resulting films are not well formed and adhesion is often poor.

1.5.2 Soft-templating

Soft-templating uses micelles of block copolymers to form the pores. These polymers typically consist of a molecule with a polar hydrophobic head and a hydrophilic hydrocarbon chain. Pluronic P-123 and Pluronic F-127 are commonly used templating polymers that are supplied as a paste and flake respectively.[44,45] The two polymers have the structure shown in Figure 1.1. The central hydrophobic portions are similar between the two, with P123 and F127 having y = 69 and 65 respectively. The major difference between the two is the length of the hydrophilic chains at each end of the molecule, with those on an F-127 molecule being over three times longer than those on P-123.

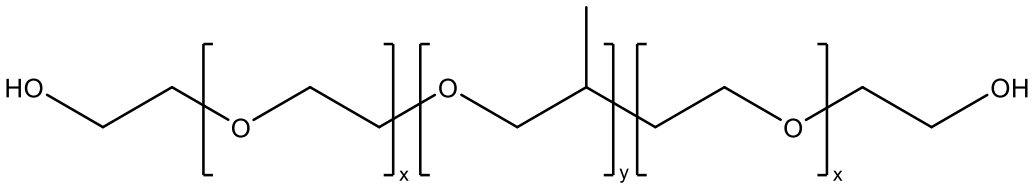

Figure 1.1: The structure of Pluronic P-123 where x = 19 and y = 69, and F-127 where x = 99 and y = 65

The self-assembly of the block copolymer is driven by evaporation (evaporation-induced self-assembly, EISA), so it is an ideal method to combine with spin-coating as the EISA can take place once the substrate has been coated. It is for this reason that a soft-templating method was chosen for this work. A solution containing a precursor to the desired porous material and the block copolymer selected can be spun onto the substrate as a liquid, producing a thin, uniform

film. Figure 1.2 illustrates the process by which the polymers can create a porous structure within a material that would otherwise not be porous.

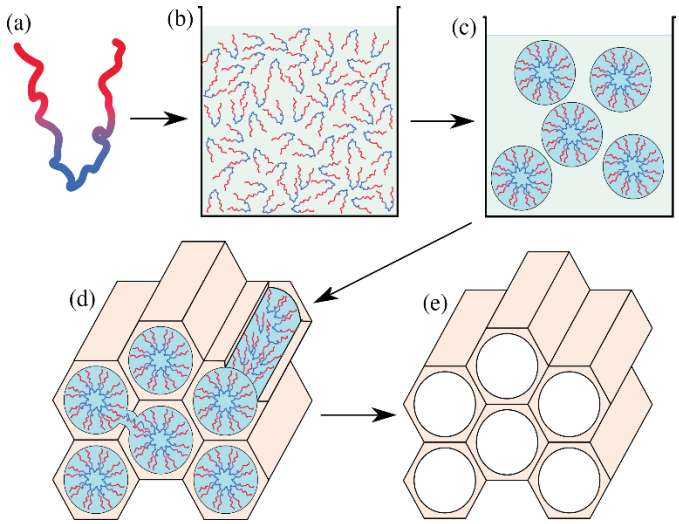

Figure 1.2: The formation of Pluronic P-123 micelles and the resulting porous structure

In Figure 1.2, A molecule of Pluronic P-123 (a) where the hydrophilic portion of the molecule is shown in red and the hydrophobic portion is shown in blue. The polymer is dissolved in a solvent (b) and a precursor is added. The polymer forms spherical micelles in solution (c) and as solvent evaporates, evaporation induced self-assembly drives the aggregation of spherical micelles into rods and then a large-scale porous structure (d). Hydrophilic end chains can become embedded in the walls, forming channels between pores. Samples are then calcined at temperatures in excess of 450 °C for several hours in order to remove the templating polymer and leave the desired porous structure. When used to create mesoporous TiO_2 from a precursor such at titanium butoxide, the precursor will hydrolyse readily in air or any water in solution. The titanium butoxide is exposed to small amounts of atmospheric moisture as the solution is stirred which will cause some hydrolysis. When the solvent is evaporating during and after the spin coating process, the exposure to atmospheric moisture will increase causing significant hydrolysis of titanium butoxide, forming titanium dioxide as the micelles form.

Pluronic P123 (poly(ethylene glycol)-*block*-poly(propylene glycol)-*block*-poly(ethylene glycol)) is an amphiphilic triblock copolymer consisting of a central hydrophobic poly(propylene glycol) chain and two hydrophilic poly(ethylene glycol) tails that is commonly used to produce mesoporous structures for TiO_2.[46] The widespread availability of this polymer means that it is ideal for use in this project. Pluronic F127 is another readily available polymer used to make mesoporous materials. The hydrophilic block is the portion of the polymer that can become embedded in the material and as these are five times longer in Pluronic F127 compared to the P123 polymer,

removal of the polymer from the final titania network is requires higher calcination temperatures.[47]

1.6 Spin coating

Spin coating is a method for producing uniform thin coatings over a flat substrate. An excess of solution containing a dissolved target material is placed on a substrate and it is rotated at speeds between 500 and 12,000 rotations per minute (rpm) to spread the solutions by centrifugal force.

Altering the spin speed, viscosity of the solution used and number of layers of the solution being coated onto the substrate can control the thickness of the films. Compared to other techniques used to produce thin films such as spray pyrolysis,[24] pulsed laser deposition,[28] and sputtering,[29] spin coating is generally more versatile, effective and economical.[31]

There have been numerous papers where titanium (IV) oxide has been spin coated onto surfaces to explore various properties including the morhpology,[31] porous structure,[32] photocatalytic activity,[33] and optical properties,[34] as well as a number of other studies investigating similar properties of mixed oxides.[31,35,36]

When spin coating a solution, the substrate is centred onto a chuck and held in place by vacuum. Any flat rigid material can be coated using a spin-coater, with silicon wafers being one of the most common substrates used with this technique. Once the substrate is secured, a guard is placed over the top to protect the user from any solution or dislodged substrate coming away from the chuck. The guard has a small hole in the top that can either be fitted with an automatic dispenser as can be seen in Figure 1.3, or it can be used to manually insert a micropipette and dispense the solution manually.

Figure 1.3: Image of a Laurell WS-650-23 spin coater[48]

When the solution is dispensed, an excess is used to ensure complete coverage. After the substrate is flooded with the solution, a large proportion will leave the substrate as the centrifugal forces thin out the liquid into a thin film. Automatic dispensing can be performed using a timed and electronically controlled micropipette. This can be programmed to dispense a certain amount of solution at a particular point in the spin coating cycle and gives extremely reproduceable processes.

1.6.1 Static and Dynamic Dispensing

When spin coating, there are two main methods for dispensing solutions onto a substrate. The solution can be dispensed onto the substrate before spinning (static dispense) or during (dynamic dispense).

Static dispense is typically used at speeds below 1000 rpm, or when using an extremely viscous solution.[42] In these cases, film quality can be compromised by the reduction in forces acting on the samples. It is usual to completely coat the substrate using this method, so will often require a much greater amount of solution when compared to dynamic spin coating. One benefit to the

static dispense method is that more solution can be added, and the pipette tip can be used to move or drag the solution across the surface to correct any mistakes. Some solvent will evaporate from the solution before the desired speed is achieved. This can result in unexpected variations in film thickness as the time between dispensing the solution and spinning the substrate is critical. This is not much of an issue with non-volatile solvents such as water, but for more volatile solvents such as chloroform, slight variations could drastically change the film thickness and quality. This variation is the main reason why static dispense does not tend to be preferred unless the spin speed and viscosity of solution mean that dynamic dispense is not possible.

Dynamic dispense is typically used unless there are any specific difficulties that cannot be overcome and result in poor film outcomes as outlined above. While this method generally affords better outcomes, it also requires more skill to execute and there are not typically any chances to correct mistakes and the consistency and precision of the user is critical to the outcomes. A micropipette is normally used to dispense around 20 µL of solution onto the substrate when it has reached the target rotational speed. The use of a micropipette varies slightly from normal usage for this application, as pushing the plunger all the way down to dispense the last of the solution will cause a bubble and compromise the film quality. If the solution is not dispensed directly onto the centre of the substrate, then the sample will have a hole in the film. Dispensing the solution as multiple droplets can also cause issues with film quality as the solvent can evaporate partly between drops to give multiple coats.

Automated dispensing can be used to provide dynamic dispense in scenarios where specific timing, dispense rate or a short time between dispensing layers can make manual dispensing impractical. A syringe pump can be used for this method, allowing a high degree of accuracy in timing and rate of dispense that cannot be achieved manually.[49]

For most applications, dynamic dispensing provides better outcomes than static dispensing and the equipment used for automated dispensing can add unnecessary costs. Aside from the few specific situations noted above, a suitably experienced user can provide the best outcomes using the dynamic dispensing method.

1.6.2 Film thickness

Predicting the film thickness has been a challenge since the development of spin coating. There are several variables that influence the spin speed including the viscosity, spin-speed and density.

$$t \propto \frac{1}{\sqrt{\omega}} \quad \textbf{1.9}$$

Equation 1.9 where *t* is the thickness and *ω* is the angular velocity is often used as an approximation of the relationship between the spin-speed and film thickness.[49] This is a greatly simplified view of the relationship between the spin speed and film thickness and only uses the angular velocity, not taking into account the viscosity of the solution, the volatility of the solvent or the behaviour of non-Newtonian fluids.

Several groups have attempted to devise an equation that can accurately predict the thickness of spin-coated films, most notably Emslie, Bonner and Peck;[50] and Meyerhofer.[51] Equation 1.10 shows Emslie, Bonner and Peck's 1958 equation for the final fluid film thickness where h_o represents the thickness of the film at the start of the process, *ω* is the angular velocity, *r* is the distance from the centre of rotation, *ρ* is the density, *η* is the viscosity and *h* is the thickness of the fluid layer, $\delta h/\delta t$ is the change of thickness and $\delta h/\delta r$ is the rate of spreading.

$$h = \frac{h_0}{\sqrt{1 + \frac{4\rho\omega^2}{3\eta} h_0^2 t}} \quad \textbf{1.10}$$

The Emslie, Bonner and Peck model is the earliest attempt at providing an equation for film thickness, but does not take into account any solvent evaporation so provides a wet film thickness, not a final dried film. It can be paired with a calculation of the solution density and concentration of solute to obtain an approximate dry film thickness. Without taking into account the solvent viscosity, surface tension or other behaviours not accounted for in this equation, a more complex model is needed.

Equation 1.11 shows Meyerhofer's equation for fluid dynamics during spin-coating, a modification of Equation 1.10 to include the uniform solvent evaporation rate, E.

$$\frac{\delta h}{\delta t} = -\frac{2\rho\omega^2 h^3}{3\eta} - E \quad \textbf{1.11}$$

Meyerhofer also proposed that the thinning process can be driven by either the flow or evaporation and that early in the process, thinning is dominated by flow and as the film becomes thinner later in the process, it is dominated by evaporation. He went on to devise an equation for the transition point between fluid thinning to evaporative thinning, shown in Equation 1.12 where *C* is the volume fraction of solute in the film and h_0 is the film thickness at the transition between flow and evaporation driven thinning.

$$E = \frac{(1-C)2\omega^2\rho h_0^3}{3\eta} \quad \textbf{1.12}$$

The equation devised by Meyerhofer for the final dry film thickness from the evaporation rate is shown in Equation 1.13 where C_0 is the initial concentration of solute and η_0 is the viscosity at C_0.

$$h_f = \left(\frac{3\eta_0 E}{2(1-C_0)\rho\omega^2}\right)^{1/3} \quad \textbf{1.13}$$

Meyerhofer made the assumption that the concentration remains at C_0 until the transition point between flow and evaporation driven thinning. There are further assumptions that can be made to allow the calculation of the final dry film without the evaporation rate as seen in Equation 1.14.

$$h_f = \left(\frac{3}{2}\right)^{\frac{1}{3}} k^{\frac{1}{3}} C_0 (1-C_0)^{-\frac{1}{3}} \rho^{-\frac{1}{3}} \eta_0^{\frac{1}{3}} \omega^{-\frac{1}{2}} \quad \textbf{1.14}$$

For many applications, the best way to predict the relationship between spin speed and film thickness is to measure the film thickness and create a 'spin-curve'. This can be challenging in certain applications, so a combination of experimental data and Meyerhofer's equation can be used.[52]

All the calculations above apply only to Newtonian liquids. For solutions with non-Newtonian behaviour, the solutions can exhibit either shear thinning or shear thickening behaviour, this can introduce some unpredictability into the thickness of spin-coated materials. The viscosity of these solutions will either increase (shear thickening) or decrease (shear thinning) with increasing shear rate. The greater the shear rate, the more shear thickening/thinning effect. This behaviour is particularly prevalent in solutions containing dissolved polymer or materials that cannot be dissolved in the solvent used.[52]

1.6.3 Spin Coating duration

The recommended spin coating duration depends on the solvent used. The more volatile the solvent, the less time is needed to completely dry the coating. Most solvents can be spin coated adequately in 30 seconds total spin time, with only certain solvents such as dichlorobenzene and glycerol needing longer periods of time.

1.6.4 Surface defects

There are a wide range of surface defects that can occur when spin coating. Some of the most common defects are comet streaks, pinhole defects and beading.[49,53]

Comet streaks are most common when spin-coating a suspension or solutions where precipitation is likely. When large particles are deposited onto the surface, the centrifugal force can drag them across the already coated surface and remove streaks of the coating from the centre of the film towards the edge.

Pinhole defects are typically a result of impurities or debris on the substrate prior to coating. Impurities on the surface will often be covered during the spin-coating process and prevent the coated material from adhering to the surface. It is vital to thoroughly clean any substrate before coating to avoid such defects in the final film.

Beading occurs most often when spin-coating at low speeds, working with viscous solutions or using volatile solvents. The area in the centre of the sample can dry quicker than the outer edges, causing a bead of solutions that does not fully dry on the spin coater and the surface tension of the solution prevents the bead of material from being removed by the centrifugal force of the spin-coating process. If the bead is still wet when the spin coater stops spinning, it can flow back towards the centre of the substrate and ruin the quality of film achieved.

To avoid edge beading, the solvent can be changed for a less volatile solvent, or a two-step spin-coating process can be used. After the spin coating has been completed, instead of allowing the sample to slow down to a stop, the speed can be increased briefly. The sudden increase in angular velocity should remove the bead from the edge.

1.7 Photocatalytic testing

Photocatalytic testing is vital to understanding the activity and mechanism of any novel photocatalysts. Careful consideration of the target molecules used, and the methods used to characterize degradation is key to a successful study.

1.7.1 Model pollutants

When testing photocatalysts, a model pollutant is typically used. This target molecule will be selected based on its proximity to the end-use pollutants, but careful consideration needs to be given to the quantitative measurements.

Testing the activity of photocatalysts can be done in several ways. Dyes such as methylene blue and methyl orange can be used in conjunction with UV-vis spectroscopy as a simple, low cost protocol for determining the activity of a photocatalyst.[16,22] This method is common in assessing the activity of semiconductor oxides as photocatalysts for water purification, but as dyes absorb visible light it can often interfere with the assessment of small bandgap photocatalysts. Many dyes have the ability to inject an electron into the conduction band of a semiconductor when photoexcited.[54] In this case, radiation is absorbed by the dye, not the photocatalyst. This property is exploited for use in dye-sensitized solar cells with materials such as TiO_2 so should be used with caution in the assessment of photocatalysts.[55]

It is preferable to use target molecules that do not absorb light in the visible or UV range. Infrared spectroscopy is a powerful technique, however, samples containing a significant proportion of water present challenges due to its extensive absorption.[56] Infrared spectroscopy is ideal when assessing photocatalytic activity using molecules such as stearic acid and degradation as a solid as opposed to an aqueous solution negates all of the problems associated with IR spectroscopy in aqueous solutions.[57]

When assessing the ability of a photocatalyst to break down plastics, it is common to form a film containing both catalyst and plastic.[58] Microplastics have also been deposited onto the surface of immobilized photocatalysts to assess activity.[4]

The photocatalytic films developed in this work could have been used either submerged in a solution or with a solid model pollutant applied. TiO_2 is widely studied as both air and water purifications, so various gaseous and soluble target molecules have been used extensively. There are significantly fewer comprehensive studies of the abilities and functioning of these materials as a surface coating used for the degradation of solid pollutants and it offers opportunities to explore the mechanism of the films through control over the gases present during the reaction.

1.8 Infrared Spectroscopy

Infrared (IR) spectroscopy is used to study the interactions between matter and infrared radiation. It can be used to identify and study molecules as gases, liquids, or solids.

Infrared light absorbed at specific wavelengths causes vibrations of molecular bonds. There are multiple vibrating modes, such as symmetric, anti-symmetric, rocking, wagging and twisting.[59] The recorded spectrum will show which wavelengths of light were absorbed by the sample. The resulting spectrum can be compared to reference materials to assign the various stretches to bonds within that sample.

IR spectroscopy can also be used quantitatively to assess the amount of a material that is present because the signal intensity is proportional to the amount of material on the surface. The areas of stretches can be compared relative to one another, but calibrations would need to be performed if an absolute concentration was required.[60]

Throughout this work, both Attenuating Total Reflectance (ATR) and Diffuse Reflectance Fourier Transform Infrared Spectroscopy (DRIFTS) will be used. The specific uses and considerations needed to effectively use the equipment for non-standard applications such as thin films will be discussed in the Methodology and Materials, Chapter 2.

1.8.1 Fourier Transform Infrared Spectroscopy - FTIR

A Fourier transform is data processing technique that is frequently used in spectroscopic techniques. It is almost always used in modern IR spectrometers to improve the speed, signal to noise ratio and offers better wavenumber accuracy. FTIR uses a Michelson interferometer with a movable mirror as depicted in Figure 1.4.

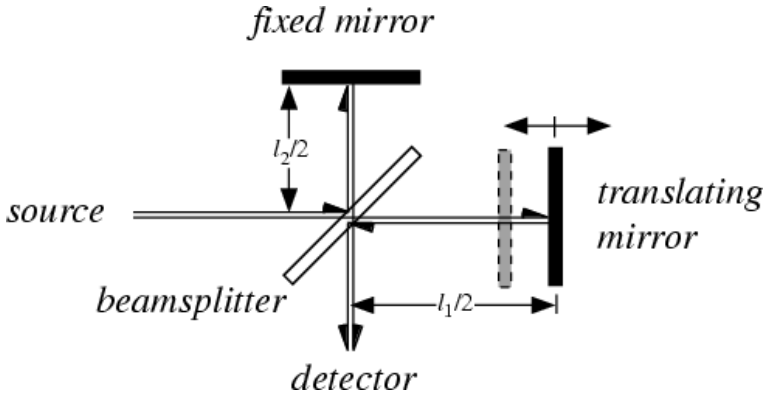

Figure 1.4: A diagram of a Michelson interferometer with a movable mirror[53]

Light is emitted from the source and half of the light travels through the beamsplitter onto a movable mirror while the other half is reflected onto a fixed mirror. The beams are then reflected back through the beamsplitter where they are combined, causing interference before going through the sample and into the detector. As the two beams combine, the movement of the translating mirror creates an interference pattern called an interferogram which can then be transformed into a spectrum by a Fourier Transform. Any infrared radiation that is absorbed by the sample will be notable in the spectrum as a series of peaks corresponding to specific wavelengths.

1.9 Aims and objectives

The aim and objective of this thesis was to assess multiple factors affecting the activity of titanium dioxide photocatalytic films. The base film formulation was explored, including the amount of templating polymer, the time and temperature of the evaporation-induced self-assembly, and hydrolysis of the precursor before spin coating. The effect of porosity was determined through photocatalytic degradation of stearic acid and XPS Argon sputtering to determine stearic acid penetration into the porous structure.

Topography was employed to determine the film depth and categorize defects that had arisen from the spin coating process. With accurate film depth measurements, the effect of film depth, spin speed and layering on the photocatalytic activity can be determined independently of one another.

Copper-doping from 0.1 to 5 wt% was used to increase the activity of the films and alter the bandgap. XPS was used to explore the oxidation state of the copper at different concentrations.

Polystyrene was also degraded on the surface of these films. 0.1 wt% copper-doped *meso*-TiO_2 produced at various spin speeds was used in this case. The activity of all photocatalysts was good, and simple changes to the method of producing films provided an effective means to alter the selectivity towards aromatic molecules while keeping good decomposition rates of the aliphatic parts of the molecule.

The mechanism of decomposition over these films was explored through photocatalytic testing in air, nitrogen and under vacuum, providing valuable insights into the Mars-van Krevelen mechanism of the decomposition of stearic acid catalysed by the photocatalytic films.

1.10 References

1 D. Lahiri, M. Nag and R. R. Ray, in *Photocatalytic Degradation of Dyes*, eds. M. Shah, S. Dave and J. Das, Elsevier, 2021, pp. 467–488.

2 F. Dong, Y. Zhang and S. Zhang, *Frontiers in Chemistry*.

3 J. D. Acuña-Bedoya, E. Luévano-Hipólito, E. I. Cedillo-González, L. P. Domínguez-Jaimes, A. M. Hurtado and J. M. Hernández-López, *Journal of Environmental Chemical Engineering*, 2021, **9**, 106208.

4 A. M. Ali, E. A. C. Emanuelsson and D. A. Patterson, *Applied Catalysis B: Environmental*, 2010, **97**, 168–181.

5 H. Huang, B. Pradhan, J. Hofkens, M. B. J. Roeffaers and J. A. Steele, *ACS Energy Lett.*, 2020, **5**, 1107–1123.

6 V. Binas, V. Stefanopoulos, G. Kiriakidis and P. Papagiannakopoulos, *Journal of Materiomics*, 2019, **5**, 56–65.

7 R. Dillert, A. Engel, J. Große, P. Lindner and D. W. Bahnemann, *Phys. Chem. Chem. Phys.*, 2013, **15**, 20876–20886.

8 A. Y. Shan, T. I. Mohd. Ghazi and S. A. Rashid, *Applied Catalysis A: General*, 2010, **389**, 1–8.

9 I. Dundar, M. Krichevskaya, A. Katerski and I. O. Acik, *Royal Society Open Science*, **6**, 181578.

10 J. Schneider, M. Matsuoka, M. Takeuchi, J. Zhang, Y. Horiuchi, M. Anpo and D. W. Bahnemann, *Chem. Rev.*, 2014, **114**, 9919–9986.

11 Electron Hole Pair (EHP) Generation | Semiconductor Theory, http://www.science-campus.com/engineering/electronics/semiconductor_theory/semiconductor_5.html, (accessed July 15, 2018).

12 R. Abe, *Journal of Photochemistry and Photobiology C: Photochemistry Reviews*, 2010, **11**, 179–209.

13 Á. Valdés and G.-J. Kroes, *J. Phys. Chem. C*, 2010, **114**, 1701–1708.

14 H. Ma, A. Brennan and S. A. Diamond, *Environmental Toxicology and Chemistry*, 2012, **31**, 2099–2107.

15 J. F. Montoya, I. Ivanova, R. Dillert, D. W. Bahnemann, P. Salvador and J. Peral, *J. Phys. Chem. Lett.*, 2013, **4**, 1415–1422.

16 T. M. Breault and B. M. Bartlett, *J. Phys. Chem. C*, 2012, **116**, 5986–5994.

17 S. K. Gharaei, M. Abbasnejad and R. Maezono, *Sci Rep*, 2018, **8**, 14192.

18 C. Dette, M. A. Pérez-Osorio, C. S. Kley, P. Punke, C. E. Patrick, P. Jacobson, F. Giustino, S. J. Jung and K. Kern, *Nano Lett.*, 2014, **14**, 6533–6538.

19 A. Khlyustova, N. Sirotkin, T. Kusova, A. Kraev, V. Titov and A. Agafonov, *Mater. Adv.*, 2020, **1**, 1193–1201.

20 M. H. N. Assadi and D. A. H. Hanaor, *Applied Surface Science*, 2016, **387**, 682–689.

21 S. A. Ansari, M. M. Khan, M. O. Ansari and M. H. Cho, *New J. Chem.*, 2016, **40**, 3000–3009.

22 R. Trofimovaite, C. M. A. Parlett, S. Kumar, L. Frattini, M. A. Isaacs, K. Wilson, L. Olivi, B. Coulson, J. Debgupta, R. E. Douthwaite and A. F. Lee, *Applied Catalysis B: Environmental*, 2018, **232**, 501–511.

23 S. K. Sahoo, B. Manoharan and N. Sivakumar, in *Perovskite Photovoltaics*, Elsevier, 2018, pp. 1–24.

24 B. B. Patil and S. H. Pawar, *Journal of Alloys and Compounds*, 2011, **509**, 414–420.

25 J. B. Mooney and S. B. Radding, *Annual Review of Materials Science*, 1982, **12**, 81–101.

26 A. Michelmore, in *Thin Film Coatings for Biomaterials and Biomedical Applications*, ed. H. J. Griesser, Woodhead Publishing, 2016, pp. 29–47.

27 D. M. Mattox, in *Handbook of Physical Vapor Deposition (PVD) Processing (Second Edition)*, ed. D. M. Mattox, William Andrew Publishing, Boston, 2010, pp. 1–24.

28 G. Balakrishnan, S. T. Sundari, P. Kuppusami, P. C. Mohan, M. P. Srinivasan, E. Mohandas, V. Ganesan and D. Sastikumar, *Thin Solid Films*, 2011, **519**, 2520–2526.

29 N. Savvides, A. Thorley, S. Gnanarajan and A. Katsaros, *Thin Solid Films*, 2001, **388**, 177–182.

30 D. Channei, A. Nakaruk, S. Phanichphant, P. Koshy and C. C. Sorrell, *Journal of Chemistry*, 2012, **2013**, e579284.

31 C. M. Firdaus, M. S. B. S. Rizam, M. Rusop and S. R. Hidayah, *Procedia Engineering*, 2012, **41**, 1367–1373.

32 B. L. Kirsch, E. K. Richman, A. E. Riley and S. H. Tolbert, *J. Phys. Chem. B*, 2004, **108**, 12698–12706.

33 Y. Ao, Y. Gao, P. Wang, C. Wang, J. Hou and J. Qian, *Materials Research Bulletin*, 2014, **49**, 223–228.

34 V. Zharvan, R. Daniyati, N. I. A. S., G. Yudoyono and Darminto, *AIP Conference Proceedings*, 2016, **1719**, 030018.

35 R. Abe, *Journal of Photochemistry and Photobiology C: Photochemistry Reviews*, 2010, **11**, 179–209.

36 H. Eskandarloo, A. Badiei and M. Behnajady, *Industrial & Engineering Chemistry Research*, 2014, **53**, 7847–7855.

37 J. Rouquerol, D. Avnir, C. W. Fairbridge, D. H. Everett, J. M. Haynes, N. Pernicone, J. D. F. Ramsay, K. S. W. Sing and K. K. Unger, *Pure Appl. Chem.*, 1994, **66**, 1739–1758.

38 A. Eftekhari, *Microporous and Mesoporous Materials*, 2017, **243**, 355–369.

39 J. Qiu, W. Yu, X. Gao and X. Li, *J Sol-Gel Sci Technol*, 2007, **44**, 235–239.

40 X. Liu, Y. Gu and J. Huang, *Chemistry – A European Journal*, 2010, **16**, 7730–7740.

41 M. R. Weatherspoon, Y. Cai, M. Crne, M. Srinivasarao and K. H. Sandhage, *Angewandte Chemie International Edition*, 2008, **47**, 7921–7923.

42 A.-H. Lu and F. Schüth, *Comptes Rendus Chimie*, 2005, **8**, 609–620.

43 L. Zhang, L. Jin, B. Liu and J. He, *Front. Chem.*, , DOI:10.3389/fchem.2019.00022.

44 M. Bohorquez, C. Koch, T. Trygstad and N. Pandit, *Journal of Colloid and Interface Science*, 1999, **216**, 34–40.

45 Y. Zhao, S.-M. Ma, B. Li, A. De Nicola, N.-S. Yu and B. Dong, *Polymers (Basel)*, 2019, **11**, 1806.

46 G. J. de A. A. Soler-Illia, C. Sanchez, B. Lebeau and J. Patarin, *Chem. Rev.*, 2002, **102**, 4093–4138.

47 M. Barczak, *New J. Chem.*, 2018, **42**, 4182–4191.

48 L. S. Coaters, Spin coaters from Laurell - WS-650-23 Spin Coater, https://laurell.com/spin-coater/?model=WS-650-23, (accessed May 16, 2022).

49 Spin Coating, https://www.ossila.com/pages/spin-coating, (accessed April 7, 2020).

50 A. G. Emslie, F. T. Bonner and L. G. Peck, *Journal of Applied Physics*, 1958, **29**, 858–862.

51 D. Meyerhofer, *Journal of Applied Physics*, 1978, **49**, 3993–3997.

52 Y. Mouhamad, P. Mokarian-Tabari, N. Clarke, R. a. L. Jones and M. Geoghegan, *Journal of Applied Physics*, 2014, **116**, 123513.

53 Defects Found in Spin Coating, Coating Systems, Inc., https://coatingsystems.com/common-defects-found-spin-coating/, (accessed May 16, 2022).

54 N. Barbero and D. Vione, *Environ. Sci. Technol.*, 2016, **50**, 2130–2131.

55 K. Sharma, V. Sharma and S. S. Sharma, *Nanoscale Research Letters*, 2018, **13**, 381.

56 G. E. Tranter, in *Reference Module in Chemistry, Molecular Sciences and Chemical Engineering*, 2016.

57 S. D. Cosham, V. Celorrio, A. N. Kulak and G. Hyett, *Dalton Trans.*, 2019, **48**, 10619–10627.

58 W. Fa, L. Guo, J. Wang, R. Guo, Z. Zheng and F. Yang, *Journal of Applied Polymer Science*, 2013, **128**, 2618–2622.

59 Infrared Spectroscopy, https://chem.libretexts.org/Bookshelves/Physical_and_Theoretical_Chemistry_Textbook_Maps/Supplemental_Modules_(Physical_and_Theoretical_Chemistry)/Spectroscopy/Vibrational_Spectroscopy/Infrared_Spectroscopy/Infrared_Spectroscopy, (accessed March 13, 2022).

60 R. A. Spragg, ed. H. A. Willis, London, United Kingdom, 1988, p. 32.

Chapter 2. Methodology and Materials

2.1 Film preparation

Titanium(IV) butoxide ($Ti(OBu)_4$) and copper (II) nitrate hydrate ($Cu(NO_3)_2 \cdot xH_2O$) were used as precursors with methanol as a solvent. Pluronic P-123 (Sigma-Aldrich) was used as the templating polymer to achieve the mesoporous structure. Pluronic P-123 (5 g) was added to anhydrous methanol (Sigma Aldrich, anhydrous 99.8%) (15 cm^3) and paraffin film was used to cover the beaker. A small hole was poked into the film using a needle and the beaker was left to stir on a magnetic stirrer until the polymer was fully dissolved. $Ti(OBu)_4$ (Sigma-Aldrich reagent grade) (10 cm^3) was added to the solution, the beaker was covered in the same manner as before and left to stir for 30 minutes. If required, $Cu(NO_3)_2$ (Copper (II) nitrate hydrate, Sigma Aldrich) was added and the solution was left to stir for a further 20 minutes. The amounts of $Cu(NO_3)_2$ used are reported in Table 2.1 below.

Desired Cu content (wt%)	**$Cu(NO_3)_2$ used (mg)**
0.1	3.88
0.5	19.5
1	39.2
2.5	99.4
5	204

Table 2.1: The amounts of copper (II) nitrate hydrate used in solutions to give copper doped samples

Cover glasses (VWR, 22 mm Ø, No. 1) were cleaned in deionised water, then acetone using an ultrasonic bath at room temperature. They were then either air dried or placed into an oven at 40 °C until the acetone had evaporated.

The titanium butoxide solution was spun onto the clean cover glasses using dynamic dispense at varying spin speeds in order to achieve differing film thicknesses. A cover glass was placed onto the chuck of the spin coater (Laurell, WS-650MZ-23NPP) and a vacuum was applied to hold it in place. Once the cover glass was spinning at the intended spin speed, 200 µL of the titanium butoxide solution was dispensed using a micropipette and the cover glass was left to spin for a further 30 seconds. When dispensing the solution onto the substrate, a micropipette is used to draw up the desired amount of solution and when the substrate is spinning at the intended speed, the pipette is inserted through the hole in the guard and held centrally less than an inch

above the sample. The plunger is swiftly depressed to the first stopping point and immediately retracted to the initial position. A single stream of solution is needed to ensure that the film forms properly, as a slow stream will result in multiple partially dried layers deposited on top of each other. It is important not to depress the plunger completely, as this will result in a bubble of solution which will interfere with the film formation. If the pipette is not central to the substrate, the solution will not cover the central portion and the film will form as a ring, leaving the substrate bare in the centre.

After spin-coating, the samples were moved into an oven (Memmert, model 30) where they were heated to 40 °C for 48 hours to facilitate the evaporation-induced self-assembly of the polymer and give the porous structure. The samples were then calcined in the furnace at 500 °C for 5 hours with a heating rate of 5 °C min^{-1}. Calcination at this temperature removes the templating polymer.

At preparation spin speeds below 1000 rpm, a thick bead of material forms around the edge of the sample. Under normal circumstances, the sample would be spun at the speed needed to get the correct thickness of film, for long enough to dry the central part of the film and then the speed would be increased to remove the bead that formed at the edge. The samples I produced cannot be completely dry after spin coating, and increasing the spin speed while still wet would disrupt the film being formed, so the beads that form on the edge have to be left in place. The high viscosity of the solution means that the beads do not flow towards the centre of the film after spin coating has completed leaving the centre of the film intact and the intended depth. The bead from round the edge of the sample is normally too thick to adhere to the substrate so will flake off after calcination.

Some samples that were intended to be non-porous were prepared using the same method, however, these samples were calcined immediately after spin-coating to avoid aggregation of the Pluronic P-123 micelles that form the porous structure.

2.2 Photocatalytic testing

2.2.1 Stearic acid

The photoactivity of the films was scrutinized with a standard stearic acid test in which DRIFTS (Diffuse Reflectance Infrared Fourier-Transform Spectroscopy) was used to monitor the surface concentration of C-H bonds of stearic acid.

200 µL of 0.1 mol dm^{-3} stearic acid (Sigma Aldrich, reagent grade, 95%) in chloroform (reagent grade) was applied to the photocatalytic films using the spin coater at 2000 rpm for 30 s. The samples were placed onto the sample holder of the DRIFTS cell (PerkinElmer Frontier). Once an IR spectrum is obtained, the sample was placed under a 72 watt single wavelength LED lamp (PCATDES)[1] with a wavelength of 365 nm for a period of time before another IR spectrum was obtained. This process was repeated multiple times until the stearic acid had been completely decomposed or a time limit for the given sample had been reached.

In order to calculate the percentage of stearic acid that had been decomposed, the IR spectrum between 2500 and 3500 cm^{-1} was used as the forked C-H absorption of stearic acid is at 2917 and 2849 cm^{-1}. A baseline was fitted to each IR spectrum using OriginLab software and the area of the C-H stretch was calculated. The area of the C-H stretch before irradiation was taken as 0 % decomposition. All areas calculated for subsequent periods of irradiation are expressed as a percentage decomposition. Figure 2.1 shows an FTIR spectrum of stearic acid on a cover glass that has been coated with a photocatalytic film alongside the baseline that has been fitted. The area between the two lines is used as a representative value of the amount of stearic acid on the surface of the photocatalyst. As the area of the C-H stretch decreases upon exposure to UV light, each subsequent value obtained after irradiation is expressed as a percentage of the area obtained before irradiation, giving a percentage decomposition over the course of the experiment.

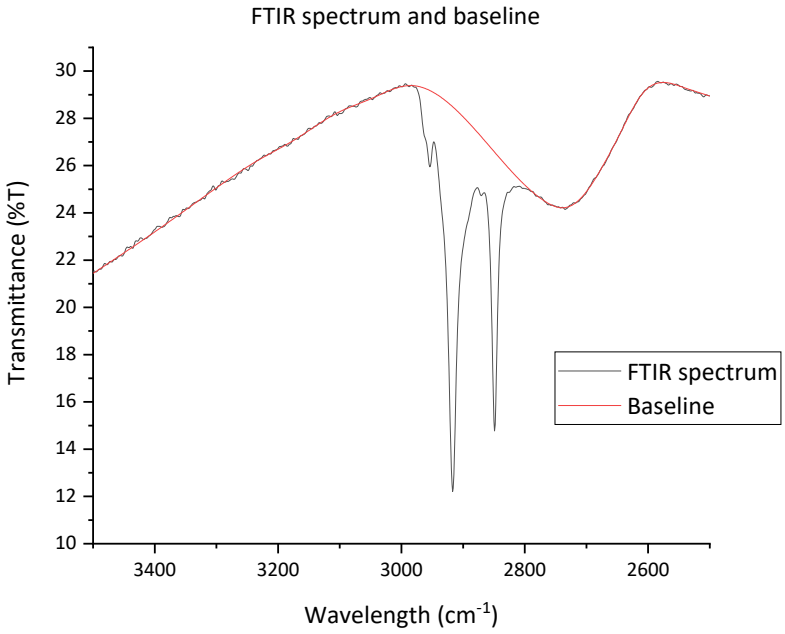

Figure 2.1: An FTIR spectrum (black) of stearic acid on a TiO_2 film with a baseline (red)

2.2.2 Polystyrene

Decomposition of polystyrene was observed in very similar way to the stearic acid. A 1 wt% solution of polystyrene (Sigma Aldrich, ave. M_w 35,000) in chloroform (reagent grade) was prepared by weighing an individual pellet of polystyrene and dissolving in the appropriate amount of solvent and then spin coated onto the photocatalyst at 2000 rpm. Analysis of these spectra required more complex fitting of the multiple absorptions present as there are both aliphatic and aromatic C-H stretches present, giving more information about the selectivity of the catalyst with respect to the two.

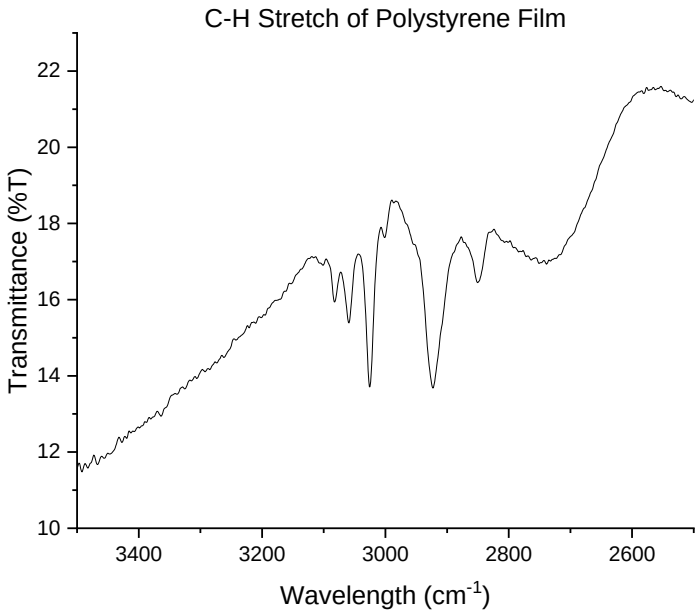

Figure 2.2: An FTIR spectrum of polystyrene on a TiO_2 photocatalytic coating

Figure 2.2 shows an FTIR spectrum of a polystyrene film on a TiO_2 coating. The area for these samples was calculated by fitting and subtracting a baseline, then curve fitting the resulting spectra in OriginLab. This approach was necessary for the polystyrene testing to get the most accurate areas for both the aliphatic and aromatic C-H stretches present in the spectrum. Appendix 6 contains the DRIFT spectra (Figure A6.1 to Figure A6.11), spectra after removal (Figure A6.12 to Figure A6.22), and after curve fitting (Figure A6.23 to Figure A6.33) over a 150 minute period of irradiation. After the areas of each fitted curve is added, the total area, as well as the aromatic and aliphatic regions independently, can be used to calculate the percentage decomposition of polystyrene over the course of the experiment.

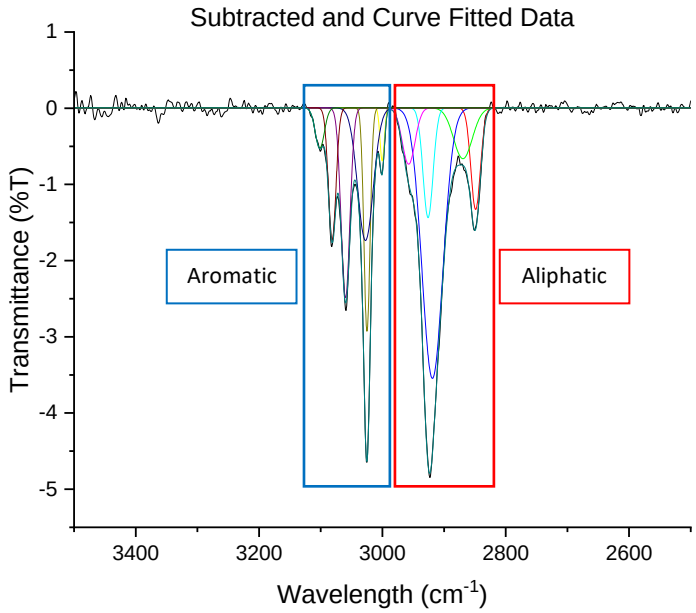

Figure 2.3: Subtracted and curve fitted spectra from Figure 2.2. The aromatic stretches are marked by a blue box and the aliphatic stretches are marked by a red box

2.2.3 Photocatalysis without air

Some samples underwent photocatalytic testing without the presence of air. Some experiments were performed under nitrogen and some under vacuum.

For samples that underwent photocatalytic testing under nitrogen, a DRIFT spectrum was obtained before the sample was placed inside a quartz tube. The tube was flushed with nitrogen before being sealed using a rubber bung. As it is not possible to obtain an IR spectrum without exposing the film to oxygen, only two IR spectra were obtained for these samples; one before, and one after irradiation. For each sample that was tested in this way, a second sample was selected that was produced from the same beaker of solution and produced at the same time and the same spin speed. This second sample underwent photocatalytic testing as was described in Section 0. The two samples give a good comparison between the rate of stearic acid decomposition over the photocatalysts in air and under nitrogen.

Another series of FTIR photocatalysis experiments were run by spin coating the photocatalyst directly onto a 3-bounce Ge ATR crystal. These samples were produced in the same way as outlined for samples on glass coverslips, the only difference being the substrate used. The FTIR spectrometer used had a sealed chamber that could be used with air, nitrogen or under vacuum.

2.2.4 Calculating rates and half-lives

As described in section 0, the amount of stearic acid remaining on the surface was expressed as a percentage of the initial amount recorded before exposure to UV light. The percentage was used as a proxy for the concentration of stearic acid in the reaction for calculations of the rate, order and half-life of reaction over the different photocatalytic films produced. Two plots were generated for each sample, with plots of % vs time and ln(%) vs time as seen below in Figure 2.4 and Figure 2.5. A linear relationship between % and time indicated that the reaction is zero order, while a linear relationship between ln(%) and time indicates a first order reaction.

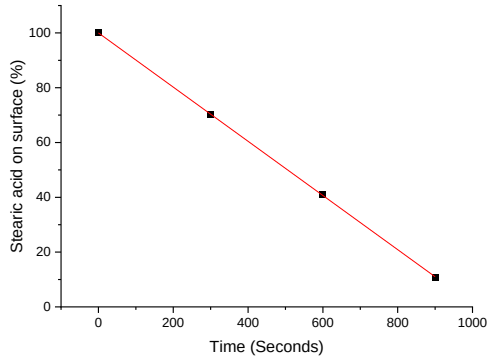

Figure 2.4: Zero order rate plot of a meso-TiO2 sample prepared at 1200 rpm

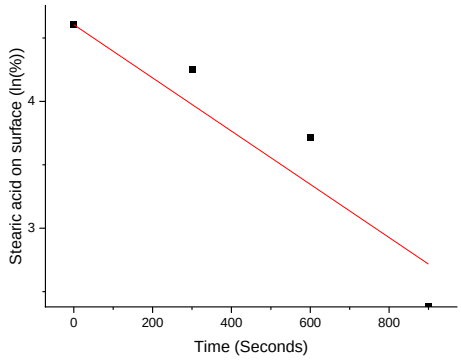

Figure 2.5: First order rate plot of a meso-TiO2 sample prepared at 1200 rpm

A linear fit of each plot was generated using OriginLab software and the slope of the linear fit is recorded as the rate constant for each reaction. The rate constants for the decomposition of stearic acid when reaction is zero and first order are not directly comparable. The equations in Table 2.2 are used to convert the rate constant half-lives to allow direct comparisons between reactions over different samples.

Zero Order	First Order
$\boldsymbol{t_{1/2} = \frac{100}{2k}}$	$t_{1/2} = \frac{0.693}{k}$

Table 2.2: Equations for calculating the half-life of a reaction from the zero or first order rate constant

The calculation for the half-life of a zero order reaction is dependent on the initial concentration, but as the data is expressed as a percentage of the initial amount of stearic acid on the surface, the initial concentration will always be 100 % so this is substituted into the equation.

2.3 Depth measurements

2.3.1 Resin encased samples

An attempt was made to calculate the thickness of films by weighing the glass coverslips before and after coating. Due to the small amount of material being applied to the surface, there were no reliable observed changes in mass. In addition to the issues encountered, measurements taken in this way would be an average thickness over the entire film and would give no information about the minimum and maximum film thicknesses.

In order to measure the film depths and gather information about the variance across the surface, films were embedded in resin and then cut to expose a cross section of the film and cover glass. Four samples were placed onto metal nuts to centre them in a 6 cm square mould and then a two-part epoxy resin (type of resin) was poured over them and left to cure overnight. The samples were then cut using a diamond edged circular saw at 2200 rpm with a feed speed of 0.100 mm s^{-1} to expose the cross section of each sample. Figure 2.6 shows the samples after being cut. The cut edges exposing the samples were then examined using SEM. Figure 2.7 shows a sample of porous, undoped TiO_2 produced at 5000 rpm. The three layers visible in the image are glass, photocatalyst and resin from top to bottom.

Figure 2.6: four samples embedded in resin and cut

Figure 2.7: SEM image showing layers of glass, photocatalytic film, and resin from top to bottom

2.3.2 Optical profilometry

The optical profilometry used in this work is a technique that can be used to extract a 3D scan from a surface and give information about surface morphology, roughness, and step height. Focus

variation is one method of performing optical profilometry that takes advantage of the limited depth of focus in brightfield images, where only a certain vertical range of the surface is in focus.[2] Multiple images are captured using different focus adjustments and the focus that leads to the maximum sharpness of the image is used to give the depth of the different positions of the sample surface. The sensor data is processed into 3D data by a computer program and analyses can be performed on this data to give accurate values for studiable characteristics such as step height.[3]

On each sample used, one half of the coating was removed by scraping off using a plastic glue spreader. This created a step between the uncoated glass coverslip and the photocatalytic coating which could be measured using optical profilometry. A Sensofar S mart profilometer was used to acquire 3D profiles of the surface at multiple points across the threshold between the two surfaces as well as being used on the intact central portion and edge of each sample to gather information about the surface of each coating.

2.4 Characterization

2.4.1 Brunauer-Emmett-Teller surface area analysis

Brunauer-Emmett-Teller (BET) theory was developed in 1938 as an extension of the Langmuir isotherm with the aim of explaining the adsorption of gas molecules onto a solid surface.[57] The BET isotherm can be used to calculate the surface area of a solid through gas adsorption analysis. The sample is degassed to remove any water or other contaminants from the surface and then cooled using liquid nitrogen and maintained at a low temperature while an adsorbate is injected into the sample cell. The volume of gas that is adsorbed onto the surface of the sample is used to calculate the surface area.

Two powders were prepared for BET analysis. For the porous powder, a solution was prepared using the same quantities as for the porous spin-coated films. For the non-porous powder, the same method was followed, omitting the templating polymer. These solutions were transferred to crucibles and placed into the oven at 40 °C for 48 hours before calcining at 500 °C for 5 hours with a heating rate of 5 °C min^{-1}. The resulting powders were then ground down to allow them to be placed into the BET sample tubes.

Surface area was measured using a Quantachrome NOVA 4200e instrument by N_2 adsorption using NovaWin v11.03 analysis software. The sample weights were 2.6344 and 2.3203 g for the non-porous and porous samples respectively. Samples were degassed under vacuum at 150 °C for

2.5 hours. Adsorption/desorption isotherms were recorded at -196 °C. BET surface areas were calculated over the relative pressure ranges 0.05-0.2 and 0.06-0.3 P/P_0 for the non-porous and porous samples respectively.

Whilst the resulting powders were representative of the porous and non-porous nature of the films, the surface area of each powder is not representative of the surface area of films produced from the same solutions. Some qualitative conclusions can be drawn from the BET surface analysis, but there is insufficient information to be able to calculate the surface area of individual films.

2.4.2 UV-vis Spectroscopy

UV-visible spectroscopy is an electronic spectroscopic technique that measures the amount of discrete wavelengths of UV and visible light that are transmitted through or absorbed by a sample. DRS-UV spectroscopy is a type of UV-vis spectroscopy that is used specifically on solid samples. The diffuse reflectance allows the characterization of these films without having to remove them from the surface. It takes several hundred identical samples to obtain less than 1 g of powder, so it is much more time and cost effective to employ techniques such as DRS-UV spectroscopy over traditional approaches.

DRS-UV spectroscopy was performed using an Agilent Technologies Cary Series UV-Vis Spectrometer scanning from 800 to 200 nm. The sample holder was packed with KBr before the coated coverslip was placed on top of the sample holder and the spectrum was recorded.

2.4.3 Tauc Plots

UV-vis spectroscopy for the characterization of photocatalysts can be used to calculate the bandgap of the material using a Tauc plot.

The square root of the product of the absorption coefficient and photon energy is plotted against the photon energy. The curve has a section of straight line which intercepts the axis at the optical band gap.

$$(\alpha \cdot h\nu)^{1/\gamma} = B(h\nu - E_g) \qquad \textbf{2.1}$$

The Tauc method assumes that the energy-dependent absorption coefficient α can be expressed as in Equation 2.1 where *h* is the Planck constant, *v* is the photon's frequency, E_g is the band gap energy and *B* is a constant.

The absorption coefficient, α, can be calculated using Equation 2.2 where *abs* is the absorption and *t* is the thickness of the film.

$$\alpha = \frac{2.303 \log(abs)}{t} \qquad \textbf{2.2}$$

When constructing a Tauc plot, αhv^2 is plotted against hv. The linear portion of the curve is extrapolated as demonstrated by the red line in Figure 2.8. The point at which the extrapolated linear region intercepts the x-axis axis gives the bandgap of the material being characterized.

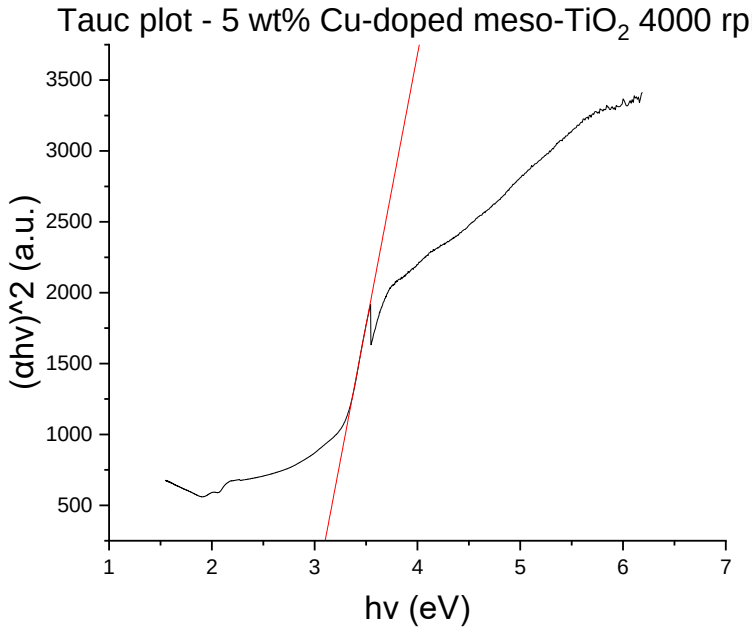

Figure 2.8: Tauc plot of a 5 wt% copper-doped meso-TiO_2 sample prepared at 4000 rpm

2.5 Fourier-Transform Infrared Spectroscopy - FTIR

2.5.1 Attenuated Total Reflectance

Attenuated total reflectance (ATR) infrared spectroscopy works by refracting IR radiation through a crystal with the sample held against the surface. The infrared radiation extends beyond the crystal to enter the surface of the sample as seen in Figure 2.9. ATR is often used with a Fourier Transform infrared spectrometer.

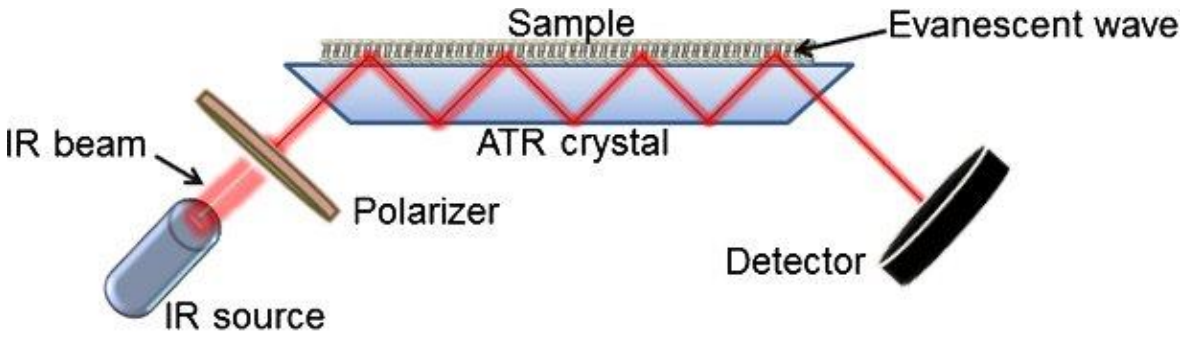

Figure 2.9: Diagram of an IR beam through a 4-bounce ATR crystal[54]

If the crystal can be removed, it is possible to deposit a material directly onto the surface of the crystal using a surface coating technique. Due to the limited penetration of the evanescent wave, it is important to select a film thin enough to penetration through the photocatalyst to the stearic acid layer.

A photocatalytic film was deposited onto a 3-bounce Ge ATR crystal as described in Section 0. When working with a substrate such as an ATR crystal that is much heavier that the glass coverslips used elsewhere in this work, it is important to ensure that the sample is accurately centered, and the vacuum is applying sufficient pressure to keep the crystal in place when spinning at high speeds. 1 mL of solution was used to ensure complete coverage of the ATR crystal as it was larger than the glass coverslips used elsewhere. All other aspects of the film preparation can be carried out as described in Section 0. Coating with stearic acid was as described previously, but 1 mL of solution was used during this process to ensure complete coverage.

2.5.2 Diffuse Reflectance

Diffuse reflectance infrared Fourier transform spectroscopy (DRIFTS) is a technique commonly applied to powders and can be used for surface coatings. DRIFTS is key to this project due to its sensitivity towards surface species and the simplicity with which it allows the qualitative and quantitative analysis of model pollutants during photocatalytic testing. Measurements of the surface are possible without compression, meaning that the spectroscopy has no impact on the photocatalytic testing.

Flat and ellipsoid mirrors are used to direct the IR beam to the samples as can be seen in Figure 2.11. The IR radiation can penetrate into the sample, reflecting off particles within the sample until exiting the sample and being directed towards the detector by another ellipsoid and flat mirror.[55]

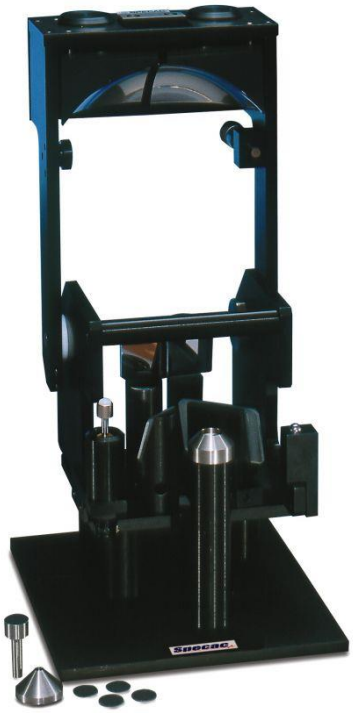

Figure 2.10: Photograph of a DRIFTS cell[56]

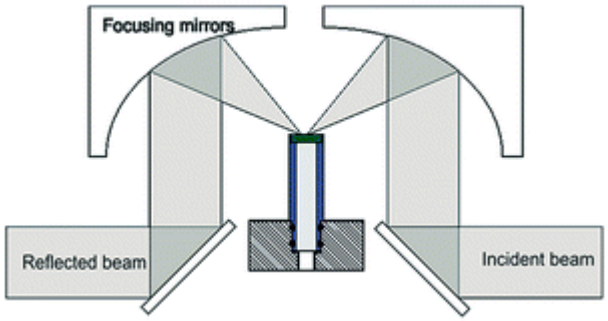

Figure 2.11: Diagram on a DRIFTS cell[55]

The FTIR instrument used for all photocatalytic testing throughout this work was a Perkin Elmer Frontier with a DRIFTS cell. The sample holder was left in place and the coated glass coverslip was placed on top. Due to the increased sample height when compared to the intended use of the DRIFTS cell, the mirrors required some height adjustment to obtain the best signal.

2.6 X-ray Diffraction

Powders were prepared for XRD by producing multiple samples with the same copper concentration and spin speed. The surface coatings from these samples were then scraped off using a scalpel blade and the powder was collected for analysis. Powder XRD was performed on a Panalytical X-pert Pro Spectrometer.

2.7 References

1 A. Sergejevs, C. T. Clarke, D. W. E. Allsopp, J. Marugán, A. Jaroenworaluck, W. Singhapong, P. Manpetch, R. Timmers, C. Casado and C. Bowen, *Photochem. Photobiol. Sci.*, , DOI:10.1039/C7PP00269F.

2 D. R. Paschotta, Optical Profilometers, https://www.rp-photonics.com/optical_profilometers.html, (accessed May 17, 2022).

3 Optical Metrology – Understanding Focus Variation, https://www.azom.com/article.aspx?ArticleID=13893, (accessed May 19, 2022).

4 S. K. Sahoo, B. Manoharan and N. Sivakumar, in *Perovskite Photovoltaics*, Elsevier, 2018, pp. 1–24.

5 B. B. Patil and S. H. Pawar, *Journal of Alloys and Compounds*, 2011, **509**, 414–420.

6 J. B. Mooney and S. B. Radding, *Annual Review of Materials Science*, 1982, **12**, 81–101.

7 A. Michelmore, in *Thin Film Coatings for Biomaterials and Biomedical Applications*, ed. H. J. Griesser, Woodhead Publishing, 2016, pp. 29–47.

8 D. M. Mattox, in *Handbook of Physical Vapor Deposition (PVD) Processing (Second Edition)*, ed. D. M. Mattox, William Andrew Publishing, Boston, 2010, pp. 1–24.

9 G. Balakrishnan, S. T. Sundari, P. Kuppusami, P. C. Mohan, M. P. Srinivasan, E. Mohandas, V. Ganesan and D. Sastikumar, *Thin Solid Films*, 2011, **519**, 2520–2526.

10 N. Savvides, A. Thorley, S. Gnanarajan and A. Katsaros, *Thin Solid Films*, 2001, **388**, 177–182.

11 D. Channei, A. Nakaruk, S. Phanichphant, P. Koshy and C. C. Sorrell, Cerium Dioxide Thin Films Using Spin Coating, https://www.hindawi.com/journals/jchem/2013/579284/, (accessed December 4, 2017).

12 C. M. Firdaus, M. S. B. S. Rizam, M. Rusop and S. R. Hidayah, *Procedia Engineering*, 2012, **41**, 1367–1373.

13 B. L. Kirsch, E. K. Richman, A. E. Riley and S. H. Tolbert, *J. Phys. Chem. B*, 2004, **108**, 12698–12706.

14 Y. Ao, Y. Gao, P. Wang, C. Wang, J. Hou and J. Qian, *Materials Research Bulletin*, 2014, **49**, 223–228.

15 V. Zharvan, R. Daniyati, N. I. A. S., G. Yudoyono and Darminto, 2016, p. 030018.

16 R. Abe, *Journal of Photochemistry and Photobiology C: Photochemistry Reviews*, 2010, **11**, 179–209.

17 H. Eskandarloo, A. Badiei and M. A. Behnajady, *Ind. Eng. Chem. Res.*, 2014, **53**, 7847–7855.

18 F. E. Ghodsi, F. Z. Tepehan and G. G. Tepehan, *Solar Energy Materials and Solar Cells*, 2001, **68**, 355–364.

19 J. Qiu, W. Yu, X. Gao and X. Li, *J Sol-Gel Sci Technol*, 2007, **44**, 235–239.

20 X. Liu, Y. Gu and J. Huang, *Chemistry – A European Journal*, **16**, 7730–7740.

21 M. R. Weatherspoon, Y. Cai, M. Crne, M. Srinivasarao and K. H. Sandhage, *Angewandte Chemie International Edition*, **47**, 7921–7923.

22 A.-H. Lu and F. Schüth, *Comptes Rendus Chimie*, 2005, **8**, 609–620.

23 L. Zhang, L. Jin, B. Liu and J. He, *Front. Chem.*, , DOI:10.3389/fchem.2019.00022.

24 G. J. de A. A. Soler-Illia, C. Sanchez, B. Lebeau and J. Patarin, *Chem. Rev.*, 2002, **102**, 4093–4138.

25 M. Barczak, *New J. Chem.*, 2018, **42**, 4182–4191.

Chapter 3. Results – Film Formulation

The synthesis and spin-coating of these films has many variables that can all affect the outcome of the finished films. The amount of P-123 used in the solution will affect the pore sizes of the resulting material,[1] as well as altering the viscosity of the solution and therefore the film thickness.[2] The soft-templating process, including the evaporation time and temperature are optimized for a traditional sol-gel method.[3-5] The small amount of solvent that remains after spin-coating means that the process normally used may not work as well with these materials.

The samples discussed in this chapter are undoped mesoporous titanium dioxide photocatalytic films, produced from a solution containing titanium butoxide and the templating polymer Pluronic P-123. This chapter seeks to systematically explore several variables, such as the film thickness, the amount of templating polymer, and the time allowed to form the porous structure. This was done to optimize a base formulation that can be used to explore other variables such as doping and film thickness going forward.

3.1 Control experiments

Control experiments were performed on 0.1 mol dm^{-3} stearic acid in chloroform, applied to a clean glass coverslip at 2000 rpm. Photocatalytic testing was performed as outlined in the Chapter 2 with five minute periods of irradiation. No measurable decomposition occurred. As no decomposition could be seen, it was not appropriate to express the data as a percentage of the area of the C-H stretch before irradiation as with other experiments. The error in measurements accounts for the variation seen.

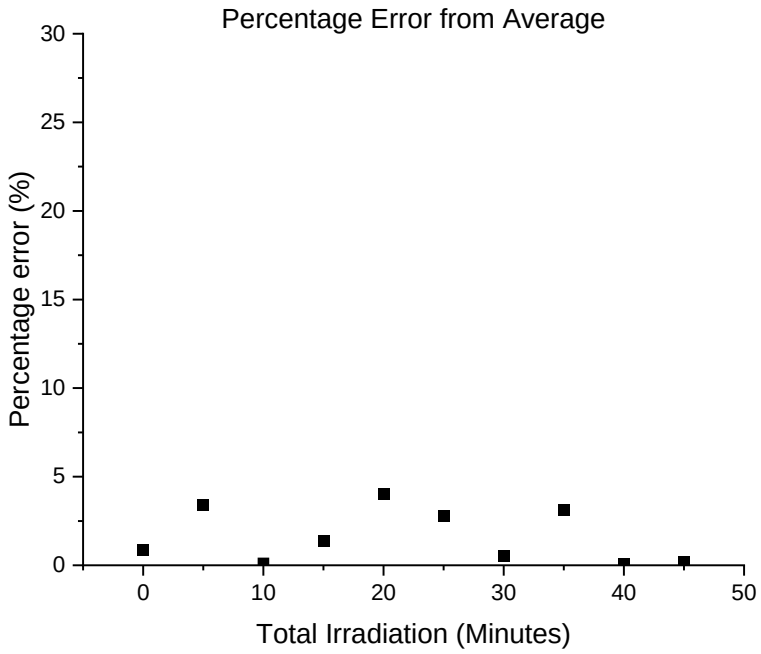

Figure 3.1: Calculated percentage errors from each spectrum in the control experiment

Figure 3.1 shows the percentage error of each spectrum when compared to the mean value for all areas. This gives a range of 0.11 to 4.04 % with a mean and median of 1.65 and 1.12 % respectively.

Equation 3.1 shows the equation for the sample standard deviations,[6] where x_i is the individual % area, $\bar{x}$ is the average mean area and N is the sample size. This gives a standard deviation of 2.76 %. The sample standard deviation was used to provide a more accurate picture than the limited results gathered could provide.

$$s = \sqrt{\frac{\sum(x_i - \bar{x})^2}{N - 1}} \qquad \textbf{3.1}$$

The amount of stearic acid remaining is proportional to the area of the stearic acid stretch remaining following reaction. In combination with the initial area of the C-H stretch before reaction, the area of each spectra can be used to calculate the percentage decomposition after each period of irradiation.

The decomposition of stearic acid is inversely proportional to the area of the C-H stretch being recorded, so larger errors should be associated with the smaller values for % decomposition. This will be done by calculating and applying the error associated with the % stearic acid present on the surface:

$$Error = 2.76 \times 10^{-2} \times 100 - '\%\ decomposition' \qquad 3.2$$

The zero minute spectra will all have an associated 2.76 % error. As all other values are calculated based on this, the variance sum law[7] should be applied resulting in:

$$Error = 2.76 + (2.76 \times 10^{-2} \times 100 - '\%\ decomposition') \qquad 3.3$$

The errors associated with the sample moving in the DRIFTS cell between spectra, variations in film thickness across the sample, temperature fluctuations from the light source and the error associated with the baseline fitting process cannot be measured independently as they are all reliant upon other processes and their associated errors. Without being able to effectively disentangle the errors from one another, it is best to be able to express them all as a single value. Other errors associated with the equipment used will also be encompassed in the errors calculated and reported above.

3.2 Investigation of the effect of Pluronic P-123 concentration

To find the optimum amount of the templating polymer, Pluronic P-123, that would yield the most active photocatalytic films, samples were prepared using different amounts of polymer while retaining the same amounts of solvent and titanium butoxide as well as keeping the spin speed at 2000 rpm when producing all samples. Figure 3.2 shows the decomposition of stearic acid over samples prepared with 0.5, 1 and 1.5 g of Pluronic P-123 in 10 mL of 0.5 mol dm^{-3} titanium butoxide in anhydrous methanol. Figure 3.2 shows that the sample with 1.5 g of P-123 is the least active, the 0.5 and 1 g samples showing very similar activities with some evidence of the higher concentration of P-123 being more active after 60 minutes. The relevant rate plots and rate constants can be found in Appendix 1, Figures A1.1 to A1.6.

The zero order rate constants and half-lives for the decomposition of stearic acid over these samples are shown in Table 3.1. Stearic acid decomposition over the sample produced with 1.5 g of Pluronic P-123 had a rate constant far smaller than the other two, however the samples produced with 0.5 and 1 g of P-123 had broadly similar rate constants with decomposition over the 1 g sample having a slightly higher rate and a much higher maximum decomposition as reflected in the half-lives, with reaction over the sample produced with 1 g of P-123 having a slightly smaller half-life than reaction over the 0.5 g sample.

Sample	Zero order rate constant	Half-life (s)
0.5 g P-123	$1.98 \times 10^{-2} \pm 1.05 \times 10^{-3}$	2517
1 g P-123	$2.06 \times 10^{-2} \pm 5.53 \times 10^{-4}$	2426
1.5 g P-123	$7.43 \times 10^{-3} \pm 7.39 \times 10^{-4}$	6732

Table 3.1: Zero order rate constants for stearic acid decomposition over samples produced with varying amount of templating polymer

On the basis of this preliminary data, the films for all subsequent experiments were made with 1 g of Pluronic P-123 for every 5×10^{-3} moles of titanium butoxide.

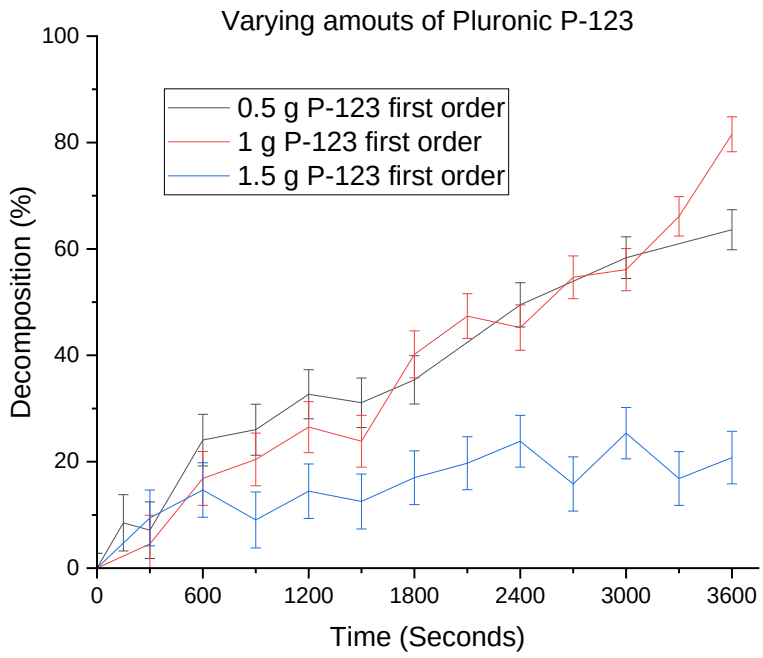

Figure 3.2: The decomposition of stearic acid over films produced with varying amounts of Pluronic P-123

3.3 Evaporation-Induced Self-Assembly

For the templating polymer to form a porous structure, it must undergo evaporation-induced self-assembly (EISA) as discussed in the introduction. The temperature of the EISA was another variable that was investigated to ensure the optimal results. The spin-coating process results in the evaporation of large amounts of the solvent used, so it was important to confirm that the EISA process was optimized in this specific use of the templating polymer. The spin-coating was ended prematurely rather than being left to spin for the 30 seconds that is recommended for a solution containing methanol[8] so that some solvent would remain in the coating. The decision was made to not explore the EISA temperature above 40 °C as the small amount of solvent left in each sample after spin-coating would need to be preserved for longer periods of time to allow the micelles to form properly. The boiling point of methanol is 64.7 °C, so raising the temperature beyond 40 °C would result in fast evaporation of the solvent that would mimic the evaporation seen with the samples that did not undergo EISA.

One set of samples underwent EISA at 40 °C for 48 hours, one set was left at room temperature for a week and another set of samples was calcined immediately. Each set of samples contained multiple samples produced at spin speeds between 500 and 4000 rpm.

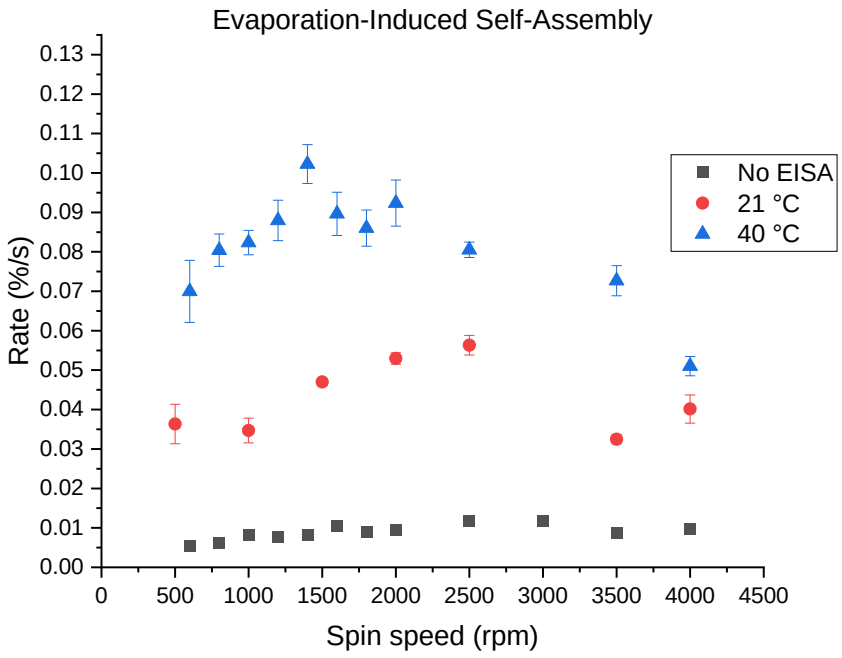

Figure 3.3: The rates of the decomposition of stearic acid over TiO_2 films plotted against the spin speeds at which they were produced. The samples produced underwent EISA at: 40°C for 48 hours (red), 21°C for a week (blue) and the final set of samples were calcined immediately after spin coating (grey)

Figure 3.3 shows the rates of stearic acid decomposition over the three set of samples plotted against the spin speed at which they were produced. The samples that didn't undergo EISA performed poorly, with the 21 °C samples showing a significant improvement. Decomposition over the samples that underwent EISA at 40 °C had significantly higher rates compared to the other samples, confirming that lowering the EISA temperature does not result in better outcomes in the activity of the final films.

3.4 Films produced from precursor and hydrolysed solutions

Titanium butoxide will readily react with small amounts of water whether from the atmosphere or in solution. The reactions between water and titanium butoxide are summarized in 3.4 and Equation 3.5 below.

$$Ti(OBu)_4 + 4\ H_2O \longleftrightarrow Ti(OH)_4 + 4\ BuOH \qquad \textbf{3.4}$$

$$Ti(OH)_4 \longleftrightarrow TiO_2 + 2\ H_2O \qquad \textbf{3.5}$$

Titanium butoxide readily hydrolyses in air, forming titanium hydroxides that readily condense to titanium dioxide and precipitate out of solution.[9] This process changes the viscosity of the solution, and may have an effect on the structure and properties of the resulting film. Spin coating a solution will also result in much more consistent and homogenous films than can be achieved by spin coating from a suspension. Films resulting from spin coating a suspension often have defects such as "comet streak type" artefacts across the surface, and the effect of using a templating polymer on a suspension as opposed to a solution may also have a significant effect on the resulting porosity as pores cannot be formed in any particles that are already formed as a result of hydrolysis at this point in the process.

Two batches of samples were prepared to investigate the effect that hydrolysis has on the activity of the resulting films. Batch one was allowed to hydrolyse and batch two isolated from atmospheric moisture. Batch one was left open to the air while stirring and allowed to hydrolyse, while batch two was covered with paraffin film and then a single small hole was poked into the film using a needle. The hole was necessary because there was some evaporation of the solvent during stirring. This evaporation provided enough increased pressure in the beaker that without the small hole the paraffin film came loose and allowed air into the beaker. A single small hole in the film provided enough pressure relief that the film was not loosened, yet there was sufficient positive pressure inside the beaker from evaporation that moisture from the air could not enter

the vessel and hydrolyze the titanium butoxide. Care was taken to keep the solution covered while spin coating so as not to allow hydrolysis at this point.

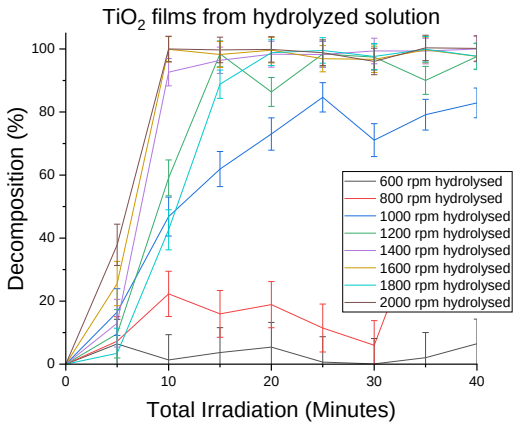

Figure 3.4: Stearic acid decomposition over mesoporous TiO_2 films produced at spin speeds from 600 to 2000 rpm from a hydrolyzed solution

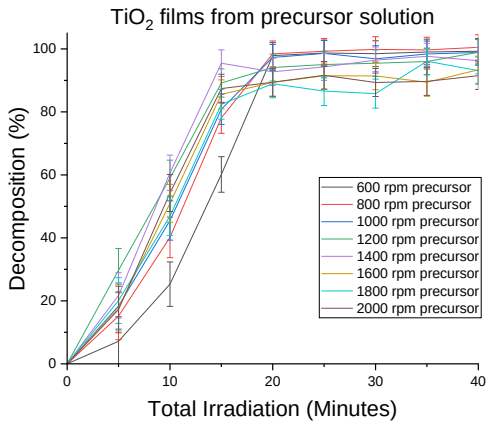

Figure 3.5: Stearic acid decomposition over mesoporous TiO_2 films produced at spin speeds from 600 to 2000 rpm from a precursor solution

Figure 3.4 shows the decomposition of stearic acid over the series of photocatalysts produced from the hydrolysed solution at spin speeds from 600 to 2000 rpm, with the maximum decompositions and time to reach these values reported in Table 3.2. The films produced at lower spin speeds perform poorly in comparison to those produced at high spin speeds, with the films produced at 1400 rpm and above reaching 100 % decomposition at or before 20 minutes total irradiation while the films produced at 1000, 800 and 600 rpm only reached decompositions of 83, 50 and 7 % respectively. As can be seen in Appendix 1, the rate constants for decomposition over these samples reflect the trend seen in the maximum decompositions. The rates of stearic acid decomposition over the hydrolysed samples continue to increase up to the sample produced at 2000 rpm, as can been seen in Figure 3.6 below.

Decomposition of stearic acid over the corresponding samples produced from the titanium butoxide that had not undergone hydrolysis is shown in Figure 3.5. In contrast to the hydrolysed films, the thicker films performed well, with the samples produced at 600, 800 and 1000 rpm reaching 100 % decomposition in 20 minutes. The samples prepared at 1200 and 1400 rpm reached 100 % decomposition within the 40 minute total irradiation, while the samples prepared at 1600 and 2000 rpm did not reach complete decomposition during the 40 minute experiment.

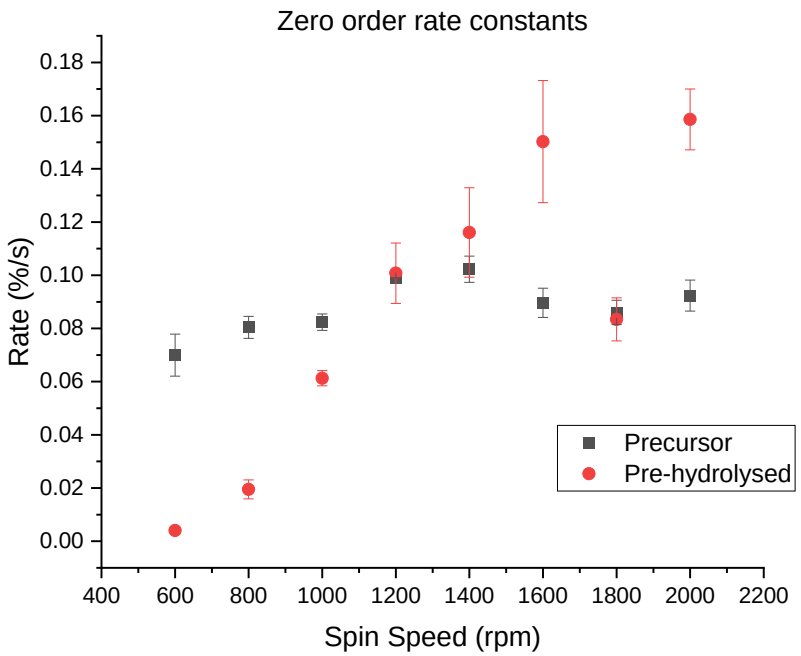

Figure 3.6: Zero order rate constants for reactions over samples produced from both precursor and hydrolysed solutions plotted against the spin speed at which the photocatalyst was produced

The zero and first order plots for stearic acid decomposition over the precursor and hydrolysed samples can be seen in Appendix 1, Figures A1.7 to A1.38. From the different plots, decomposition over all samples made from both solutions follow a zero order reaction mechanism. Table 3.2 shows the half-lives of decomposition over the hydrolysed and precursor samples as well as their maximum decompositions and Figure 3.6 shows the zero order rate constants.

The reaction half-lives of the precursor samples formed at low spin speeds are significantly higher than those for the hydrolysed samples formed at low spin speeds, however, the half-lives do not consider the fact that the hydrolysed samples reached a comparatively low maximum decomposition early in the experiment. In both groups of samples, the half-lives of the reaction decrease when increasing the spin speed that the photocatalyst was formed at, with significant differences between the two groups.

	Half-lives (s)		Maximum decomposition (%)	
Spin speed	**Hydrolysed**	**Precursor**	**Hydrolysed**	**Precursor**
600	12315	714	5.40 ± 5.37	97.87 ± 2.82
800	2567	621	18.89 ± 5.00	98.45 ± 2.80
1000	815	607	84.67 ± 3.18	97.30 ± 2.83
1200	496	505	98.46 ± 2.80	89.20 ± 3.06
1400	430	488	96.43 ± 2.86	95.48 ± 2.88
1600	332	557	99.89 ± 2.76	85.57 ± 3.16
1800		581	98.83 ± 2.79	
2000	315	541	99.99 ± 2.76	87.40 ± 3.11

Table 3.2: The half-lives of the decomposition of stearic acid over precursor and hydrolyzed samples and their maximum decompositions

The samples produced at low spin speeds are very different between the two sets of samples. Decomposition over the hydrolysed samples have extremely poor rates and maximum decompositions, whereas decomposition over the precursor samples reach completion in around 20 minutes total irradiation and have rate constants that are 17 and 4 times larger than those of decomposition over the samples produced at 600 and 800 rpm from the hydrolysed solution respectively. Decomposition over the samples produced at 1200 rpm have very similar rate constants to the precursor's being 2 % smaller than the rate constant of decomposition over the hydrolysed samples. The rate of decomposition over the hydrolysed samples continues to increase with increasing spin speed, with reaction over the sample produced at 2000 rpm having a rate 1.7 times larger than reaction over its precursor counterpart.

One issue that cannot be fully appreciated from the decomposition alone is the quality of the resulting films and the issues caused by working with a suspension as opposed to a solution. The higher viscosity of the solution results in much thicker films which have a much higher tendency to flake off the surface, so they must be handled with delicacy during and after the spin coating process. Many of the samples produced had to be disposed of due to large comet streaks across the surface leaving gaps where very little photocatalyst remained. The more viscous solution also presented a problem with large beads forming round the edge of the sample. Normally this would be removed by increasing the spin speed for a short period of time, causing the bead to be removed, however, the coatings on these films need to retain as much solvent as possible during this process so that the slow evaporation can help to form the porous structure. As such, it would

affect the resulting film if the bead was removed so it is left in place where it later flakes off during the calcination, leaving a ring of bare coverslip around the photocatalyst.

3.5 Summary

Before undertaking this work, it was unclear whether the formulations that are often used to produce photocatalytic mesoporous TiO_2 by a sol-gel method would be directly applicable to the spin-coating of thin films of the same materials.

The Pluronic P-123 concentration was varied to ensure the correct pore size was present in the finished films to give the most active films.

The time and temperature for EISA of the films was also explored, although this procedure did not change from the procedure that is used for a sol-gel method of producing powders. The effects of EISA at 40 °C for 48 hours did show a marked improvement when compared to either immediate calcination of the films after spin-coating or leaving the films at room temperature for an extended period.

The hydrolysis of the solution is not an important consideration when producing mesoporous titanium dioxide as a powder using a sol-gel method. It will always occur during the gelling and EISA step of the process and the precipitation will not form defects in the final product as it will with spin-coated films. The increased viscosity of the hydrolysed solution caused poor adhesion to the substrate and vastly increased the number of visible surface defects in the films. Given the progressive nature of the hydrolysis of the solution, the solution became increasingly more difficult to work with as the pipette tip became blocked and before a reasonable number of samples could be produced, the solution became too viscous to draw up into the pipette. Despite showing higher rates over photocatalysts prepared at higher spin-speeds, the physical properties of the hydrolysed solution made it impractical to use going forward.

The work set out in this chapter ensured that the base formulation of the mesoporous titanium dioxide films was optimized to allow the exploration of other variables in these materials going forward.

3.6 References

1 Y. Zhao, S.-M. Ma, B. Li, A. De Nicola, N.-S. Yu and B. Dong, *Polymers (Basel)*, 2019, **11**, 1806.

2 U. G. Lee, W.-B. Kim, D. H. Han and H. S. Chung, *Symmetry*, 2019, **11**, 1183.

3 F. Atay and D. Durmaz, *Journal of Elec Materi*, 2020, **49**, 5542–5551.

4 M. I. Khan, K. A. Bhatti, R. Qindeel, H. S. Althobaiti and N. Alonizan, *Results in Physics*, 2017, **7**, 1437–1439.

5 J. R. M. Ângelo, Ph.D., Universidade do Porto (Portugal).

6 A. P. King and R. J. Eckersley, in *Statistics for Biomedical Engineers and Scientists*, eds. A. P. King and R. J. Eckersley, Academic Press, 2019, pp. 1–21.

7 Variance Sum Law I, https://stats.libretexts.org/Bookshelves/Introductory_Statistics/Book%3A_Introductory_Statistics_(Lane)/03%3A_Summarizing_Distributions/3.18%3A_Variance_Sum_Law_I_-_Uncorrelated_Variables, (accessed February 17, 2022).

8 Spin Coating, https://www.ossila.com/pages/spin-coating, (accessed April 7, 2020).

9 M. J. Velasco, F. Rubio, J. Rubio and J. L. Oteo, *Spectroscopy Letters*, 1999, **32**, 289–304.

Chapter 4. Film Thickness and Topography

4.1 Introduction

Surface metrology methods can be categorised as either contact or non-contact techniques. Contact techniques such as atomic force microscopy (AFM) can be used to obtain 3D profiles of surfaces but are slow and best at measuring much smaller areas than needed in this case.[1] Non-contact techniques can be used to generate 3D surface topographic images as well as 2D profiles.[2] Non-contact methods can offer advantages when working with soft materials or materials with large vertical steps that need to be accurately measured, however, the optical properties of the materials (transparent or reflective) can pose significant disadvantages over contact methods.[3,4]

As addressed in the introduction, the film thickness of spin coated materials that contain large amounts of polymer or undissolved materials often exhibit non-Newtonian behaviour and so the film thicknesses produced can be unpredictable.[5] The shear thinning or thickening behaviour can result in films becoming thicker or thinner than would be expected at high spin speeds.[6–9] It is necessary to use a range of measurements across the entire spin-coating speed range to be used, as the shear stresses may not introduce variations from the predicted behaviour until higher spin speeds.[10]

AFM was not suitable to use on these samples due the large step height to be measured and the limitations of the probe size. The large number of samples that needed to be recorded in order to obtain reliable graphs of film thickness against the preparation spin speed were also better suited to the quicker technique of optical profilometry.

Before surface metrology was decided upon, several samples were embedded in resin, and a cross-section was cut through the sample and resin then SEM was used to image the exposed edge. Despite lowering the rate at which the sample was fed into the saw, the photocatalyst tore out of the surface and a small air gap was present during the resin pour. These two factors meant that images did not show the sample and the air gap that remained was significantly larger than the surface coating.

4.2 Film Thickness Measurements Using Optical Profilometry

Samples were prepared by scraping half of the film off the glass coverslip using a plastic glue spreader. Figure 4.1 shows a greyscale image of a sample under magnification. The left hand side of the image shows the intact TiO_2 film, and the right hand side is the bare glass coverslip where the film was removed.

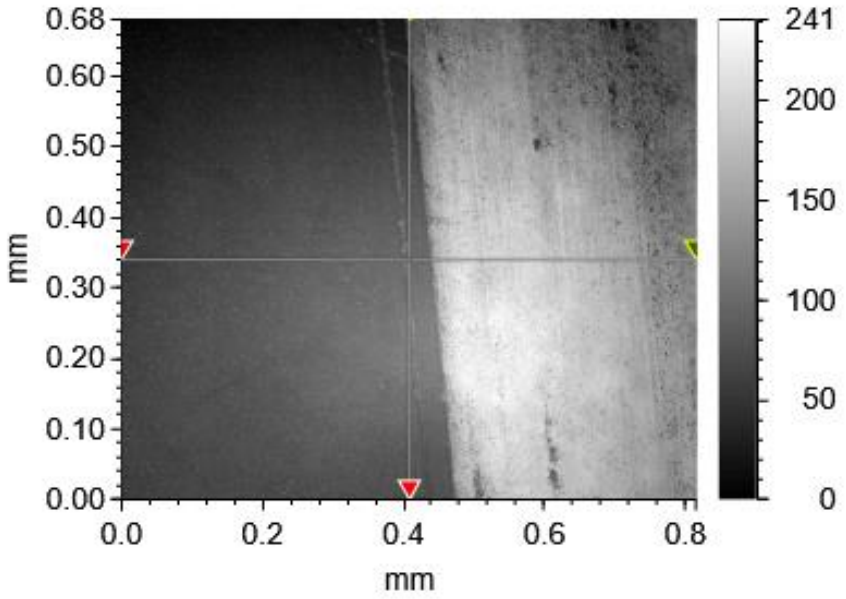

Figure 4.1: Greyscale image of the surface of a 0.5 wt% Cu-doped meso-TiO_2 surface coating prepared at a spin speed of 2000 rpm. The right hand side of this area of the sample has been scraped off the surface as described in Chapter 2, leaving the bare glass coverslip on this side

Focus-Variation metrology was performed using a Sensofar S mart sensor, capturing the threshold between the coated and uncoated surfaces. The data obtained was processed using SensoMAP software. The surface was levelled, and then the difference between the coated and uncoated surfaces was calculated using the average value from the glass and the maximum value from the surface coating.

SensoMAP software was used to generate reports with the mean heights of two pre-defined areas of each sample as well as the minimum and maximum values. It was necessary to remove a large number of outliers from the glass surface due to its transparent and reflective nature by adding a cut-off threshold for measurements. When removing areas of the surface ahead of the surface metrology measurements, it was common to have areas that were damaged, especially near the step between the two surfaces. User error in the placement of the sample before acquisition can also have areas of missing film in the calculation area. Out of the measurements in

the SensoMAP report, the most accurate measurement for the height of the film was the maximum height of the film minus the average height of the glass. This method did mean that any debris on the surface was introduced into the calculations, but these were removed from any further calculations of average film thickness.

Figure 4.2 shows a 3D view of the data collected. The green area toward the bottom of the image is the glass coverslip and the top of the image shows the TiO_2 film. The colour of each area correlates to the z-height in the scale on the right hand side of the figure.

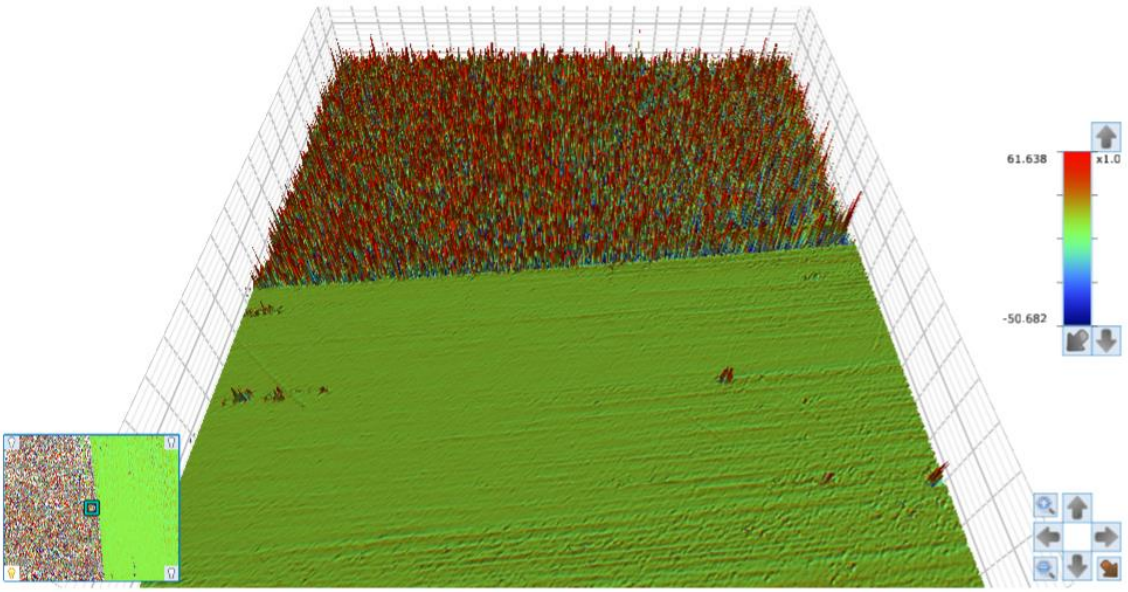

Figure 4.2: 3D view of a heat map of the surface of a 0.5 wt% Cu-doped meso-TiO_2 surface coating prepared at a spin speed of 2000 rpm

Figure 4.3 shows a closer view of region at the edge of the remaining film. The green glass coverslip on the right hand side of the image is flat aside from some small pieces of debris which can be easily removed. The left hand side of the figure shows the texture of the film and demonstrates well why the average height of the film could not be used.

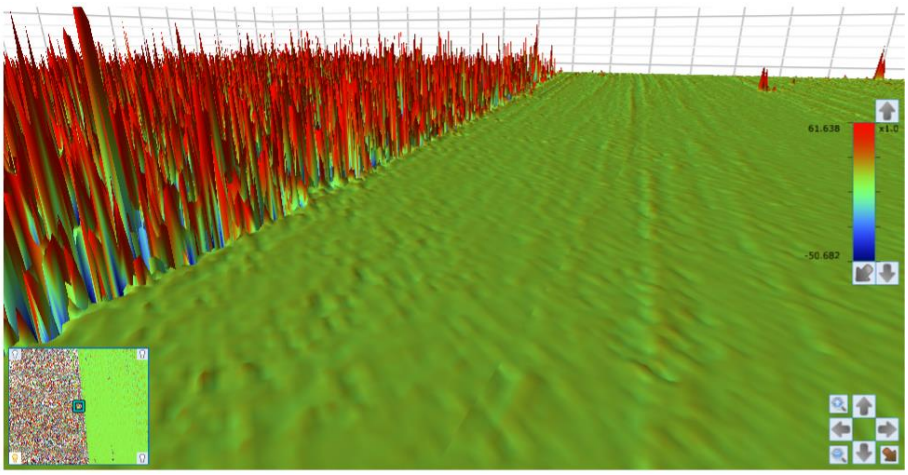

Figure 4.3: A closer view of the edge between the TiO_2 film and the bare glass coverslip

The channels in the TiO_2 films are too deep and numerous to give an accurate mean height over the area of the film, so the maximum height for that portion of the image was chosen as a metric instead.

Figure 4.4 to Figure 4.9 on page 50 show plots of the film thickness against preparation spin speeds for samples with different copper contents fitted with an exponential curve. As the preparation spin speed increases, the film thickness decreases towards a minimum value. These values have been reported as the minimum film thickness in Table 4.1 as well as the film thickness at a preparation speed of 500 rpm. The changes in film thickness at high spin-speeds is limited beyond 4000 rpm in all groups of samples.

Copper Doping (wt%)	**Minimum Film Thickness (µm)**	**Film Thickness at 500 rpm (µm)**
Undoped	14.6	33.3
0.1	2.9	18.8
0.5	5.4	49.3
1	22.4	49.2
2.5	23.4	59.9
5	12.5	49.3

Table 4.1: A table of the film thickness tended towards by samples with varying copper content

The minimum film thicknesses increased with increasing copper content, except for the undoped and 5 wt% copper films. The copper nitrate inhibited hydrolysis of the titanium butoxide, so the undoped solution was much more viscous than the copper containing solutions, hence the increase in thickness of these samples.

The initial film thicknesses, at a preparation spin speed of 500 rpm is consistent within the copper doped samples between 0.5 and 5 wt% with the exception of the 2.5 wt% samples. At the same range of thicknesses, the 1 and 2.5 wt% samples have film thicknesses within 1 µm of each other.

Despite having similar depths between samples prepared at spin speeds of 500 rpm, the 0.5 wt% samples are significantly thinner than the samples with different copper content at produced at higher spin speeds, with all samples produced at spin speeds over 2000 rpm having a depth under 7.5 µm.

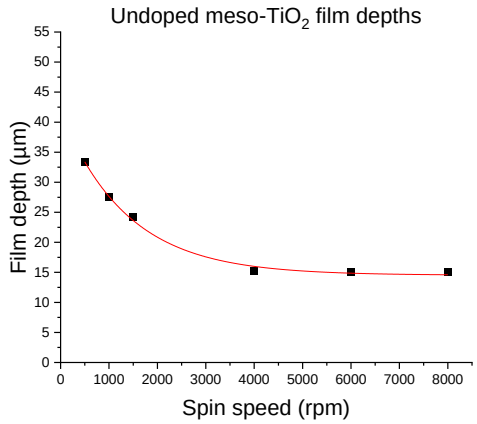

Figure 4.4: The film thicknesses of undoped meso-TiO_2 coatings

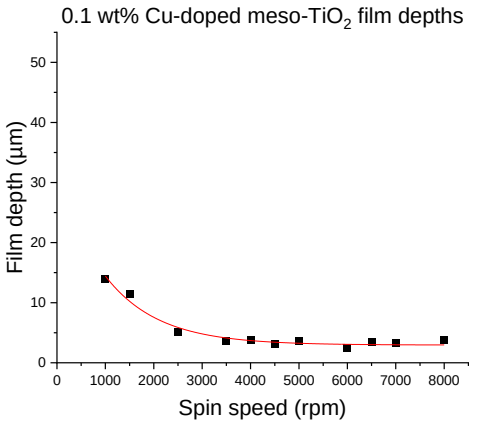

Figure 4.5: The film thicknesses of 0.1 wt% copper doped meso-TiO_2 surface coatings

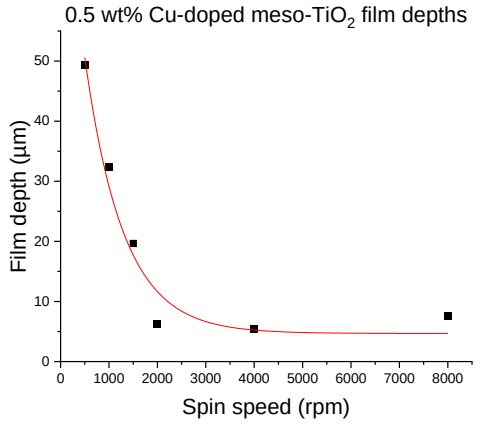

Figure 4.6: The film thicknesses of 0.5 wt% copper doped meso-TiO_2 surface coatings

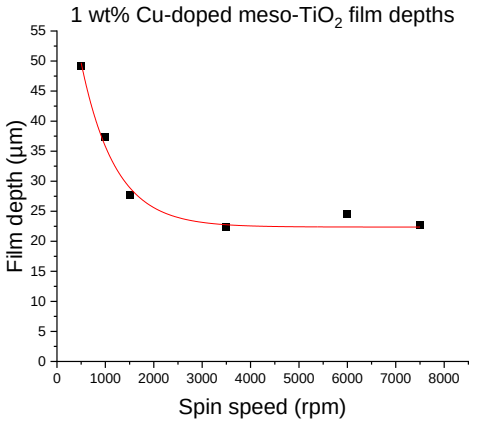

Figure 4.7: The film thicknesses of 1 wt% copper doped meso-TiO_2 surface coatings

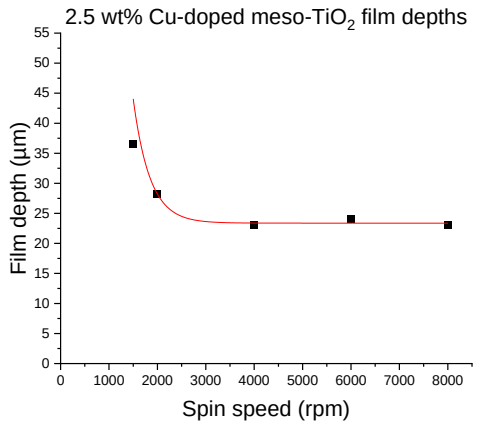

Figure 4.8: The film thicknesses of 2.5 wt% copper doped meso-TiO_2 surface coatings

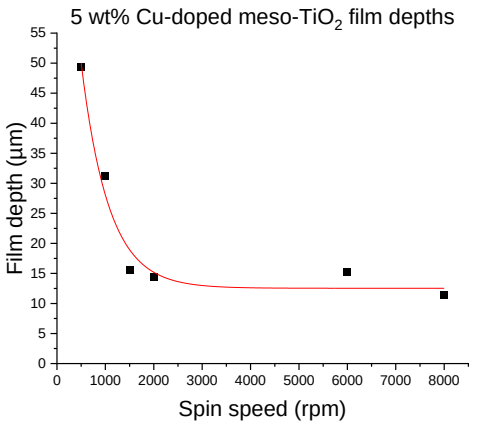

Figure 4.9: The film thicknesses of 5 wt% copper doped meso-TiO_2 surface coatings

4.3 Fluid Behaviour While Spin-Coating

When spin coating Newtonian fluids, the film thickness will be proportional to the square root of the angular velocity. As can be seen in Figure 4.11 to Figure 4.16 on page 53, the films produced in this work do not follow this behaviour. They show two distinct linear regions in each group of samples, with the initial left-hand line [A] and the right-hand line [B]. Both areas of Figure 4.11 to Figure 4.16 were fitted to Equation 4.1:

$$t = mx + c \tag{4.1}$$

where *t* is the thickness, *c* is the intercept and *m* is the slope. The intercepts and slopes of all linear fits are reported in Table 4.2.

Copper Doping (wt%)	Slope [A]	Intercept [A]	Slope [B]	Intercept [B]
Undoped	$-5.63\times10^{-1} \pm 4.48\times10^{-2}$	45.7 ± 1.42	$-7.61\times10^{-3} \pm 4.29\times10^{-3}$	15.7 ± 0.33
0.1	$-4.84\times10^{-1} \pm 6.02\times10^{-2}$	29.6 ± 2.46	$-7.27\times10^{-3} \pm 1.75\times10^{-2}$	3.93 ± 1.30
0.5	$-1.90 \pm 6.30\times10^{-2}$	92.2 ± 2.23	$-3.11\times10^{-2} \pm 3.37\times10^{-2}$	4.39 ± 2.30
1	$-1.31 \pm 2.37\times10^{-2}$	79.7 ± 0.748	$2.34\times10^{-2} \pm 7.95\pm10^{-2}$	21.6 ± 5.98
2.5	-1.40	90.9	$3.49\times10^{-3} \pm 4.56\times10^{-2}$	23.1 ± 3.53
5	$-2.06 \pm 6.47\times10^{-2}$	95.6 ± 2.05	$-4.83\times10^{-2} \pm 6.98\times10^{-2}$	17.1 ± 5.10

Table 4.2: Table of the slopes and intercepts of the graphs in Figure 4.11 to Figure 4.16 where line [A] is the left hand line on each plot

It is common for suspensions or solutions containing dissolved polymers to exhibit non-Newtonian behaviour, providing an explanation of the change in behaviour seen in the spin-coated solution at different spin speeds. At low spin speeds, the relationship between thickness and spin speed follows the expected behaviour of Newtonian fluids because the shear forces at lower speeds are not great enough to induce any shear thickening behaviour in the solution. As the spin speed increases, the shear forces and viscosity of the solution increase, causing an increasing deviation from the expected film thickness. Figure 4.10 shows the relationship between the shear rate and viscosity for Newtonian, shear thickening and shear thinning liquids. At low shear rates, the differences between the viscosity of the three types of liquids is negligible as would be the case for three solutions of similar properties at low spin speeds. As the shear rate increases, the viscosity of the non-Newtonian liquids changes exponentially. This behaviour of shear thickening non-Newtonian liquids would explain the thicknesses seen with the spin coated

samples. As the spin speed increases, the viscosity of the solution also increases, causing the film thickness to decrease at a much lower rate than expected from the low spin speed trend.

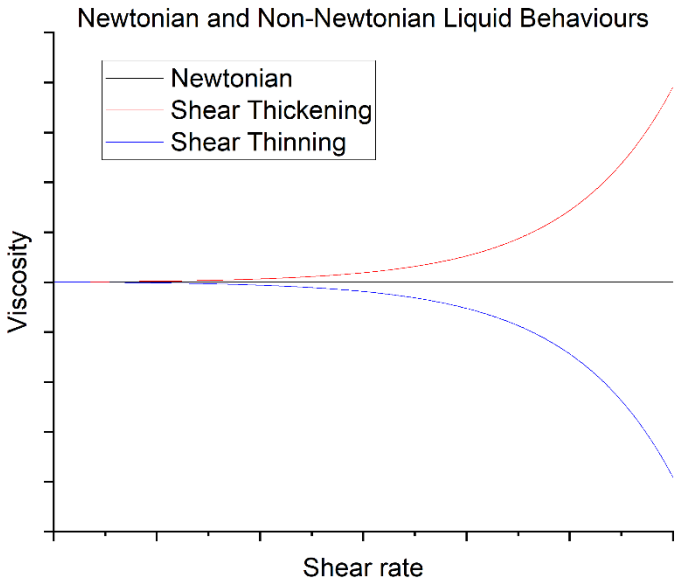

Figure 4.10: The relationship between the viscosity and shear rate for Newtonian (black), non-Newtonian shear thickening (red) and non-Newtonian shear thinning liquids (blue)[11]

Figure 4.11 to Figure 4.16 show the conflict between the centrifugal forces spreading the solution over the surface and the increasing viscosity of the solution as the shear force increases. The linear fit at lower √ω values follows the expected behaviour for Newtonian fluids as the shear rate is low enough to be insignificant at low spin speeds. As the spin speed increases, the film depth gradually increases compared to the expected values. The gradients of the high spin speed linear fits for all groups of samples are within an error margin of zero. The point at which the two linear fits converge (Table 4.3) is the critical shear rate in rpm for the onset of shear thickening of the solutions. After the critical shear rate, the films do not change in depth with increasing spin speed.

Copper doping:	**Undoped**	**0.1 wt%**	**0.5 wt%**	**1 wt%**	**2.5 wt%**	**5 wt%**
Critical shear rate (rpm)	2930	2894	2065	1890	2324	1527

Table 4.3: The transition point between centrifugal force and shear thickening led film depths

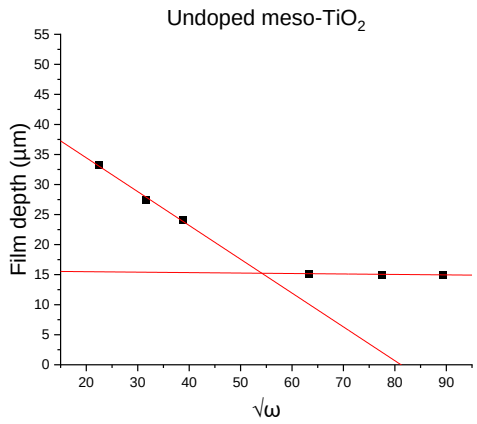

Figure 4.11: The film thicknesses of undoped meso-TiO_2 surface coatings plotted against the square root of the spin-speed (√ω) and linear fits

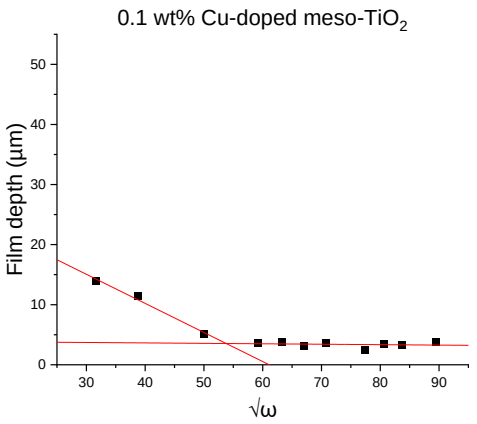

Figure 4.12: The film thicknesses of 0.1 wt% Cu-doped meso-TiO_2 surface coatings plotted against the square root of the spin-speed (√ω) and linear fits

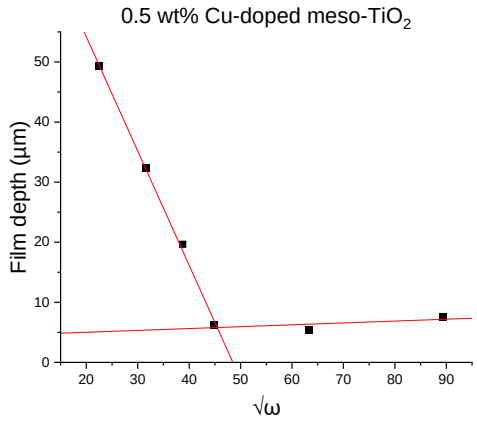

Figure 4.13: The film thicknesses of 0.5 wt% Cu-doped meso-TiO_2 surface coatings plotted against the square root of the spin-speed (√ω) and linear fits

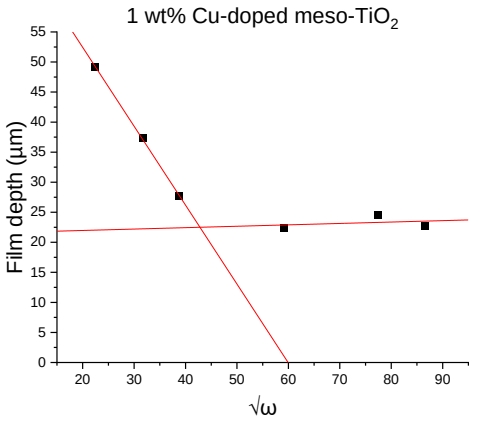

Figure 4.14: The film thicknesses of 1 wt% Cu-doped meso-TiO_2 surface coatings plotted against the square root of the spin-speed (√ω) and linear fits

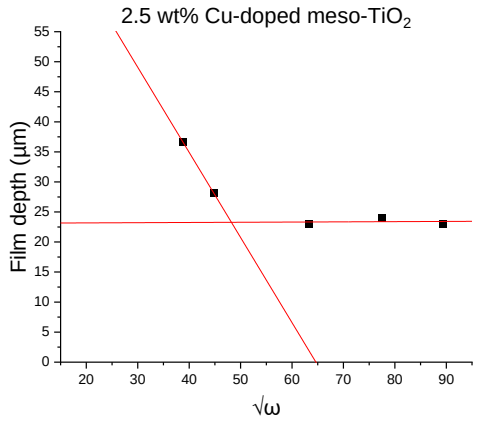

Figure 4.15: The film thicknesses of 2.5 wt% Cu-doped meso-TiO_2 surface coatings plotted against the square root of the spin-speed (√ω) and linear fits

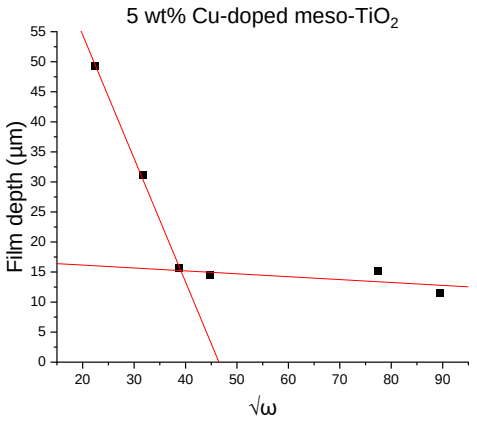

Figure 4.16: The film thicknesses of 5 wt% Cu-doped meso-TiO_2 surface coatings plotted against the square root of the spin-speed (√ω) and linear fits

4.4 Surface metrology

Surface metrology was performed on an intact part of the coatings near the centre of each sample. After levelling in the same way described in Section 0, a linear cross section of each sample was taken to compare the surface roughness and texture to one another.

Figure 4.18 shows the surface height across a 1.1 mm cross section of the surface of the 0.1 wt% copper-doped samples produced at spin speeds from 1000 to 8000 rpm. Images of the surfaces these cross sections are taken from can be found in Appendix 3. Figure 4.17 shows the surface image of a sample. The cross sections of these samples were obtained by recording the height changes across a one dimensional area of the sample surface, represented by the red line below. This process gives a graphical representation of the surface roughness that can be easily compared to other samples as is shown in Figure 4.18 to Figure 4.23. When the features that need to be compared are minimal in height, this approach is very effective when compared to the heat maps shown later in this chapter.

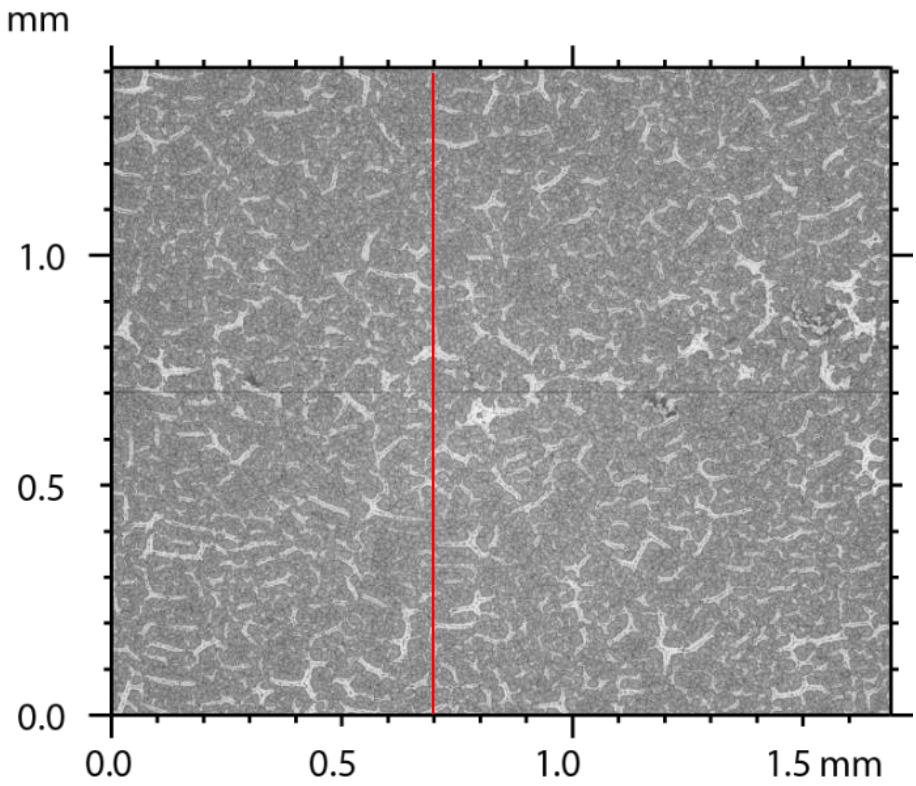

Figure 4.17: The surface of a 2.5 wt% copper doped **meso-*TiO_2* *film prepared at 500 rpm, with a red line indicating where the cross section was recorded.***

The peaks and troughs of the cross sections represent the channels that are visible on the image above. The 2-dimensional cross section allows easy comparisons of the channel depths and widths over the surface of each sample.

The surfaces at the centre of these films are remarkably similar, with all exhibiting the same cracked appearance and having similar cross sections. There is very little variation in the depth or width of the channels in the surface, with the deepest measuring approximately 1.5 µm deep. The average widths of the channels at their mid points are around 12 µm across the samples produced at lower spin speeds, increasing to 15 and 14 µm at preparation spin speeds of 4500 and 8000 rpm respectively.

Cross sections of the undoped films (Figure 4.19) show similar channel depths, but they are significantly wider than the 0.1 wt% copper films. At lower preparation spin speeds, there is a greater proportion of wide, deep channels, with most channels over 1 µm deep and around 15 µm wide.

The channels in the 0.5 wt% copper doped films (Figure 4.20) have average widths of 18 µm in the sample prepared at 1500 rpm and 16 µm in samples prepared at spin speeds from 4000 to 8000 rpm. The average depths of the channels are 2 µm in the sample prepared at 1500 rpm, 1 µm in the sample prepared at 4000 rpm, 3 µm in the sample prepared at 6000 and 1 µm in the sample prepared at 8000 rpm.

The 1 wt% copper-doped samples (Figure 4.21) had consistent channel widths at 15 µm. The sample prepared at 500 rpm had 4 µm deep channels, while the other samples had channels around 1 µm deep. The 2.5 wt% copper doped samples (Figure 4.22) are consistent in both the depth and width of their channels. The 5 wt% copper doped samples (Figure 4.23) had 3 µm deep channels in the sample prepared at 500 rpm, with channels in samples produced at all other spin speeds measuring around 1 µm.

The undoped and 0.5 to 2.5 wt% copper doped samples differed from the 0.1 wt% samples in their appearances. The cracked appearance was present in the thicker films, but the size of the islands between channels reduced significantly as the preparation spin speed increased until a nearly homogenous appearance is achieved at higher spin speeds.

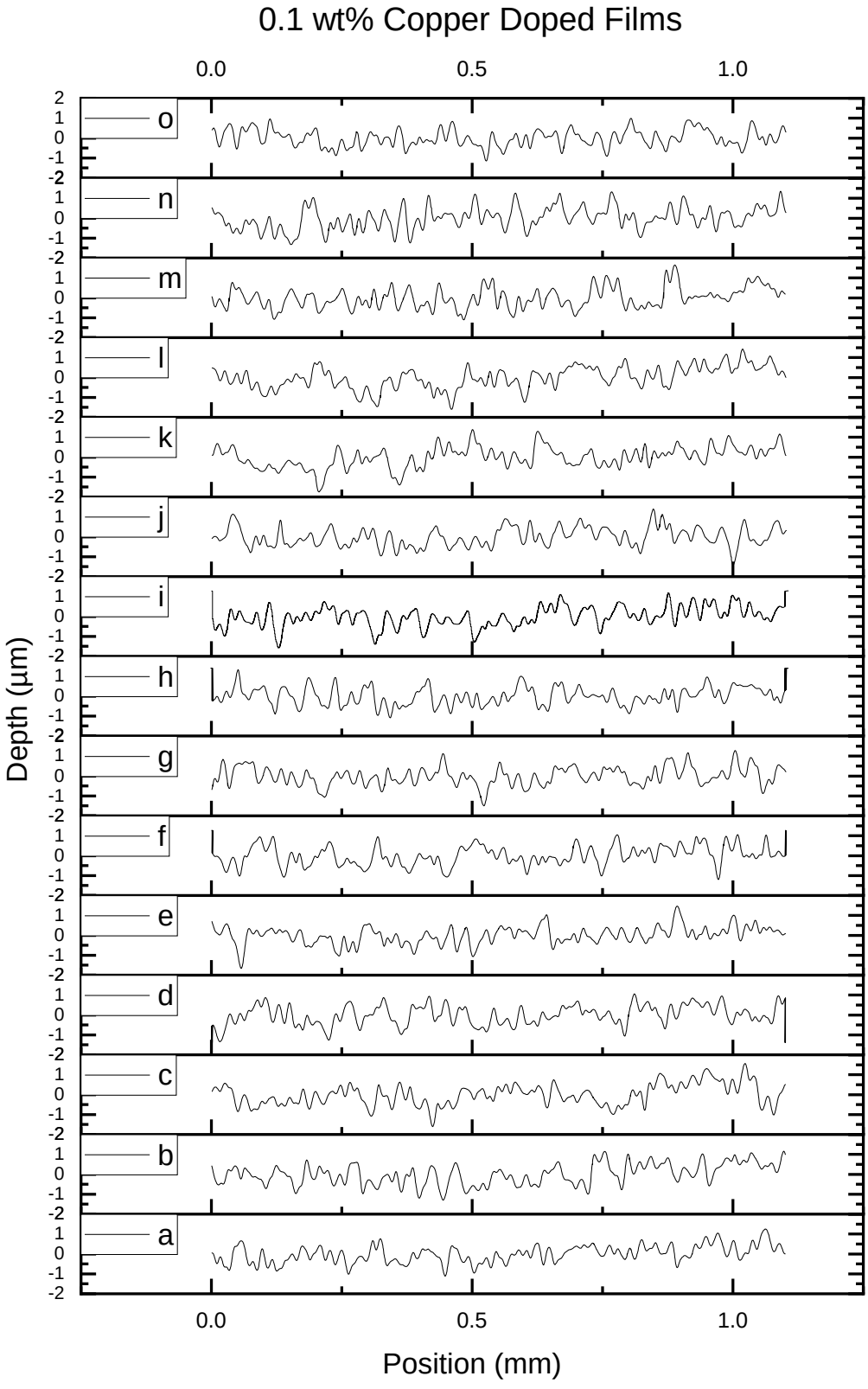

Figure 4.18: A cross section of the surface of 0.1 wt% copper dope meso-TiO_2 surface coatings produced at spin speeds of (a) 1000, (b) 1500, (c) 2000, (d) 2500, (e) 3000, (f) 3500, (g) 4000, (h) 4500, (i) 5000, (j) 5500, (k) 6000, (l) 6500, (m) 7000, (n) 7500 and (o) 8000 rpm

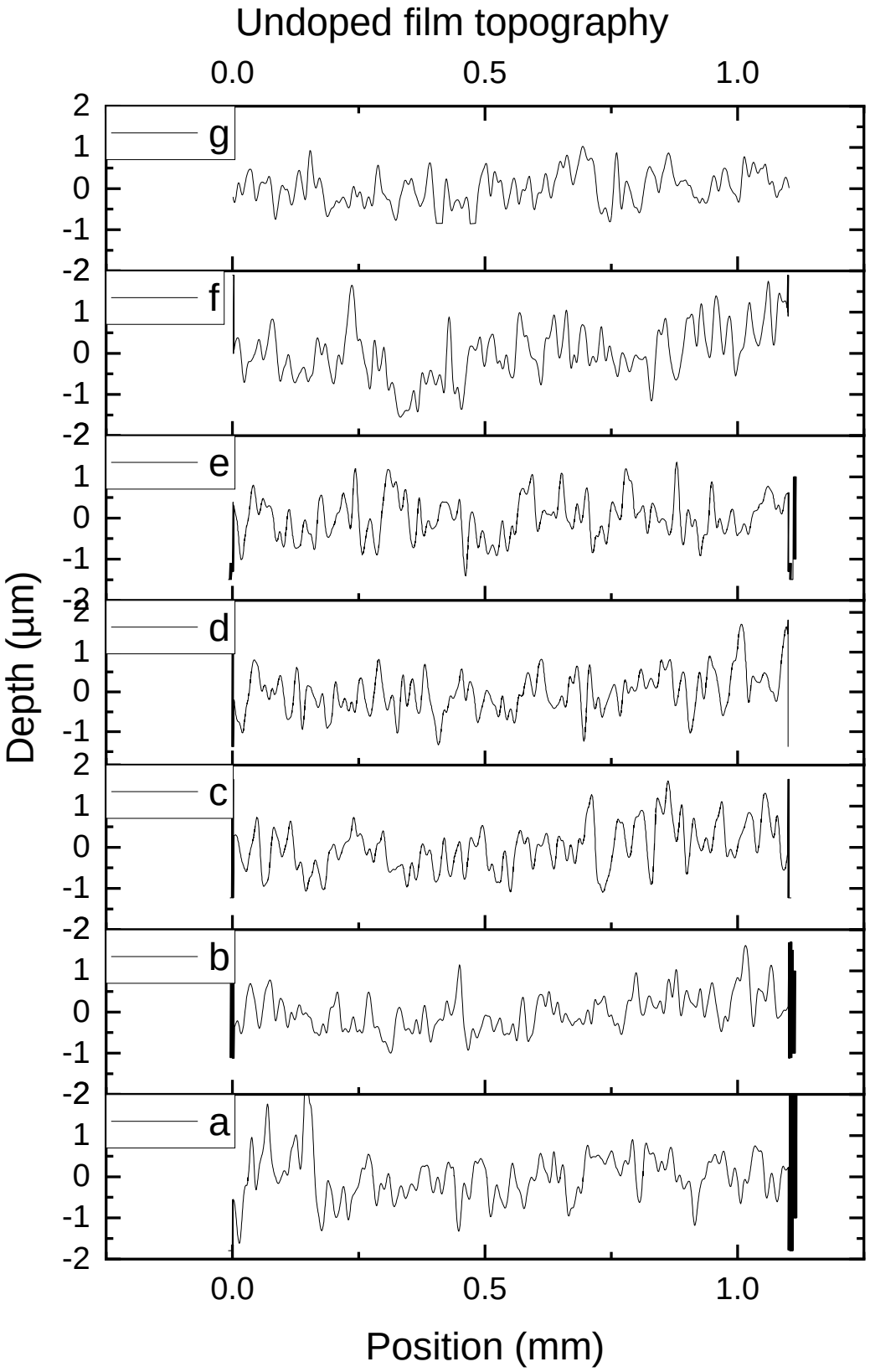

Figure 4.19: A cross section of the surface of undoped meso-TiO_2 surface coatings produced at spin speeds of (a) 500, (b) 1000, (c) 1500, (d) 2000, (e) 4000, (f) 6000 and (g) 8000 rpm

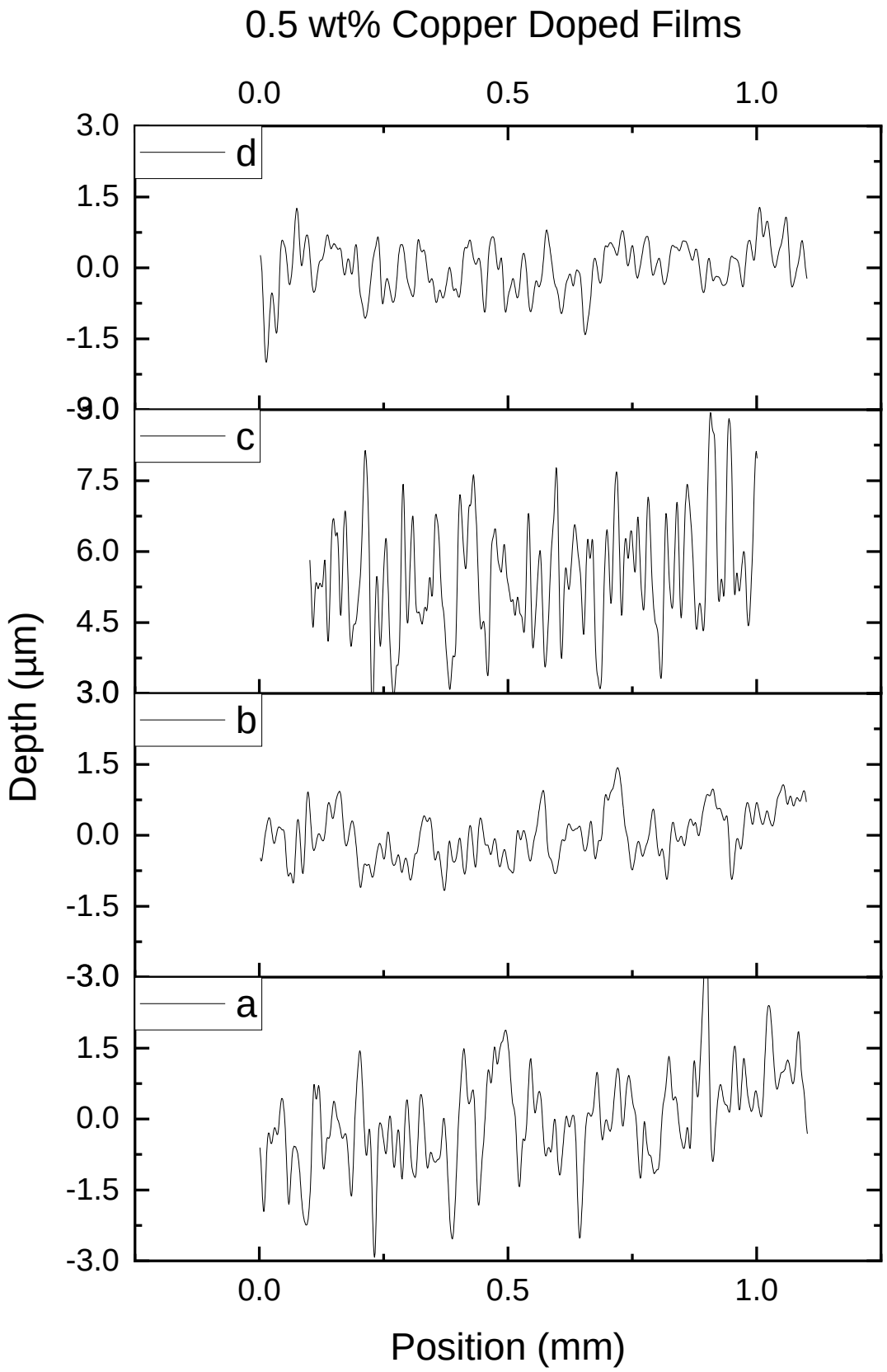

Figure 4.20: A cross section of the surface of 0.5 wt% copper doped meso-TiO_2 surface coatings produced at spin speeds of (a) 1500, (b) 4000, (c) 6000 and (d) 8000 rpm

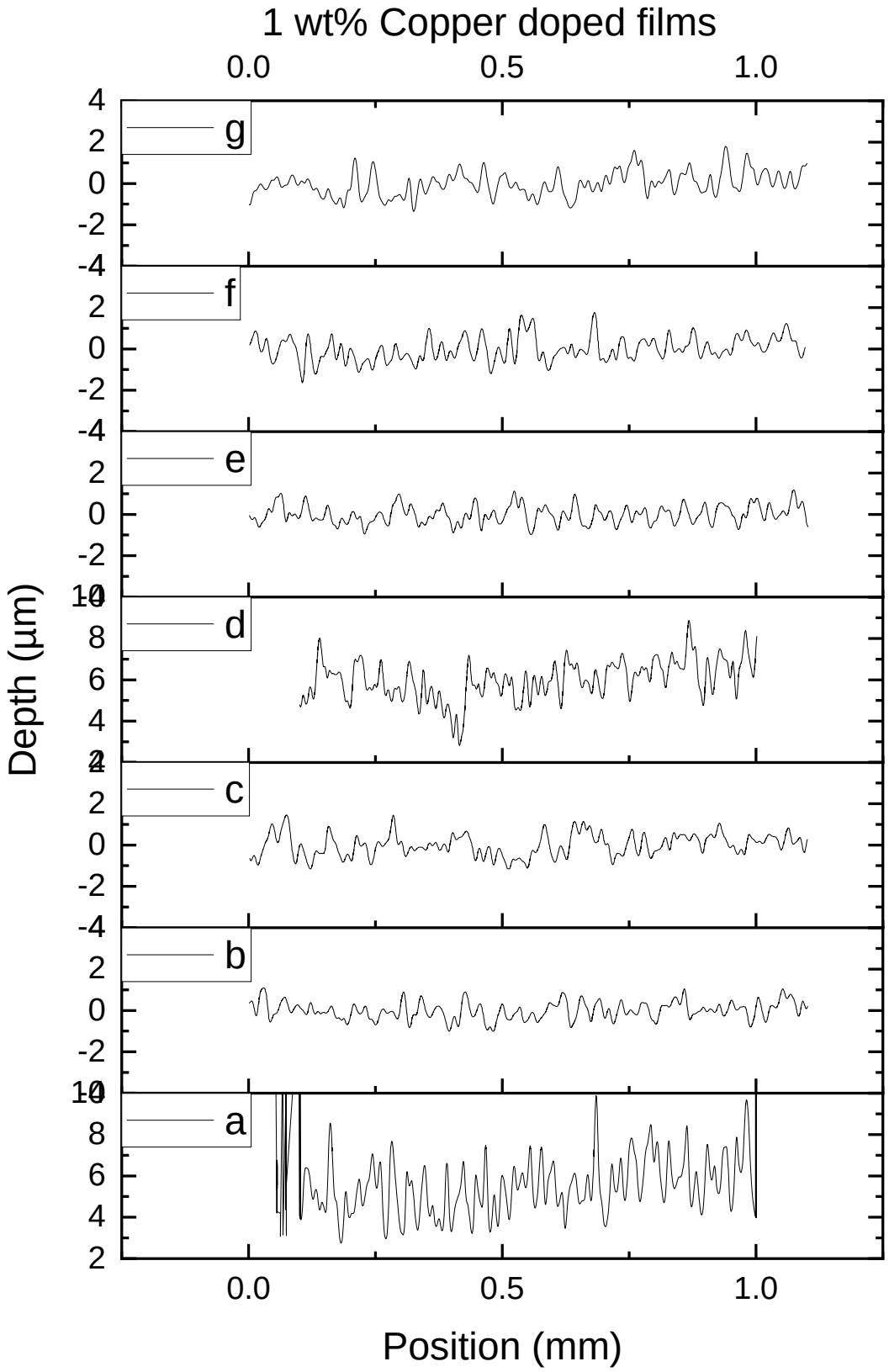

Figure 4.21: A cross section of the surface of 1 wt% copper doped meso-TiO_2 surface coatings produced at spin-speeds of (a) 500, (b) 1000, (c) 1500, (d) 2000, (e) 3500, (f) 6000 and (g) 7500 rpm

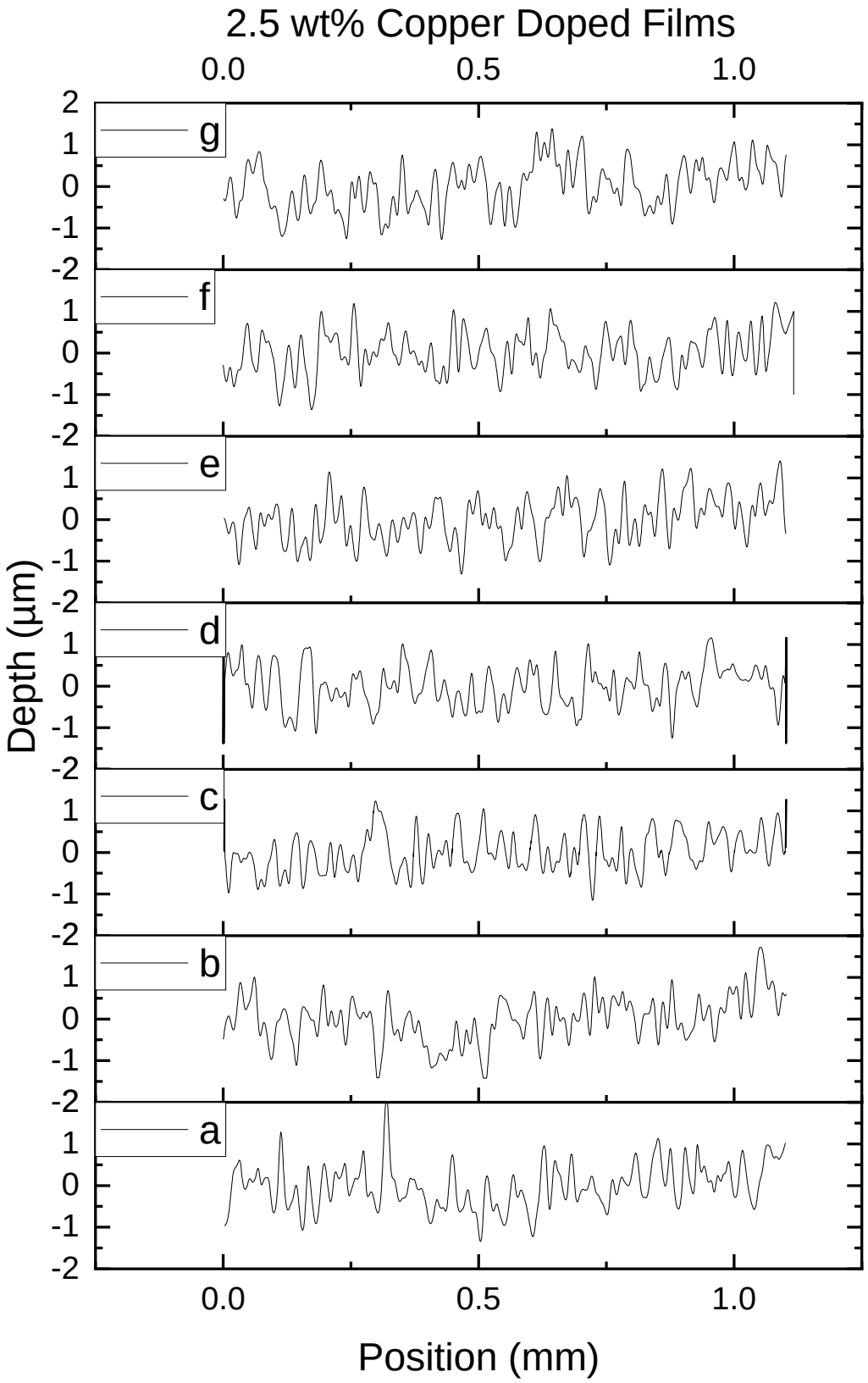

Figure 4.22: A cross section of the surface of 2.5 wt% copper doped meso-TiO_2 surface coatings produced at spin-speeds of (a) 500, (b) 1000, (c) 1500, (d) 2000, (e) 4000, (f) 6000 and (g) 7500 rpm

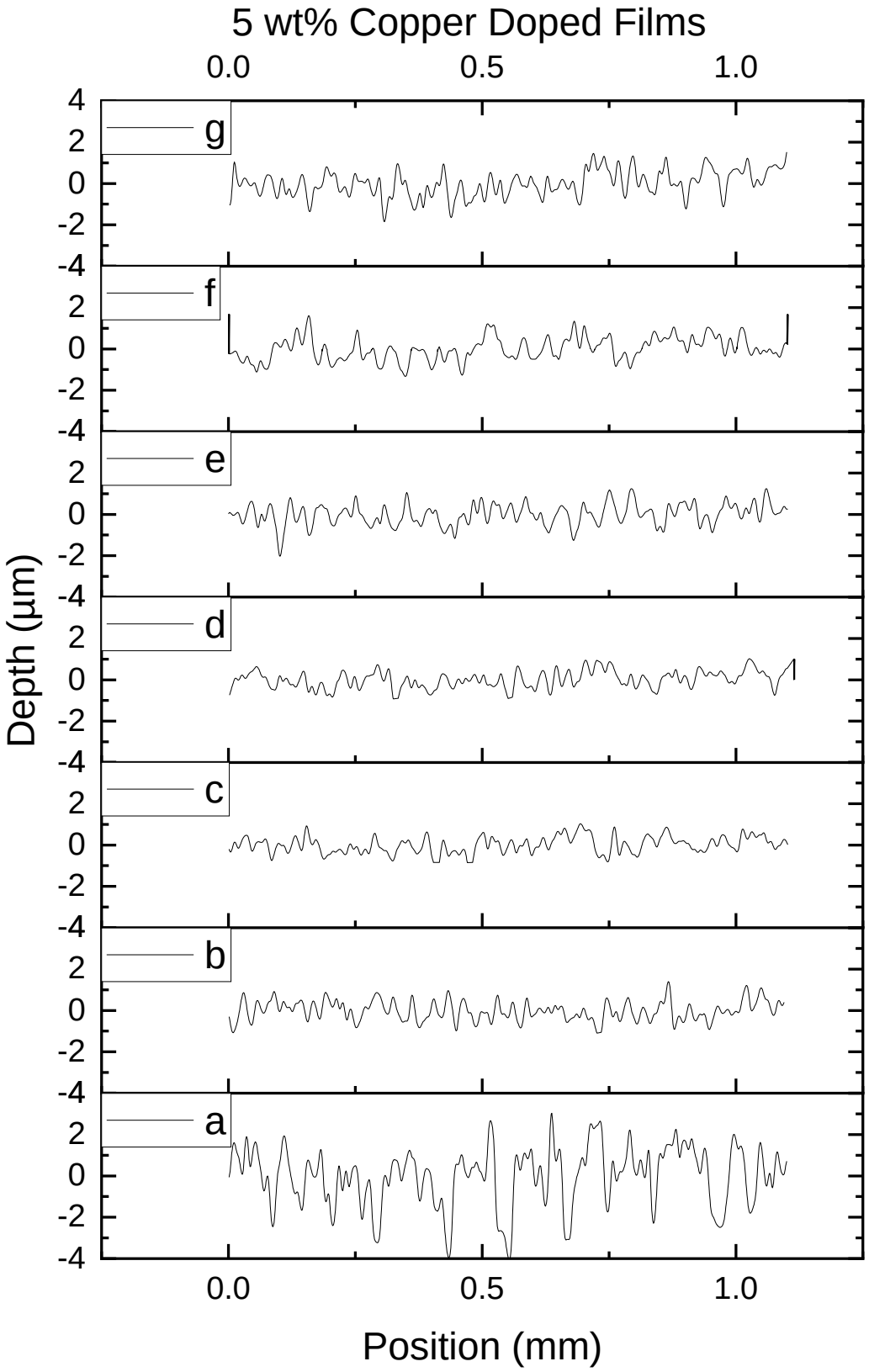

Figure 4.23: A cross section of the surface of 5 wt% copper doped meso-TiO_2 surface coatings produced at spin-speeds of (a) 500, (b) 1000, (c) 1500, (d) 2000, (e) 4000, (f) 6000 and (g) 8000 rpm

4.5 Edge topography

Surface metrology was also performed at the edge of each sample as shown in Figure 4.24. These were processed in the same way as the metrology in the centre of the films. A heat map was produced from each sample to give a 3-dimensional representation of the surface of each sample. The x- and y axes of each image have a scale indicating the size of the image and the z-height of each pixel is represented by a colour. The colour scale on the right of each figure shows the range associated with each heat map.

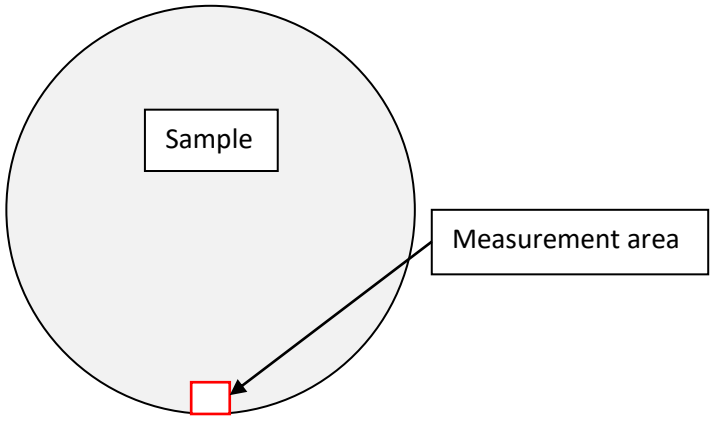

Figure 4.24: Schematic of the areas of each sample used for the edge topography in Figure 4.25 to Figure 4.32

There was significant "beading" at the edge of samples produced at lower spin speeds.[12] This is a known issue with spin-coating at low spin speeds and is described in the introduction.

Figure 4.25 and Figure 4.26 show the edge of an undoped *meso*-TiO_2 sample produced at 500 rpm. The beading is worse at low spin speeds and the beading on the sample produced at 500 rpm was so extensive that it could not be adequately imaged within the 1.4 by 1.7 mm area of a single topographic scan. The beading on this sample resulted in a loss of the coating in some areas as can be seen by the blue areas of the heat maps in Figure 4.25 and Figure 4.26. The beading on this sample is roughly 2 mm wide and over 120 µm deep in places. The texture of the surface changes drastically from the edge towards the centre of the sample as the film thickness decreases. The light pink area in the centre of Figure 4.25 is the highest point in the image. When compared to the turquoise area immediately either side of this feature and the height colour scale to the right of the image, this island of material is approximately 120 µm high. Toward the top and bottom of Figure 4.25, there are areas of the glass substrate depicted in blue next to areas of photocatalyst that appear yellow-green, indicating that the film depth in these areas is

around 70 µm deep. Toward the centre of the sample prepared at 500 rpm, seen in Figure 4.26, the cracked areas of missing film get smaller until there are only shallow channels through the topmost 4 µm as seen in Figure 4.19. It is important to note that the colour scale in Figure 4.26 is different to the previous figure of the same sample, meaning that similar colour changes in the two images indicate a smaller height change in the latter.

The samples prepared at 1000 and 1500 rpm (Figure 4.27 and Figure 4.28) have a similar pattern of beading and high surface roughness at the edge towards a lower film depth and more homogenous surface towards the centre of the sample. These samples also have areas of missing photocatalyst where the thickness has caused low adhesion to the substrate. In some cases, the areas were missing after calcination, but in others they came loose after handling. The beading on the sample produced at 1000 rpm measures 0.8 mm wide, while the beading on the sample produced at 1500 rpm measured approximately 0.5 mm.

Films produced at spin speeds of 2000 rpm and above (Figure 4.29 to Figure 4.32) did not show any areas of missing film despite similar handling to the others. As the preparation spin speed increases, the beading decreases until it is not noticeable at this scale in films produced at 6000 rpm and above.

The undoped samples are characteristic of the beading and cracking seen at the edges of all films, regardless of copper doping.

All the blue and turquoise areas in Figure 4.25 to Figure 4.28 show areas of missing photocatalyst. These areas of bare glass are caused by the beading causing thicker than expected film depths and ultimately poor adhesion. As the preparation spin speed increases to and above 2000 rpm in Figure 4.29 to Figure 4.32, there are no more areas of bare glass or damaged photocatalytic film. This is because the higher spin speeds cause a significant reduction in the beading at the edge of the films.

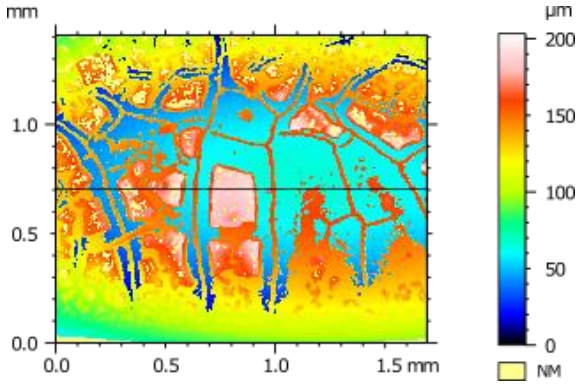

Figure 4.25: Metrology depth heat map of the edge of an undoped meso-TiO_2 film produced at 500 rpm

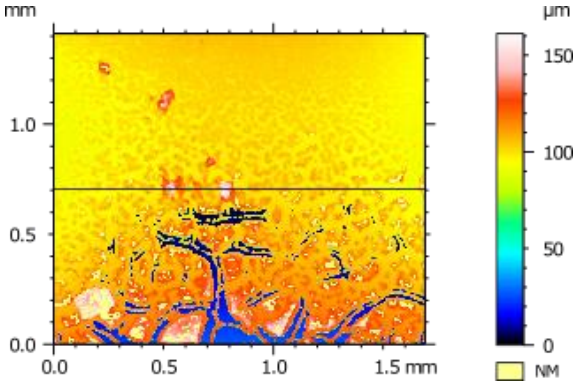

Figure 4.26: Metrology depth heat map of the near edge of an undoped meso-TiO_2 film produced at 500 rpm

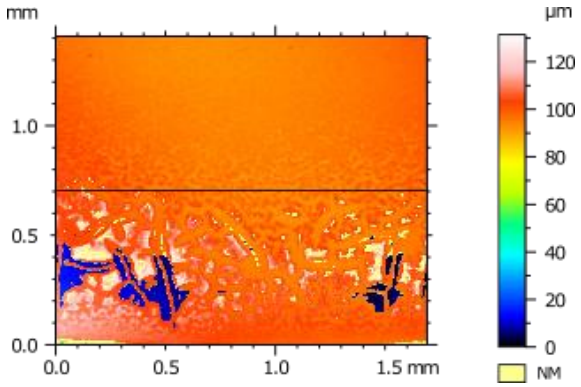

Figure 4.27: Metrology depth heat map of the edge of an undoped meso-TiO_2 film produced at 1000 rpm

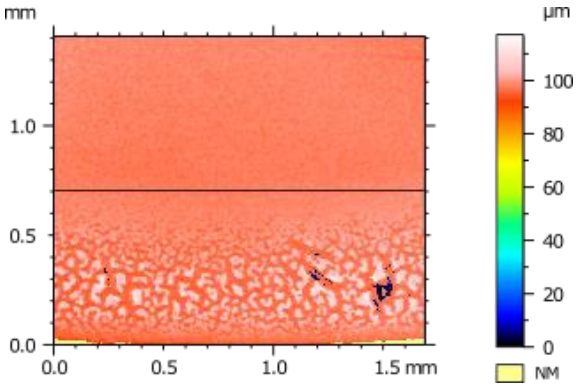

Figure 4.28: Metrology depth heat map of the edge of an undoped meso-TiO_2 film produced at 1500 rpm

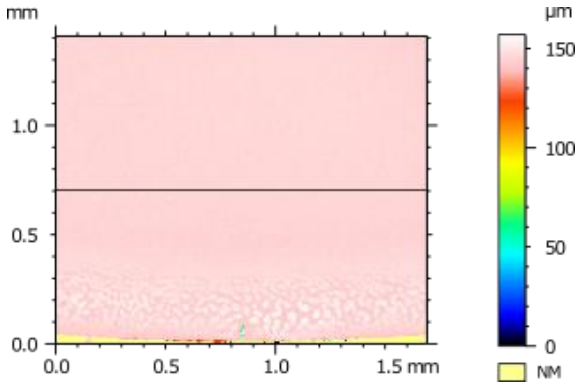

Figure 4.29: Metrology depth heat map of the edge of an undoped meso-TiO_2 film produced at 2000 rpm

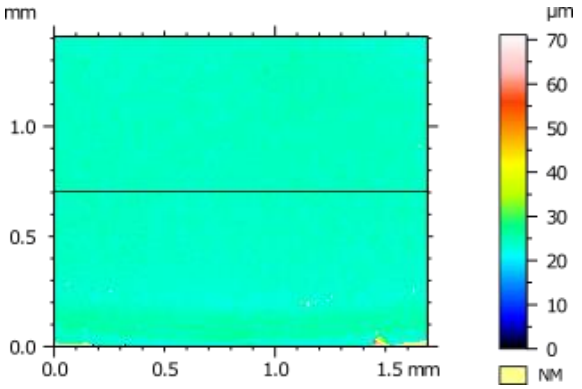

Figure 4.30: Metrology depth heat map of the edge of an undoped meso-TiO_2 film produced at 4000 rpm

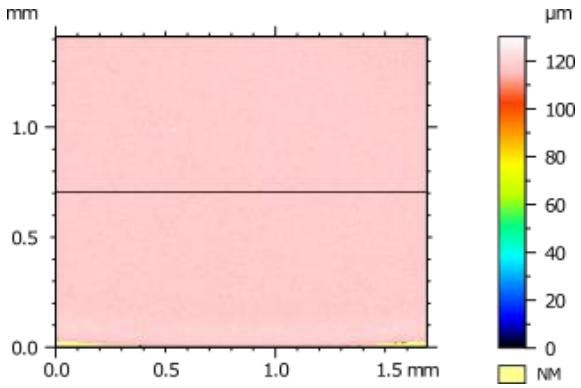

Figure 4.31: Metrology depth heat map of the edge of an undoped meso-TiO_2 film produced at 6000 rpm

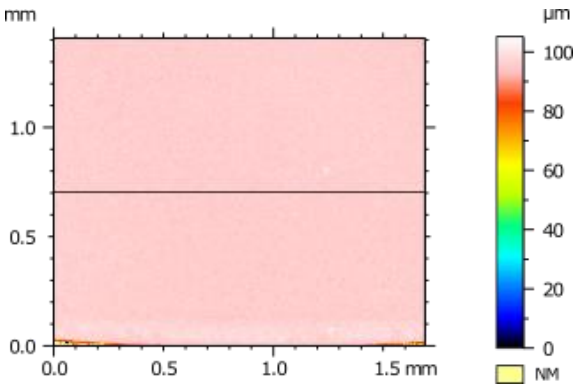

Figure 4.32: Metrology depth heat map of the edge of an undoped meso-TiO_2 film produced at 8000 rpm

4.6 Discussion

Acquiring an accurate profile of the uncoated glass coverslip proved challenging due to its transparency. As well as the missing data, there were a significant number of points that were inaccurate and had to be removed when processing the data.

The surface roughness of the coatings also presented a challenge. The software uses the average surface height of each area to calculate the step height, giving a film thickness of around 0.05 µm, but the metrology of the surface showed surface roughness of 2 µm on the thinnest films. The average height of the films was calculated using all areas of the coating, including any areas where the coating had been scratched, flaked off, and any surface roughness inherent in the material. This resulted in the recorded height being far lower than it is. The maximum height of the coating was used instead of the average. This gave much more reliable measurements of the step height, but also resulted in many unusable measurements due to debris on the surface that artificially increased the maximum height of the film.

Polymeric fluids are known to exhibit non-Newtonian behaviour and provide challenges when spin-coating. Accurate film depths were used to plot against $\sqrt{\omega}$, shedding light on the relationship between the preparation spin speed these films were prepared at and the depth of the resulting films. At low preparation spin speeds, the spin-coating solution showed Newtonian behaviour, but as the angular velocity increases the fluids start to show non-Newtonian behaviour. Plots of the film depth against $\sqrt{\omega}$ allowed the calculation of the critical shear rate for the onset of shear thickening and linear fits can be used to give the accurate film depth predictions of other films made from the same solutions. The critical shear rate and viscosity of the solutions change with the introduction of copper nitrate. The amount of copper nitrate added to the solution does not correlate with the critical shear rate nor the final film depths but there is no obvious explanation for such behaviour.

The beading at the edge of the undoped film prepared at 500 rpm measured over 90 µm in places, well above the 33 µm measured at the centre of the film. This significant change in height is due to the variation in film depth across the surface of spin-coated materials, as well as the beading that can occur when using low spin speeds or highly viscous solutions. When spin coating, a two-step process would normally be used to remove this beading, but that was not performed on these materials as the solvent intentionally wasn't fully evaporated before finishing the spin coating to optimise the EISA process.

4.7 Conclusion

Accurately measuring the film depths has revealed the nature of the solution used and will help to explain the activity of these materials as photocatalysts.

Spin-speed controls the film thickness below the critical shear rate, but at higher spin-speeds, no change is seen in film depth. The ability to accurately measure film thickness and predict the depth of subsequent films produced from the same solution is vital to being able to tailor the samples and their properties.

The thickness of these samples can be controlled within bounds that are dictated by the solution used. The non-Newtonian nature of the solution dictates the minimum thickness achievable and the spin-speed at which the minimum is achieved. The critical shear rate changes depending on the amount of copper nitrate in the solution and does not correlate with the minimum film depth.

4.8 References

1 L. M. Picco, L. Bozec, A. Ulcinas, D. J. Engledew, M. Antognozzi, M. A. Horton and M. J. Miles, *Nanotechnology*, 2006, **18**, 044030.

2 J. W. Haus, in *Fundamentals and Applications of Nanophotonics*, ed. J. W. Haus, Woodhead Publishing, 2016, pp. 185–210.

3 M. Conroy and J. Armstrong, *Journal of Physics: Conference Series*, 2006, **13**, 458.

4 W. Häßler-Grohne, D. Hueser, K.-P. Johnsen, C. Frase and H. Bosse, *Measurement Science and Technology*, 2011, **22**, 094003.

5 C. J. Lawrence and W. Zhou, *Journal of Non-Newtonian Fluid Mechanics*, 1991, **39**, 137–187.

6 Spin Coating, https://www.ossila.com/pages/spin-coating, (accessed April 7, 2020).

7 D. Meyerhofer, *Journal of Applied Physics*, 1978, **49**, 3993–3997.

8 A. G. Emslie, F. T. Bonner and L. G. Peck, *Journal of Applied Physics*, 1958, **29**, 858–862.

9 Y. Mouhamad, P. Mokarian-Tabari, N. Clarke, R. a. L. Jones and M. Geoghegan, *Journal of Applied Physics*, 2014, **116**, 123513.

10 P.-C. Nkinamubanzi, S. Mantellato and R. J. Flatt, in *Science and Technology of Concrete Admixtures*, eds. P.-C. Aïtcin and R. J. Flatt, Woodhead Publishing, 2016, pp. 353–377.

11 RheoSense, Viscosity of Newtonian and Non-Newtonian Fluids, https://www.rheosense.com/applications/viscosity/newtonian-non-newtonian, (accessed March 14, 2022).

12 Defects Found in Spin Coating, Coating Systems, Inc., https://coatingsystems.com/common-defects-found-spin-coating/, (accessed May 16, 2022).

Chapter 5. Results – Varying the Spin Speed and Layering

This chapter aims to explore the effect that the spin-coating process has on the surface coatings formulated in the previous chapter, as it is a widely used method for creating these titanium dioxide thin films.[1–3] There is a large amount of literature on both doped and undoped mesoporous titanium dioxide,[4–12] and thin films of these materials have been well studied,[2,4,6,8] yet there is very little literature exploring the effect that the spin coating process has on the resulting photocatalysts and their activity.

Some research groups have explored the use of layered spin coated films as a way of controlling the film thickness,[1–3,9] with some reporting an increase in activity with increasing numbers of layers.[1,3] Layering titanium dioxide films was explored by Khan et al. where it was discovered that the grain size increased, and the band gap decreased as layers were added,[2] suggesting that layering would have a beneficial effect on the photoactivity.[3]

Whilst adding layers certainly increases thickness of the catalyst, an alternative approach is to use the spin speed the sample is prepared at to influence the coating thickness. None of the papers that explored the layering of spin-coated titanium dioxide have tried to compare layered films to films produced at a variety of spin speeds. In this chapter as well as producing films with different numbers of layers, the preparation spin speed was altered to see what effect could be seen in the activity of the resulting films. The comparison between these two groups of samples will help to decipher whether any changes in activity come from changes in films thickness and therefore the amount of material present, or other effects from the spin-coating process.

There are several different ways that the thickness of a film can be influenced during production depending on the technique used. Dip coating, where the substrate is immersed in a solution and dried to form a film uses the withdrawal rate from the solution to control thickness.[13] The thickness of a film produced using the doctor blade technique is controlled by the distance the blade is placed from the surface as a highly viscous solution is deposited onto a surface and a blade is moved across the surface at a maintained distance to deposit a wet film.[14] Spin-coating uses increasing centrifugal force and rapid evaporation of solvent to produce thinner films. It is unclear how this might affect the templating polymer and the resulting photocatalytic films.

5.1 Varying the thickness by layering

A series of films were produced by layering multiple porous TiO_2 films on top of one another, with the total number of layers being between 1 and 10. The samples were allowed to partially dry on the spin coater, but were not placed in the oven, or calcined between the addition of each successive layer. This gave the best opportunity for the addition of multiple layers to increase the film depth, while retaining the porous structure throughout the entire depth of the samples.

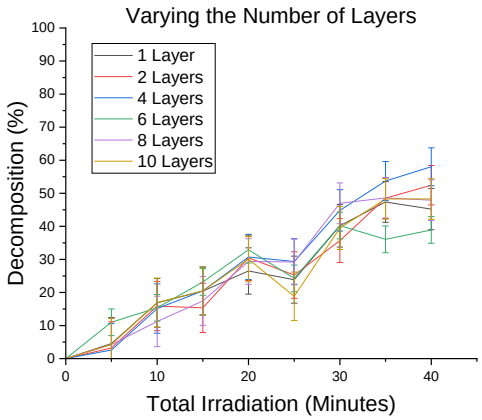

Figure 5.1: A graph showing the decomposition of stearic acid over layered, mesoporous TiO_2 films

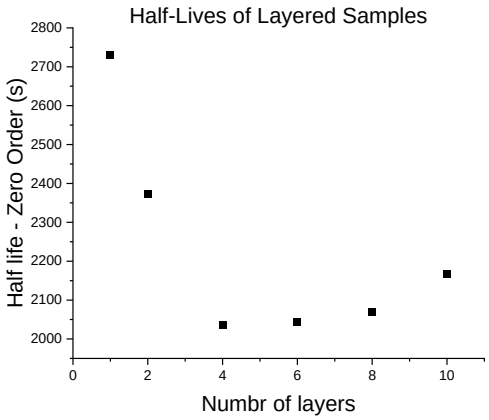

Figure 5.2: A graph showing the half-lives of stearic acid decomposition over layered photocatalysts

Figure 5.1 shows the decomposition of stearic acid over these films over the course of 40 minutes. Figure 5.2 and Table 5.1 show the half-lives of stearic acid decomposition over the layered films against the number of layers. The half-lives decrease rapidly with increasing numbers of photocatalyst coatings until 4 layers where it starts to increase with increasing layers. All samples showed zero order kinetics with respect to the decomposition of stearic acid.

Number of layers	Half-lives (s)
1	2729
2	2327
4	2035
6	2043
8	2069
10	2166

Table 5.1: Half-lives of the decomposition of stearic acid over layered samples

Despite the decreasing half-lives of stearic acid decomposition over these samples, they still perform significantly worse than samples where the preparation spin speed dictates the film

thickness. None of the samples were able to decompose more than 60 % of the stearic acid within 40 minutes.

The inability of these samples to completely decompose the stearic acid on the surface is unusual for their composition and the spin speed they were produced at. The increased time spent on the spin coater has the potential to remove more solvent than desired for the EISA process to be effective. This could explain the greatly increased half-lives seen in these samples when compared to samples that were spin-coated with the reduced spin-time used in other samples.

5.2 Varying the film thickness by spin speed

5.2.1 Low spin speeds from 600 to 2000 rpm

A series of films produced at spin speeds between 600 and 2000 rpm were tested to see how quickly they decomposed stearic acid. According to Meyerhofer,[15] for a Newtonian fluid, the square of the spin speed is inversely proportional to the thickness of the resulting film, with higher spin speeds producing thinner films. There are a number of other factors that help to determine the final resulting film thickness, but no single equation has been devised that will accurately determine the film thickness in all applications.[15–18]

Preparation spin speed (rpm)	**Maximum Decomposition (%)**	**Time to Maximum Decomposition (minutes ± 2.5)**
600	97.9 ± 4.1	20
800	98.5 ± 4.1	20
1000	97.3 ± 4.2	20
1200	96.0 ± 4.2	35
1400	96.4 ± 4.2	30
1600	93.4 ± 4.3	40
1800	93.1 ± 4.3	40
2000	91.5 ± 4.4	40

Table 5.2: The maximum decomposition and time to reach these values by samples produced with spin speeds between 600 and 2000 rpm. The first values within the stated error of 100 % decomposition were reported as the maximum decomposition at the given time.

Table 5.2 shows the maximum decomposition of stearic acid during the 40 minute irradiation of the photocatalysts as well as the time taken to reach 100 % decomposition for those that

decomposed all the stearic acid before the end of the experiment. The thickest film, produced at 600 rpm, decomposed 98 % of the stearic acid over 20 minutes, with the sample prepared at 2000 rpm decomposing 91.5 % over 20 minutes, but failing to decompose the remaining stearic acid over the final 20 minutes.

There is a clear trend of increasing activity with increasing preparation spin speed up to 1400 rpm, as can be seen from the half-lives in Figure 5.4. The samples produced at 800 and 1000 rpm both reached similar maximum decompositions by 20 minutes, but the half-life of the sample produced at 1000 rpm is significantly lower. This trend in decreasing half-life continues until the sample produced at 1400 rpm where the half life begins to increase until the preparation spin speed reaches 1800 rpm. The half-life of the sample produced at 2000 rpm drops to 541 s, but paired with the maximum decomposition of 91.5 % at 20 minutes, it is a less effective photocatalyst than the half-life in isolation suggests.

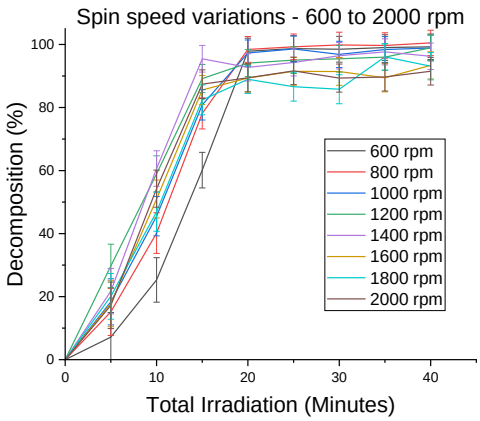

Figure 5.3: The decomposition of stearic acid over mesoporous TiO_2 films produced at spin speeds between 600 and 2000 rpm over 40 minutes

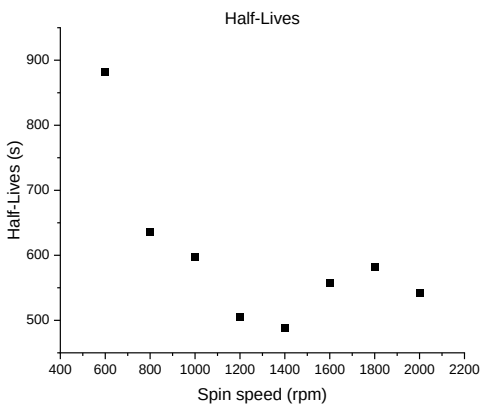

Figure 5.4: The half-lives of stearic acid decomposition over photocatalytic samples produced at spin speeds from 600 to 2000 rpm

5.2.2 Spin speeds from 600 to 8000 rpm

Figure 5.5 shows the half-lives of stearic acid decomposition over samples produced at spin speeds between 600 and 8000 rpm. As the spin speed used to produce each photocatalytic film is increased, the activity of the sample increases, with the sample prepared at 600 rpm having a half-life of 881 seconds, and the most active sample was prepared at 7000 rpm having a half-life of 205 seconds.

The zero and first order rate plots for the *meso*-TiO_2 samples discussed in this chapter are in Appendix 1, Figure A1.51 to Figure A1.66. As can be seen from the plots, the samples produced at spin speeds from 500 to 2500 rpm show zero order kinetics with respect to the decomposition of stearic acid, however, stearic acid decomposition over the samples produced from 3000 to 8000 rpm shows first order kinetics.

Reactions over samples produced at spin speeds from 600 to 2000 rpm exhibit zero order kinetics and have half-lives ranging from 881 seconds over the sample produced at 600 rpm, decreasing to a minimum half-life of 488 seconds over the sample produced at 1400 rpm before increasing to 581 and 541 seconds over the samples produced at 1800 and 2000 rpm respectively. Stearic acid decomposition over samples produced at spin speeds from 3000 rpm to 8000 rpm exhibit first order kinetics, with half-lives decreasing from 389 seconds over the sample produced at 3000 rpm through to 205 seconds over the sample produced at 7000 rpm. The half-life of the reaction over the sample produced at 8000 rpm shows a slight increase to 255 seconds.

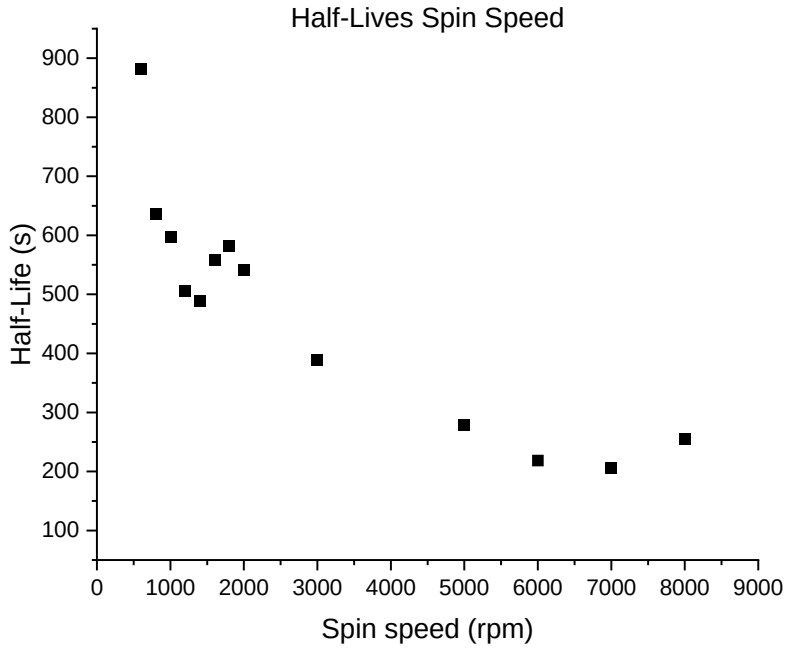

Figure 5.5: The half-lives of stearic acid decomposition over meso-TiO_2 samples produced at spin speeds of 600 to 8000 rpm

5.2.3 Half-Lives and Film Thickness

The film depths for single layer films produced at spin speeds between 500 and 8000 rpm were calculated as described in Chapter 4. Samples produced at spin speeds below 3000 rpm follow the expected relationship between spin speed and film depth for Newtonian fluids,[13] but the

thickness of samples produced at spin speeds of 3000 rpm and above is dominated by shear thickening of the fluid so there is very little change in film thickness.

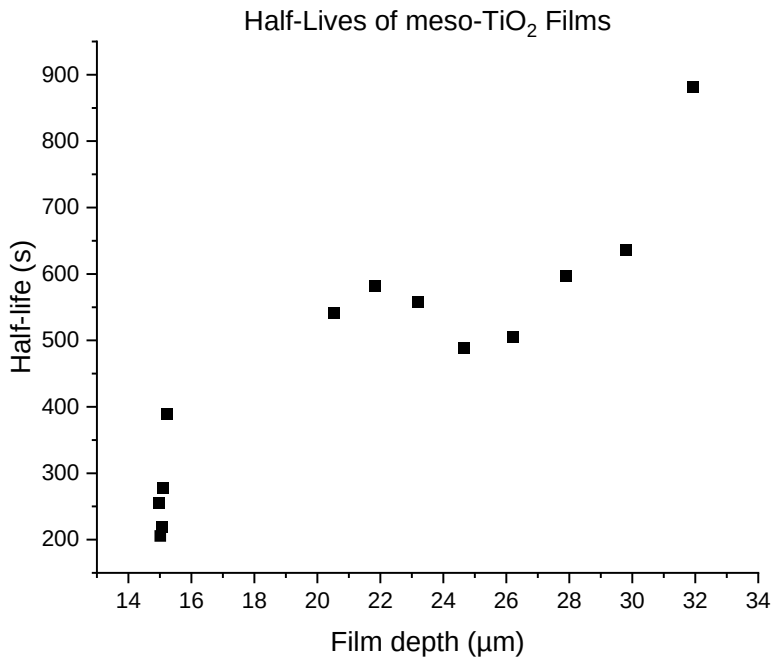

Figure 5.6: Half-lives of stearic acid decomposition over meso-TiO_2 films plotted against the film depths of the photocatalysts

Figure 5.6 shows the half-lives of the relevant reaction plotted against the film depth of the photocatalyst. The trend between spin speed during photocatalyst preparation and the half-life of reaction over the films is preserved at photocatalyst preparation speeds between 500 and 3000 rpm, where the final film depth is dominated by the preparation spin speed. For samples produced at spin speeds above 3000 rpm, where shear thickening dictates the resulting film thickness, the film thickness stays the same when spin speed is changed.

Increased film depth of porous films will result in a higher surface area, an increase in surface oxygen species, and more material capable of absorbing UV light. This should result in an increased activity and therefore a decrease in half-life of reaction over these samples. Figure 5.6 shows the half-lives of the decomposition of stearic acid over these samples, plotted against the measured film depth. Instead of observing the expected trend of half-life reducing with increasing film depth, the half-life increases as film depth increases. The topmost surfaces are the only part of the photocatalytic films that are in contact with the stearic acid as shown in Chapter 8. The

topography and imaging of the surfaces of these films showed that there are marked changes in the surface roughness and homogeneity of the surface appearance. These changes were correlated to spin speed and continued to progress after the spin speed increased above the critical shear rate and the film depths reached their minimum. This combination of evidence suggests that the formation mechanics of the film during the spin-coating process are influencing the surface and leading to an increased activity as the films get thinner and the spin speed increases.

5.3 Tauc plots

Tauc plots of the photocatalytic films prepared at spin speeds of 500 and 4000 rpm (Figure 5.7 and Figure 5.8) gave bandgaps of 3.13 and 3.17 eV respectively. These values are within the error for these measurements, so the preparation spin speed between 500 and 4000 rpm in these undoped films can be discounted as a contributing factor. While the bandgaps do not change between preparation spin speeds of 500 and 4000 rpm, they are slightly lower than would be expected from anatase TiO_2.

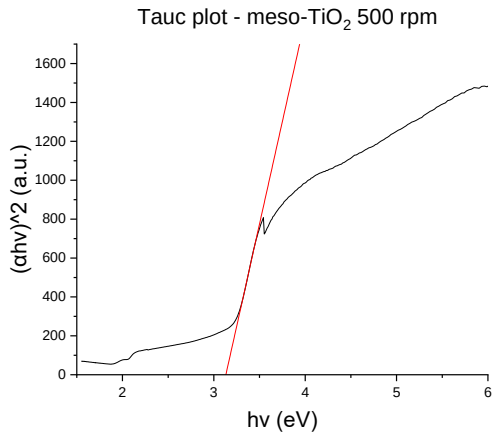

Figure 5.7: Tauc plot of a meso-TiO_2 film prepared at 500 rpm

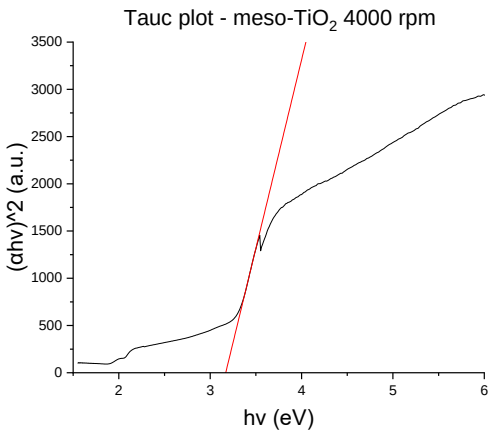

Figure 5.8: Tauc plot of a meso-TiO_2 film prepared at 500 rpm

5.4 Discussion

The layering of spin-coated films has been reported in the literature to result in increasing activity.[1,3] Layered films can be produced by depositing multiple layers of the spin coating solution onto the surface with or without calcination in between layers. Typically, at low preparation spin

speeds, there are a significant number of film defects when working with these solutions. Beading and thick single layers cause poor adhesion, especially at the edges and at low preparation spin speeds, there were a high number of failed or partly damaged and missing films. Layering could provide a way of achieving greater film depths without compromising the integrity of the film.

In the present work the half-lives of the photocatalytic decomposition of a layer of stearic acid on the layered films reached a minimum at 4 layers. The 25 % decrease in reaction half-life over a photocatalyst that has been prepared with 1 to 4 layers was much more significant than the subsequent increase in half-life as the number of layers was increased to 10. Atay produced multi-layered TiO_2 films by sol-gel spin-coating and XRD patterns of the samples indicated improvements in crystallization levels.[3] They found the optimal number of layer to be 6-7 when produced at 2500 rpm and calcined at 600 °C. Gent found that adding multiple layers of mesoporous TiO_2 by dip coating resulted in lowered bandgap energy with increasing numbers of coatings.[8] Khan used a sol-gel spin-coating techniques to produce multilayer TiO_2 films[2] and, similar to the samples produced in this work, samples were not calcined between the addition of additional layers and samples were produced with between 1 and 4 layers at 2400 rpm. Grain size was calculated and found to increase with the increasing number of layers.

The layered films produced in this chapter were not directly comparable to the other samples tested in this chapter as the light source was serviced in between the photocatalytic testing on the layered films and samples produced by varying the preparation spin speed but the trends can be compared and a 25 % decrease in the half-life of reaction over the samples prepared at 2000 rpm would result in a half-life of 403 seconds.

The layered films were all produced at 2000 rpm. Knowing that the preparation spin speed also affects the activity of the resulting samples, in future work, it would be worthwhile exploring if the effect of layering on the rate of stearic acid decomposition was similar when films were deposited sequentially at other spin speeds. The samples produced at 7000 rpm were the most active of the samples produced at varied spin speeds and it is plausible that layering could be used to further improve the functioning of these photocatalysts.

The half-lives of the decomposition of stearic acid over the films produced at different spin speeds varied from 205 to 881 seconds. The most active films were produced at high spin speeds, where despite very little change in film depth, the half-lives continued to reduce over samples produced using a spin speed of up to 7000 rpm.

Samples produced at spin speeds from 500 to 2500 rpm showed zero order kinetics for the degradation of stearic acid. From preparation spin speeds of 3000 to 8000 rpm, reaction over the samples followed first order kinetics. The change in kinetics was mirrored by the forces driving the film thicknesses. At preparation spin speeds below 2930 rpm, the film thickness is proportional to $\sqrt{\omega}$ as is expected for Newtonian fluids.[15] Above 2930 rpm, the increased angular velocity causes increasing shear thickening that prevents the films from becoming thinner at higher spin speeds. Given that the thickness does not change in samples prepared at spin speeds from 3000 to 8000 rpm, the forces involved in the spin coating process are the most likely factor that could change the activity of these films but there isn't any direct evidence to account for why the spin speed should affect catalytic performance, different grain size, different morphological features could all have subtle effects and in future work a closer look at these properties should be carried out.

One of the drawbacks of titanium dioxide as a photocatalyst is the large bandgap at 3.2 eV. Tauc plots of samples of spin coated *meso*-TiO_2 showed bandgaps of 3.13 to 3.17 eV, slightly below the bandgaps of commercially available TiO_2. Changes in bandgap energy of TiO_2 have been linked to grain size, surface oxygen species and doping[19–21] and since the preparation spin speed has a significant effect on catalytic activity there may be a link between all these factors.

5.5 References

1 Institute of Microengineering and Nanoelectronics (IMEN), Universiti Kebangsaan Malaysia,43600, Bangi, Selangor, Malaysia and S. N. Sadikin, *Int. J. Electrochem. Sci.*, 2017, 5529–5538.

2 M. I. Khan, K. A. Bhatti, R. Qindeel, H. S. Althobaiti and N. Alonizan, *Results in Physics*, 2017, **7**, 1437–1439.

3 F. Atay and D. Durmaz, *Journal of Elec Materi*, 2020, **49**, 5542–5551.

4 Z. Bai, Y. Hu, S. Yan, W. Shan and C. Wei, *RSC Adv.*, 2017, **7**, 1966–1974.

5 Z. Xiong, J. Ma, W. J. Ng, T. D. Waite and X. S. Zhao, *Water Research*, 2011, **45**, 2095–2103.

6 J. H. Pan, Z. Lei, W. I. Lee, Z. Xiong, Q. Wang and X. S. Zhao, *Catal. Sci. Technol.*, 2011, **2**, 147–155.

7 V. Kalousek, J. Tschirch, D. Bahnemann and J. Rathousky, *Superlattices and Microstructures*, 2008, **44**, 506–513.

8 E. Gent, D. H. Taffa and M. Wark, *Coatings*, 2019, **9**, 625.

9 J. Rathouský, M. Slabová, K. Macounová and A. Zukal, in *Studies in Surface Science and Catalysis*, eds. A. Sayari and M. Jaroniec, Elsevier, 2002, vol. 141, pp. 599–606.

10 A.-H. Lu and F. Schüth, *Comptes Rendus Chimie*, 2005, **8**, 609–620.

11 L. Zhang, L. Jin, B. Liu and J. He, *Front. Chem.*, , DOI:10.3389/fchem.2019.00022.

12 R. Trofimovaite, C. M. A. Parlett, S. Kumar, L. Frattini, M. A. Isaacs, K. Wilson, L. Olivi, B. Coulson, J. Debgupta, R. E. Douthwaite and A. F. Lee, *Applied Catalysis B: Environmental*, 2018, **232**, 501–511.

13 J. E. ten Elshof, in *Epitaxial Growth of Complex Metal Oxides*, eds. G. Koster, M. Huijben and G. Rijnders, Woodhead Publishing, 2015, pp. 69–93.

14 R. Cherrington and J. Liang, in *Design and Manufacture of Plastic Components for Multifunctionality*, eds. V. Goodship, B. Middleton and R. Cherrington, William Andrew Publishing, Oxford, 2016, pp. 19–51.

15 D. Meyerhofer, *Journal of Applied Physics*, 1978, **49**, 3993–3997.

16 A. G. Emslie, F. T. Bonner and L. G. Peck, *Journal of Applied Physics*, 1958, **29**, 858–862.

17 Y. Mouhamad, P. Mokarian-Tabari, N. Clarke, R. a. L. Jones and M. Geoghegan, *Journal of Applied Physics*, 2014, **116**, 123513.

18 Y. Yan, P. Zhou, S.-X. Zhang, X.-G. Guo and D.-M. Guo, *Chinese Physics B*, 2018, **27**, 068104.

19 Y.-C. Lee, Y.-S. Chang, L. Teoh, Y. Huang and Y. Shen, *Journal of Sol-Gel Science and Technology*, 2010, **56**, 33–38.

20 C. Dette, M. A. Pérez-Osorio, C. S. Kley, P. Punke, C. E. Patrick, P. Jacobson, F. Giustino, S. J. Jung and K. Kern, *Nano Lett.*, 2014, **14**, 6533–6538.

21 T. M. Breault and B. M. Bartlett, *J. Phys. Chem. C*, 2012, **116**, 5986–5994.

Chapter 6. Results – Copper doping

Copper has been investigated as a dopant for titania due to its ability to increase the photocatalytic degradation properties of undoped titania.[1–5] The range of copper content in materials studied varies widely from mixed oxides to single atom Cu(I) surface species.[6–8]

Instead of modifying materials that are already formed, the decision was made to introduce the copper into the material before spin-coating. All the copper-doped *meso*-TiO_2 films were produced in the same way as undoped films except for the addition of copper nitrate while stirring the solution.

Appendix 2 contains the rate plots and rate constants of stearic acid decomposition over all samples discussed in this chapter. Figures A2.1 to A2.154 concern the 5 wt% copper-doped samples, Figure A2.155 to A2.188 concern the 2.5 wt% copper doped samples, Figures A2.189 to A2.274 concern the 1 wt% coper doped samples, Figures A2.275 to A2.312 concern the 0.5 wt% copper-doped samples and Figures A2.313 to A2.382 concern the 0.1 wt% copper doped samples. Appendix 5, Figure A5.1 to Figure A5.442, contains DRIFT spectra of stearic acid on the samples discussed in this chapter.

6.1 Photocatalytic testing

6.1.1 Stearic Acid Decomposition over 5 wt% Copper-Doped *meso*-TiO_2

Zero and first order reaction plots of the degradation of stearic acid on 5 wt% Cu-doped *meso*-TiO_2 films showed that the order of the reaction changed with the spin speed used to produce the photocatalytic films. Reaction over samples produced at spin speeds from 500 to 1500 and 6000 to 8000 rpm showed first order reaction kinetics, while reaction over the samples produced at spin speeds from 2000 to 5500 rpm showed zero order reaction kinetics.

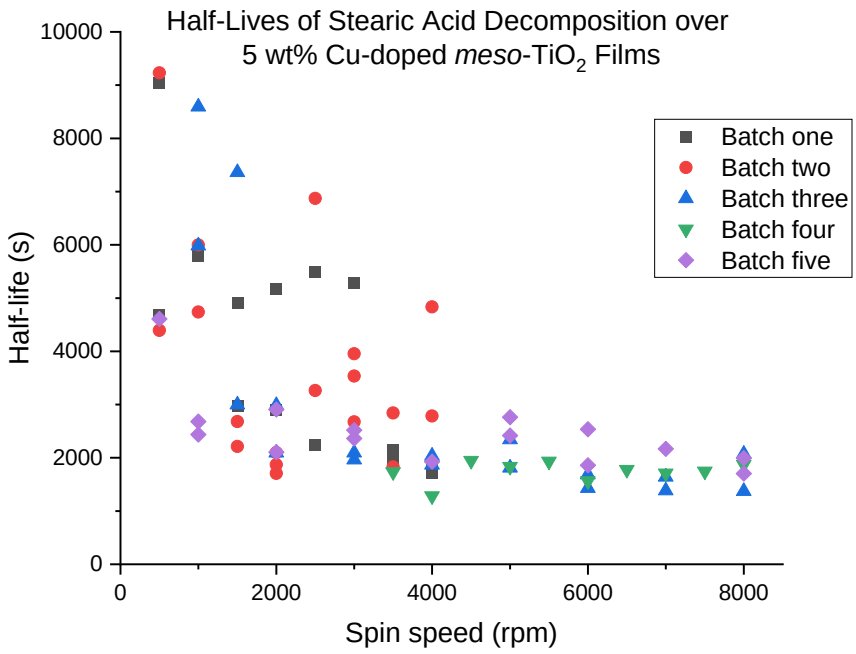

Figure 6.1: Half-lives of stearic acid decomposition on 5 wt% copper-doped meso-TiO_2 samples plotted against the spin speed at which they were produced

Figure 6.1 shows the half-lives of stearic acid decomposition on all 5 wt% Cu samples tested showing the reactivity of each separate batch produced. Each batch was produced from a single solution, and each sample was treated identically. The separate batches had a wide range of half-lives at lower preparation spin speeds, but the half-lives were much more consistent when the photocatalytic films were produced at speeds above 4000 rpm. At lower preparation spin speeds, even within a single batch, there was significant scatter, with some half-lives nearly double those of samples produced at the same spin-speed from the same solution.

This issue of consistency was due in large part to adhesion issues in samples produced at lower spin speeds, as the technique gave films that tended to be fragile and partly flake off or become detached when handled during the photocatalytic testing. The inconsistency in reaction half-lives reduced with thinner films. At higher preparation spin speeds, the half-lives are consistent, even across the different batches. No major changes in activity can be observed at the spin speeds used to produce photocatalytic films where reaction over the photocatalysts changes between zero and first order kinetics. The trends are gradual across the range of preparation spin speeds tested.

Even at their most active, the 5 wt% films are still significantly less active than the undoped films as can be seen in Figure 6.2 below.

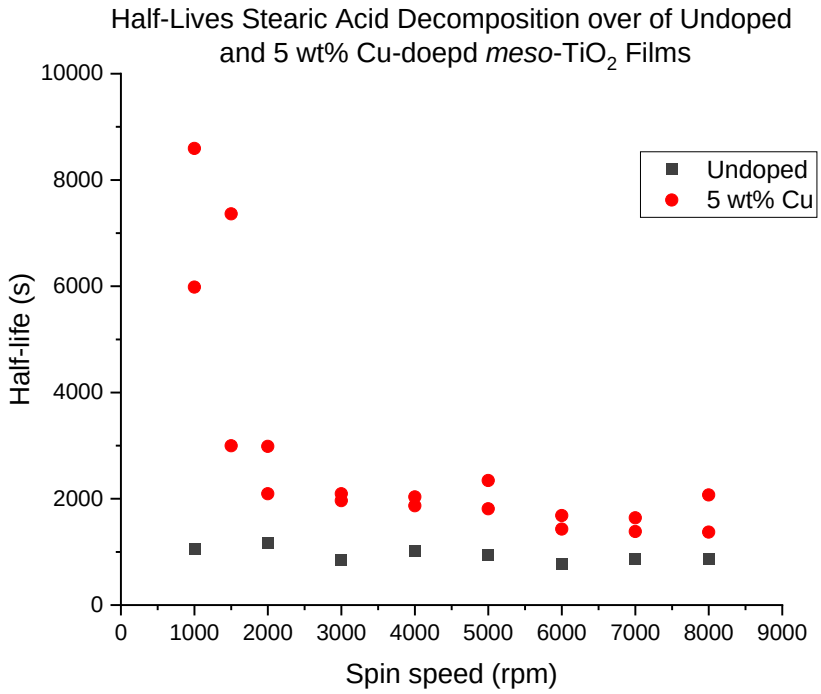

Figure 6.2: half-lives of stearic acid decomposition on undoped and 5 wt% copper-doped titanium dioxide photocatalytic films as a function of the spin speed used to produce the photocatalytic films

Figure 6.3 shows the average half-lives of stearic acid decomposition on 5 wt% copper-doped *meso*-TiO_2 films plotted against the film depth calculated in Chapter 4. At preparation spin speeds around 500 rpm, the films measure around 50 µm in depth and above preparation spin speeds of 1500 rpm, they are approximately 13 µm in depth with very little change in depth at higher preparation spin speeds. As discussed in Chapter 4 shear thickening starts to affect the film depth at preparation spin speeds above 1500 rpm which also coincides with the change in the kinetics of reaction over these films from first order to zero order described above. Despite less than 2 µm changes in film depth when the preparation spin speed changes from 2000 to 8000 rpm, there is a reduction in the calculated half-lives of the reaction over these samples from 2500 to 1700 seconds. The effect of the spin coating process is therefore not simply related to the film depth.

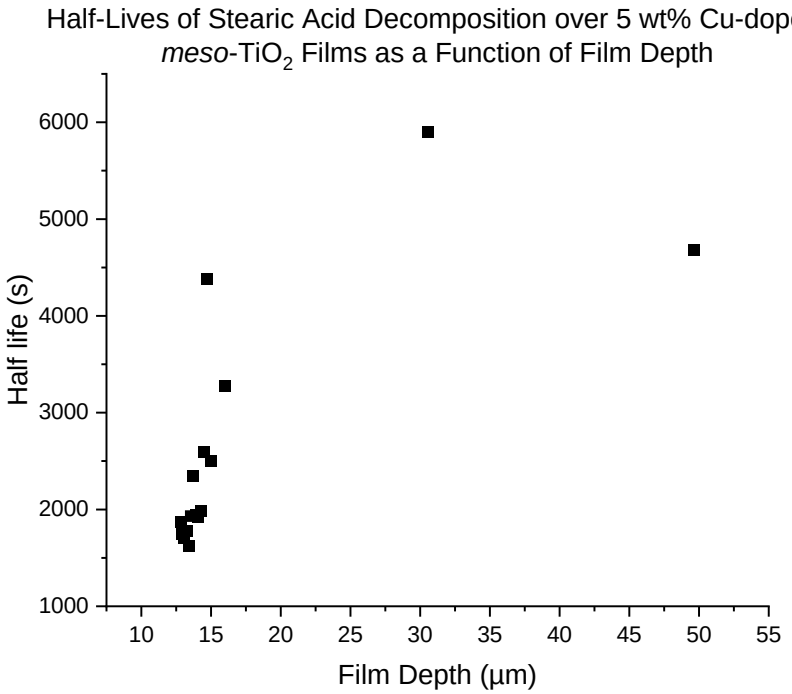

Figure 6.3: The half-lives of stearic acid decomposition on 5 wt% Cu-doped meso-TiO_2 plotted against the film depth

Tauc plots (Figure 6.5 to Figure 6.9 on page 83) for samples produced at 500, 1000, 2000, 3000 and 4000 rpm gave band gaps from 2.68 to 3.03 eV. Figure 6.4 shows a plot of the calculated bandgaps against the spin speed at which they were prepared. The band gap increases with increasing preparation spin-speed, with the sample prepared at 500 rpm having a band gap of 2.68 eV with a sharp increase up to 2.88 eV for the material prepared at 1000 rpm. There is a slight increase in band gap energy from the sample prepared at 1000 rpm to the sample prepared at 4000 rpm where the band gap energy was calculated at 3.04 eV.

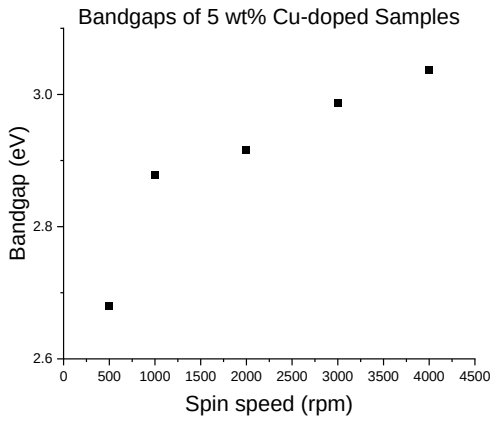

Figure 6.4: The bandgaps calculated from the Tauc plots below plotted against the spin speed at which they were prepared

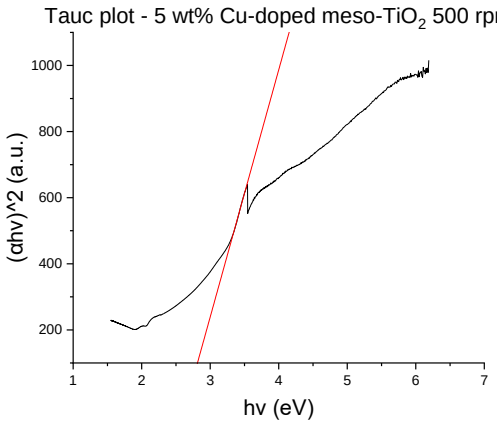

Figure 6.5: Tauc plot of a 5 wt% copper-doped meso-TiO_2 sample produced at 500 rpm

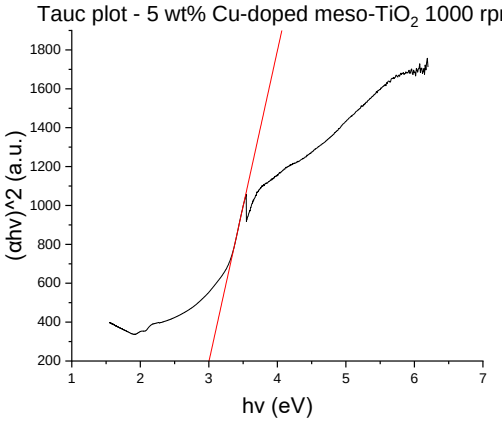

Figure 6.6: Tauc plot of a 5 wt% copper-doped meso-TiO_2 sample produced at 1000 rpm

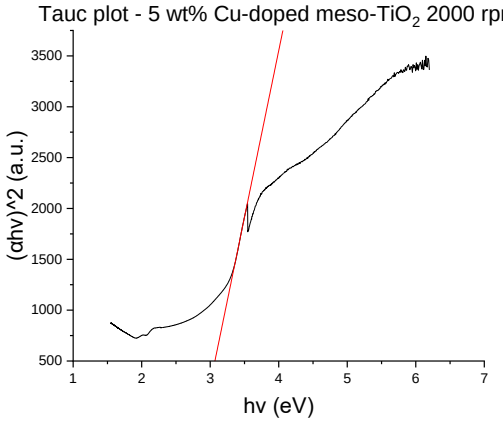

Figure 6.7: Tauc plot of a 5 wt% copper-doped meso-TiO_2 sample produced at 2000 rpm

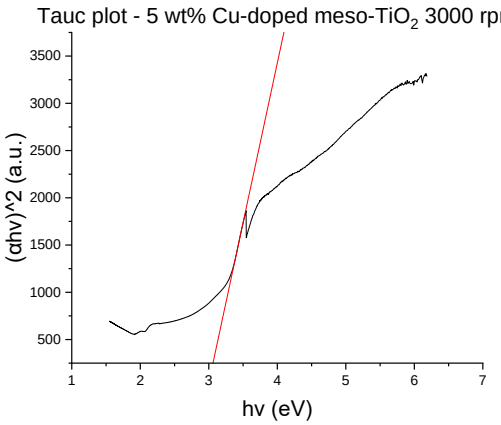

Figure 6.8: Tauc plot of a 5 wt% copper-doped meso-TiO_2 sample produced at 3000 rpm

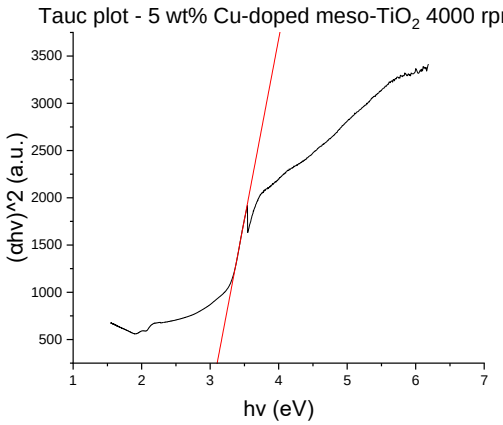

Figure 6.9: Tauc plot of a 5 wt% copper-doped meso-TiO_2 sample produced at 4000 rpm

6.1.2 Stearic Acid Decomposition over 2.5 wt% Copper-Doped *meso*-TiO_2

As with the 5 % samples above, Stearic acid decomposition over the thickest and thinnest films produced with 2.5 % copper content showed first order kinetics, with reaction over the photocatalysts prepared from 3000 to 7000 rpm exhibiting zero order kinetics.

Despite being more active than the 5 wt% samples, these samples were still less active than the undoped films. The half-lives of stearic acid decomposition over the samples in this section are significantly lower at low preparation spin speeds compared to reaction over the 5 wt% Cu-doped films as can be seen in Figure 6.13. The half-lives of these samples increase by over 500 seconds from samples prepared at 500 to 1500 rpm. Reaction over samples prepared at spin speeds from 2000 to 8000 rpm shows a gradual decrease in half-life, but very little change can be observed.

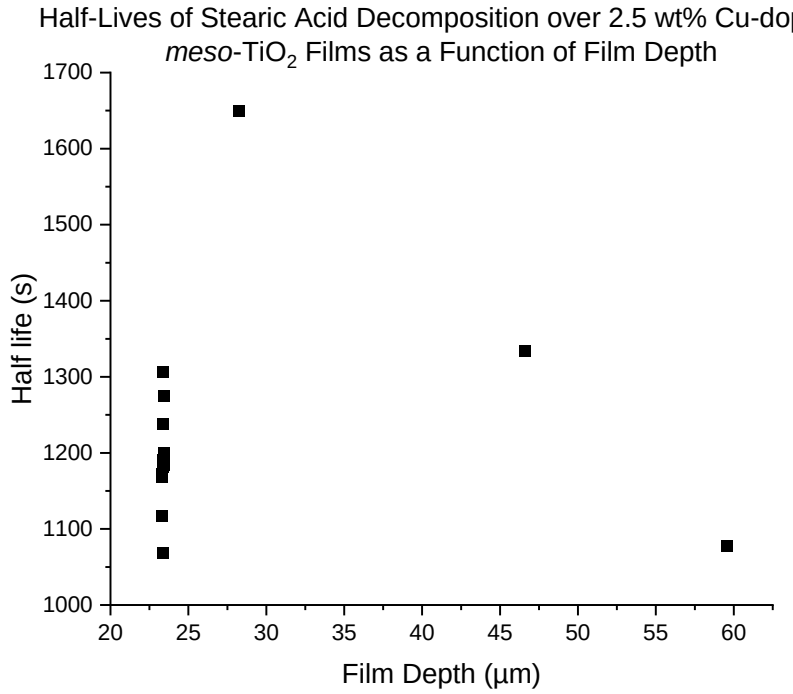

Figure 6.10: The half-lives of stearic acid decomposition over 2.5 wt% Cu-doped meso-TiO_2 plotted against the photocatalyst film depth

As with the 5 wt% copper-doped samples, the transition from first order to zero order kinetics of stearic acid decomposition coincides with the critical shear rate as discussed in Chapter 4. There is a large linear increase in half life with decreasing film thickness from 60 to 25 µm film thickness. As shear thickening forces drive the film thickness below 25 µm and the film thickness does not change, there is no correlation between film thickness and half-life.

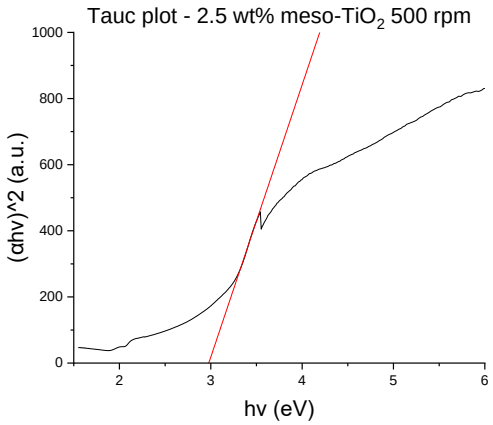

Figure 6.11: Tauc plot of a 2.5 wt% meso-TiO_2 sample produced at 500 rpm

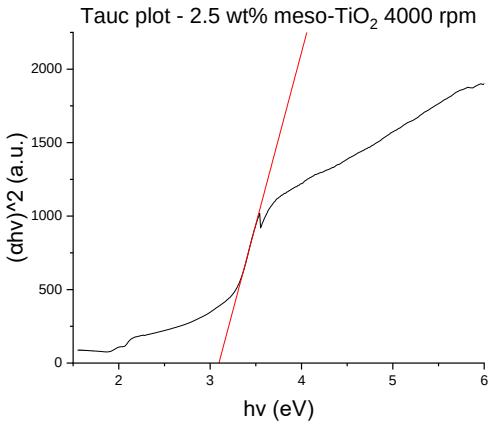

Figure 6.12: Tauc plot of a 2.5 wt% meso-TiO_2 sample produced at 4000 rpm

Tauc plots for samples prepared at spin speeds of 500 and 4000 rpm (Figure 6.11 and Figure 6.12) gave band gaps of 2.97 and 3.09 eV respectively. Unlike the 5 wt% samples, the change here is minimal and not outside of the errors associated with these measurements. The conclusion must be that the band gap of the 2.5 wt% films does not change with the preparation spin speed between 500 and 4000 rpm.

6.1.3 Stearic Acid Decomposition over 1 wt% Copper-Doped *meso*-TiO_2

The half-lives of stearic acid decomposition over the 1 wt% copper-doped films are higher than those for undoped films. There is a slight decrease in half-life with preparation spin speed from 2500 to 8000 rpm from 1473 to 996 seconds.

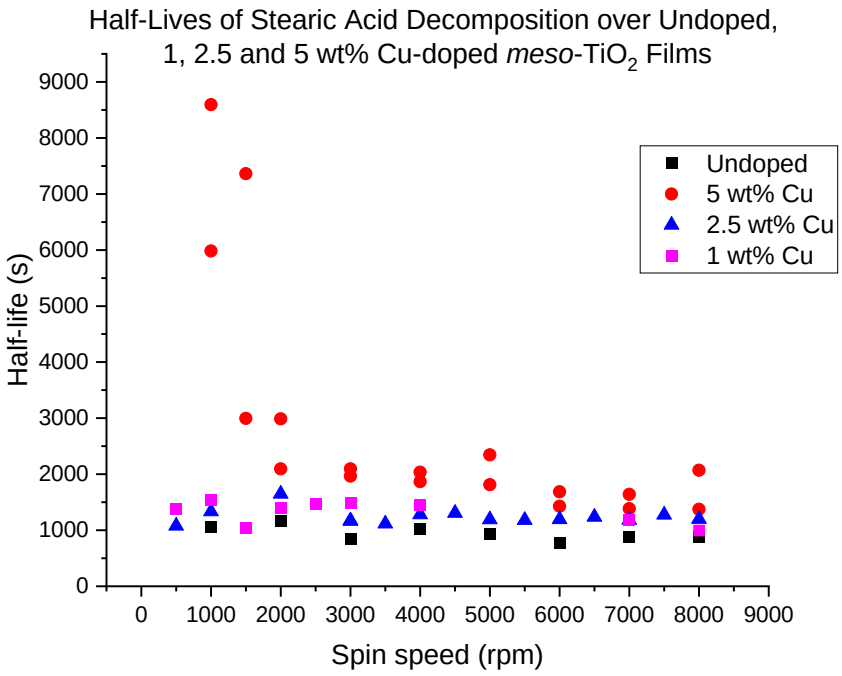

Figure 6.13: The half-lives of stearic acid decomposition on undoped, 1, 2.5 and 5 wt% Cu-doped meso-TiO_2 photocatalysts plotted against preparation spin speed

The gradual reduction in half-life of the decomposition reaction seen when plotted against preparation spin speed Figure 6.13 is not repeated when the half-life of the reaction over 1 wt% Cu samples are plotted against film thickness, Figure 6.14. The shear thickening forces dominate in these samples from a preparation spin speed of 1900 rpm and the reaction half-life gradually declines from preparation spin speeds of 2000 to 8000 rpm. It was not possible to determine which reactions progressed by zero or first order kinetics for this group of samples.

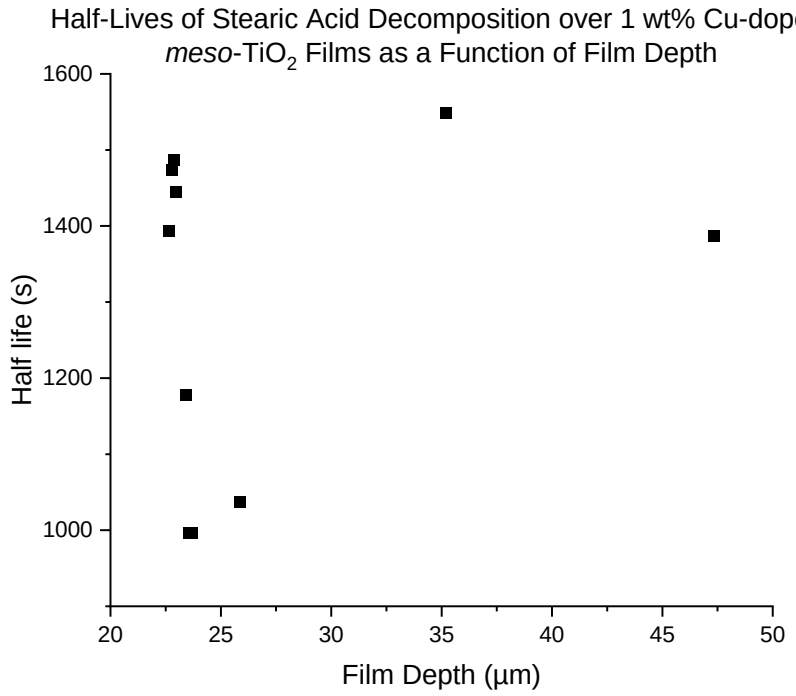

Figure 6.14: The half-lives of stearic acid decomposition on 1 wt% Cu-doped meso-TiO_2 films plotted against film depth

Tauc plots of samples produced at 500 and 4000 rpm (Figure 6.15 and Figure 6.16) gave band gaps of 3.05 and 3.13 eV. As with the 2.5 wt% samples, this is within a margin of error for these calculations so will not be considered an increase in band gap energy.

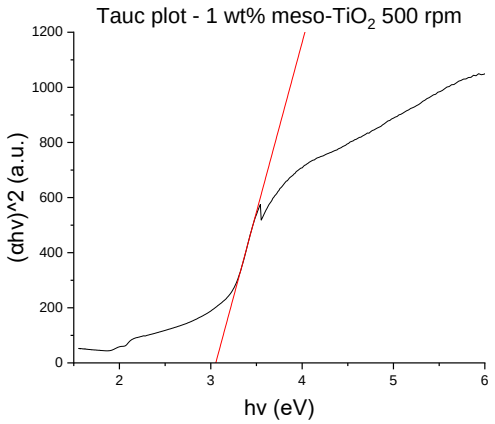

Figure 6.15: Tauc plot of a 1 wt% meso-TiO_2 sample produced at 500 rpm

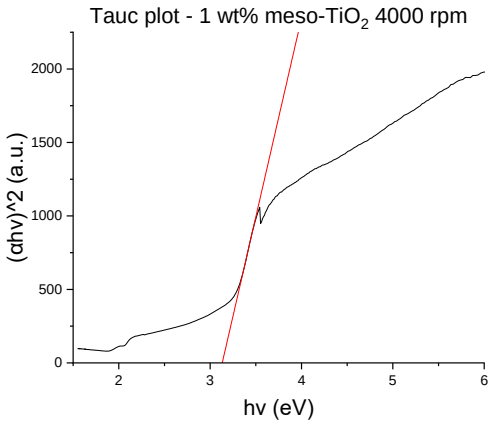

Figure 6.16: Tauc plot of a 1 wt% meso-TiO_2 sample produced at 4000 rpm

6.1.4 Stearic Acid Decomposition over 0.5 wt% Copper-Doped *meso*-TiO_2

The 0.5 wt% Cu-doped samples all showed zero order kinetics with respect to the decomposition of stearic acid.

In contrast to the 5, 2.5 and 1 wt% copper doped samples, the 0.5 wt% samples have significantly lower reaction half-lives than the undoped films at preparation spin speeds above 2000 rpm. The half-lives increase up to a preparation spin speed of 4000 rpm before reducing back down towards 8000 rpm. There is an increase in activity seen at preparation speeds of 6000 rpm that is also seen in the undoped films.

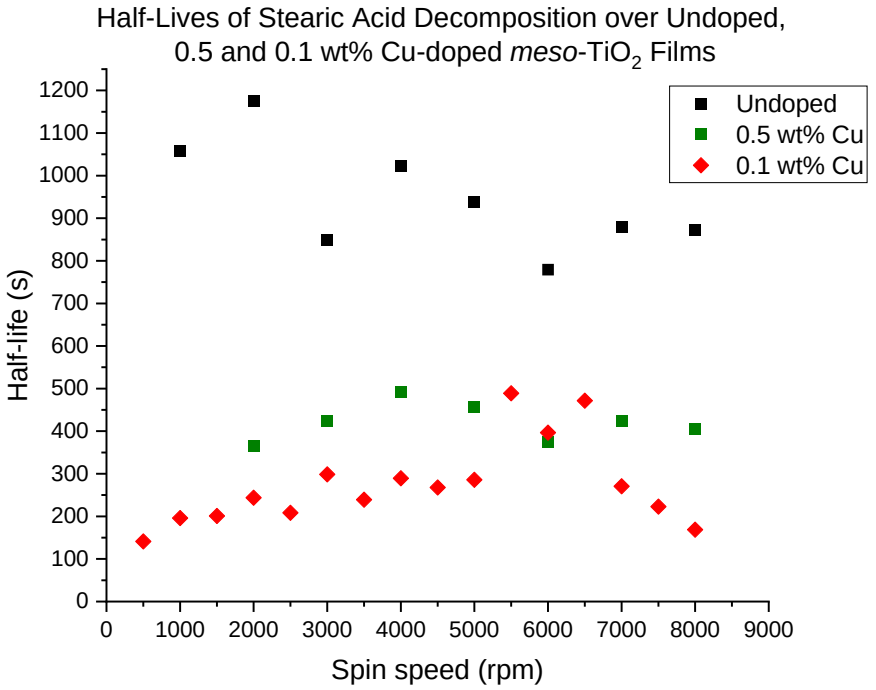

Figure 6.17: The half-lives of stearic acid decomposition over undoped, 0.1 and 0.5 wt% copper-doped meso-TiO_2 films

The 0.5 wt% copper-doped samples produced at 500 and 1000 rpm had half-lives of 3614 and 3369 seconds respectively. These half-lives were not plotted in Figure 6.17 as the scale would have hidden the detail of the other samples. Reaction half-lives over samples produced at 500 and 1000 rpm are far higher than the other 0.5 wt% samples as well as the undoped, 1 and 2.5 wt% samples discussed previously. The samples prepared at spin speeds from 2000 to 8000 rpm fall within the region of preparation spin speeds where shear thickening dominates in determining the film thickness. Within this group of samples, changes in half-lives are determined by the spin speed used to prepare the film, not the film thickness.

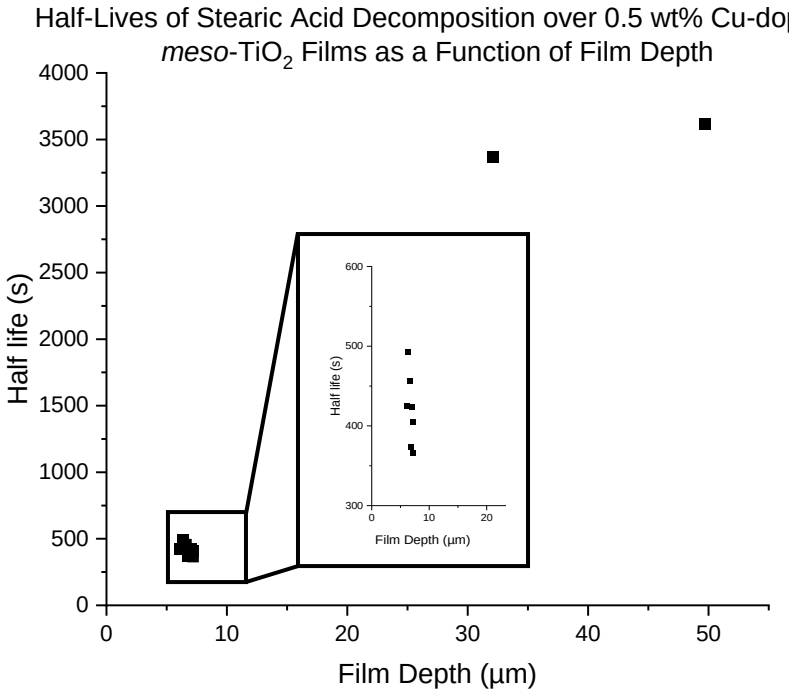

Figure 6.18: The half-lives of stearic acid decomposition on 0.5 wt% copper-doped meso-TiO_2 films plotted against film depth

6.1.5 Stearic Acid Decomposition over 0.1 wt% Copper-Doped *meso*-TiO_2

Stearic acid decomposition over the 0.1 wt% copper-doped samples exhibits zero order kinetics as seen with the 0.5 wt% samples. They are also significantly more active than other doped films. The thickest film, produced at 500 rpm is the most active with the activity of other films decreasing until a preparation spin speed of 6000 rpm as can be seen in Figure 6.17. The samples prepared at 7000 and 8000 rpm show an increase in activity, but they remain less active than the sample prepared at 500 rpm.

Figure 6.19 shows the half-lives of the reaction over these samples against film depth. The critical shear rate of the solution used to prepare these samples is at 2890 rpm. Unlike the other groups of samples in this chapter, there is no notable change in activity or kinetics at this transition point.

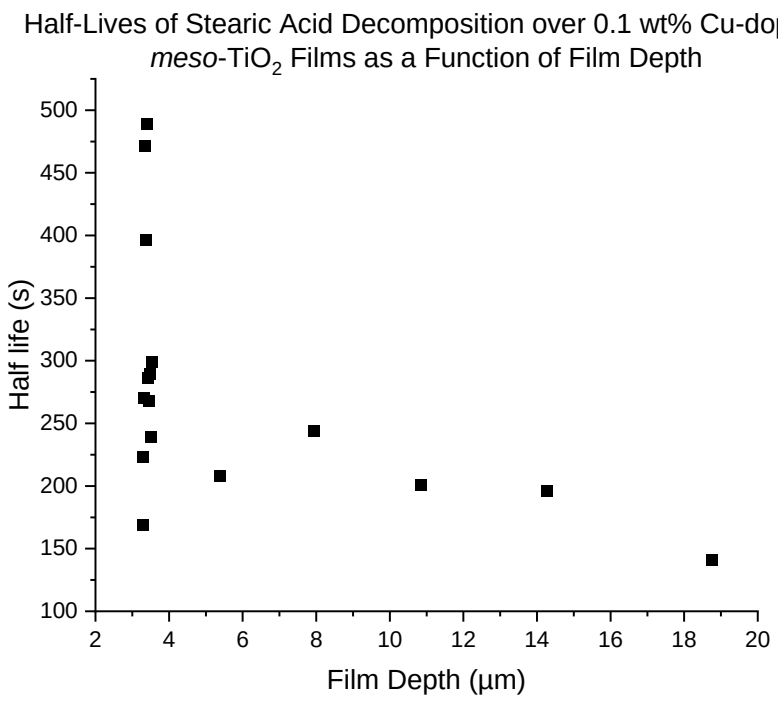

Figure 6.19: The half-lives of stearic acid decomposition on 0.1 wt% copper-doped meso-TiO_2 films plotted against film depth

Tauc plots of 0.1 wt% copper-doped films can be found on page 91. There is no trend between preparation spin speed and band gap energy for these films. The average band gap of these films is 3.11 eV. This is higher than other band gap energies reported in this chapter.

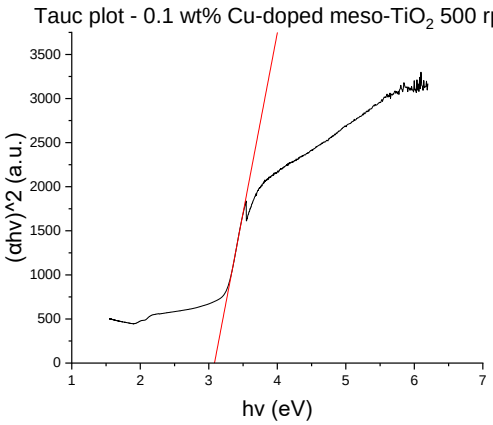

Figure 6.20: Tauc plot of a 0.1 wt% copper-doped meso-TiO_2 sample produced at 500 rpm

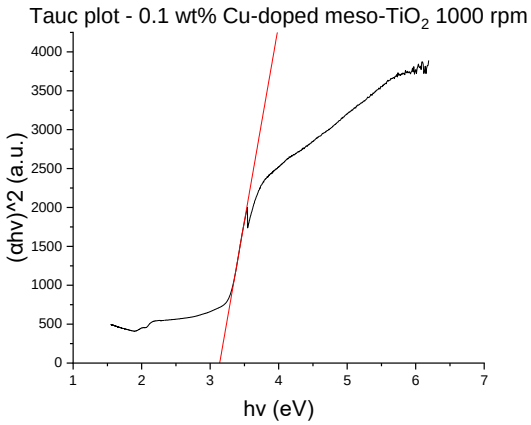

Figure 6.21: Tauc plot of a 0.1 wt% copper-doped meso-TiO_2 sample produced at 1000 rpm

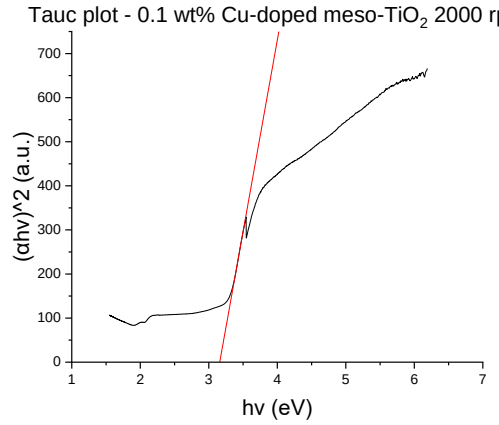

Figure 6.22: Tauc plot of a 0.1 wt% copper-doped meso-TiO_2 sample produced at 2000 rpm

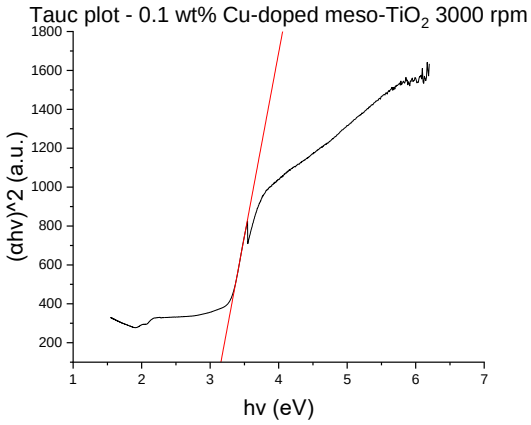

Figure 6.23: Tauc plot of a 0.1 wt% copper-doped meso-TiO_2 sample produced at 3000 rpm

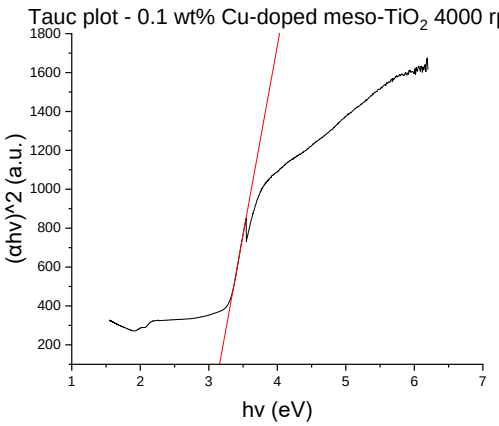

Figure 6.24: Tauc plot of a 0.1 wt% copper-doped meso-TiO_2 sample produced at 4000 rpm

6.2 X-ray Photoelectron Spectroscopy

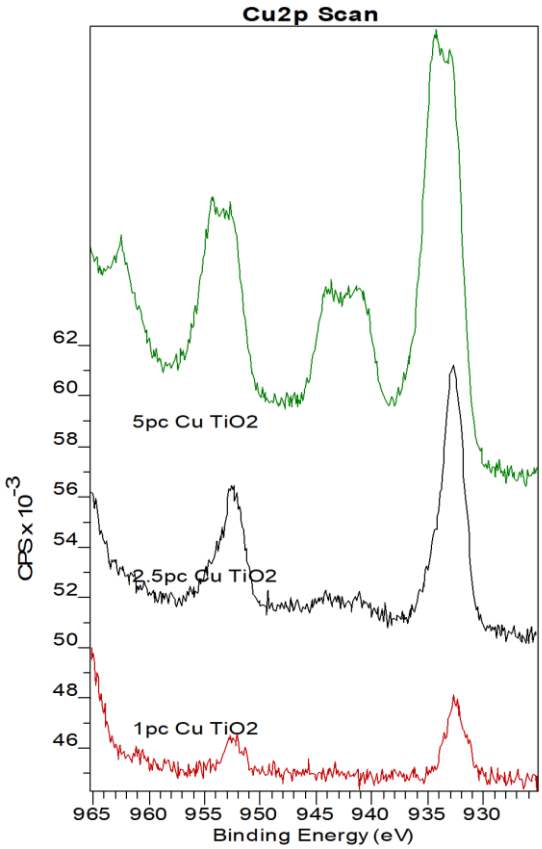

Figure 6.25: XP spectra showing the Cu2p scans of 1, 2.5 and 5 wt% Cu-doped mesoporous TiO_2 films

The Cu2p scans of 5 %, 2.5 % and 1 % Cu-doped *meso*-TiO_2 films before photocatalysis are shown in Figure 6.25. These show that by varying the amount of copper present in the samples, we also alter the oxidation state of the copper in the samples. The strong satellites present in the spectrum of the 5 % sample scans are indicative of Cu(II). The weak satellites present in the spectrum of the 2.5 % samples suggest that Cu(I) is present, instead of the Cu(II) seen in the 5 % sample. The 1 % Cu-doped films showed no satellites. This could indicate the presence of Cu(0), however it is more likely that it is the result of a weak signal stemming from the low amount of copper in the sample.

6.3 X-ray Diffraction

A series of powders were produced by producing multiple identical surface coatings and then scraping the films off the surface into a fine powder. A scalpel blade was used to remove the photocatalyst from the surface of the films. This led to areas of the glass coverslip chipping off

and being incorporated into the resulting powder. This approach allowed analysis of the surface coatings without being limited by the small amount of material on the surface of each sample. Six powders were produced in this way, with 5, 2.5 and 1 wt% copper-doped *meso*-TiO_2, prepared at 500 and 4000 rpm. The undoped meso-TiO_2 powder used for BET surface area measurements was also analysed by XRD.

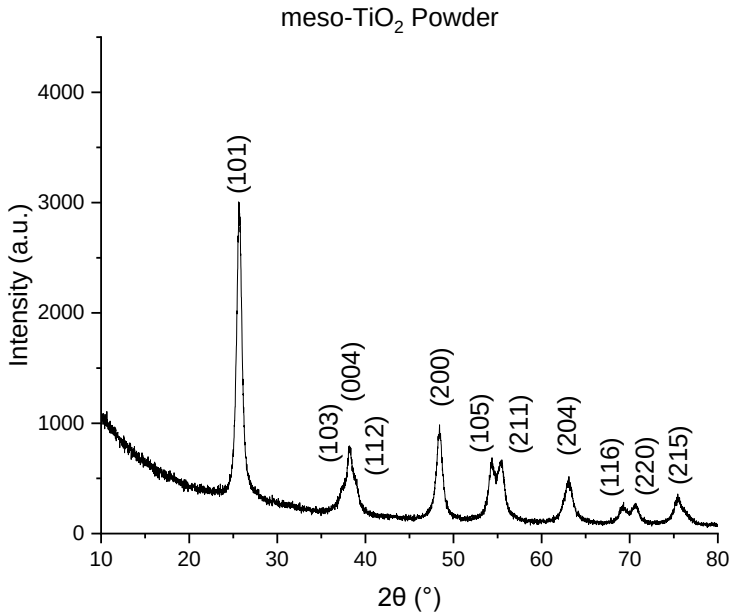

Figure 6.26: XRD of a meso-TiO_2 powder

Figure 6.26 shows the XRD pattern of the undoped powder. The powder is anatase TiO_2. The templating polymer does not affect the crystal structure of the TiO_2 as anatase is expected to be the dominant structure for TiO_2 calcined at 500 °C.

Figure 6.27 to Figure 6.32 show the XRD patterns of powders all copper doped powders. The patterns all show that the TiO_2 is present as anatase. The diffraction peaks were indexed to (101), (103), (004), (112), (200), (105), (211), (204), (116), (220) and (215) planes of anatase TiO_2. As no peaks could be attributed to copper, it is implied that copper is doped into the TiO_2 lattice.

There are several peaks present that cannot be attributed to other phases of TiO_2, copper oxides or metallic copper. They are marked with blue vertical lines in Figure 6.31 on page 96. These peaks are significantly broader in the sample prepared at 4000 rpm and have been attributed to the glass coverslips that were damaged when removing the photocatalyst.

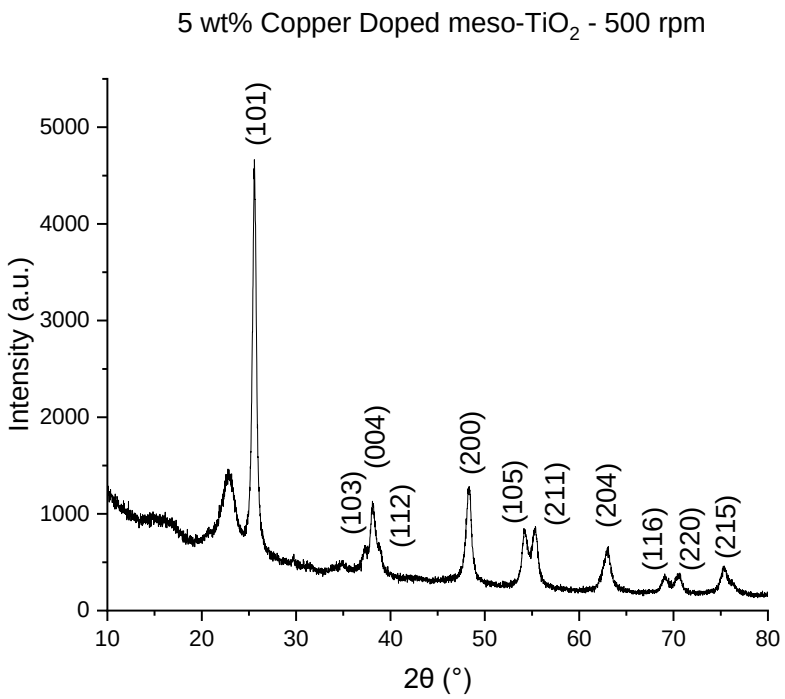

Figure 6.27: XRD pattern of 5 wt% copper doped meso-TiO_2 films produced at 500 rpm and scraped into a powder

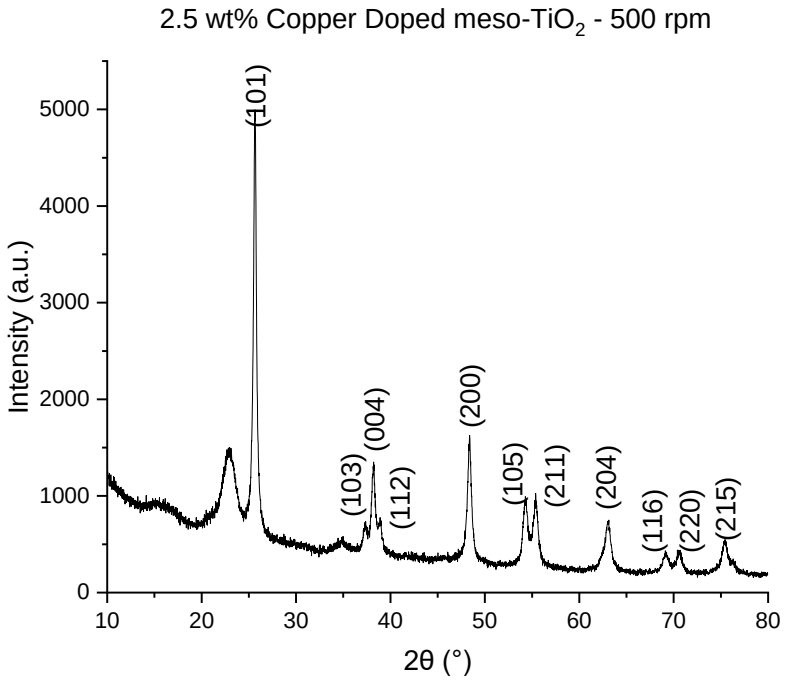

Figure 6.28: XRD pattern of 2.5 wt% copper doped meso-TiO_2 films produced at 500 rpm and scraped into a powder

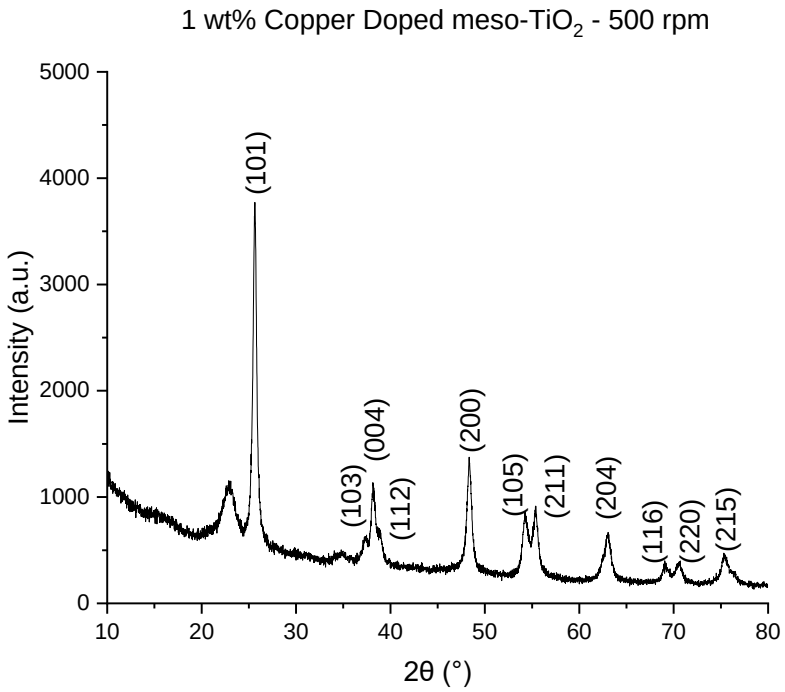

Figure 6.29: XRD pattern of 1 wt% copper doped meso-TiO_2 films produced at 500 rpm and scraped into a powder

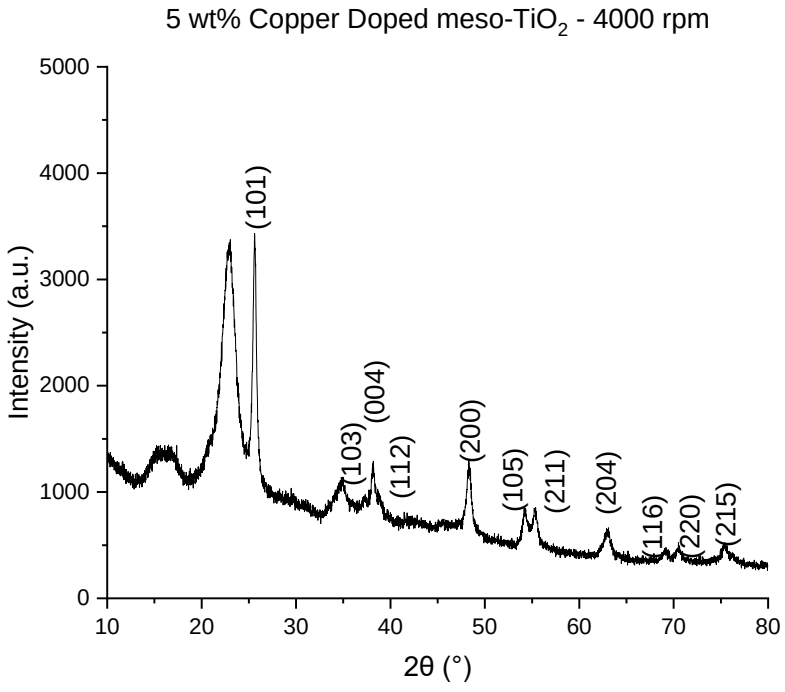

Figure 6.30: XRD pattern of 5 wt% copper doped meso-TiO_2 films produced at 4000 rpm and scraped into a powder

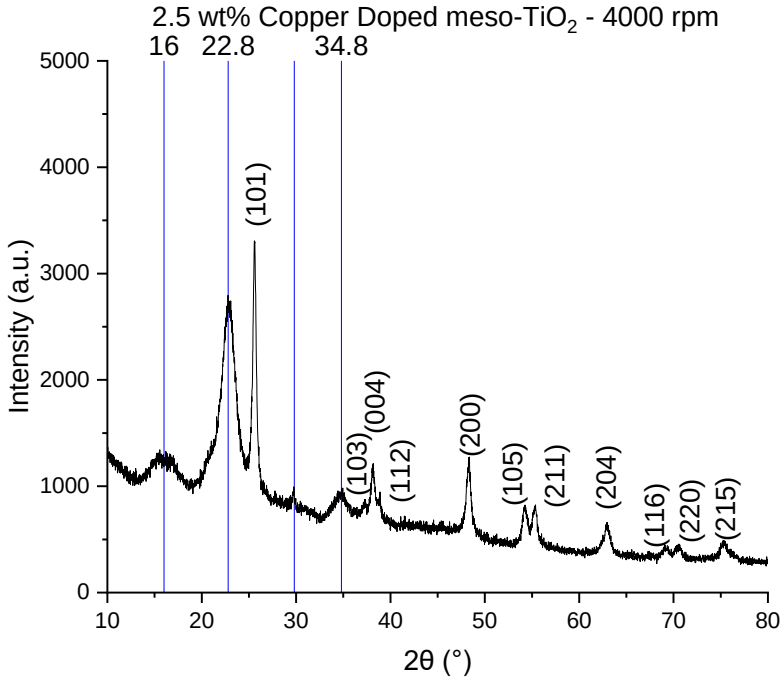

Figure 6.31: XRD pattern of 2.5 wt% copper doped meso-TiO_2 films produced at 4000 rpm and scraped into a powder

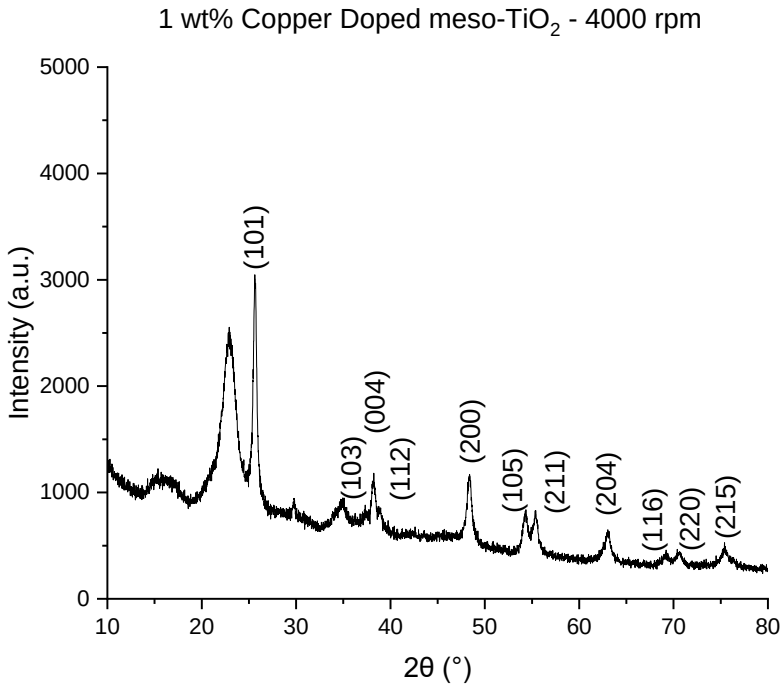

Figure 6.32: XRD pattern of 1 wt% copper doped meso-TiO_2 films produced at 4000 rpm and scraped into a powder

6.4 Discussion

Copper doping of TiO_2 has previously been shown to increase the photocatalytic activity, including several claims that it decreases the recombination rate of photoinduced electron-hole pairs on the photocatalyst.[6,9] There is very little literature about the effect of the spin-coating process on the activity of such materials.

Figure 6.33 shows the median half-lives of reaction over all copper-doped samples used. The least active samples are the 5 wt% Cu-doped samples, regardless of preparation spin speed. One limitation of these experiments is the use of a single wavelength light source. The 2.7 eV bandgap calculated for the thickest sample corresponds to blue light in the visible region. It would be best to test these samples under a light source that encompasses visible light as well as other frequencies of UV light to ensure that the lightsource is not hindering the reaction.

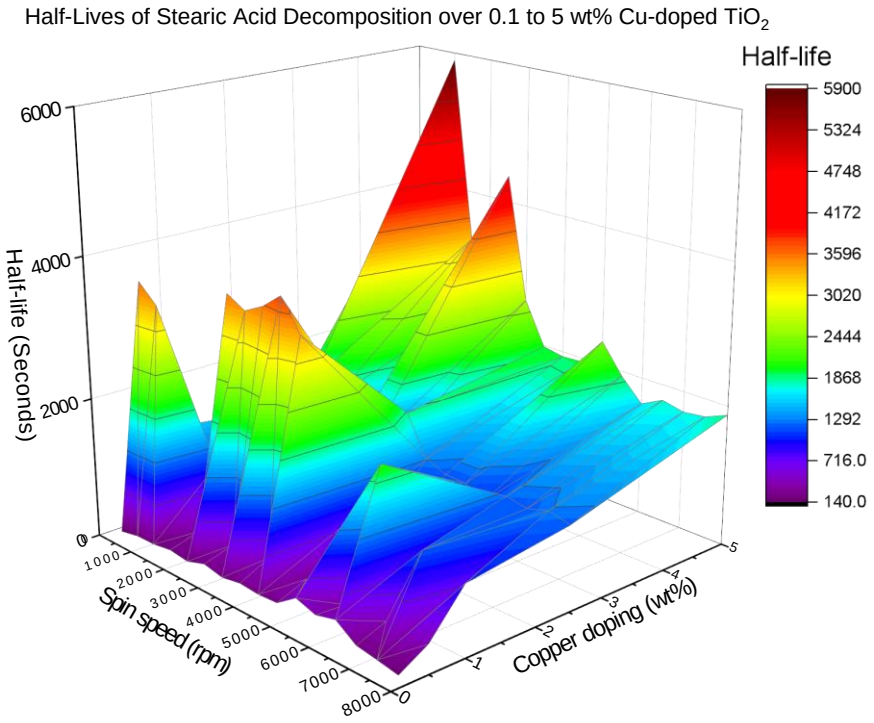

Figure 6.33: A 3D colourmap surface showing the half-lives of samples produced at 500 to 8000 rpm, with 0.1 to 5 wt% copper content

Generally, the activity increased with decreasing copper content. Undoped samples perform similarly to the 2.5 wt% Cu-doped samples. Some samples with 1 wt% copper doping have greater half-lives than the 2.5 wt% samples, but at higher preparation spin speeds the 1 wt% samples perform better than the 2.5 wt% copper doped samples.

The presence of Cu(II) in copper-doped TiO_2 is common and well reported as crystalline or amorphous CuO clusters and in substitutional positions.[10–13] Cu(I) is reported less often, but has also been characterised as Cu_2O clusters or in substitutional positions.[14,15] XPS confirmed the presence of Cu(II) in the 5 wt% copper-doped films and Cu(I) in the 2.5 and 1 wt% films. XRD supported the inclusion of both copper species in substitutional positions in the anatase TiO_2 lattice or as amorphous or fine secondary precipitates.[16] Cu(0) has been reported in literature, but could not be confirmed with XPS due to the weak signal from the 1 wt% copper-doped sample.[14,15]

Previous studies have shown that Cu(II) can act as traps for photogenerated electrons.[17] Despite literature evidence suggesting that the presence of Cu(II) would improve the catalyst, the 5 wt% copper-doped films are all less active than undoped films produced at the same spin speed or film thickness. The copper in these samples could be forming amorphous or fine secondary precipitates that inhibit the photocatalytic activity of the TiO_2 lattice.

The rate plots of the decomposition of stearic acid over copper doped films showed a mixture of zero and first order kinetics. In all groups of samples where the kinetics could be determined, the kinetics changed at the same preparation spin speed that was determined to be the critical shear rate in Chapter 4. It is unclear what could cause this effect on the kinetics of the resulting films as the XRD does not show any changes to the structure of the films, but the change of behaviour could be related to mesostructural parameters such as grain size, or the effectiveness of the coherence of the coating which might affect the porosity.

The work in this chapter represents a comprehensive study of the effect of spin-speed, film thickness and copper-doping on mesoporous TiO_2 films and could be used to effectively tailor the properties of photocatalytic mesoporous copper-doped TiO_2 films using the copper content, preparation spin speed and film thickness.

6.5 References

1 G. K. Mor, O. K. Varghese, R. H. T. Wilke, S. Sharma, K. Shankar, T. J. Latempa and K.-S. Choi, *Nano Lett.*, 2008, **8**, 3555–3555.

2 J. Araña, J. M. Doña-Rodríguez, O. González-Díaz, E. Tello Rendón, J. A. Herrera Melián, G. Colón, J. A. Navío and J. Pérez Peña, *Journal of Molecular Catalysis A: Chemical*, 2004, **215**, 153–160.

3 H. S. Park, D. H. Kim, S. J. Kim and K. S. Lee, *Journal of Alloys and Compounds*, 2006, **415**, 51–55.

4 Y. Xu, D. Liang, M. Liu and D. Liu, *Materials Research Bulletin*, 2008, **43**, 3474–3482.

5 M. Sahu and P. Biswas, *Nanoscale Research Letters*, 2011, **6**, 441.

6 R. Trofimovaite, C. M. A. Parlett, S. Kumar, L. Frattini, M. A. Isaacs, K. Wilson, L. Olivi, B. Coulson, J. Debgupta, R. E. Douthwaite and A. F. Lee, *Applied Catalysis B: Environmental*, 2018, **232**, 501–511.

7 A. E. Baber, X. Yang, H. Y. Kim, K. Mudiyanselage, M. Soldemo, J. Weissenrieder, S. D. Senanayake, A. Al-Mahboob, J. T. Sadowski, J. Evans, J. A. Rodriguez, P. Liu, F. M. Hoffmann, J. G. Chen and D. J. Stacchiola, *Angewandte Chemie International Edition*, 2014, **53**, 5336–5340.

8 T. H. Nguyen, T. L. Nguyen, T. D. T. Ung and Q. L. Nguyen, *Adv. Nat. Sci: Nanosci. Nanotechnol.*, 2013, **4**, 025002.

9 X. Yang, S. Wang, H. Sun, X. Wang and J. Lian, *Transactions of Nonferrous Metals Society of China*, 2015, **25**, 504–509.

10 X. H. Xia, Y. Gao, Z. Wang and Z. J. Jia, *Journal of Physics and Chemistry of Solids*, 2008, **69**, 2888–2893.

11 A. Maury-Ramirez, K. Demeestere and N. De Belie, *Journal of Hazardous Materials*, 2012, **211–212**, 218–225.

12 G. Sivalingam, K. Nagaveni, M. S. Hegde and G. Madras, *Applied Catalysis B: Environmental*, 2003, **45**, 23–38.

13 J.-N. Nian, S.-A. Chen, C.-C. Tsai and H. Teng, *J. Phys. Chem. B*, 2006, **110**, 25817–25824.

14 송강용, 권영태, 최광진 and 이완인, *Bulletin of the Korean Chemical Society*, 1999, **20**, 957–960.

15 R. López, R. Gómez and M. E. Llanos, *Catalysis Today*, 2009, **148**, 103–108.

16 M. H. N. Assadi and D. A. H. Hanaor, *Applied Surface Science*, 2016, **387**, 682–689.

17 V. Polliotto, S. Livraghi, A. Krukowska, M. V. Dozzi, A. Zaleska-Medynska, E. Selli and E. Giamello, *ACS Appl. Mater. Interfaces*, 2018, **10**, 27745–27756.

Chapter 7. Photocatalytic Decomposition of Polystyrene

Plastics represent an environmental challenge due to their widespread use and inability to degrade naturally. In 1950, the estimated global production of plastic was around 2 metric tons.[1] Between 1950 and 2018, around 6 billion tons of plastic was produced globally, with around 21 % incinerated or recycled and the other 79 % left untreated.[2] 2,361,000 tonnes of plastic packaging waste was generated in the UK in 2018, with a 43.8 % recovery or recycling rate.[3] With misleading symbols on plastics such as the Green Dot and the confusing Mobius loops with plastic resin codes, the general public is getting ever more confused about what can be recycled with their local authority and large amounts of recyclable plastics are still making their way into landfill.[4,5] With over a million tonnes of plastics remaining unrecycled in the UK every year, a practical solution needs to be developed that does not rely upon the burning or burying of these materials.

Fragmentation of plastics into nanoparticles that pollute our waterways and oceans is a growing cause for concern as the material is a mixture of plastics that cannot be reliably identified for recycling.[6–8] Even if plastics cannot be fully decomposed by photocatalysis, partial degradation would allow quicker biodegradation for any plastics that do enter landfill.[9]

Most work into the photocatalytic degradation of polystyrene has focused on polystyrene-TiO_2 composite films or reactions in solution.[10–12] The presence of phenyl rings in its repeating units cause significant challenges to the photocatalytic degradation of polystyrene.

7.1 Photocatalytic testing – Polystyrene

Photocatalytic testing was performed using the 0.1 wt% copper doped films as these were the most active at decomposing stearic acid in Chapter 6. Eight samples were produced at spin speeds from 1000 to 8000 rpm for polystyrene degradation. 20 µL of a 1 wt% solution of polystyrene in chloroform was deposited at 2000 rpm, resulting in a thin film of polystyrene over the photocatalyst.

Two test experiments were performed as a proof of concept. After 30 minutes of constant irradiation, little to no decomposition was observed. The sample was then left under the light source overnight. The DRIFTS spectrum the following day showed that no polystyrene was left on

the surface. The decision was made to conduct experiments by using 15 minute periods of irradiation for a total of 150 minutes. This gave percentage degradations between 25 and 70 %.

The DRIFTS spectra were individually fitted with multiple curves and the areas of the peaks associated with the aliphatic and aromatic areas were separated so analysis could determine the rates for decomposition of the aliphatic and aromatic sections of the molecule separately. The total area could not be taken as the stearic acid decomposition rates were. This might be misleading due to the mixture of aromatic and aliphatic bonds in the molecule. If the aliphatic bonds were being targeted selectively by the photocatalyst, then it could lead to harmful by-products and the catalyst would not be effective at reducing plastic pollution.

7.1.1 Total Degradation

The percentage decomposition of polystyrene over the photocatalytic films is shown in Figure 7.1. The movement of samples in the holder caused a lot more variations in signal intensity than was seen during the degradation of stearic acid. Most samples tested had large variations in the decomposition, but all samples showed a gradual decline in the amount of polystyrene on the surface over the course of the experiment.

Figure 7.2 shows the half-lives of polystyrene decomposition. There is large variation in the half-lives seen, but the majority fall within the 8000 to 12000 second range. These are far greater than the 150 to 500 second half-lives seen for stearic acid degradation on these films, but still mark a dramatic increase over natural degradation.

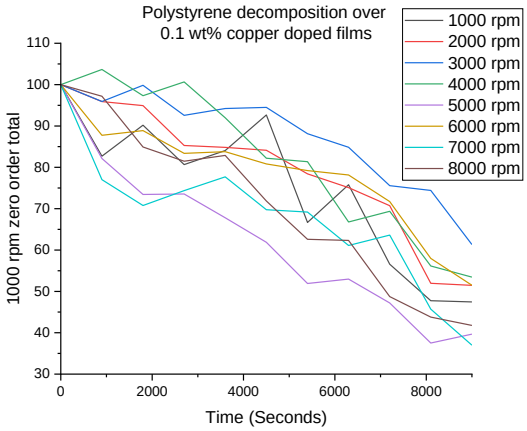

Figure 7.1: The percentage decomposition of polystyrene over 0.1 wt% copper-doped samples produced at spin speeds between 1000 and 8000 rpm

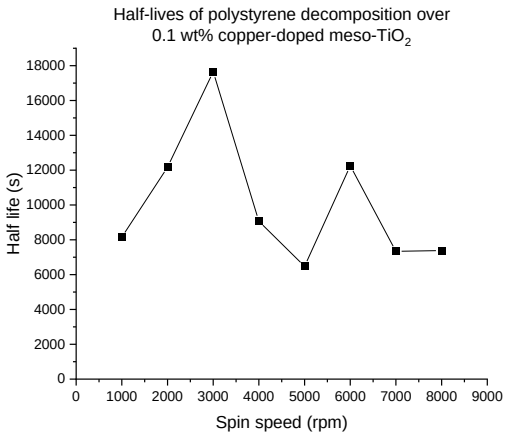

Figure 7.2: Half-lives of polystyrene decomposition plotted against the spin speed used to produce the photocatalytic film

7.1.2 Aromatic and Aliphatic Degradation

The DRIFTS spectra for the polystyrene films allowed the degradation of C-H bonds from the aromatic and aliphatic parts of the molecule to be calculated separately. The half-lives of aliphatic degradation were significantly lower than for the aromatic degradation over catalysts prepared at lower spin speeds. As the preparation spin speed increased, the half-lives of the degradation of aromatic hydrogens were considerably lower, indicating that the samples produced at higher spin speeds showed greater selectivity towards aromatic compounds.

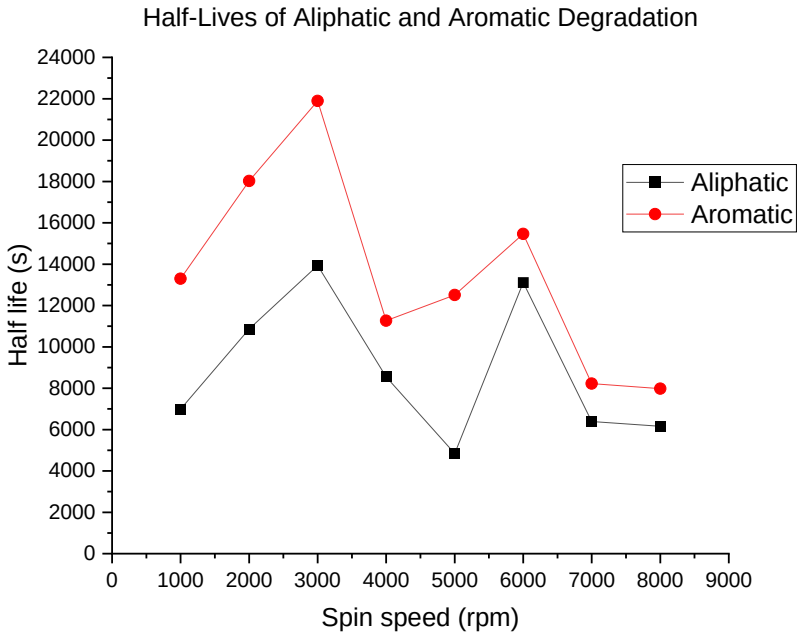

Figure 7.3: Half-lives of the decomposition of aromatic and aliphatic parts of polystyrene

7.2 Conclusion

The 0.1 wt% copper-doped *meso*-TiO_2 photocatalysts developed throughout this work have been shown to offer effective decomposition of polystyrene. The degradation of polystyrene is significantly slower than the degradation of stearic acid over the same catalyst family, but these samples are still effective photocatalysts for this use.

The spin speed used to produce that photocatalytic film influences the selectivity, with higher spin speeds providing decreased half-lives for the degradation of aromatic compounds, while maintaining low half-lives of the aliphatic parts of the polymer. As seen in Chapter 4, the thickness

of these films plateaus at preparation spin speeds above 3000 rpm, so the change in selectivity is influenced by the preparation spin speed, not film depth.

Despite selectivity towards aliphatic C-H bonds, both aliphatic and aromatic C-H stretches lose intensity throughout the 150 minute irradiation suggesting two separate mechanisms, with different radicals being formed with each. If one radical was more selective towards the aromatic C-H bonds and changing the preparation spin speed had an effect on the properties of the films then it would be possible to influence the mechanism this way.

These materials offer an inexpensive and effective means of plastic degradation that provide good selectivity towards both the phenyl ring of polystyrene and the hydrocarbon links between them.

7.3 References

1 R. Geyer, J. R. Jambeck and K. L. Law, *Science Advances*, 2017, **3**, e1700782.

2 S. K. Tulashie, E. K. Boadu, F. Kotoka and D. Mensah, *Construction and Building Materials*, 2020, **241**, 118044.

3 Department for Environment Food & Rural Affairs, *UK Statistics on Waste*, 2021.

4 What Do the Plastic Recycling Symbols Mean?, https://www.willshees.co.uk/news/information-guides/what-do-the-plastic-recycling-symbols-mean/, (accessed March 13, 2022).

5 D. Roy, E. Berry and M. Dempster, *PLOS ONE*, 2022, **17**, e0267284.

6 N. Laskar and U. Kumar, *Environmental Technology & Innovation*, 2019, **14**, 100352.

7 X. Lim, *Nature*, 2021, **593**, 22–25.

8 H. Du and J. Wang, *Gondwana Research*, 2021, **98**, 63–75.

9 S. Dinoop lal, T. Sunil Jose, C. Rajesh, P. Anju Rose Puthukkara, K. Savitha Unnikrishnan and K. J. Arun, *European Polymer Journal*, 2021, **153**, 110493.

10 J. D. Acuña-Bedoya, E. Luévano-Hipólito, E. I. Cedillo-González, L. P. Domínguez-Jaimes, A. M. Hurtado and J. M. Hernández-López, *Journal of Environmental Chemical Engineering*, 2021, **9**, 106208.

11 W. Fa, L. Guo, J. Wang, R. Guo, Z. Zheng and F. Yang, *Journal of Applied Polymer Science*, 2013, **128**, 2618–2622.

12 J. Shang, M. Chai and Y. Zhu, *Environ. Sci. Technol.*, 2003, **37**, 4494–4499.

Chapter 8. The Role of Surface Oxygen Species

8.1 Introduction

The photocatalytic oxidation of organic molecules by TiO_2 photocatalysts has been studied comprehensively over the last several decades.[1–6] Despite this, the mechanisms of the photocatalytic oxidation process are not clear as detailed in recent reviews.[5–8] The role of lattice oxygen in TiO_2 photocatalysts is poorly understood due to the challenges of studying these systems. Typically, the mechanism of TiO_2 photocatalysis is studied using TiO_2 powders in an aqueous solution containing the reactant. This system involves three oxygen sources: the lattice oxygen from the photocatalyst itself, oxygen from the solvent, and the surrounding atmosphere.

$$TiO_2 + h\nu \rightarrow e_{CB}^- + h_{VB}^+ \quad \textbf{8.1}$$

$$H_2O + h_{VB}^+ \rightarrow \bullet OH + H^+ \quad \textbf{8.2}$$

$$O_2 + e_{CB}^- \rightarrow O_2^{\bullet -} \quad \textbf{8.3}$$

$$O_2^{\bullet -} + H^+ \rightarrow {}^{\bullet}OOH \quad \textbf{8.4}$$

$${}^{\bullet}OOH + e_{CB}^- \rightarrow HOO^- \quad \textbf{8.5}$$

$$HOO^- + H^+ \rightarrow H_2O_2 \quad \textbf{8.6}$$

$$O_2^{\bullet -} + C_xH_y \rightarrow H_2O + CO_2 \quad \textbf{8.7}$$

$${}^{\bullet}OOH + \text{pollutant} \rightarrow H_2O + CO_2 \quad \textbf{8.8}$$

Equations 8.1 to 8.8 outline a typical proposed reaction mechanism by which TiO_2 photocatalysts oxidize organic pollutants. The absorbed photon excites an electron from the valence band to the conduction band generating a positive hole, and leaving an electron in the conduction band (the electron-hole pair).[9] The excited electron can undergo redox reactions in order to break down pollutants in contact with the surface of the material.[10] Oxidation of water or hydroxyl ions by the positive hole can produce hydroxyl radicals, which are powerful oxidants of organic compounds.[11] The photo-excited electron in the conduction band can react with oxygen to produce a superoxide radical anion ($O^{\bullet -}{}_2$) which, when protonated, forms a hydroperoxide radical (${}^{\bullet}OOH$). Equations 1-6 summarize the mechanism by which the reactive oxygen species are produced and Equations 7

and 8 demonstrate how the superoxide radical anion and hyperoxide radical can react with pollutants to give water and carbon dioxide as products.[12]

Experiments using $H_2{}^{18}O$ in the solvent and $^{18}O_2$ in the surrounding atmosphere have shown labelled oxygen incorporated into both intermediates and final reaction products.[13] As it is not possible to remove both the solvent and atmospheric oxygen sources in these experiments, it is not possible to determine the source of oxygen incorporated into the products. It is also possible that labelled oxygen is merely replacing lattice oxygen that has been lost during the reaction and is being incorporated into the products through a Mars-van Krevelen type mechanism.

These results are further complicated by the hypothesized role of surface radicals as opposed to the radicals formed from adsorbed H_2O and O_2 in Equations 8.2 and 8.3. There are two distinct types of surface oxygen species present on TiO_2, terminal hydroxides ($-OH^-$) and bridging hydroxides ($>OH^-$). Equations 8.9 to 8.11 outline a mechanism by which these surface lattice oxygen species can generate surface lattice radicals depending on the experimental pH.[13–16] Previous studies have shown that the $-OH^-$ species will readily exchange with water in the dark at room temperature.[17]

$$h_{VB}{}^+ + (>O^{2-}) \rightarrow (-O^{\bullet -}) \qquad pH > pH_{zpc} \qquad \textbf{8.9}$$

$$h_{VB}{}^+ + (>OH^-) \rightarrow (-OH^{\bullet}) \qquad pH < pH_{zpc} \qquad \textbf{8.10}$$

$$C_xH_y + (-OH^{\bullet}/-O^{\bullet -}) \rightarrow C_xH_{y-1}{}^{\bullet} + H^+ + (>OH^-/>O^{2-}) \qquad \textbf{8.11}$$

Isotopically labelled titania ($Ti^{18}O_2$), produced in a closed vacuum apparatus from titanium tetrachloride and $H_2{}^{18}O$ has also been used to probe the mechanism of these reactions further, producing a $Ti^{18}O_2$ purity of 97-99 %.[18–21] Montoya et al.[13] studied the photooxidation of benzene over $Ti^{16}O_2$ and $Ti^{18}O_2$ photocatalyst by tracking the evolution of $C^{16}O_2$ and $C^{16}O^{18}O$ under UV light irradiation. The specific surface area of the two photocatalysts were determined from BET surface analysis to be 32.1 and 52.7 m^2g^{-1} for $Ti^{18}O_2$ and $Ti^{16}O_2$ respectively. Both labelled and unlabeled TiO_2 showed evolution of $C^{16}O$ and $C^{16}O^{18}O$. The presence of $C^{16}O^{18}O$ when using $Ti^{16}O_2$ was attributed to the natural presence of ^{18}O in water used for the synthesis of the $Ti^{16}O_2$. The two samples produced flow rates of 17.2 and 22.8 $\mu molh^{-1}$ for $Ti^{18}O_2$ and $Ti^{16}O_2$ respectively, with the difference accounted for in the increased surface area of the $Ti^{16}O_2$ sample. The $Ti^{16}O_2$ sample had a constant $C^{16}O^{18}O$: $C^{16}O_2$ ratio of 0.62 % while the $Ti^{18}O_2$ sample showing an increased ratio at 0.97 % shortly after irradiation, before reducing down to 0.66 % giving a value of 0.17 % ^{18}O enrichment between 25 and 85 minutes. The author states that the only possible source of ^{18}O is the bridging surface oxygen species of $Ti^{18}O_2$, therefore the bridging oxygen species must be

incorporated into the evolved CO_2. However, the author did not explore the exchange of $>^{18}OH^-$ and $-^{16}OH^-$ species, which would result in $-^{18}OH^-$ which would freely exchange with the solvent as outlined in Equations 8.9 and 8.10. Further, photoinduced oxygen isotopic exchange could also account for the $C^{18}O^{16}O$ detected. This process was discounted by Montoya et al. as it is unlikely in the presence of organic molecules that can be readily photooxidized,[22] yet there was no mention of a storage method that would limit the samples exposure to moisture, UV or visible light to avoid this process taking place between preparation of the samples and their use.

Work by Ali et al. showed evidence for a Mars-van Krevelen type mechanism in zinc oxide thin film catalysts,[233] however, they were unable to remove the liquid or gaseous oxygen and instead, drew their conclusions from observing the morphology and rates of reaction over the catalysts while varying the flow rate of oxygen through the solution containing the catalyst and reactants.

Several authors have described the kinetics of photocatalytic degradation of gaseous NO over TiO_2 using a Langmuir-Hinshelwood-type rate law shown in Equation 8.12.[24–26]

$$^{r}rNO = k_{NO} \frac{k_{NO}[NO]}{1 + K_{NO}[NO]} \qquad \textbf{8.12}$$

Dillert et al.[27] used TiO_2 to degrade gaseous NO. As the photocatalyst was prepared by pressing, it was possible to control the amount of oxygen present in the gas mixture. The carrier gas was varied between nitrogen, compressed oil free air and oxygen, with the humidity remaining constant at 50 ± 2 % in all experiments. By changing the amount of molecular oxygen available to the photocatalyst, Dillert concluded that molecular oxygen was the only suitable electron acceptor in the reaction mixture as experiments run using N_2 as the carrier gas showed no NO decomposition.[27] In NO decomposition over TiO_2, the importance of humidity was outlined by Hunger et al.[28] where it was found that a maximum rate was obtained at around 50 % humidity. This is used as the humidity for all NO degradation experiments discussed here, adding in another source of oxygen to the reaction mixtures.

Photodegradation of NO can be performed using a solid photocatalyst and a gaseous mixture of reactants.[27,28] Experiments to determine the role of molecular oxygen in these systems are relatively easy, because oxygen can simply be excluded from the mixture. The systems that are currently used to probe the photodegradation of model organic pollutants usually have the target molecule and photocatalyst in solution, so performing these experiments without the presence of molecular oxygen or other gases in the reaction mixture is significantly more difficult. As the work undertaken during this project involves a solid photocatalyst, solid reactant and the atmosphere surrounding it, it offers a unique approach to the study of these reactions. The atmosphere

surrounding the samples can be replaced with nitrogen while under UV irradiation to eliminate all sources of oxygen except the lattice and surface oxygen species of the photocatalyst.

8.2 Porous and non-porous films

Non-porous TiO_2 films are a challenge to produce, as they need to be as comparable to the porous films as possible. Despite there being large amounts of literature on both titanium dioxide films and mesoporous titanium dioxide,[10–12,29–34] there is very little literature directly comparing the two. To make any direct comparisons, it is important to have porous and non-porous films that are similar to each other in every way other than their porosity. This can be particularly challenging for techniques like spin-coating where the film thickness is correlated to the viscosity of the solution, as the films resulting from these solutions will have different thicknesses with the different solutions used.

The Pluronic P-123 altered the viscosity of the solution so it would be needed in the solution to give the same film thickness between the porous and non-porous samples. Without the polymer, the titanium butoxide also hydrolysed at a much faster rate and the resulting precipitate rendered the solution unusable for spin-coating quicker than the films could be produced on the spin-coater. The few films that could be produced had defects similar to those seen in Chapter 3 with the hydrolysed solution, but the solution was so viscous that most of the surface coatings simply flaked off the surface due to too much material being retained on the surface.

To obtain the most comparable groups of films, the choice was made to include the templating polymer in the solution for both porous and non-porous films, but to prevent the self-assembly stage of the process by calcining the films immediately after spin-coating. The evaporation induced self-assembly that occurs over the 48 hour period that the samples are in the oven at 40 °C is the step that give samples their mesoporous structure,[32,35] so omitting this step will result in the polymer being removed during the calcination step before forming aggregated micelles and therefore the mesoporous structure.

The non-porous films have a similar relationship between activity and preparation spin speed as the porous films discussed in Chapter 4, with increasing spin speed resulting in more active films. As can be seen in Figure 8.1, the overall activity of these films is extremely poor in comparison. Reaction over the sample produced at 1600 rpm had the highest maximum decomposition at 29.8 % (Table 8.1), while the sample produced at 2000 rpm had the highest reaction rate (Table 8.2).

Table 8.1 shows the maximum decomposition for the non-porous films and their porous counterparts.

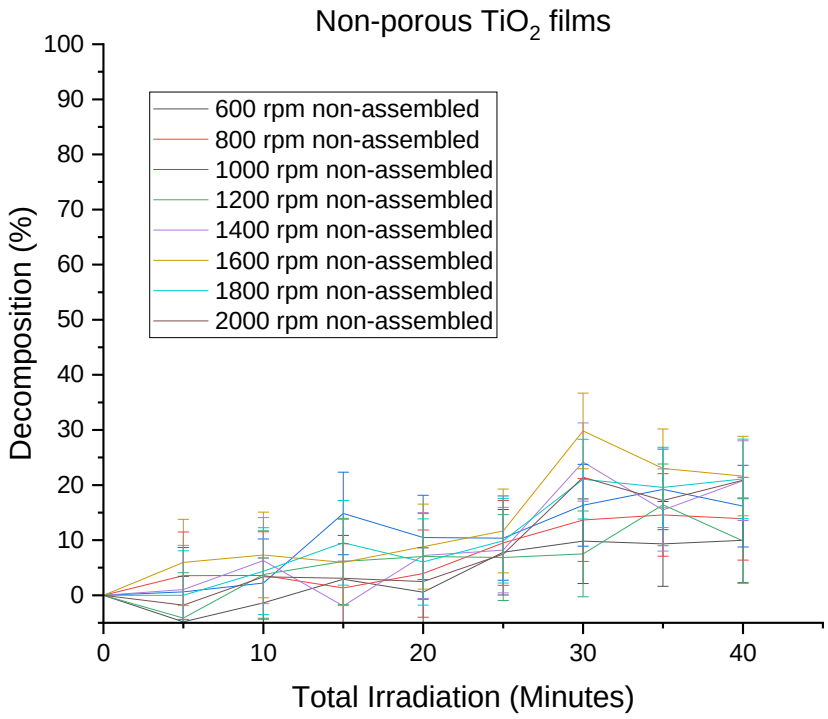

Figure 8.1: The decomposition of stearic acid over non-porous TiO_2 films

Spin speed (rpm)	Non-porous		Porous	
	Max. Decomposition (%)	**Time to Max. Decomposition (minutes ±2.5)**	**Max. Decomposition (%)**	**Time to Max. Decomposition (minutes ±2.5)**
600	9.8 ± 7.7	30	97.9 ± 4.1	20
800	14.6 ± 7.5	35	98.5 ± 4.1	20
1000	19.2 ± 7.3	35	97.3 ± 4.2	20
1200	16.4 ± 7.4	35	96.0 ± 4.2	35
1400	24.2 ± 7.1	30	96.4 ± 4.2	30
1600	29.9 ± 6.9	30	93.4 ± 4.3	40
2000	21.4 ± 7.2	30	91.5 ± 4.4	40

Table 8.1: The maximum extent of decomposition of stearic acid over porous and non-porous films

Figure 8.2 shows the decomposition of stearic acid over both porous and non-porous TiO_2 films. The half-lives for both groups of samples are reported in Table 8.2. The half-lives for the non-porous samples are over 10 times higher than for their equivalent porous sample.

Spin speed (rpm)	**Half-lives (s)**	
	Non-porous	**Porous**
600	9064	714
800	8202	621
1000	6057	607
1200	6431	568
1400	6153	488
1600	4741	557
1800	5633	581
2000	5285	541

Table 8.2: Zero order rate constants for stearic acid decomposition over porous and non-porous samples produced at spin speeds between 600 and 2000 rpm

8.2.1 Brunauer-Emmett-Teller (BET) surface area analysis

Solutions of polymer, solvent and precursor were produced using the same method as for the films. The solution was placed into a crucible and left to undergo EISA (Evaporation Induced Self-Assembly) and calcination before being removed. The non-porous powder did not contain any templating polymer. BET surface area calculations showed that the non- porous powder had a surface area of 27.7 m^2g^{-1} and the porous sample had a surface area of 47.4 m^2g^{-1}.

The increase in surface area seen is likely to be amplified in the spin-coated samples, as both samples were present as powders for the BET, whereas the non-porous samples that have been spin-coated only have the area on the very surface of the films available for adsorption.

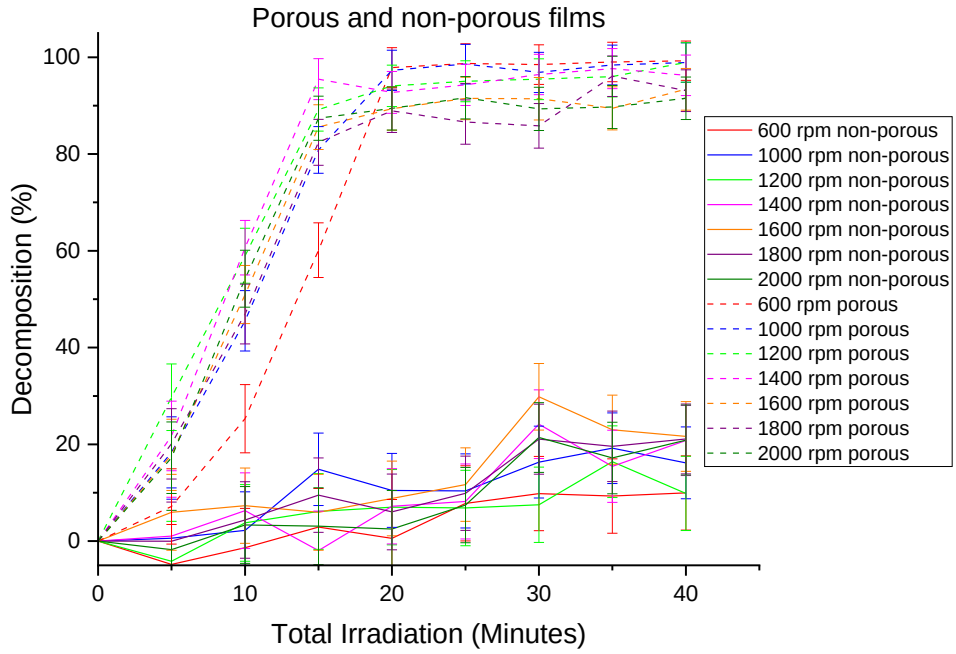

Figure 8.2: The decomposition of stearic acid over both porous and non-porous TiO_2 films where the solid lines are non-porous samples, and the dashed lines are porous.

8.2.2 XPS Sputtering to Determine Stearic Acid Penetration

To explore the relationship between porosity, film thickness and the photocatalytic activity of the films, three films were coated with stearic acid before using XPS and argon sputtering to get a profile of C1s spectra through the depth of the films. One possible way the porosity could be changing the activity of the films is if the stearic acid was entering the pores, causing a greater proportion of it to be in contact with the surface at any time. If this is the cause of the changes in activity for the porous and non-porous samples, it might also be responsible for the changes in activity with the changing preparation spin speeds.

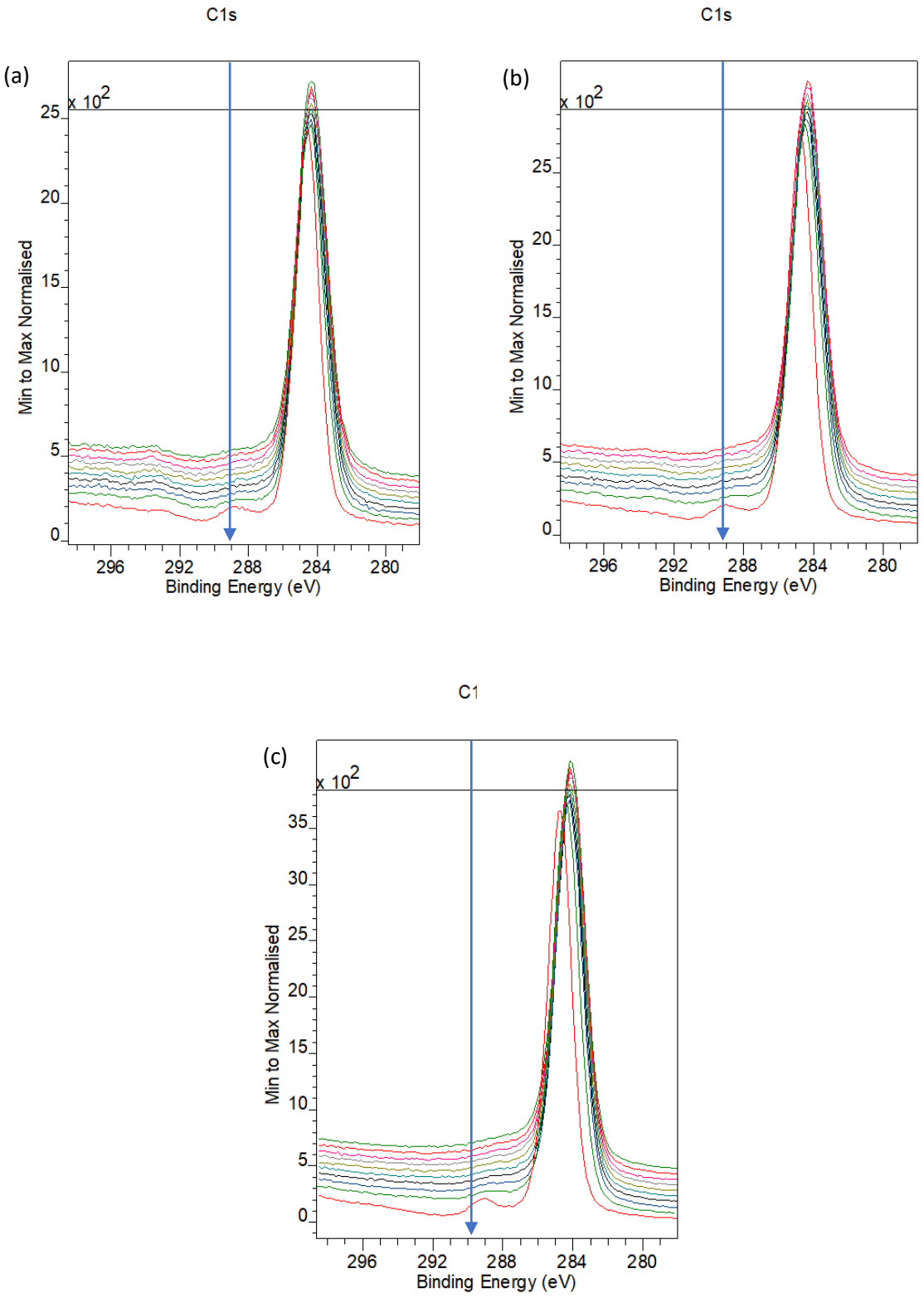

Figure 8.3: XPS C1s spectra of (a) thick mesoporous, (b) thin mesoporous and (c) non-porous TiO_2 films through the depth of the samples. The arrows at 289.2 eV on each spectrum mark the peak associated with the carbon in the carboxylic acid of stearic acid.

The three XP spectra in Figure 8.3 show the different carbon species present through the depth of the samples. To differentiate between the C1s peak associated with any residual polymer, or other carbon based contaminants, it is important to consider the structure of each of these.

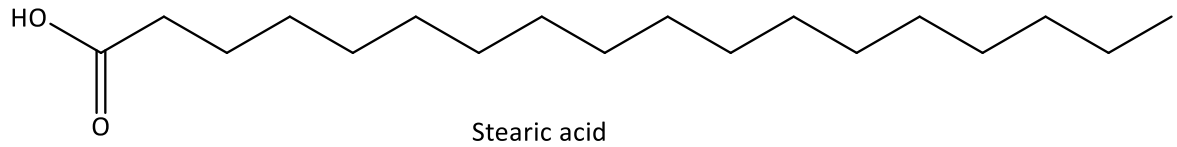

Stearic acid

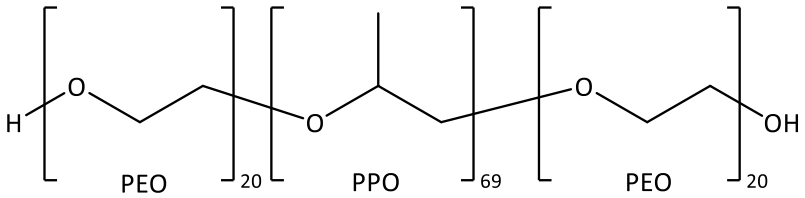

Pluronic P-123

Figure 8.4: The structures of stearic acid and Pluronic P-123

Figure 8.4 above, shows that the structure of stearic acid is a carboxylic acid on an 18-carbon backbone. This will give two separate peaks on a C1s XP spectrum. We can attribute the C-C peak at 284.8 eV to the C_{17} chain of the stearic acid, the polymer, and other carbon based contaminants. The smaller peak at 289.2 eV (marked with an arrow on Figure 8.3) can be attributed to the carbon of the carboxylic acid in the stearic acid. As the O=C-OH peak at 289.2 eV can be solely attributed to the stearic acid, the presence of that peak can be used to determine the relative penetration of stearic acid into the porous structure of the films. Penetration across all three samples is minimal and consistent, showing that stearic acid penetration into the pores of the samples cannot be responsible for their differing rates of decomposition. Due to the porous nature of the samples, it isn't possible to accurately estimate the depth of each layer shown in Figure 8.3.

Sample	**Half-life (s)**
Non-porous	6057
Thick, porous	607
Thin, porous	1027

Table 8.3: The half-lives of stearic acid decomposition over the non-porous and thick, porous and thin, porous samples

8.3 Photodegradation of Stearic Acid in Nitrogen

Two samples were used to determine the role of oxygen on the activity and mechanism. To remove any atmospheric oxygen from the reaction, a sample was placed inside a quartz tube, flushed with nitrogen and sealed, as described in the experimental section.

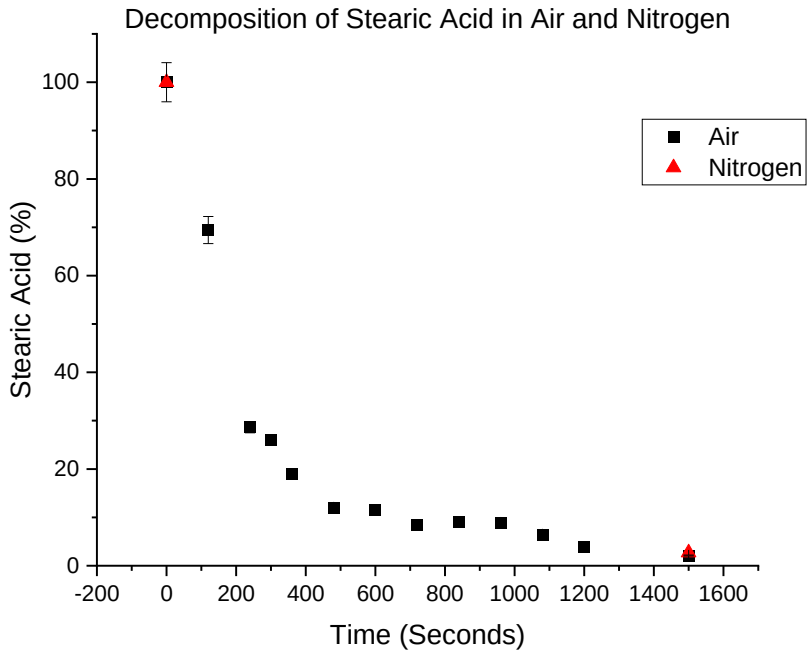

Figure 8.5: Decomposition of stearic acid over a 0.1 wt% Cu-doped meso-TiO_2 thin film produced at 3500 rpm

Figure 8.5 shows the decomposition of stearic acid over two 0.1 wt% Cu-doped mesoporous TiO_2 films produced at 3500 rpm from the same batch, to provide two samples that are as comparable as possible. The sample that was run in nitrogen was sealed, so it wasn't possible to obtain IR spectra at regular intervals as with the sample run in air. After irradiation, the quartz tube used to contain the sample and nitrogen had an area of visible condensation immediately surrounding the sample. Decomposition after the 25 minute total irradiation was almost identical between the two samples, with the air and nitrogen samples decomposing 97.9 and 97.3 % of the stearic acid respectively.

Comparisons between the two samples are not ideal since the sample run in nitrogen had a 25 minute period of continuous irradiation, whereas the irradiation of the sample run in air was broken up into several minute intervals. The exponential decay of signal intensity for stearic acid over the sample run in air indicates first order process.

8.4 Photodegradation of Stearic Acid Under Vacuum

To investigate the role of molecular oxygen in the decomposition of stearic acid further, a 0.1 wt% Cu-doped film was spin-coated directly onto a 3-bounce Ge ATR crystal. The film was prepared in the same way as described in the experimental section, except for the substrate being the ATR crystal instead of the usual glass coverslips and a larger volume of solution was used to guarantee complete coverage of the crystal. The experimental configuration of the ATR experiment brings the IR beam into contact with the underside of the titania film instead of the stearic acid as is the case in the DRIFTS experiments. The experiment therefore requires as thin a film as possible due to the limited penetration of the IR beam. The ATR crystal was coated at a spin speed of 8000 rpm with a 0.1 wt% copper doped photocatalyst so that the resulting spectra showed as much of the stearic acid as possible.

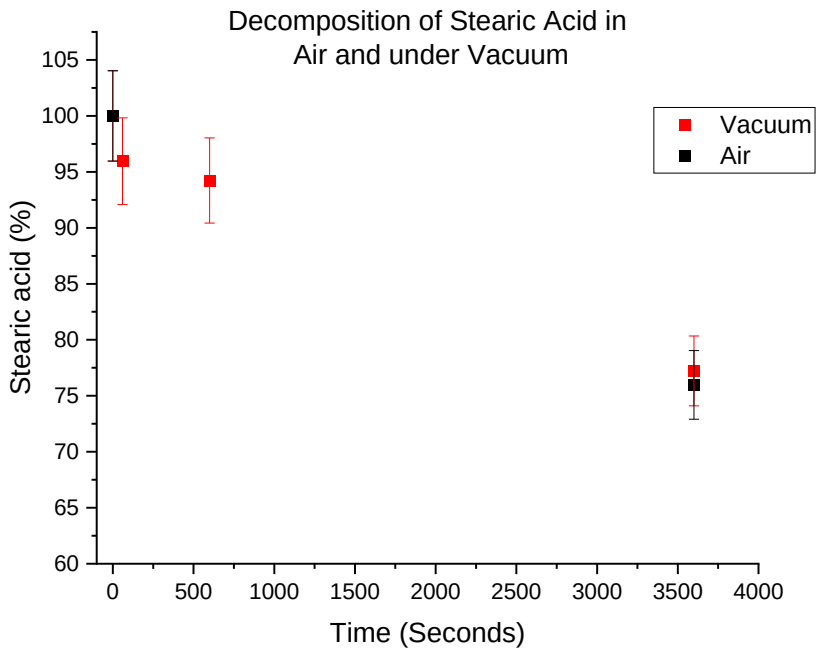

Figure 8.6: Decomposition of stearic acid in air (black) and under vacuum (red)

The ATR-FTIR used could be operated under vacuum or with a flow of air. The sample was placed into the FTIR and placed under vacuum before being exposed to UV light for 60 minutes, with IR spectra taken at 1, 10 and 60 minute intervals. Subsequently, air was flowed through the apparatus and the experiment repeated, with IR spectra recorded at 60 minutes and 17.5 hours. Figure 8.6 shows the degradation of stearic acid in both air and under vacuum over 60 minutes. After 60 minutes, they reached 22.8 and 24.0 % decomposition respectively. The sample run in air

reached a total decomposition of 34.06 % after the 17.5 hour irradiation. Due to space constraints in the chamber, the lightsource used for these experiments was less powerful than the one used for other experiments, so they cannot be directly compared to the other rates obtained.

As seen with the sample run under nitrogen, the extent of degradation of the stearic acid is almost identical whether the sample is irradiated in the presence of oxygen or not. This is in direct conflict with most current theories about the role of molecular oxygen in the mechanism of these materials.

8.5 Discussion

The samples and reactants used in these experiments lend themselves well to obtaining details about the reaction mechanism and the sources of oxygen used in the photocatalytic degradation of organic molecules by these films.

Apart from the oxygen in the catalyst itself, the only source of oxygen that couldn't be removed from the reaction mixture was the oxygen contained within the carboxylic acid group of stearic acid. Equation 8.13 shows the complete decomposition of stearic acid. Given that there are 35 C-H bonds in each molecule of stearic acid, if the oxygen of the carboxylic acid was the only oxygen species involved in the decomposition, there would be a maximum 11 % decomposition as measured using the C-H stretch.

$$26\ O_2 + C_{18}H_{36}O_2 \rightarrow 18\ H_2O + 18\ CO_2 \qquad \textbf{8.13}$$

As the decomposition seen in experiments without atmospheric oxygen exceeds the 11 % threshold, it can be concluded that either surface or lattice oxygen species from the TiO_2 must be involved in the mechanism. Experiments conducted in nitrogen, air and under vacuum all reached > 20 % decomposition of the stearic acid present, it can be determined that the oxygen from the carboxylic acid cannot be responsible for the decomposition, leaving either lattice or surface oxygen species from the catalyst as responsible for the decomposition.

Two mechanisms that have been proposed for these reactions involve either hyperoxide radicals produced after molecular oxygen combines with an electron, Equation 8.3, or from surface oxygen species combining with holes to form surface radicals as seen in Equations 8.9 and 8.10. It is clear from the results obtained, that the molecular oxygen pathway cannot be the only mechanism utilized by these films, as the reactions still progress at similar rates without any molecular oxygen present.

If the reactions with and without the presence of molecular oxygen were progressing by different mechanisms, we would expect a difference in the percentage decomposition between the samples run in air and their equivalent samples run under nitrogen or vacuum. The very close similarity in decomposition rates under the different conditions indicates that the reactions are either progressing by the same mechanism or have the same rate limiting factor in both experiments.

It is possible that the molecular oxygen route is kinetically favourable while molecular oxygen is present in the reaction mixture and the reaction is progressing through this mechanism in the experiments conducted in air, while the experiments performed without molecular oxygen present progress by a surface oxygen mechanism. If that were the case, then the two experiments having near identical rates of decomposition would be reliant upon the two different mechanisms having a common rate limiting step. There are several factors that could be responsible for the similarity in the rates of the two reactions, including the amount of stearic acid in contact with the surface, the intensity of light the sample is exposed to, and levels of electron hole recombination.

After confirming that the reaction progresses at the same rate whether in air, nitrogen or under vacuum, molecular oxygen can be ruled out as having a direct role in the mechanism, so the mechanism must progress using either surface or lattice oxygen species contained within the catalyst. The large increase in activity seen in the mesoporous films when compared to the non-porous films supports this hypothesis as there is an increase to the surface area and therefore the number of surface oxygen species as confirmed by BET analysis.

The reaction mechanism of these films may vary from the mechanism that TiO_2 takes when in solution. A solvent could enable the propagation of radicals away from the surface, but this is unlikely to happen in the gas phase. Other mechanistic studies using only solid and gas phase reaction mixtures have focused on NO or other gaseous pollutants.[26,32]

The only likely mechanism by which the reaction can proceed is a Mars van Krevelen mechanism. There is evidence that other photocatalysts proceed by this mechanism, but it has previously been accepted that molecular oxygen plays a pivotal role in the mechanism of TiO_2 photocatalysis.[13,23]

8.6 References

1 M. Anne. Fox and M. T. Dulay, *Chem. Rev.*, 1993, **93**, 341–357.

2 M. R. Hoffmann, S. T. Martin, Wonyong. Choi and D. W. Bahnemann, *Chemical Reviews*, 1995, **95**, 69–96.

3 J. Peral, X. Domènech and D. F. Ollis, *Journal of Chemical Technology & Biotechnology*, 1997, **70**, 117–140.

4 A. Fujishima, T. N. Rao and D. A. Tryk, 2000, 21.

5 D. Friedmann, C. Mendive and D. Bahnemann, *Applied Catalysis B: Environmental*, 2010, **99**, 398–406.

6 M. A. Henderson, *Surface Science Reports*, 2011, **66**, 185–297.

7 V. Augugliaro, M. Bellardita, V. Loddo, G. Palmisano, L. Palmisano and S. Yurdakal, *Journal of Photochemistry and Photobiology C: Photochemistry Reviews*, 2012, **13**, 224–245.

8 J. F. Montoya, M. F. Atitar, D. W. Bahnemann, J. Peral and P. Salvador, *J. Phys. Chem. C*, 2014, **118**, 14276–14290.

9 Electron Hole Pair (EHP) Generation | Semiconductor Theory, http://www.science-campus.com/engineering/electronics/semiconductor_theory/semiconductor_5.html, (accessed May 24, 2022).

10 R. Abe, *Journal of Photochemistry and Photobiology C: Photochemistry Reviews*, 2010, **11**, 179–209.

11 Á. Valdés and G.-J. Kroes, *J. Phys. Chem. C*, 2010, **114**, 1701–1708.

12 H. Ma, A. Brennan and S. A. Diamond, *Environmental Toxicology and Chemistry*, 2012, **31**, 2099–2107.

13 J. F. Montoya, I. Ivanova, R. Dillert, D. W. Bahnemann, P. Salvador and J. Peral, *J. Phys. Chem. Lett.*, 2013, **4**, 1415–1422.

14 R. F. Howe and Michael. Gratzel, *J. Phys. Chem.*, 1987, **91**, 3906–3909.

15 O. I. Micic, Y. Zhang, K. R. Cromack, A. D. Trifunac and M. C. Thurnauer, *J. Phys. Chem.*, 1993, **97**, 7277–7283.

16 N. M. Dimitrijevic, Z. V. Saponjic, B. M. Rabatic, O. G. Poluektov and T. Rajh, *J. Phys. Chem. C*, 2007, **111**, 14597–14601.

17 Shinri. Sato, *J. Phys. Chem.*, 1987, **91**, 2895–2897.

18 L. Kavan, M. Zukalova, M. Ferus, J. Kürti, J. Koltai and S. Civiš, *Physical Chemistry Chemical Physics*, 2011, **13**, 11583.

19 S. Civiš, M. Ferus, M. Zukalová, P. Kubát and L. Kavan, *The Journal of Physical Chemistry C*, 2012, **116**, 11200–11205.

20 S. Civiš, M. Ferus, P. Kubát, M. Zukalová and L. Kavan, *The Journal of Physical Chemistry C*, 2011, **115**, 11156–11162.

21 O. Frank, M. Zukalova, B. Laskova, J. Kürti, J. Koltai and L. Kavan, *Physical Chemistry Chemical Physics*, 2012, **14**, 14567.

22 H. Courbon, M. Formenti and P. Pichat, *J. Phys. Chem.*, 1977, **81**, 550–554.

23 A. M. Ali, E. A. C. Emanuelsson and D. A. Patterson, *Applied Catalysis B: Environmental*, 2010, **97**, 168–181.

24 S. Devahasdin, C. Fan, K. Li and D. H. Chen, *Journal of Photochemistry and Photobiology A: Chemistry*, 2003, **156**, 161–170.

25 H. Wang, Z. Wu, W. Zhao and B. Guan, *Chemosphere*, 2007, **66**, 185–190.

26 A. Folli, S. B. Campbell, J. A. Anderson and D. E. Macphee, *Chemistry*, 2011, **220**, 85–93.

27 R. Dillert, A. Engel, J. Große, P. Lindner and D. W. Bahnemann, *Phys. Chem. Chem. Phys.*, 2013, **15**, 20876–20886.

28 M. Hunger, G. Hüsken and H. J. H. Brouwers, *Cement and Concrete Research*, 2010, **40**, 313–320.

29 G. Ali, J. Nisar, M. Iqbal, A. Shah, M. Abbas, M. R. Shah, U. Rashid, I. A. Bhatti, R. A. Khan and F. Shah, *Waste Manag Res*, 2020, **38**, 202–212.

30 J. R. M. Ângelo, Ph.D., Universidade do Porto (Portugal).

31 Z. Bai, Y. Hu, S. Yan, W. Shan and C. Wei, *RSC Adv.*, 2017, **7**, 1966–1974.

32 J. Rathouský, M. Slabová, K. Macounová and A. Zukal, in *Studies in Surface Science and Catalysis*, eds. A. Sayari and M. Jaroniec, Elsevier, 2002, vol. 141, pp. 599–606.

33 Y. Deng, S. Peng, H. Liu, S. Li and Y. Chen, *Front. Environ. Sci. Eng.*, 2019, **13**, 21.

34 Z. Xiong, J. Ma, W. J. Ng, T. D. Waite and X. S. Zhao, *Water Research*, 2011, **45**, 2095–2103.

35 J. N. Kondo, T. Yamashita, T. Katou, B. Lee, D. Lu, M. Hara and K. Domen, in *Studies in Surface Science and Catalysis*, eds. A. Sayari and M. Jaroniec, Elsevier, 2002, vol. 141, pp. 265–272.

Chapter 9. Conclusions

The main aim of this study was to explore the use of spin-coating to produce mesoporous titanium dioxide photocatalysts and assess the multiple factors that can affect the activity of the resulting films. This was approached by looking closely at the fundamental aspects of sol-gel spin-coating and exploring the affect that they have on the activity of the surface coatings produced.

The formulation was assessed in Chapter 3. The concentration of Pluronic P-123 and EISA time and temperature was varied to ensure that the porosity of the samples would give the most active samples. Hydrolysis of the solution was a considerable problem when spin-coating but would not pose an issue when making powders from this type of sol-gel synthesis. This work was vital to the whole project as it gave the best possible starting point to explore film thickness, preparation spin speed, and copper doping and other variables.

Surface metrology was employed to gather information about the topography of the films, surface defects and film depth. These film depth measurements shed light on the non-Newtonian nature of the solution used during spin-coating. The bounds within which the film thickness could be controlled with the spin-speed used to produce films varied from one solution to another. The critical shear rate and the viscosity of the solution dictate the minimum film depth that can be achieved. Both values changed considerably with the amount of copper nitrate in the solution and no relationship between the three values could be found that would help to predict the properties of future solutions.

Photocatalytic testing on layered films revealed a significant increase in activity with increasing layers up to four layers. Increasing the number of layers above four led to a decrease in the activity.

There is very little literature suggesting that the preparation spin speed affects anything more than the film thickness yet varying the spin-speed of films resulted in changes in activity well beyond the critical shear rate and into the region where the film depth did not change.

Bandgaps were calculated for these films at 3.13 and 3.17 eV, below the commercially available TiO_2. Changes in bandgap energy have been linked to grain size and surface oxygen species. Either of these could be influenced by the preparation spin speed changes in absence of the changes in depth and could explain the changes in activity seen at increasing preparation spin speeds.

Copper doping above 1 wt% proved to be detrimental to the activity of the films. At 0.5 and 0.1 wt%, the activity increased with decreasing copper content. XRD of powders revealed the films to be present as anatase. No peaks could be attributed to copper, suggesting that it is present in substitutional positions or amorphous clusters. XPS revealed differing oxidation states of the copper depending on the doping amount. The 5 wt% copper-doped films showed changes in the bandgap energy with preparation spin speed.

The 0.1 wt% copper-doped samples were the most active films and as such were selected for photodegradation of polystyrene. Photocatalytic testing over a range of samples produced at differing spin-speeds revealed tuneable selectivity to the decomposition of aromatic or aliphatic C-H bonds.

9.1 Future work

Increasing the number of layers and decreasing the preparation spin speed independently resulted in a decrease in the half-life of stearic acid decomposition over these films. It would be beneficial to explore the effect of combining the two methods to see if two effects are independent of each other when multi-layered films are produced at high spin speeds.

Producing powders from scraped surface coatings to allow BET surface area analysis and XRD of a wider range of samples would be beneficial. The small amount of material on each surface coating means that several hundred identical samples would need to be produced to obtain 1 g of powder representative of a single sample. These powders could also be used for other analytical techniques to gain a better understanding of the differences between samples produced at different spin speeds and number of layers.

Stearic acid decomposition over photocatalytic films performed under nitrogen or vacuum was limited to a single film of stearic acid. Multiple layers of stearic acid could be added, or other coating methods could be utilised to provide a much greater amount of stearic acid on the surface. This would give valuable information about the upper limit that the films are able to decompose. The samples would also benefit from characterisation before and after photocatalytic testing without molecular oxygen before they are expose to the air. This would give valuable insight into any changes that happen to the films during this process and could shed further light on the mechanism.

Appendix 1: Rate Plots and Rates of Stearic Acid Decomposition on Undoped Samples

A: 1.1 Rate plots for stearic acid decomposition over samples produced with varying amounts of P-123

Zero order rate plots for stearic acid decomposition on samples with varying amounts of Pluronic P-123 and the rate constants

A1.1

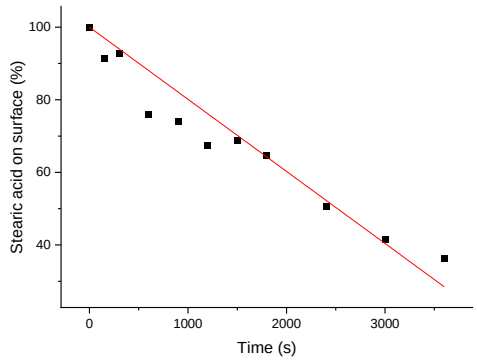

0.5 g P-123

R^2: 0.99245

Rate constant: $1.98 \times 10^{-2} \pm 1.05 \times 10^{-3}$

A1.2

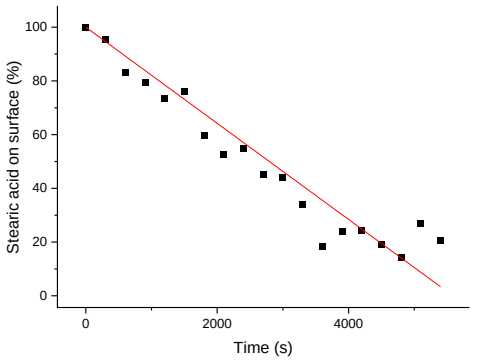

1 g P-123

R^2: 0.99601

Rate constant: $2.06 \times 10^{-2} \pm 5.53 \times 10^{-4}$

A1.3

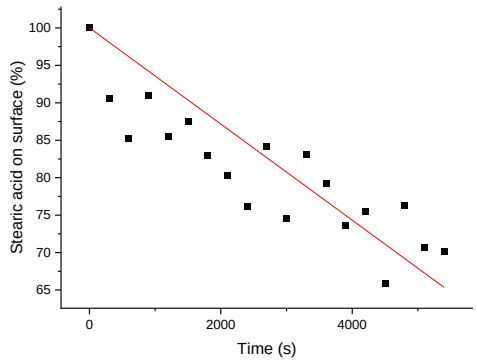

1.5 g P-123

R^2: 0.99557

Rate constant: $7.43 \times 10^{-3} \pm 7.39 \times 10^{-4}$

First order rate plots for samples with varying amounts of Pluronic P-123 and the rate constants

A1.4

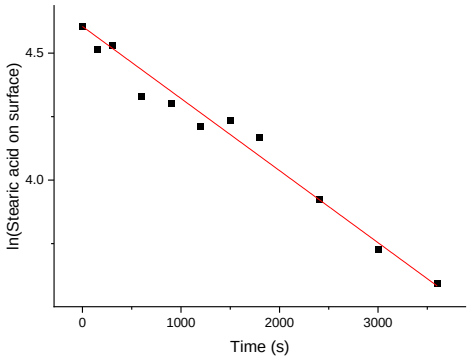

0.5 g P-123

R^2: 0.99984

Rate constant: $2.84 \times 10^{-4} \pm 8.76 \times 10^{-6}$

A1.5

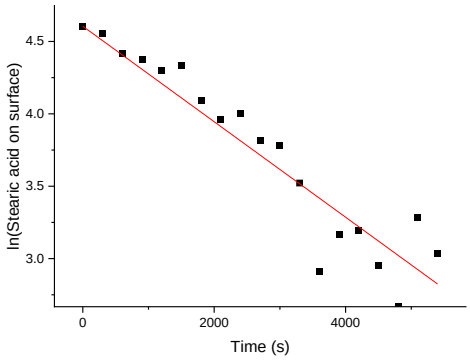

1 g P-123

R^2: 0.99708

Rate constant: $3.30 \times 10^{-4} \pm 1.49 \times 10^{-5}$

A1.6

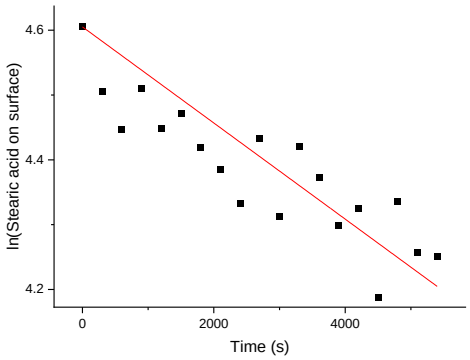

1.5 g P-123

R^2: 0.9998

Rate constant: $7.42 \times 10^{-5} \pm 4.53 \times 10^{-6}$

A: 1.2 Rate plots for stearic acid decomposition over samples produced from precursor and pre-hydrolysed solutions

Zero order rate plots and the rate constants for stearic acid decomposition on samples made using a precursor solution at spin speeds from 600 to 2000 rpm

A1.7	A1.8
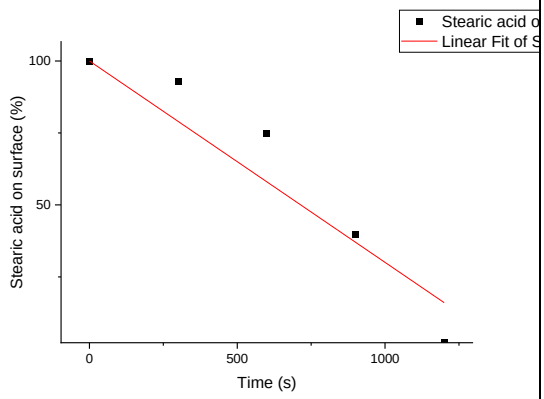	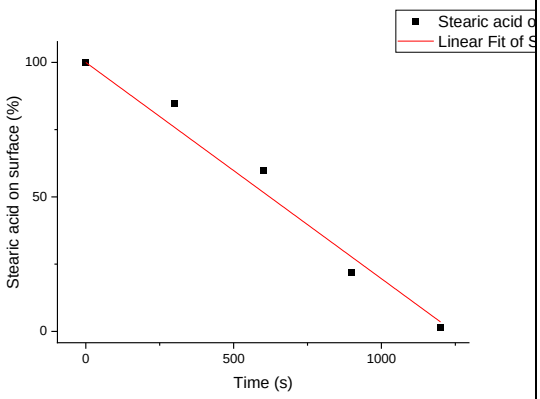
600 rpm R^2: 0.96751 Rate constant: $6.99 \times 10^{-2} \pm 7.88 \times 10^{-3}$	800 rpm R^2: 0.98923 Rate constant: $8.04 \times 10^{-2} \pm 4.12 \times 10^{-3}$
A1.9	**A1.10**
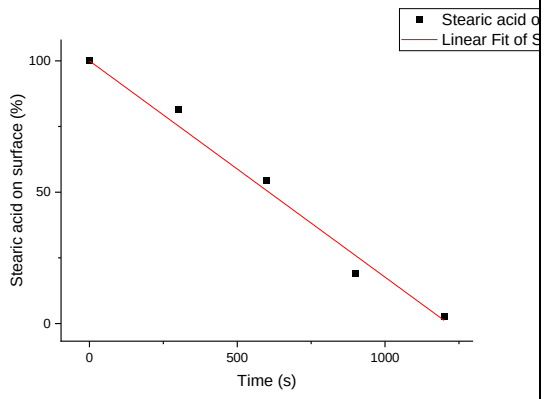	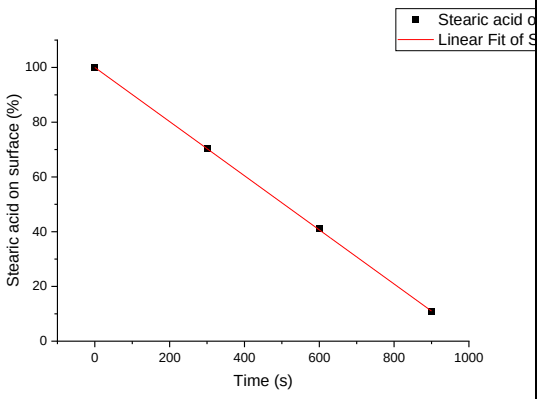
1000 rpm R^2: 0.99356 Rate constant: $8.24 \times 10^{-2} \pm 3.09 \times 10^{-3}$	1200 rpm R^2: 0.99999 Rate constant: $9.89 \times 10^{-2} \pm 2.12 \times 10^{-4}$

A1.11

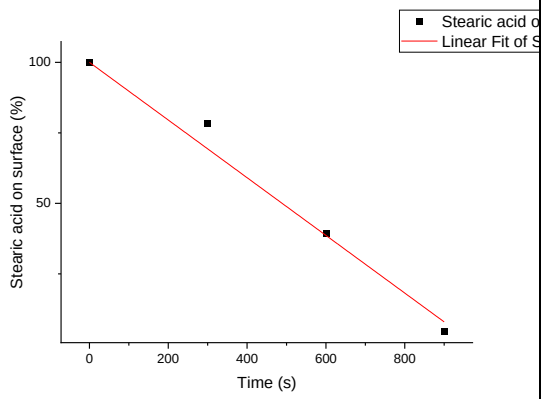

1400 rpm

R^2: 0.99304

Rate constant: $1.02 \times 10^{-1} \pm 4.94 \times 10^{-3}$

A1.12

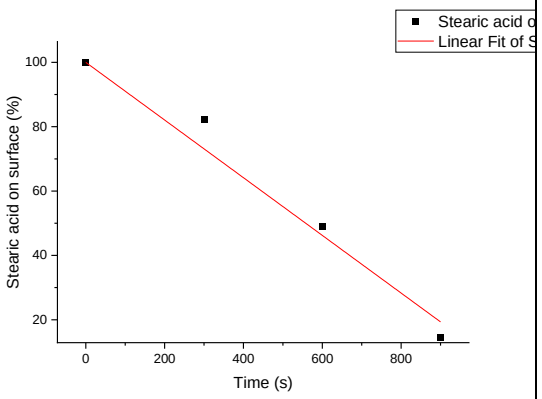

1600 rpm

R^2: 0.99215

Rate constant: $8.96 \times 10^{-2} \pm 5.49 \times 10^{-3}$

A1.13

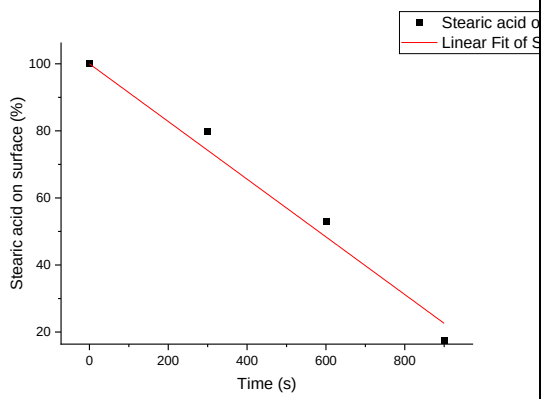

1800 rpm

R^2: 0.99456

Rate constant: $8.60 \times 10^{-2} \pm 4.59 \times 10^{-3}$

A1.14

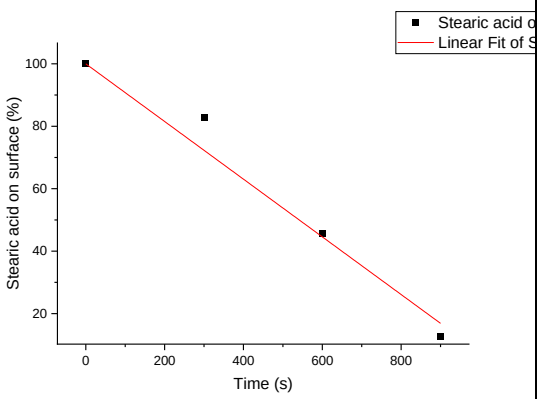

2000 rpm

R^2: 0.99098

Rate constant: $9.24 \times 10^{-2} \pm 5.85 \times 10^{-3}$

Zero order rate plots and the rate constants for stearic acid decomposition on samples made using a hydrolysed solution at spin speeds from 600 to 2000 rpm

A1.15 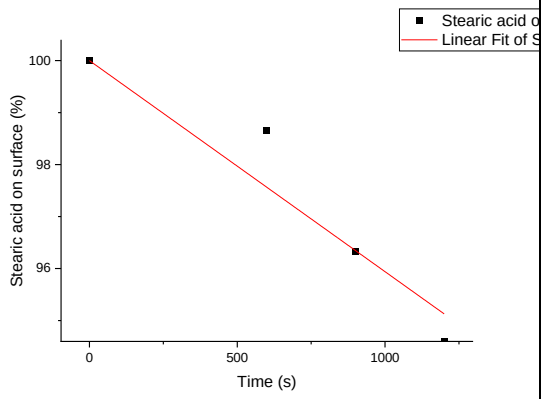 600 rpm R^2: 0.99995 Rate constant: $4.06 \times 10^{-3} \pm 4.32 \times 10^{-4}$	A1.16 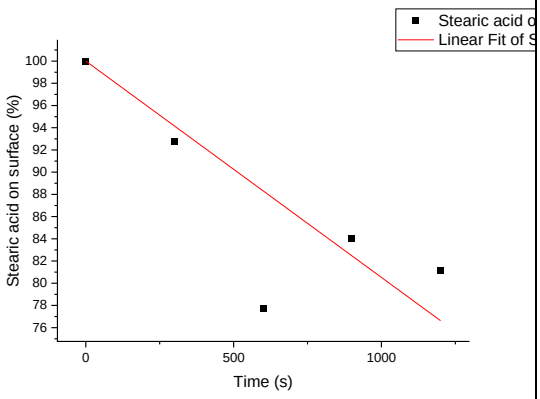 800 rpm R^2: 0.99551 Rate constant: $1.95 \times 10^{-2} \pm 3.57 \times 10^{-3}$
A1.17 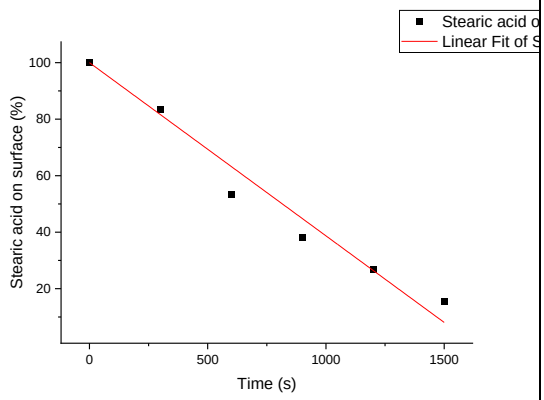 1000 rpm R^2: 0.98904 Rate constant: $6.13 \times 10^{-3} \pm 2.86 \times 10^{-3}$	A1.18 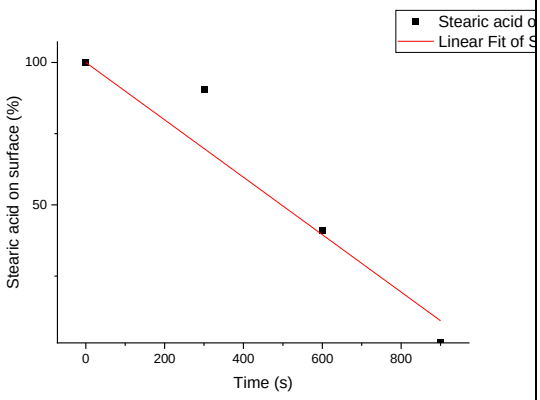 1200 rpm R^2: 0.96732 Rate constant: $1.01 \times 10^{-1} \pm 1.13 \times 10^{-2}$

A1.19

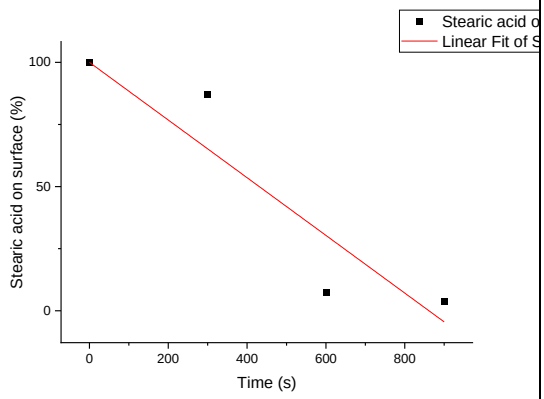

1400 rpm

R^2: 0.91913

Rate constant: $1.16 \times 10^{-1} \pm 1.68 \times 10^{-2}$

A1.20

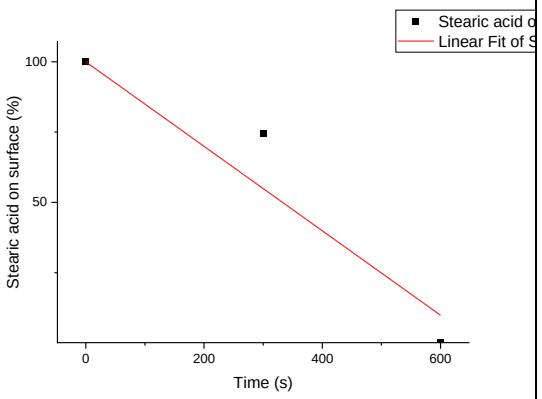

1600 rpm

R^2: 0.95413

Rate constant: $1.50 \times 10^{-1} \pm 2.30 \times 10^{-2}$

A1.21

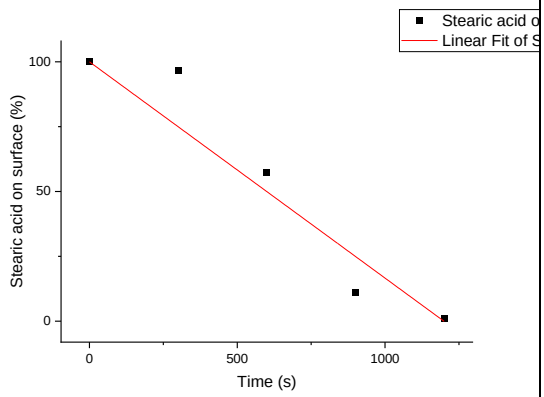

1800 rpm

R^2: 0.9609

Rate constant: $8.34 \times 10^{-2} \pm 8.11 \times 10^{-3}$

A1.22

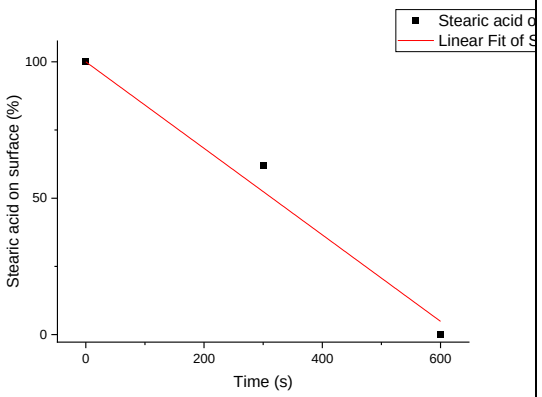

2000 rpm

R^2: 0.98726

Rate constant: $1.59 \times 10^{-1} \pm 1.14 \times 10^{-2}$

First order rate plots and the rate constants for stearic acid decomposition on samples made using a precursor solution at spin speeds from 600 to 2000 rpm

A1.23 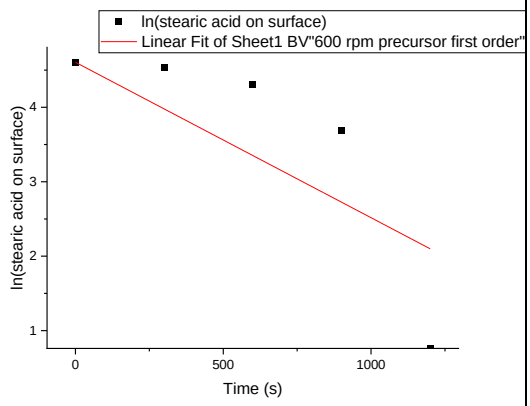 600 rpm R^2: 0.93386 Rate constant: $2.09 \times 10^{-3} \pm 6.04 \times 10^{-4}$	A1.24 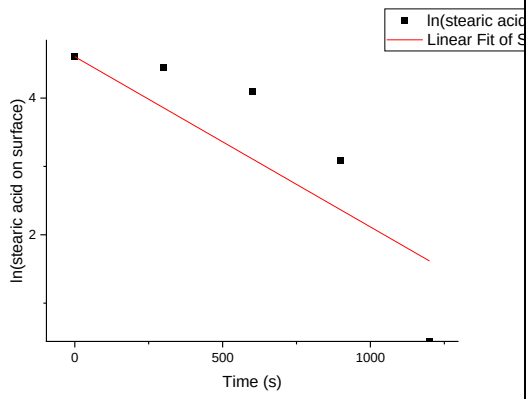 800 rpm R^2: 0.94054 Rate constant: $2.49 \times 10^{-3} \pm 5.45 \times 10^{-4}$
A1.25 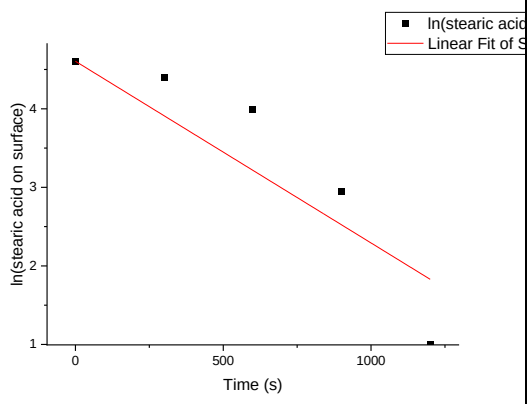 1000 rpm R^2: 0.96734 Rate constant: $2.31 \times 10^{-3} \pm 4.00 \times 10^{-4}$	A1.26 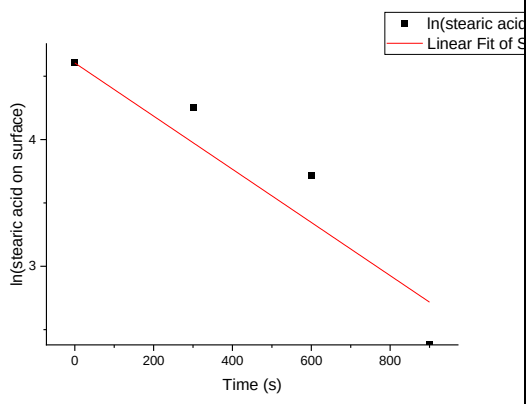 1200 rpm R^2: 0.99261 Rate constant: $2.10 \times 10^{-3} \pm 2.93 \times 10^{-4}$

A1.27

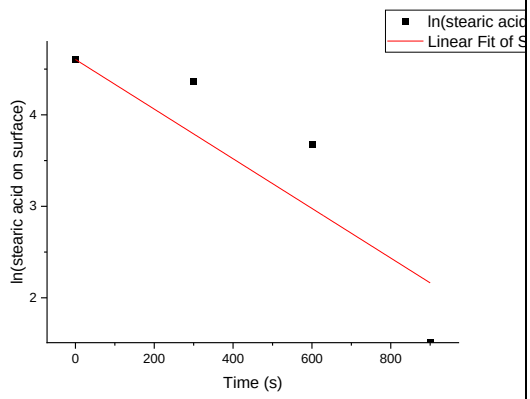

1400 rpm

R^2: 0.97059

Rate constant: $2.71 \times 10^{-3} \pm 5.72 \times 10^{-4}$

A1.28

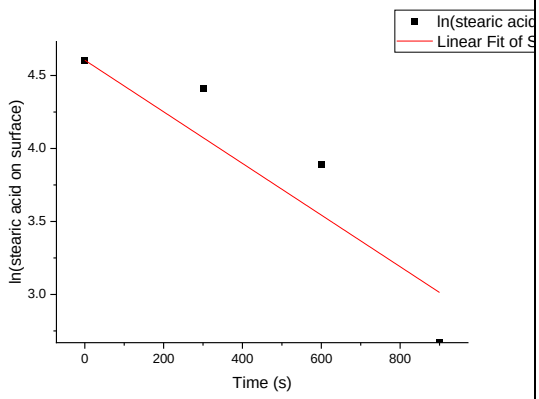

1600 rpm

R^2: 0.99255

Rate constant: $1.77 \times 10^{-3} \pm 3.05 \times 10^{-4}$

A1.29

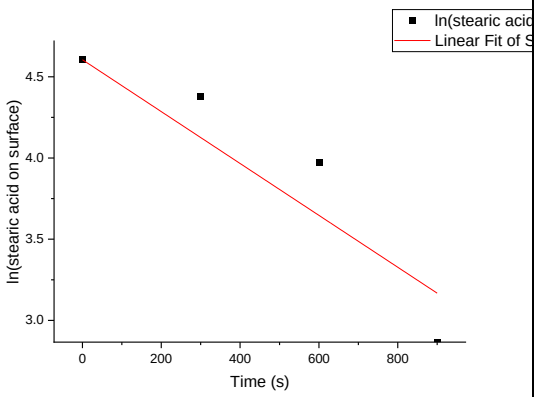

1800 rpm

R^2: 0.99459

Rate constant: $1.60 \times 10^{-3} \pm 2.63 \times 10^{-4}$

A1.30

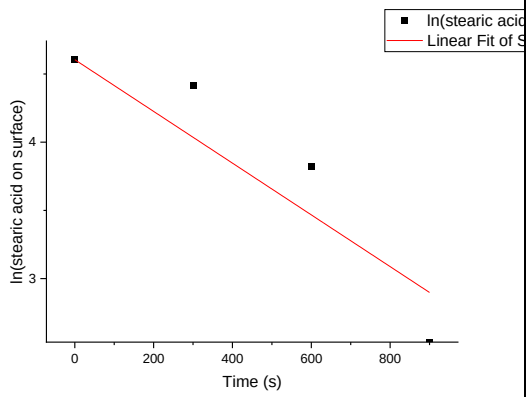

2000 rpm

R^2: 0.99128

Rate constant: $1.90 \times 10^{-3} \pm 3.27 \times 10^{-4}$

First order rate plots and the rate constants for stearic acid decomposition on samples made using a hydrolysed solution at spin speeds from 600 to 2000 rpm

A1.31 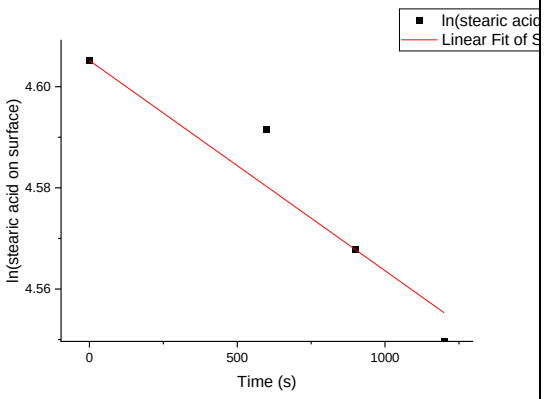 600 rpm R^2: 1 Rate constant: $4.16 \times 10^{-5} \pm 4.54 \times 10^{-6}$	A1.32 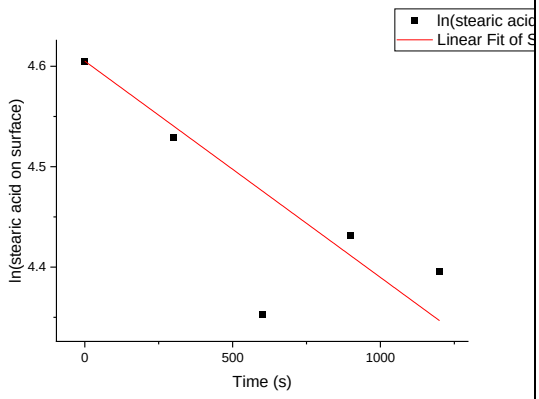 800 rpm R^2: 0.99977 Rate constant: $2.15 \times 10^{-4} \pm 4.09 \times 10^{-5}$
A1.33 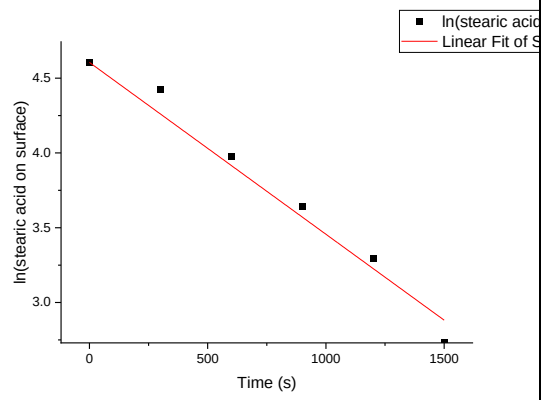 1000 rpm R^2: 0.99915 Rate constant: $1.15 \times 10^{-3} \pm 5.03 \times 10^{-5}$	A1.34 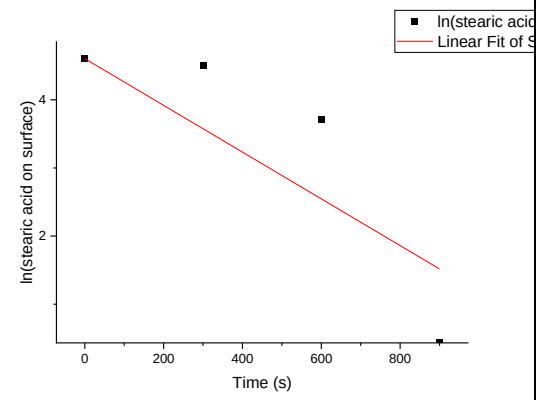 1200 rpm R^2: 0.9184 Rate constant: $3.43 \times 10^{-3} \pm 9.48 \times 10^{-4}$

A1.35

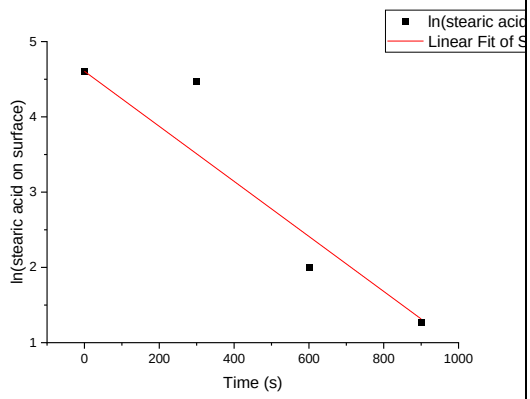

1400 rpm

R^2: 0.96889

Rate constant: $3.66 \times 10^{-3} \pm 5.37 \times 10^{-4}$

A1.36

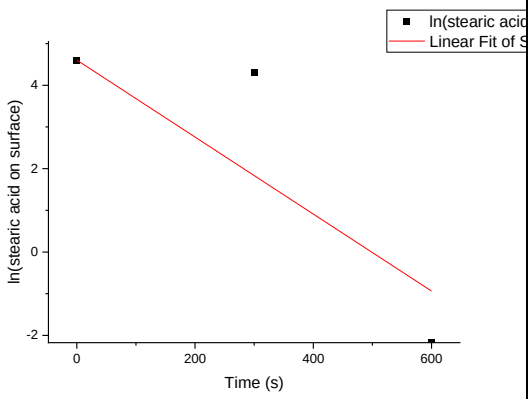

1600 rpm

R^2: 0.74183

Rate constant: $9.24 \times 10^{-3} \pm 2.92 \times 10^{-3}$

A1.37

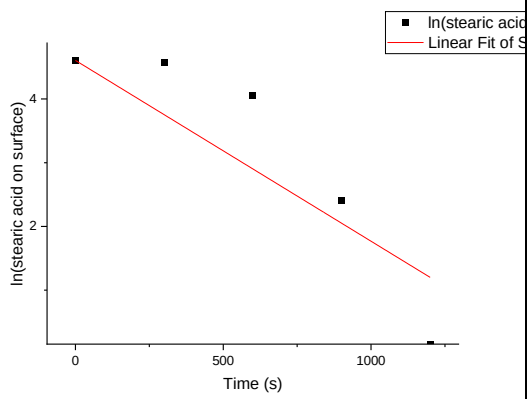

1800 rpm

R^2: 0.93771

Rate constant: $2.84 \times 10^{-3} \pm 5.45 \times 10^{-4}$

A1.38

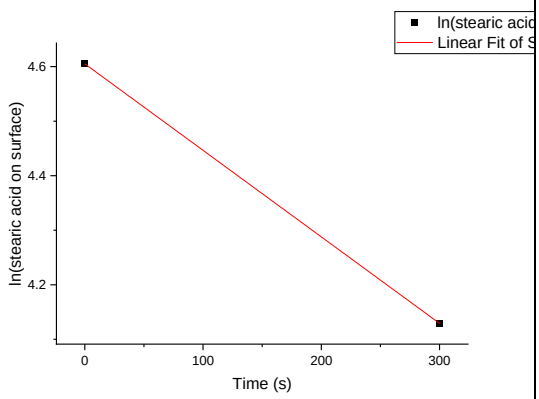

2000 rpm

R^2: 1

Rate constant: $1.59 \times 10^{-3} \pm 6.20 \times 10^{-10}$

A: 1.3 Rate plots for stearic acid decomposition over layered samples

Zero order rate plots and the rate constants for stearic acid decomposition on samples with a number of layers between 1 and 10, produced at a spin speed of 2000 rpm

A1.39

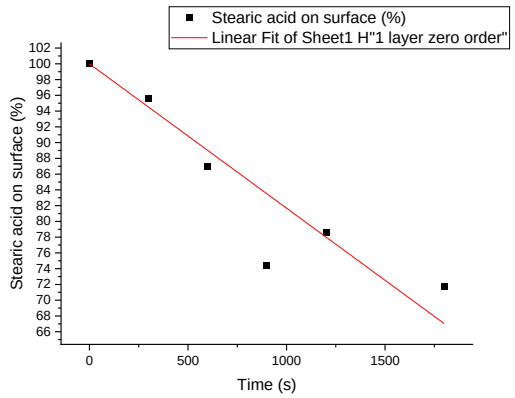

1 layer

R^2: 0.99694

Rate constant: $1.83 \times 10^{-2} \pm 1.93 \times 10^{-3}$

A1.40

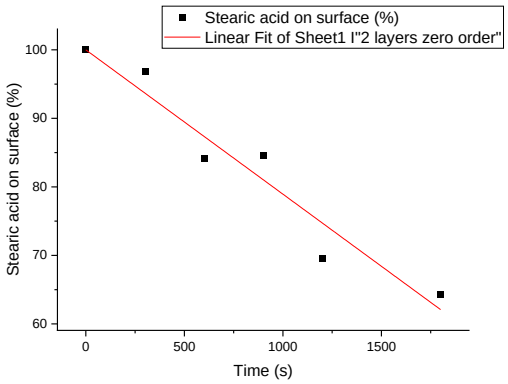

2 layers

R^2: 0.99816

Rate constant: $2.11 \times 10^{-2+ \pm 1.48} \times 10^{-3}$

A1.41

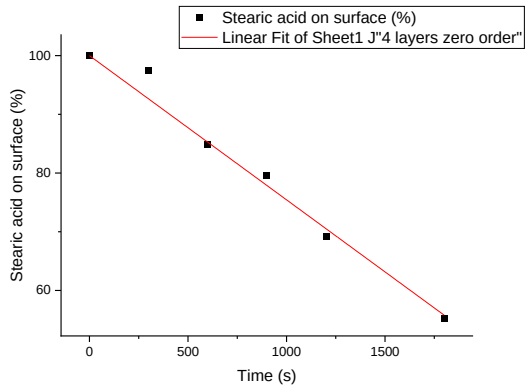

4 layers

R^2: 0.99919

Rate constant: $2.47 \times 10^{-2} \pm 9.62 \times 10^{-4}$

A1.42

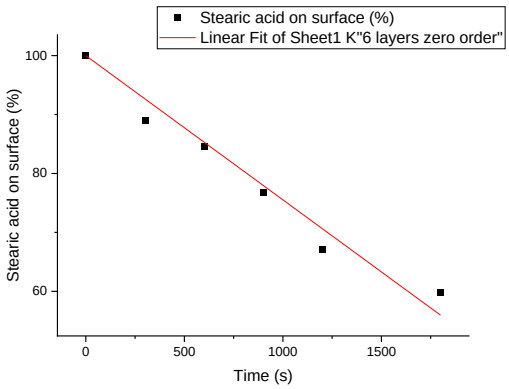

6 layers

R^2: 0.9987

Rate constant: $2.45 \times 10^{-2} \pm 1.19 \times 10^{-3}$

A1.43	A1.44
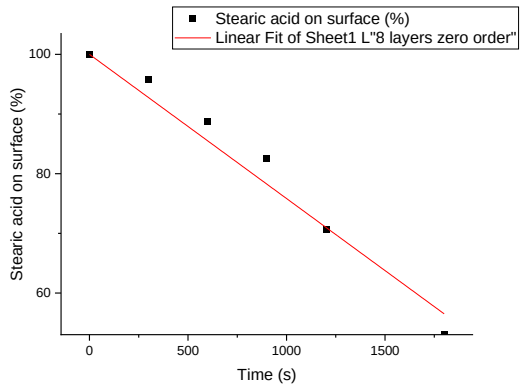	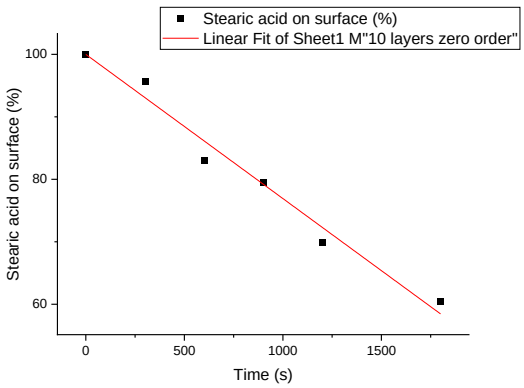
8 layers	10 layers
R^2: 0.99855	R^2: 0.99923
Rate constant: $2.42 \times 10^{-2} \pm 1.30 \times 10^{-3}$	Rate constant: $2.31 \times 10^{-2} \pm 9.43 \times 10^{-4}$

First order rate plots and the rate constants for stearic acid decomposition on samples with the number of layers between 1 and 10, produced at a spin speed of 2000 rpm

A1.45	A1.46
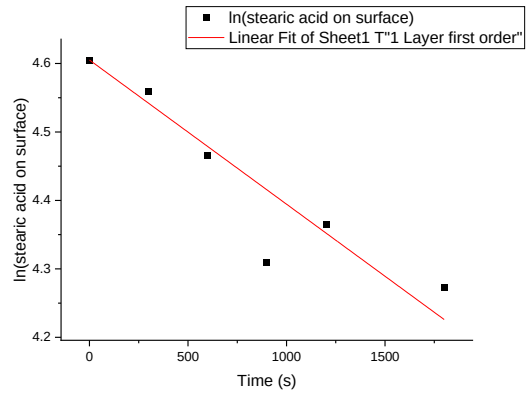	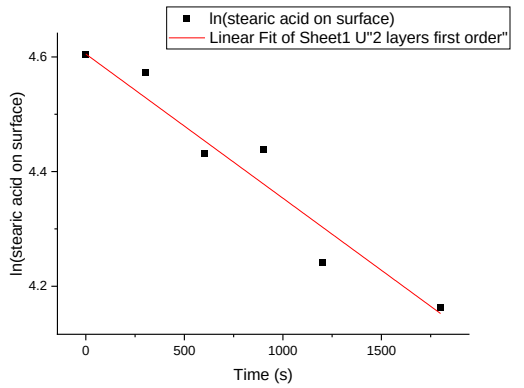
1 layer	2 layers
R^2: 0.99986	R^2: 0.9999
Rate constant: $2.11 \times 10^{-4} \pm 2.18 \times 10^{-5}$	Rate constant: $2.52 \times 10^{-4} \pm 1.82 \times 10^{-5}$

A1.47

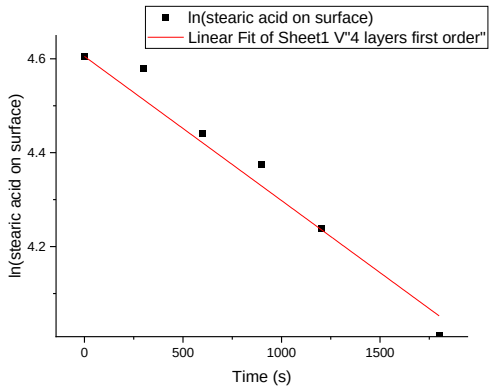

layers

R^2: 0.99991

Rate constant: $3.07 \times 10^{-4} \pm 1.71 \times 10^{-5}$

A1.48

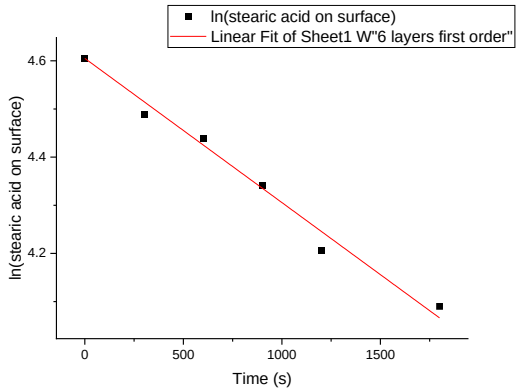

6 layers

R^2: 0.99997

Rate constant: $2.99 \times 10^{-4} \pm 1.02 \times 10^{-5}$

A1.49

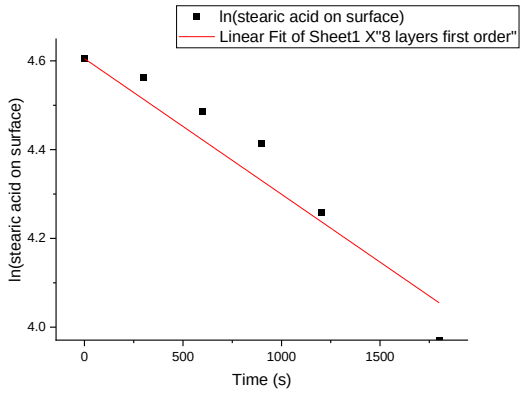

8 layers

R^2: 0.99978

Rate constant: $3.06 \times 10^{-4} \pm 2.65 \times 10^{-5}$

A1.50

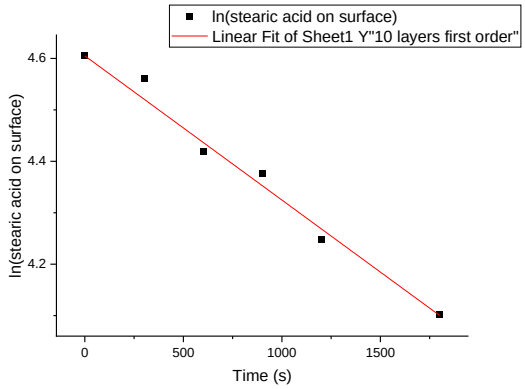

10 layers

R^2: 0.99997

Rate constant: $2.80 \times 10^{-4} \pm 9.90 \times 10^{-6}$

A: 1.4 Rate plots for stearic acid decomposition over samples produced at spin speeds from 600 to 2000 rpm

Zero order rate plots and the rate constants for stearic acid decomposition on samples produced at spin speeds from 600 to 2000 rpm

A1.51 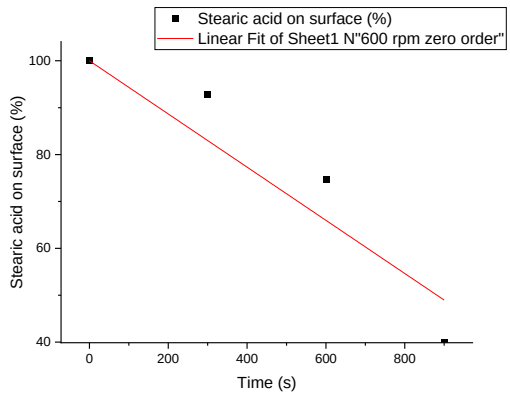 600 rpm R^2: 0.98678 Rate constant: $5.67 \times 10^{-2} \pm 8.22 \times 10^{-3}$	A1.52 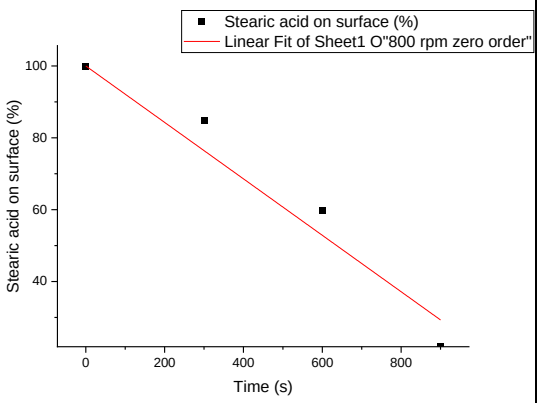 800 rpm R^2: 0.98903 Rate constant: $7.86 \times 10^{-2} \pm 6.80 \times 10^{-3}$
A1.53 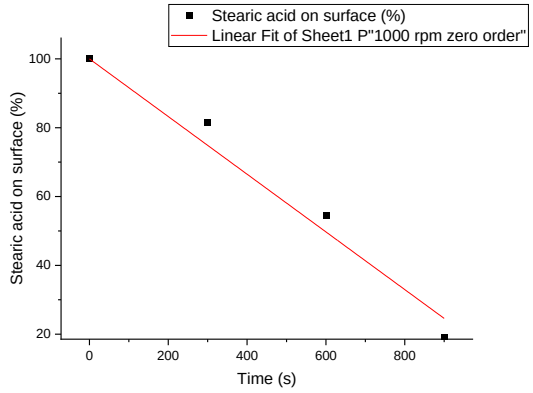 1000 rpm R^2: 0.99346 Rate constant: $8.38 \times 10^{-2} \pm 5.10 \times 10^{-3}$	A1.54 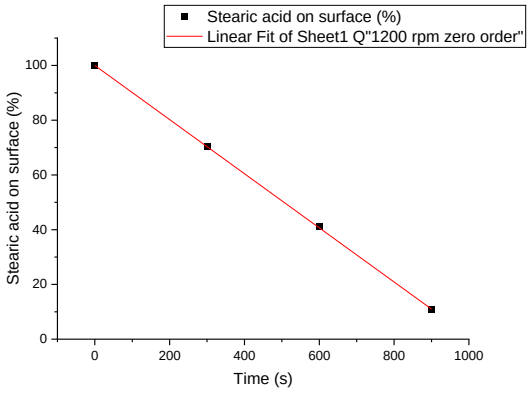 1200 rpm R^2: 0.99999 Rate constant: $9.89 \times 10^{-2} \pm 2.12 \times 10^{-4}$

A1.55

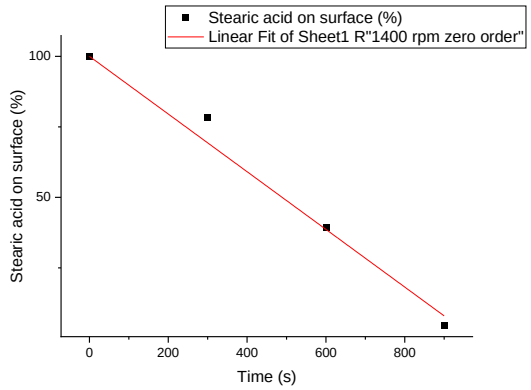

1400 rpm

R^2: 0.99304

Rate constant: $1.02 \times 10^{-1} \pm 4.94 \times 10^{-3}$

A1.56

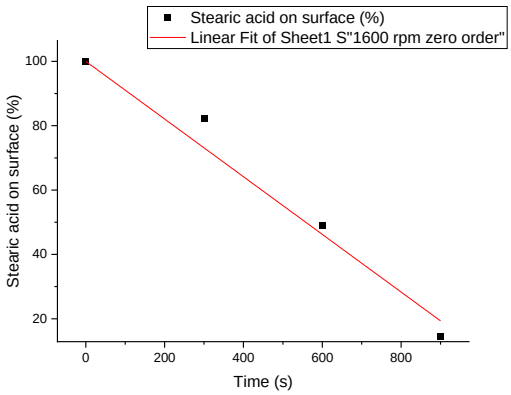

1600 rpm

R^2: 0.99215

Rate constant: $8.96 \times 10^{-2} \pm 5.49 \times 10^{-3}$

A1.57

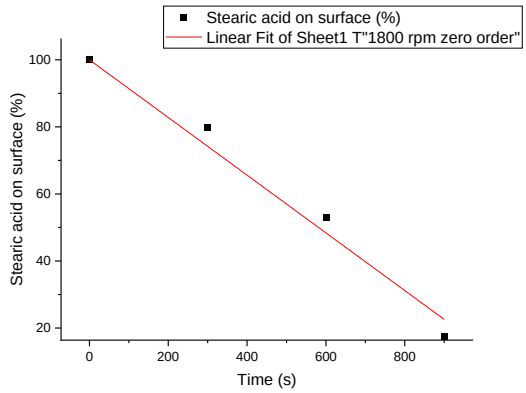

1800 rpm

R^2: 0.99456

Rate constant: $8.60 \times 10^{-2} \pm 4.59 \times 10^{-3}$

A1.58

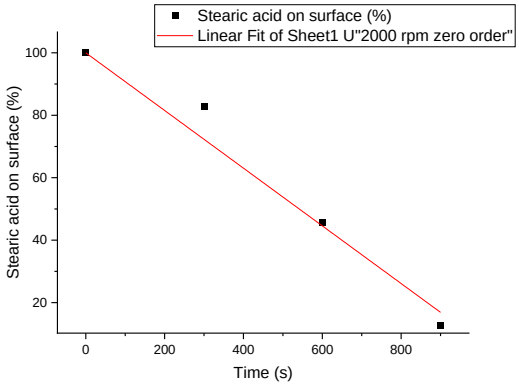

2000 rpm

R^2: 0.99098

Rate constant: $9.24 \times 10^{-2} \pm 5.58 \times 10^{-3}$

First order rate plots and the rate constants for stearic acid decomposition on samples produced at spin speeds from 600 to 2000 rpm

A1.59 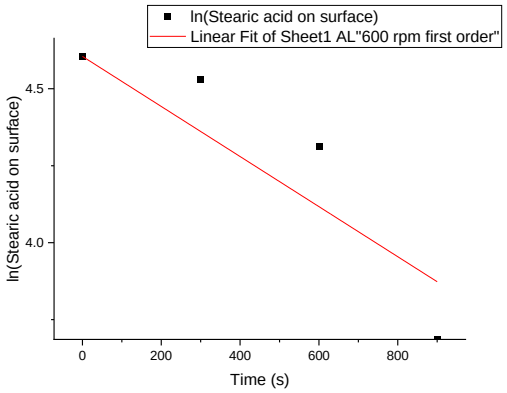 600 rpm R^2: 0.99815 Rate constant: $8.13 \times 10^{-4} \pm 1.65 \times 10^{-4}$	A1.60 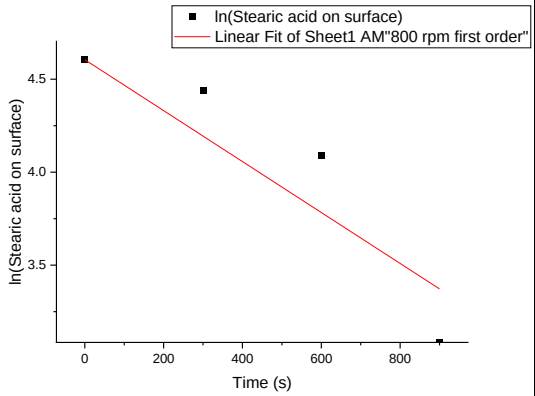 800 rpm R^2: 0.99526 Rate constant: $1.37 \times 10^{-3} \pm 2.51 \times 10^{-4}$
A1.61 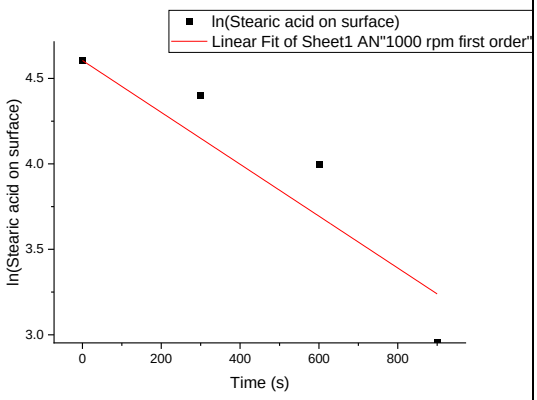 1000 rpm R^2: 0.99514 Rate constant: $1.52 \times 10^{-3} \pm 2.51 \times 10^{-4}$	A1.62 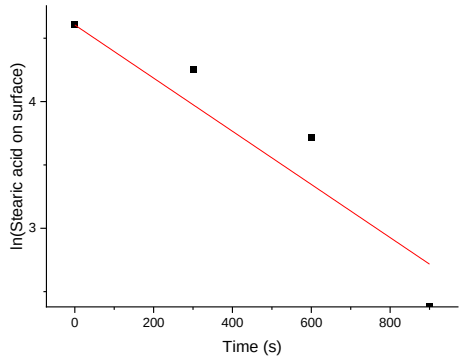 1200 rpm R^2: 0.99261 Rate constant: $2.10 \times 10^{-3} \pm 2.93 \times 10^{-4}$

A1.63

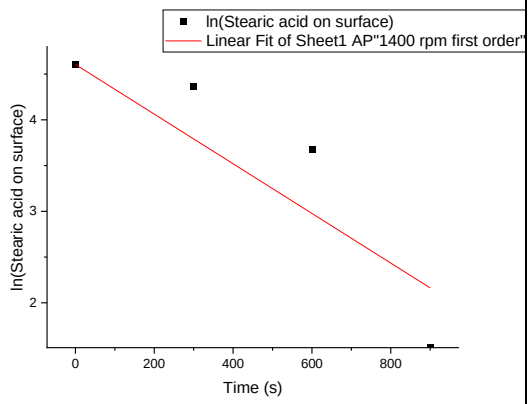

1400 rpm

R^2: 0.97059

Rate constant: $2.71 \times 10^{-3} \pm 5.72 \times 10^{-4}$

A1.64

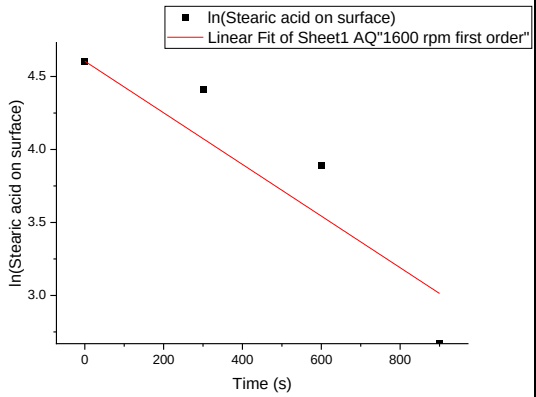

1600 rpm

R^2: 0.99255

Rate constant: $1.77 \times 10^{-3} \pm 3.05 \times 10^{-4}$

A1.65

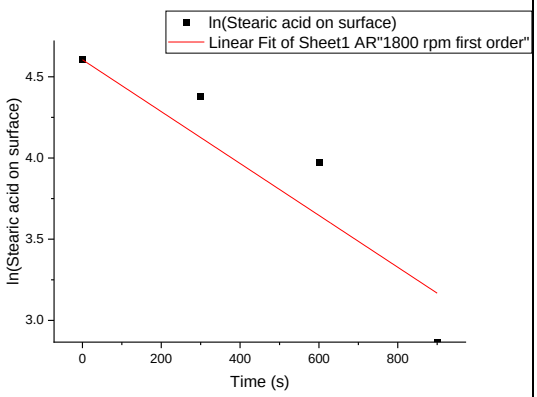

1800 rpm

R^2: 0.99459

Rate constant: $1.60 \times 10^{-3} \pm 2.63 \times 10^{-4}$

A1.66

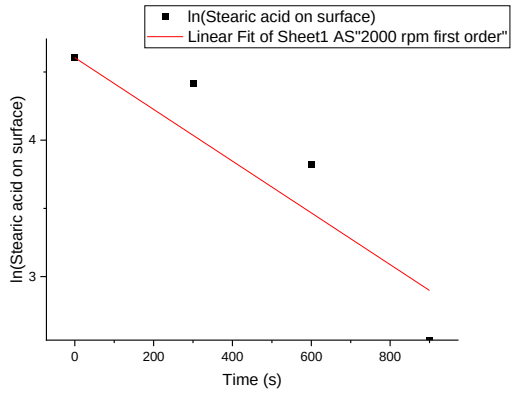

2000 rpm

R^2: 0.99128

Rate constant: 1.90×10^{-3} 3.27×10^{-4}

Appendix 2: Stearic acid decomposition on copper doped samples

A: 2.1 Rate plots for stearic acid decomposition over 5 wt% Copper-doped *meso*-TiO_2 samples

Preparation spin speeds, zero order rate plots and rate constants for stearic acid decomposition on 5 wt% copper-doped *meso*-TiO_2 samples

A2.1	A2.2
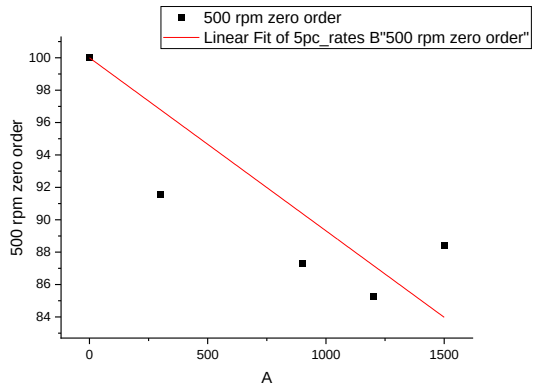	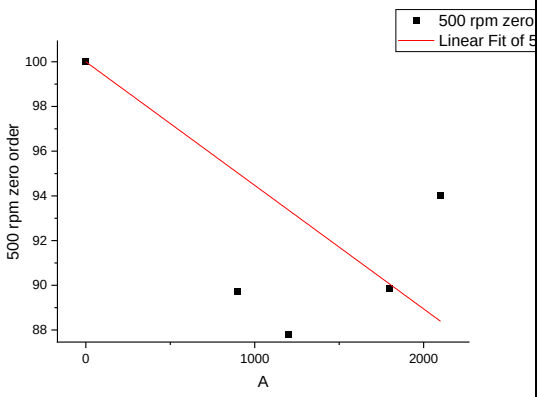
500 rpm R^2: 0.99815 Rate constant: 0.01068 ± 0.00182	500 rpm R^2: 0.99734 Rate constant: 0.00553 ± 0.00151
A2.3	**A2.4**
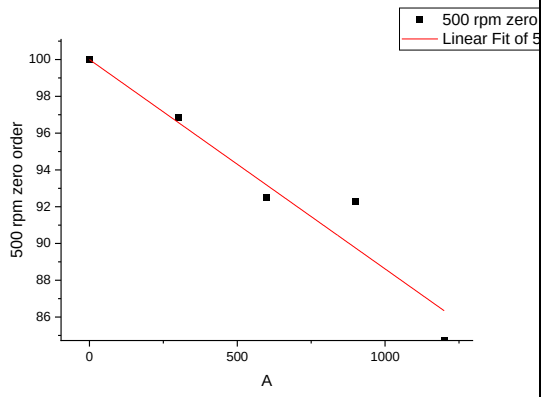	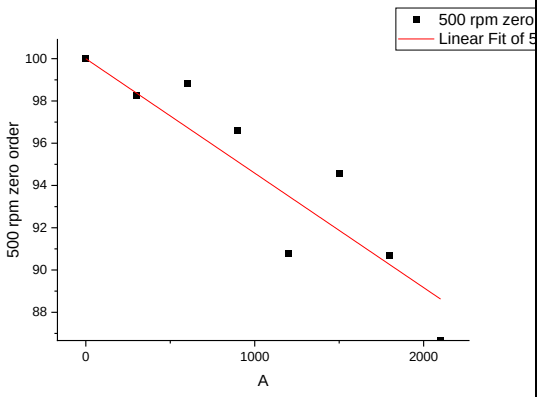
500 rpm R^2: 0.99973 Rate constant: 0.01138 ± 9.32102E-4	500 rpm R^2: 0.9996 Rate constant: 0.00542 ± 5.3298E-4

A2.5 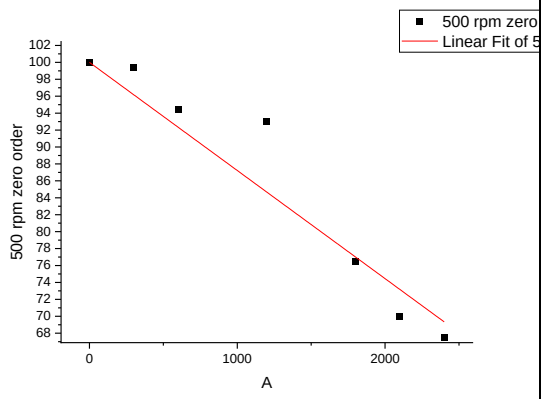 500 rpm R^2: 0.99783 Rate constant: 0.01278 ± 0.00103	A2.6 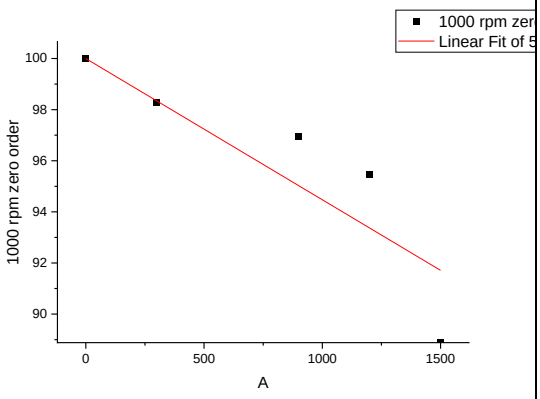 1000 rpm R^2: 0.99956 Rate constant: 0.00553 ± 9.37606E-4
A2.7 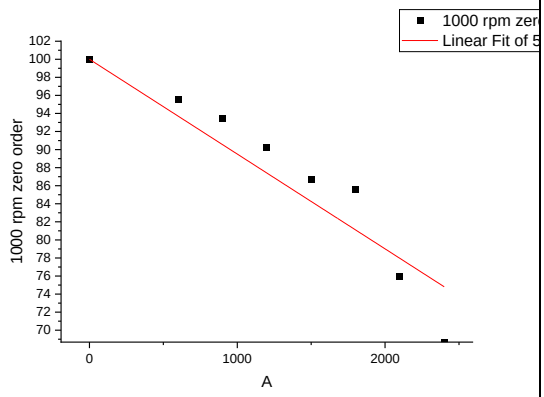 1000 rpm R^2: 0.99838 Rate constant: 0.0105 ± 8.24905E-4	A2.8 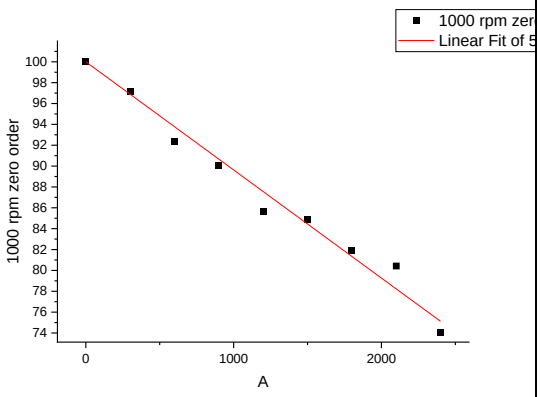 1000 rpm R^2: 0.99979 Rate constant: 0.01037 ± 2.9373E-4

A2.9

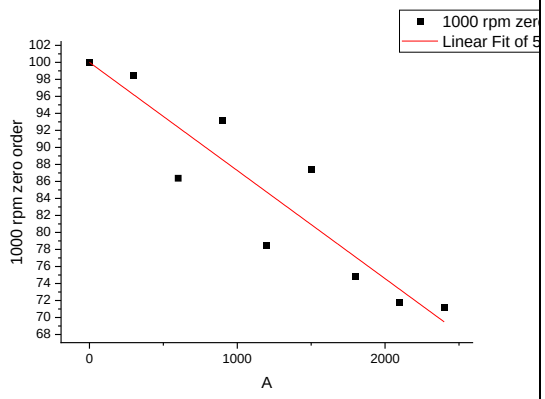

1000 rpm

R^2: 0.99734

Rate constant: 0.01272 ± 0.00103

A2.10

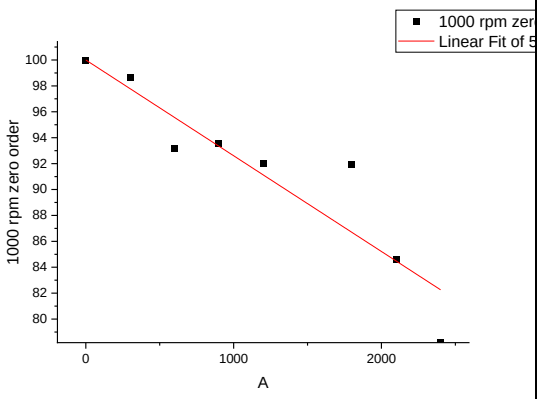

1000 rpm

R^2: 0.99913

Rate constant: 0.00739 ± 6.75474E-4

A2.11

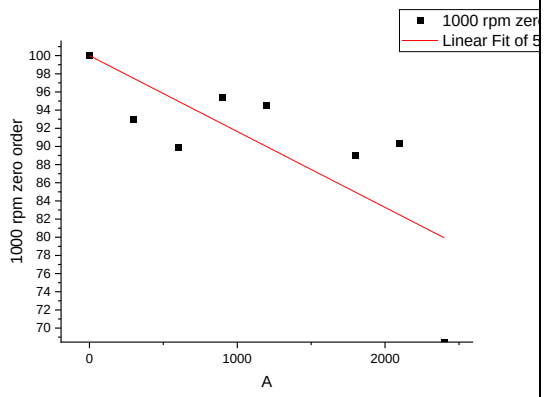

1000 rpm

R^2: 0.99501

Rate constant: 0.00836 ± 0.00159

A2.12

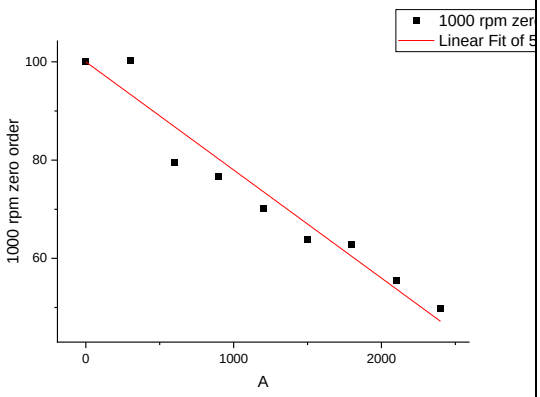

1000 rpm

R^2: 0.99666

Rate constant: 0.02201 ± 0.00101

A2.13

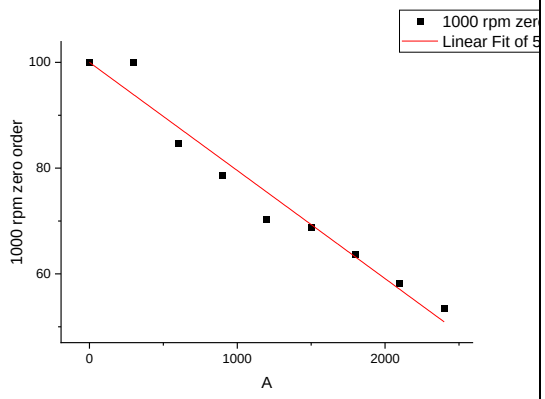

1000 rpm

R^2: 0.9981

Rate constant: 0.02045 ± 7.83337E-4

A2.14

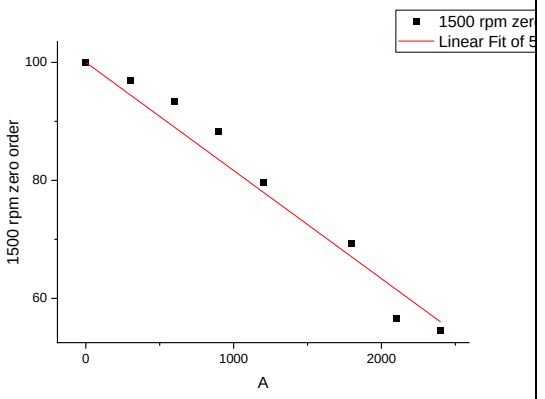

1500 rpm

R^2: 0.99826

Rate constant: 0.01833 ± 8.48701E-4

A2.15

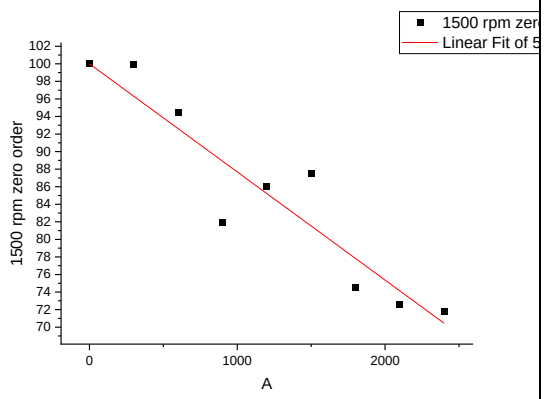

1500 rpm

R^2: 0.99804

Rate constant: 0.01232 ± 8.901E-4

A2.16

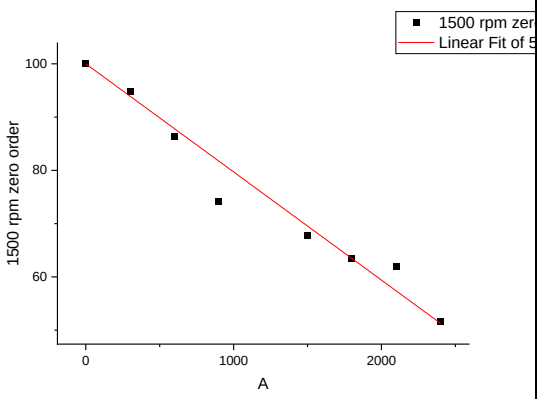

1500 rpm

R^2: 0.99792

Rate constant: 0.02347 ± 8.50825E-4

A2.17

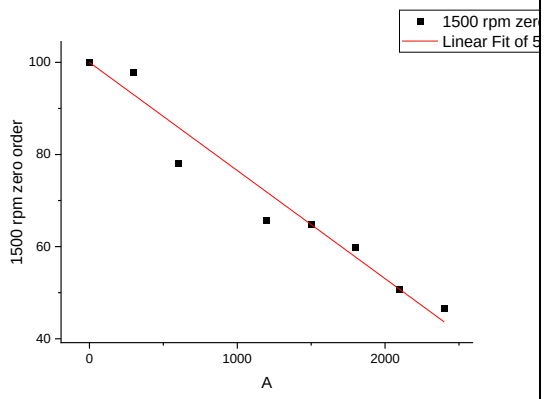

1500 rpm

R^2: 0.99631

Rate constant: 0.02347 ± 0.00106

A2.18

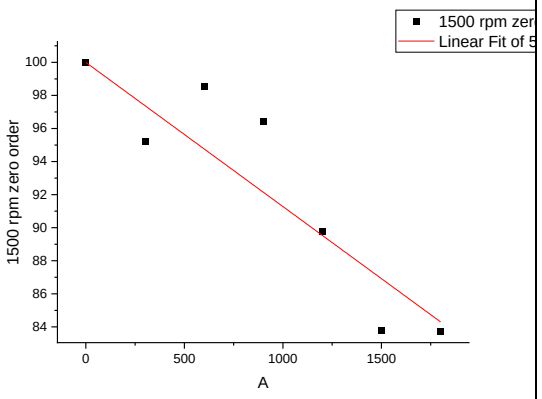

1500 rpm

R^2: 0.99908

Rate constant: 0.00872 ± 9.81742E-4

A2.19

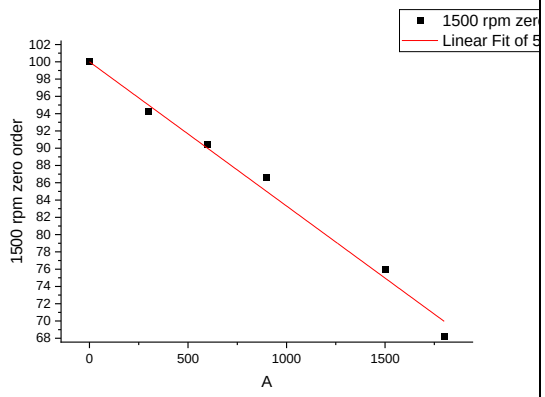

1500 rpm

R^2: 0.9998

Rate constant: 0.01669 ± 4.71523E-4

A2.20

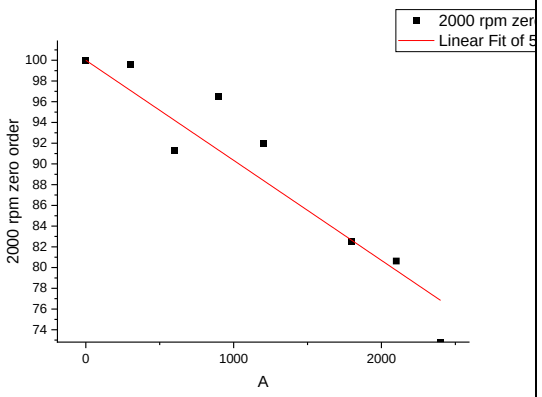

2000 rpm

R^2: 0.99874

Rate constant: 0.00965 ± 7.95808E-4

A2.21

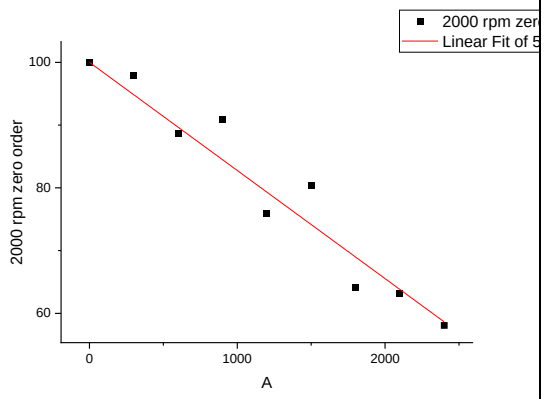

2000 rpm

R^2: 0.99761

Rate constant: 0.01723 ± 9.27168E-4

A2.22

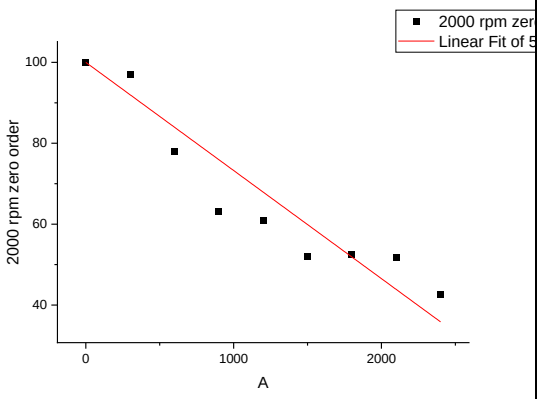

2000 rpm

R^2: 0.9884

Rate constant: 0.02674 ± 0.00174

A2.23

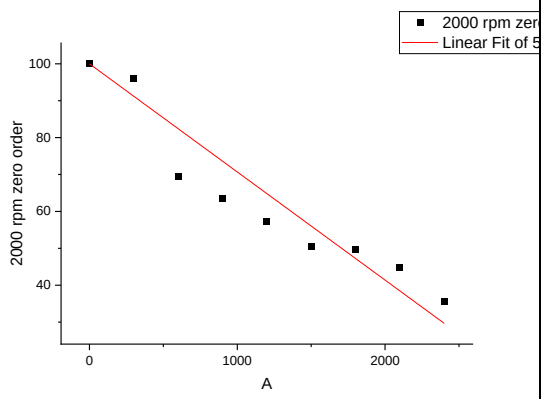

2000 rpm

R^2: 0.98683

Rate constant: 0.02931 ± 0.00178

A2.24

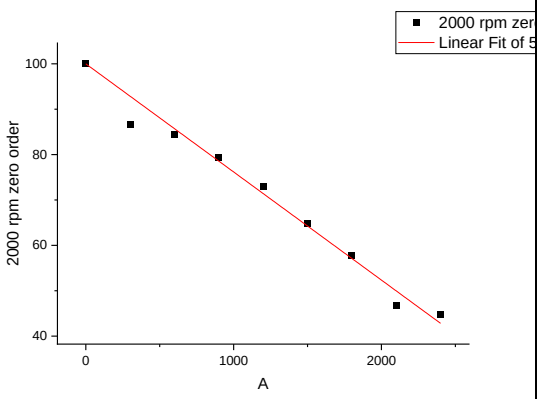

2000 rpm

R^2: 0.99866

Rate constant: 0.02383 ± 6.23077E-4

A2.25

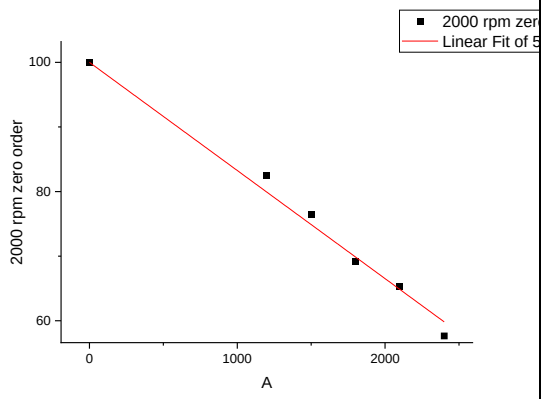

2000 rpm

R^2: 0.99951

Rate constant: 0.01674 ± 4.09783E-4

A2.26

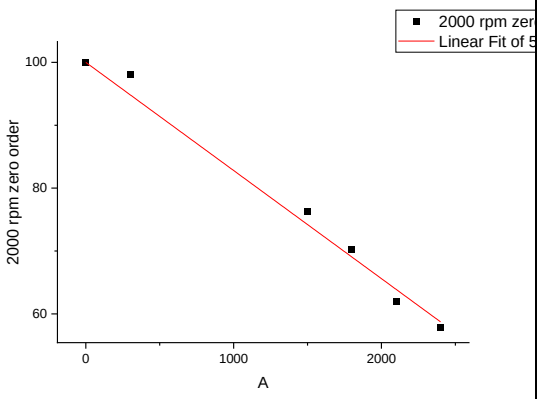

2000 rpm

R^2: 0.99934

Rate constant: 0.0172 ± 5.12344E-4

A2.27

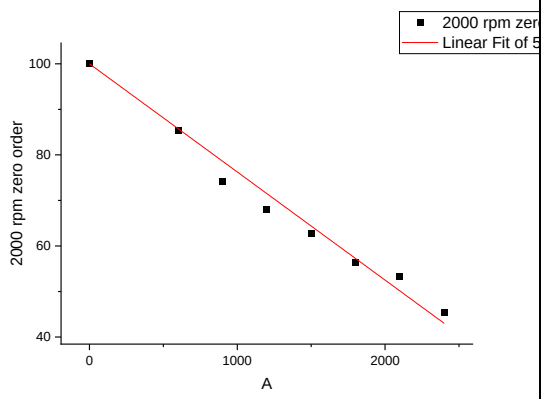

2000 rpm

R^2: 0.99848

Rate constant: 0.02375 ± 6.40689E-4

A2.28

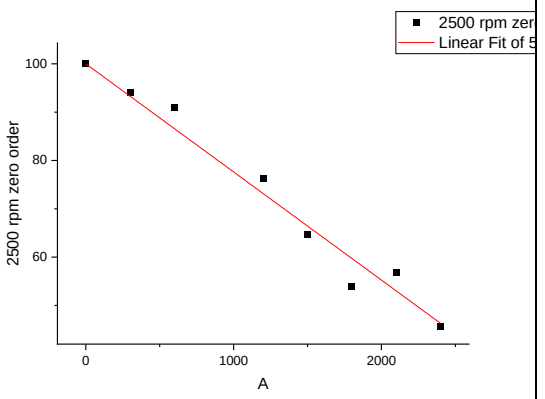

2500 rpm

R^2: 0.99793

Rate constant: 0.02238 ± 8.17448E-4

A2.29

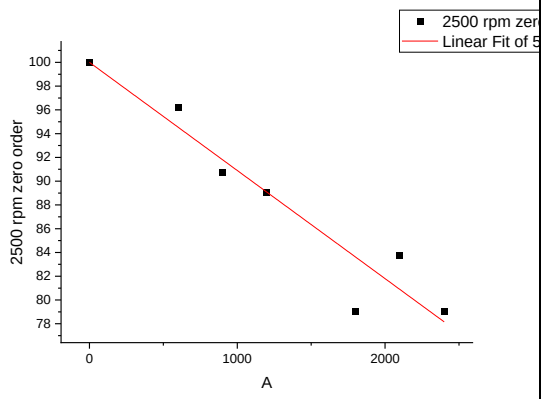

2500 rpm

R^2: 0.99928

Rate constant: 0.0091 ± 5.94447E-4

A2.30

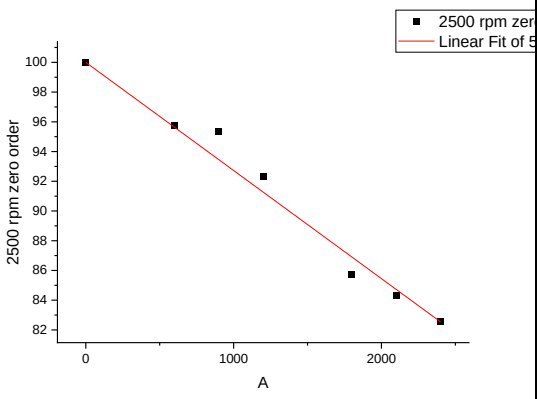

2500 rpm

R^2: 0.99987

Rate constant: 0.00727 ± 2.56044E-4

A2.31

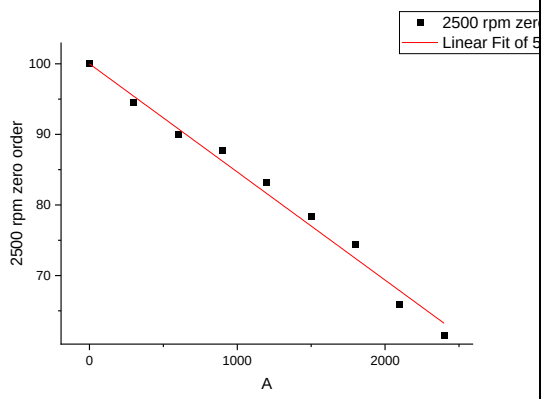

2500 rpm

R^2: 0.99965

Rate constant: 0.01532 ± 3.58548E-4

A2.32

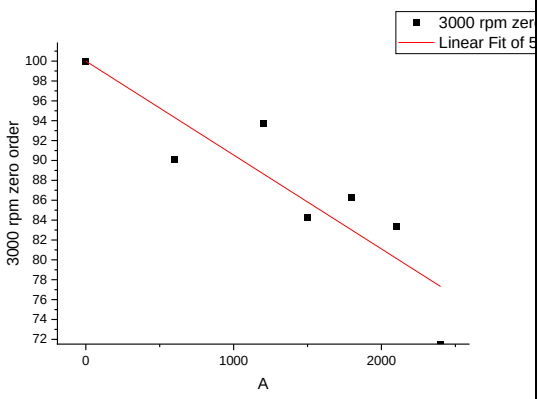

3000 rpm

R^2: 0.99782

Rate constant: 0.00945 ± 9.76024E-4

A2.33

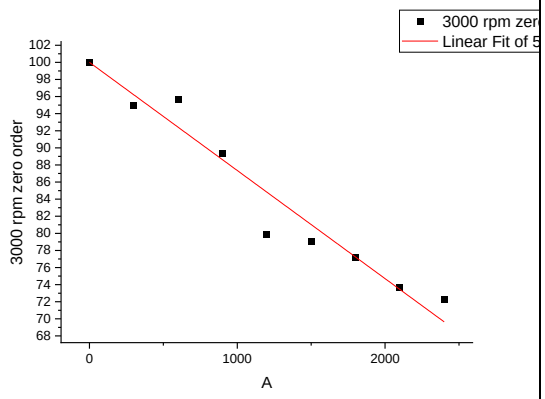

3000 rpm

R^2: 0.99917

Rate constant: 0.01265 ± 5.72923E-4

A2.34

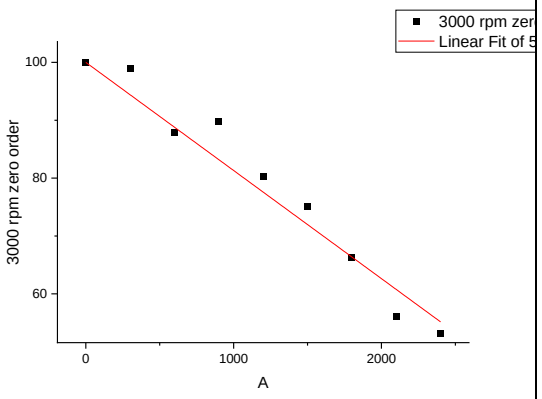

3000 rpm

R^2: 0.99787

Rate constant: 0.01868 ± 8.66017E-4

A2.35

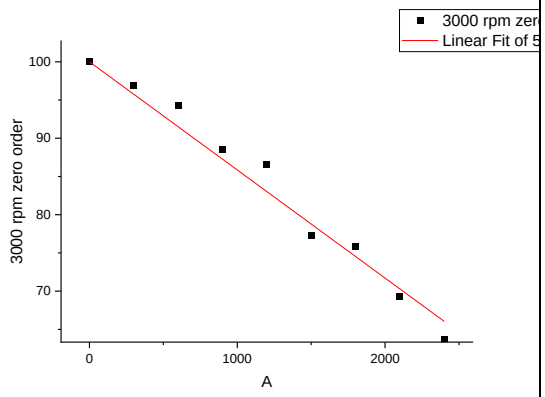

3000 rpm

R^2: 0.99941

Rate constant: 0.01415 ± 4.79592E-4

A2.36

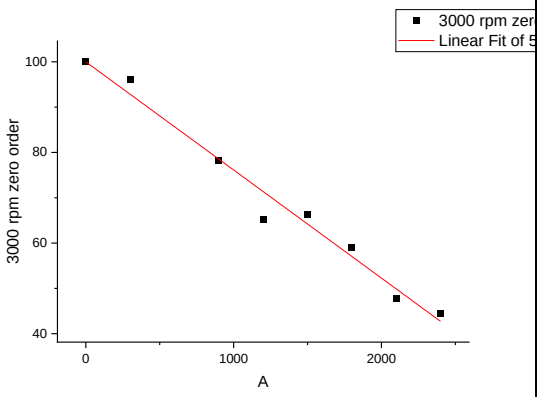

3000 rpm

R^2: 0.99824

Rate constant: 0.02386 ± 7.13926E-4

A2.37

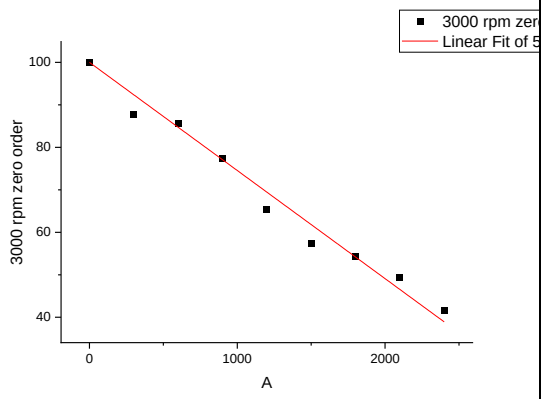

3000 rpm

R^2: 0.99819

Rate constant: 0.02545 ± 7.06866E-4

A2.38

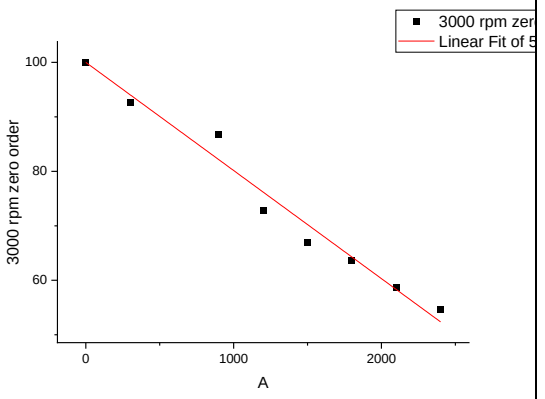

3000 rpm

R^2: 0.99877

Rate constant: 0.01985 ± 6.30468E-4

A2.39

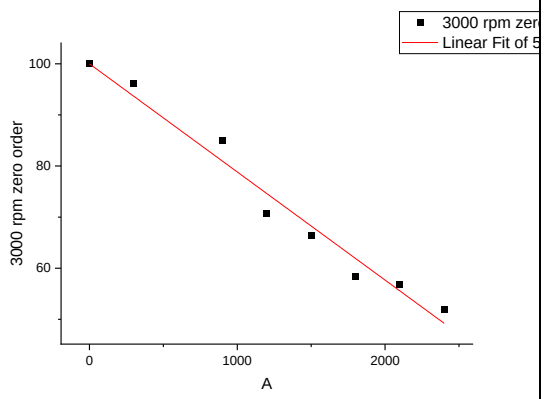

3000 rpm

R^2: 0.99843

Rate constant: 0.02116 ± 7.02448E-4

A2.40

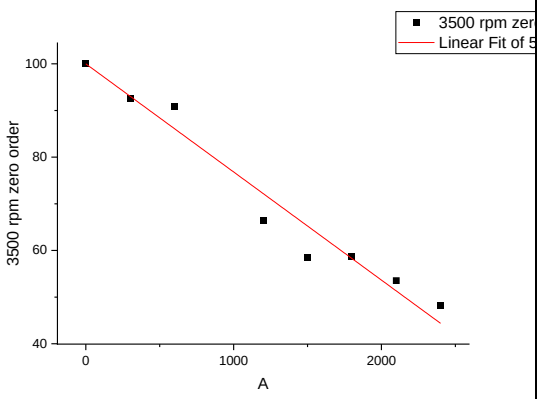

3500 rpm

R^2: 0.99675

Rate constant: 0.02317 ± 0.001

A2.41

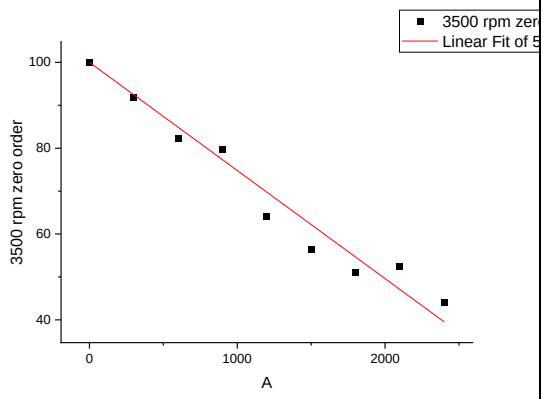

3500 rpm

R^2: 0.99656

Rate constant: 0.02519 ± 9.79394E-4

A2.42

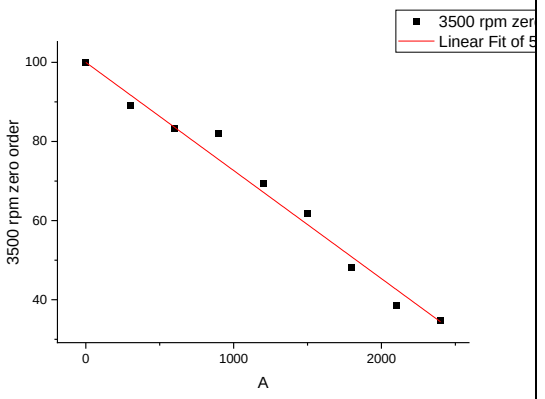

3500 rpm

R^2: 0.99786

Rate constant: 0.02733 ± 7.65031E-4

A2.43

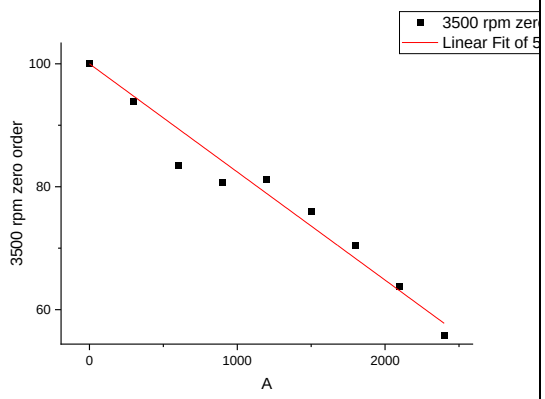

3500 rpm

R^2: 0.99866

Rate constant: 0.01759 ± 6.78947E-4

A2.44

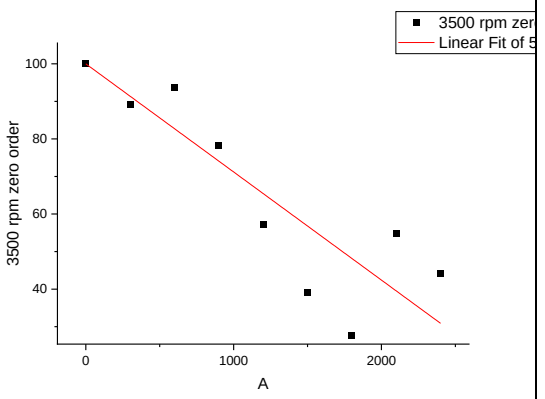

3500 rpm

R^2: 0.96503

Rate constant: 0.0288 ± 0.00303

A2.45

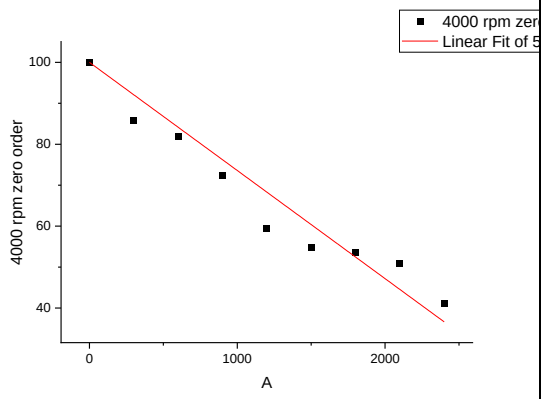

4000 rpm

R^2: 0.99406

Rate constant: 0.02641 ± 0.00124

A2.46

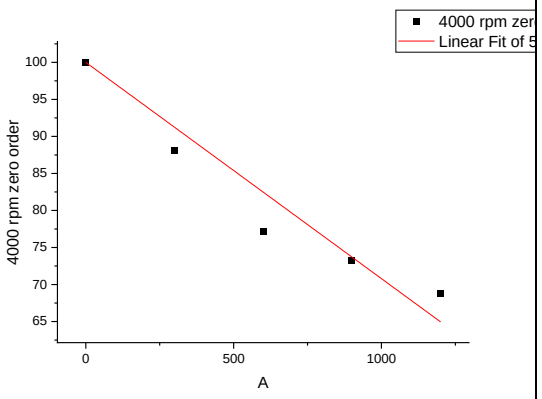

4000 rpm

R^2: 0.99802

Rate constant: 0.0292 ± 0.00223

A2.47

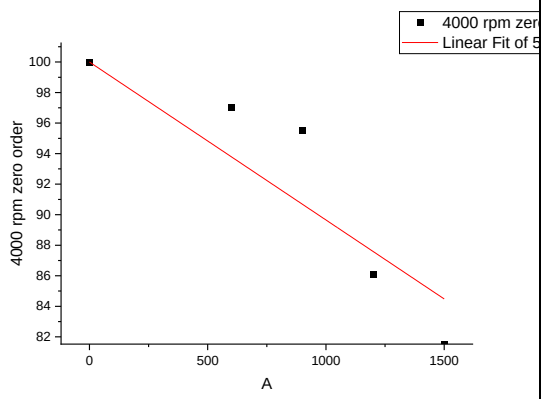

4000 rpm

R^2: 0.9987

Rate constant: 0.01035 ± 0.00151

A2.48

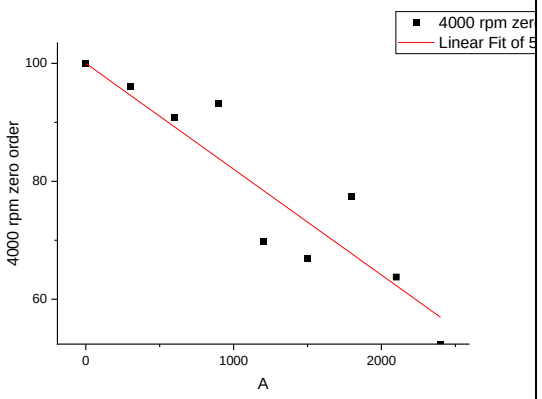

4000 rpm

R^2: 0.99376

Rate constant: 0.01795 ± 0.00148

A2.49

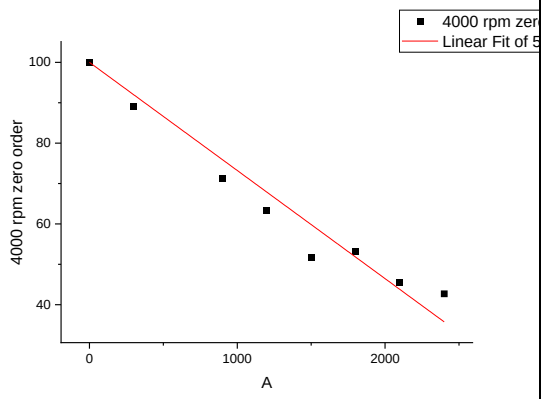

4000 rpm

R^2: 0.99467

Rate constant: 0.02678 ± 0.00116

A2.50

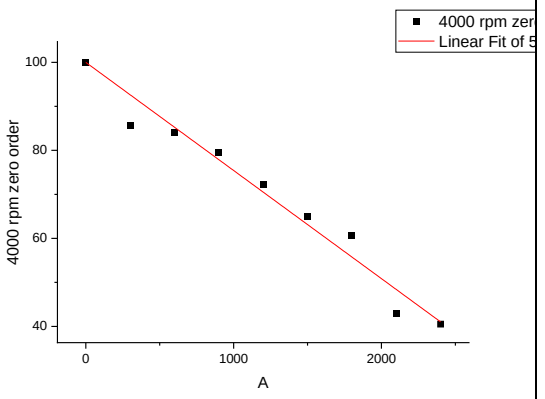

4000 rpm

R^2: 0.99727

Rate constant: 0.02457 ± 8.84074E-4

A2.51

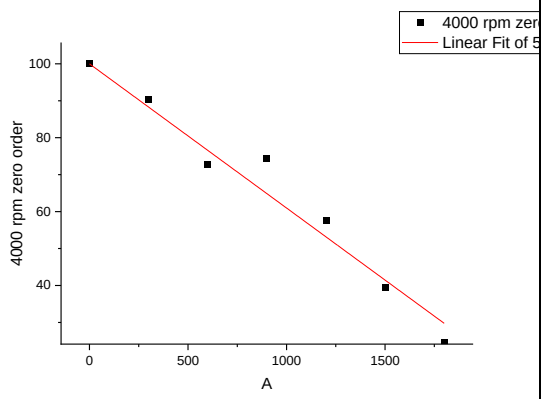

4000 rpm

R^2: 0.99453

Rate constant: 0.03902 ± 0.00181

A2.52

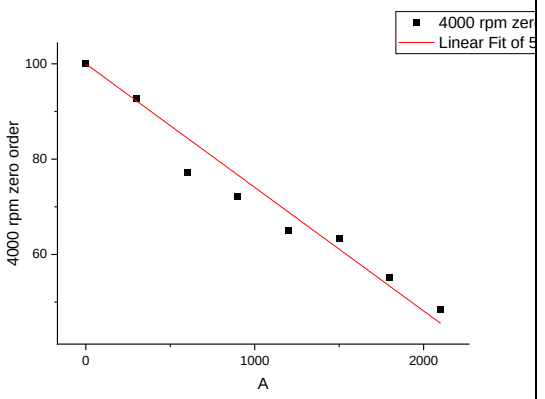

4000 rpm

R^2: 0.99725

Rate constant: 0.02593 ± 0.00109

A2.53

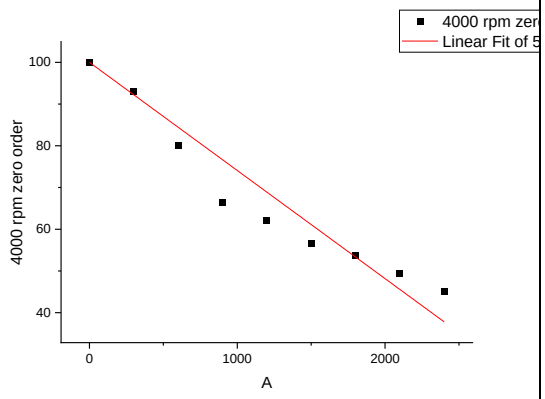

4000 rpm

R^2: 0.99339

Rate constant: 0.02592 ± 0.00133

A2.54

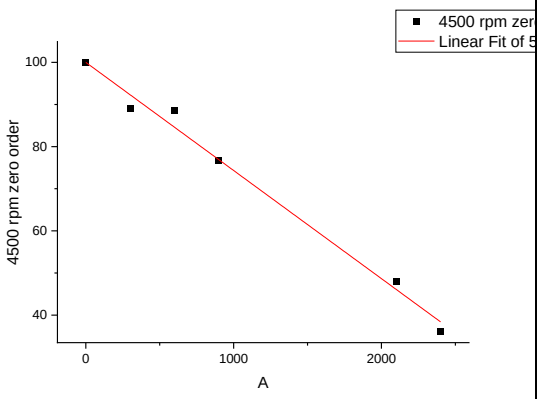

4500 rpm

R^2: 0.99882

Rate constant: 0.02567 ± 7.77877E-4

A2.55

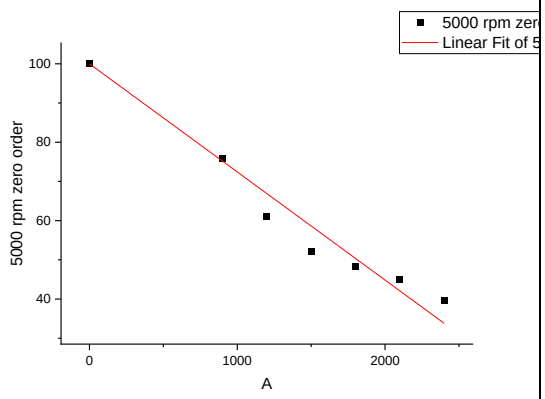

5000 rpm

R^2: 0.99487

Rate constant: 0.02758 ± 0.00107

A2.56

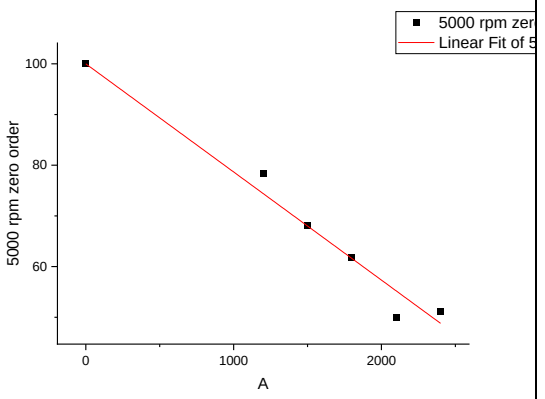

5000 rpm

R^2: 0.99802

Rate constant: 0.02133 ± 7.57707E-4

A2.57

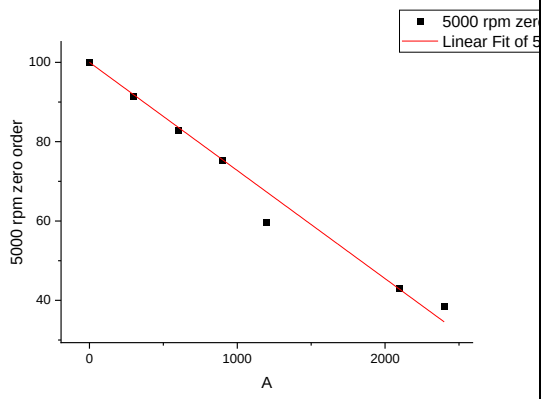

5000 rpm

R^2: 0.99769

Rate constant: 0.02726 ± 9.8407E-4

A2.58

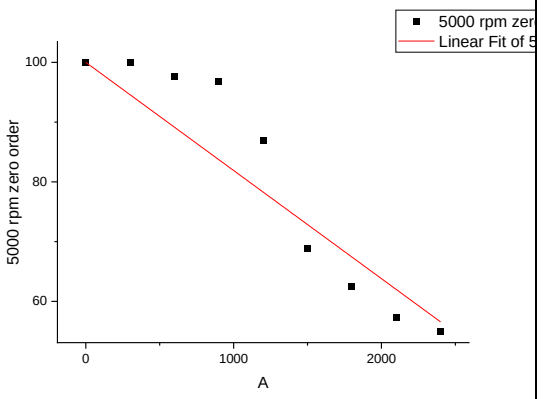

5000 rpm

R^2: 0.99243

Rate constant: 0.0181 ± 0.00168

A2.59

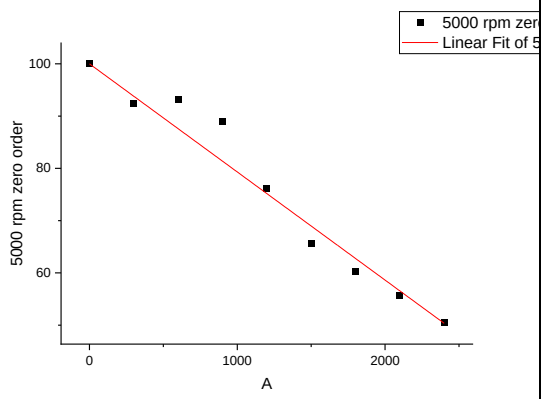

5000 rpm

R^2: 0.99769

Rate constant: 0.02069 ± 8.72269E-4

A2.60

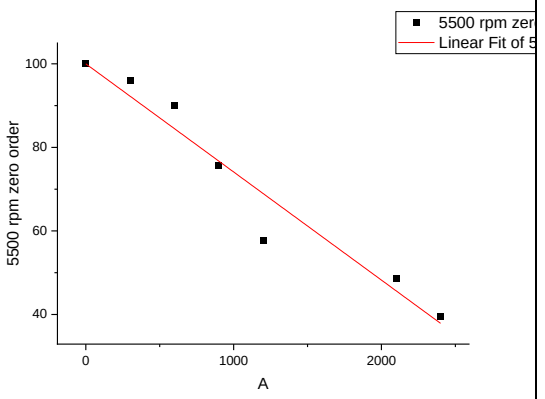

5500 rpm

R^2: 0.99479

Rate constant: 0.02588 ± 0.00153

A2.61

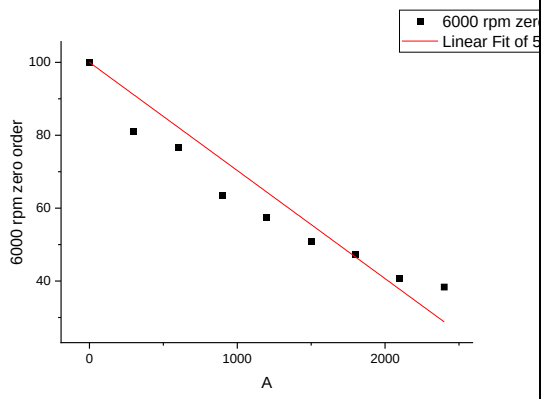

6000 rpm

R^2: 0.98794

Rate constant: 0.02966 ± 0.00166

A2.62

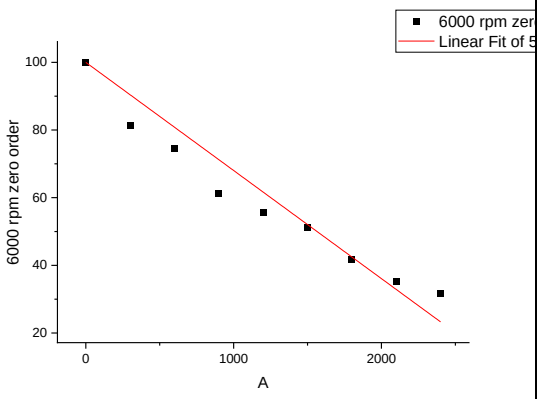

6000 rpm

R^2: 0.98957

Rate constant: 0.03196 ± 0.0015

A2.63

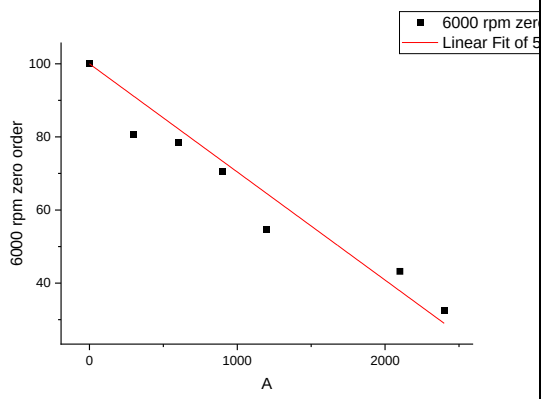

6000 rpm

R^2: 0.99045

Rate constant: 0.02959 ± 0.00189

A2.64

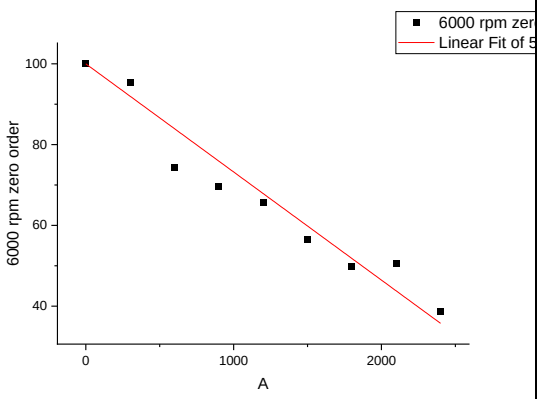

6000 rpm

R^2: 0.99446

Rate constant: 0.02677 ± 0.00121

A2.65

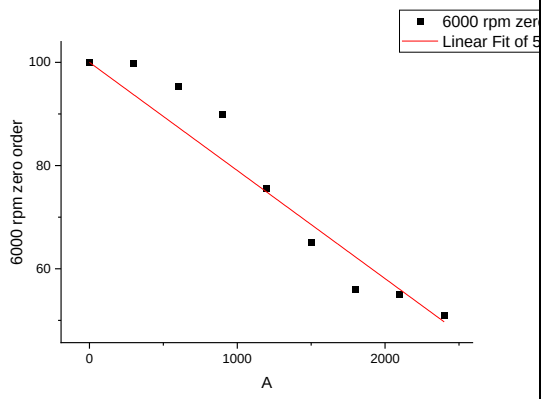

6000 rpm

R^2: 0.99542

Rate constant: 0.02096 ± 0.00124

A2.66

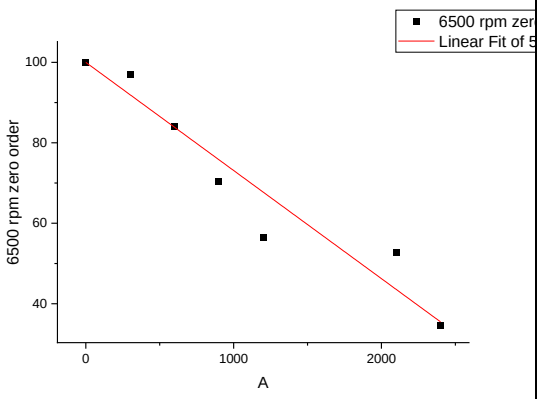

6500 rpm

R^2: 0.99197

Rate constant: 0.02688 ± 0.00185

A2.67

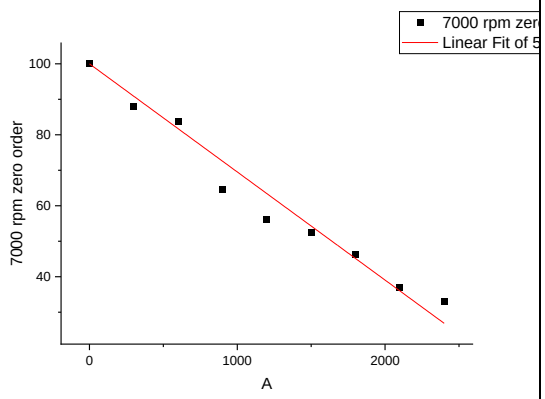

7000 rpm

R^2: 0.99511

Rate constant: 0.03047 ± 0.00108

A2.68

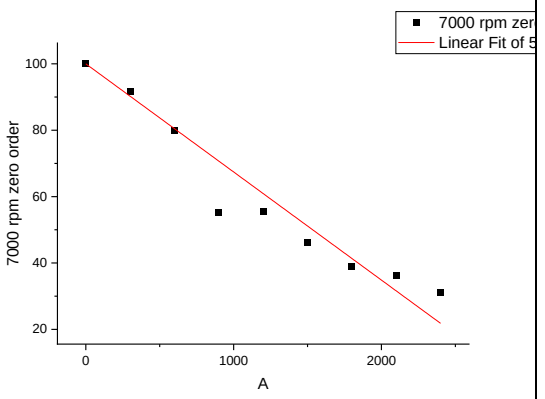

7000 rpm

R^2: 0.98762

Rate constant: 0.03257 ± 0.00166

A2.69 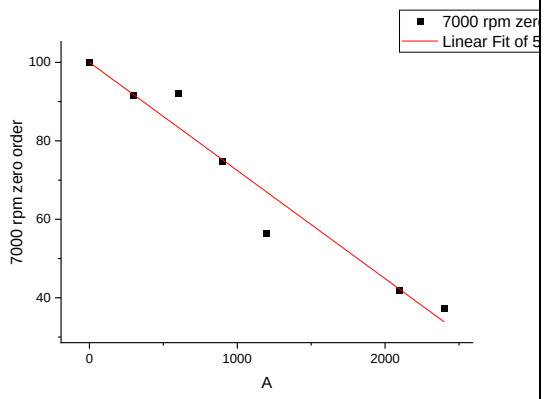 7000 rpm R^2: 0.99406 Rate constant: 0.02756 ± 0.0016	A2.70 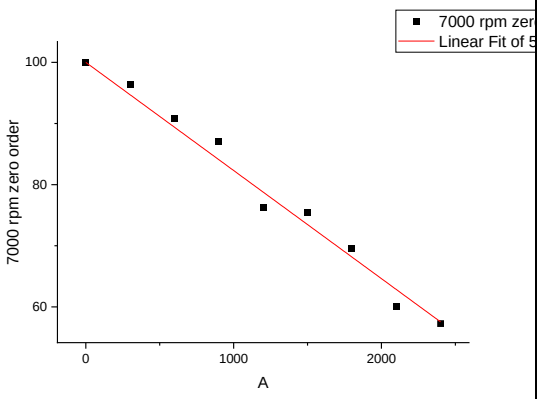 7000 rpm R^2: 0.99934 Rate constant: 0.01769 ± 4.82064E-4
A2.71 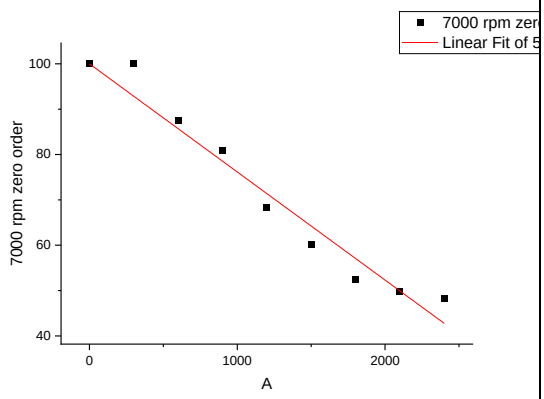 7000 rpm R^2: 0.99692 Rate constant: 0.02384 ± 9.6622E-4	A2.72 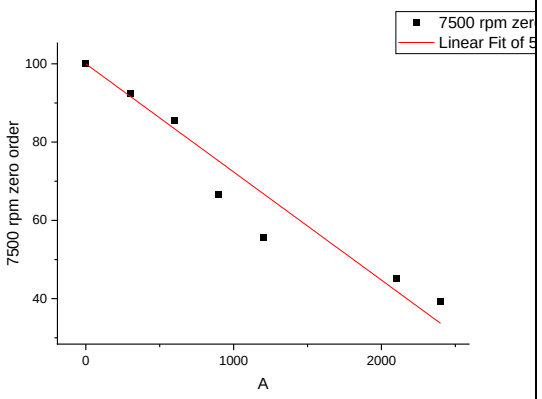 7500 rpm R^2: 0.99231 Rate constant: 0.02763 ± 0.00178

A2.73

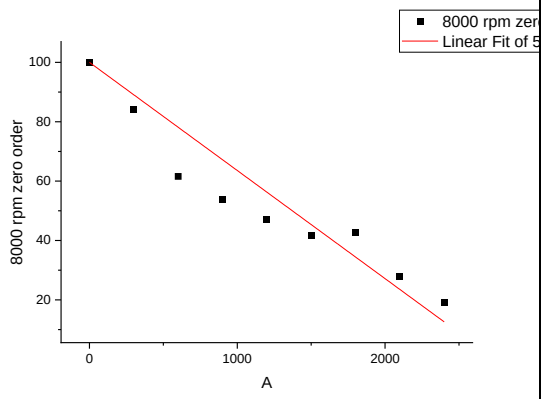

8000 rpm

R^2: 0.97416

Rate constant: 0.03642 ± 0.00219

A2.74

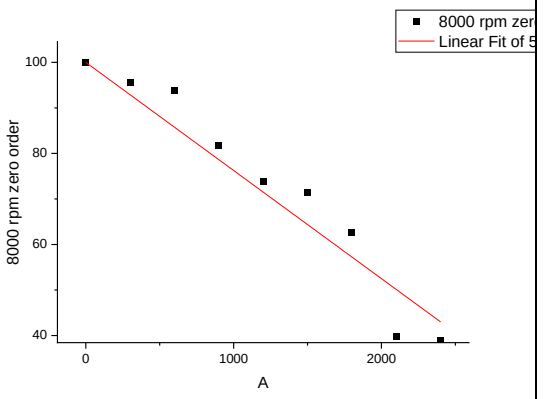

8000 rpm

R^2: 0.99385

Rate constant: 0.02375 ± 0.00139

A2.75

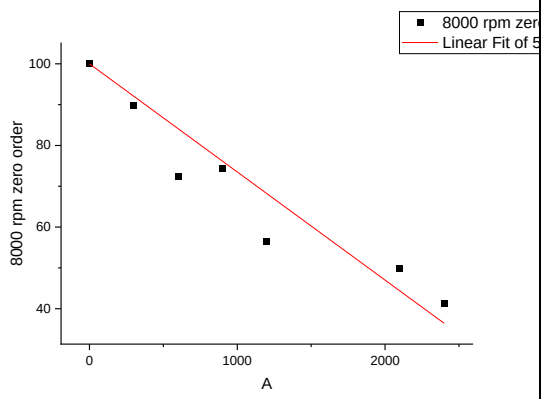

8000 rpm

R^2: 0.98906

Rate constant: 0.0265 ± 0.0021

A2.76

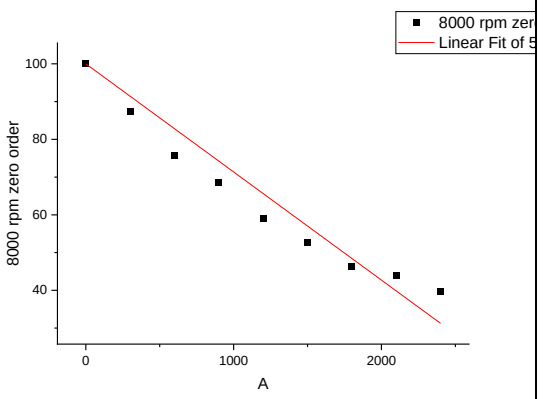

8000 rpm

R^2: 0.9929

Rate constant: 0.02864 ± 0.00131

A2.77

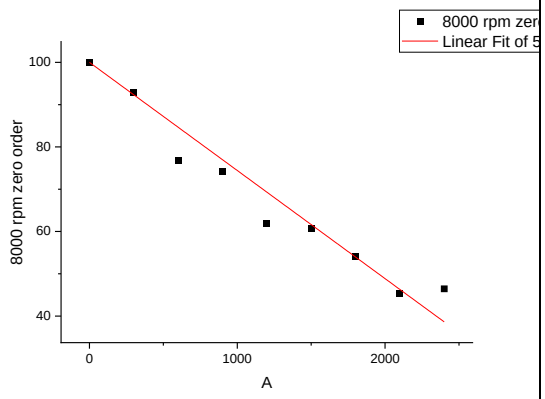

8000 rpm

R^2: 0.9953

Rate constant: 0.02557 ± 0.00113

Preparation spin speed and the first order rate plots and rate constants for stearic acid decomposition on 5 wt% copper-doped *meso*-TiO_2 samples

A2.78 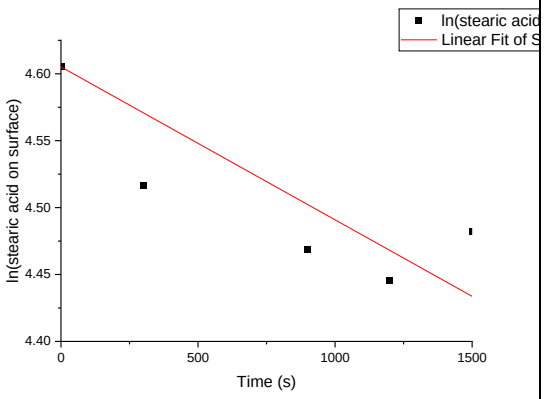 500 rpm R^2: 0.99992 Rate constant: 1.14324E-4 ± 1.93684E-5	A2.79 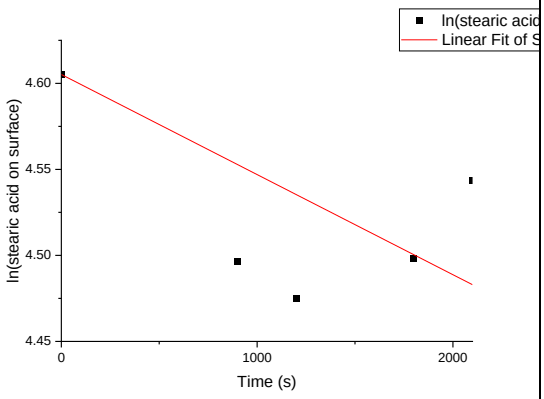 500 rpm R^2: 0.99987 Rate constant: 5.81907E-5 ± 1.6244E-5
A2.80 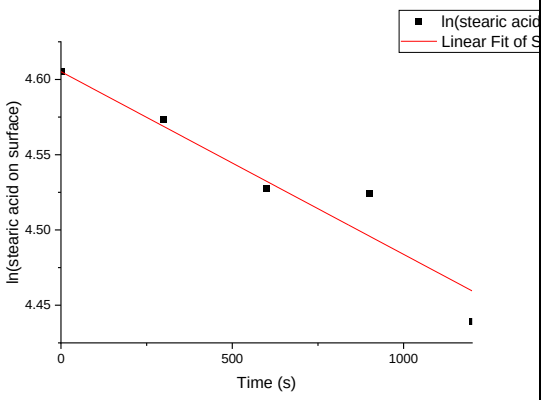 500 rpm R^2: 0.99998 Rate constant: 1.21358E-4 ± 1.08503E-5	A2.81 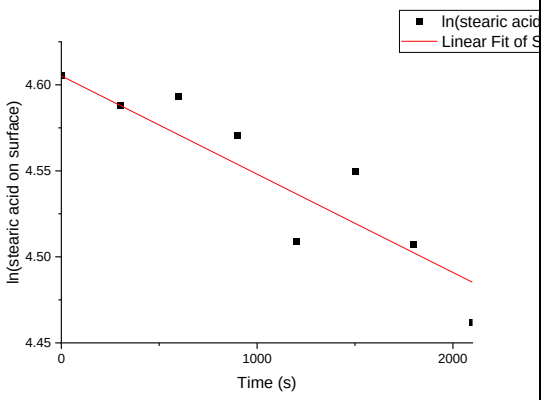 500 rpm R^2: 0.99998 Rate constant: 5.71227E-5 ± 5.85191E-6

A2.82

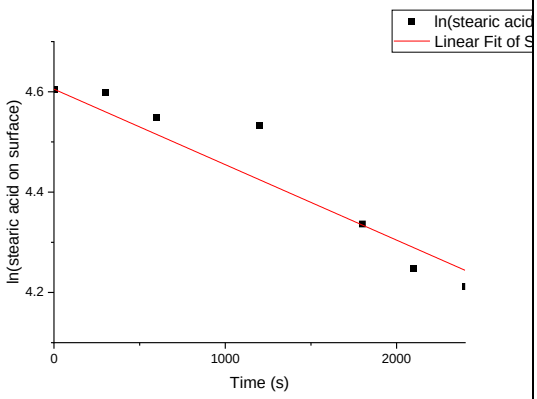

500 rpm

R^2: 0.99986

Rate constant: 1.50408E-4 ± 1.36211E-5

A2.83

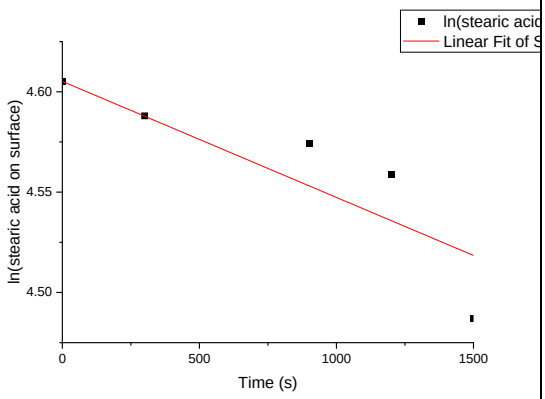

1000 rpm

R^2: 0.99998

Rate constant: 5.78236E-5 ± 1.02933E-5

A2.84

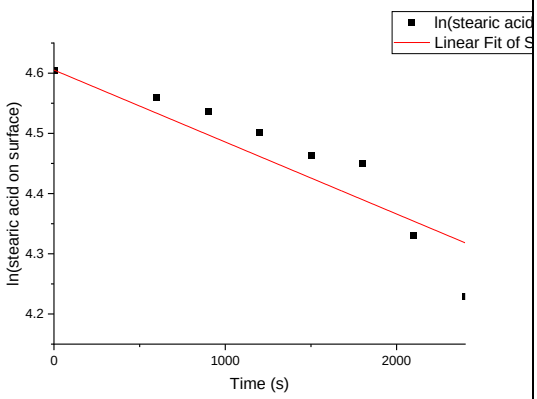

1000 rpm

R^2: 0.99988

Rate constant: 1.19536E-4 ± 1.16021E-5

A2.85

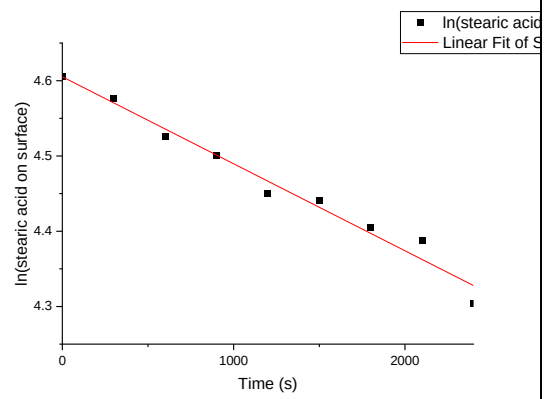

1000 rpm

R^2: 0.99999

Rate constant: 1.15569E-4 ± 3.4351E-6

A2.86

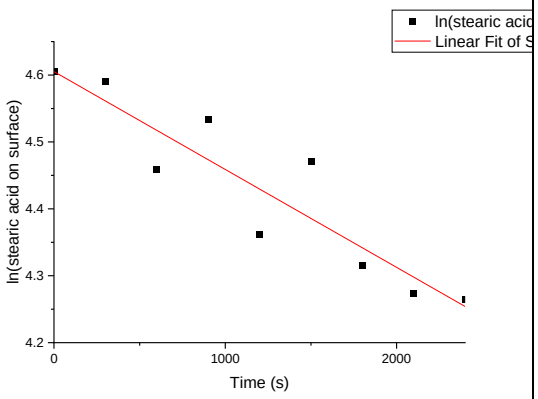

1000 rpm

R^2: 0.99987

Rate constant: 1.46295E-4 ± 1.19949E-5

A2.87

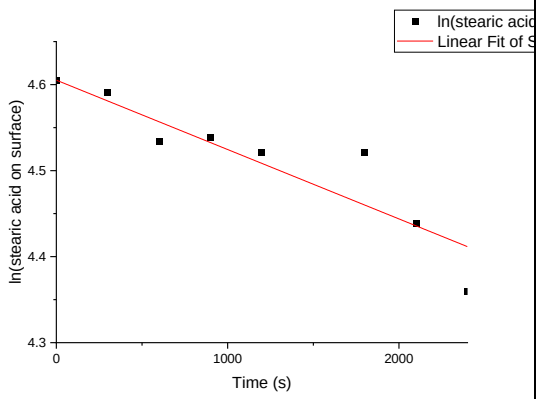

1000 rpm

R^2: 0.99995

Rate constant: 8.06514E-5 ± 8.06338E-6

A2.88

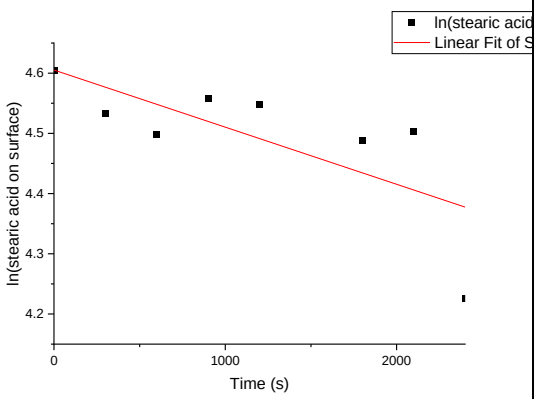

1000 rpm

R^2: 0.99968

Rate constant: 9.48514E-5 ± 1.98875E-5

A2.89

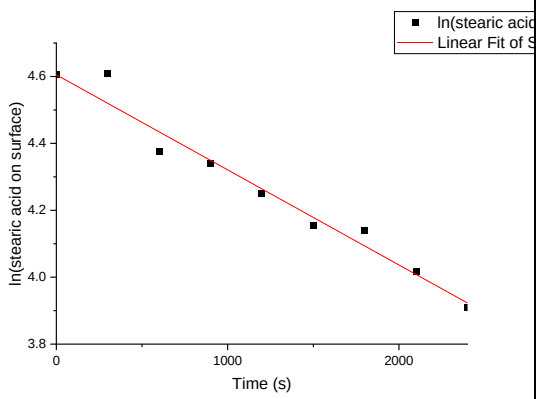

1000 rpm

R^2: 0.9999

Rate constant: 2.84261E-4 ± 9.94434E-6

A2.90

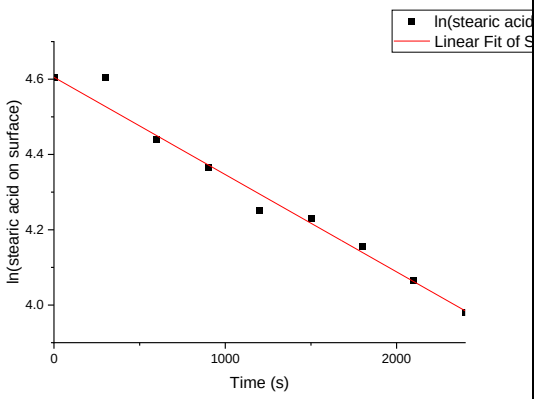

1000 rpm

R^2: 0.99994

Rate constant: 2.5851E-4 ± 7.52704E-6

A2.91

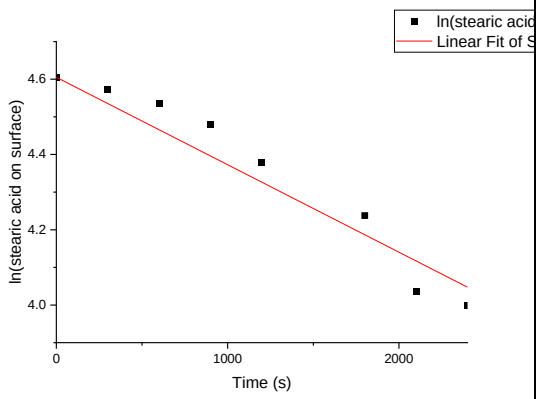

1500 rpm

R^2: 0.99979

Rate constant: 2.32395E-4 ± 1.56628E-5

A2.92

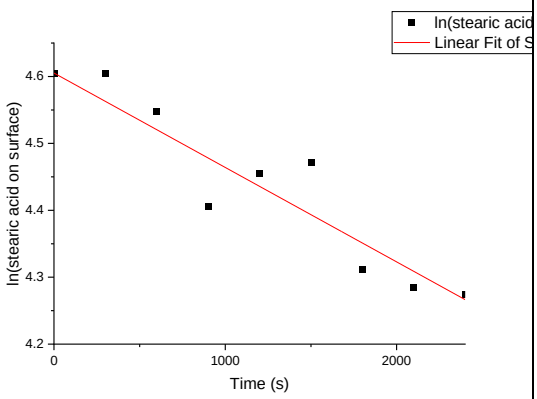

1500 rpm

R^2: 0.9999

Rate constant: 1.41116E-4 ± 1.05528E-5

A2.93

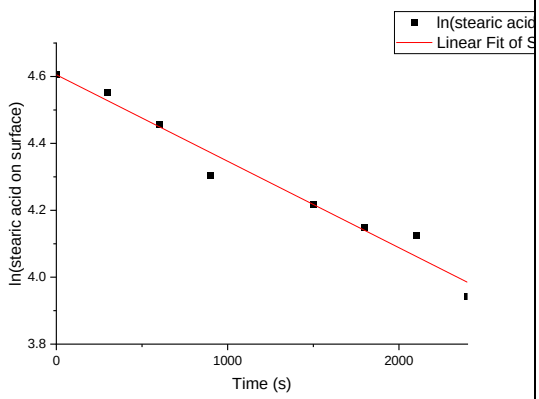

1500 rpm

R^2: 0.99991

Rate constant: 2.58479E-4 ± 9.68929E-6

A2.94

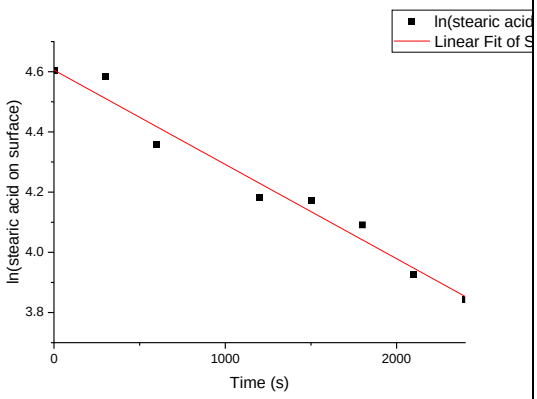

1500 rpm

R^2: 0.99988

Rate constant: 3.13148E-4 ± 1.11257E-5

A2.95

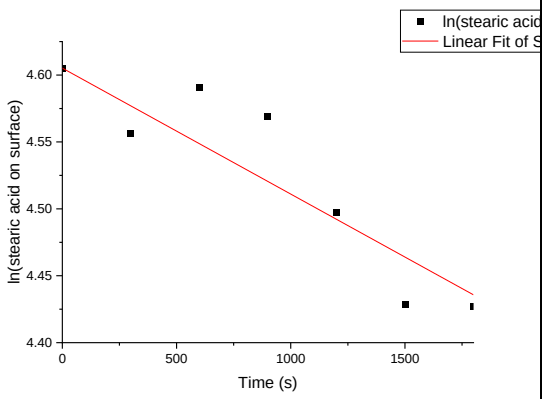

1500 rpm

R^2: 0.99995

Rate constant: 9.41251E-5 ± 1.09342E-5

A2.96

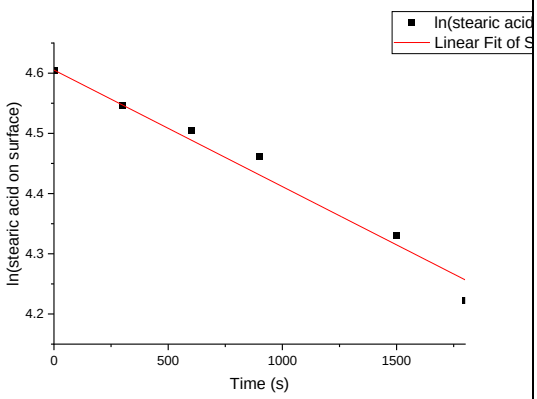

1500 rpm

R^2: 0.99997

Rate constant: 1.93549E-4 ± 8.72118E-6

A2.97

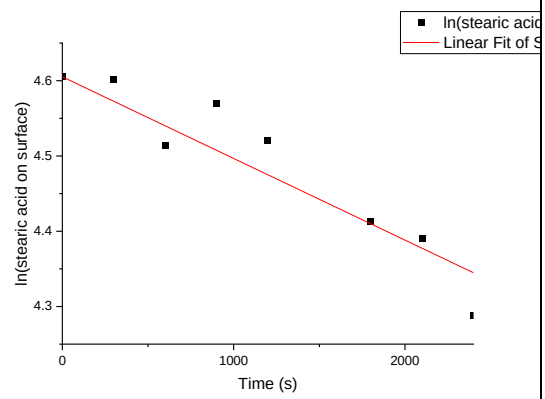

2000 rpm

R^2: 0.99992

Rate constant: 1.0848E-4 ± 9.84071E-6

A2.98

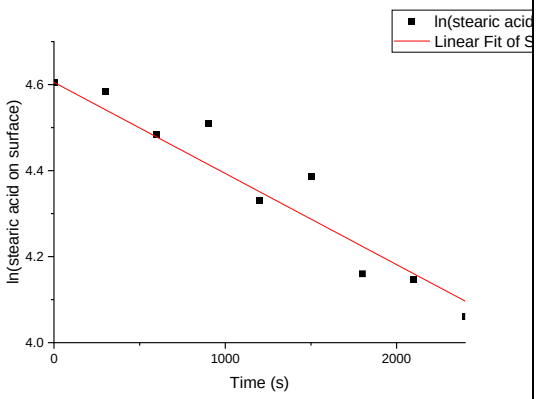

2000 rpm

R^2: 0.99983

Rate constant: 2.11868E-4 ± 1.34702E-5

A2.99

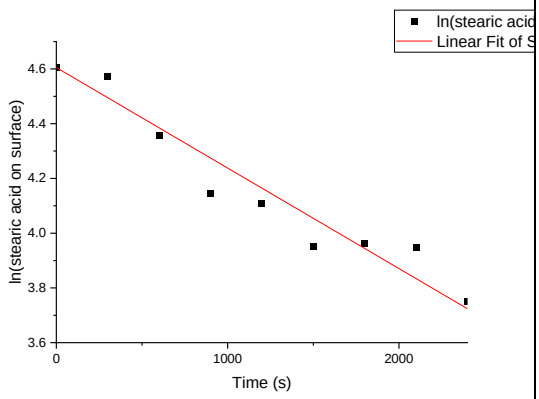

2000 rpm

R^2: 0.99963

Rate constant: 3.67184E-4 ± 1.87385E-5

A2.100

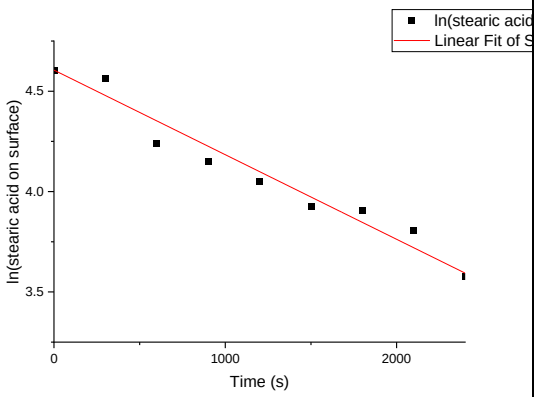

2000 rpm

R^2: 0.99969

Rate constant: 4.21398E-4 ± 1.68389E-5

A2.101

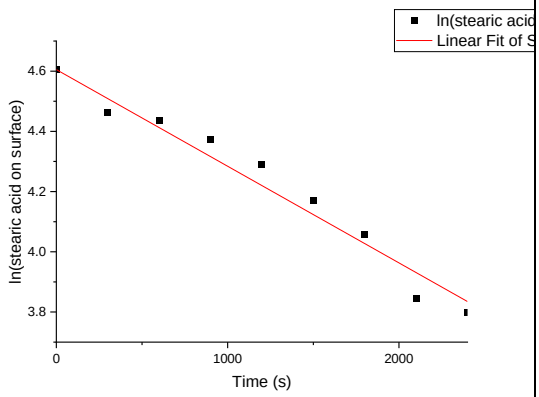

2000 rpm

R^2: 0.99984

Rate constant: 3.20999E-4 ± 1.24384E-5

A2.102

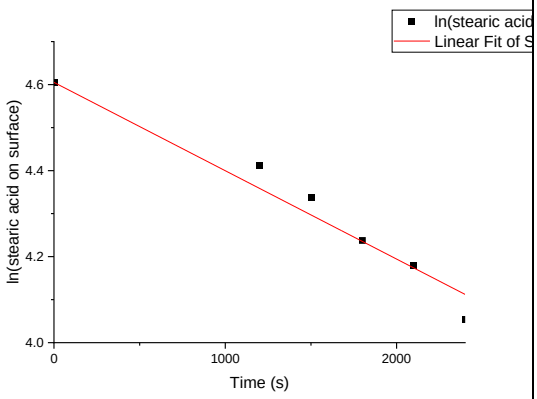

2000 rpm

R^2: 0.99992

Rate constant: 2.05408E-4 ± 9.5716E-6

A2.103

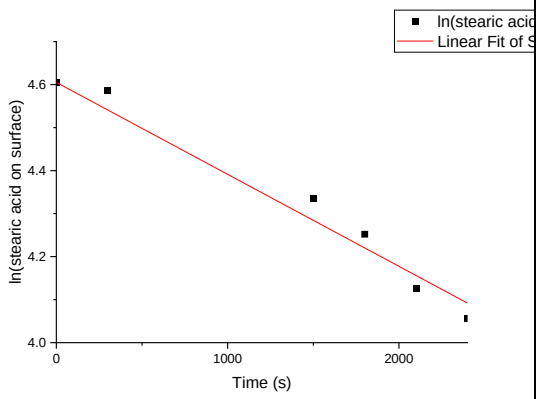

2000 rpm

R^2: 0.99992

Rate constant: 2.13864E-4 ± 9.8315E-6

A2.104

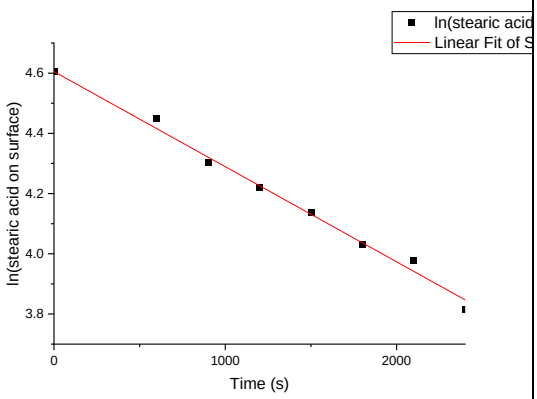

2000 rpm

R^2: 0.99997

Rate constant: 3.15937E-4 ± 5.28271E-6

A2.105

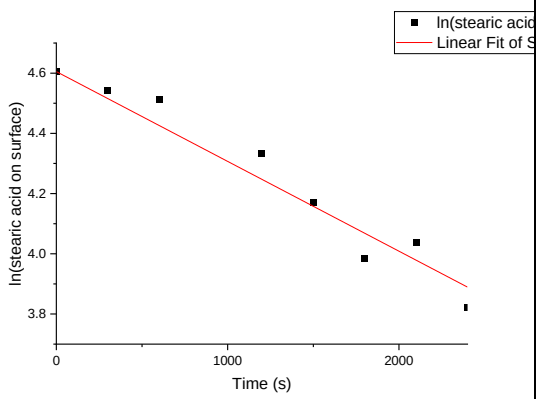

2500 rpm

R^2: 0.99976

Rate constant: 2.98245E-4 ± 1.57497E-5

A2.106

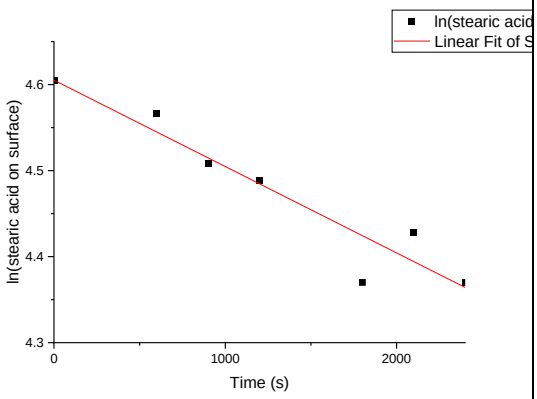

2500 rpm

R^2: 0.99996

Rate constant: 1.00418E-4 ± 6.96696E-6

A2.107

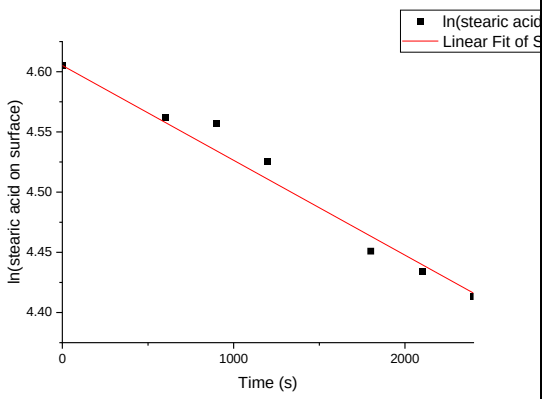

2500 rpm

R^2: 0.99999

Rate constant: 7.87475E-5 ± 3.16143E-6

A2.108

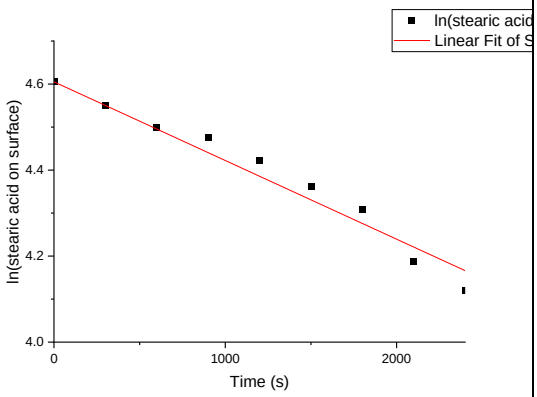

2500 rpm

R^2: 0.99995

Rate constant: 1.82908E-4 ± 7.31579E-6

A2.109

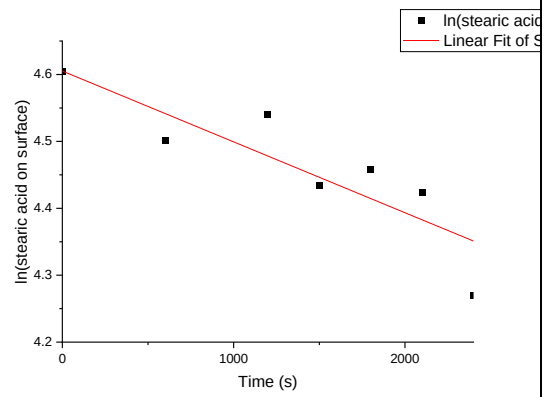

3000 rpm

R^2: 0.99987

Rate constant: 1.05881E-4 ± 1.22151E-5

A2.110

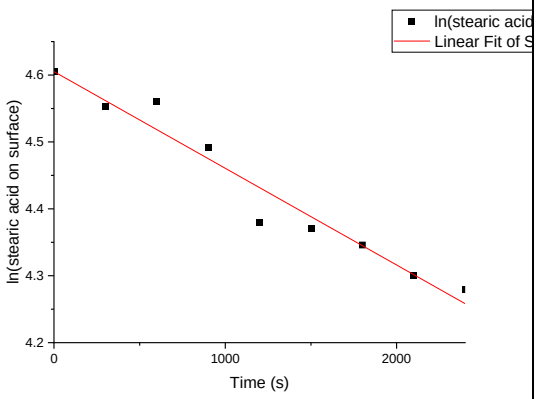

3000 rpm

R^2: 0.99996

Rate constant: 1.44529E-4 ± 6.20299E-6

A2.111

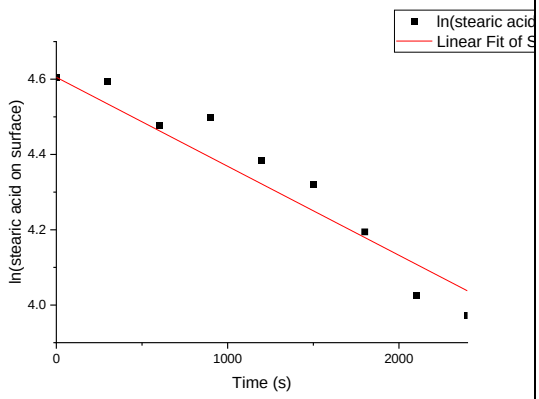

3000 rpm

R^2: 0.99977

Rate constant: 2.36475E-4 ± 1.54873E-5

A2.112

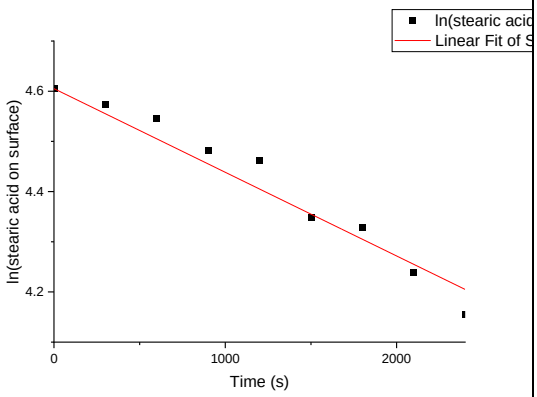

3000 rpm

R^2: 0.99994

Rate constant: 1.6672E-4 ± 8.02213E-6

A2.113

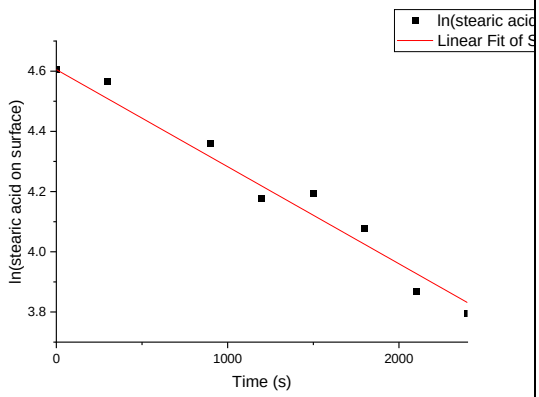

3000 rpm

R^2: 0.99984

Rate constant: 3.22444E-4 ± 1.2651E-5

A2.114

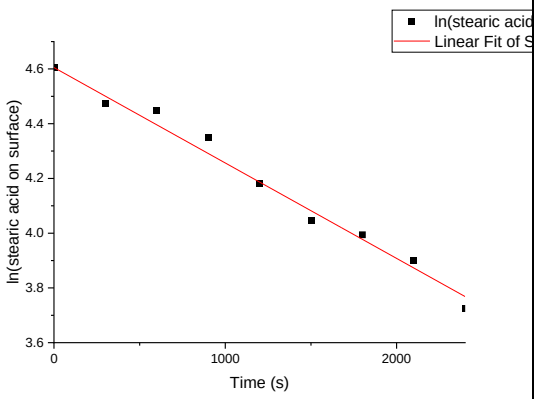

3000 rpm

R^2: 0.99992

Rate constant: 3.48652E-4 ± 8.54012E-6

A2.115

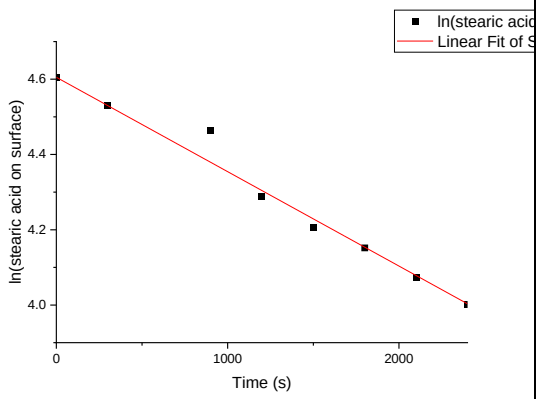

3000 rpm

R^2: 0.99994

Rate constant: 2.508E-4 ± 7.88988E-6

A2.116

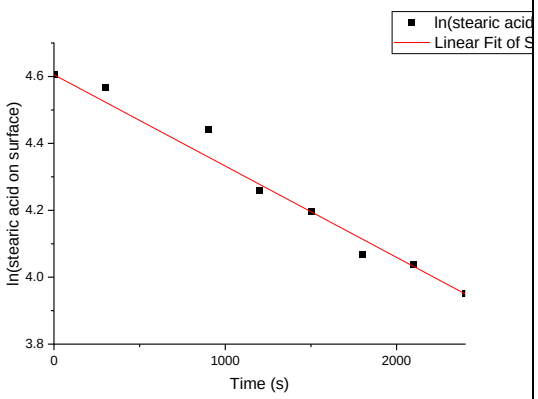

3000 rpm

R^2: 0.99991

Rate constant: 2.72923E-4 ± 9.46424E-6

A2.117

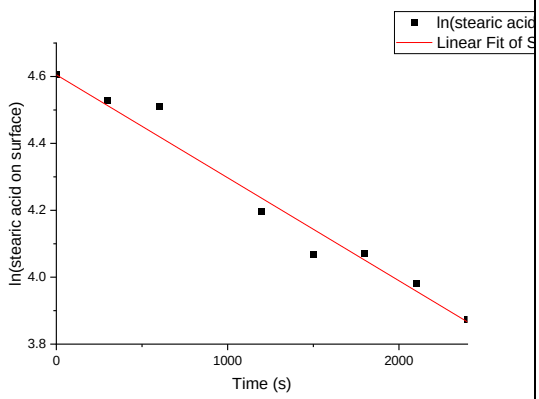

3500 rpm

R^2: 0.99987

Rate constant: 3.07825E-4 ± 1.15904E-5

A2.118 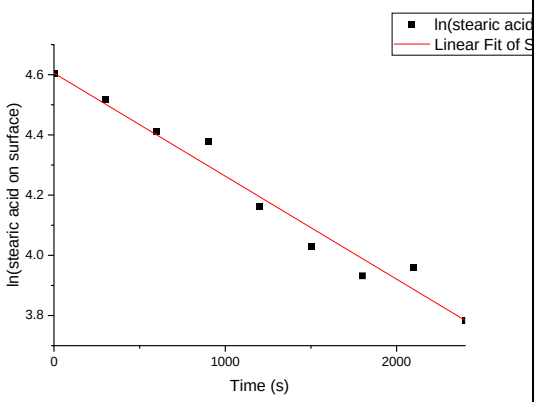 3500 rpm R^2: 0.99986 Rate constant: 3.42169E-4 ± 1.17727E-5	A2.119 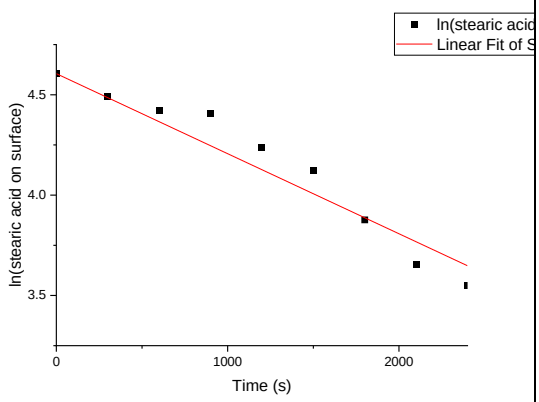 3500 rpm R^2: 0.99944 Rate constant: 3.98771E-4 ± 2.30429E-5
A2.120 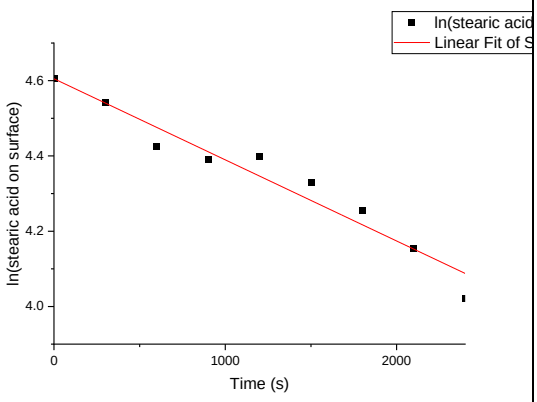 3500 rpm R^2: 0.99991 Rate constant: 2.15536E-4 ± 9.66699E-6	A2.121 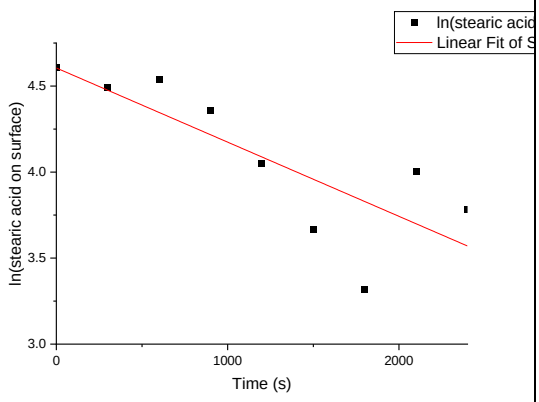 3500 rpm R^2: 0.99599 Rate constant: 4.31181E-4 ± 6.07752E-5

A2.122

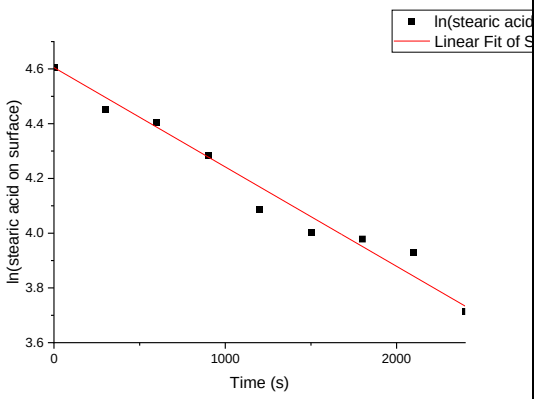

4000 rpm

R^2: 0.99985

Rate constant: 3.63109E-4 ± 1.19492E-5

A2.123

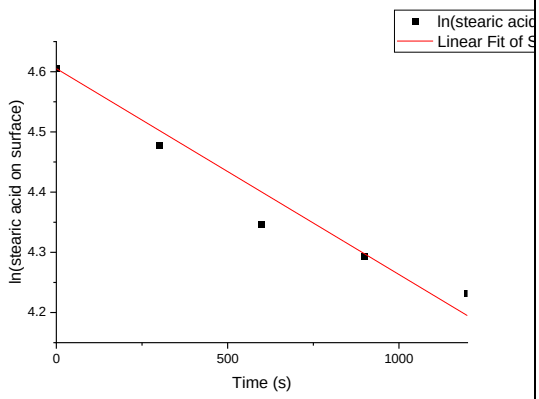

4000 rpm

R^2: 0.99994

Rate constant: 3.4196E-4 ± 2.12915E-5

A2.124

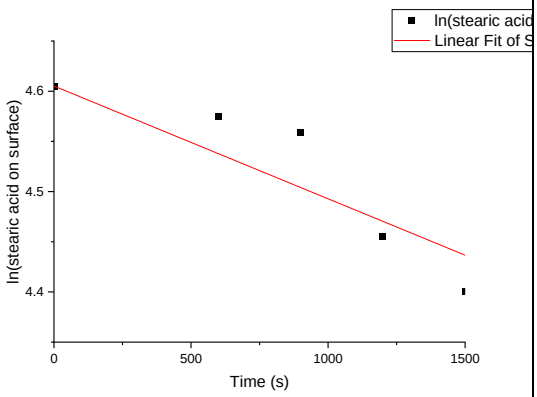

4000 rpm

R^2: 0.99993

Rate constant: 1.12366E-4 ± 1.74209E-5

A2.125

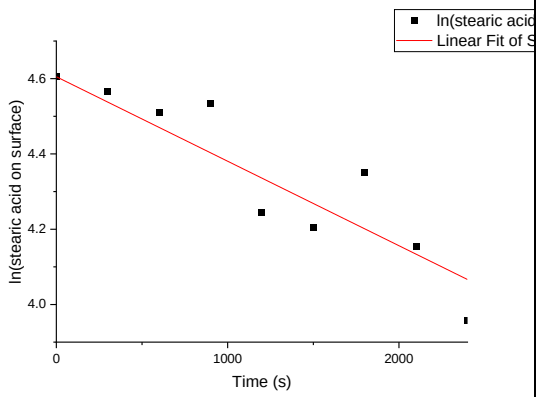

4000 rpm

R^2: 0.99956

Rate constant: 2.24493E-4 ± 2.12296E-5

A2.126

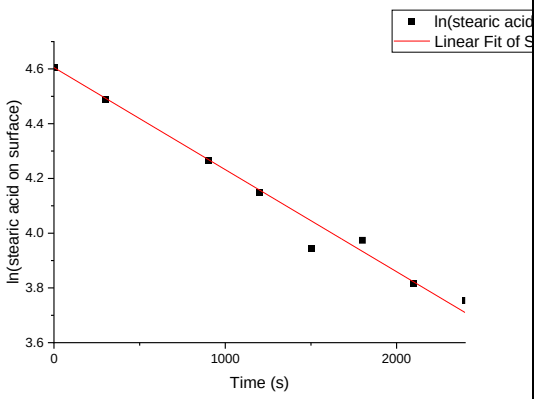

4000 rpm

R^2: 0.99988

Rate constant: 3.72969E-4 ± 1.05905E-5

A2.127

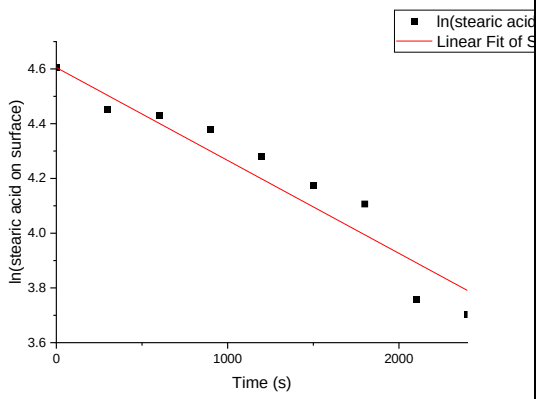

4000 rpm

R^2: 0.99957

Rate constant: 3.39396E-4 ± 2.03816E-5

A2.128

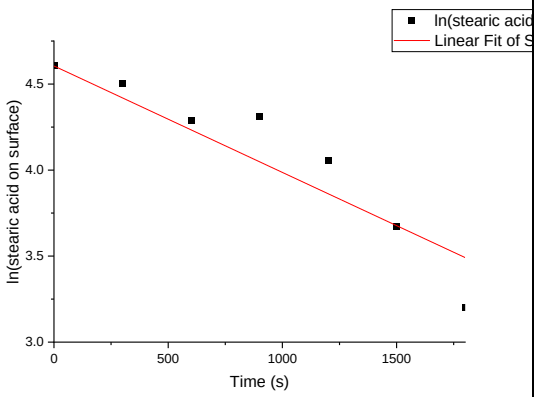

4000 rpm

R^2: 0.99805

Rate constant: 6.18715E-4 ± 6.35566E-5

A2.129

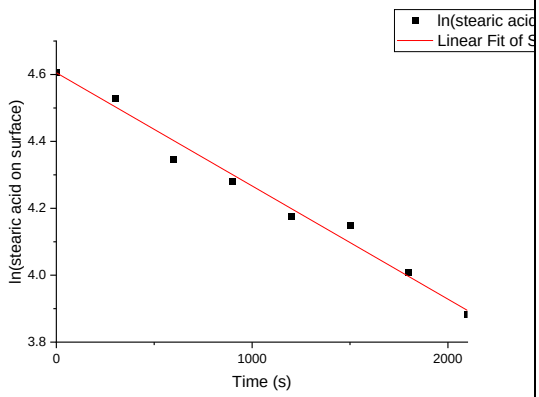

4000 rpm

R^2: 0.99994

Rate constant: 3.38317E-4 ± 9.3029E-6

A2.130

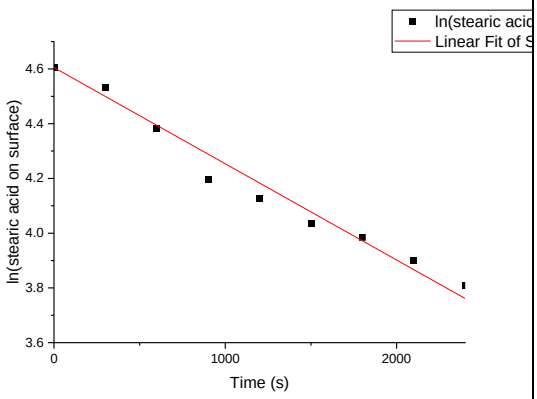

4000 rpm

R^2: 0.99987

Rate constant: 3.51547E-4 ± 1.10204E-5

A2.131

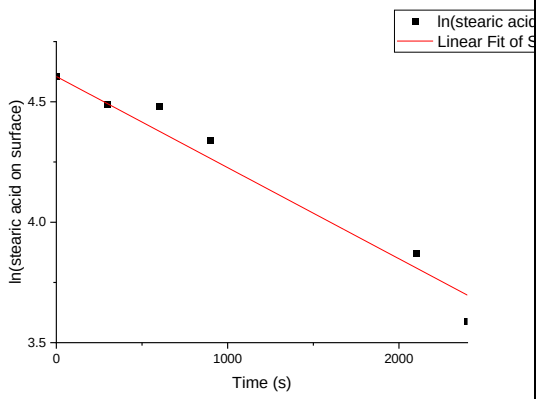

4500 rpm

R^2: 0.99965

Rate constant: 3.78372E-4 ± 2.35972E-5

A2.132

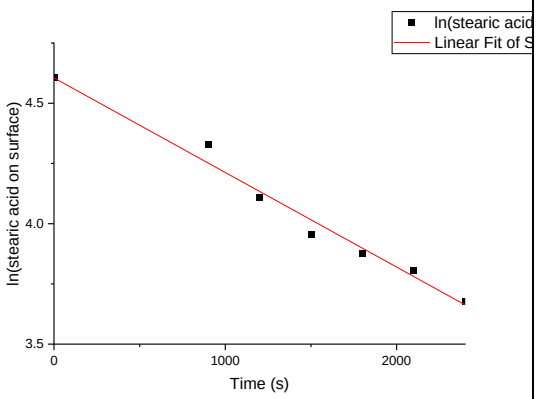

5000 rpm

R^2: 0.99988

Rate constant: 3.92643E-4 ± 1.03606E-5

A2.133

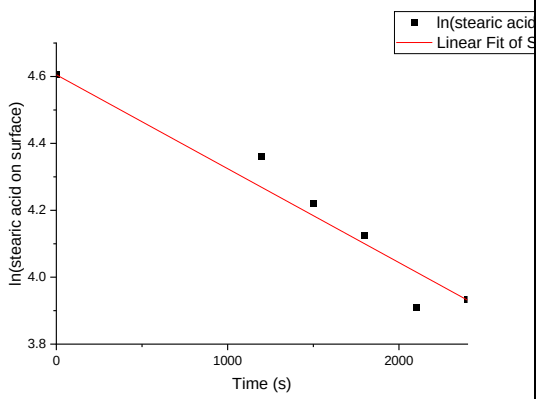

5000 rpm

R^2: 0.99975

Rate constant: 2.80698E-4 ± 1.59666E-5

A2.134

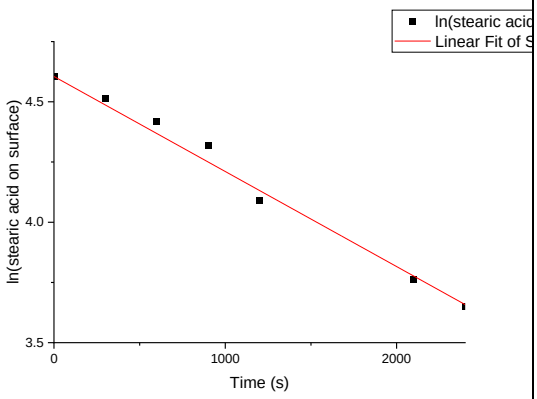

5000 rpm

R^2: 0.9999

Rate constant: 3.94574E-4 ± 1.14698E-5

A2.135

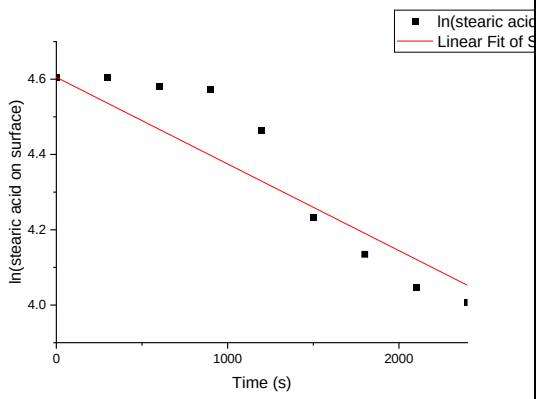

5000 rpm

R^2: 0.99949

Rate constant: 2.30322E-4 ± 2.31188E-5

A2.136

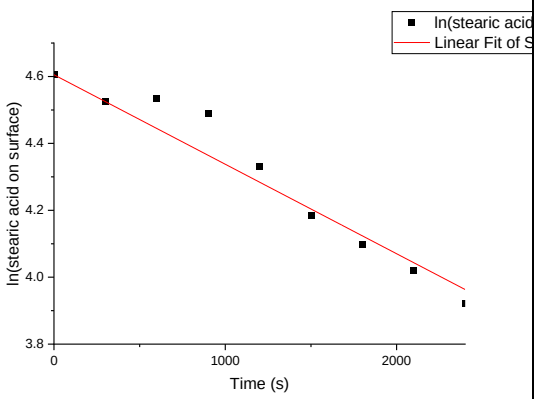

5000 rpm

R^2: 0.9998

Rate constant: 2.67472E-4 ± 1.41311E-5

A2.137

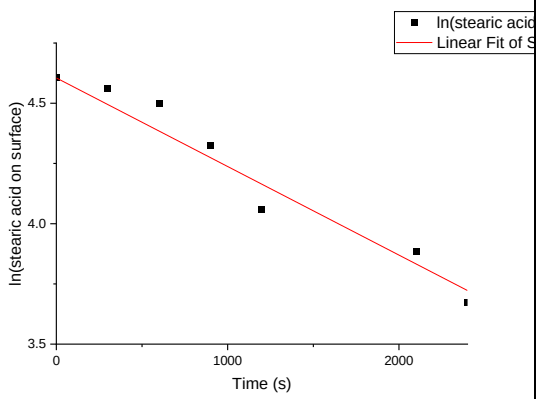

5500 rpm

R^2: 0.99966

Rate constant: 3.67761E-4 ± 2.18119E-5

A2.138

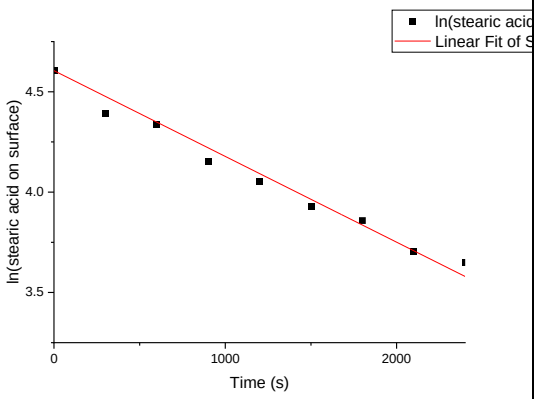

6000 rpm

R^2: 0.99985

Rate constant: 4.2724E-4 ± 1.17166E-5

A2.139

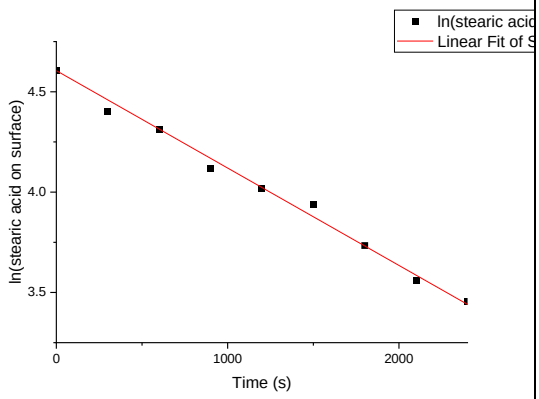

6000 rpm

R^2: 0.99992

Rate constant: 4.85219E-4 ± 8.61496E-6

A2.140

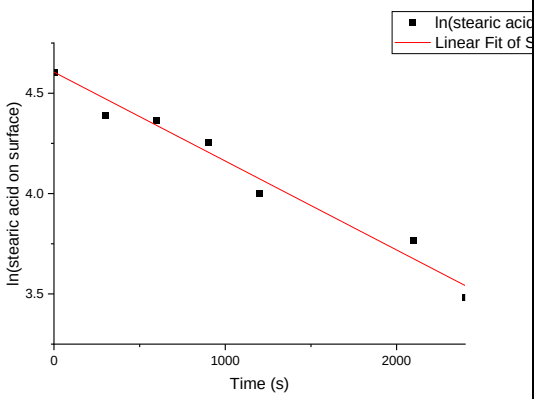

6000 rpm

R^2: 0.99974

Rate constant: 4.43026E-4 ± 1.86857E-5

A2.141

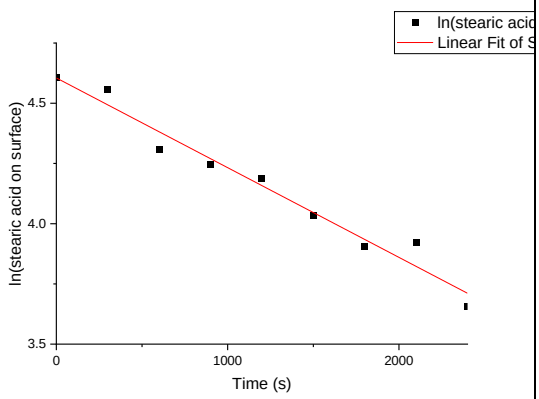

6000 rpm

R^2: 0.99982

Rate constant: 3.72514E-4 ± 1.30708E-5

A2.142

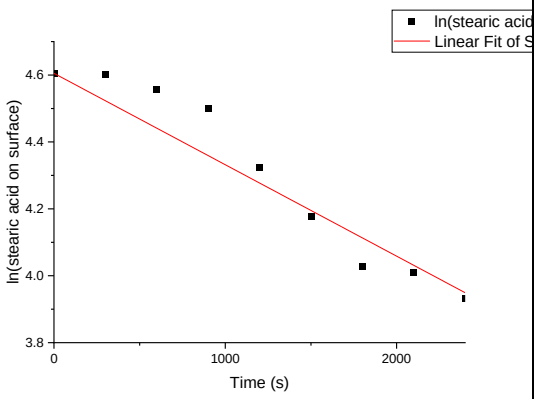

6000 rpm

R^2: 0.99966

Rate constant: 2.73261E-4 ± 1.84376E-5

A2.143

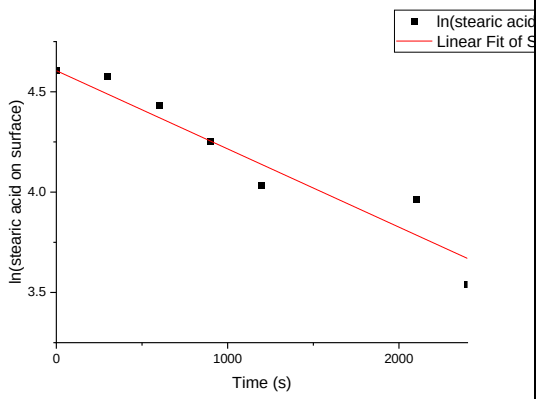

6500 rpm

R^2: 0.99934

Rate constant: 3.89786E-4 ± 3.00751E-5

A2.144

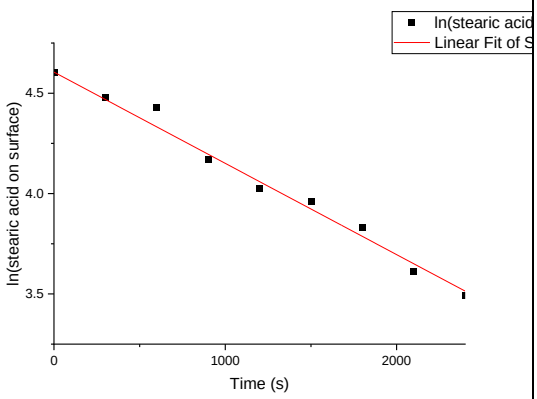

7000 rpm

R^2: 0.99988

Rate constant: 4.54579E-4 ± 1.05027E-5

A2.145

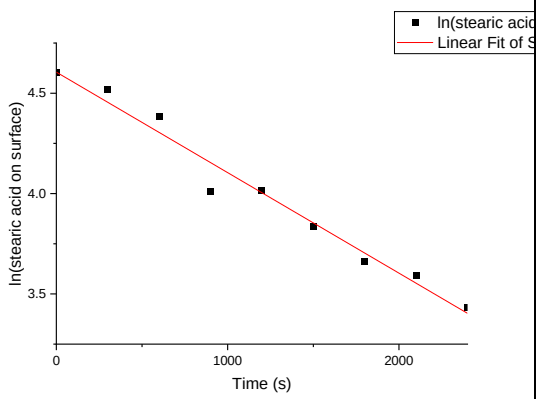

7000 rpm

R^2: 0.99973

Rate constant: 5.00761E-4 ± 1.54757E-5

A2.146

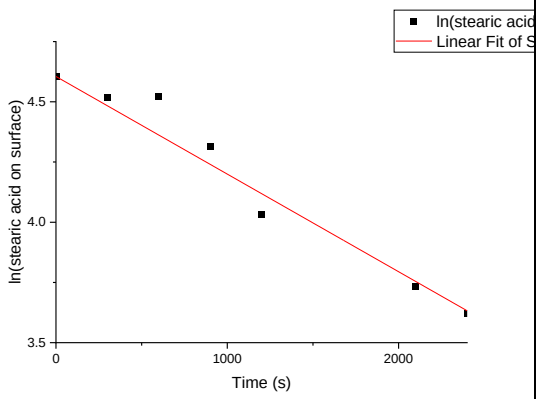

7000 rpm

R^2: 0.99962

Rate constant: 4.05292E-4 ± 2.28939E-5

A2.147

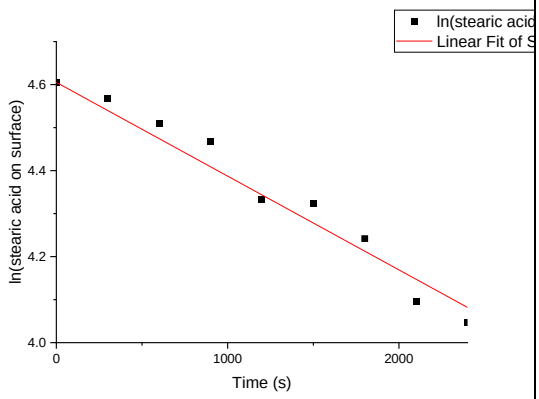

7000 rpm

R^2: 0.99992

Rate constant: 2.18003E-4 ± 9.12353E-6

A2.148

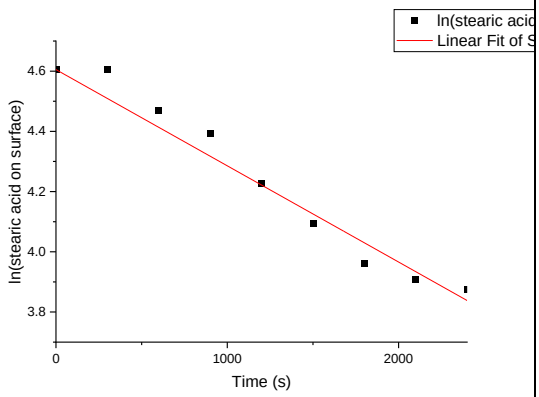

7000 rpm

R^2: 0.99982

Rate constant: 3.19575E-4 ± 1.33424E-5

A2.149

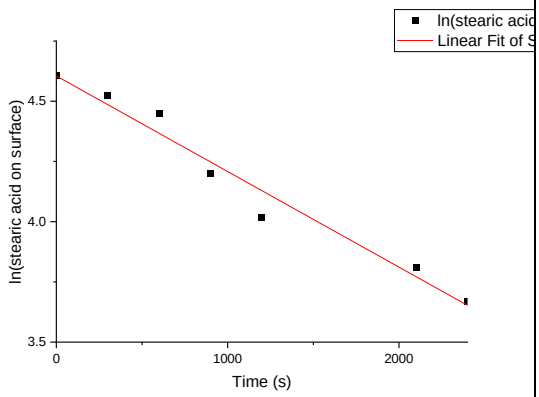

7500 rpm

R^2: 0.99977

Rate constant: 3.96884E-4 ± 1.77699E-5

A2.150

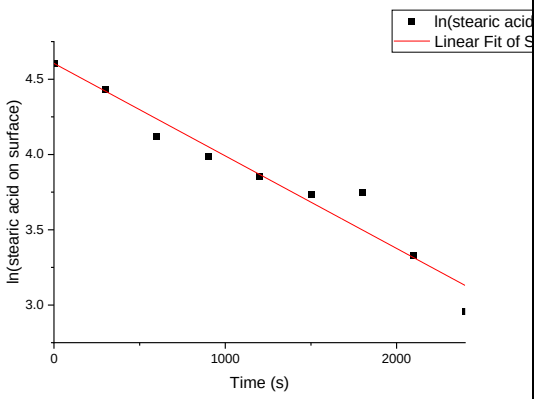

8000 rpm

R^2: 0.99906

Rate constant: 3.34541E-4 ± 3.22199E-5

A2.151

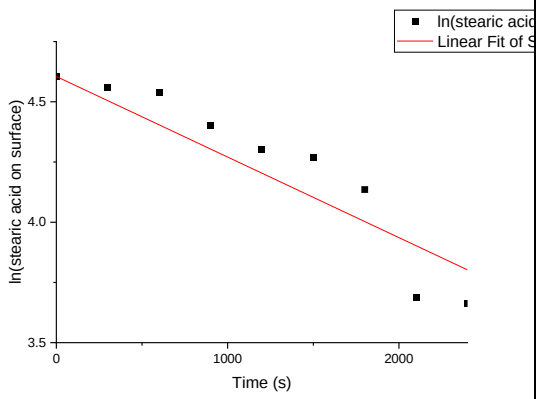

8000 rpm

R^2: 0.99895

Rate constant: 6.14563E-4 ± 2.79053E-5

A2.152

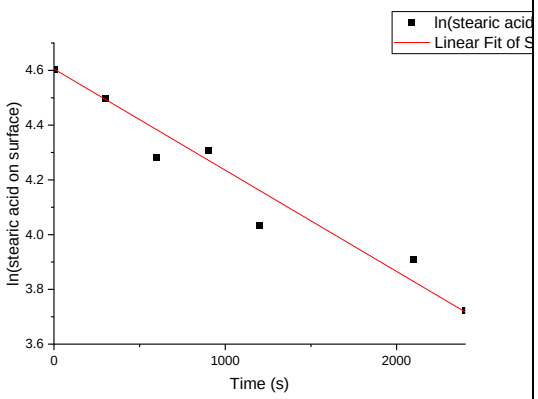

8000 rpm

R^2: 0.99967

Rate constant: 3.69773E-4 ± 2.11818E-5

A2.153

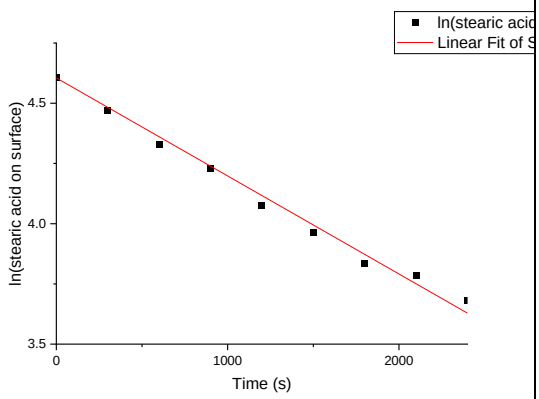

8000 rpm

R^2: 0.99993

Rate constant: 4.06944E-4 ± 7.9166E-6

A2.154

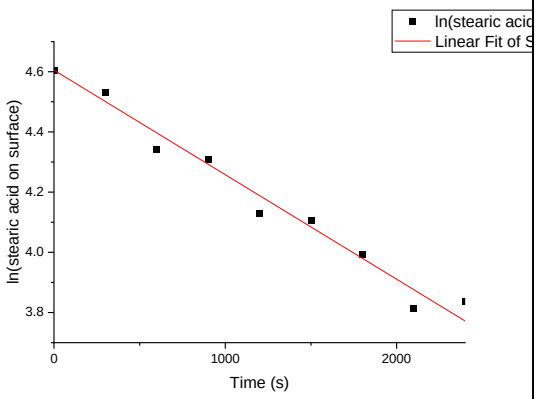

8000 rpm

R^2: 0.99988

Rate constant: 3.47183E-4 ± 1.07011E-5

A: 2.2 Rate plots for stearic acid decomposition over 2.5 wt% Copper-doped *meso*-TiO_2 samples

Preparation spin speed, zero order rate plots and rate constants for stearic acid decomposition on 2.5 wt% copper-doped *meso*-TiO_2 samples

<table>
<tr>
<td>A2.155
 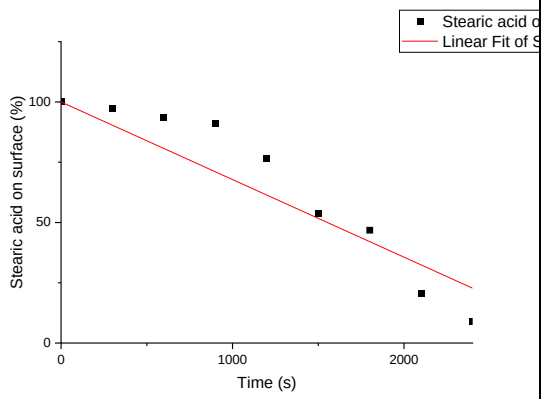

500 rpm
R^2: 0.97206
Rate constant: 0.03219 ± 0.00285</td>
<td>A2.156
 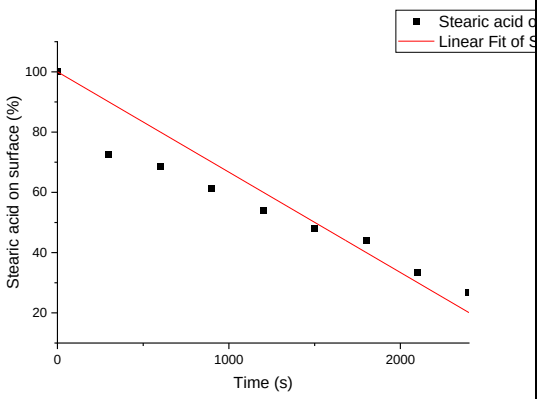

1000 rpm
R^2: 0.97857
Rate constant: 0.03329 ± 0.00206</td>
</tr>
<tr>
<td>A2.157
 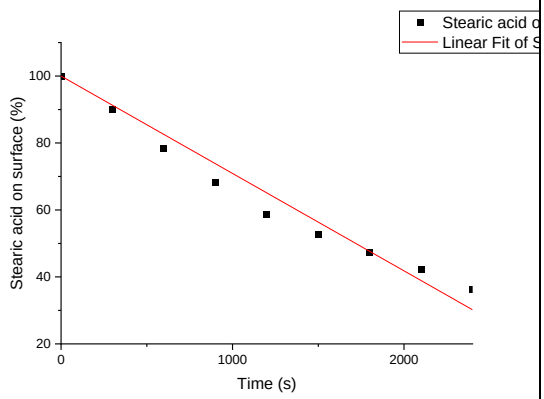

2000 rpm
R^2: 0.99582
Rate constant: 0.02909 ± 0.00101</td>
<td>A2.158
 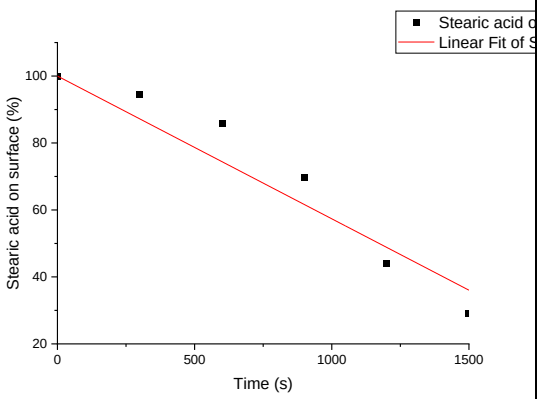

3000 rpm
R^2: 0.9887
Rate constant: 0.04264 ± 0.00359</td>
</tr>
</table>

A2.159	A2.160
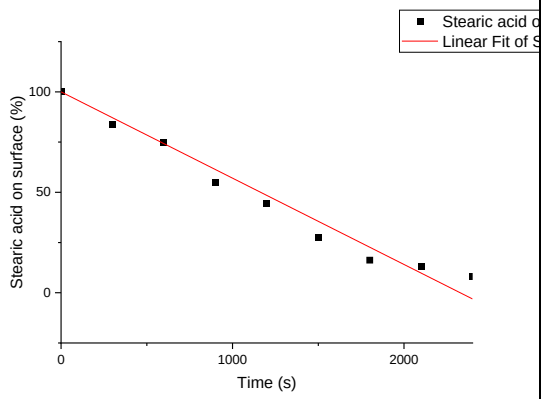	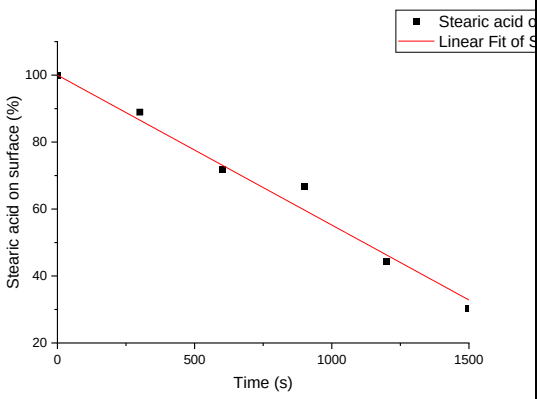
3000 rpm	3500 rpm
R^2: 0.98794	R^2: 0.99733
Rate constant: 0.04296 ± 0.00145	Rate constant: 0.04477 ± 0.00165
A2.161	**A2.162**
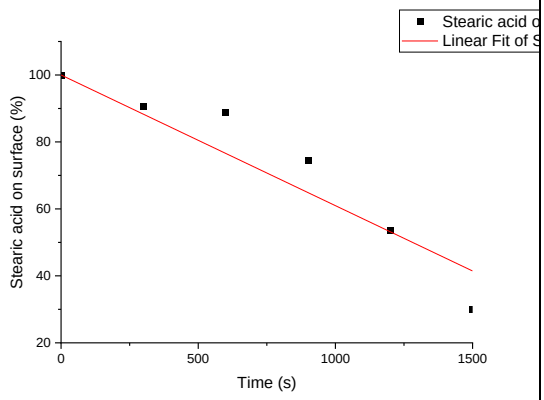	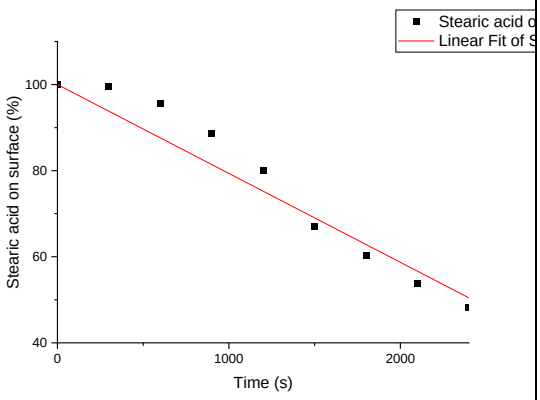
4000 rpm	4000 rpm
R^2: 0.98721	R^2: 0.99613
Rate constant: 0.03903 ± 0.00391	Rate constant: 0.02065 ± 0.00115

A2.163

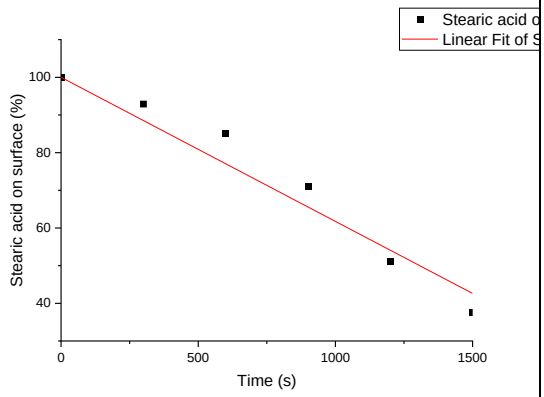

4500 rpm

R^2: 0.99494

Rate constant: 0.03825 ± 0.00244

A2.164

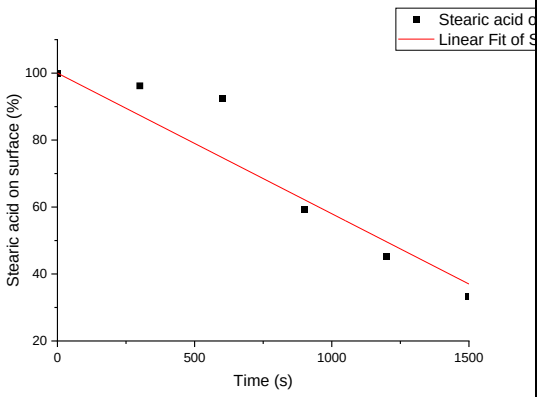

5000 rpm

R^2: 0.98489

Rate constant: 0.04199 ± 0.00419

A2.165

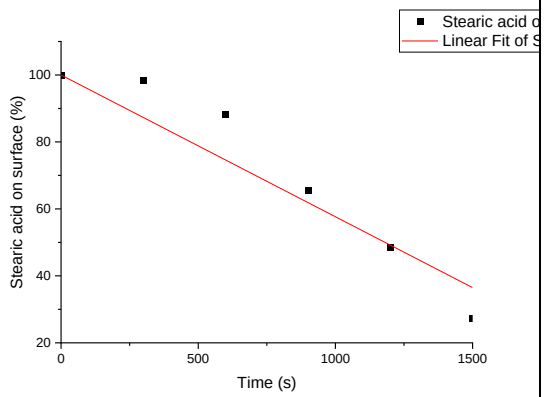

5500 rpm

R^2: 0.98613

Rate constant: 0.04234 ± 0.00403

A2.166

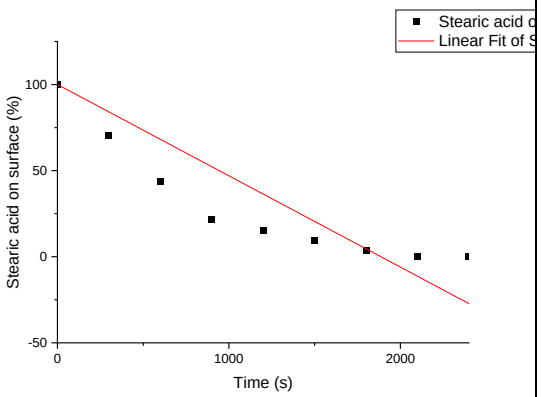

6000 rpm

R^2: 0.79949

Rate constant: 0.05302 ± 0.00464

A2.167 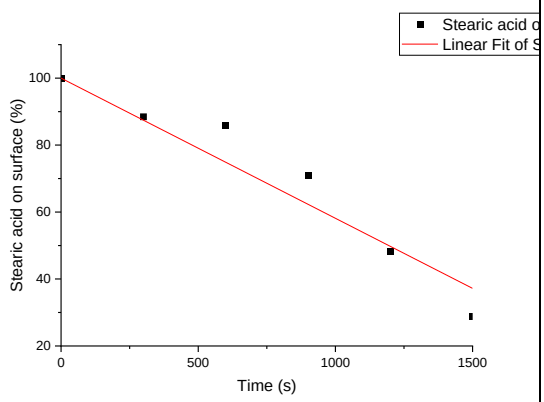 6000 rpm R^2: 0.99018 Rate constant: 0.04186 ± 0.00332	A2.168 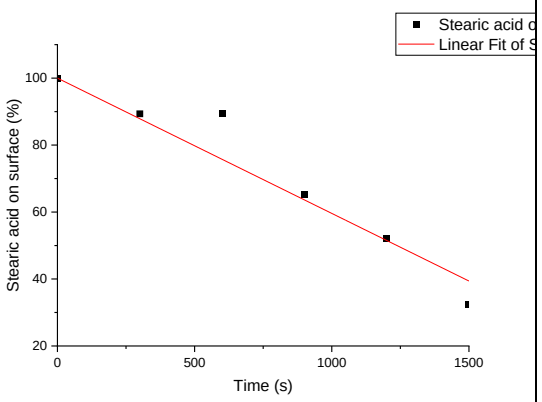 6500 rpm R^2: 0.99157 Rate constant: 0.0404 ± 0.0031
A2.169 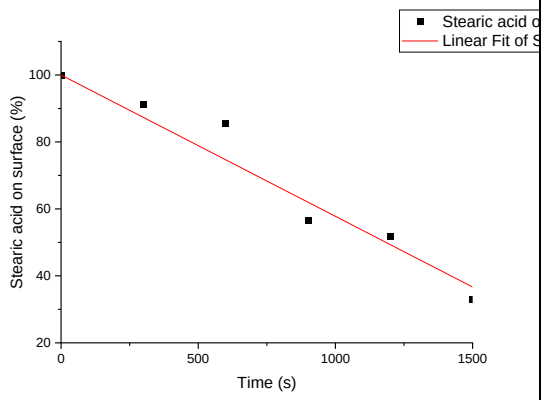 7000 rpm R^2: 0.99333 Rate constant: 0.04222 ± 0.00271	A2.170 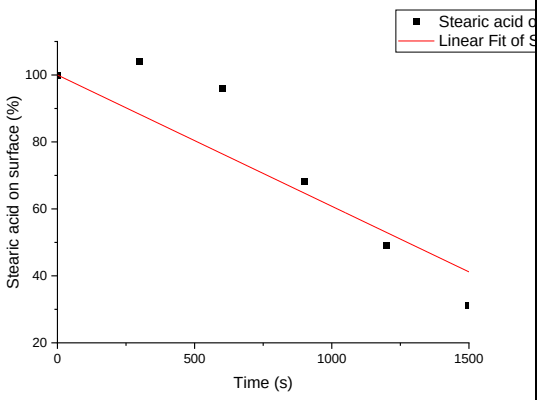 7500 rpm R^2: 0.9761 Rate constant: 0.03921 ± 0.00554

A2.171

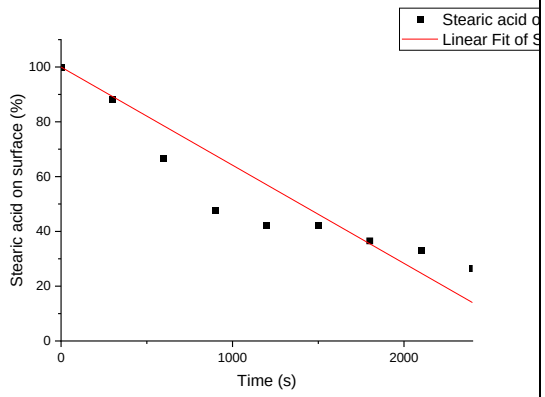

8000 rpm

R^2: 0.96354

Rate constant: 0.03583 ± 0.00262

Preparation spin speed and first order rate plots and rate constants for stearic acid decomposition on 2.5 wt% copper-doped *meso*-TiO_2 samples

A2.172 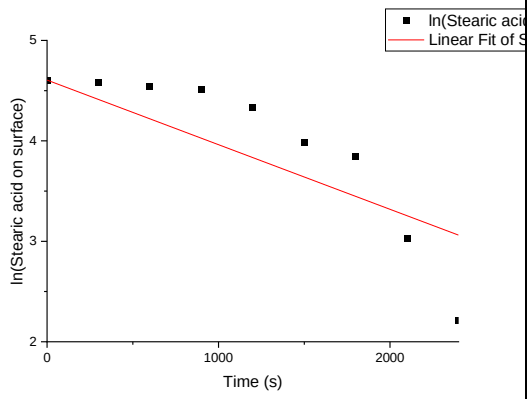 500 rpm R^2: 0.98722 Rate constant: 6.43198E-4 ± 1.0649E-4	A2.173 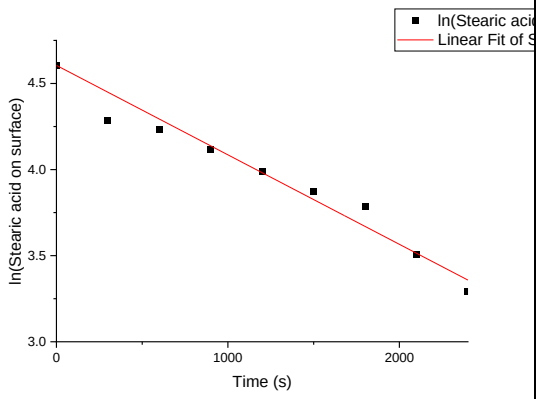 1000 rpm R^2: 0.99959 Rate constant: 5.19591E-4 ± 1.88015E-5
A2.174 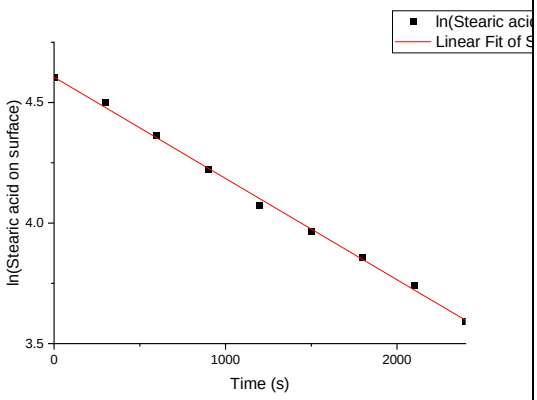 2000 rpm R^2: 0.99999 Rate constant: 4.20093E-4 ± 3.52874E-6	A2.175 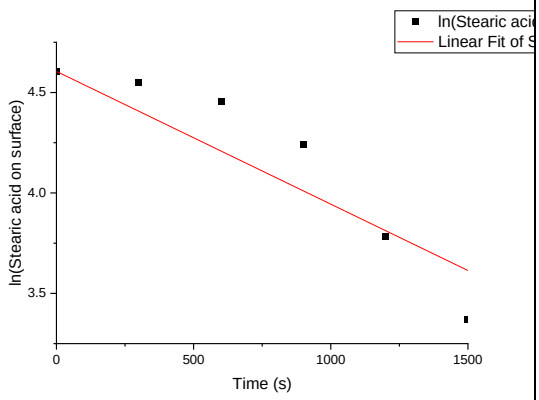 3000 rpm R^2: 0.9978 Rate constant: 6.60865E-4 ± 8.82957E-5

A2.176

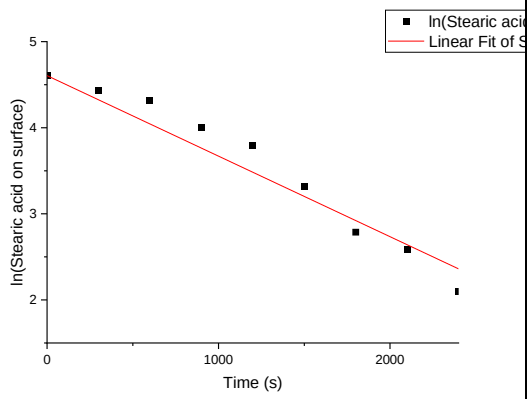

3000 rpm

R^2: 0.9968

Rate constant: 9.3518E-4 ± 4.81941E-5

A2.177

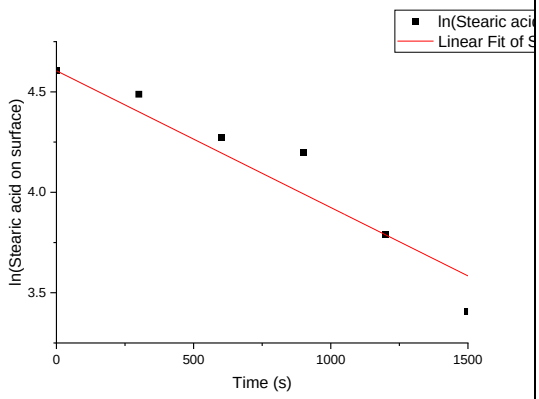

3500 rpm

R^2: 0.99897

Rate constant: 6.80805E-4 ± 5.98752E-5

A2.178

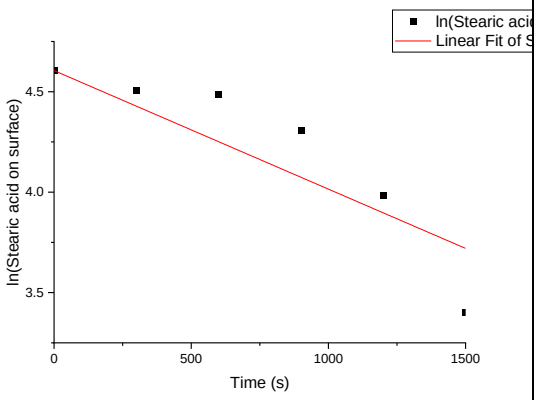

4000 rpm

R^2: 0.99747

Rate constant: 5.90066E-4 ± 9.57259E-5

A2.179

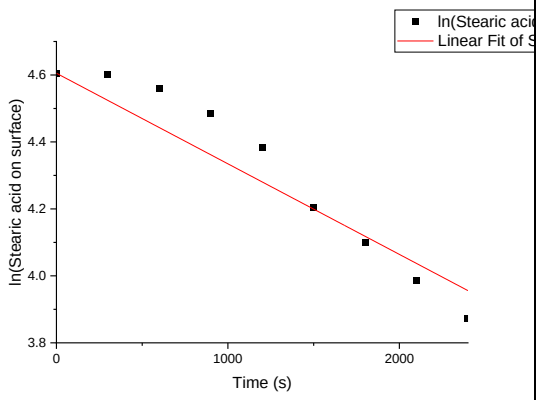

4000 rpm

R^2: 0.99963

Rate constant: 2.70495E-4 ± 1.93141E-5

A2.180

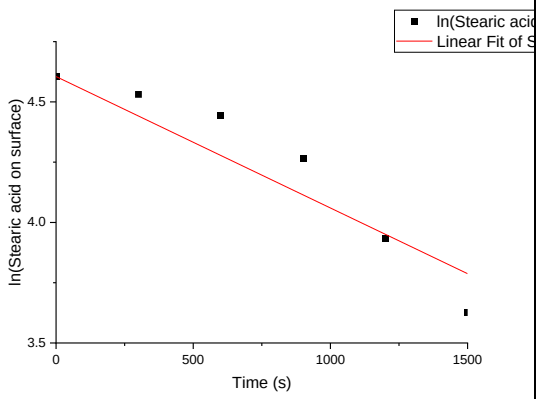

4500 rpm

R^2: 0.99907

Rate constant: 5.45145E-4 ± 5.82333E-5

A2.181

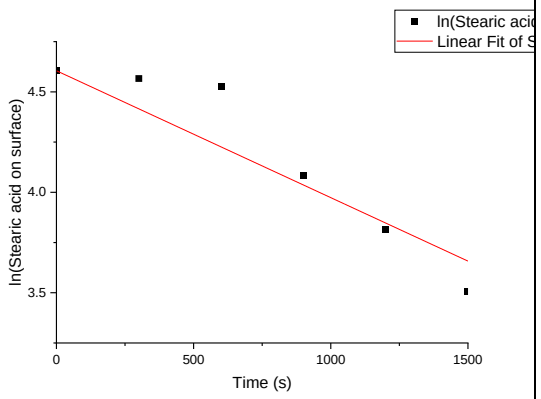

5000 rpm

R^2: 0.99841

Rate constant: 6.31725E-4 ± 7.53256E-5

A2.182

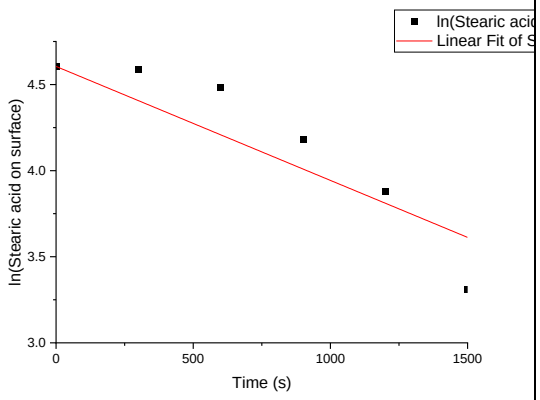

5500 rpm

R^2: 0.99737

Rate constant: 6.61842E-4 ± 9.67918E-5

A2.183

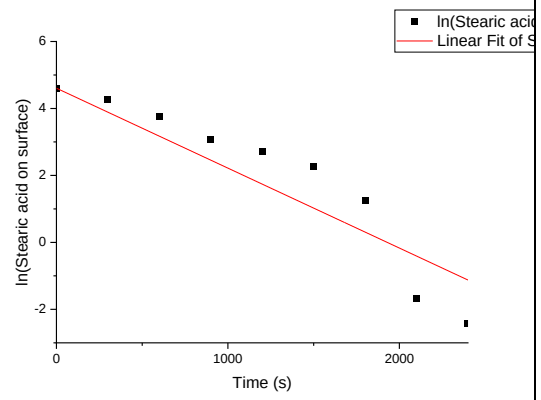

6000 rpm

R^2: 0.90089

Rate constant: 0.00239 ± 2.2693E-4

A2.184

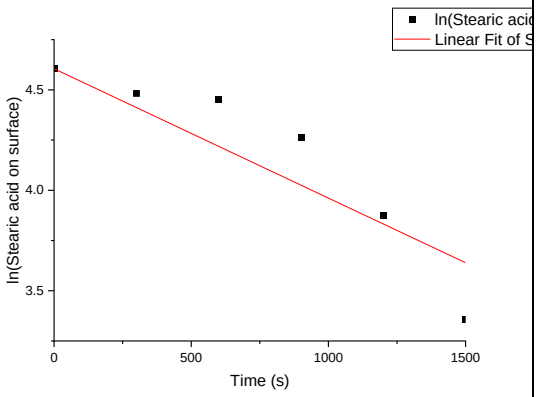

6000 rpm

R^2: 0.99775

Rate constant: 6.43832E-4 ± 8.9477E-5

A2.185

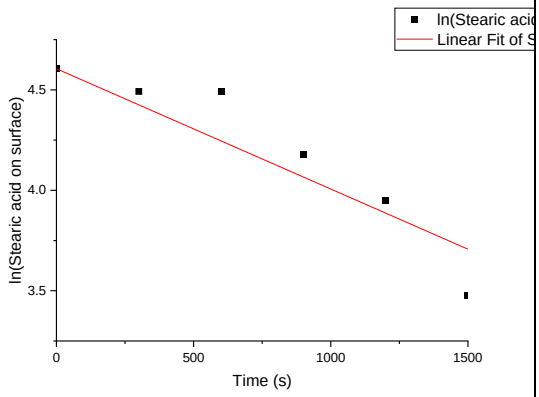

6500 rpm

R^2: 0.99848

Rate constant: 5.98858E-4 ± 7.39065E-5

A2.186

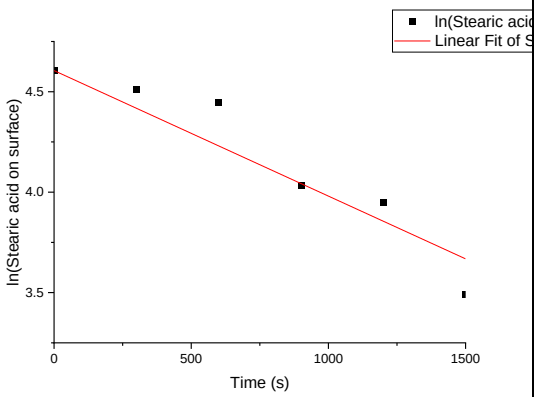

7000 rpm

R^2: 0.99891

Rate constant: 6.2473E-4 ± 6.22409E-5

A2.187

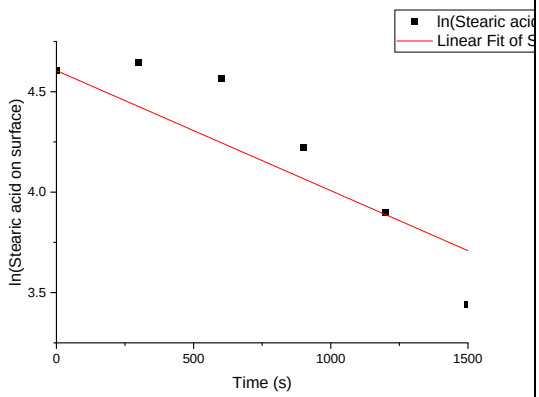

7500 rpm

R^2: 0.99728

Rate constant: 5.97549E-4 ± 9.96124E-5

A2.188

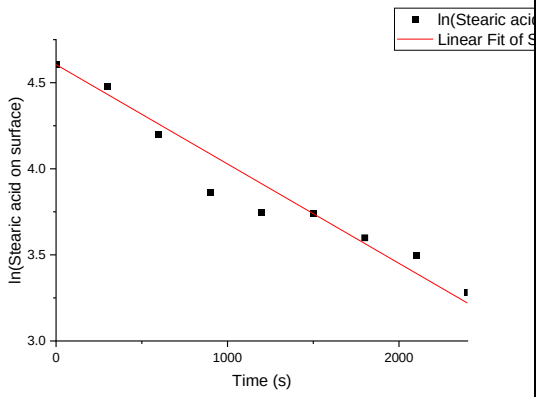

8000 rpm

R^2: 0.99919

Rate constant: 5.77212E-4 ± 2.5939E-5

A: 2.3 Rate plots for stearic acid decomposition over 1 wt% Copper-doped *meso*-TiO_2 samples

Preparation spin speed, zero order rate plots and rate constants for stearic acid decomposition on 1 wt% copper-doped *meso*-TiO_2 samples

<table>
<tr>
<td>A2.189
 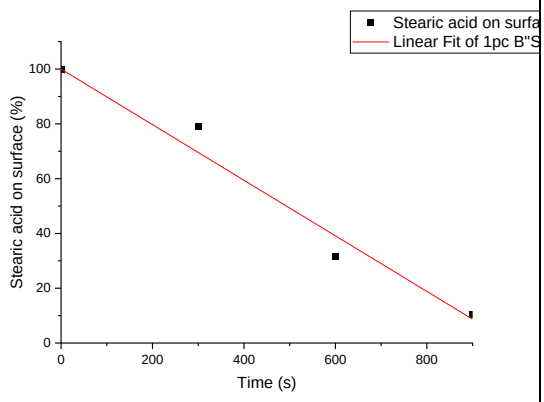

500 rpm
R^2: 0.9885
Rate constant: 0.10144 ± 0.0063</td>
<td>A2.190
 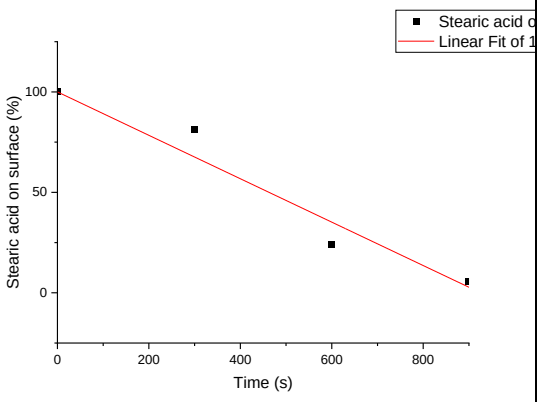

500 rpm
R^2: 0.97477
Rate constant: 0.10804 ± 0.00929</td>
</tr>
<tr>
<td>A2.191
 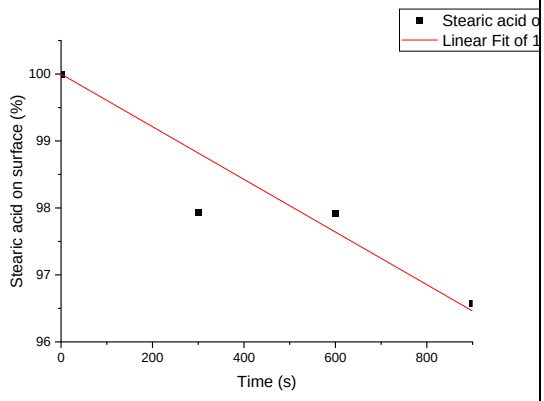

500 rpm
0.00393 ± R^2: 0.99997
Rate constant: 0.00393 ± 4.80223E-4</td>
<td>A2.192
 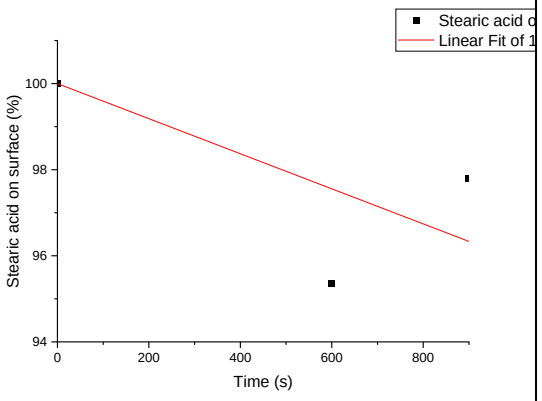

500 rpm
R^2: 0.99964
Rate constant: 0.00407 ± 0.00173</td>
</tr>
</table>

A2.193

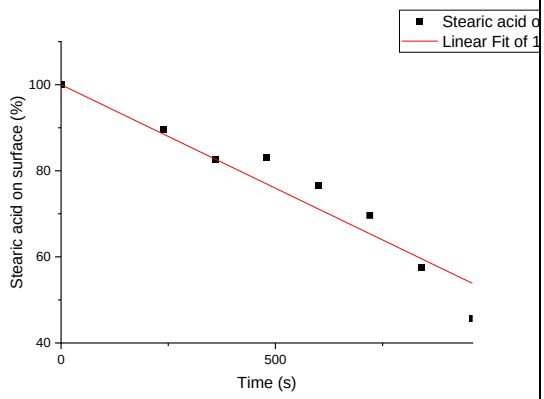

500 rpm

R^2: 0.99368

Rate constant: 0.04808 ± 0.00279

A2.194

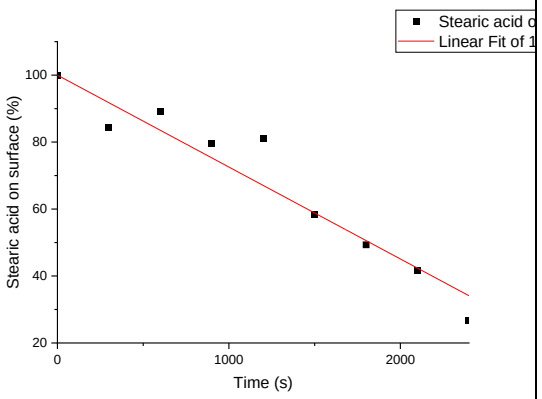

500 rpm

R^2: 0.99147

Rate constant: 0.02745 ± 0.00155

A2.195

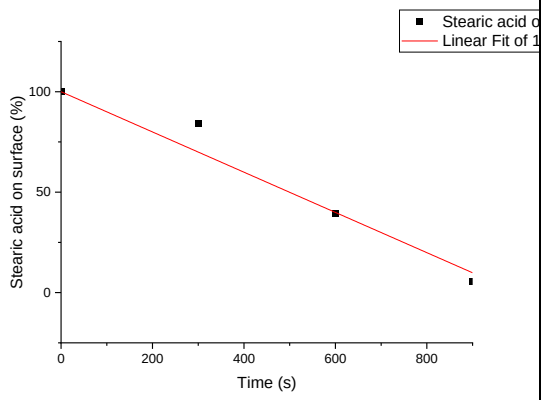

1000 rpm

R^2: 0.98441

Rate constant: 0.10014 ± 0.00759

A2.196

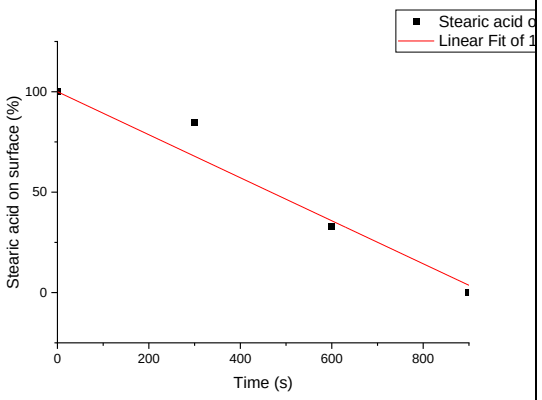

1000 rpm

R^2: 0.97777

Rate constant: 0.10706 ± 0.00897

A2.197	A2.198
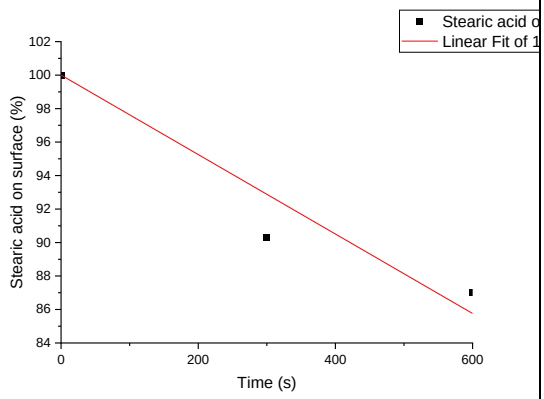	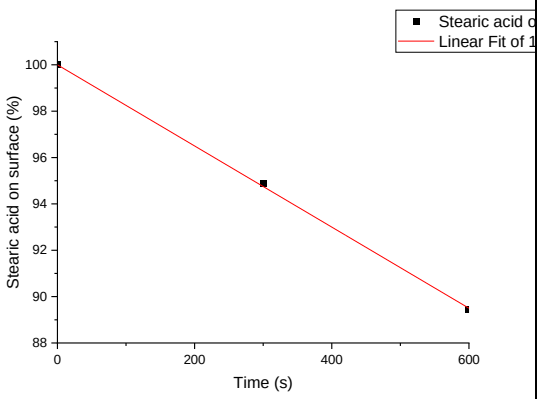
1000 rpm	1000 rpm
R^2: 0.99952	R^2: 1
Rate constant: 0.02373 ± 0.00302	Rate constant: 0.0175 ± 1.55602E-4
A2.199	**A2.200**
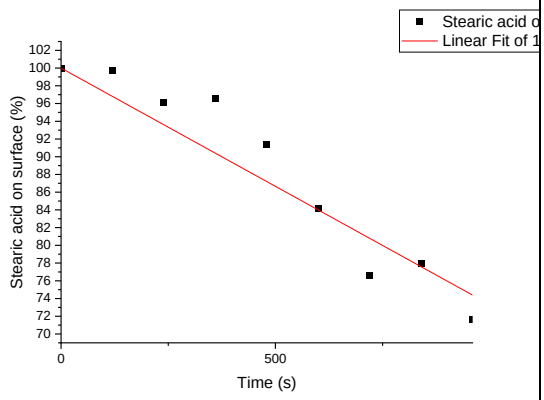	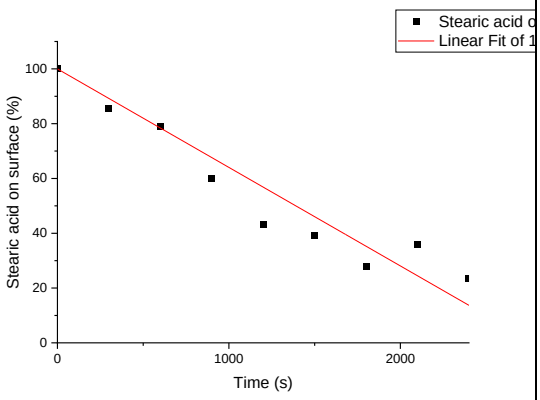
1000 rpm	1000 rpm
R^2: 0.99805	R^2: 0.98011
Rate constant: 0.02929 ± 0.00159	Rate constant: 0.03596 ± 0.002

A2.201

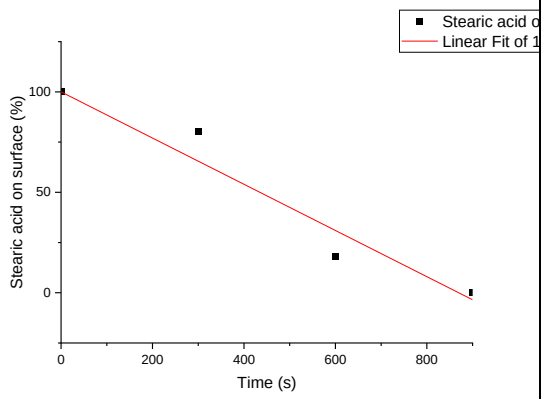

1500 rpm

R^2: 0.96754

Rate constant: 0.115 ± 0.0104

A2.202

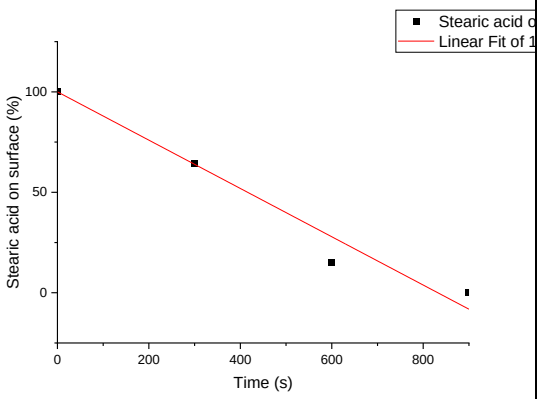

1500 rpm

R^2: 0.97788

Rate constant: 0.12021 ± 0.00793

A2.203

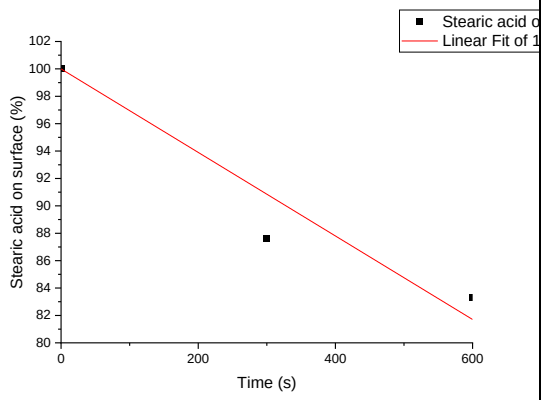

1500 rpm

R^2: 0.99919

Rate constant: 0.03049 ± 0.00383

A2.204

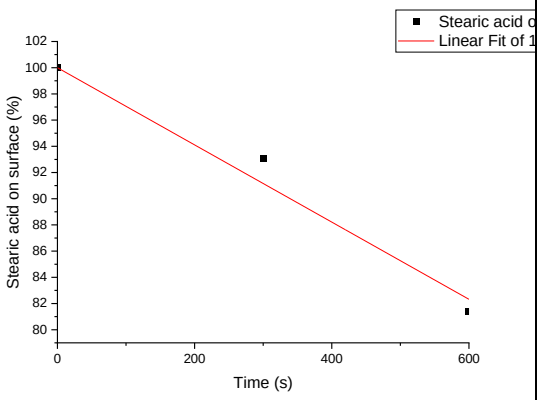

1500 rpm

R^2: 0.99973

Rate constant: 0.02946 ± 0.00226

A2.205

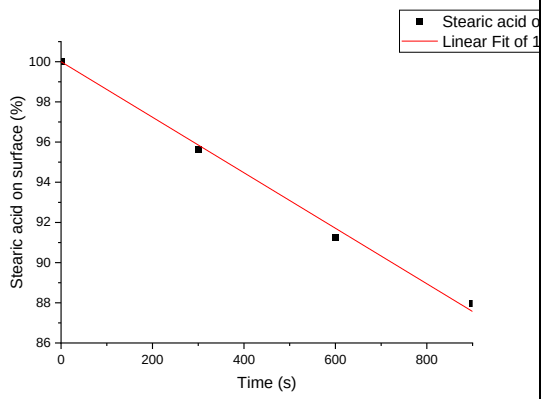

2000 rpm

R^2: 0.99998

Rate constant: 0.01382 ± 3.30146E-4

A2.206

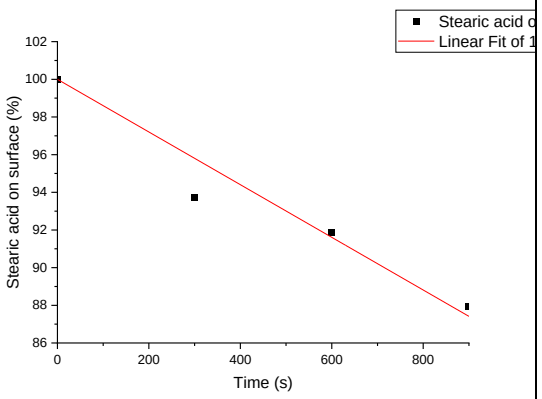

2000 rpm

R^2: 0.99982

Rate constant: 0.01399 ± 0.00111

A2.207

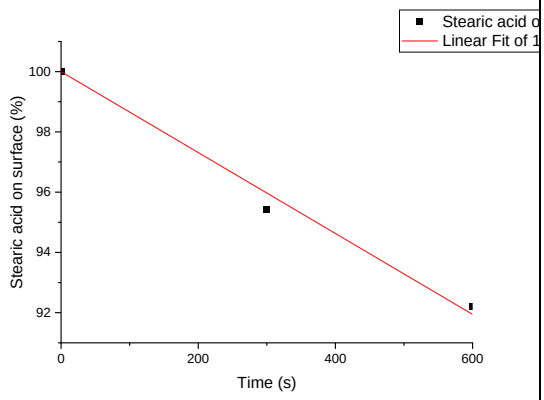

2000 rpm

R^2: 0.99998

Rate constant: 0.01343 ± 6.28969E-4

A2.208

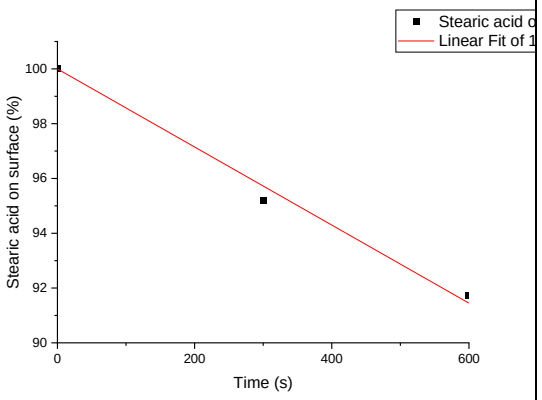

2000 rpm

R^2: 0.99998

Rate constant: 0.01425 ± 6.38627E-4

A2.209

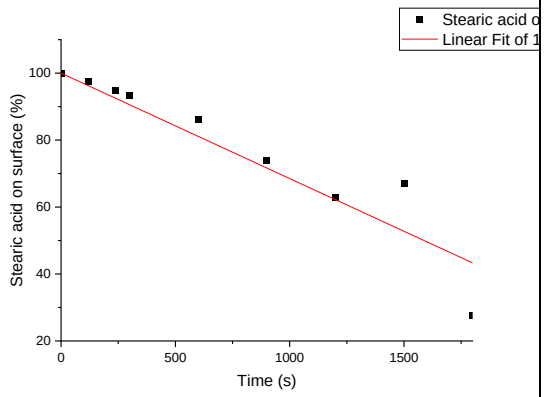

2000 rpm

R^2: 0.98315

Rate constant: 0.03588 ± 0.00222

A2.210

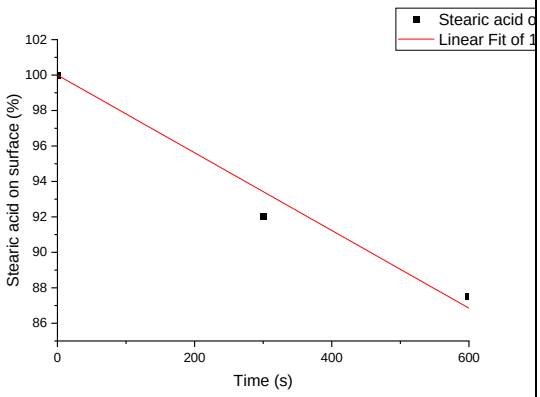

2500 rpm

R^2: 0.99986

Rate constant: 0.02191 ± 0.00162

A2.211

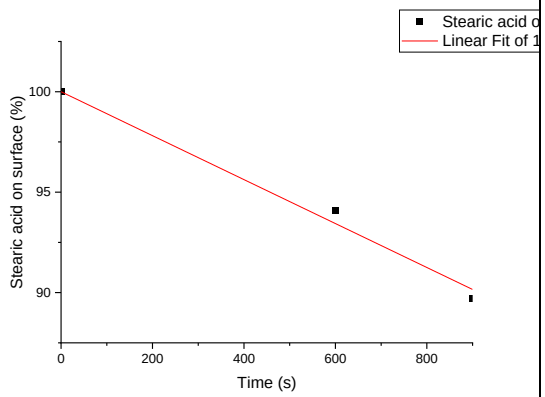

2500 rpm

R^2: 0.99997

Rate constant: 0.01094 ± 5.00843E-4

A2.212

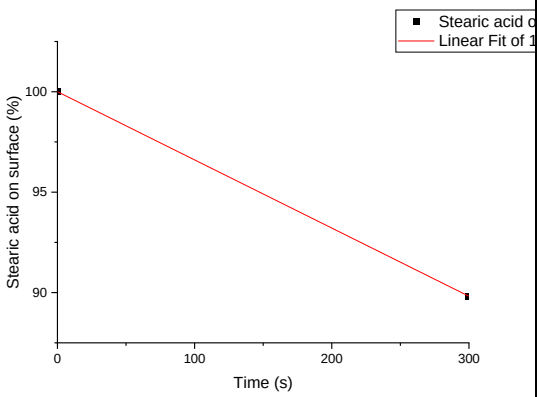

2500 rpm

R^2: 1

Rate constant: 0.03393

A2.213

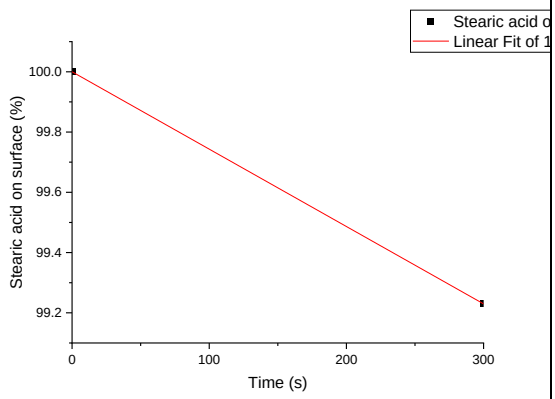

2500 rpm

R^2: 1

Rate constant: 0.00257

A2.214

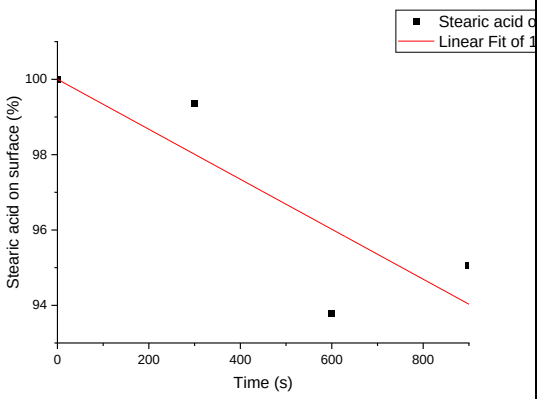

3000 rpm

R^2: 0.99972

Rate constant: 0.00663 ± 0.00144

A2.215

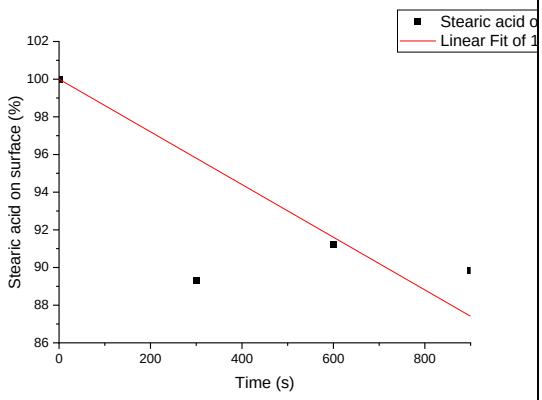

3000 rpm

R^2: 0.99812

Rate constant: 0.01399 ± 0.00358

A2.216

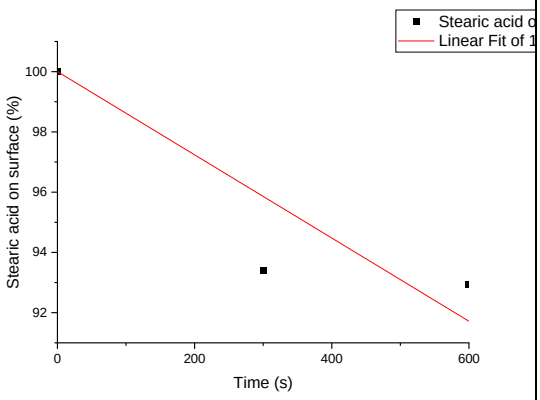

3000 rpm

R^2: 0.99959

Rate constant: 0.0138 ± 0.0029

A2.217	A2.218
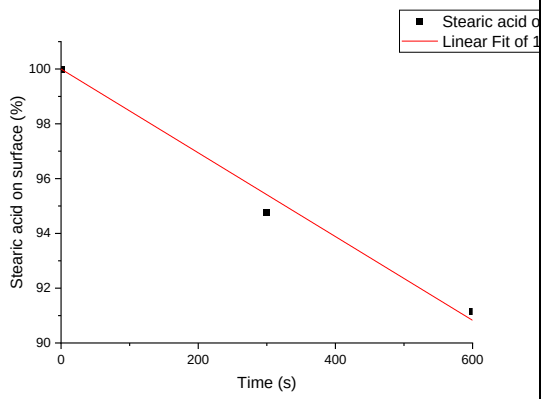	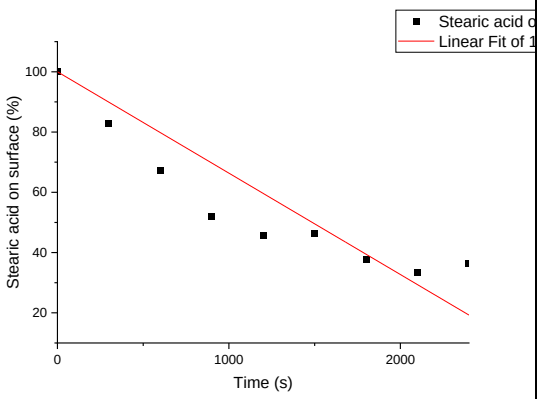
3000 rpm	3000 rpm
R^2: 0.99997	R^2: 0.96386
Rate constant: 0.01529 ± 7.8238E-4	Rate constant: 0.03364 ± 0.00266
A2.219	**A2.220**
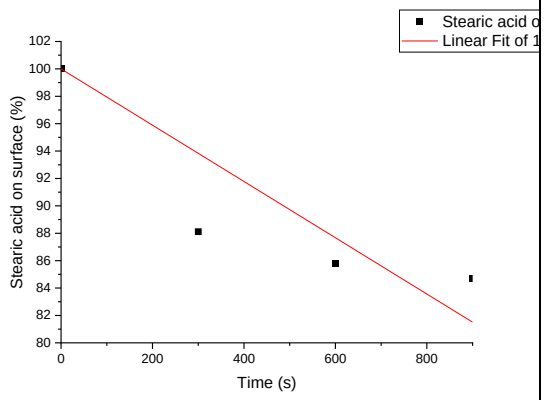	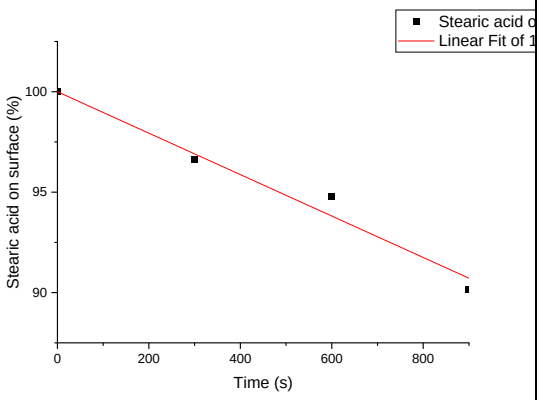
3500 rpm	3500 rpm
R^2: 0.99809	R^2: 0.99995
Rate constant: 0.02055 ± 0.0035	Rate constant: 0.01031 ± 5.92203E-4

A2.221	A2.222
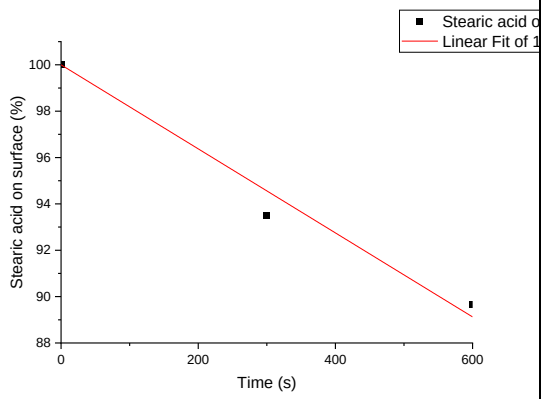	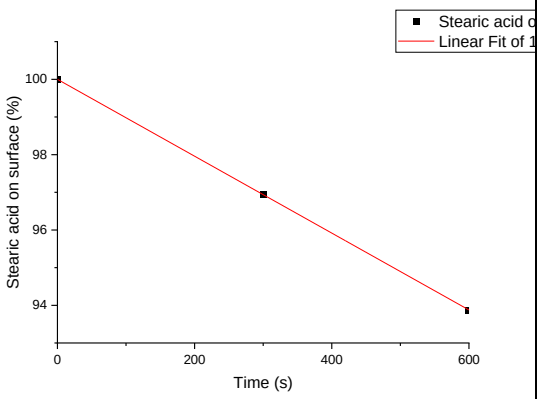
3500 rpm	3500 rpm
R^2: 0.99992	R^2: 1
Rate constant: 0.01813 ± 0.00123	Rate constant: 0.01021 ± 4.89092E-9
A2.223	**A2.224**
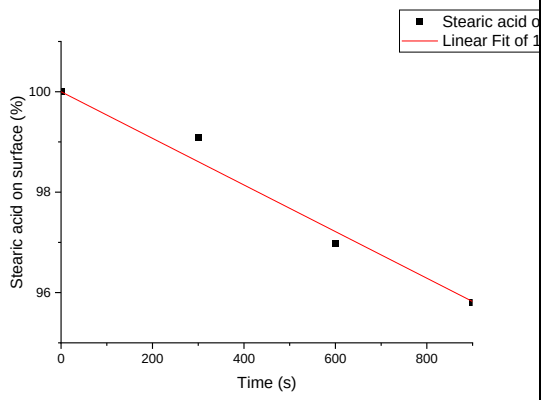	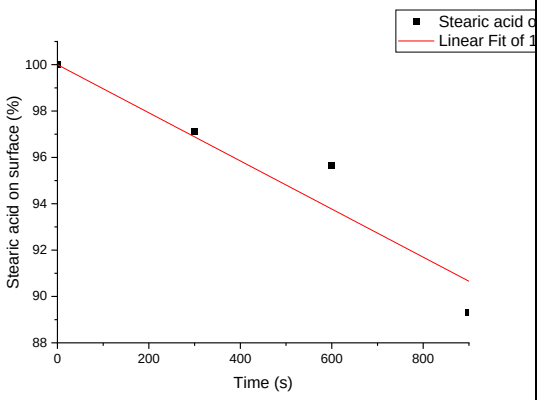
4000 rpm	4000 rpm
R^2: 0.99999	R^2: 0.99981
Rate constant: 0.00464 ± 2.73732E-4	Rate constant: 0.01038 ± 0.00119

A2.225

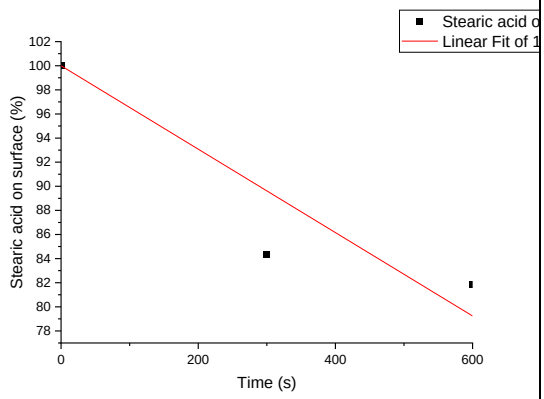

4000 rpm

R^2: 0.99781

Rate constant: 0.0346 ± 0.00622

A2.226

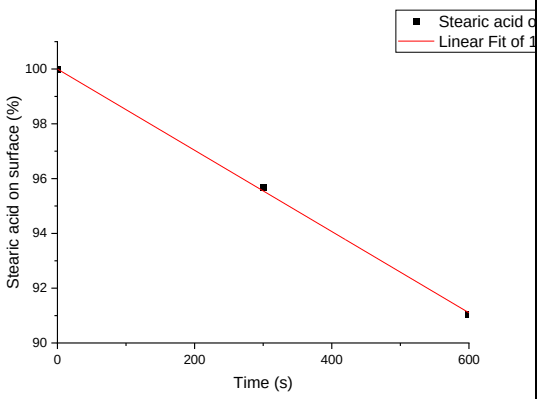

4000 rpm

R^2: 1

Rate constant: 0.01483 ± 1.34796E-4

A2.227

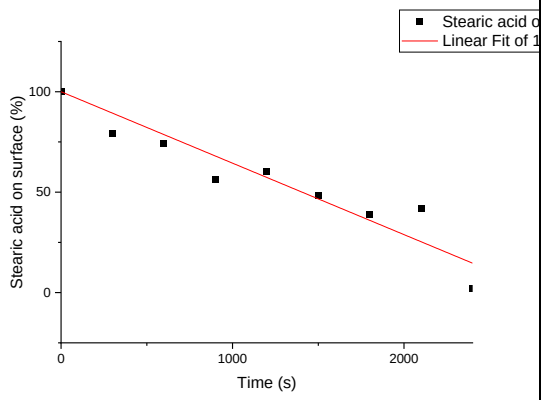

4000 rpm

R^2: 0.97715

Rate constant: 0.03556 ± 0.00218

A2.228

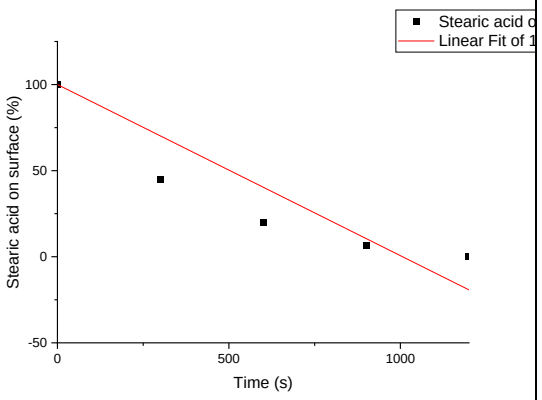

5000 rpm

R^2: 0.85383

Rate constant: 0.09936 ± 0.01161

A2.229

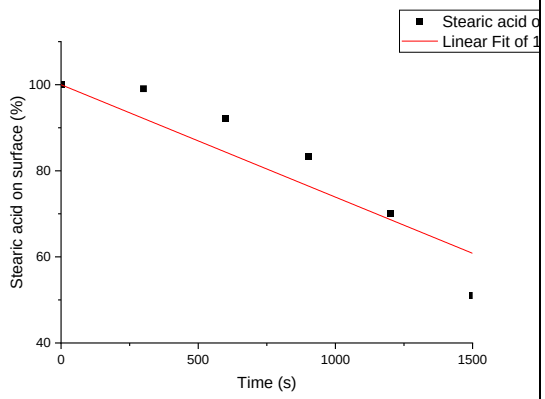

6000 rpm

R^2: 0.99285

Rate constant: 0.02611 ± 0.00321

A2.230

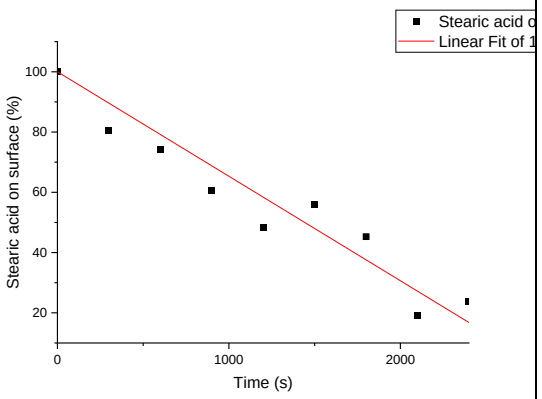

7000 rpm

R^2: 0.98318

Rate constant: 0.03467 ± 0.00186

A2.231

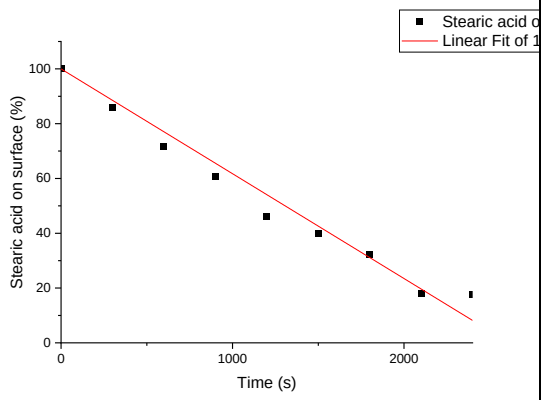

8000 rpm

R^2: 0.99209

Rate constant: 0.03826 ± 0.00123

Preparation spin speed and first order rate plots and rate constants for stearic acid decomposition on 1 wt% copper-doped *meso*-TiO_2 samples

A2.232 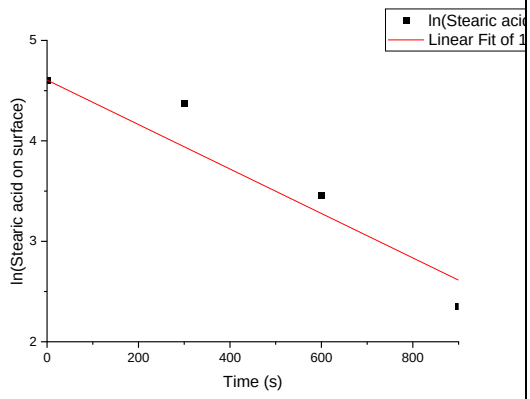 500 rpm R^2: 0.99343 Rate constant: 0.00221 ± 2.74546E-4	A2.233 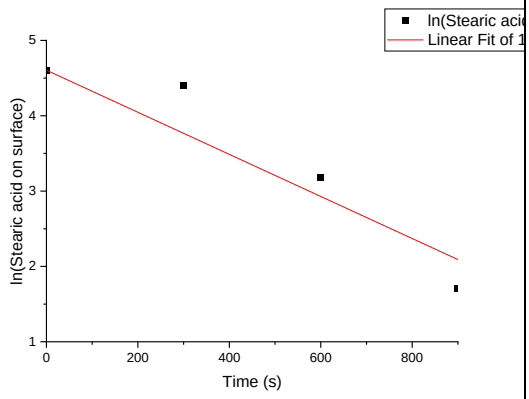 500 rpm R^2: 0.9849 Rate constant: 0.00279 ± 4.00851E-4
A2.234 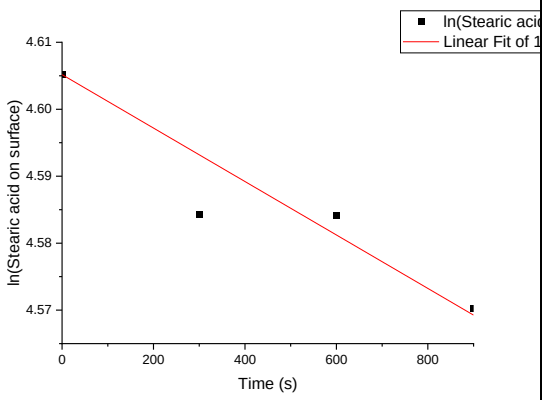 500 rpm R^2: 1 Rate constant: 3.99071E-5 ± 4.83752E-6	A2.235 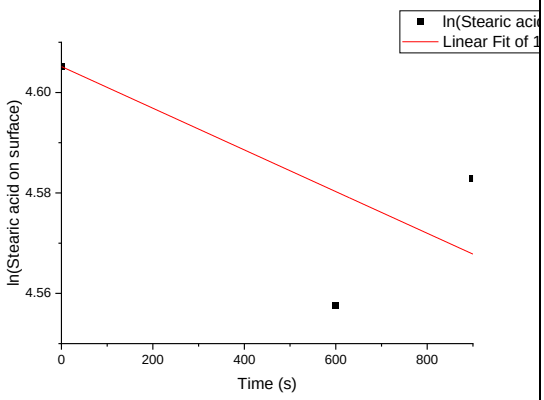 500 rpm R^2: 0.99998 Rate constant: 4.14964E-5 ± 1.77753E-5

A2.236

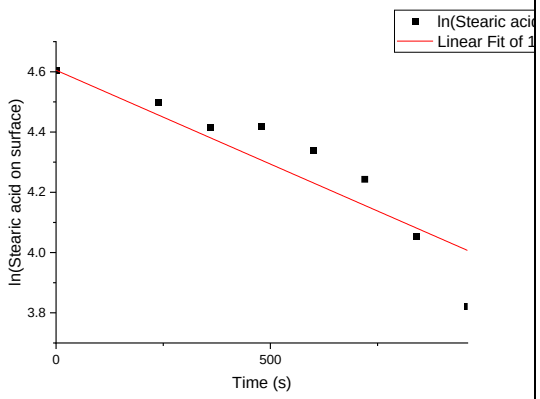

500 rpm

R^2: 0.99867

Rate constant: 7.71982E-4 ± 6.46812E-5

A2.237

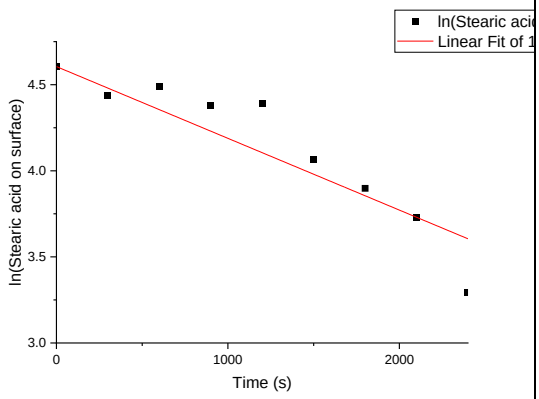

500 rpm

R^2: 0.99832

Rate constant: 4.16704E-4 ± 3.98799E-5

A2.238

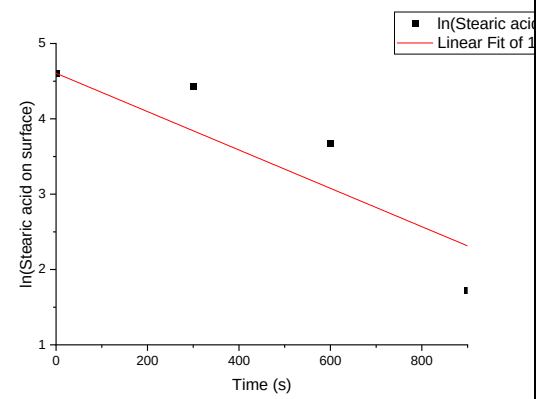

1000 rpm

R^2: 0.97553

Rate constant: 0.00255 ± 5.27355E-4

A2.249

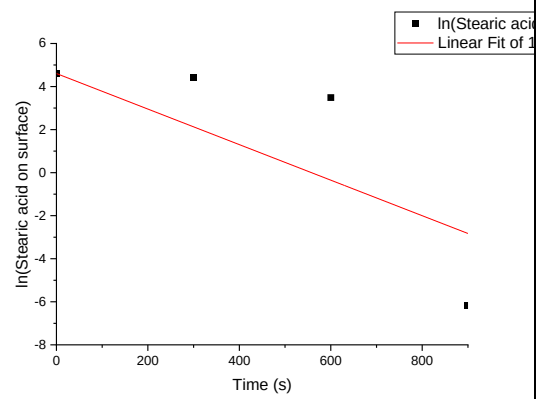

1000 rpm

R^2: 0.54315

Rate constant: 0.00826 ± 0.00287

A2.240

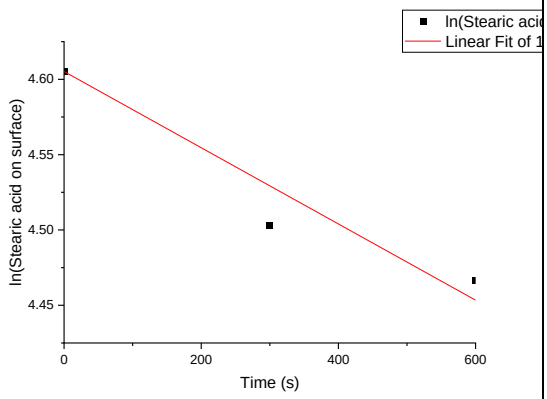

1000 rpm

R^2: 0.99998

Rate constant: 2.52931E-4 ± 3.06169E-5

A2.241

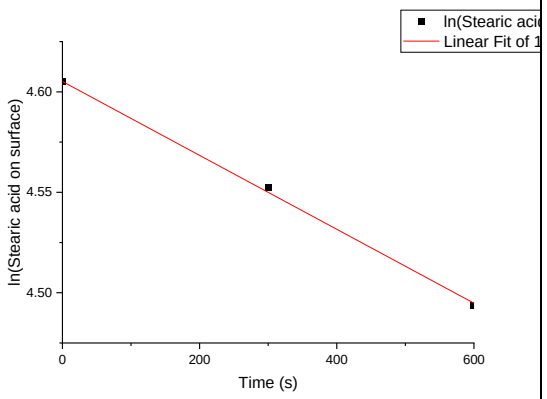

1000 rpm

R^2: 1

Rate constant: 1.83926E-4 ± 3.11049E-6

A2.242

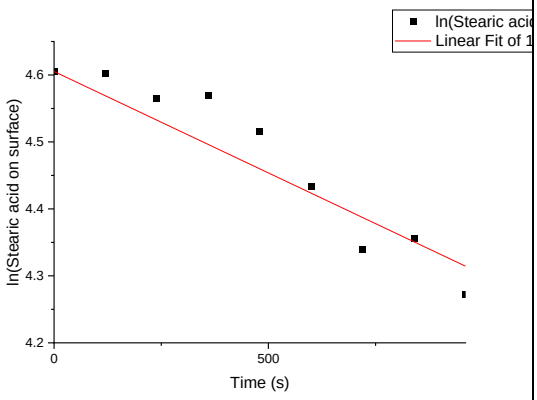

1000 rpm

R^2: 0.99985

Rate constant: 3.49544E-4 ± 2.2801E-5

A2.243

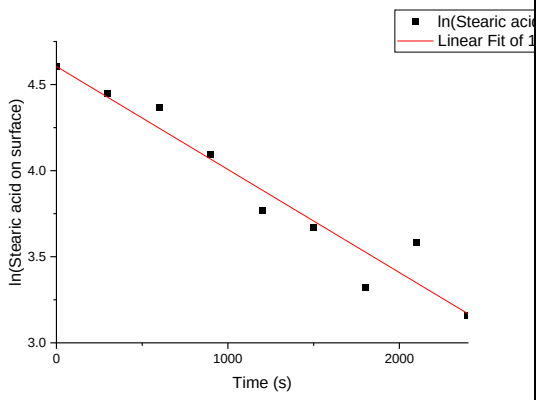

1000 rpm

R^2: 0.99895

Rate constant: 5.98352E-4 ± 2.96214E-5

A2.244

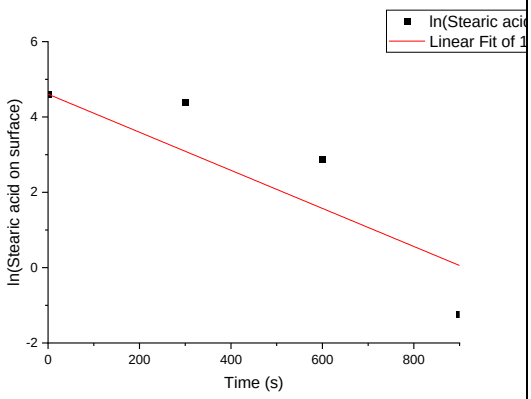

1500 rpm

R^2: 0.86461

Rate constant: 0.00505 ± 0.00116

A2.245

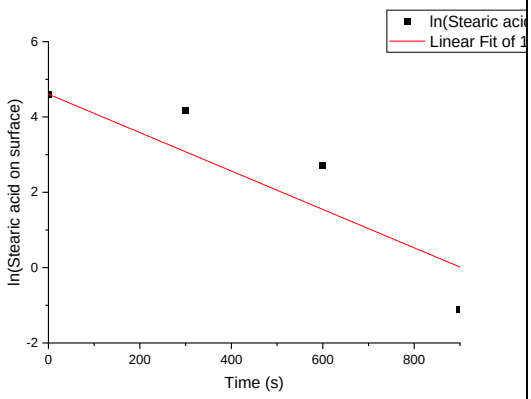

1500 rpm

R^2: 0.8918

Rate constant: 0.0051 ± 0.00101

A2.246

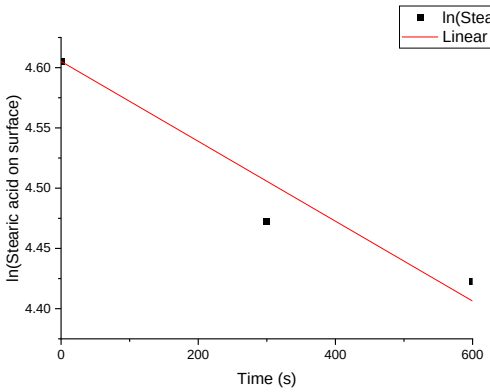

1500 rpm

R^2: 0.99997

Rate constant: 3.31387E-4 ± 3.88615E-5

A2.247

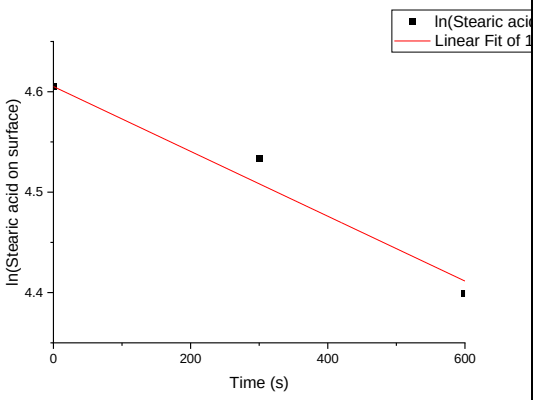

1500 rpm

R^2: 0.99998

Rate constant: 3.22782E-4 ± 2.96044E-5

A2.248

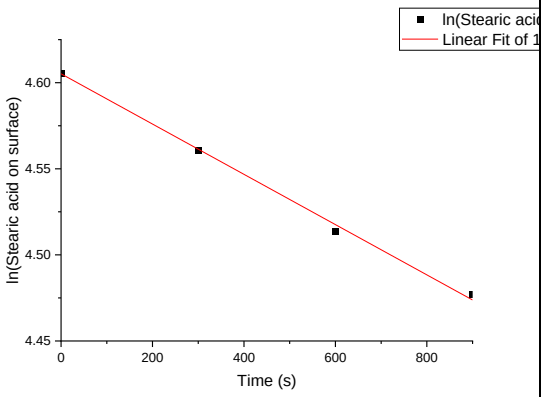

2000 rpm

R^2: 1

Rate constant: 1.45972E-4 ± 2.63849E-6

A2.249

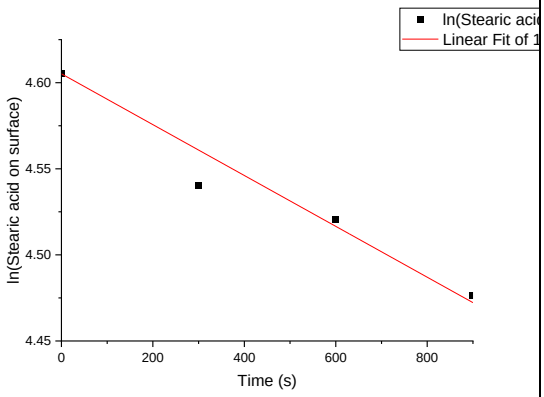

2000 rpm

R^2: 0.99999

Rate constant: 1.47667E-4 ± 1.09903E-5

A2.250

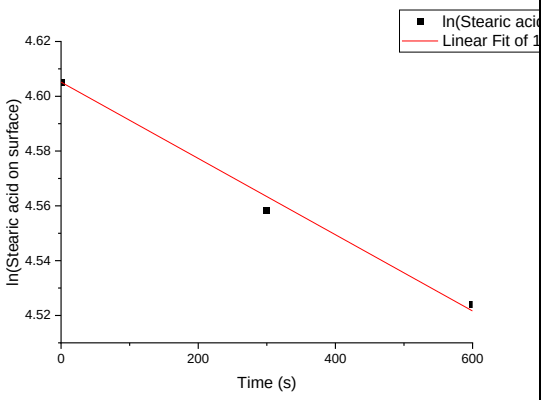

2000 rpm

R^2: 1

Rate constant: 1.39251E-4 ± 5.79252E-6

A2.251

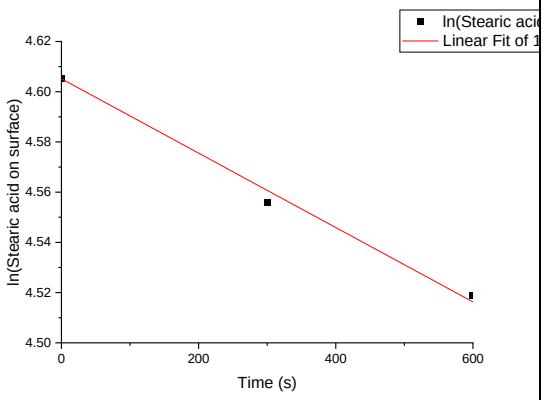

2000 rpm

R^2: 1

Rate constant: 1.48136E-4 ± 5.80575E-6

A2.252

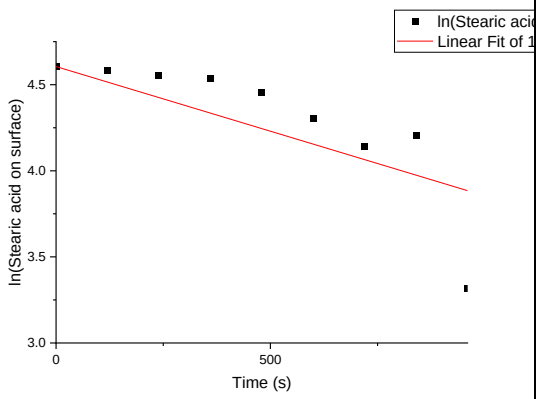

2000 rpm

R^2: 0.98324

Rate constant: 0.00132 ± 2.21659E-4

A2.253

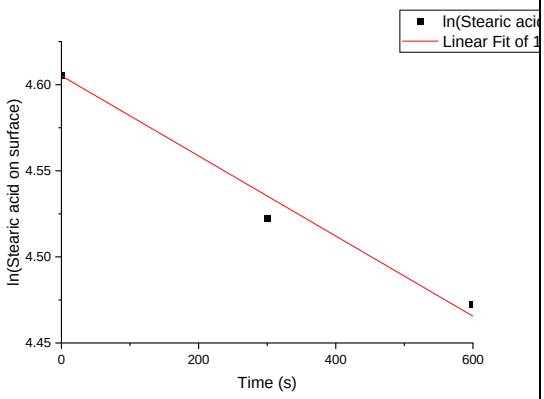

2500 rpm

R^2: 0.99999

Rate constant: 2.32664E-4 ± 1.53415E-5

A2.254

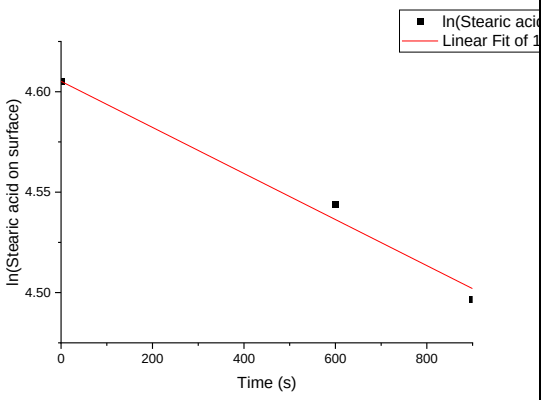

2500 rpm

R^2: 1

Rate constant: 1.14664E-4 ± 6.06788E-6

A2.255

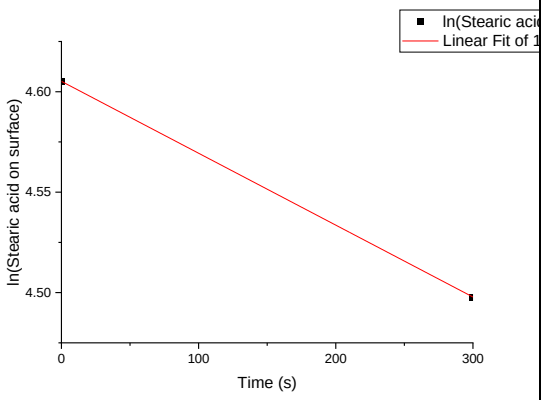

2500 rpm

R^2: 1

Rate constant: 3.57888E-4 ± 6.1996E-10

A2.256

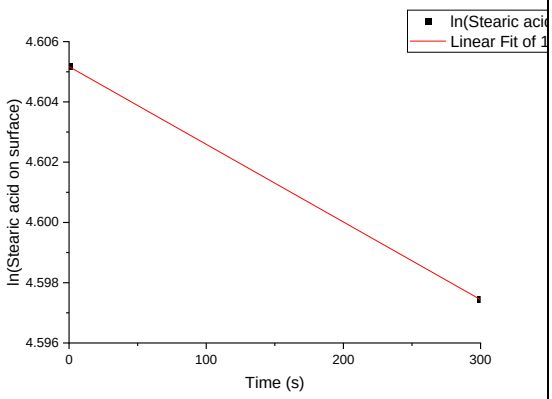

2500 rpm

R^2: 1

Rate constant: 2.57735E-5 ± 6.1996E-10

A2.257

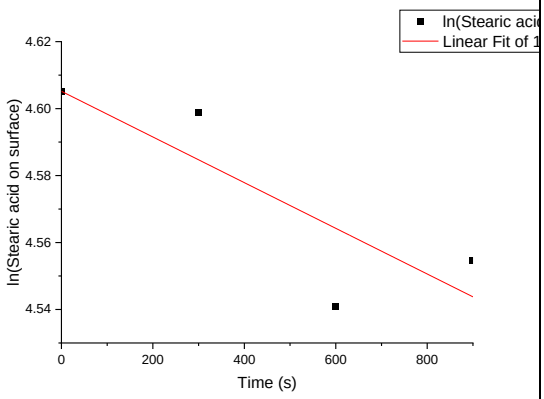

3000 rpm

R^2: 0.99999

Rate constant: 6.82113E-5 ± 1.50093E-5

A2.258

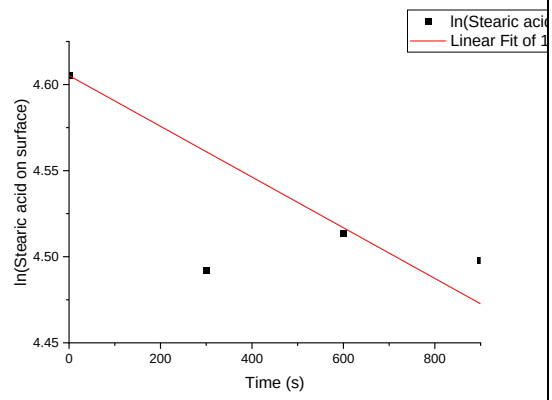

3000 rpm

R^2: 0.99991

Rate constant: 1.47256E-4 ± 3.79097E-5

A2.259

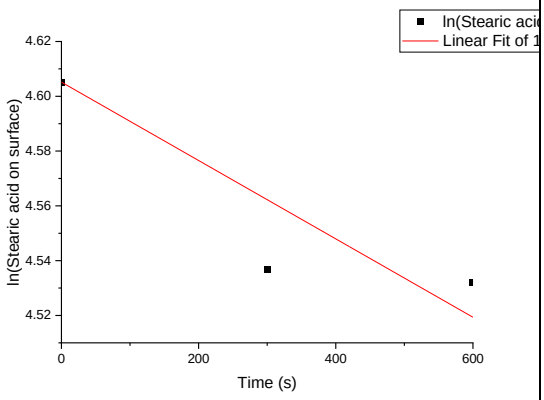

3000 rpm

R^2: 0.99998

Rate constant: 1.43046E-4 ± 2.98778E-5

A2.260

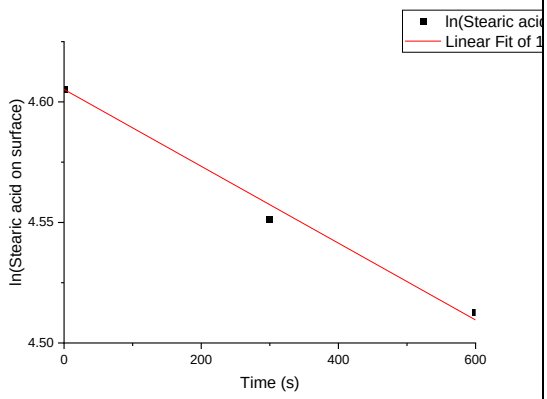

3000 rpm

R^2: 1

Rate constant: 1.59385E-4 ± 7.21176E-6

A2.261

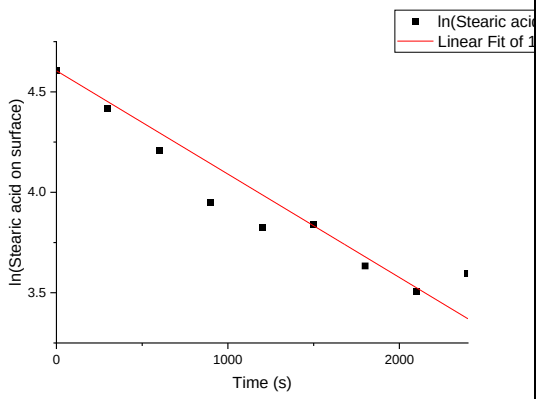

3000 rpm

R^2: 0.999

Rate constant: 5.14464E-4 ± 2.92444E-5

A2.262

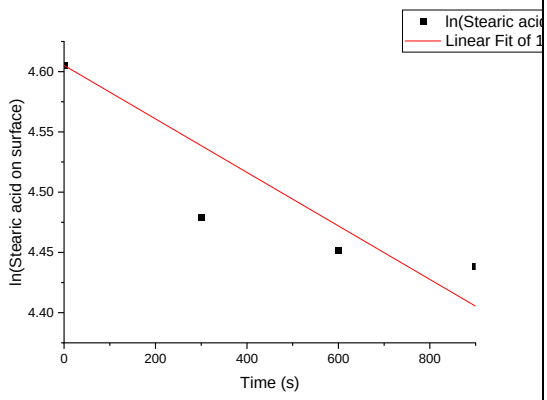

3500 rpm

R^2: 0.99992

Rate constant: 2.21958E-4 ± 3.6738E-5

A2.263

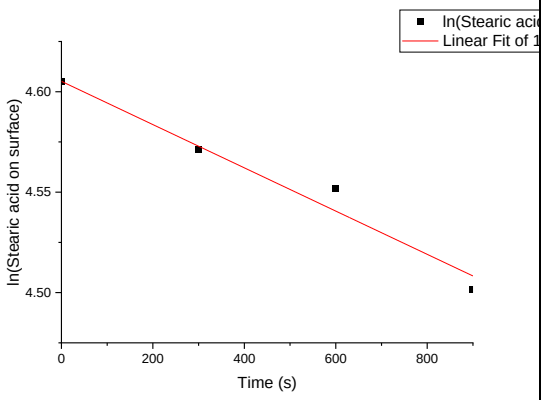

3500 rpm

R^2: 1

Rate constant: 1.07647E-4 ± 6.70578E-6

A2.264

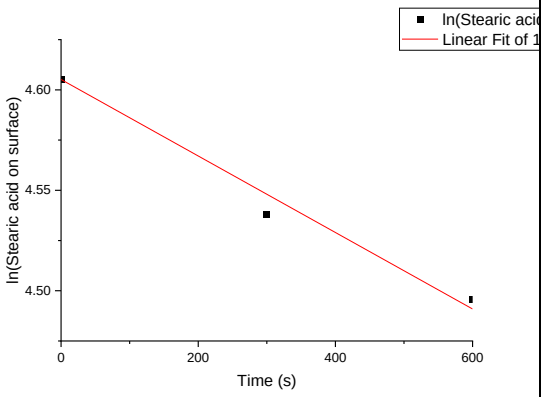

3500 rpm

R^2: 1

Rate constant: 1.90418E-4 ± 1.1642E-5

A2.265

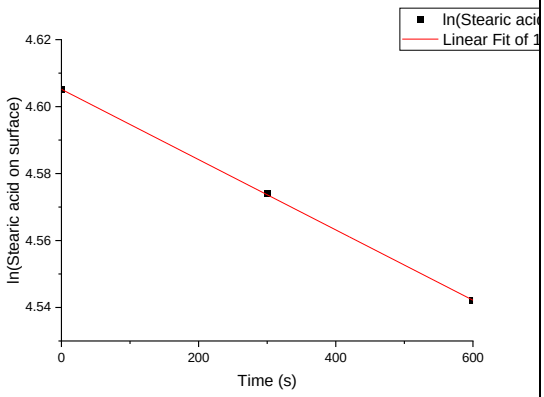

3500 rpm

R^2: 1

Rate constant: 1.04989E-4 ± 4.70583E-7

A2.266

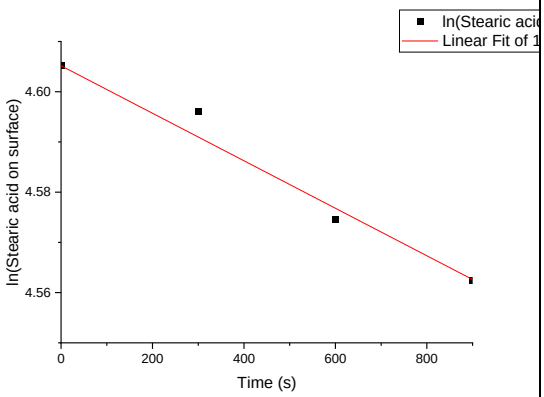

4000 rpm

R^2: 1

Rate constant: 4.72897E-5 ± 2.82884E-6

A2.267

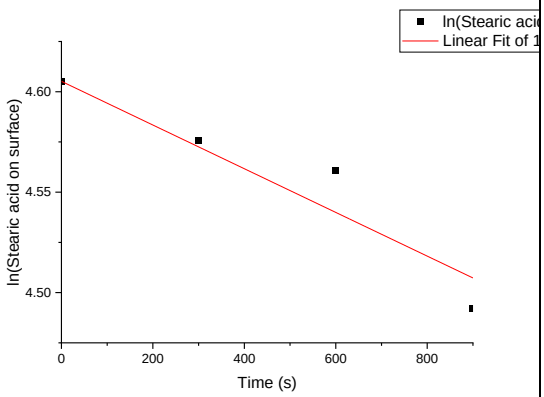

4000 rpm

R^2: 0.99999

Rate constant: 1.0875E-4 ± 1.32696E-5

A2.268

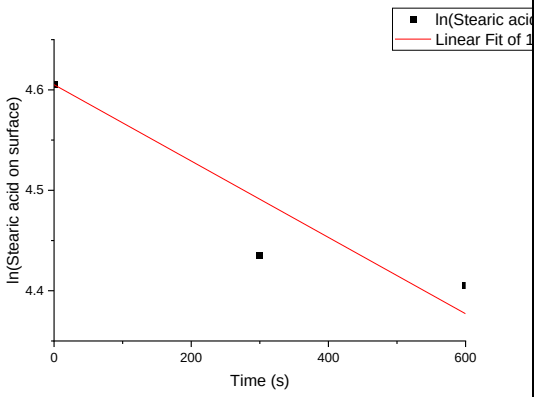

4000 rpm

R^2: 0.9999

Rate constant: 3.80118E-4 ± 6.62604E-5

A2.269

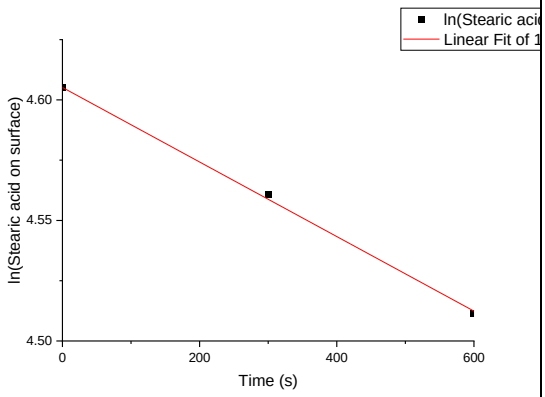

4000 rpm

R^2: 1

Rate constant: 1.54624E-4 ± 2.44698E-6

A2.270

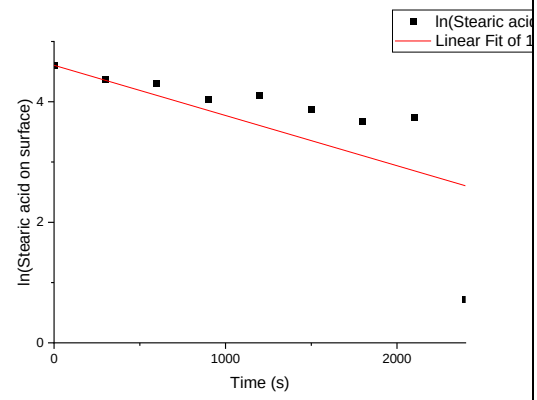

4000 rpm

R^2: 0.95659

Rate constant: 8.33161E-4 ± 1.88263E-4

A2.271

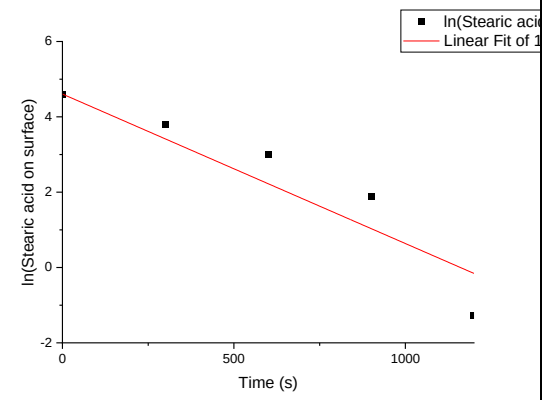

5000 rpm

R^2: 0.93088

Rate constant: 0.00397 ± 5.0531E-4

A2.272

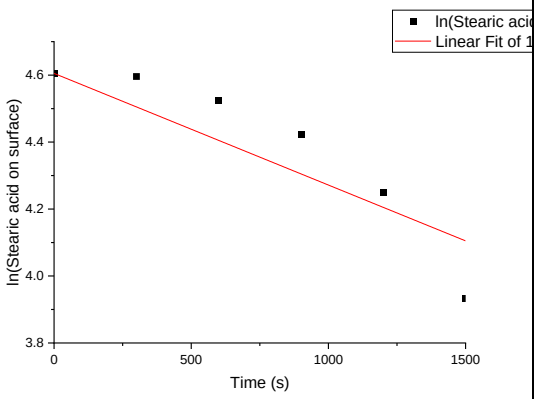

6000 rpm

R^2: 0.99929

Rate constant: 3.33474E-4 ± 5.24796E-5

A2.273

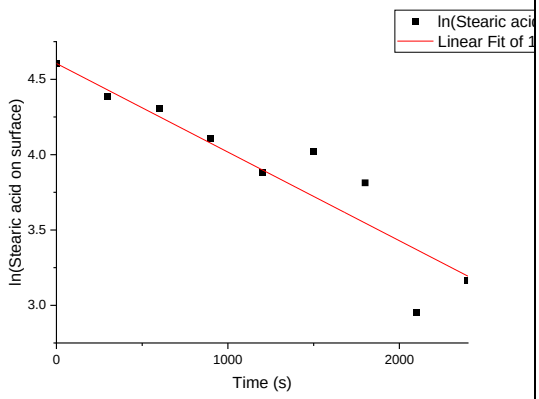

7000 rpm

R^2: 0.99725

Rate constant: 5.88231E-4 ± 4.8336E-5

A2.274

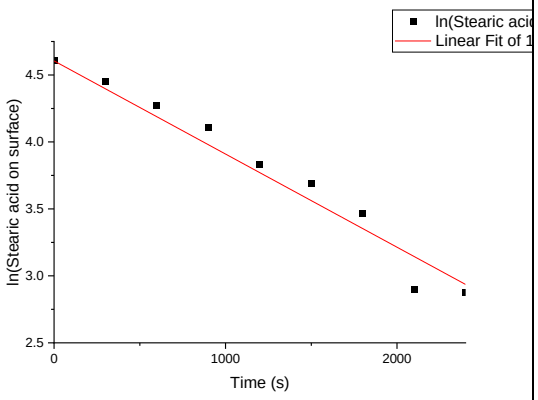

8000 rpm

R^2: 0.99894

Rate constant: 6.95515E-4 ± 2.91859E-5

A: 2.4 Rate plots for stearic acid decomposition over 0.5 wt% Copper-doped *meso*-TiO_2 samples

Preparation spin speed, zero order rate plots and rate constants for stearic acid decomposition on 0.5 wt% copper-doped *meso*-TiO_2 samples

A2.275 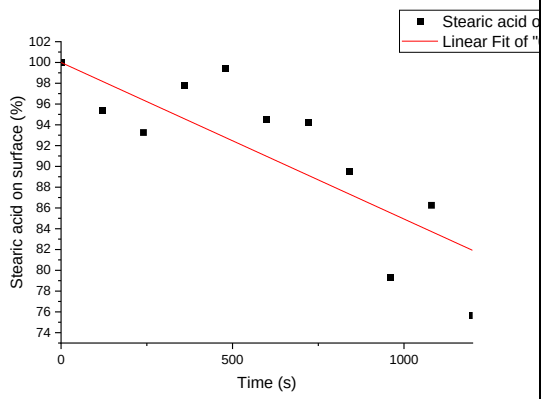 500 rpm R^2: 0.99762 Rate constant: 0.01507 ± 0.0019	A2.276 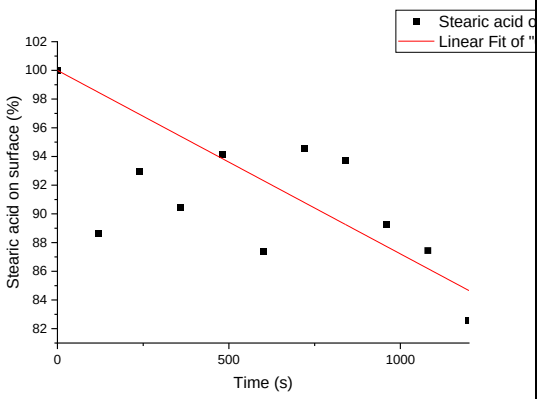 500 rpm R^2: 0.99754 Rate constant: 0.01279 ± 0.00192
A2.277 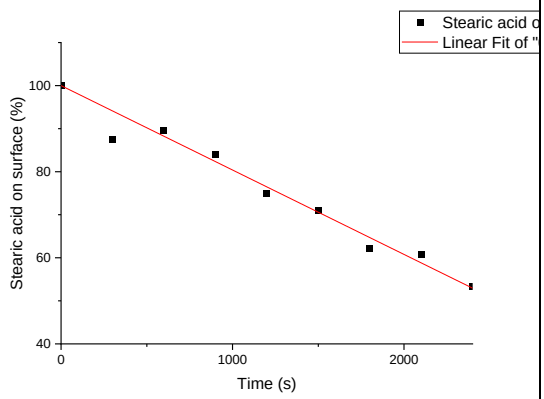 1000 rpm R^2: 0.99869 Rate constant: 0.01961 ± 6.53817E-4	A2.278 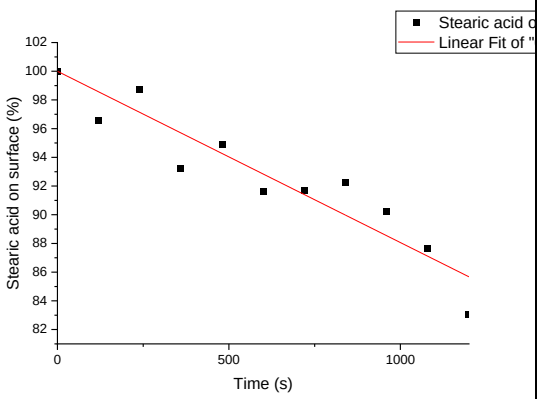 1000 rpm R^2: 0.99966 Rate constant: 0.01194 ± 7.28519E-4

A2.279	A2.280
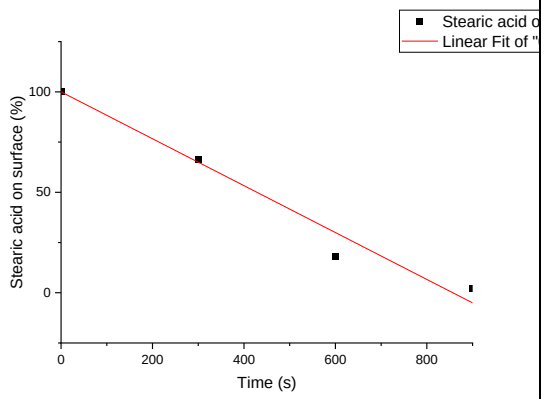	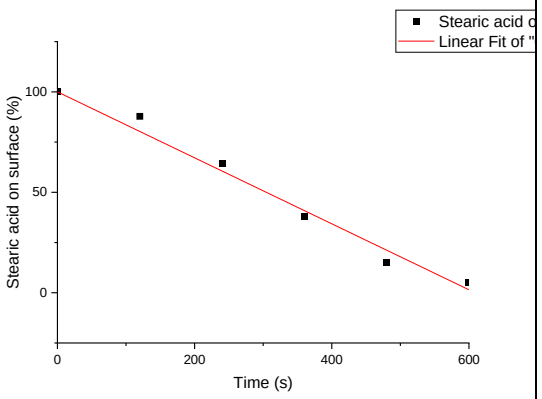
2000 rpm R^2: 0.98269 Rate constant: 0.11672 ± 0.00711	2000 rpm R^2: 0.99365 Rate constant: 0.16418 ± 0.00561
A2.281	**A2.282**
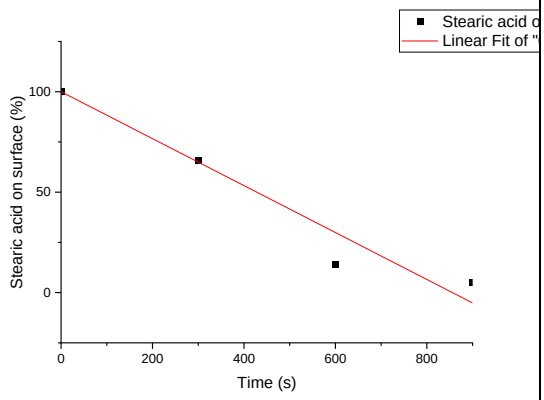	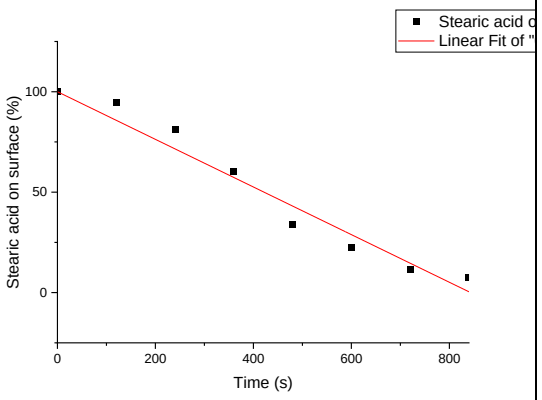
3000 rpm R^2: 0.96733 Rate constant: 0.11683 ± 0.00971	3000 rpm R^2: 0.98658 Rate constant: 0.11856 ± 0.00508

A2.283

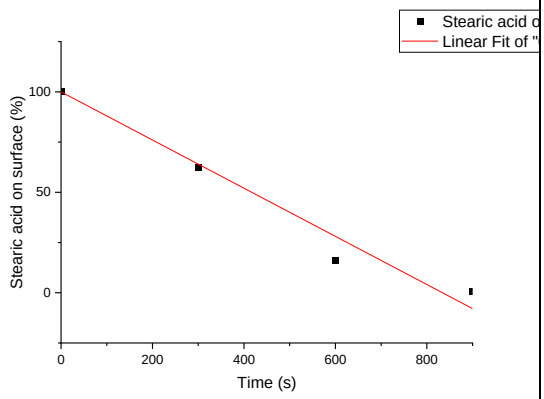

4000 rpm

R^2: 0.97975

Rate constant: 0.11987 ± 0.00754

A2.284

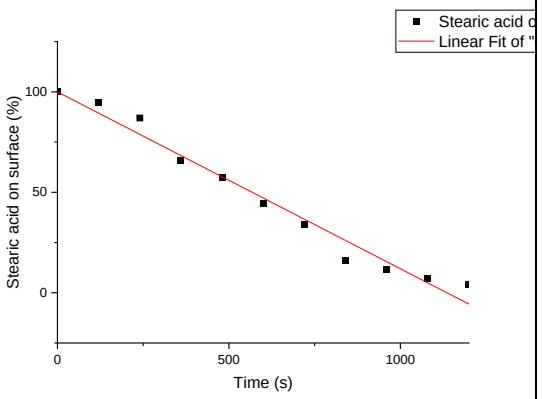

4000 rpm

R^2: 0.9904

Rate constant: 0.08803 ± 0.00244

A2.285

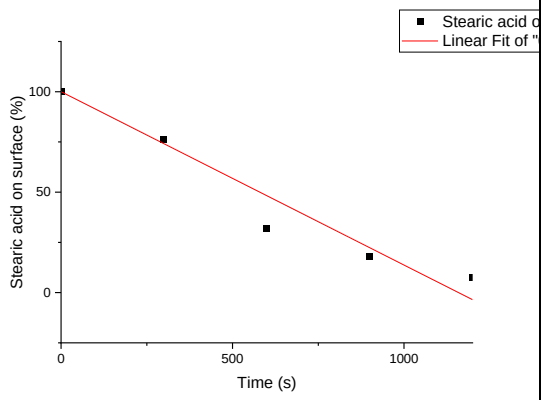

5000 rpm

R^2: 0.96976

Rate constant: 0.08629 ± 0.0062

A2.286

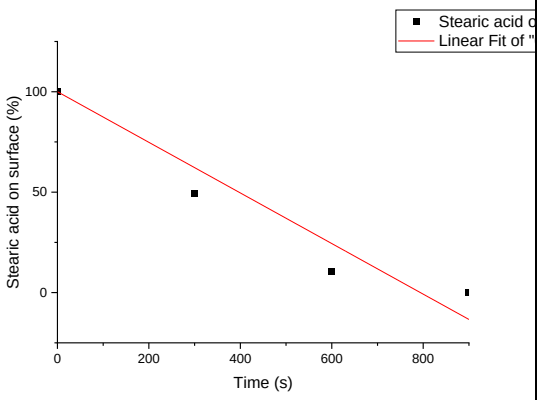

5000 rpm

R^2: 0.94292

Rate constant: 0.12596 ± 0.01192

A2.287

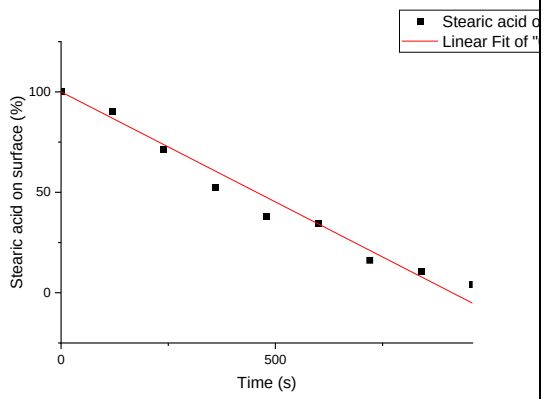

5000 rpm

R^2: 0.98865

Rate constant: 0.10957 ± 0.00353

A2.288

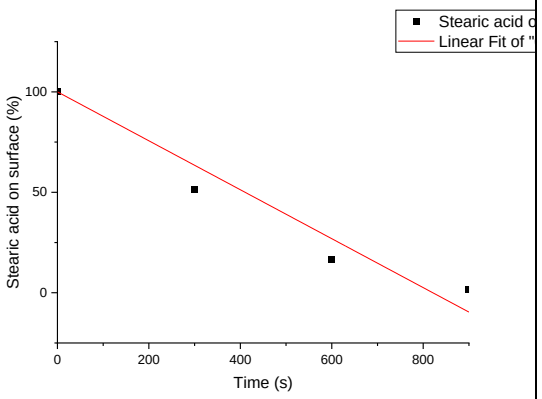

6000 rpm

R^2: 0.96057

Rate constant: 0.12181 ± 0.01005

A2.289

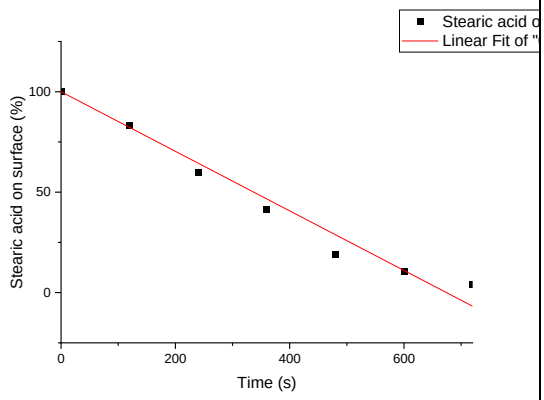

6000 rpm

R^2: 0.98647

Rate constant: 0.14828 ± 0.00579

A2.290

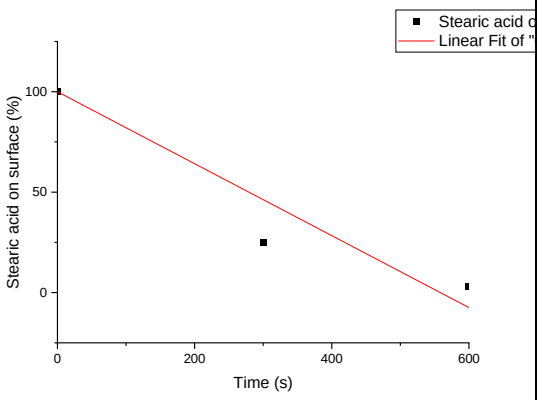

7000 rpm

R^2: 0.91947

Rate constant: 0.17908 ± 0.02518

A2.291

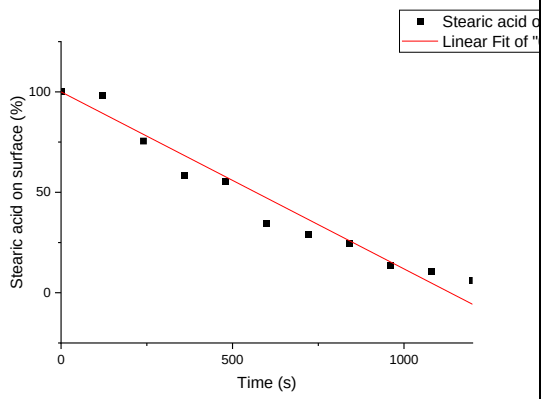

7000 rpm

R^2: 0.98147

Rate constant: 0.08812 ± 0.00325

A2.292

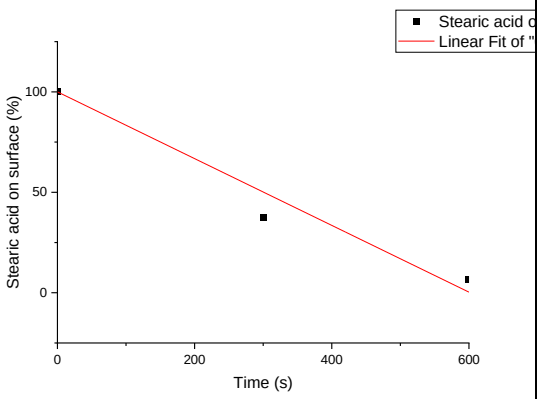

8000 rpm

R^2: 0.97301

Rate constant: 0.16616 ± 0.01512

A2.293

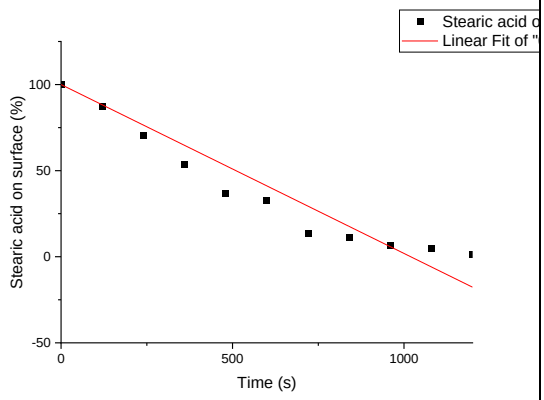

8000 rpm

R^2: 0.95143

Rate constant: 0.09808 ± 0.00475

Preparation spin speed and first order rate plots and rate constants for stearic acid decomposition on 0.5 wt% copper-doped *meso*-TiO_2 samples

A2.294 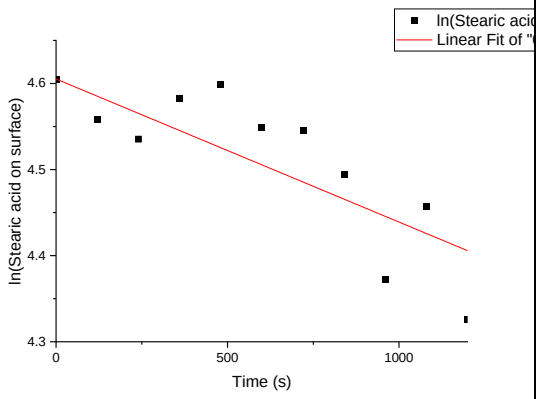 500 rpm R^2: 0.99987 Rate constant: 1.6616E-4 ± 2.22459E-5	A2.295 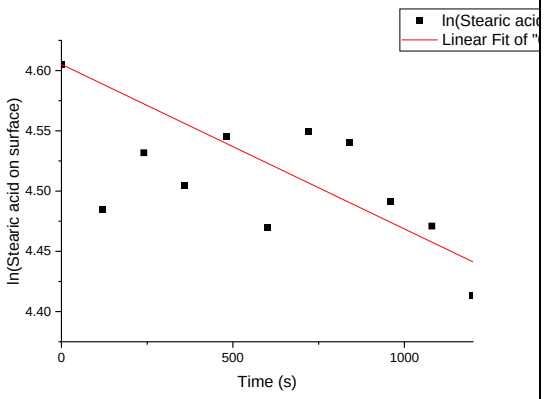 500 rpm R^2: 0.99988 Rate constant: 1.36545E-4 ± 2.05789E-5
A2.296 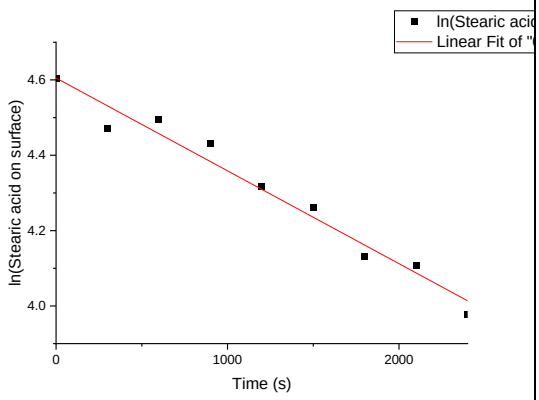 1000 rpm R^2: 0.99993 Rate constant: 2.46433E-4 ± 8.55462E-6	A2.297 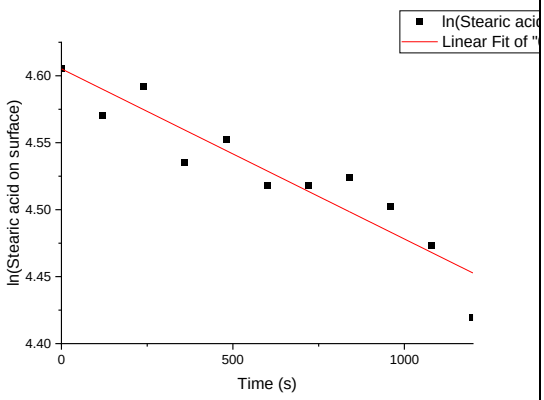 1000 rpm R^2: 0.99998 Rate constant: 1.27033E-4 ± 8.11722E-6

A2.298 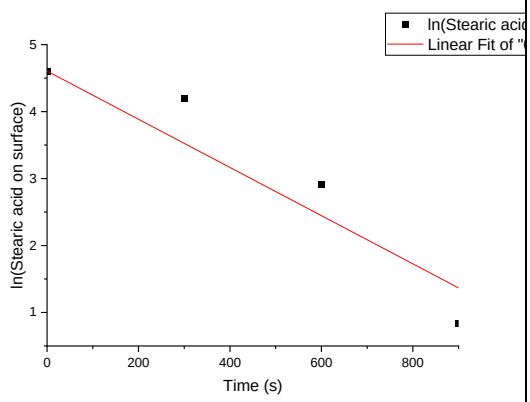 2000 rpm R^2: 0.97386 Rate constant: 0.0036 ± 4.98635E-4	A2.299 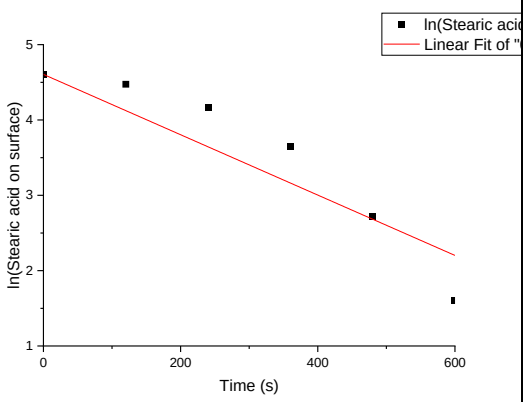 2000 rpm R^2: 0.98567 Rate constant: 0.00401 ± 4.9665E-4
A2.300 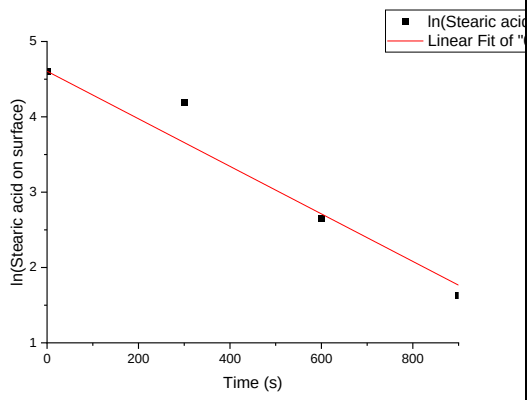 3000 rpm R^2: 0.99173 Rate constant: 0.00316 ± 2.81884E-4	A2.301 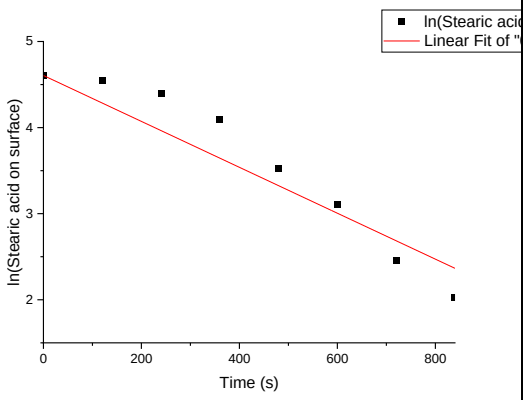 3000 rpm R^2: 0.99291 Rate constant: 0.00267 ± 2.2021E-4

A2.302

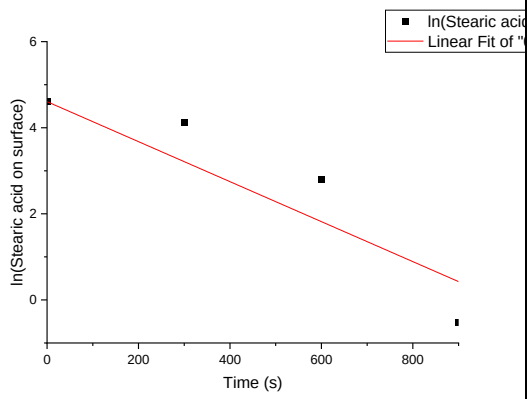

4000 rpm

R^2: 0.92243

Rate constant: 0.00464 ± 8.44434E-4

A2.303

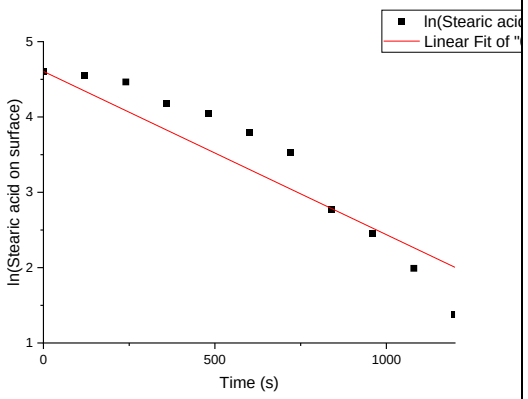

4000 rpm

R^2: 0.98843

Rate constant: 0.00217 ± 1.6427E-4

A2.304

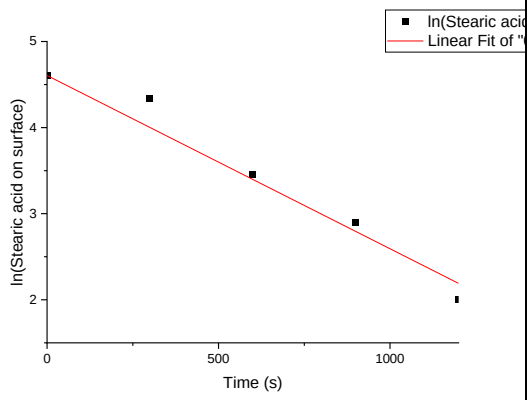

5000 rpm

R^2: 0.99693

Rate constant: 0.00201 ± 1.20863E-4

A2.305

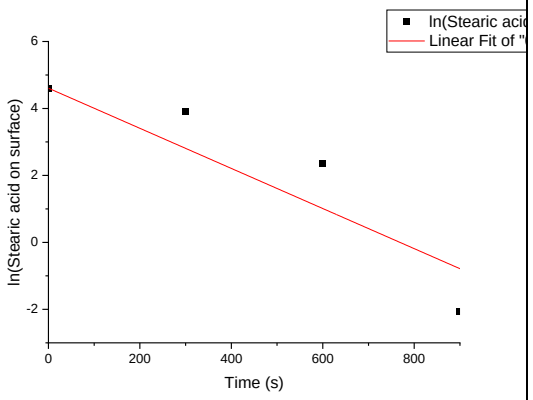

5000 rpm

R^2: 0.86703

Rate constant: 0.00599 ± 0.0011

A2.306

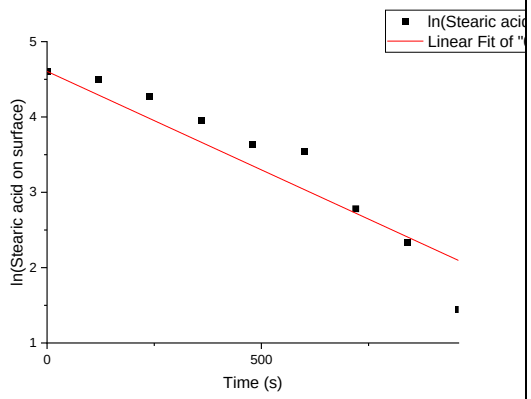

5000 rpm

R^2: 0.99051

Rate constant: 0.00261 ± 2.04452E-4

A2.307

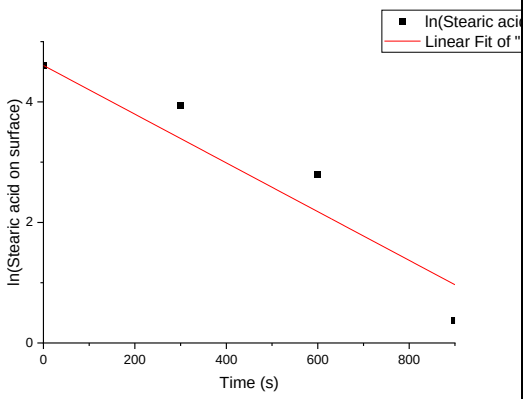

6000 rpm

R^2: 0.96933

Rate constant: 0.00404 ± 5.21402E-4

A2.308

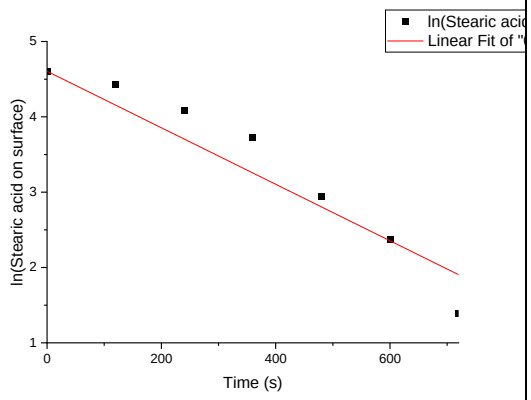

6000 rpm

R^2: 0.99037

Rate constant: 0.00375 ± 3.03312E-4

A2.309

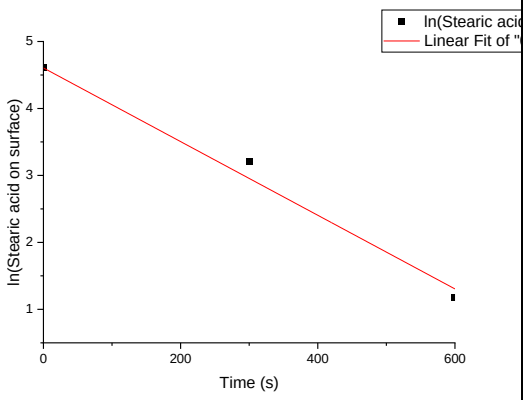

7000 rpm

R^2: 0.99615

Rate constant: 0.0055 ± 3.06542E-4

A2.310

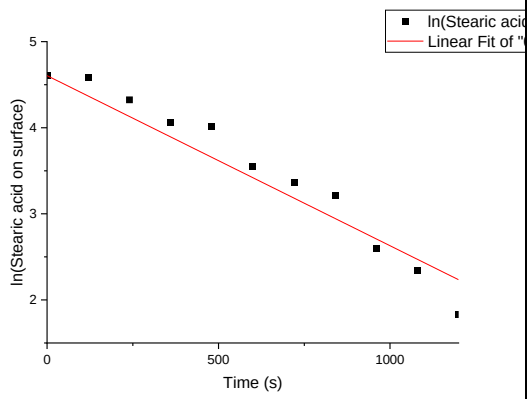

7000 rpm

R^2: 0.99577

Rate constant: 0.00198 ± 9.96707E-5

A2.311

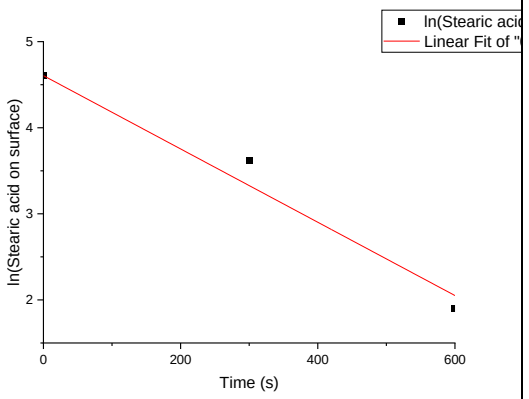

8000 rpm

R^2: 0.9958

Rate constant: 0.00426 ± 3.4347E-4

A2.312

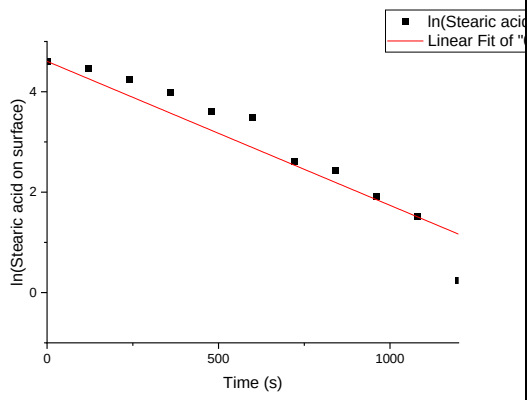

8000 rpm

R^2: 0.98379

Rate constant: 0.00287 ± 1.77881E-4

A: 2.5 Rate plots for stearic acid decomposition over 0.1 wt% Copper-doped *meso*-TiO_2 samples

Preparation spin speed, zero order rate plots and rate constants for stearic acid decomposition on 0.1 wt% copper-doped *meso*-TiO_2 samples

A2.313 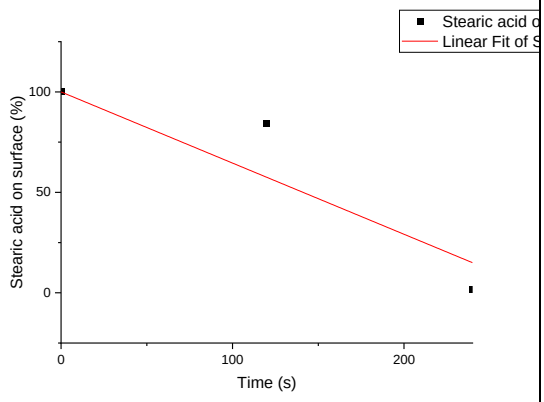 500 rpm R^2: 0.92136 Rate constant: 0.35426 ± 0.07891	A2.314 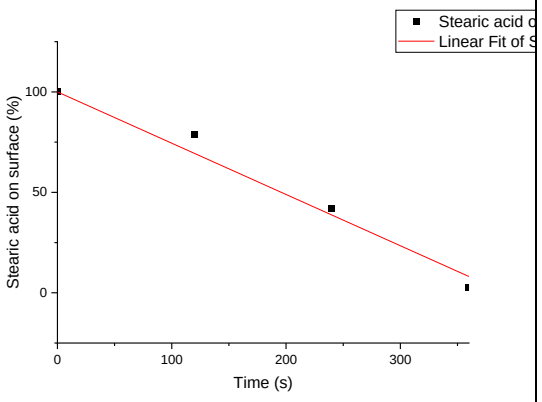 1000 rpm R^2: 0.99027 Rate constant: 0.25524 ± 0.01474
A2.315 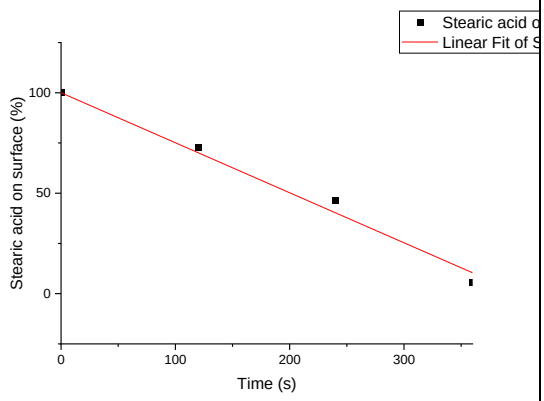 1500 rpm R^2: 0.99496 Rate constant: 0.24894 ± 0.01045	A2.316 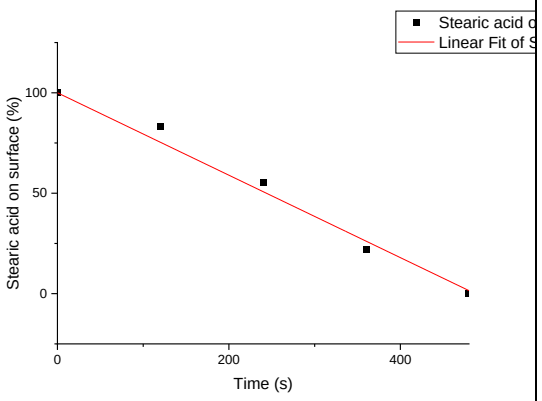 2000 rpm R^2: 0.99371 Rate constant: 0.20515 ± 0.00773

A2.317 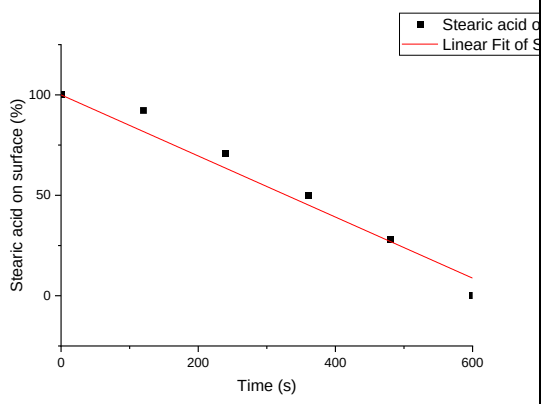 2500 rpm R^2: 0.98848 Rate constant: 0.15206 ± 0.00806	A2.318 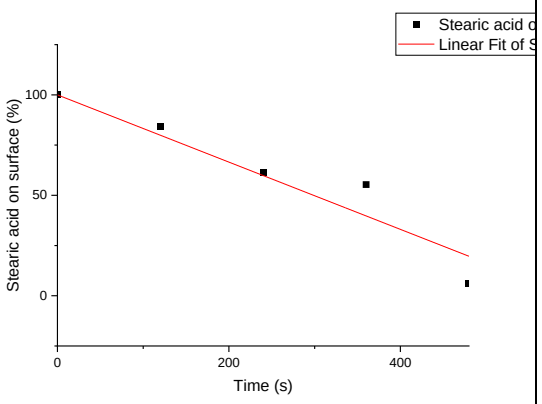 3000 rpm R^2: 0.97663 Rate constant: 0.16737 ± 0.0161
A2.319 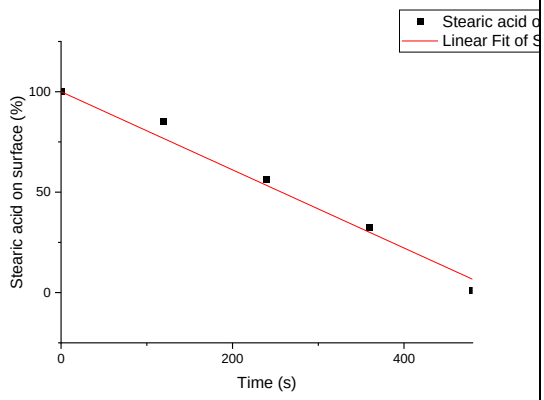 3500 rpm R^2: 0.99317 Rate constant: 0.19447 ± 0.00824	A2.320 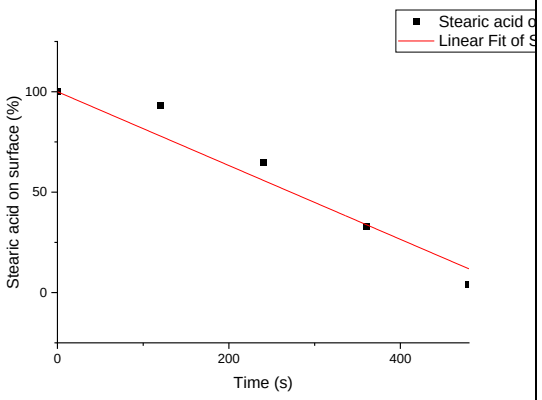 4000 rpm R^2: 0.98069 Rate constant: 0.1837 ± 0.01465

A2.321

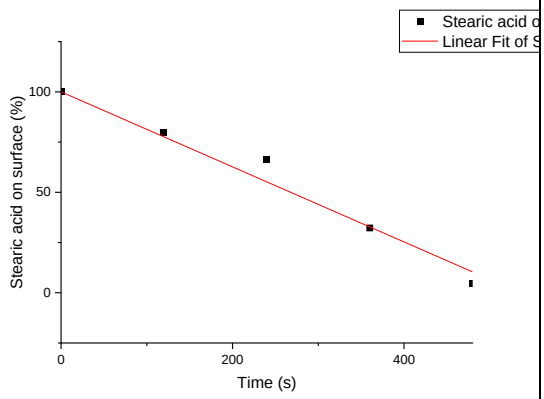

4500 rpm

R^2: 0.99075

Rate constant: 0.18674 ± 0.00967

A2.322

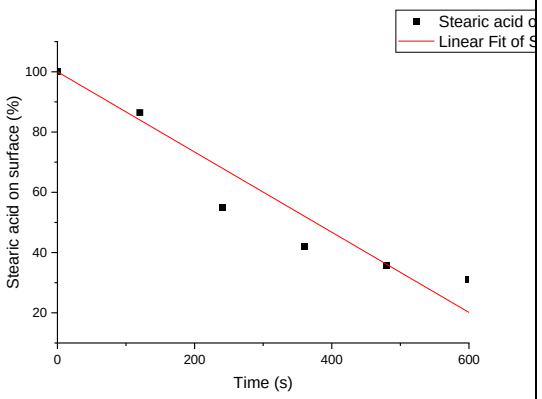

5000 rpm

R^2: 0.98059

Rate constant: 0.1331 ± 0.01001

A2.323

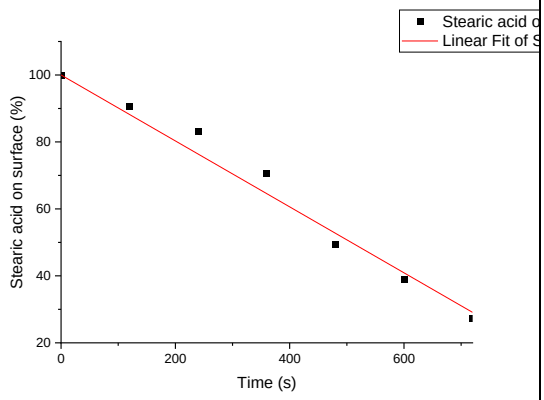

5500 rpm

R^2: 0.9964

Rate constant: 0.09848 ± 0.00369

A2.324

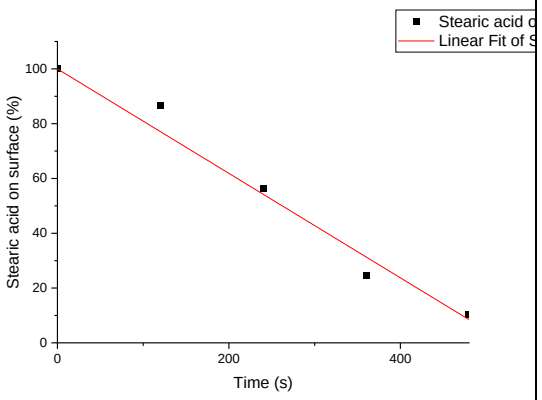

6000 rpm

R^2: 0.99183

Rate constant: 0.19065 ± 0.00899

A2.325

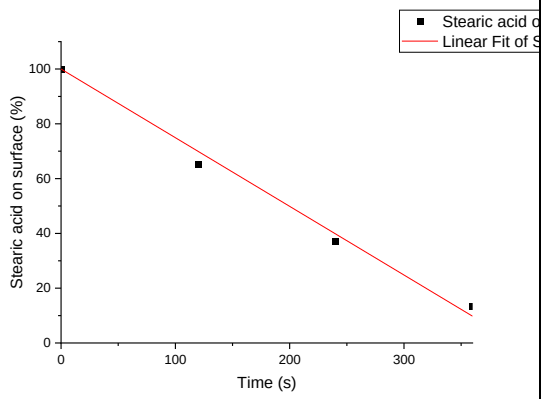

2500 rpm

R^2: 0.99623

Rate constant: 0.25065 ± 0.00859

A2.326

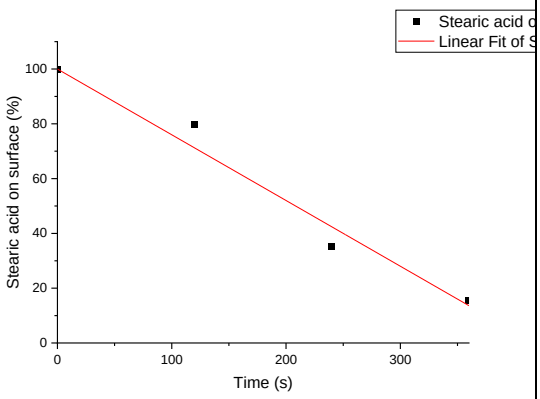

2500 rpm

R^2: 0.99042

Rate constant: 0.23996 ± 0.01455

A2.327

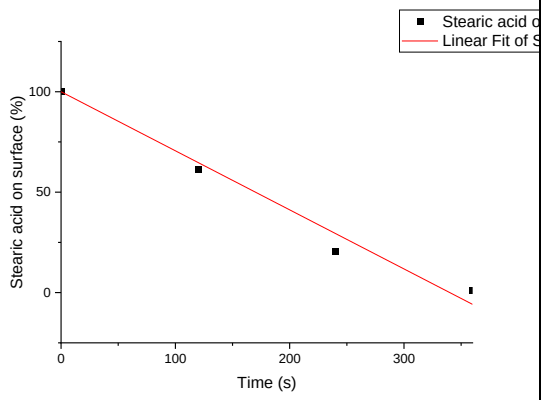

3000 rpm

R^2: 0.98633

Rate constant: 0.29404 ± 0.0155

A2.328

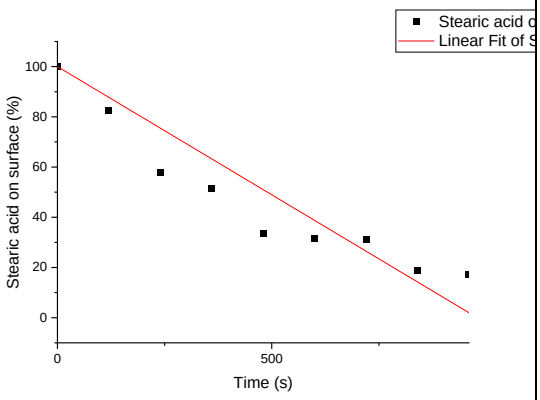

3000 rpm

R^2: 0.95264

Rate constant: 0.10209 ± 0.0069

A2.329

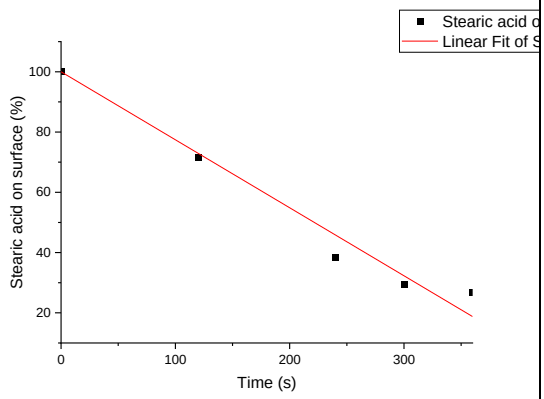

3500 rpm

R^2: 0.99105

Rate constant: 0.22566 ± 0.01055

A2.330

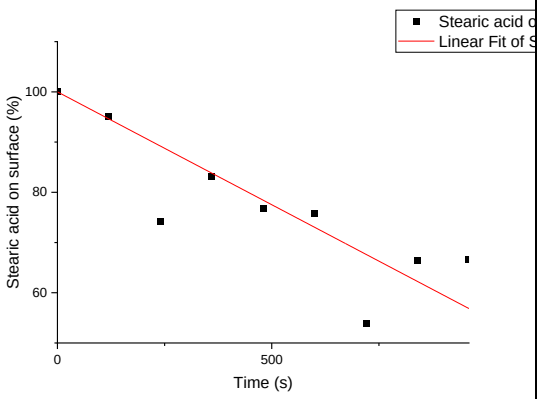

4000 rpm

R^2: 0.98893

Rate constant: 0.04494 ± 0.00479

A2.331

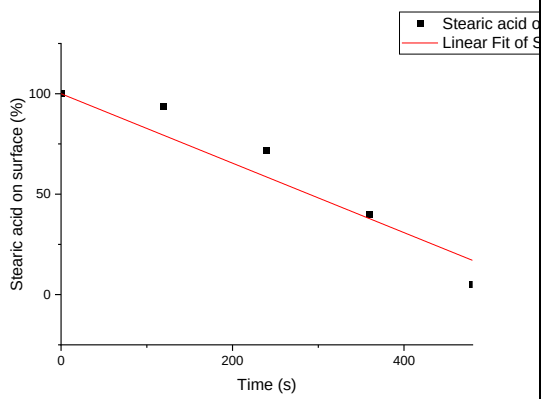

4000 rpm

R^2: 0.9733

Rate constant: 0.17284 ± 0.0178

A2.332

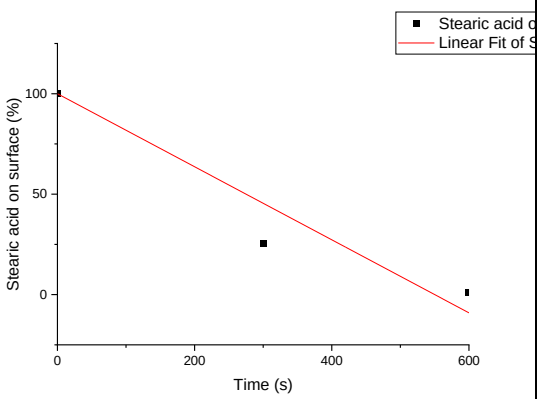

4000 rpm

R^2: 0.92868

Rate constant: 0.18178 ± 0.02371

A2.333	A2.334
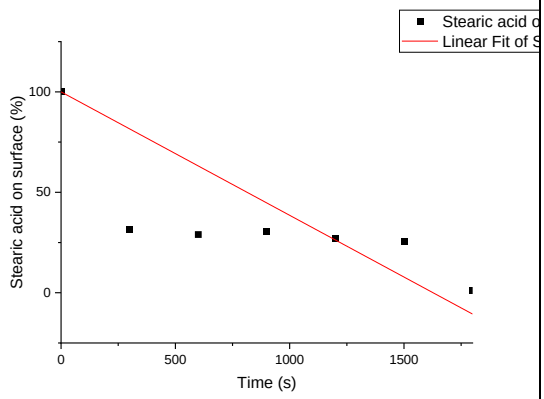	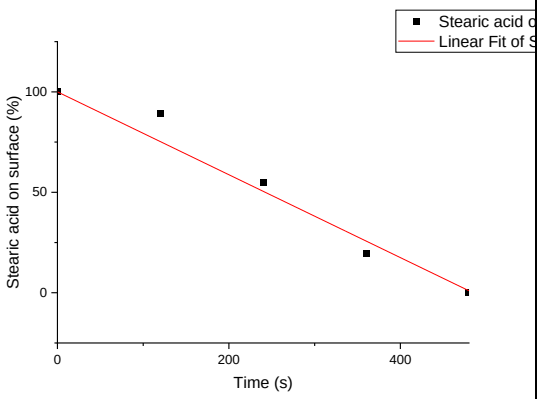
4000 rpm R^2: 0.64389 Rate constant: 0.06145 ± 0.00937	4500 rpm R^2: 0.98526 Rate constant: 0.20626 ± 0.01207
A2.335	**A2.336**
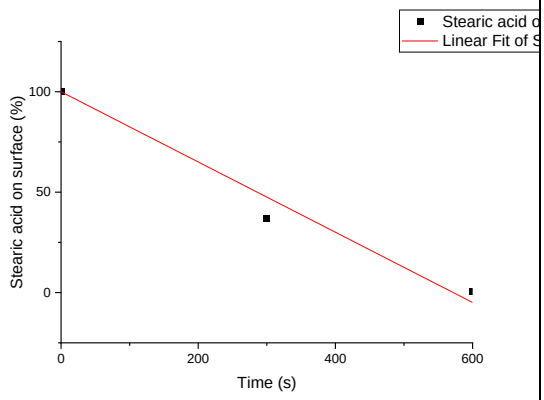	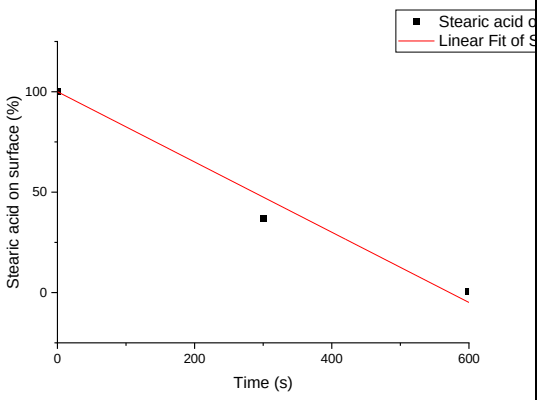
4500 rpm R^2: 0.98183 Rate constant: 0.17484 ± 0.01237	5000 rpm R^2: 0.98183 Rate constant: 0.17484 ± 0.01237

A2.337

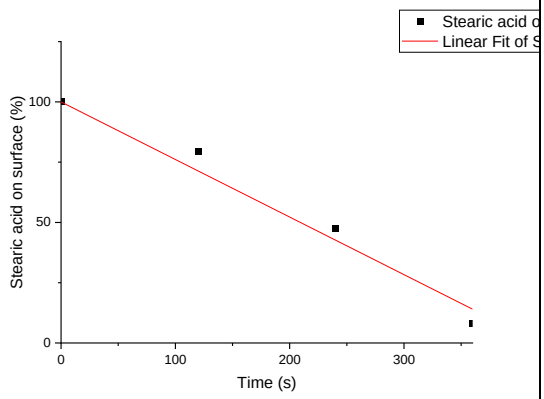

5000 rpm

R^2: 0.99115

Rate constant: 0.23884 ± 0.0143

A2.338

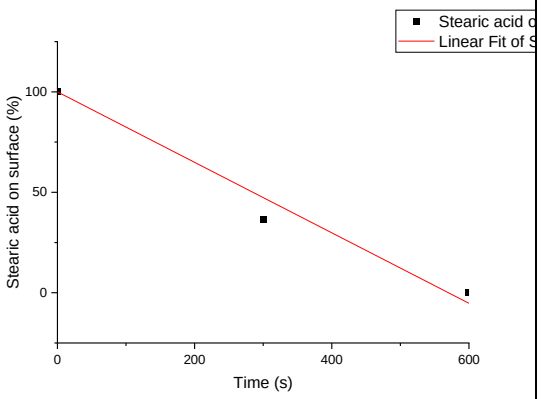

5500 rpm

R^2: 0.98048

Rate constant: 0.1754 ± 0.0128

A2.339

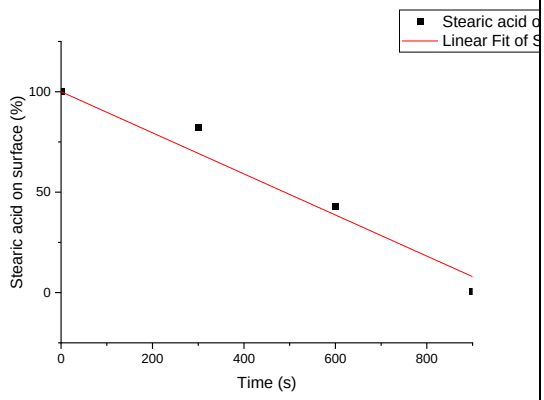

5500 rpm

R^2: 0.98295

Rate constant: 0.10227 ± 0.00793

A2.340

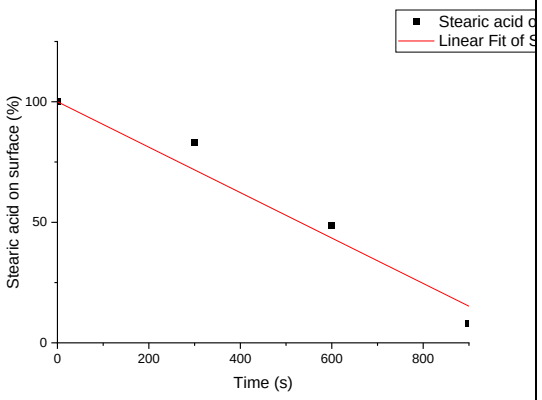

6000 rpm

R^2: 0.98566

Rate constant: 0.09423 ± 0.00741

A2.341

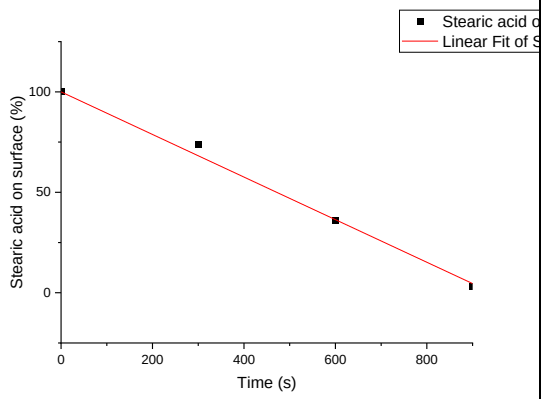

6500 rpm

R^2: 0.99707

Rate constant: 0.10603 ± 0.00312

A2.342

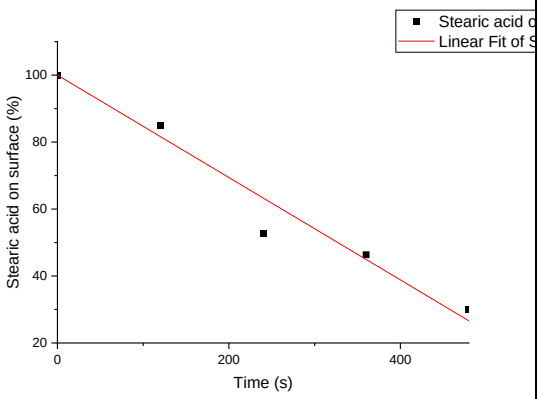

7000 rpm

R^2: 0.9927

Rate constant: 0.15289 ± 0.00882

A2.343

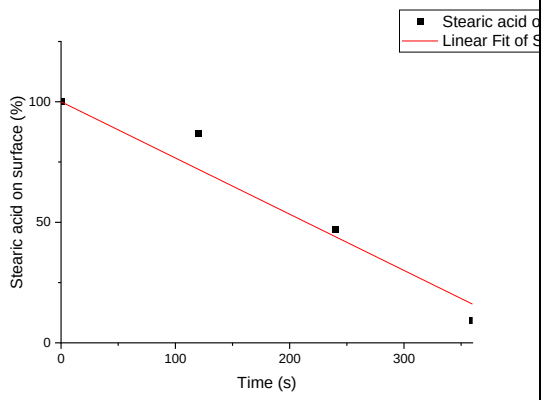

7000 rpm

R^2: 0.98131

Rate constant: 0.23321 ± 0.02144

A2.344

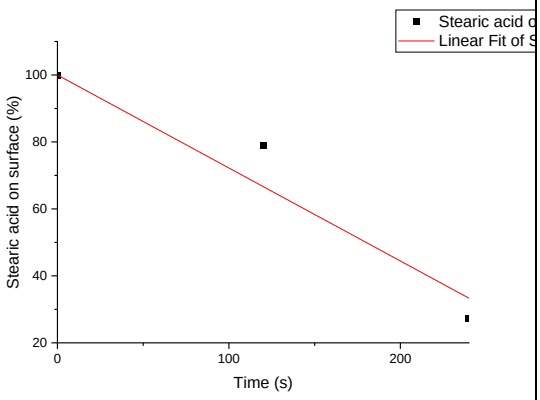

7500 rpm

R^2: 0.98356

Rate constant: 0.27774 ± 0.03593

A2.345

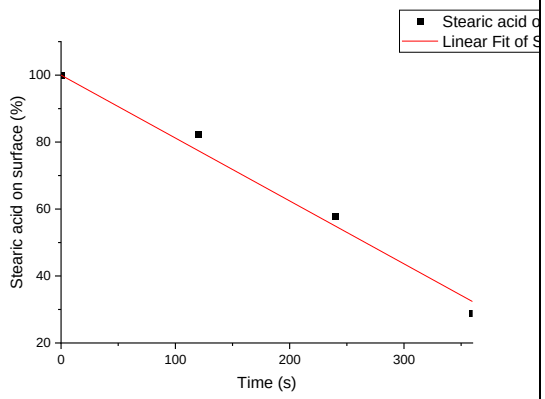

7500 rpm

R^2: 0.9972

Rate constant: 0.18788 ± 0.00852

A2.346

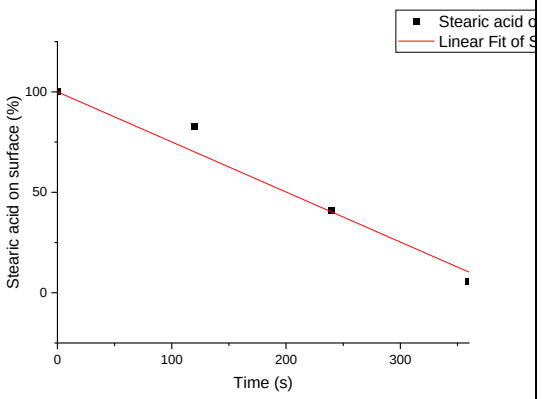

8000 rpm

R^2: 0.98646

Rate constant: 0.24921 ± 0.01767

A2.347

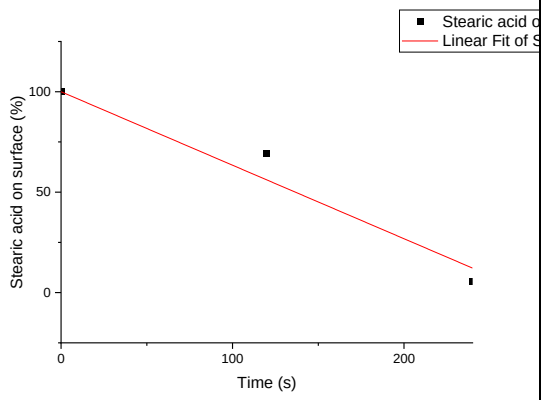

8000 rpm

R^2: 0.97827

Rate constant: 0.36585 ± 0.03862

Preparation spin speed and first order rate plots and rate constants for stearic acid decomposition on 0.1 wt% copper-doped *meso*-TiO_2 samples

A2.348 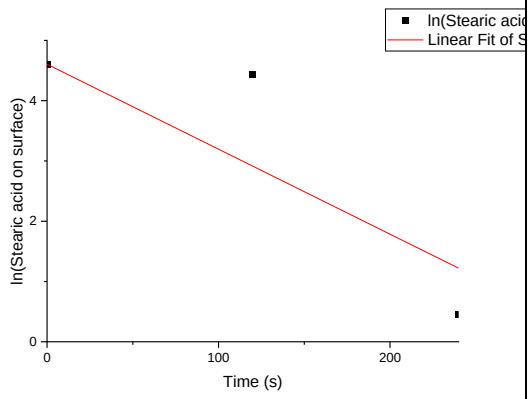 500 rpm R^2: 0.89444 Rate constant: 0.0141 ± 0.00448	A2.349 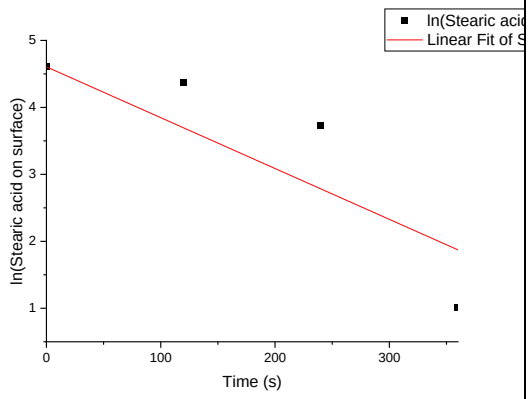 1000 rpm R^2: 0.94915 Rate constant: 0.00759 ± 0.00187
A2.350 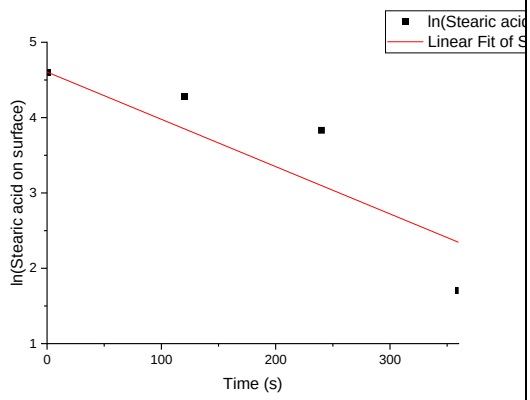 1500 rpm R^2: 0.9736 Rate constant: 0.00628 ± 0.00137	A2.351 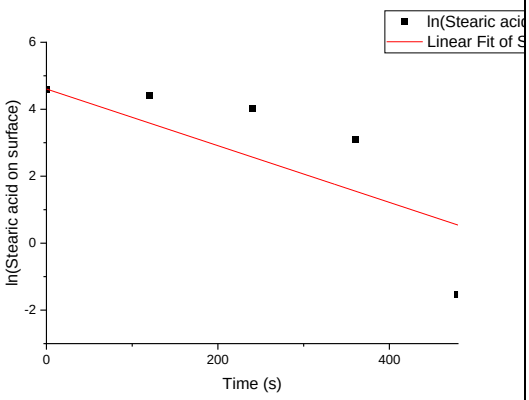 2000 rpm R^2: 0.82765 Rate constant: 0.00847 ± 0.00234

A2.352

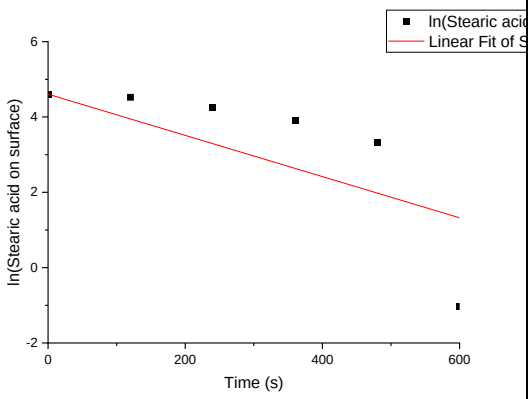

2500 rpm

R^2: 0.85985

Rate constant: 0.00547 ± 0.0016

A2.353

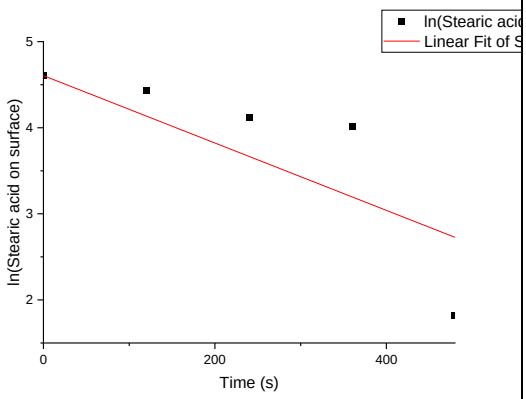

3000 rpm

R^2: 0.97101

Rate constant: 0.00391 ± 0.00102

A2.354

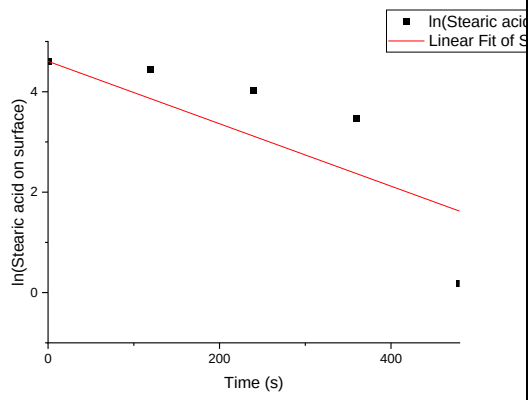

3500 rpm

R^2: 0.9192

Rate constant: 0.00621 ± 0.00161

A2.355

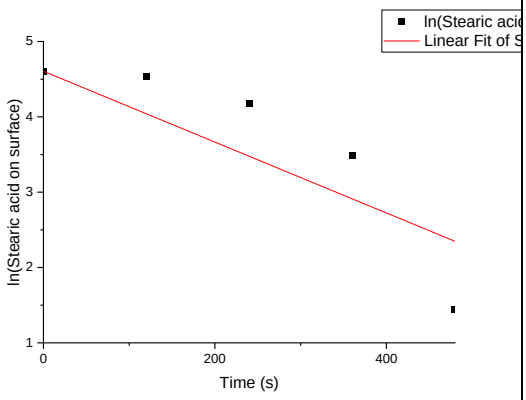

4000 rpm

R^2: 0.96779

Rate constant: 0.0047 ± 0.00105

A2.356

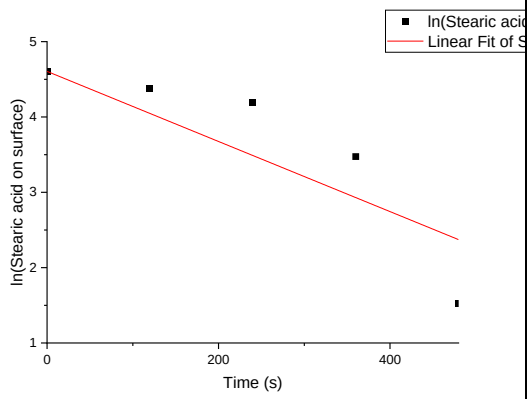

4500 rpm

R^2: 0.97206

Rate constant: 0.00465 ± 9.67732E-4

A2.357

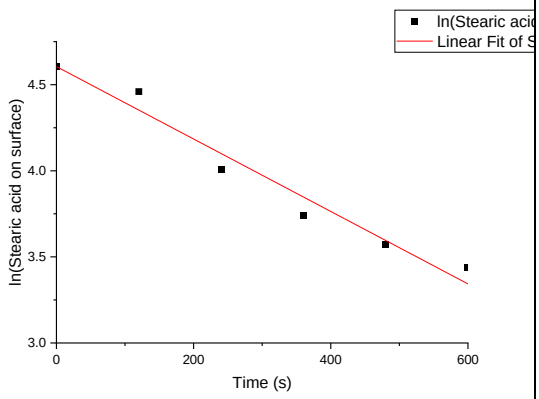

5000 rpm

R^2: 0.99948

Rate constant: 0.0021 ± 1.0261E-4

A2.358

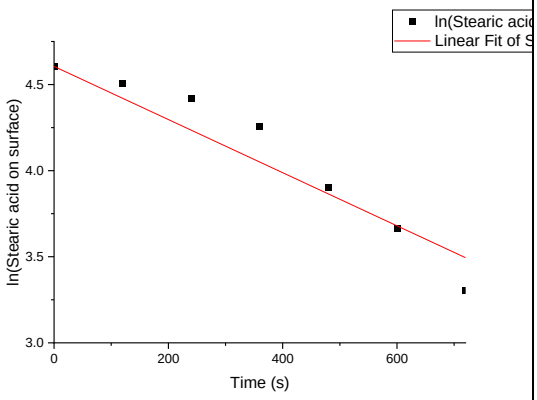

5500 rpm

R^2: 0.99879

Rate constant: 0.00154 ± 1.24976E-4

A2.359

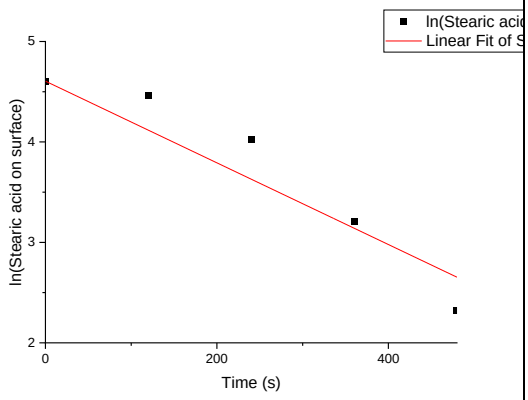

6000 rpm

R^2: 0.99327

Rate constant: 0.00407 ± 4.769E-4

A2.360 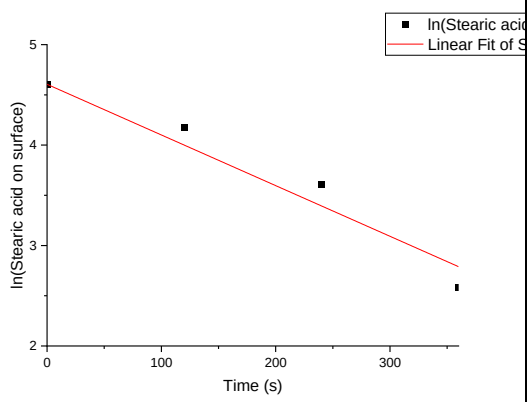 2500 rpm R^2: 0.99729 Rate constant: 0.00504 ± 4.4318E-4	A2.361 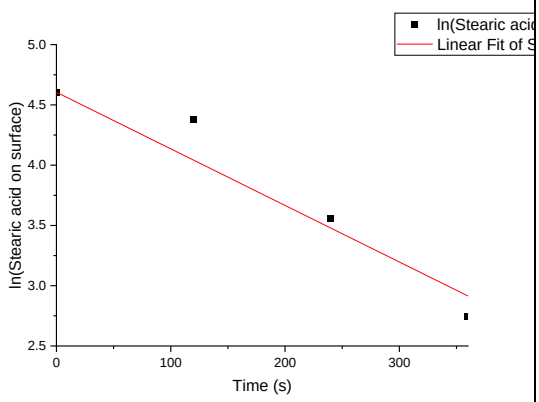 2500 rpm R^2: 0.99675 Rate constant: 0.0047 ± 4.94222E-4
A2.362 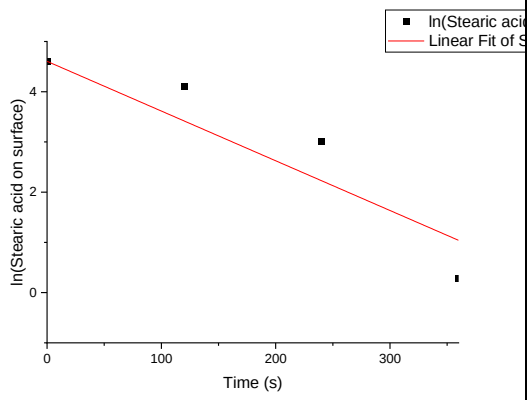 3000 rpm R^2: 0.9527 Rate constant: 0.0099 ± 0.00167	A2.363 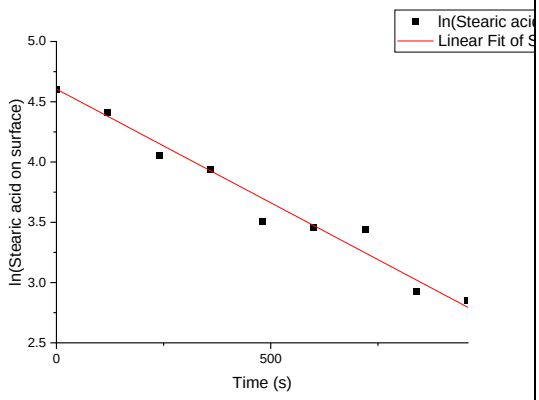 3000 rpm R^2: 0.99914 Rate constant: 0.00189 ± 6.4025E-5

A2.364 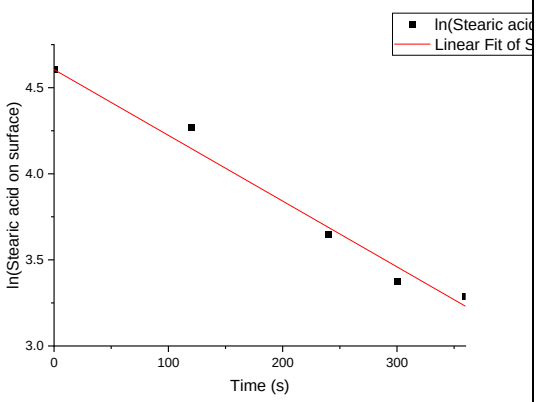 3500 rpm R^2: 0.99956 Rate constant: 0.00382 ± 1.50664E-4	A2.365 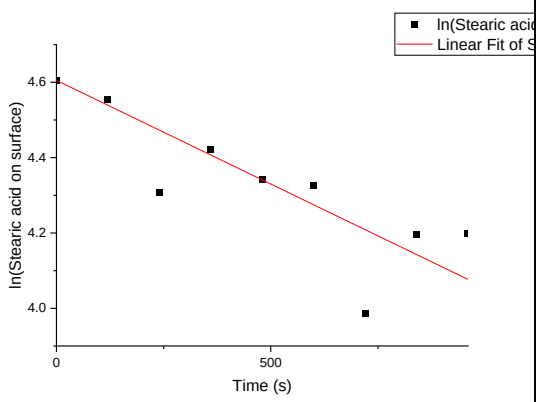 4000 rpm R^2: 0.99934 Rate constant: 5.5039E-4 ± 6.46753E-5
A2.366 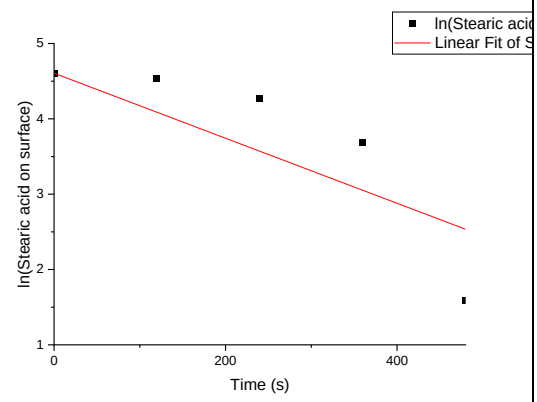 4000 rpm R^2: 0.96699 Rate constant: 0.00432 ± 0.00108	A2.367 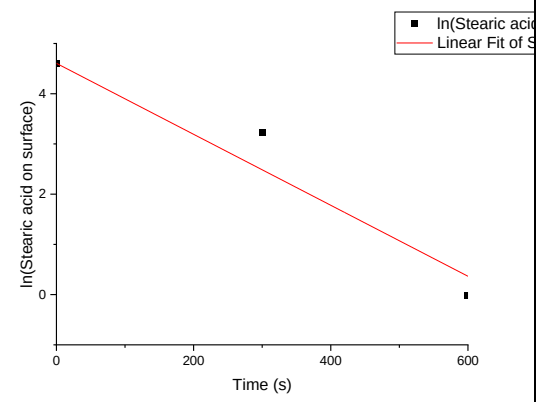 4000 rpm R^2: 0.96693 Rate constant: 0.00707 ± 8.80558E-4

A2.368

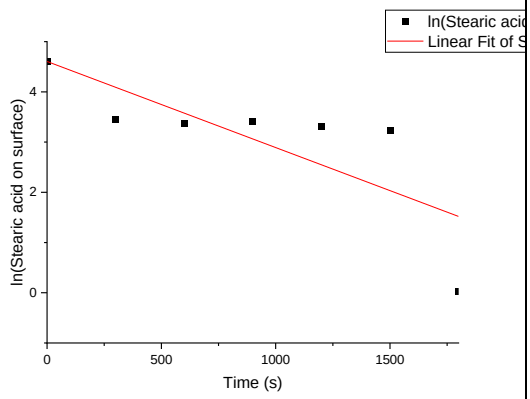

4000 rpm

R^2: 0.92713

Rate constant: 0.00171 ± 3.13807E-4

A2.369

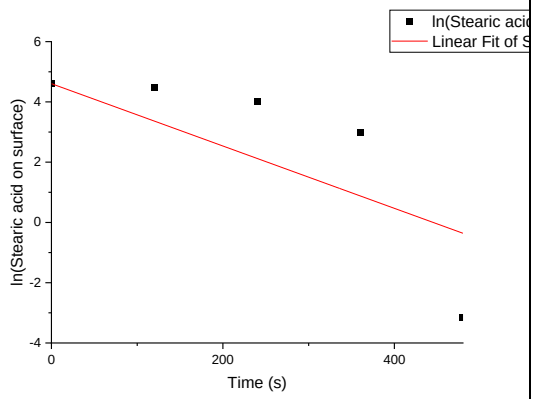

4500 rpm

R^2: 0.72166

Rate constant: 0.01034 ± 0.00313

A2.370

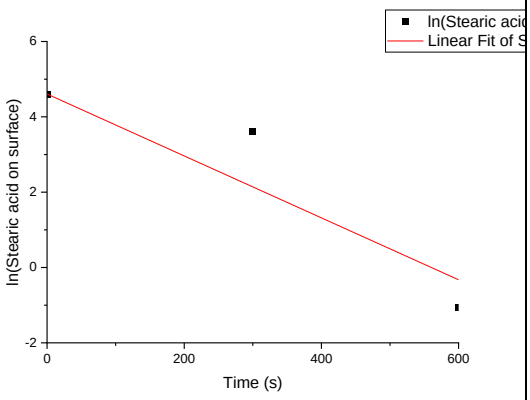

4500 rpm

R^2: 0.88503

Rate constant: 0.00822 ± 0.00174

A2.371

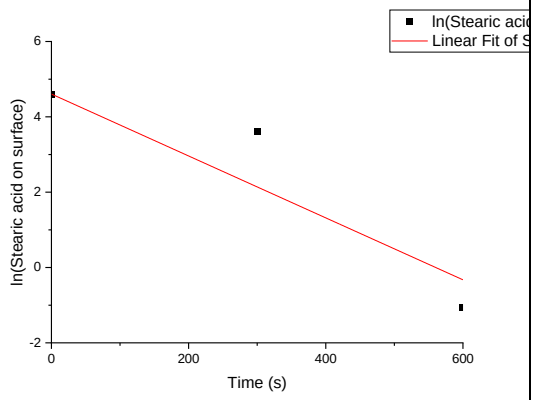

5000 rpm

R^2: 0.88503

Rate constant: 0.00822 ± 0.00174

A2.372	A2.373
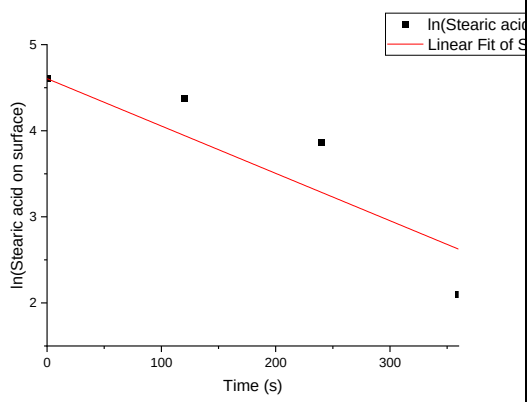 5000 rpm R^2: 0.98232 Rate constant: 0.0055 ± 0.00114	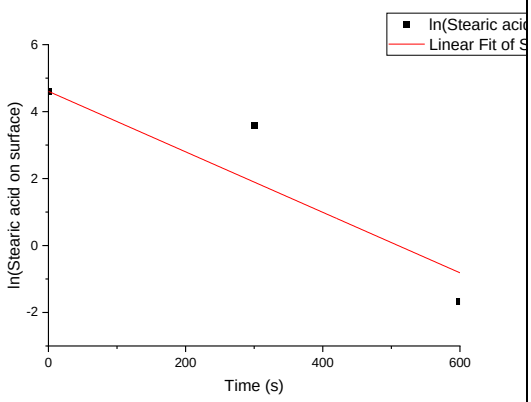 5500 rpm R^2: 0.85282 Rate constant: 0.00903 ± 0.00201
A2.374	**A2.375**
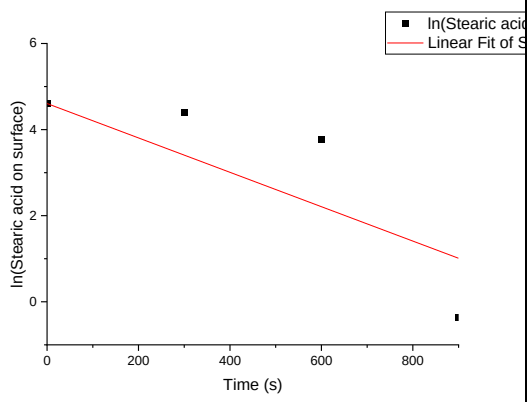 5500 rpm R^2: 0.87143 Rate constant: 0.00399 ± 0.00118	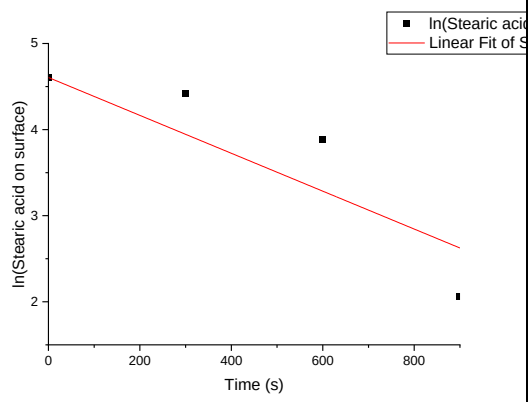 6000 rpm R^2: 0.98001 Rate constant: 0.0022 ± 4.88294E-4

A2.376 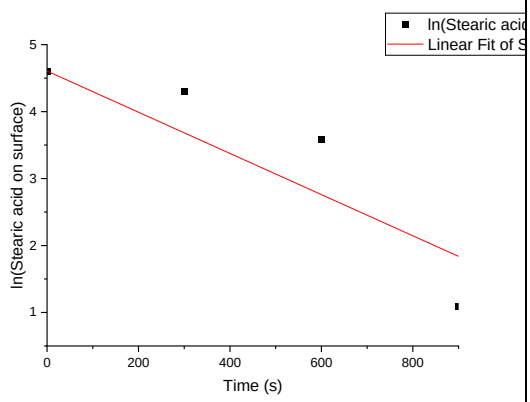 6500 rpm R^2: 0.95957 Rate constant: 0.00308 ± 6.56496E-4	A2.377 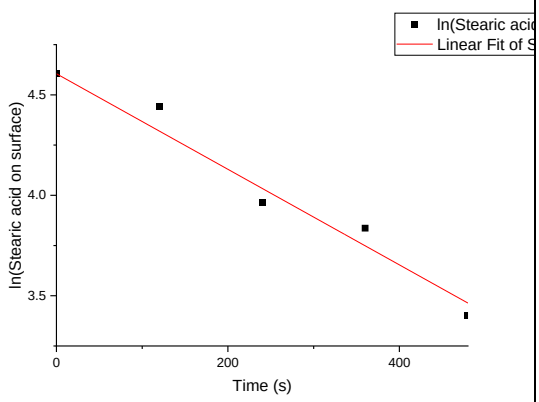 7000 rpm R^2: 0.99953 Rate constant: 0.00238 ± 1.33696E-4
A2.378 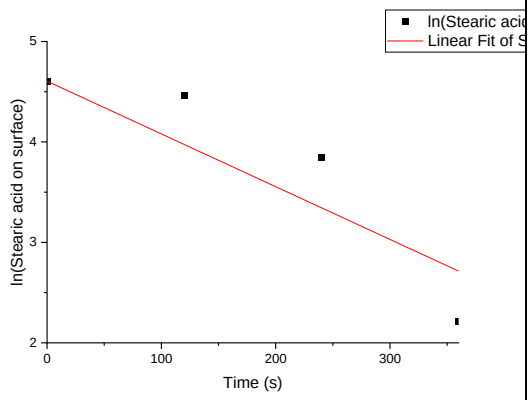 7000 rpm R^2: 0.98375 Rate constant: 0.00525 ± 0.00111	A2.379 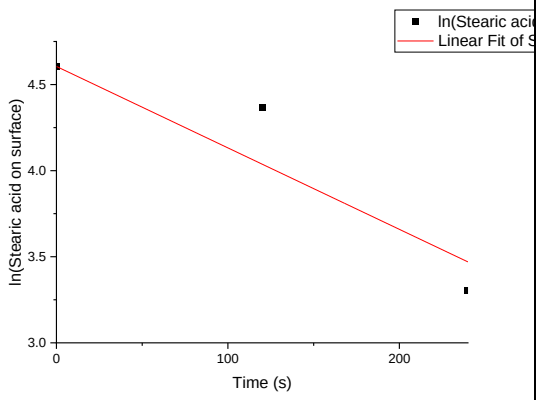 7500 rpm R^2: 0.99601 Rate constant: 0.00473 ± 9.72927E-4

A2.380

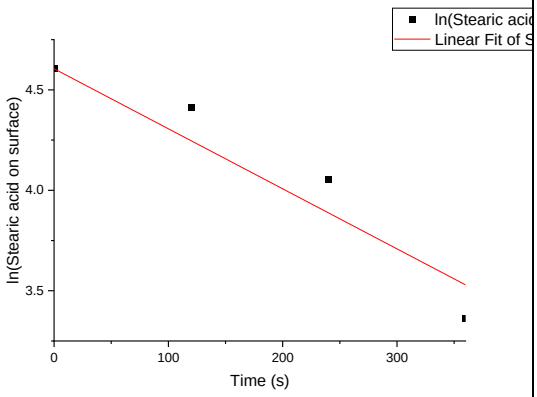

7500 rpm

R^2: 0.99839

Rate constant: 0.00299 ± 3.69719E-4

A2.381

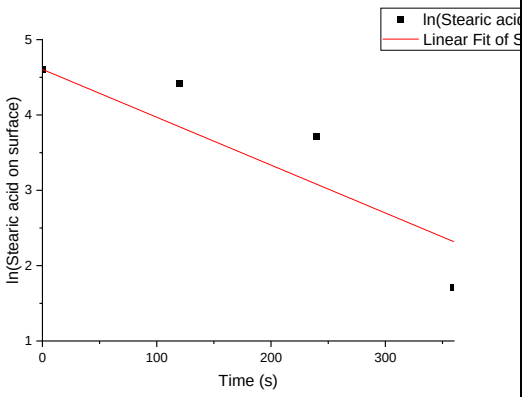

8000 rpm

R^2: 0.97429

Rate constant: 0.00635 ± 0.00135

A2.382

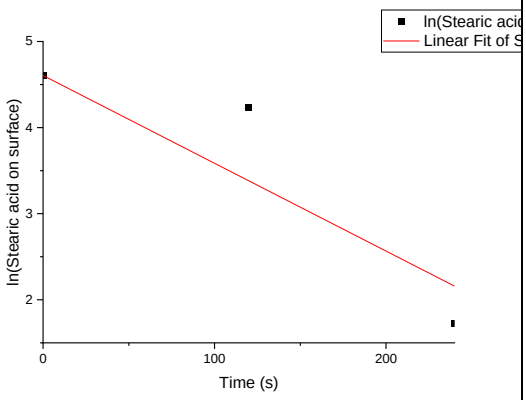

8000 rpm

R^2: 0.96745

Rate constant: 0.0102 ± 0.00252

Appendix 3: Surface Images

Surface images of the centre of photocatalytic films. The preparation spin speed and copper content is listed below each image.

A3.1

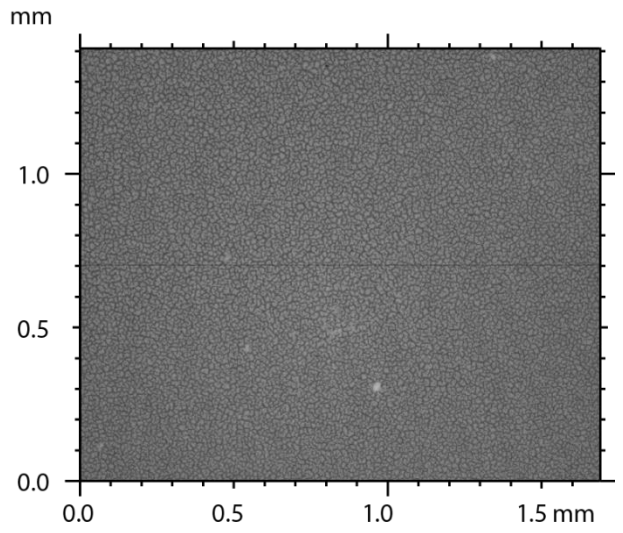

Undoped – 500 rpm

A3.2

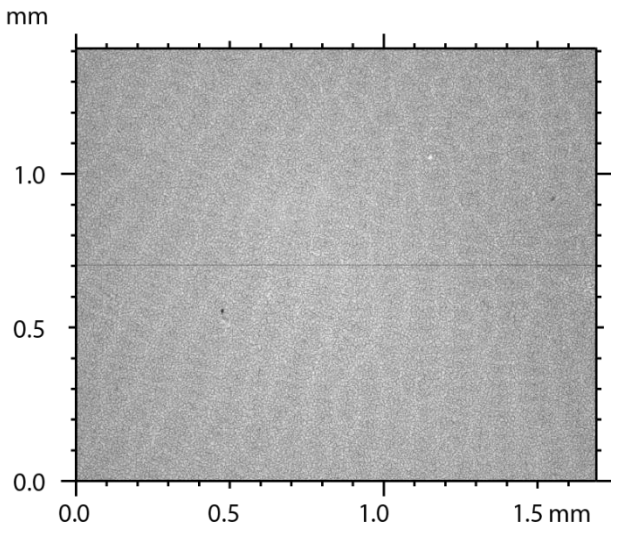

Undoped – 1000 rpm

A3.3

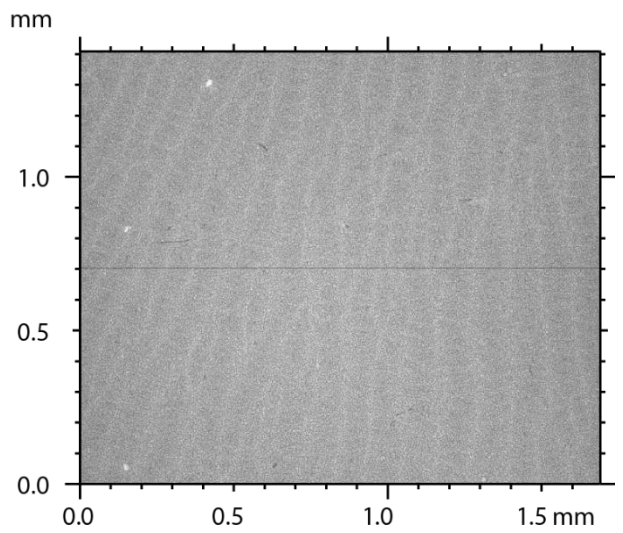

Undoped – 1500 rpm

A3.4

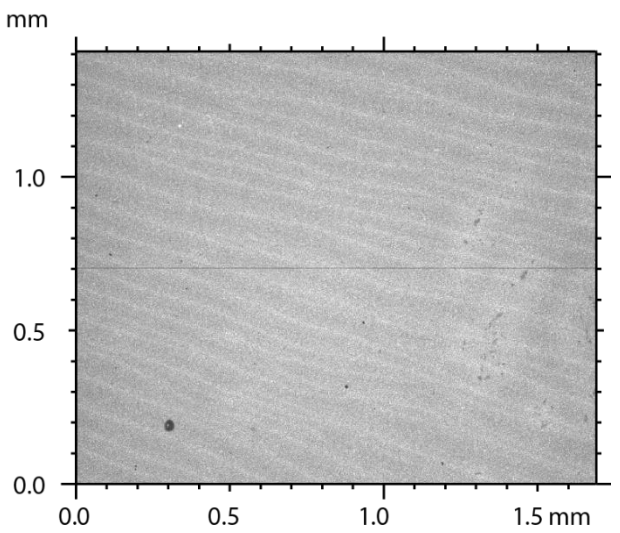

Undoped – 2000 rpm

A3.5

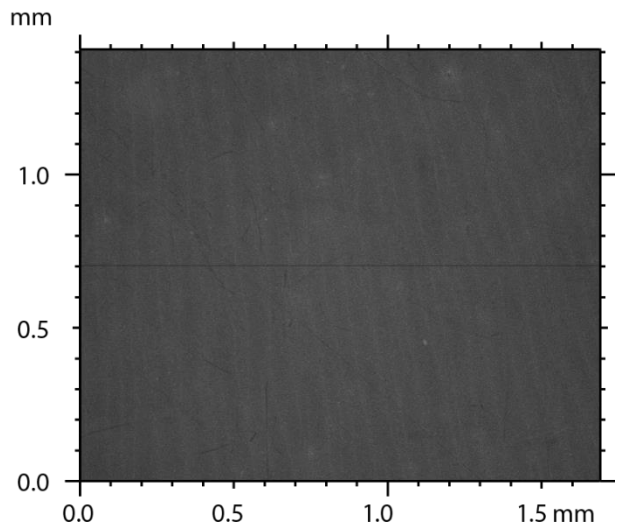

Undoped – 4000 rpm

A3.6

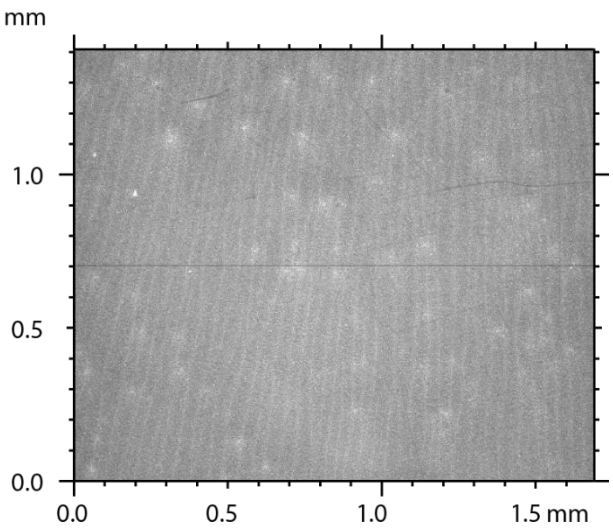

Undoped – 6000 rpm

A3.7

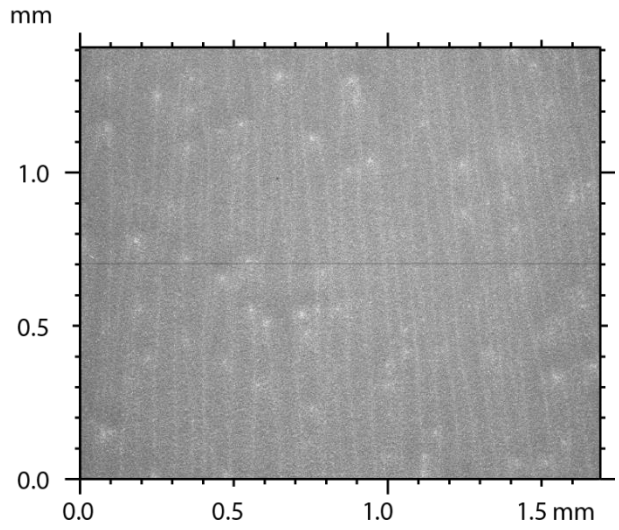

Undoped – 8000 rpm

A3.8

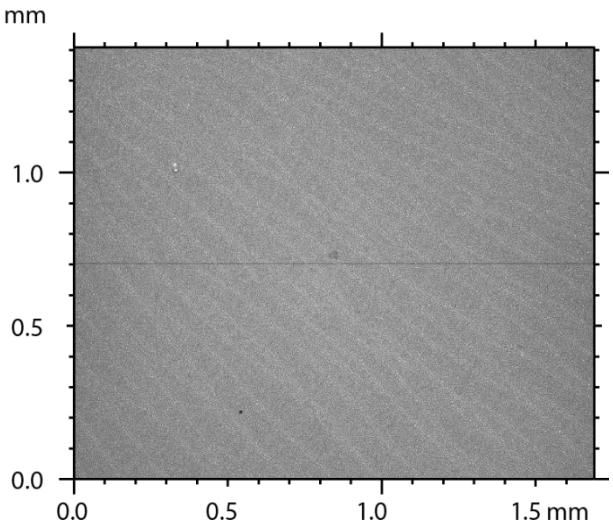

5 wt% – 1500 rpm

A3.9

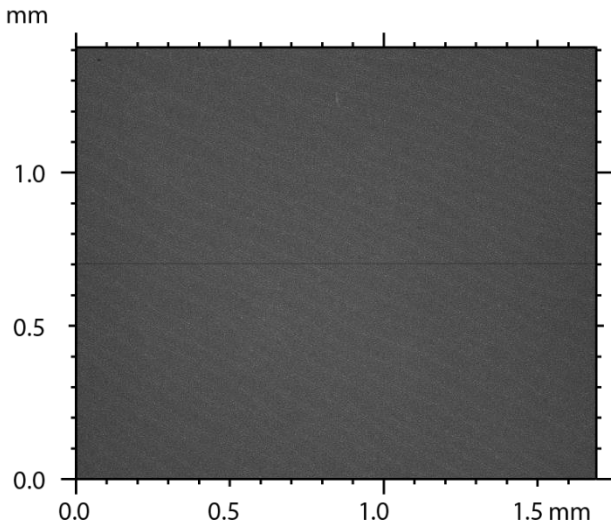

5.0% wt% – 2000 rpm

A3.10

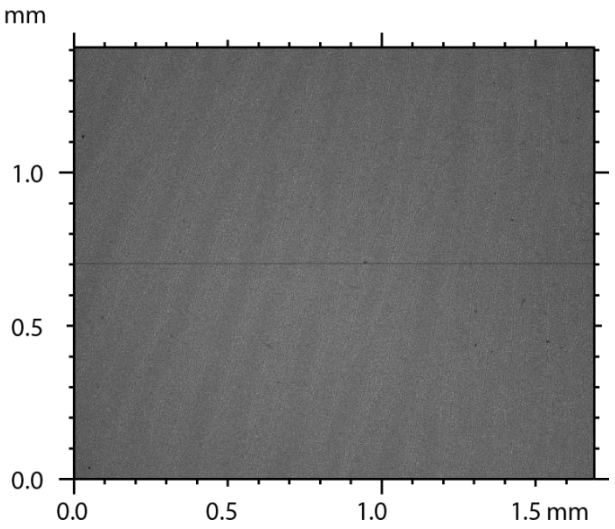

5.0% wt% – 6000 rpm

A3.11

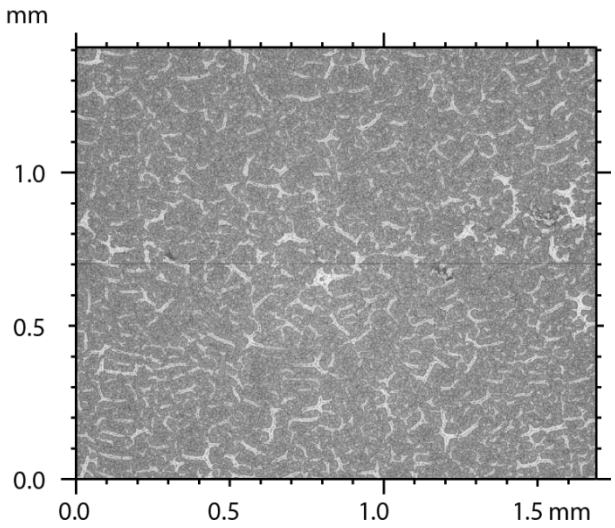

2.5% wt% – 500 rpm

A3.12

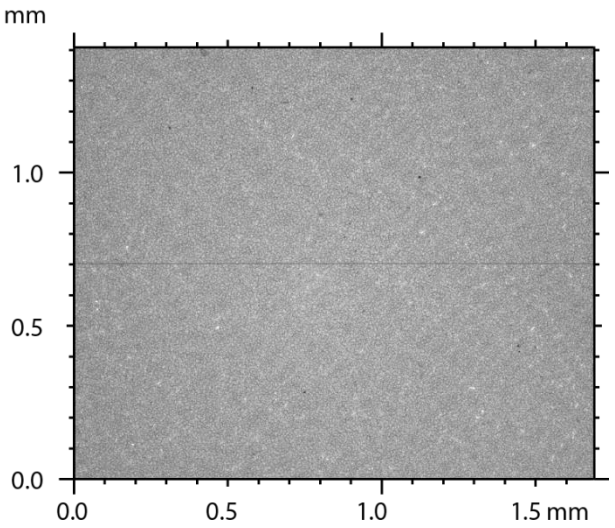

2.5% wt% – 1000 rpm

A3.13

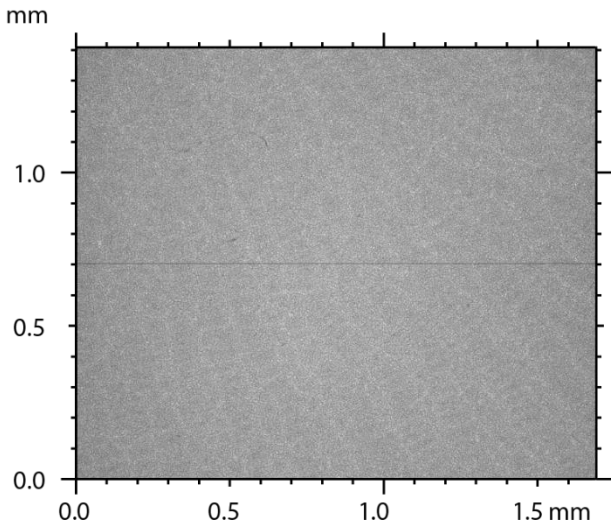

2.5% wt% – 1500 rpm

A3.14

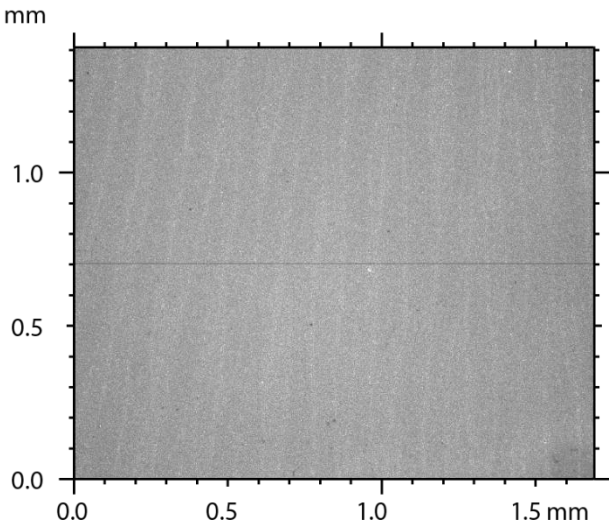

2.5% wt% – 2000 rpm

A3.15

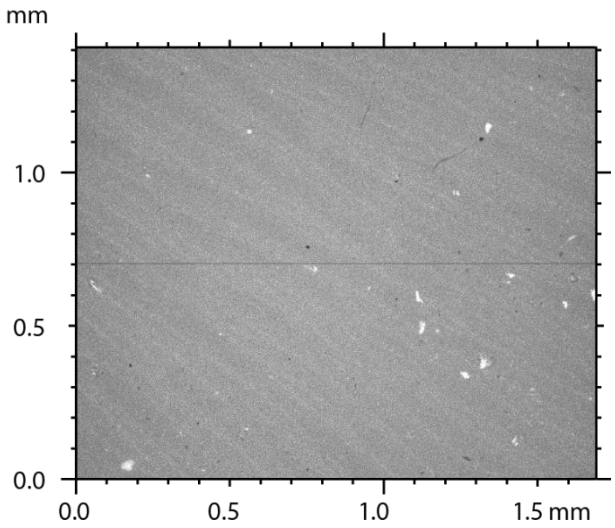

2.5% wt% – 4000 rpm

A3.16

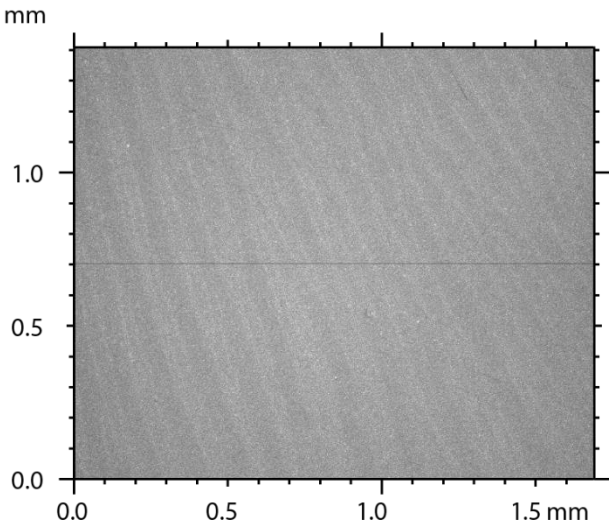

2.5% wt% – 6000 rpm

A3.17

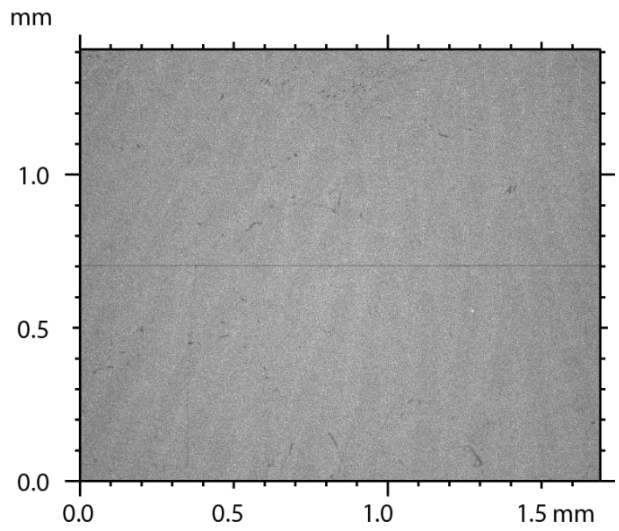

2.5% wt% – 7500 rpm

A3.18

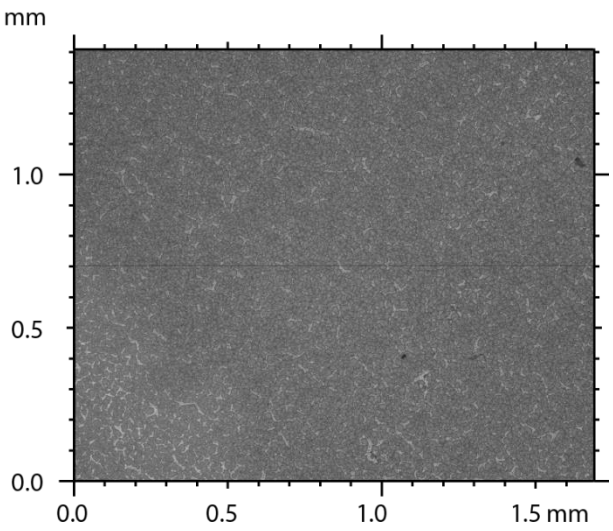

1.0% wt% – 500 rpm

A3.19

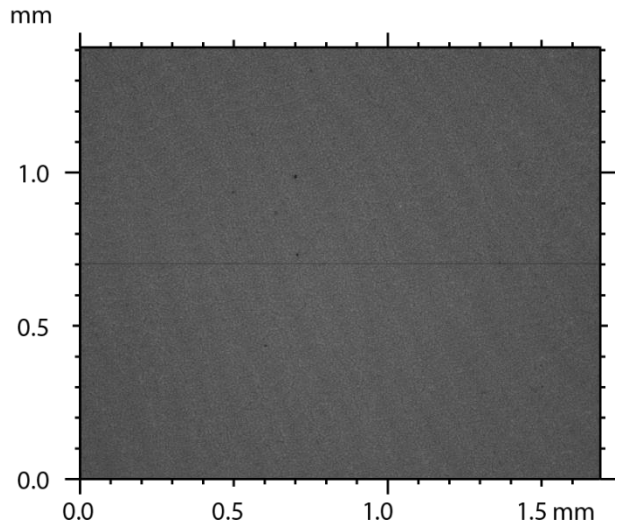

1.0% wt% – 1000 rpm

A3.20

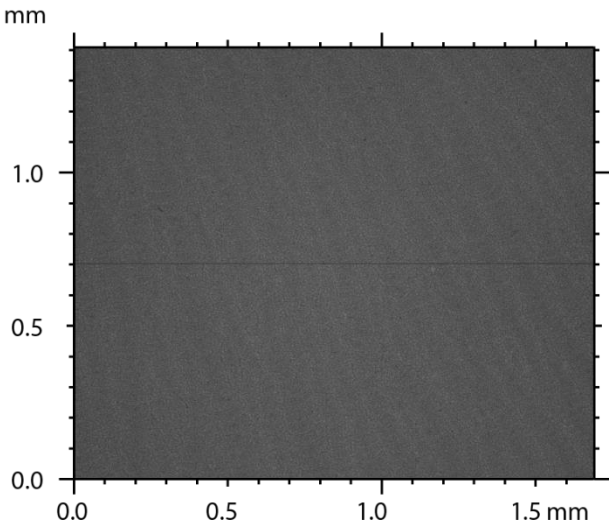

1.0% wt% – 1500 rpm

A3.21

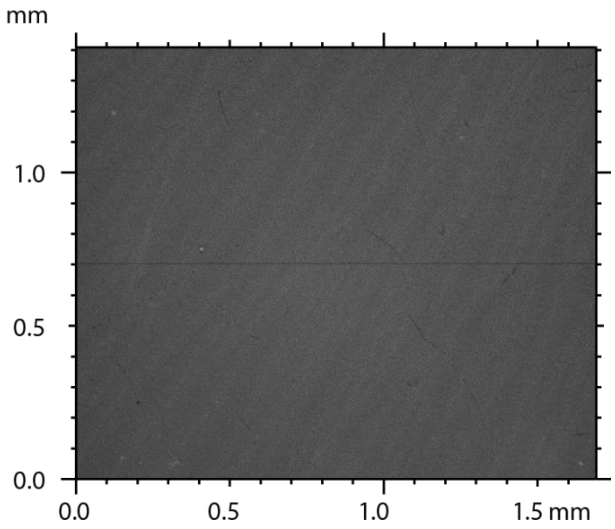

1.0% wt% – 2000 rpm

A3.22

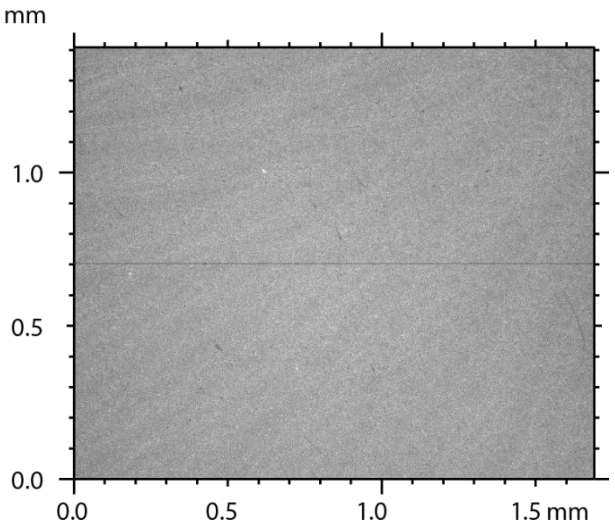

1.0% wt% – 3500 rpm

A3.23

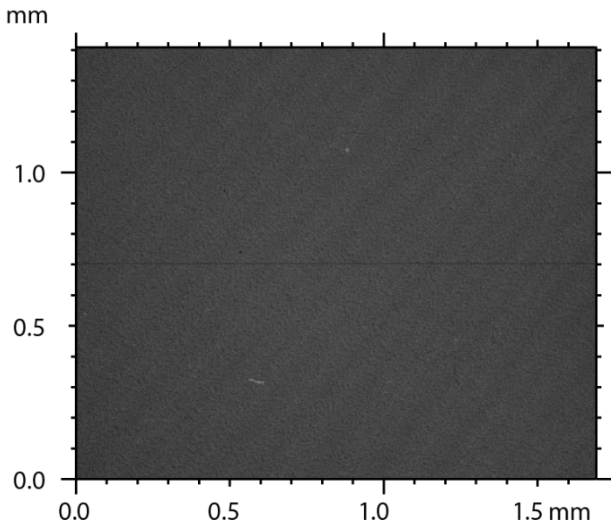

1.0% wt% – 6000 rpm

A3.24

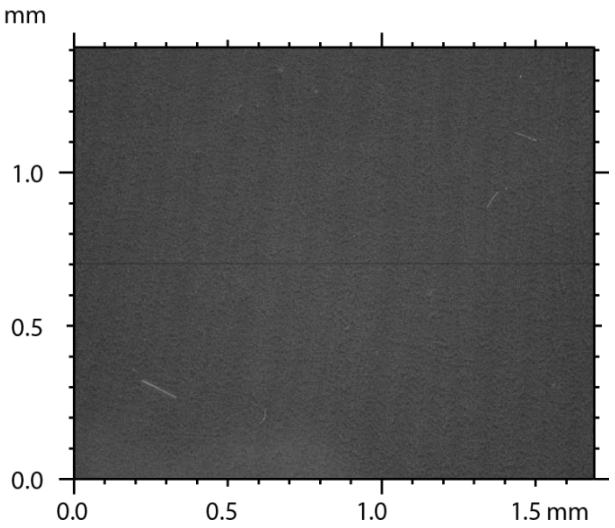

1.0% wt% – 7500 rpm

A3.25

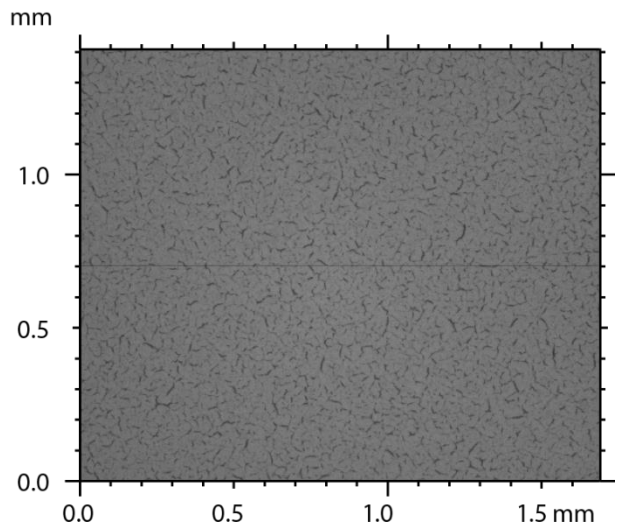

0.5% wt% – 500 rpm

A3.26

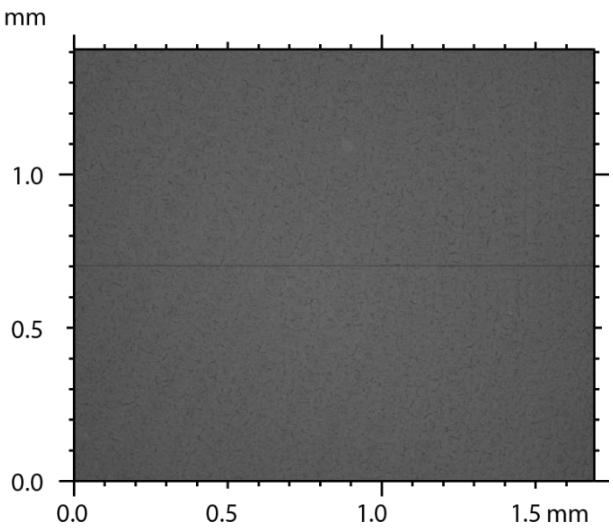

0.5% wt% – 1000 rpm

A3.27

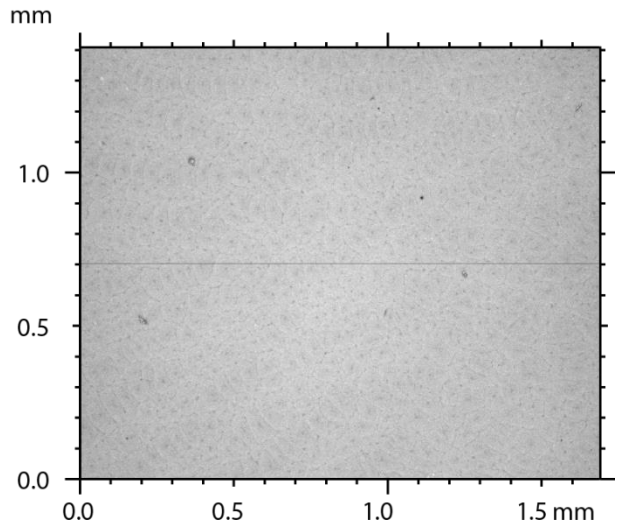

0.5% wt% – 1500 rpm

A3.28

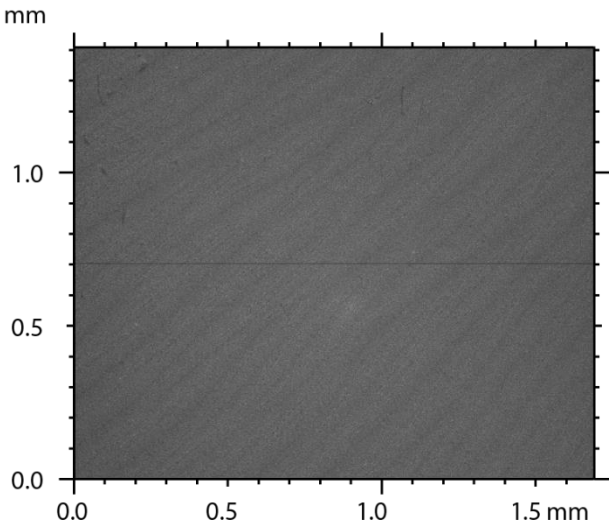

0.5% wt% – 4000 rpm

A3.29

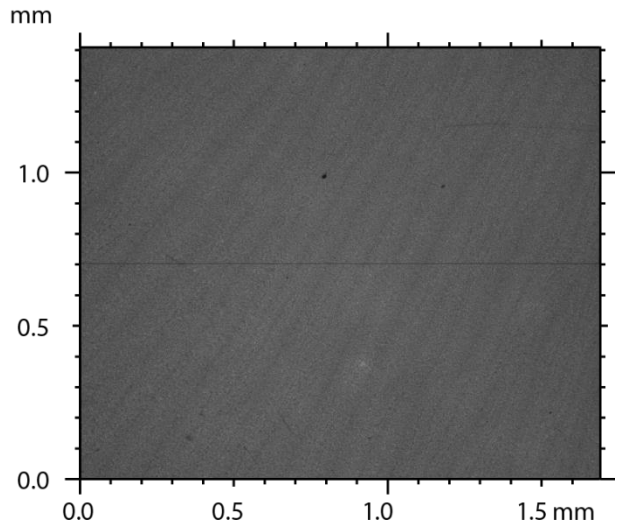

0.5% wt% – 6000 rpm

A3.30

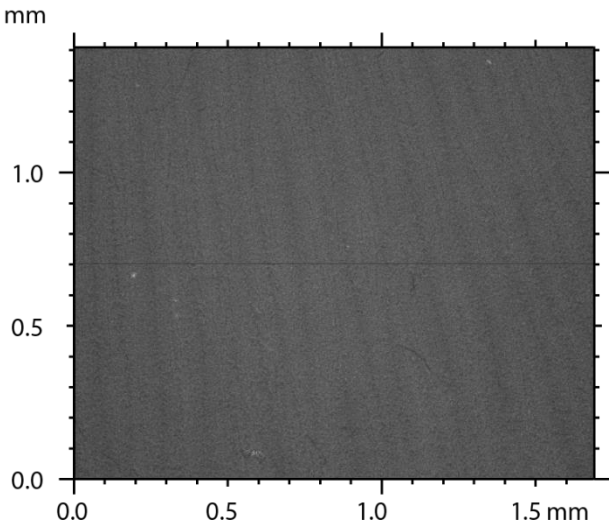

0.5% wt% – 8000 rpm

A3.31

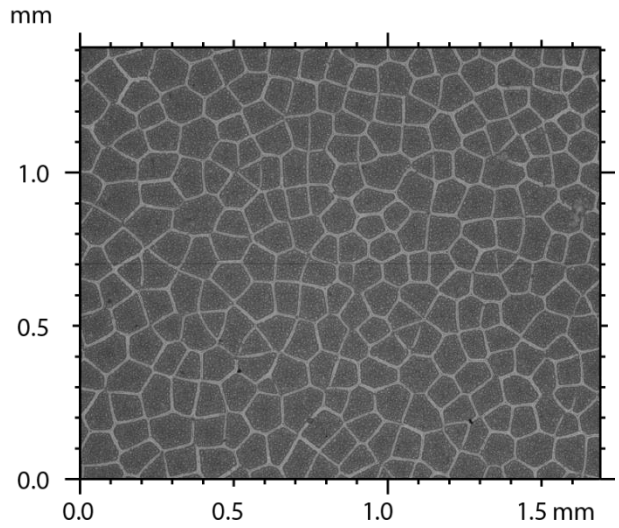

5.0% wt% – 500 rpm

A3.32

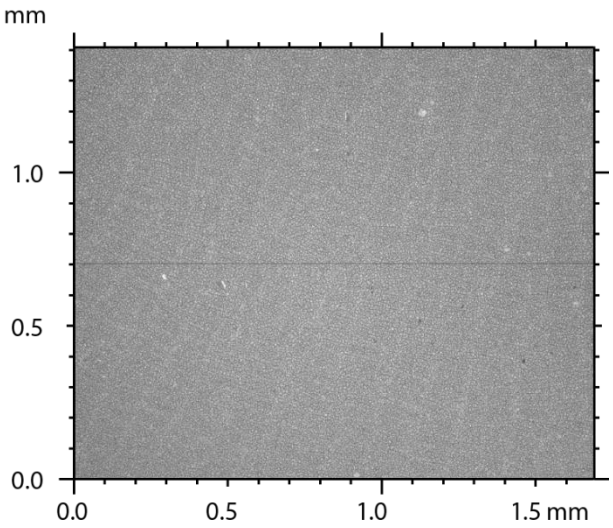

5.0% wt% – 1000 rpm

A3.33

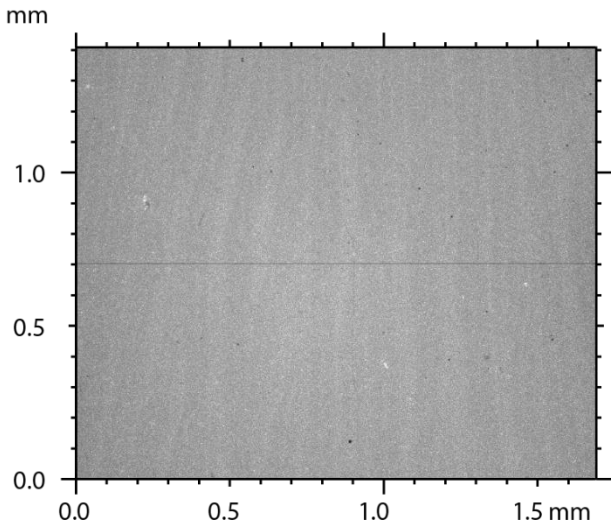

5.0% wt% – 4000 rpm

A3.34

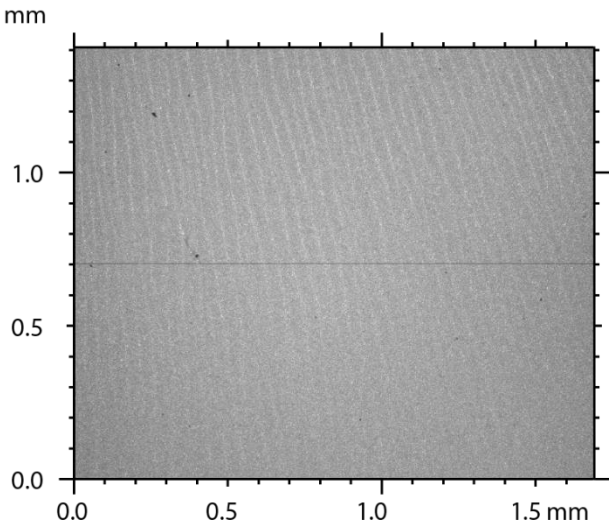

5.0% wt% – 8000 rpm

A3.35

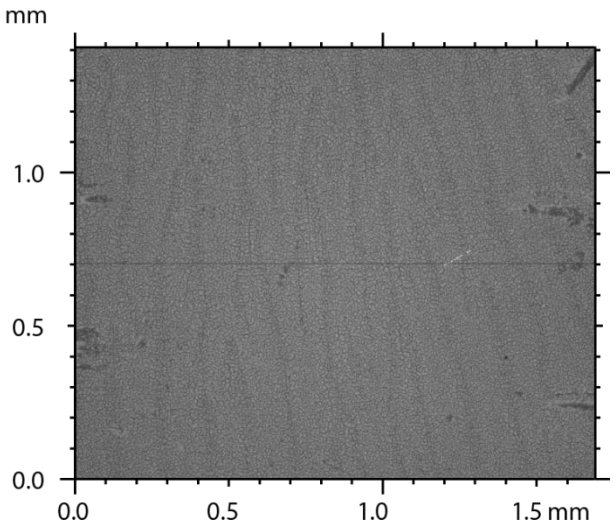

0.1% wt% – 1000 rpm

A3.37

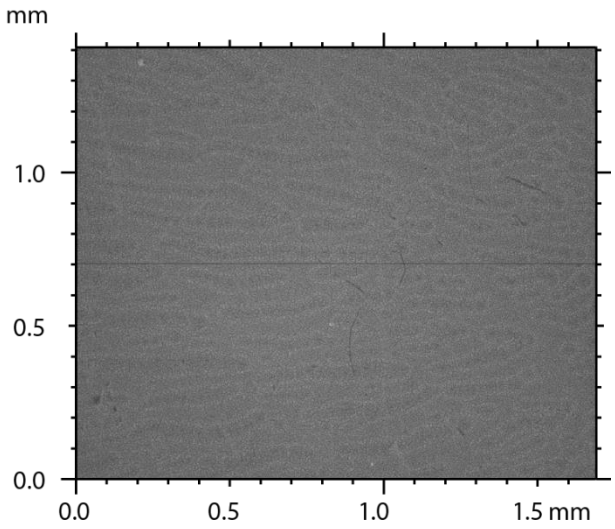

0.1% wt% – 1500 rpm

A3.38

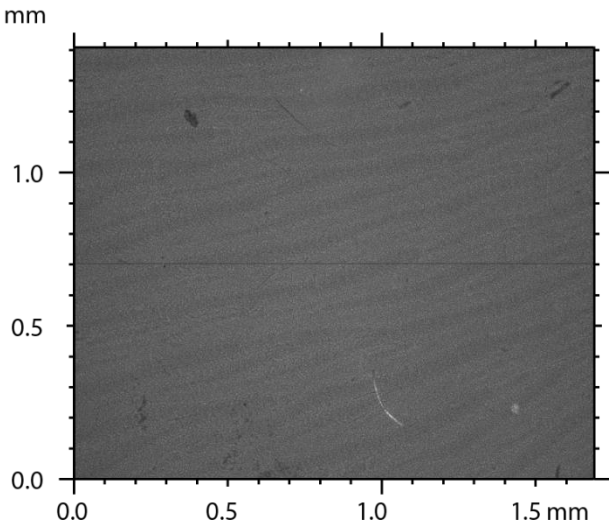

0.1% wt% – 2000 rpm

A3.39

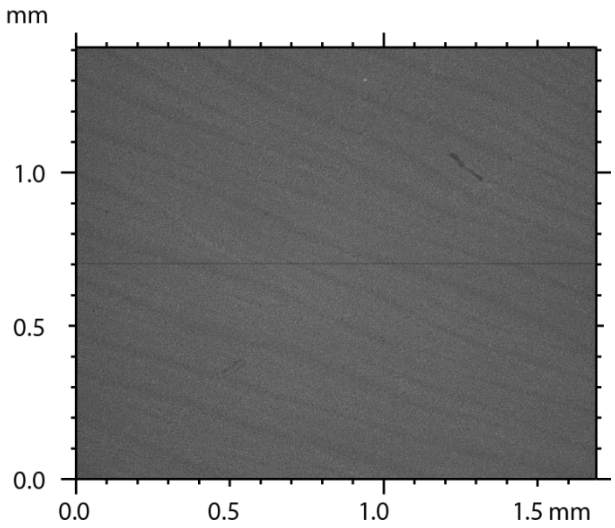

0.1% wt% – 2500 rpm

A3.40

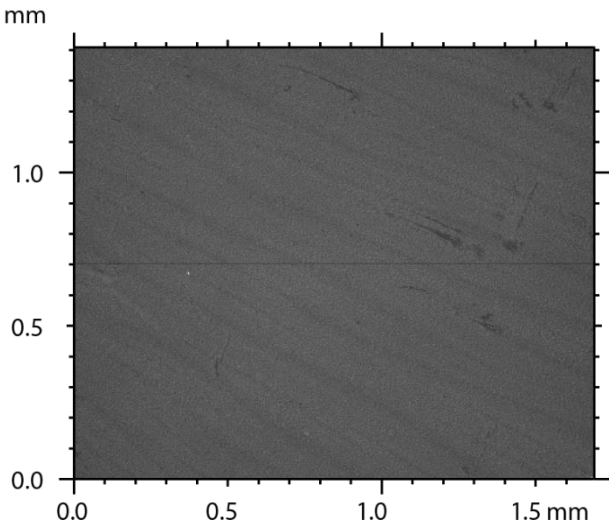

0.1% wt% – 3000 rpm

A3.41

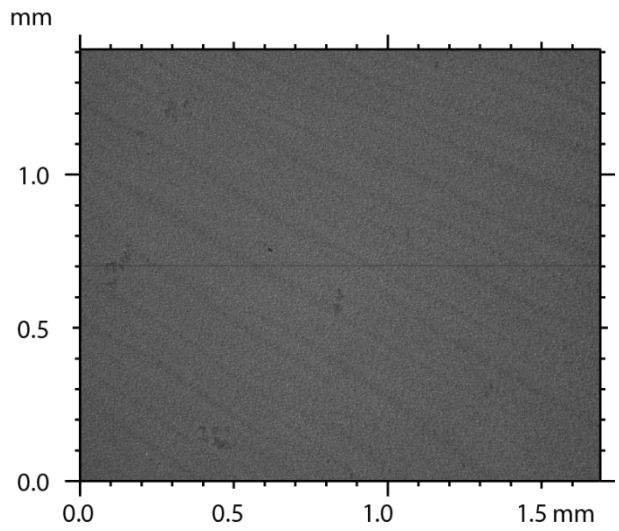

0.1% wt% – 3500 rpm

A3.42

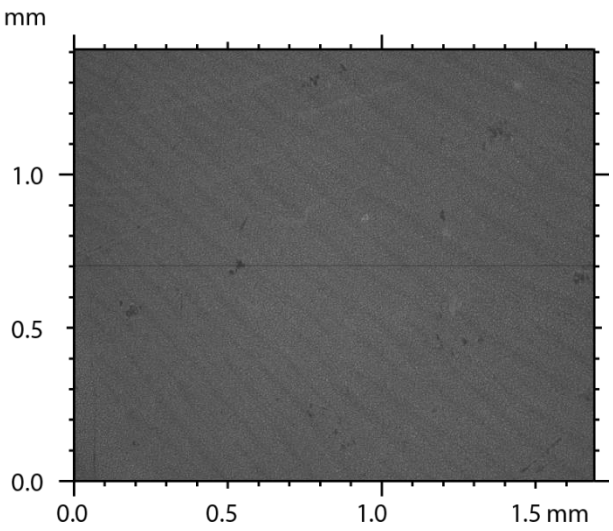

0.1% wt% – 4000 rpm

A3.43

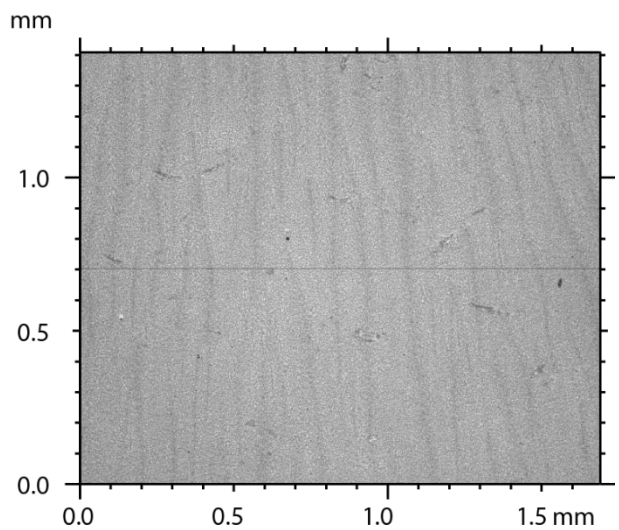

0.1% wt% – 4500 rpm

A3.44

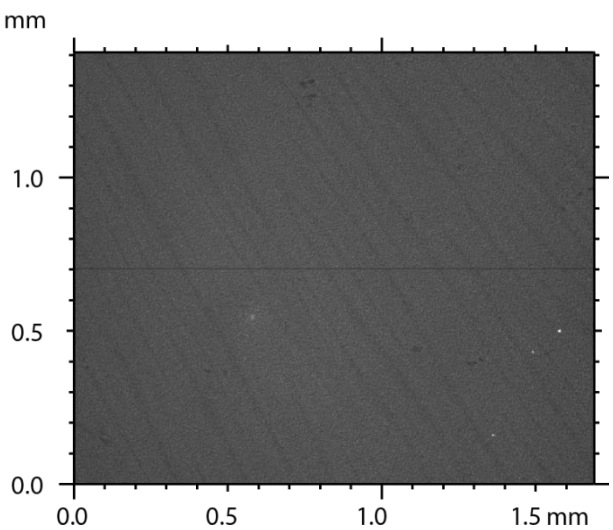

0.1% wt% – 5000 rpm

A3.45

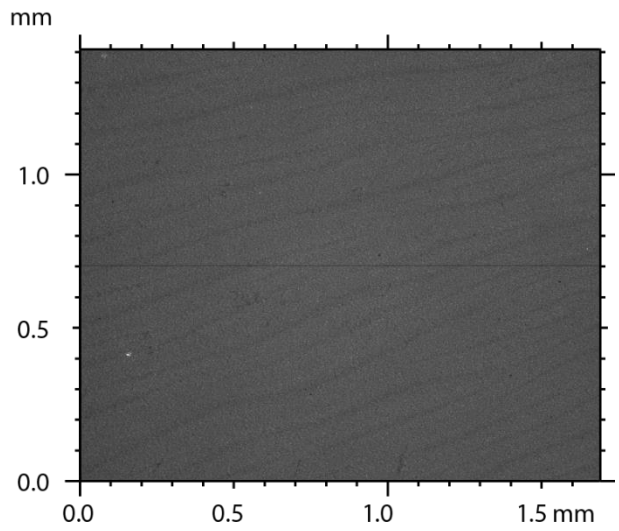

0.1% wt% – 5500 rpm

A3.46

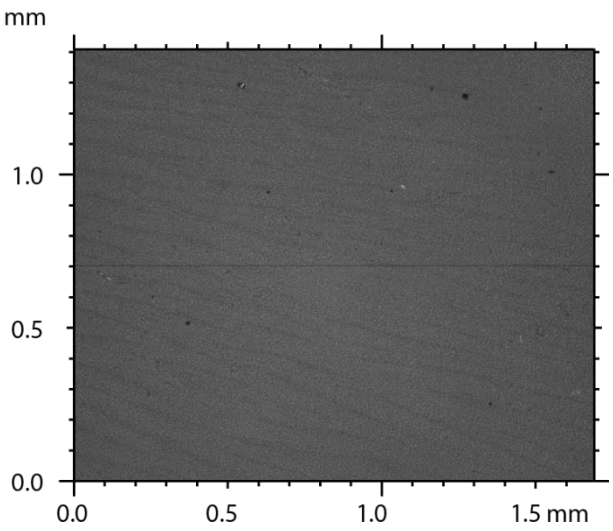

0.1% wt% – 6000 rpm

A3.47

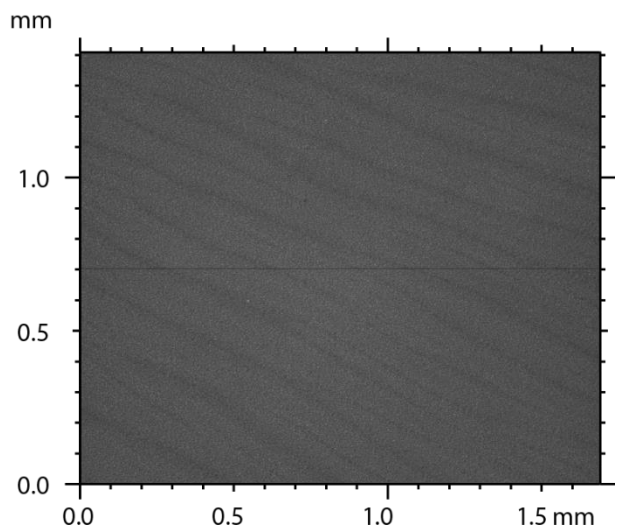

0.1% wt% – 6500 rpm

A3.48

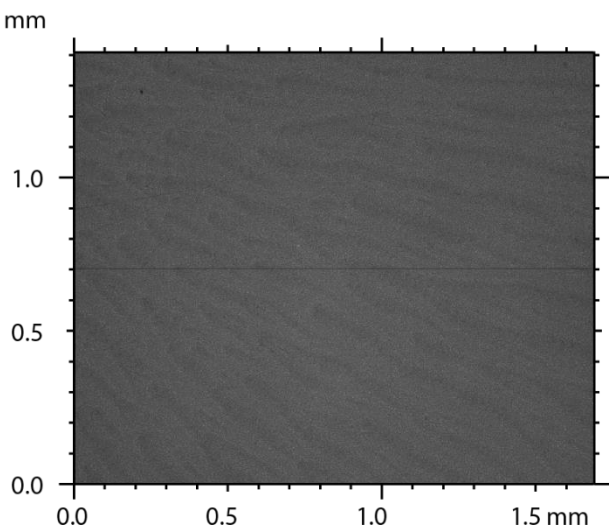

0.1% wt% – 7000 rpm

A3.49	A3.50
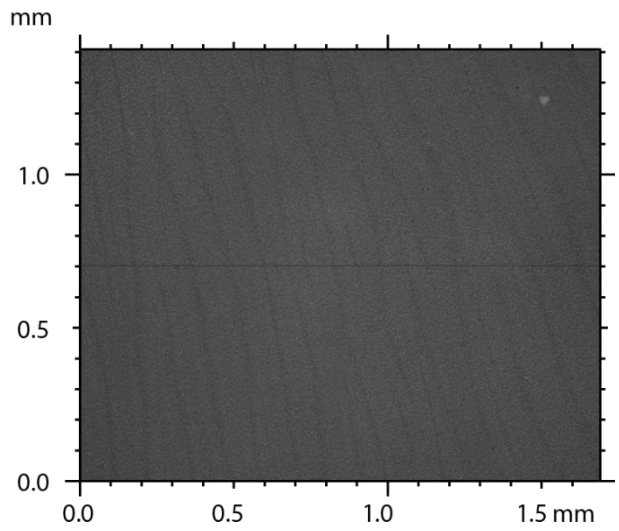	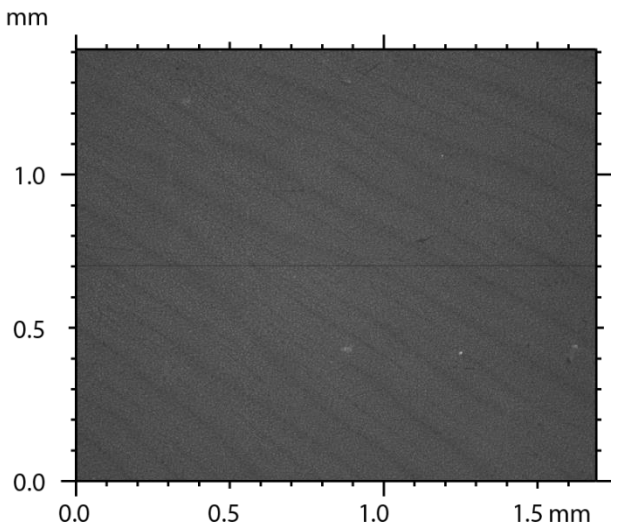
0.1% wt% – 7500 rpm	0.1% wt% – 8000 rpm

Appendix 4: Metrology Depth Maps – Edges

Depth map of the edge of photocatalytic films. The preparation spin speed and copper content is listed below each image.

A4.1

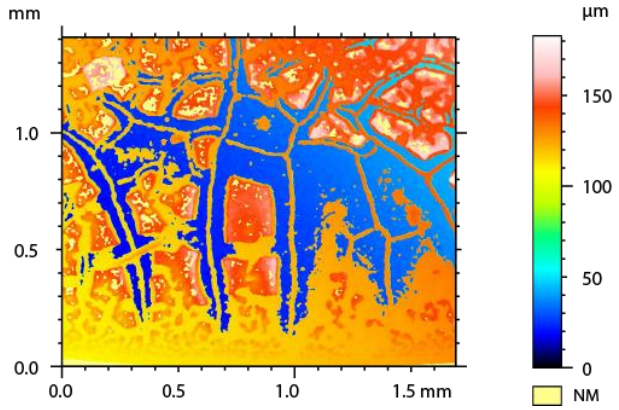

Undoped – 500 rpm

A4.2

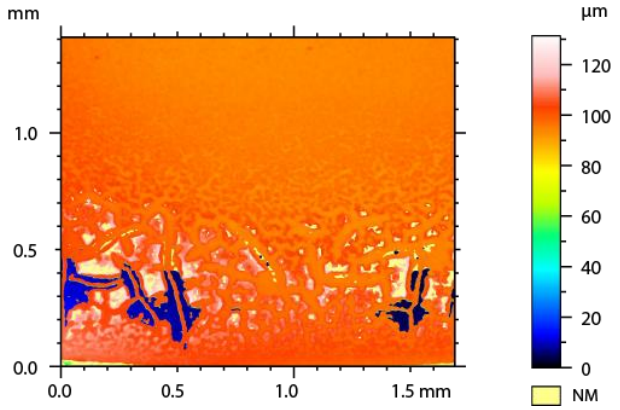

Undoped – 1000 rpm

A4.3

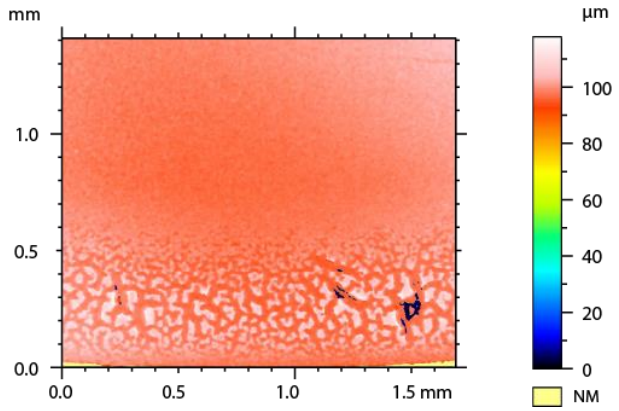

Undoped – 1500 rpm

A4.4

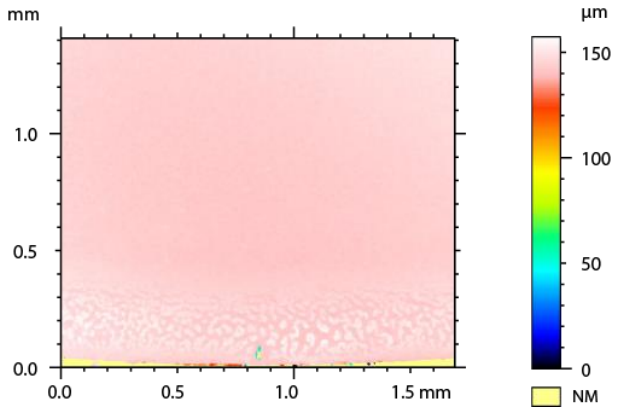

Undoped – 2000 rpm

A4.5

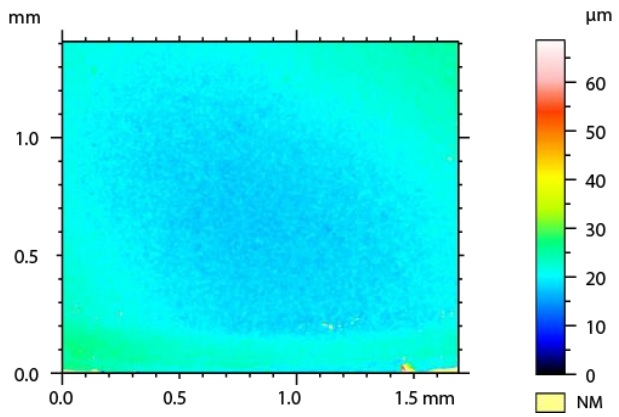

A4.6

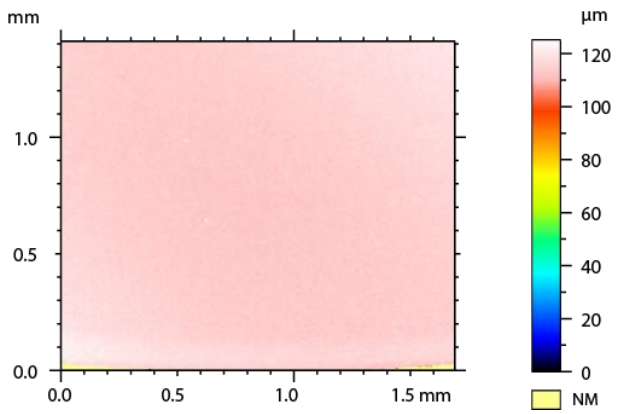

Undoped – 4000 rpm	Undoped – 6000 rpm
A4.7 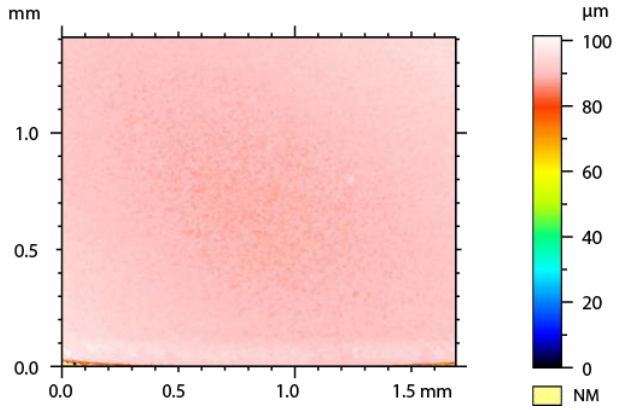 Undoped – 8000 rpm	A4.8 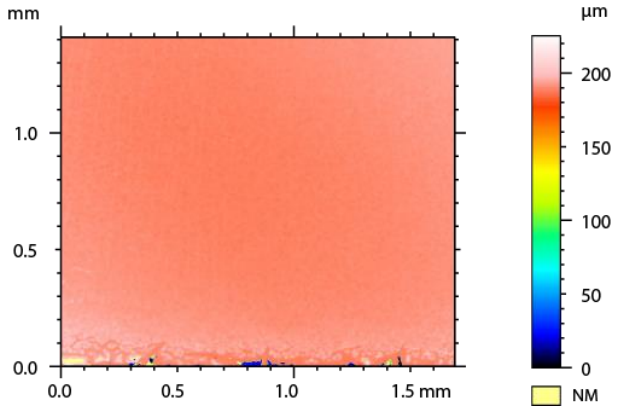 5 wt% – 1500 rpm
A4.9 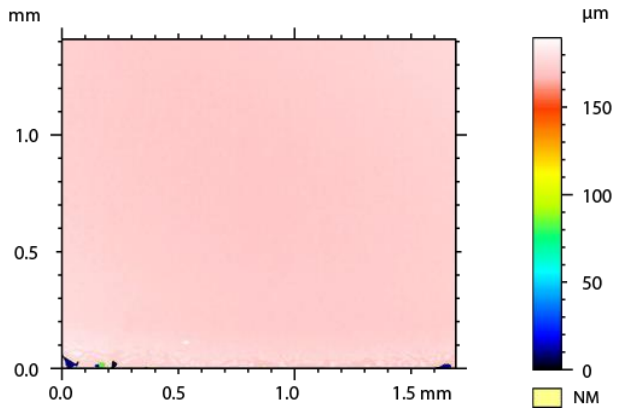 5 wt% – 2000 rpm	A4.10 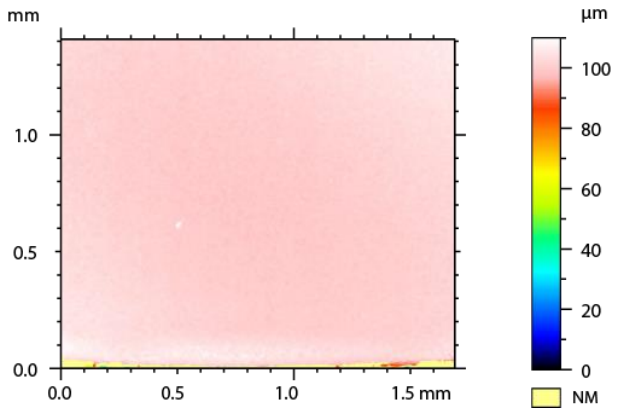 5 wt% – 6000 rpm
A4.11 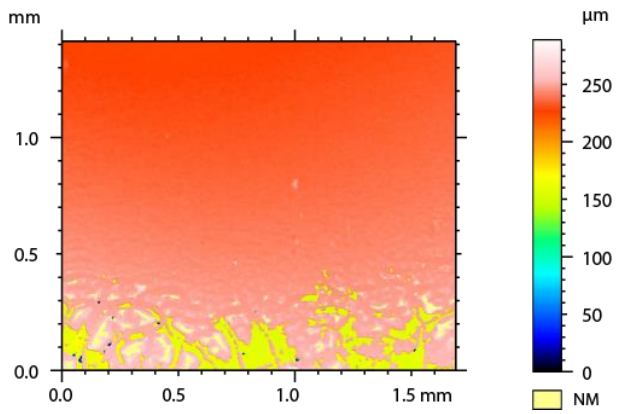 2.5 wt% – 500 rpm	A4.12 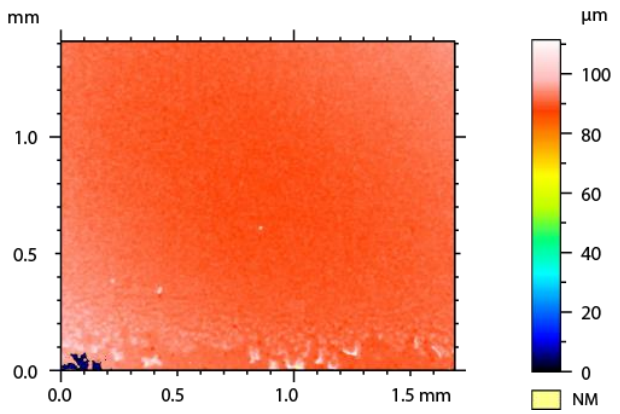 2.5 wt% – 1000 rpm

A4.13

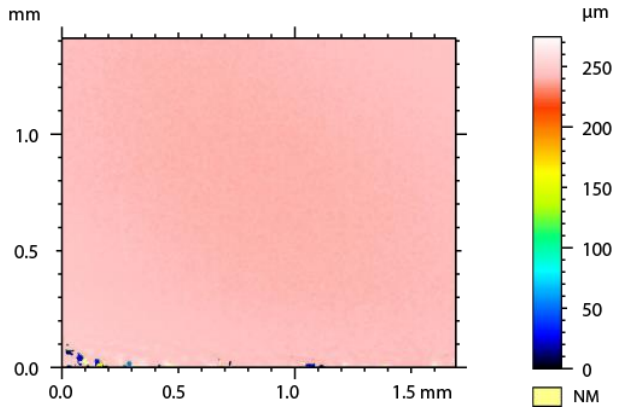

2.5 wt% – 1500 rpm

A4.14

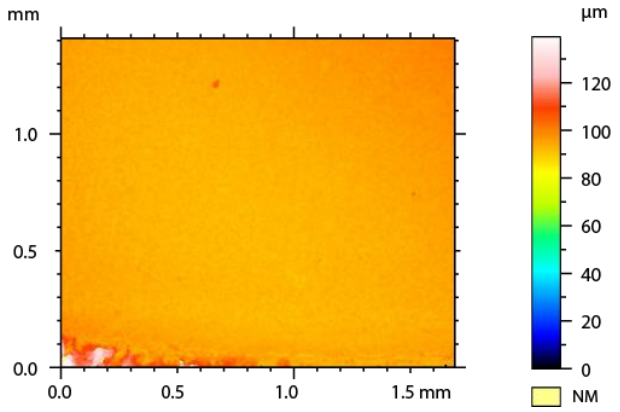

2.5 wt% – 2000 rpm

A4.15

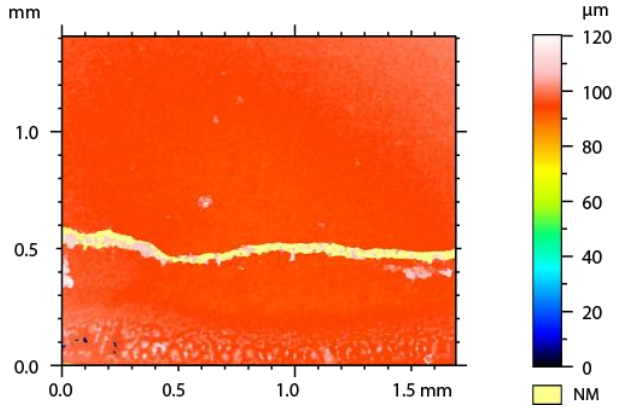

2.5 wt% – 4000 rpm

A4.16

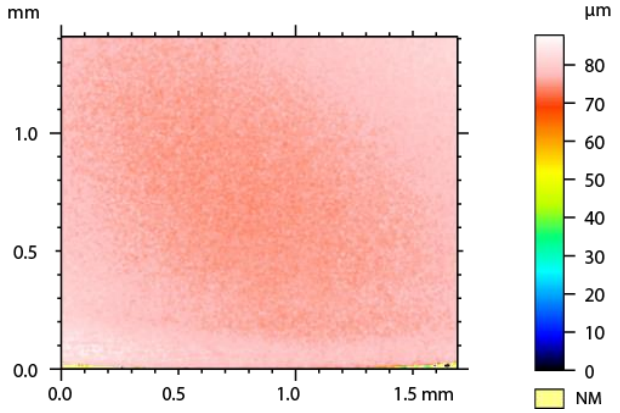

2.5 wt% – 6000 rpm

A4.17

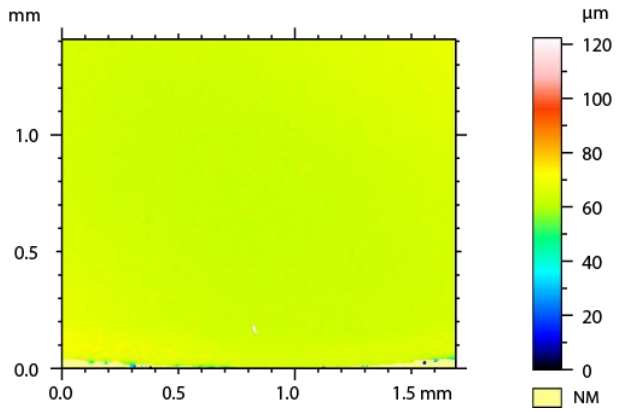

2.5 wt% – 7500 rpm

A4.18

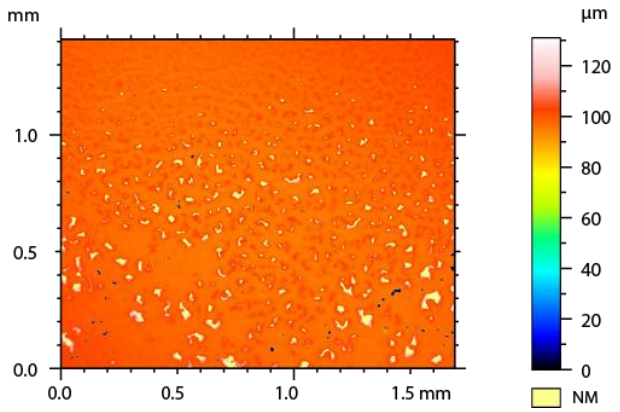

1 wt% – 500 rpm

A4.19

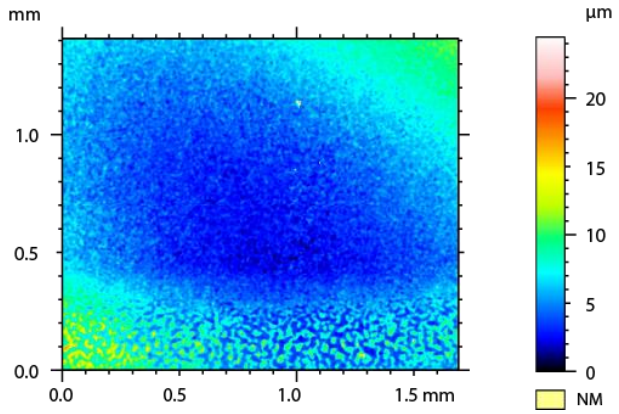

1 wt% – 1500 rpm

A4.20

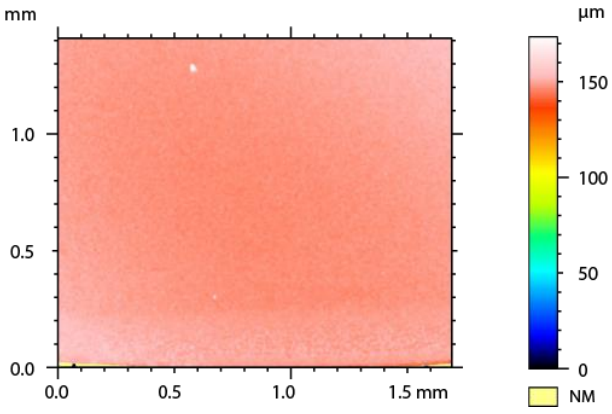

1 wt% – 3500 rpm

A4.21

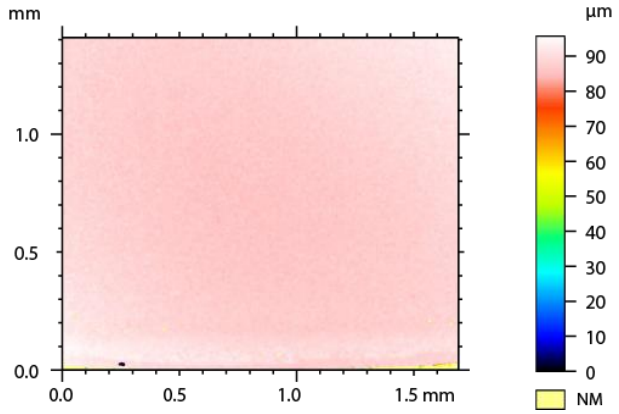

1 wt% – 6000 rpm

A4.22

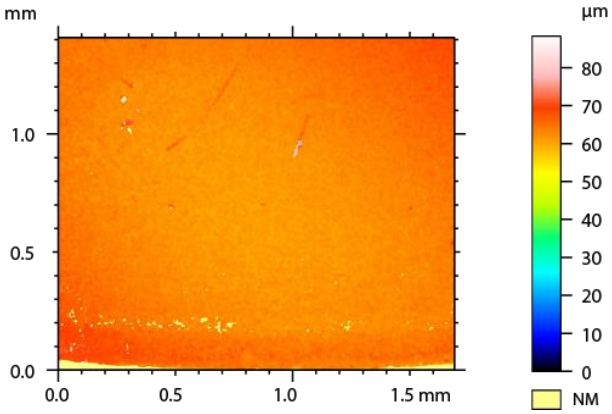

1 wt% – 7500 rpm

A4.23

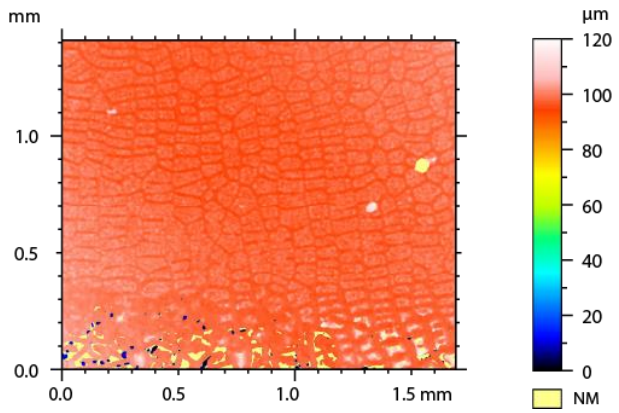

5 wt% – 500 rpm

A4.24

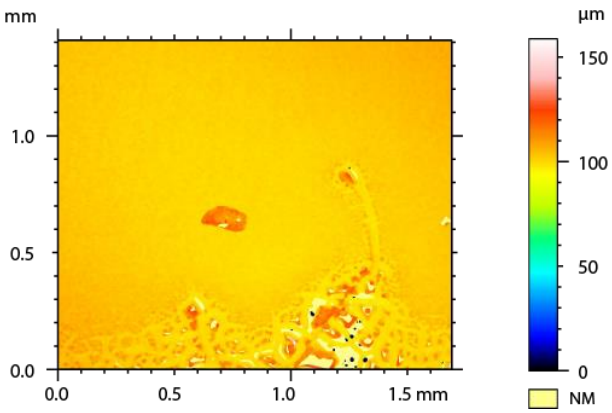

5 wt% – 1000 rpm

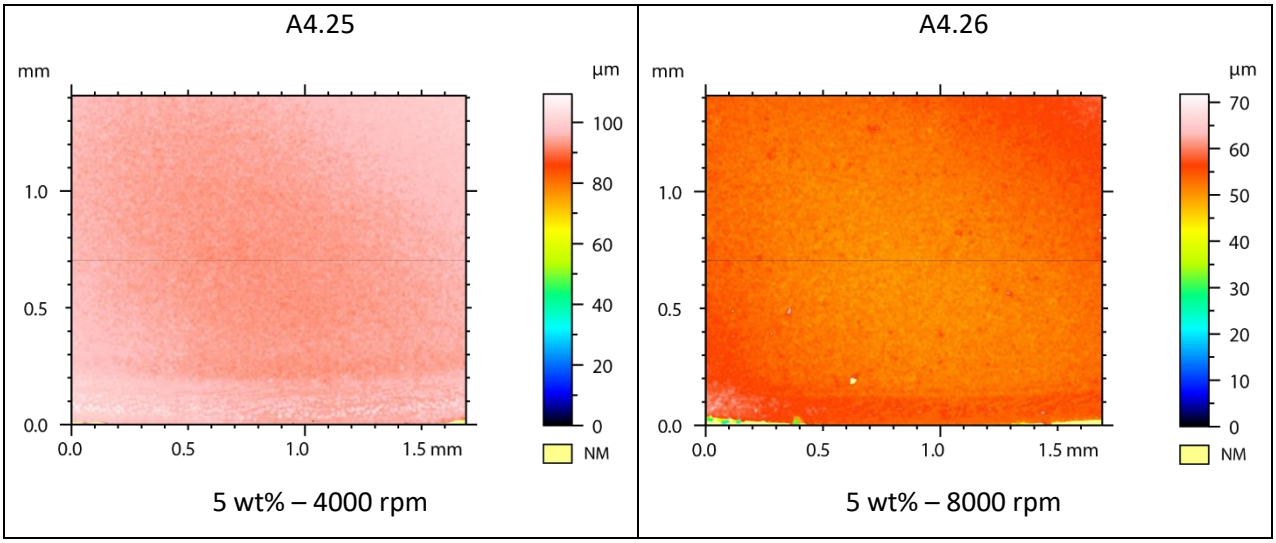
A4.25
mm
µm
1.0
0.5
0.0
0.0
0.5
1.0
1.5 mm
100
80
60
40
20
0
NM
5 wt% – 4000 rpm
A4.26
mm
µm
1.0
0.5
0.0
0.0
0.5
1.0
1.5 mm
70
60
50
40
30
20
10
0
NM
5 wt% – 8000 rpm

Appendix 5: FTIR Spectra of Stearic Acid on Photocatalytic Films

A: 5.1 DRIFT spectra of stearic acid on and undoped *meso*-TiO_2 film prepared at 1000 rpm

These FTIR spectra show the C-H stretch of stearic acid that was used during photocatalytic testing to monitor the progress of the reaction with exposure to UV light. The total irradiation time is listed on each graph.

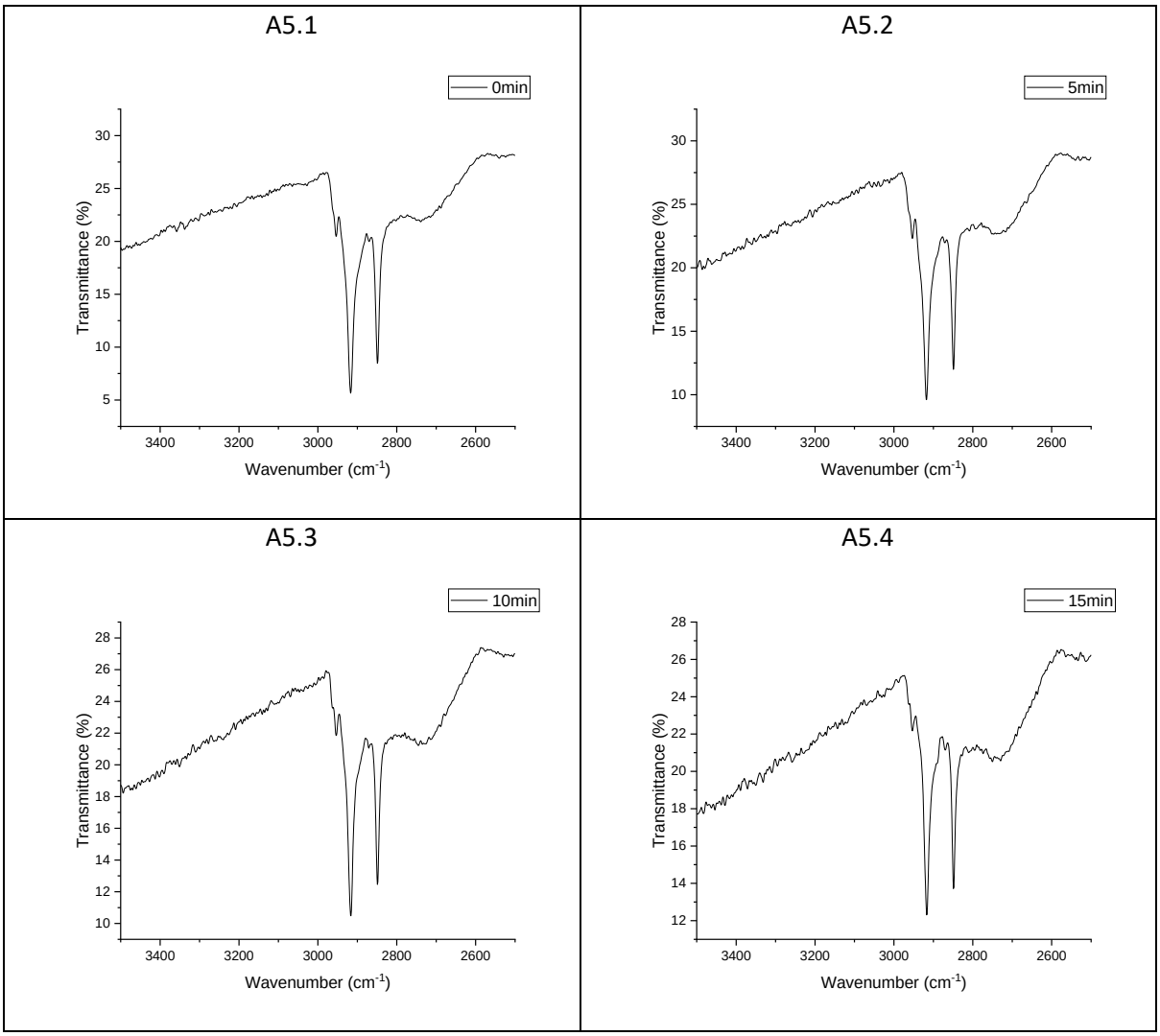

A5.5

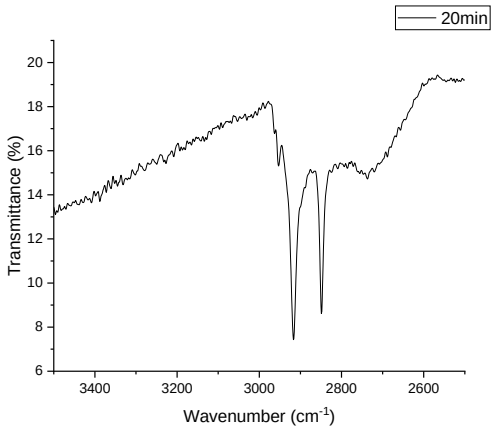

A5.6

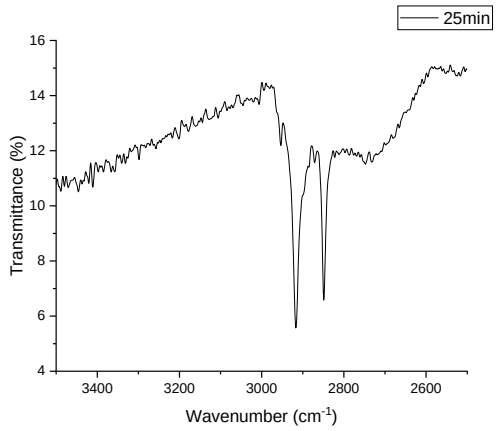

A5.7

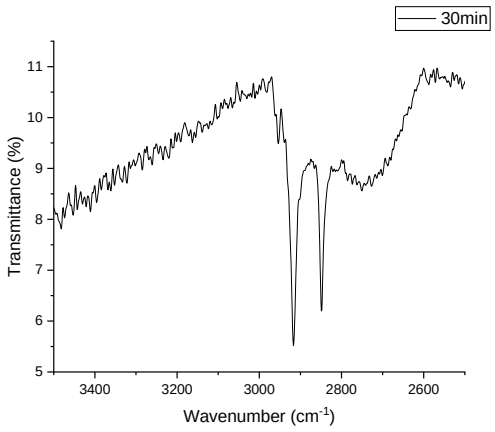

A5.8

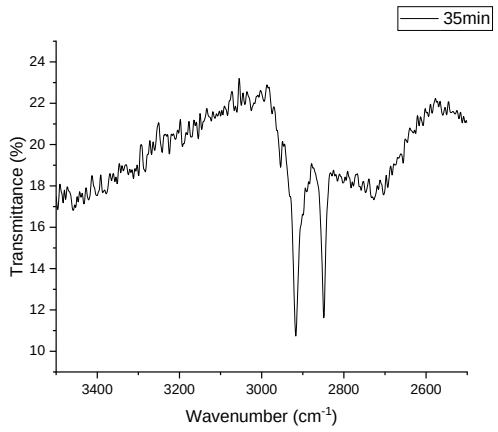

A5.9

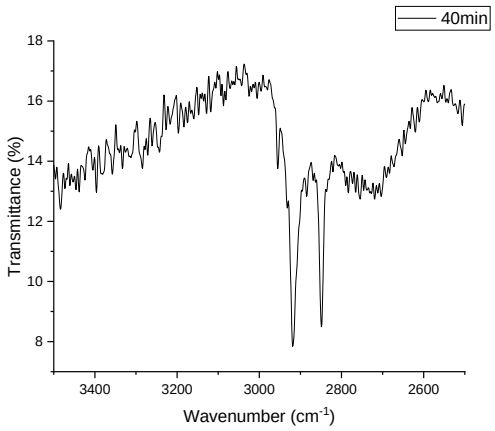

A: 5.2 DRIFT spectra of stearic acid on and undoped *meso*-TiO_2 film prepared at 2000 rpm

These FTIR spectra show the C-H stretch of stearic acid that was used during photocatalytic testing to monitor the progress of the reaction with exposure to UV light. The total irradiation time is listed on each graph.

A5.10

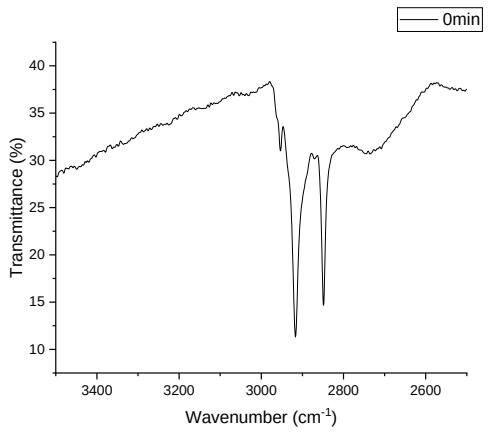

A5.11

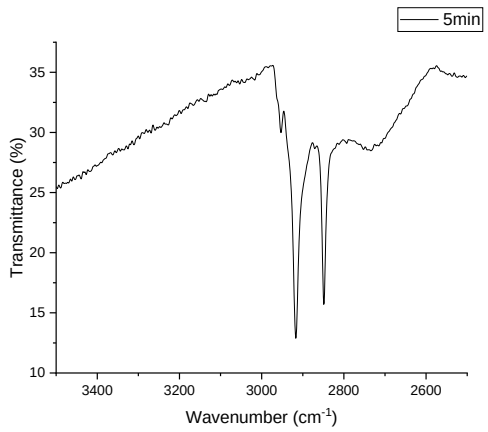

A5.12

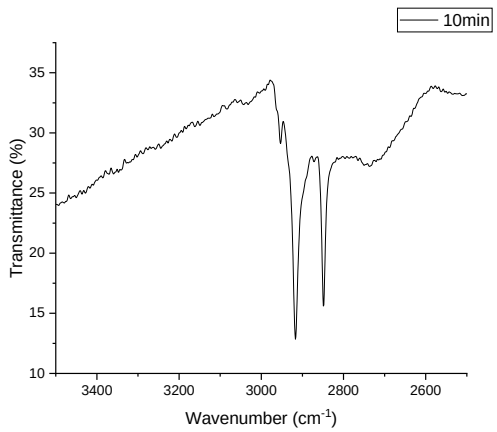

A5.13

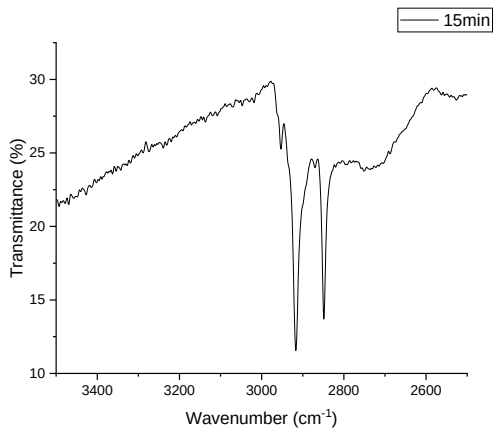

A5.14

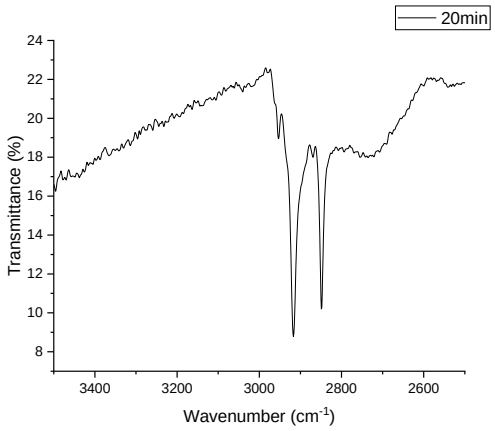

A5.15

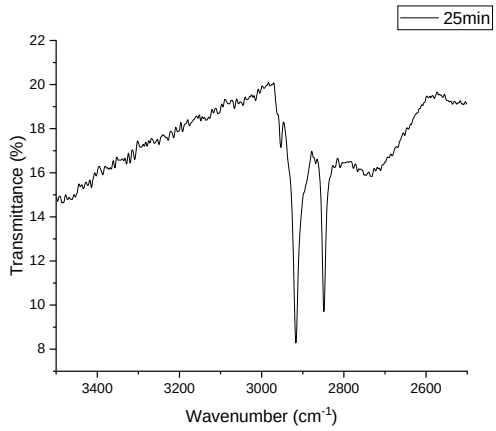

A5.16

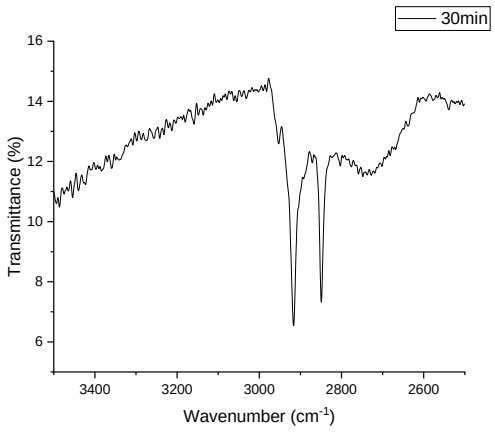

A5.17

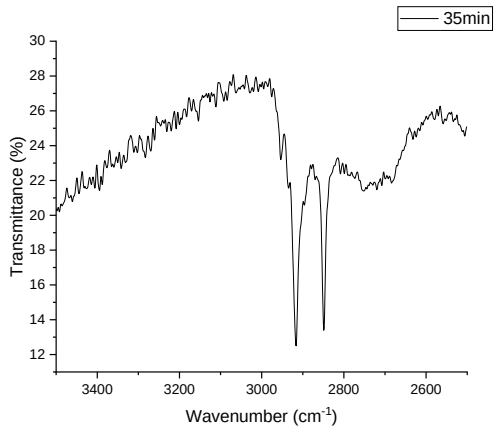

A5.18

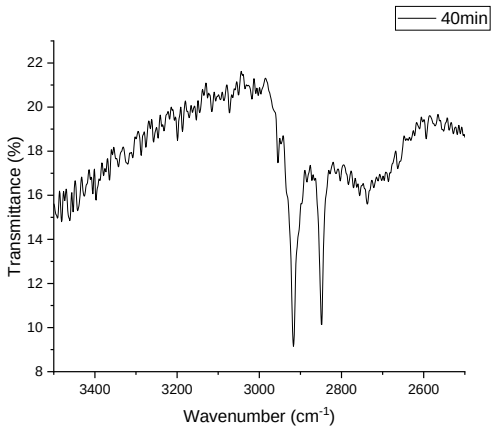

A: 5.3 DRIFT spectra of stearic acid on and undoped *meso*-TiO_2 film prepared at 3000 rpm

These FTIR spectra show the C-H stretch of stearic acid that was used during photocatalytic testing to monitor the progress of the reaction with exposure to UV light. The total irradiation time is listed on each graph.

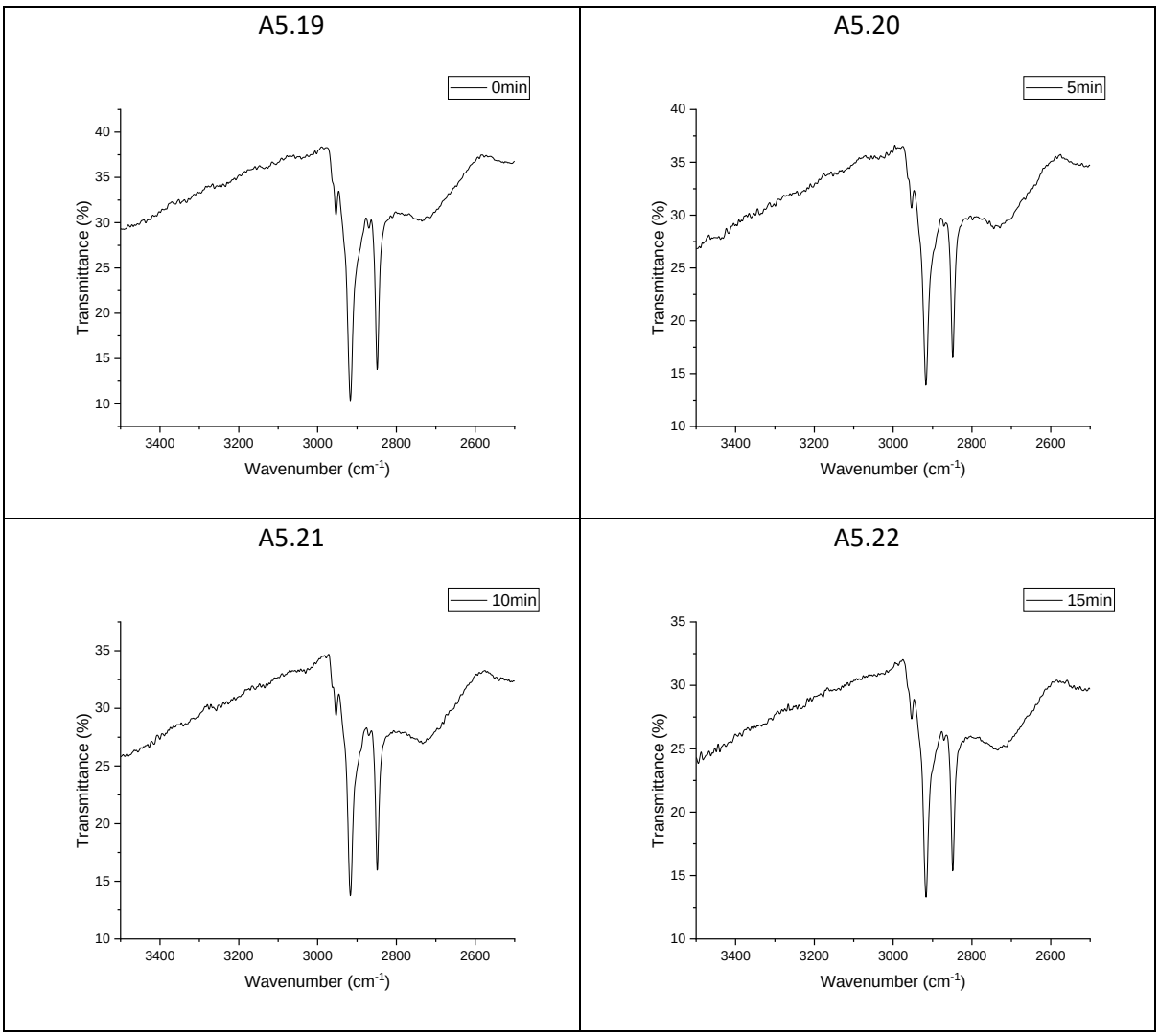

A5.23

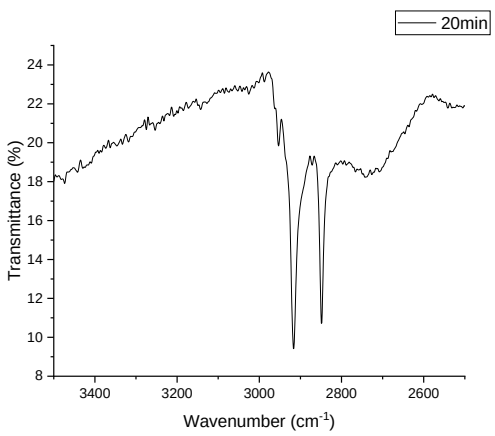

A5.24

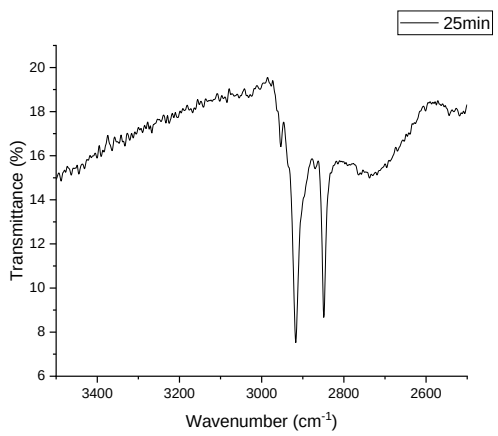

A5.25

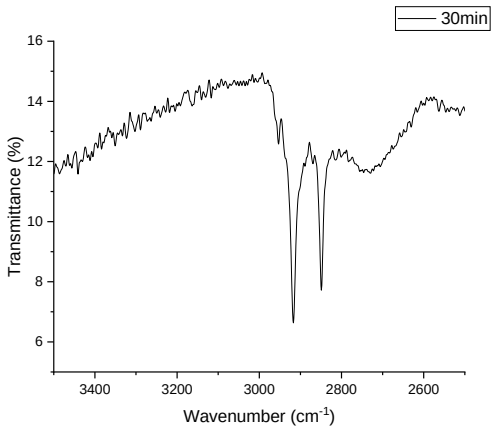

A5.26

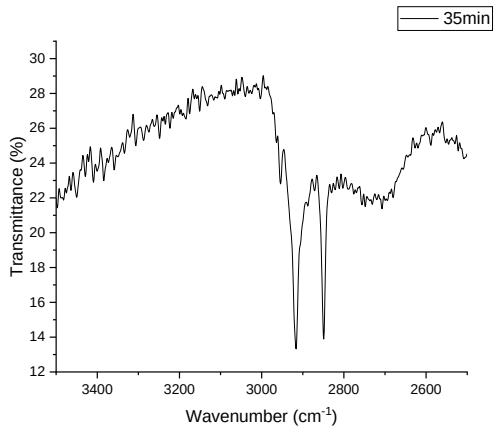

A5.27

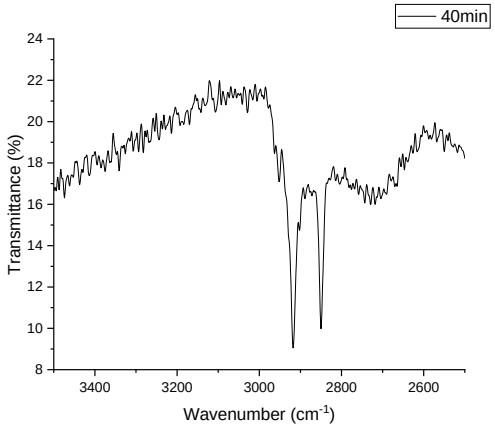

A: 5.4 DRIFT spectra of stearic acid on and undoped *meso*-TiO_2 film prepared at 4000 rpm

These FTIR spectra show the C-H stretch of stearic acid that was used during photocatalytic testing to monitor the progress of the reaction with exposure to UV light. The total irradiation time is listed on each graph.

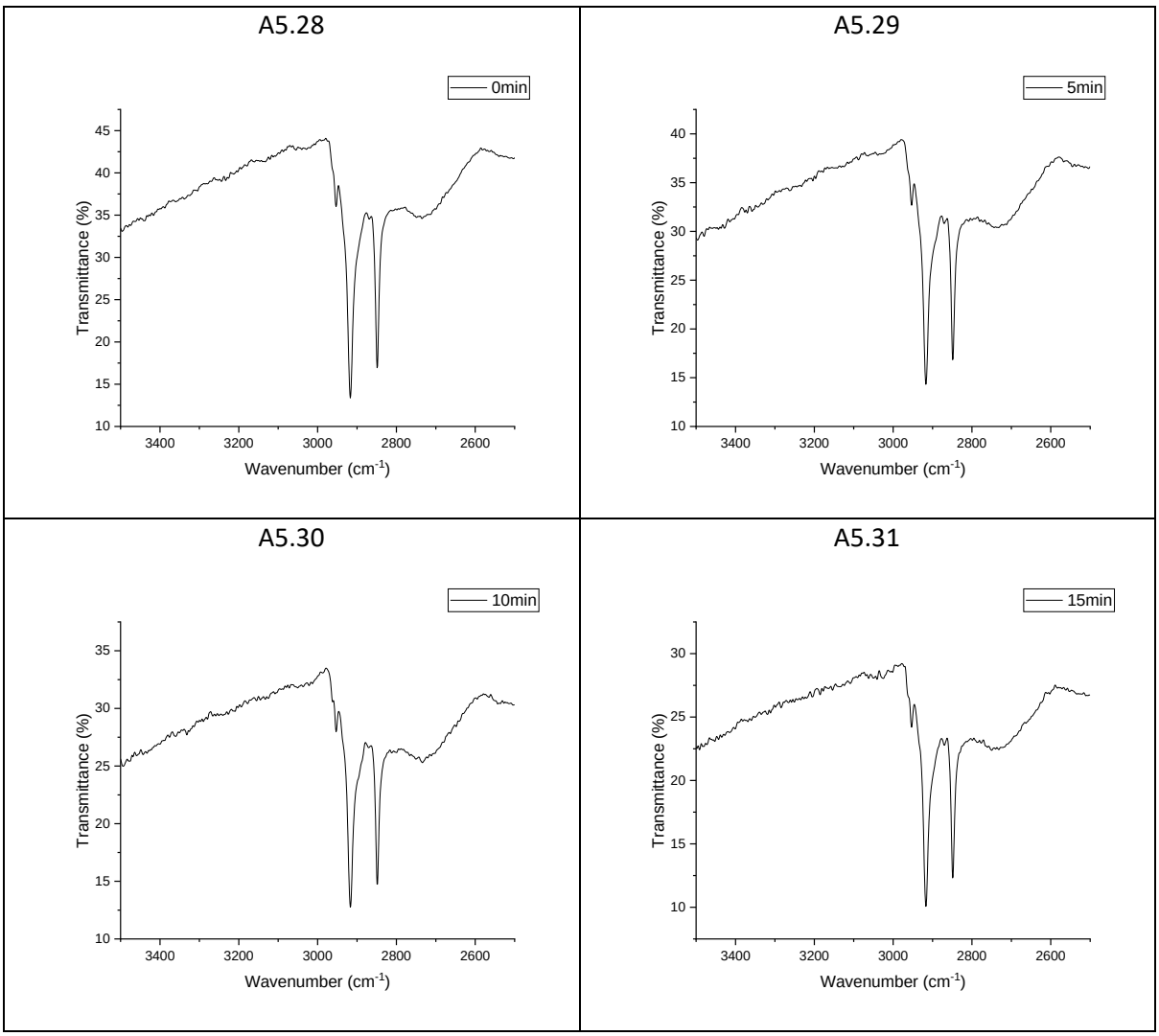

A5.32

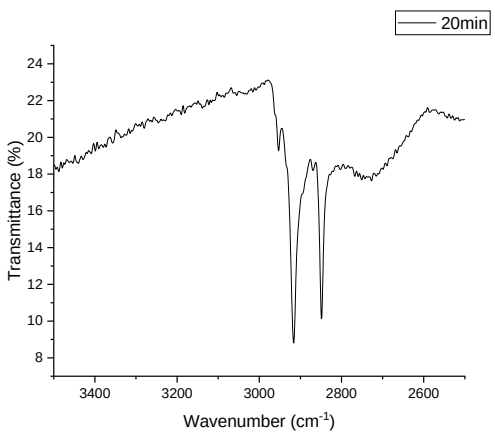

A5.33

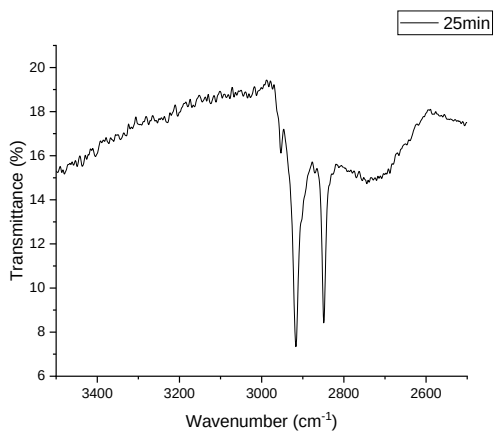

A5.34

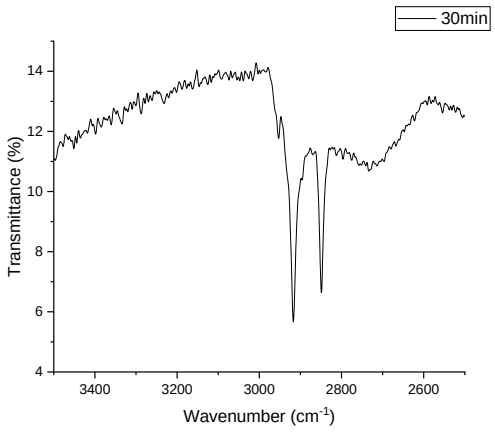

A5.35

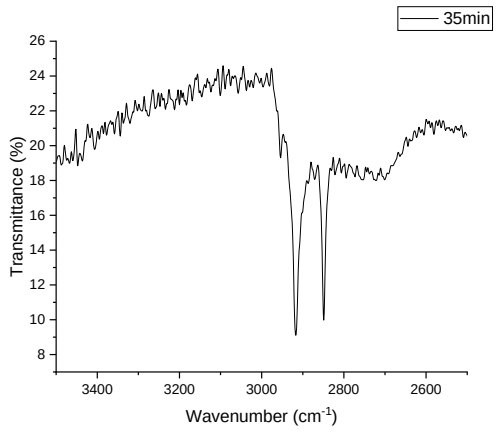

A5.36

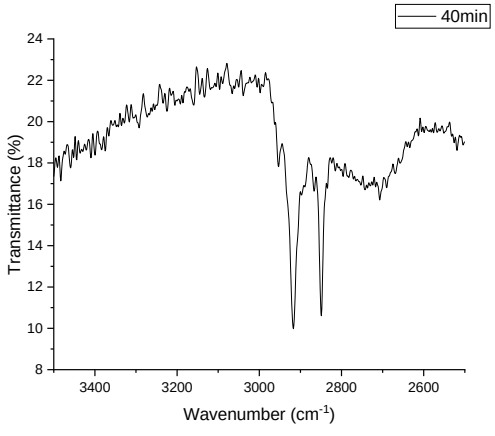

A: 5.5 DRIFT spectra of stearic acid on and undoped *meso*-TiO_2 film prepared at 5000 rpm

These FTIR spectra show the C-H stretch of stearic acid that was used during photocatalytic testing to monitor the progress of the reaction with exposure to UV light. The total irradiation time is listed on each graph.

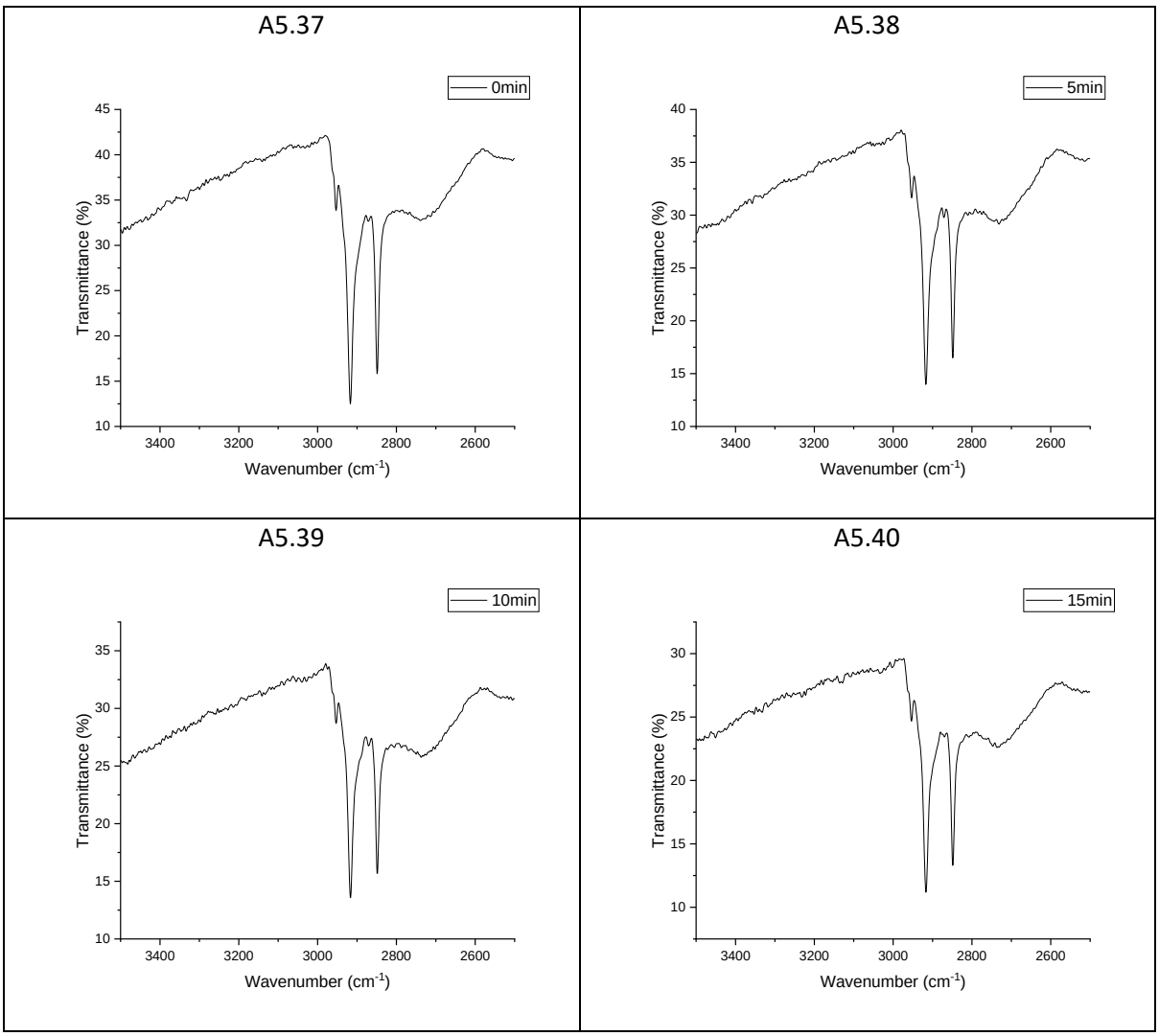

A5.41

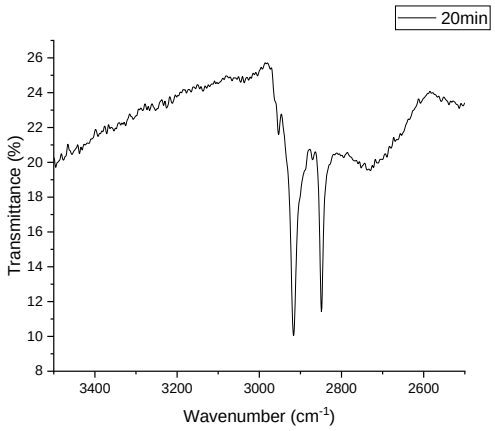

A5.42

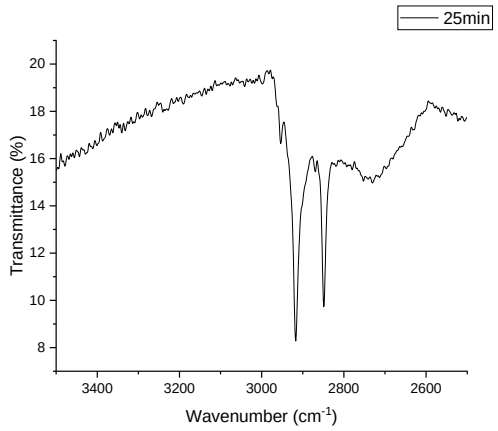

A5.43

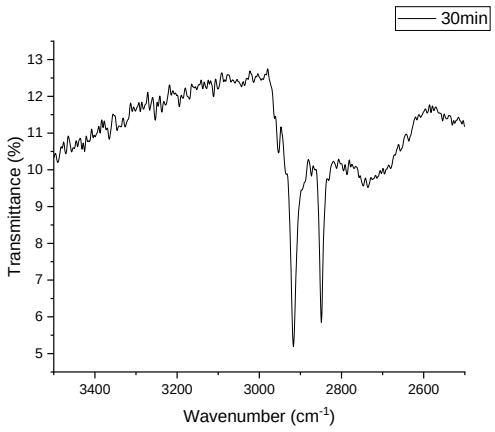

A5.44

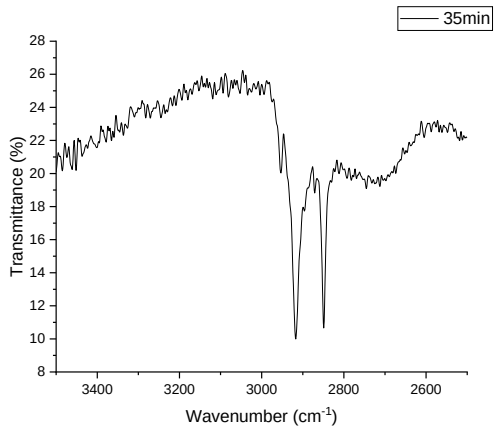

A5.45

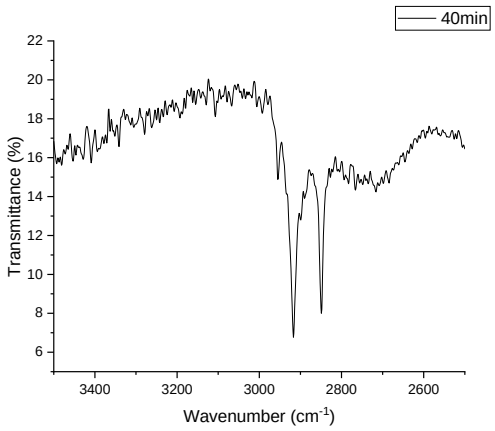

A: 5.6 DRIFT spectra of stearic acid on and undoped *meso*-TiO_2 film prepared at 6000 rpm

These FTIR spectra show the C-H stretch of stearic acid that was used during photocatalytic testing to monitor the progress of the reaction with exposure to UV light. The total irradiation time is listed on each graph.

A5.46

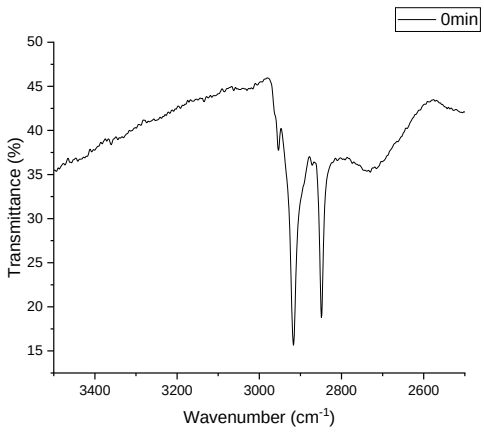

A5.47

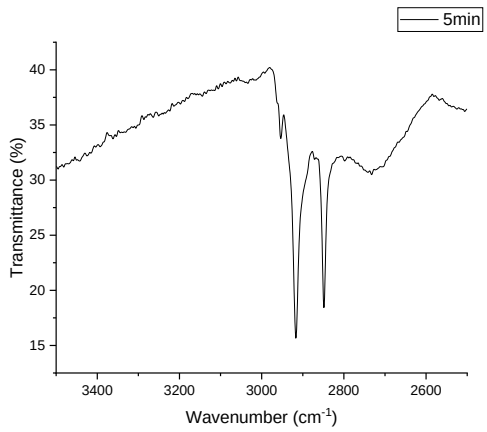

A5.48

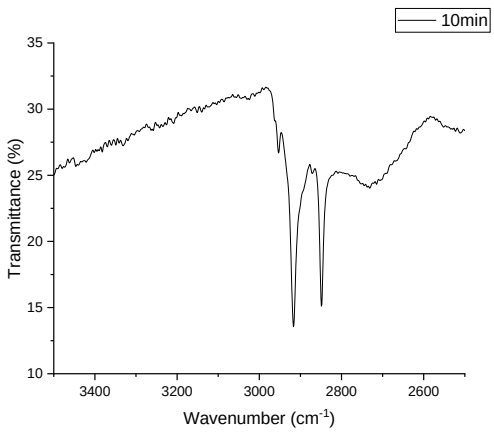

A5.49

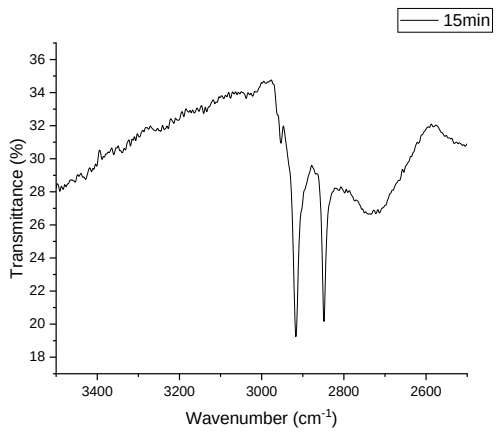

A5.50

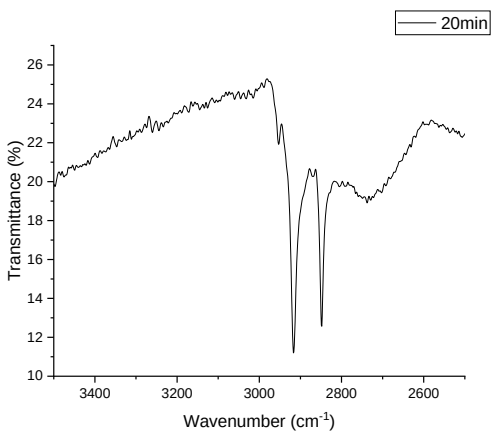

A5.51

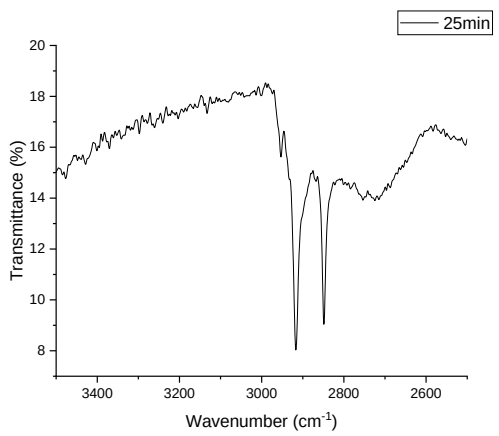

A5.52

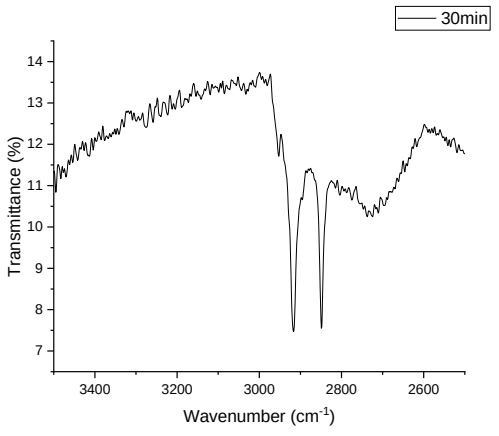

A5.53

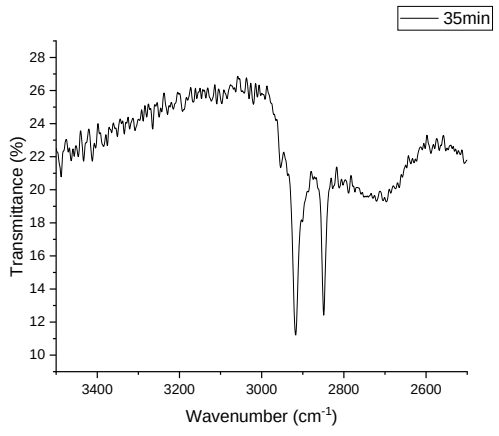

A5.54

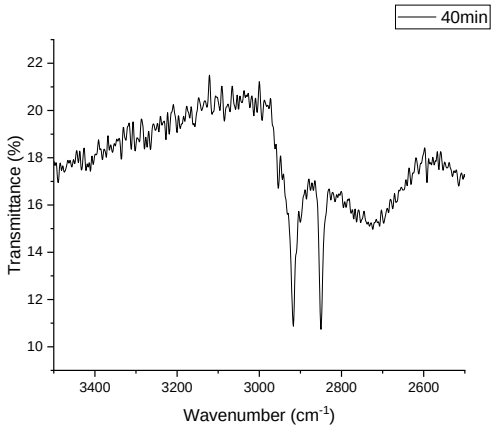

A: 5.7 DRIFT spectra of stearic acid on and undoped *meso*-TiO_2 film prepared at 7000 rpm

These FTIR spectra show the C-H stretch of stearic acid that was used during photocatalytic testing to monitor the progress of the reaction with exposure to UV light. The total irradiation time is listed on each graph.

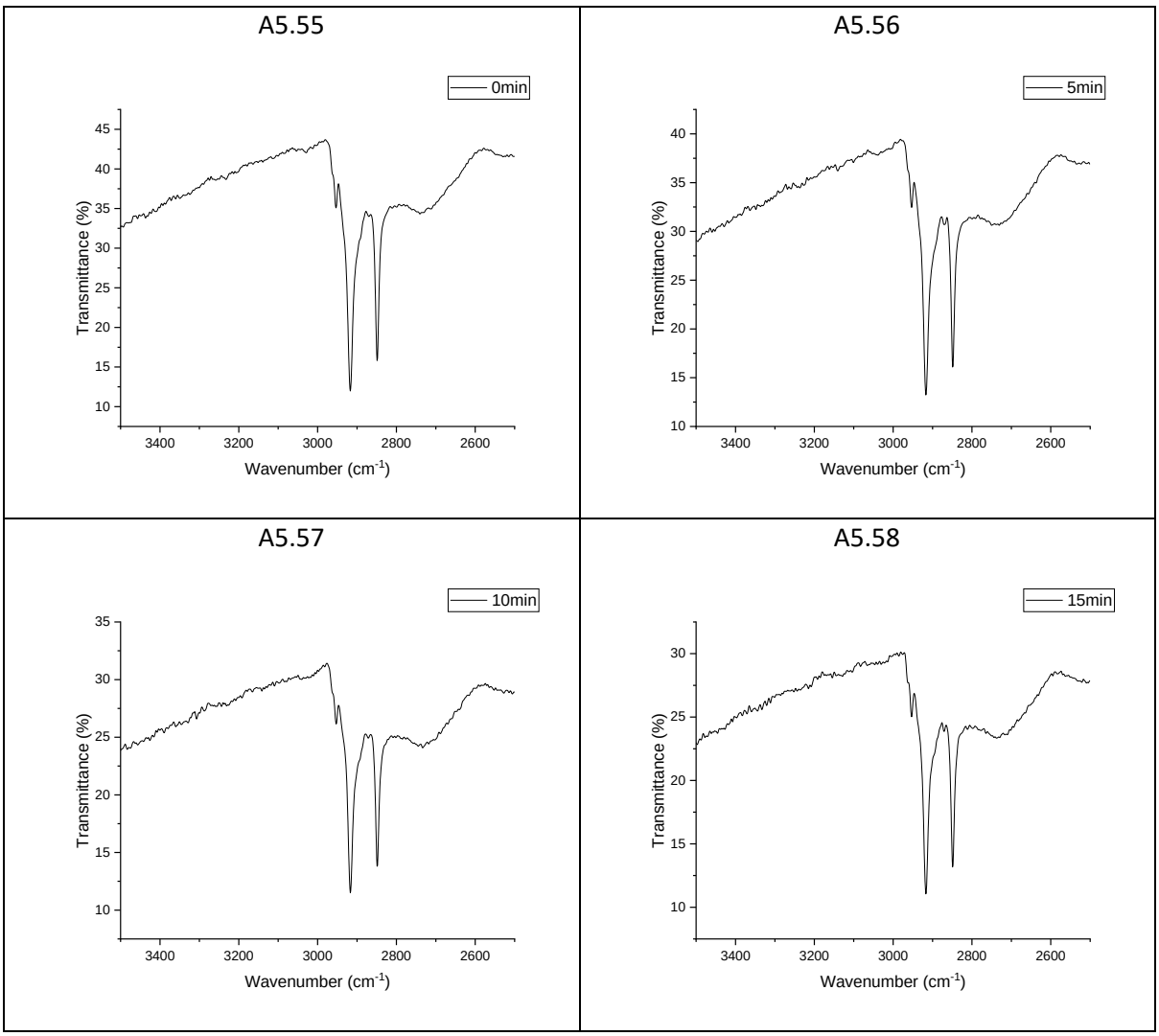

A5.59

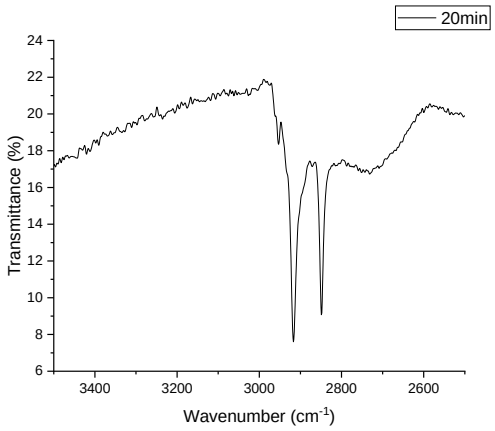

A5.60

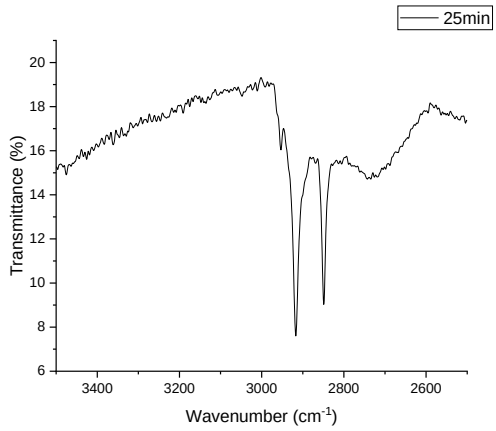

A5.61

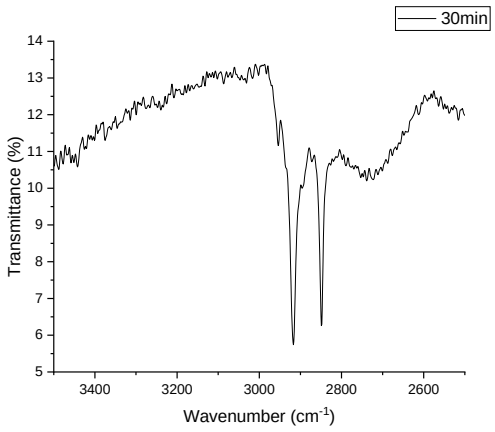

A5.62

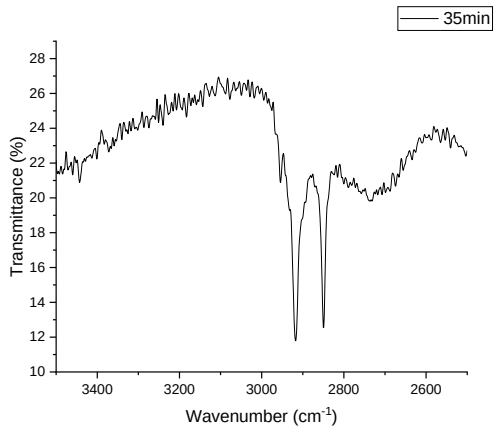

A5.63

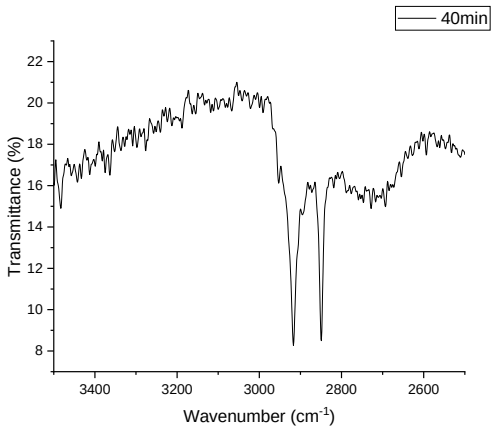

A: 5.8 DRIFT spectra of stearic acid on and undoped *meso*-TiO_2 film prepared at 8000 rpm

These FTIR spectra show the C-H stretch of stearic acid that was used during photocatalytic testing to monitor the progress of the reaction with exposure to UV light. The total irradiation time is listed on each graph.

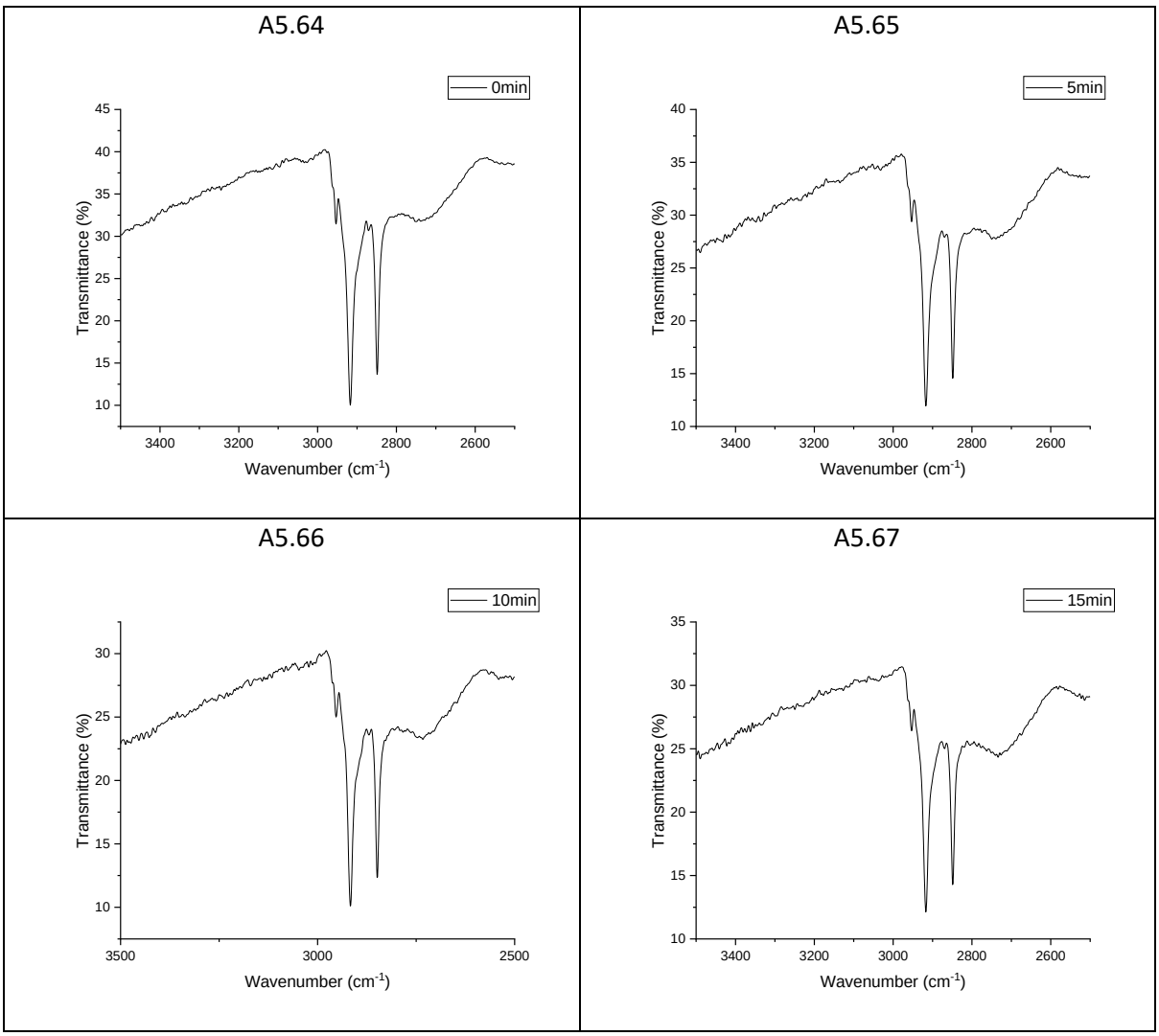

A5.68

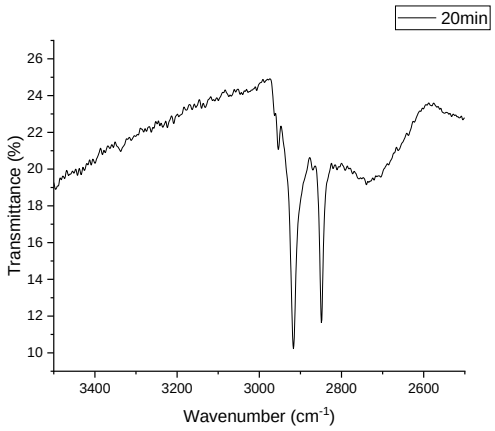

A5.69

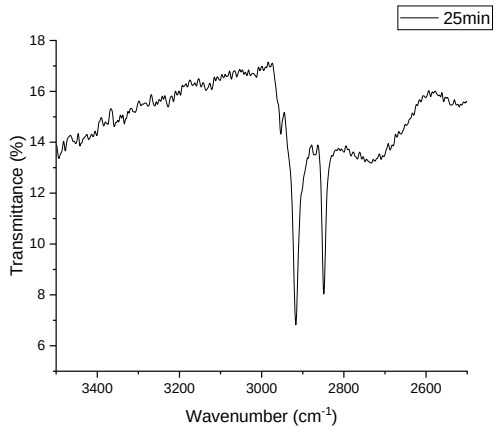

A5.70

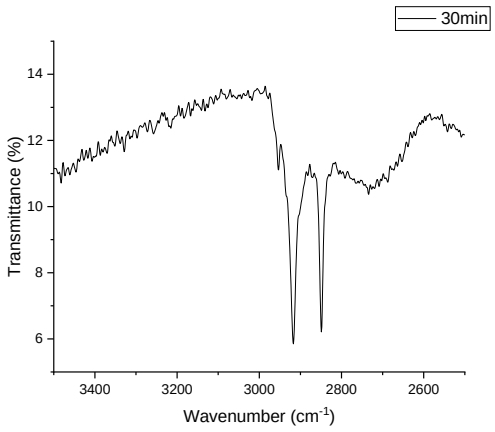

A5.71

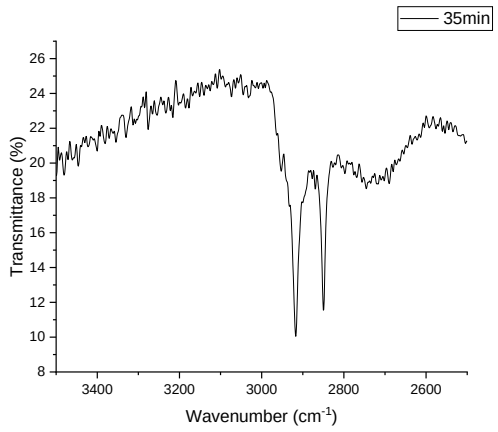

A5.72

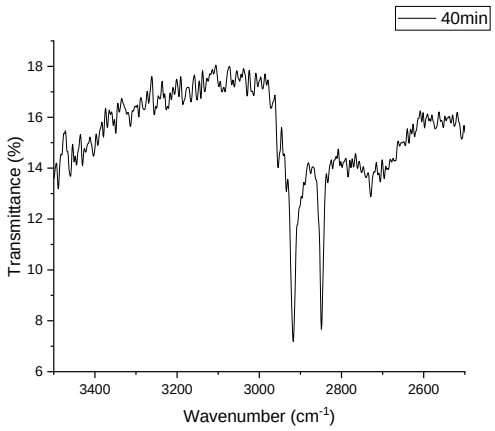

A: 5.9 DRIFT spectra of stearic acid on a 5 wt% Cu-doped *meso*-TiO_2 film prepared at 500 rpm

These FTIR spectra show the C-H stretch of stearic acid that was used during photocatalytic testing to monitor the progress of the reaction with exposure to UV light. The total irradiation time is listed on each graph.

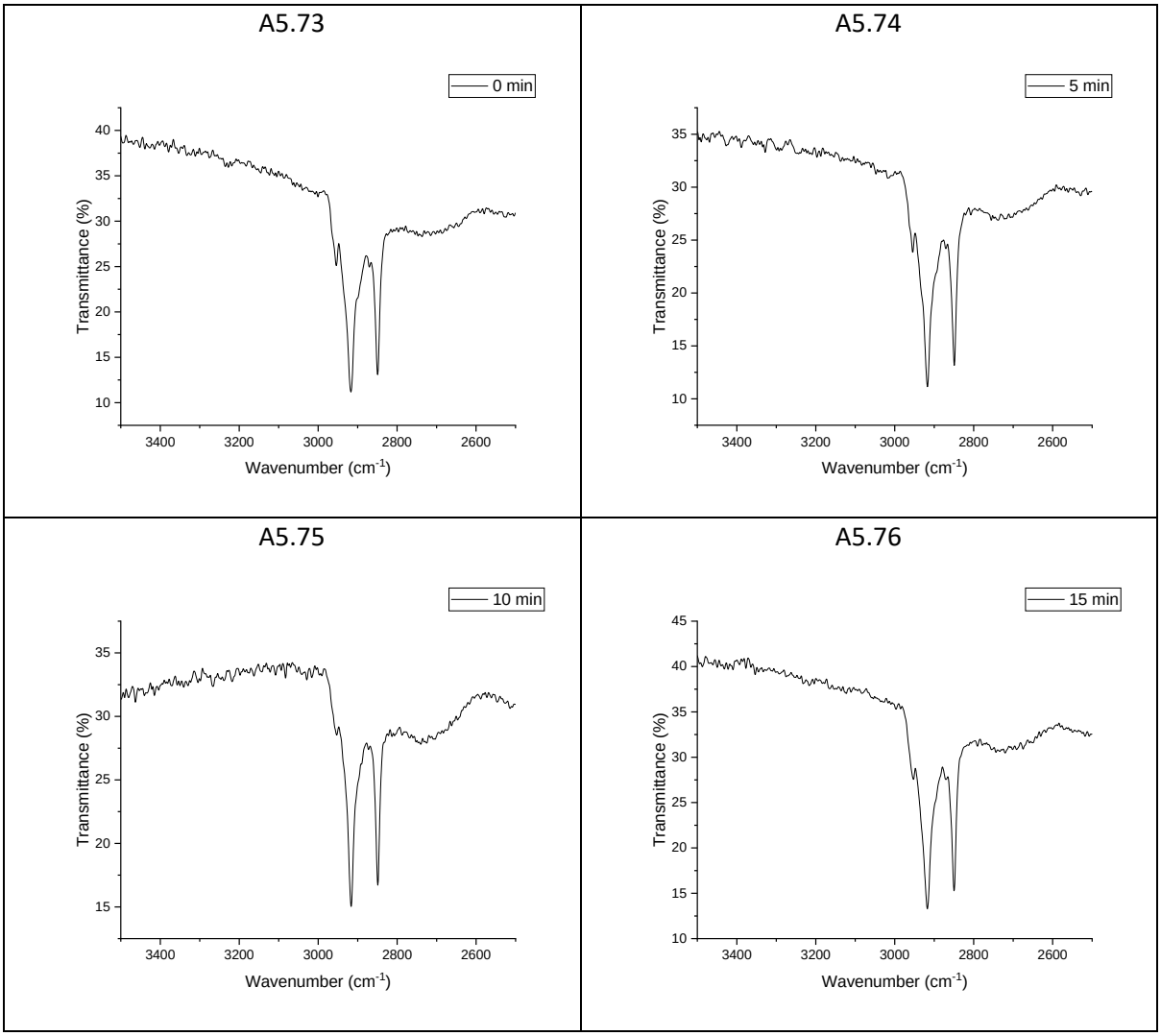

A5.77

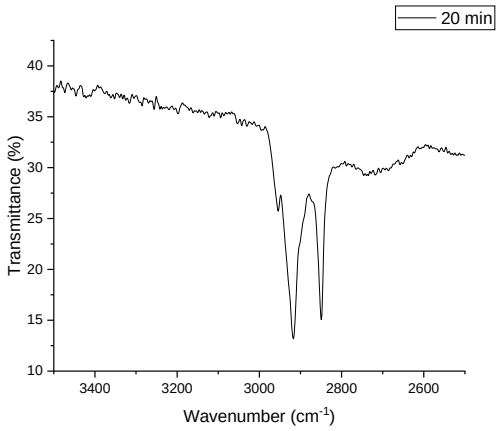

A5.78

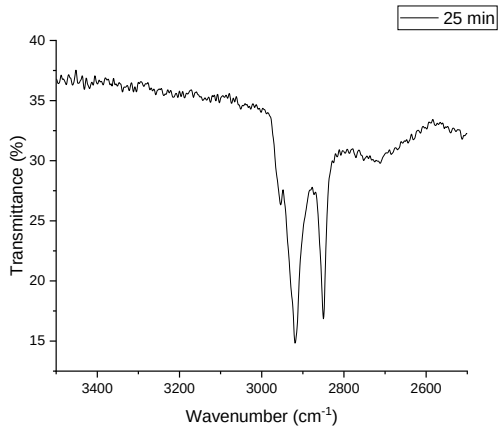

A5.79

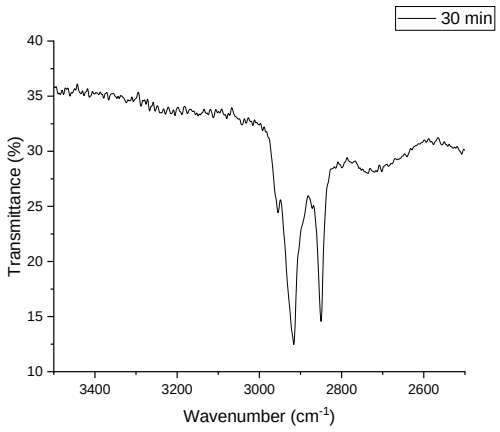

A5.80

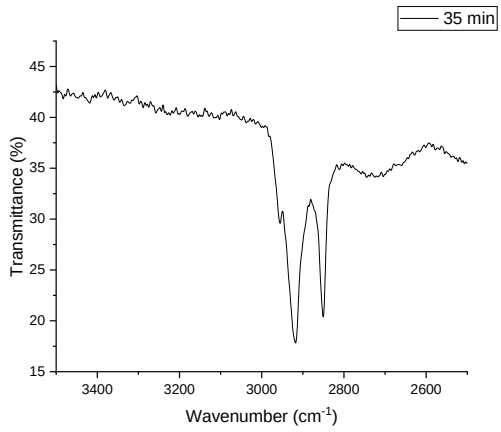

A5.81

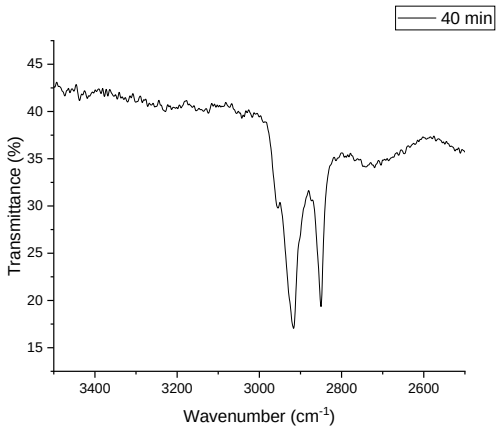

A: 5.10 DRIFT spectra of stearic acid on a 5 wt% Cu-doped *meso*-TiO_2 film prepared at 1000 rpm

These FTIR spectra show the C-H stretch of stearic acid that was used during photocatalytic testing to monitor the progress of the reaction with exposure to UV light. The total irradiation time is listed on each graph.

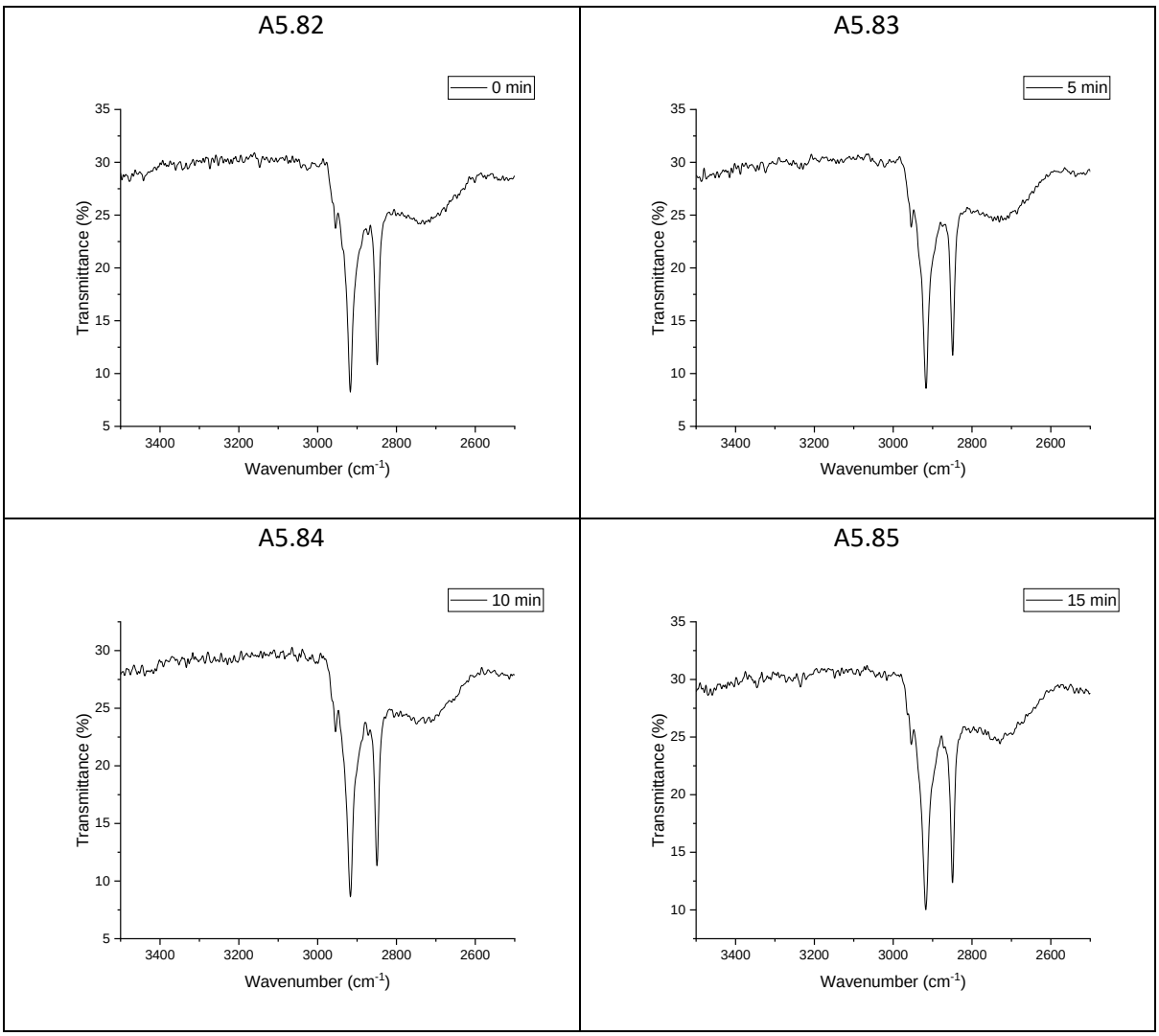

A5.86

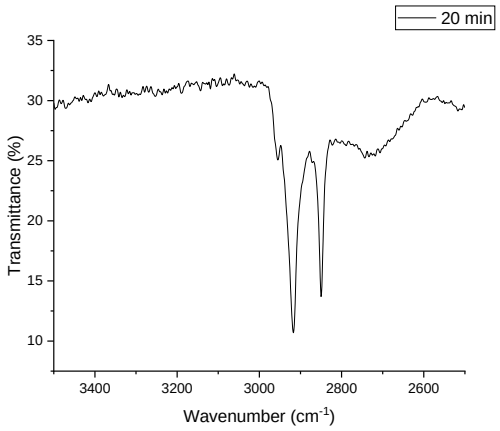

A5.87

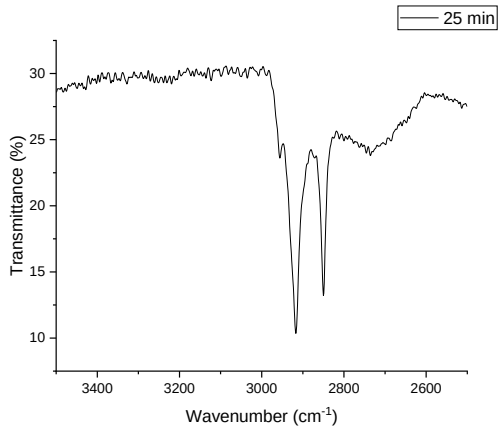

A5.88

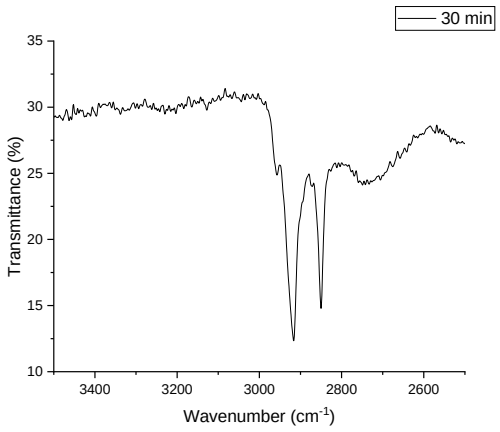

A5.89

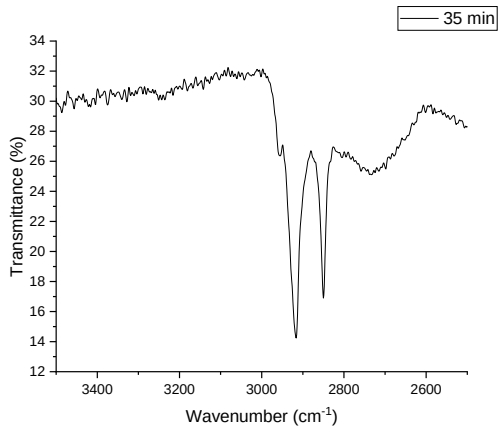

A5.90

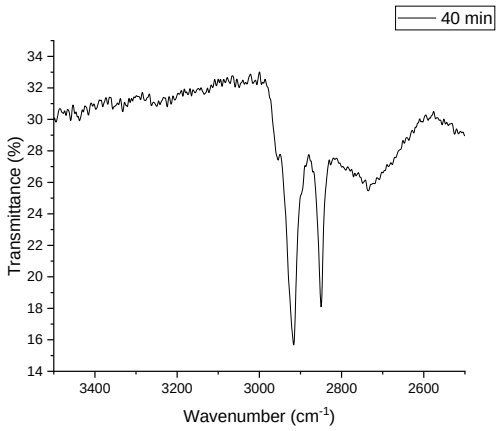

A: 5.11 DRIFT spectra of stearic acid on a 5 wt% Cu-doped *meso*-TiO_2 film prepared at 2000 rpm

These FTIR spectra show the C-H stretch of stearic acid that was used during photocatalytic testing to monitor the progress of the reaction with exposure to UV light. The total irradiation time is listed on each graph.

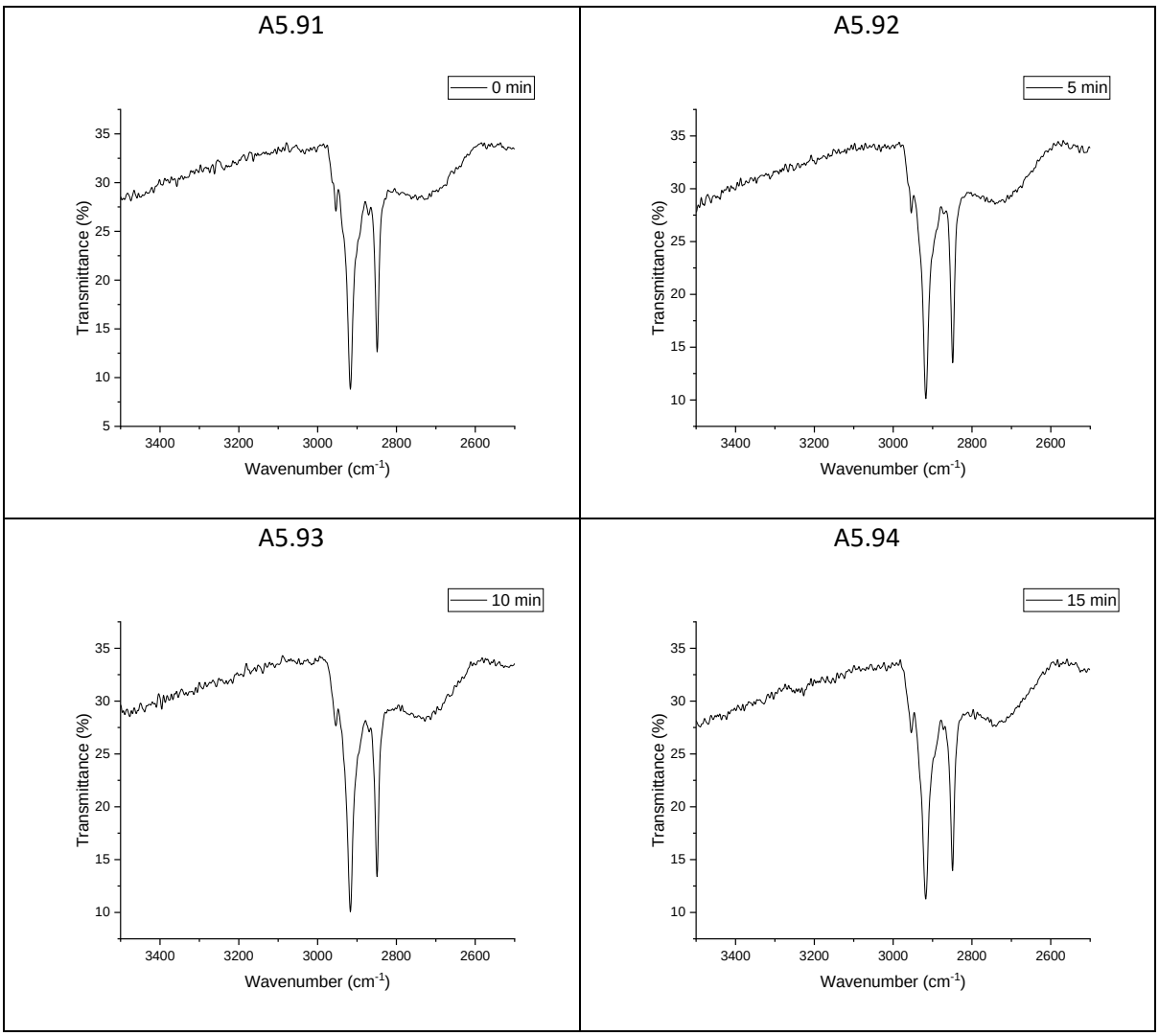

A5.95

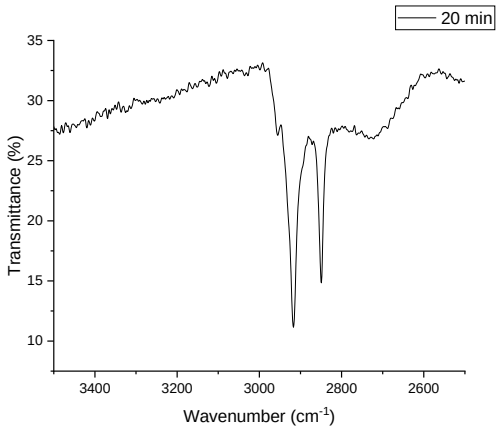

A5.96

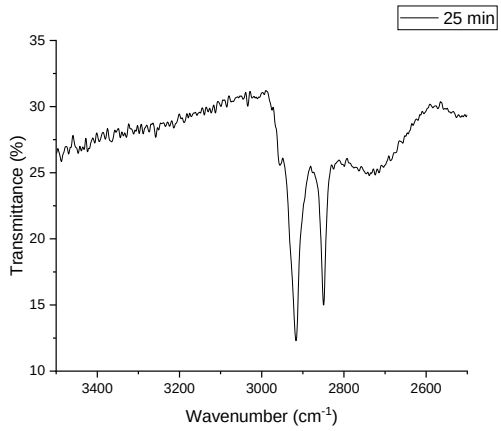

A5.97

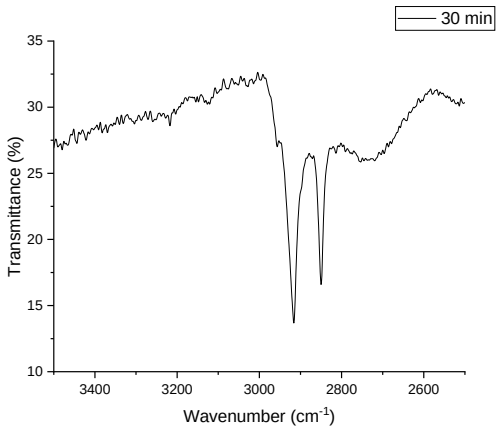

A5.98

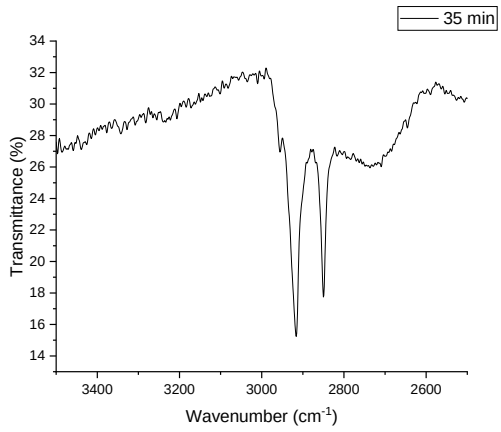

A5.99

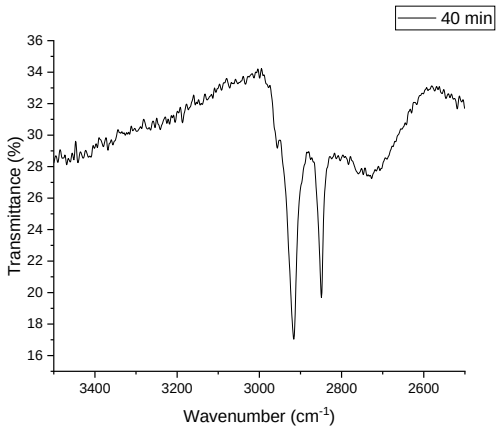

A: 5.12 DRIFT spectra of stearic acid on a 5 wt% Cu-doped *meso*-TiO_2 film prepared at 3000 rpm

These FTIR spectra show the C-H stretch of stearic acid that was used during photocatalytic testing to monitor the progress of the reaction with exposure to UV light. The total irradiation time is listed on each graph.

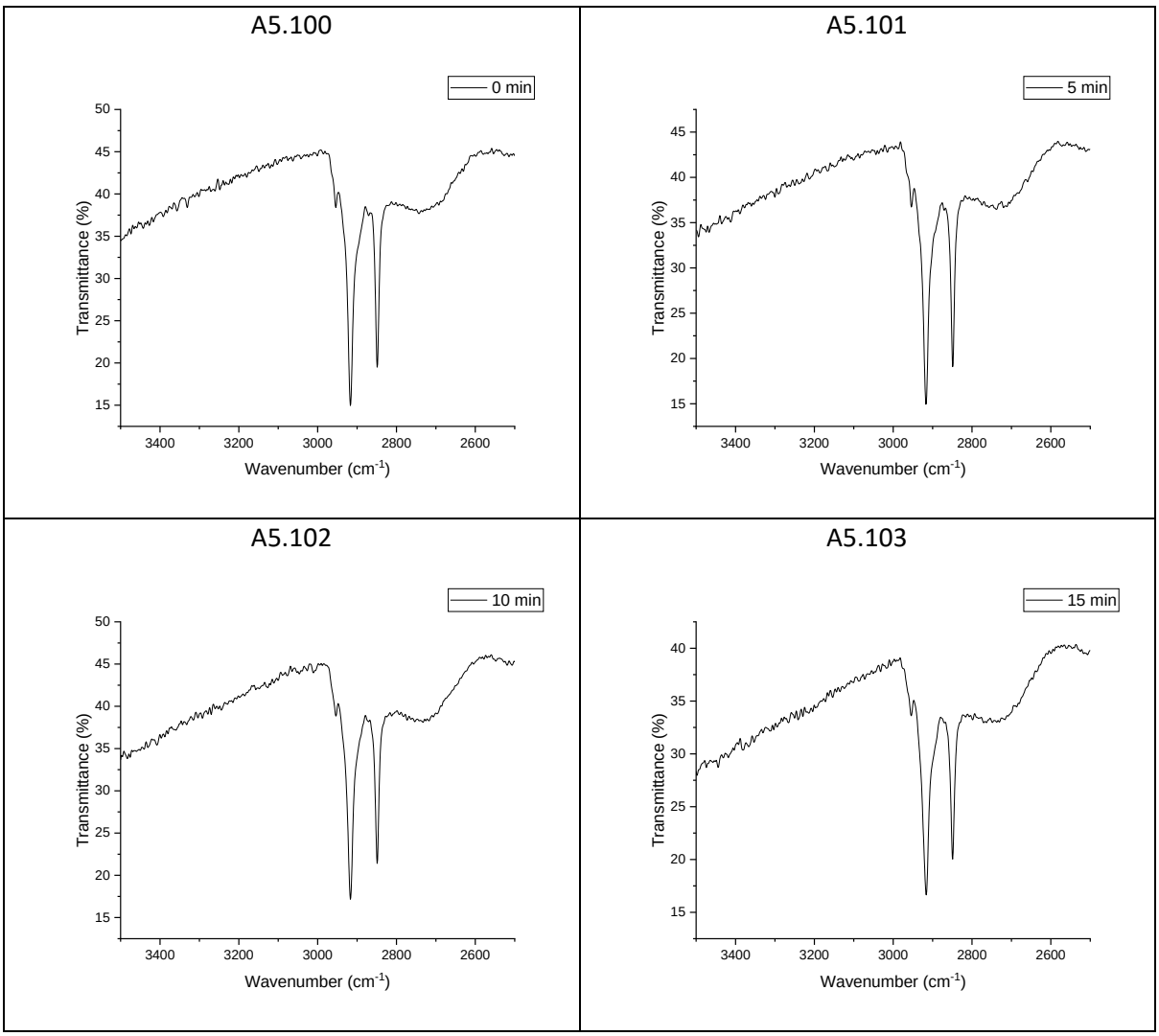

A5.104

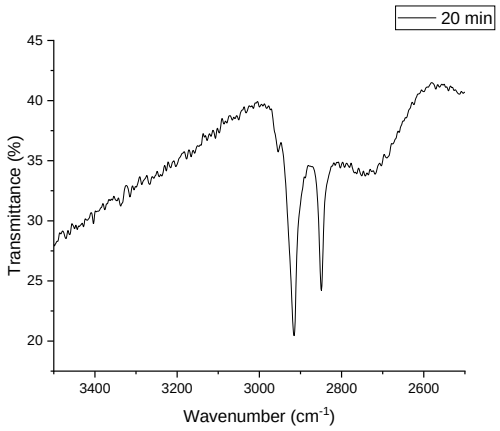

A5.105

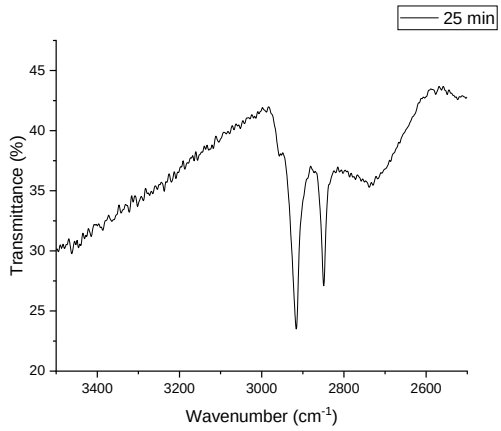

A5.106

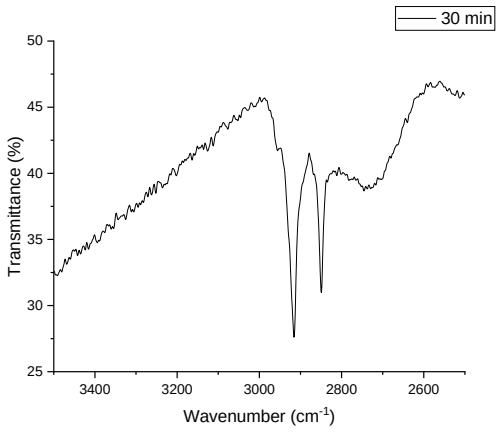

A5.107

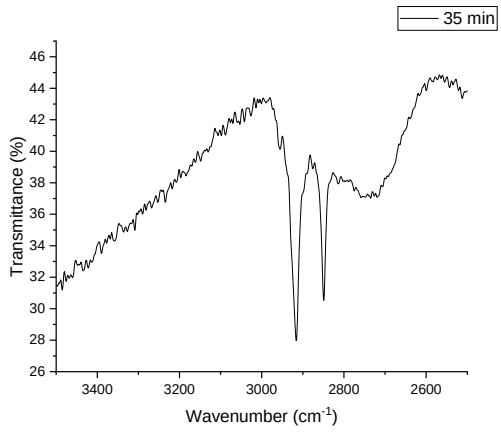

A5.108

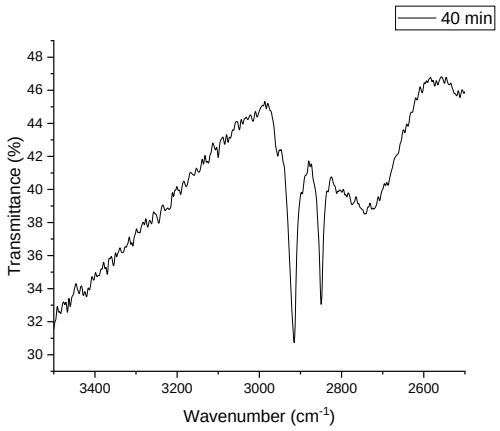

A: 5.13 DRIFT spectra of stearic acid on a 5 wt% Cu-doped *meso*-TiO_2 film prepared at 4000 rpm

These FTIR spectra show the C-H stretch of stearic acid that was used during photocatalytic testing to monitor the progress of the reaction with exposure to UV light. The total irradiation time is listed on each graph.

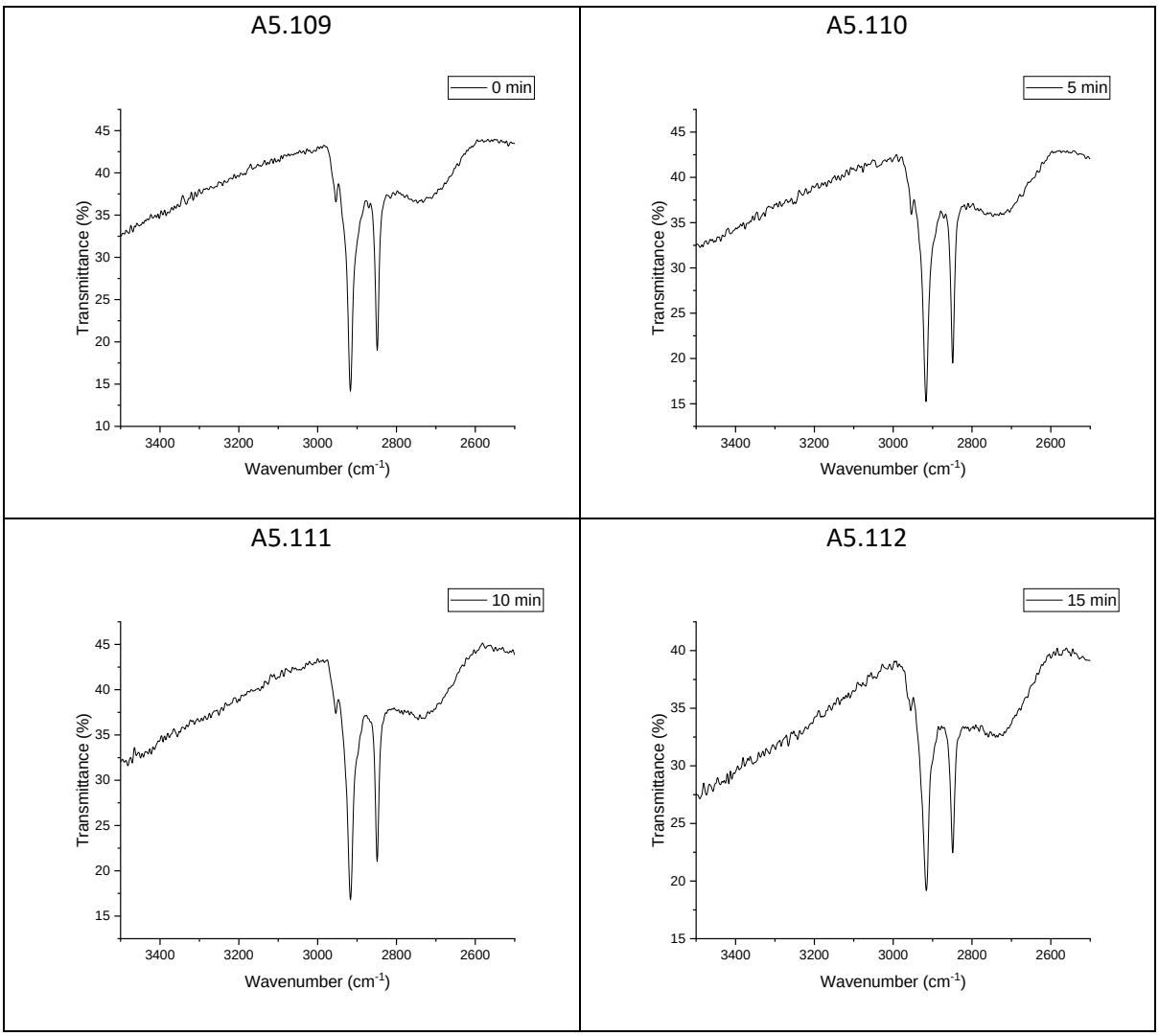

A5.113

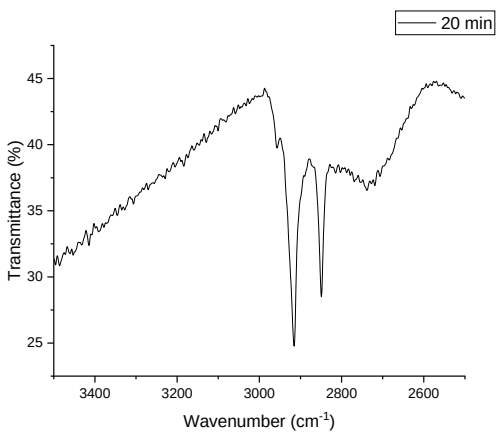

A5.114

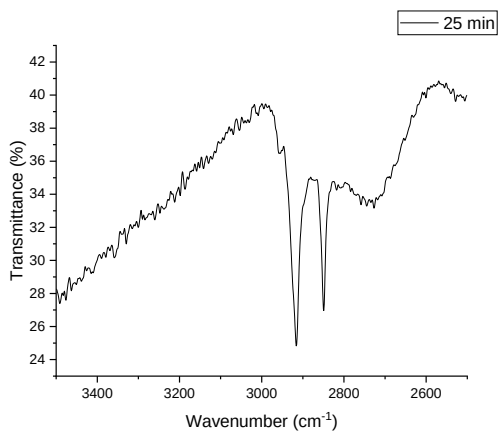

A5.115

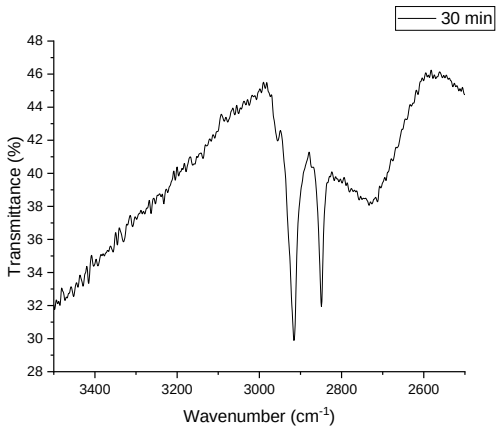

A5.116

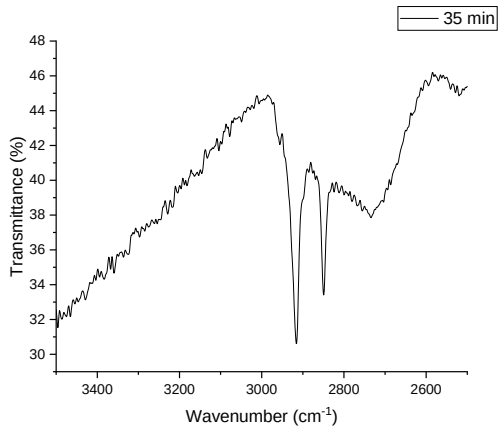

A5.117

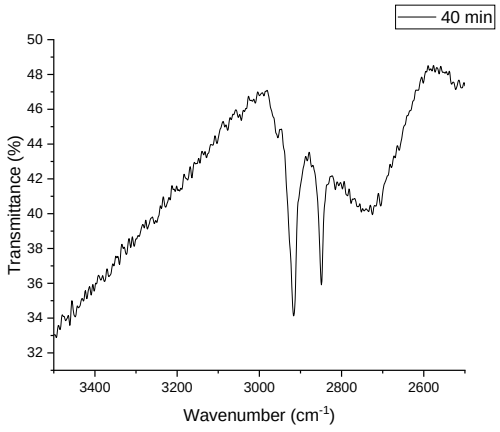

A: 5.14 DRIFT spectra of stearic acid on a 5 wt% Cu-doped *meso*-TiO_2 film prepared at 5000 rpm

These FTIR spectra show the C-H stretch of stearic acid that was used during photocatalytic testing to monitor the progress of the reaction with exposure to UV light. The total irradiation time is listed on each graph.

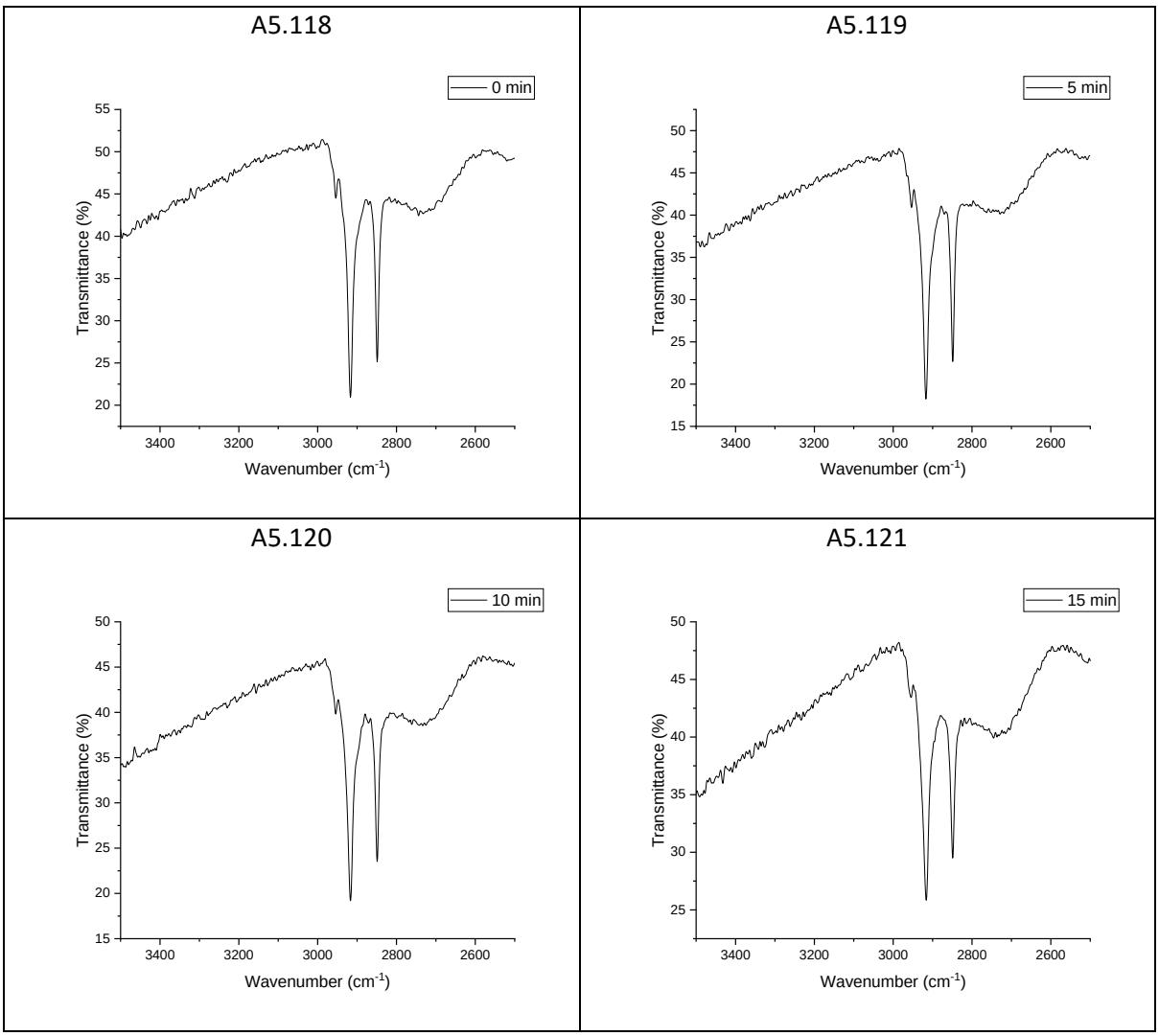

A5.122

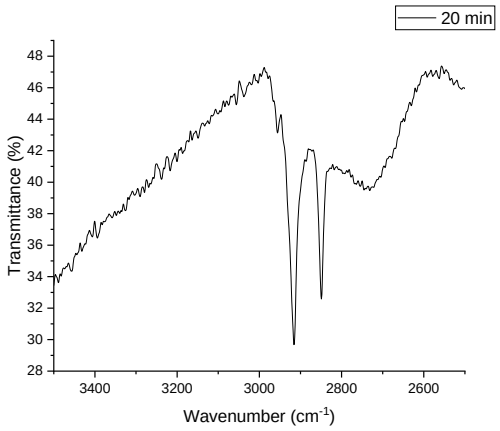

A5.123

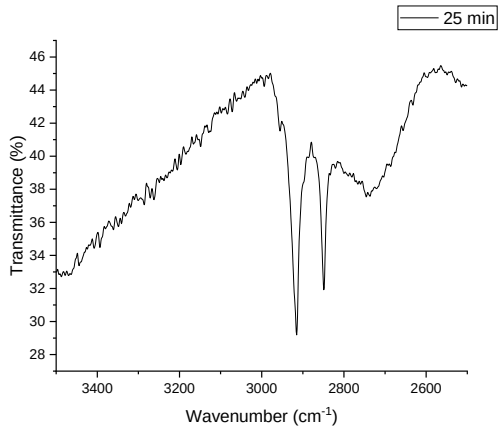

A5.124

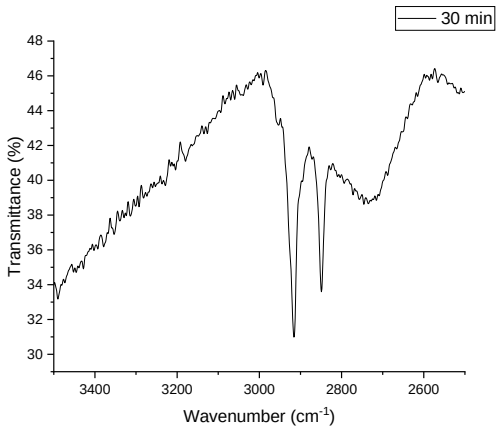

A5.125

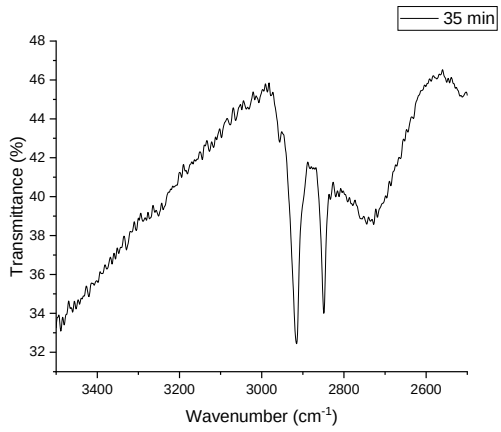

A5.126

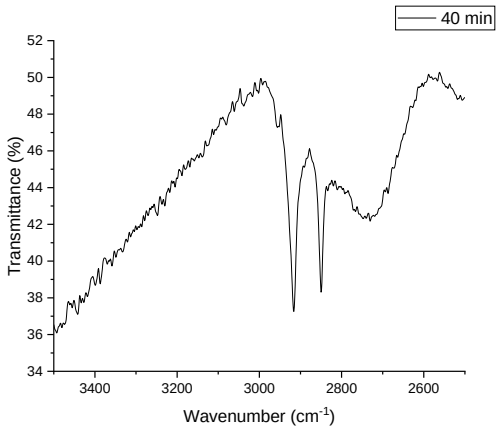

A: 5.15 DRIFT spectra of stearic acid on a 5 wt% Cu-doped *meso*-TiO_2 film prepared at 6000 rpm

These FTIR spectra show the C-H stretch of stearic acid that was used during photocatalytic testing to monitor the progress of the reaction with exposure to UV light. The total irradiation time is listed on each graph.

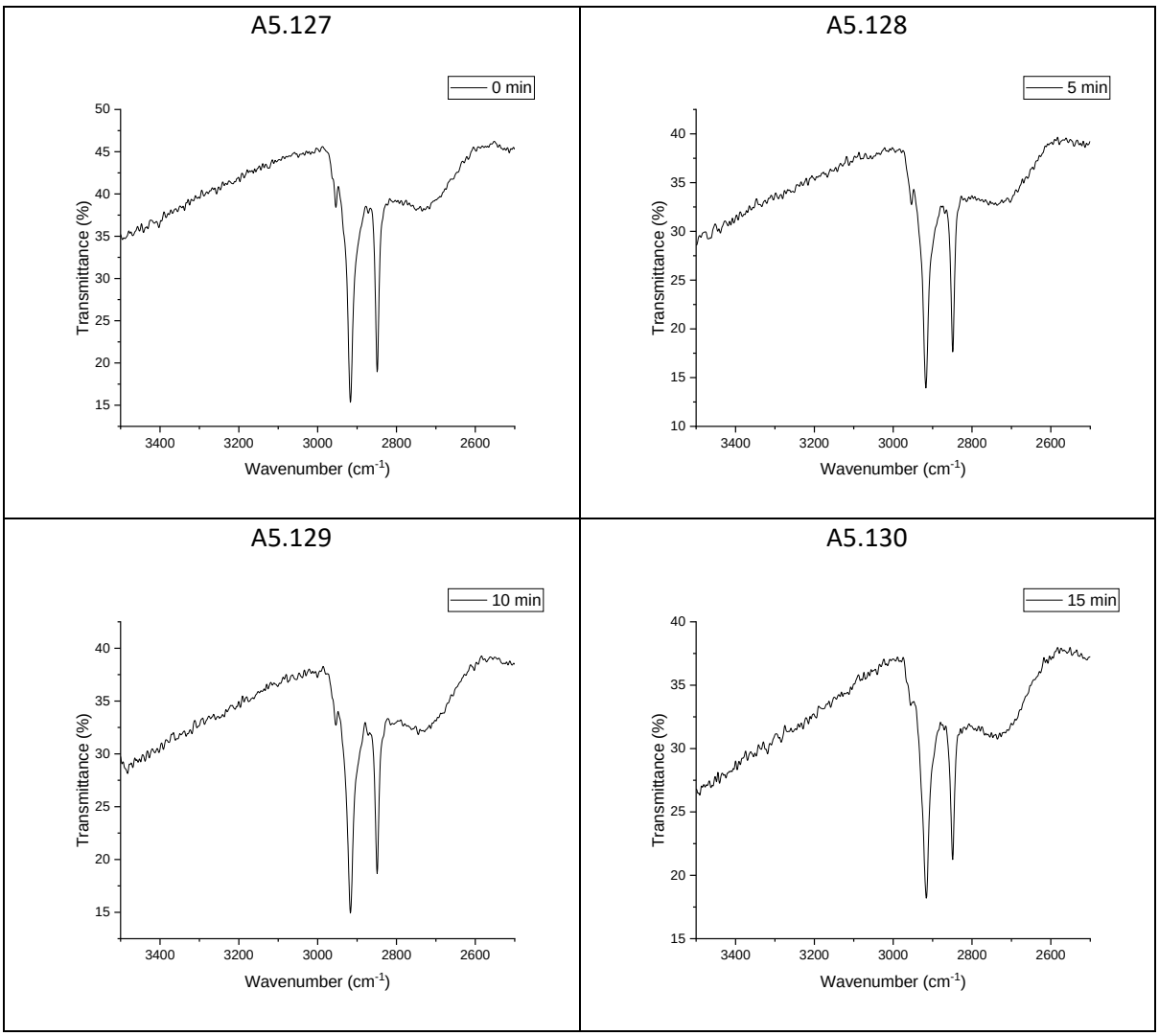

A5.131

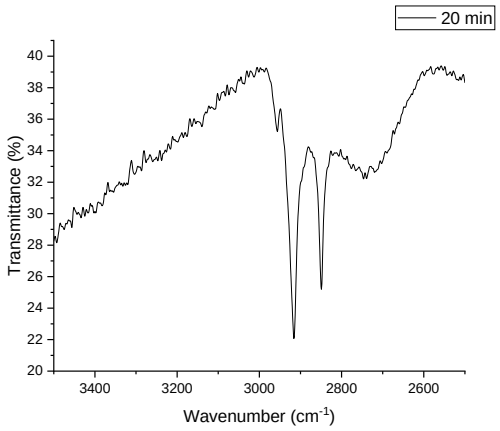

A5.132

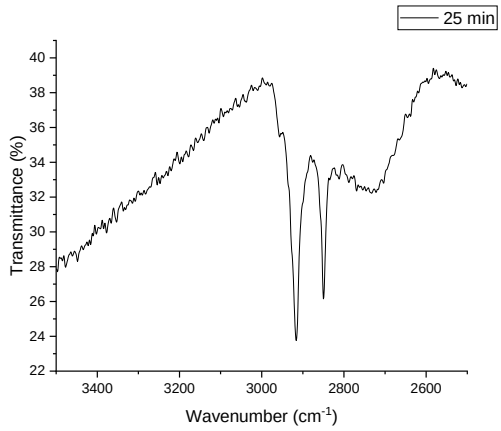

A5.133

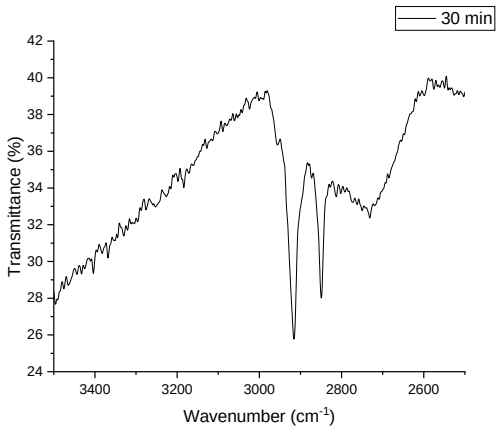

A5.134

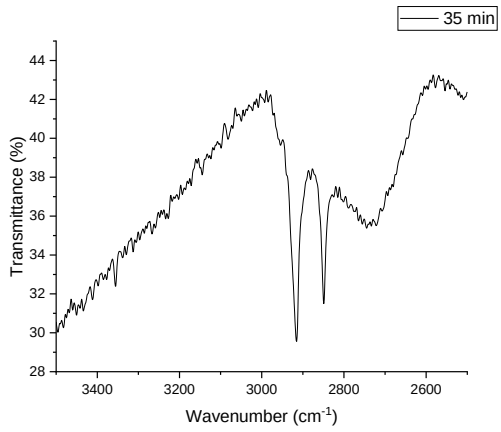

A5.135

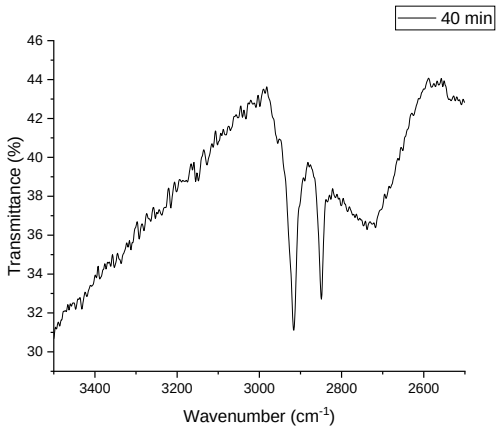

A: 5.16 DRIFT spectra of stearic acid on a 5 wt% Cu-doped *meso*-TiO_2 film prepared at 7000 rpm

These FTIR spectra show the C-H stretch of stearic acid that was used during photocatalytic testing to monitor the progress of the reaction with exposure to UV light. The total irradiation time is listed on each graph.

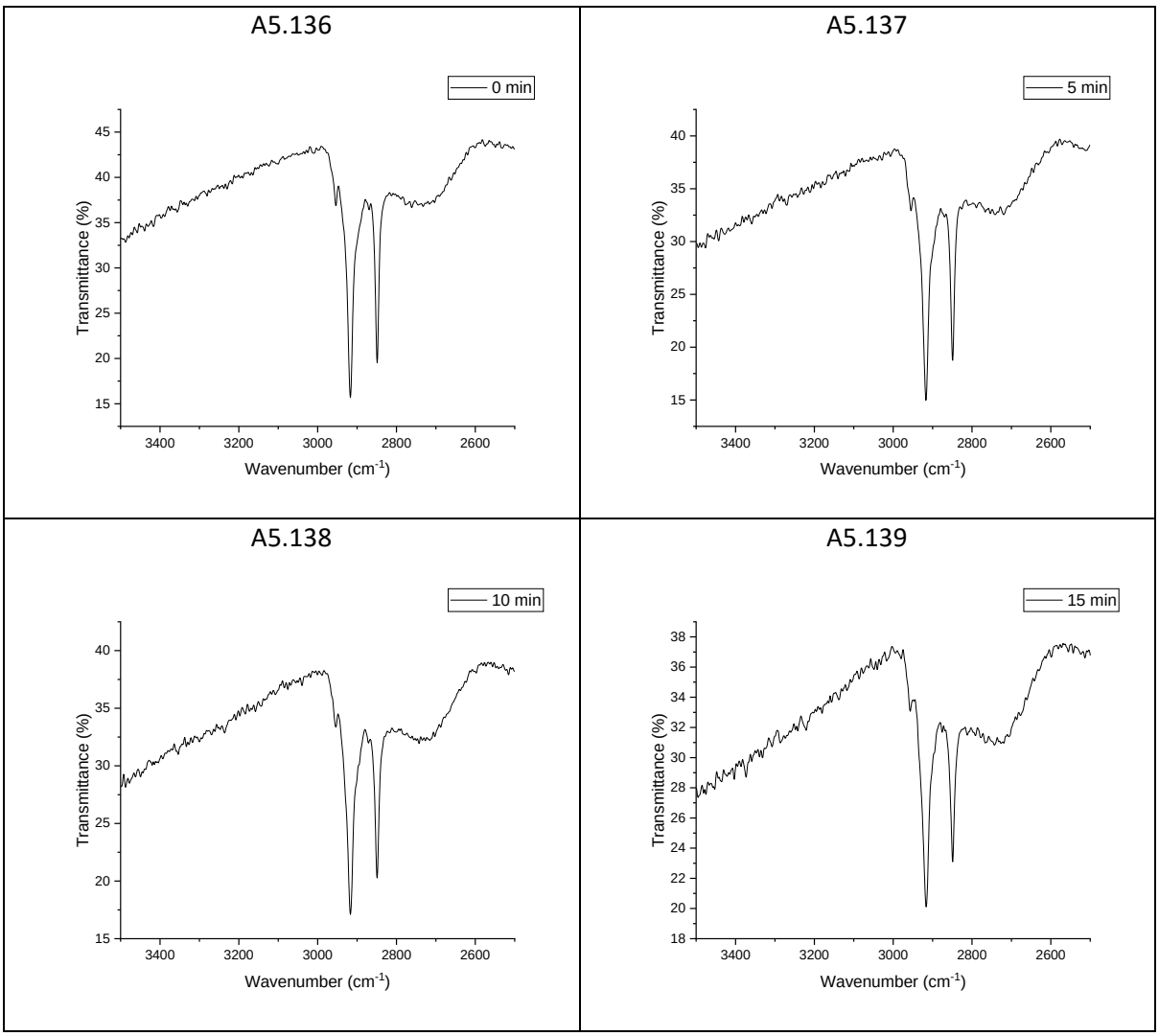

A5.140

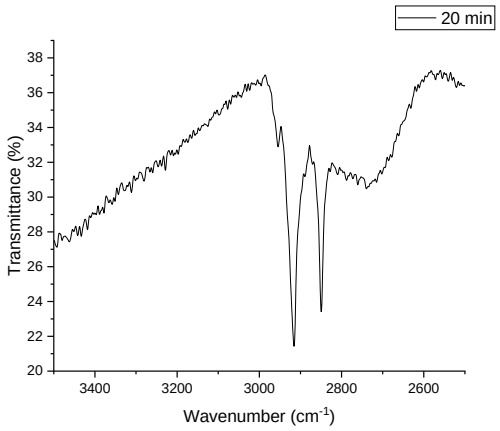

A5.141

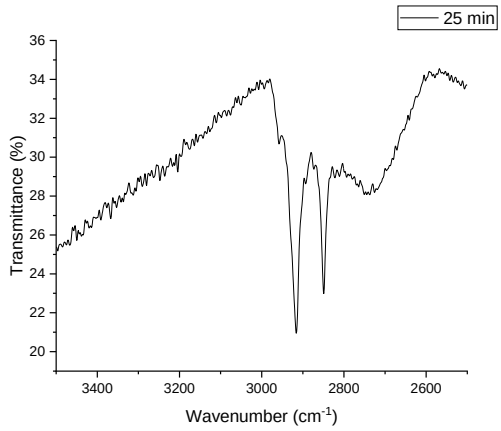

A5.142

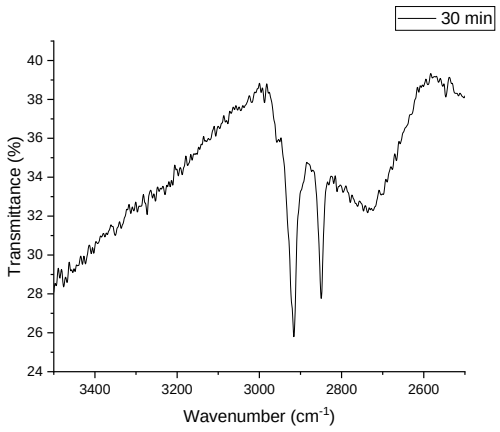

A5.143

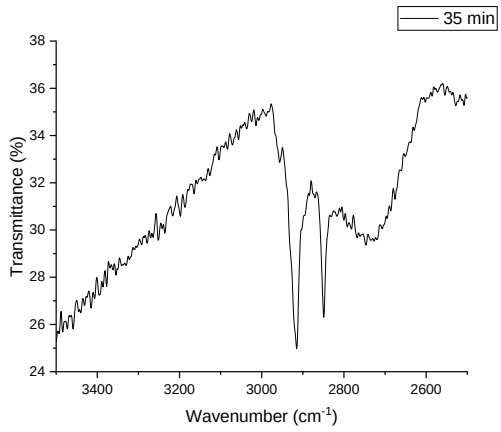

A5.144

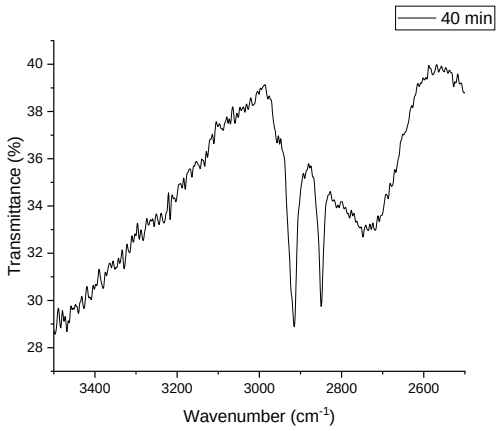

A: 5.17 DRIFT spectra of stearic acid on a 5 wt% Cu-doped *meso*-TiO_2 film prepared at 8000 rpm

These FTIR spectra show the C-H stretch of stearic acid that was used during photocatalytic testing to monitor the progress of the reaction with exposure to UV light. The total irradiation time is listed on each graph.

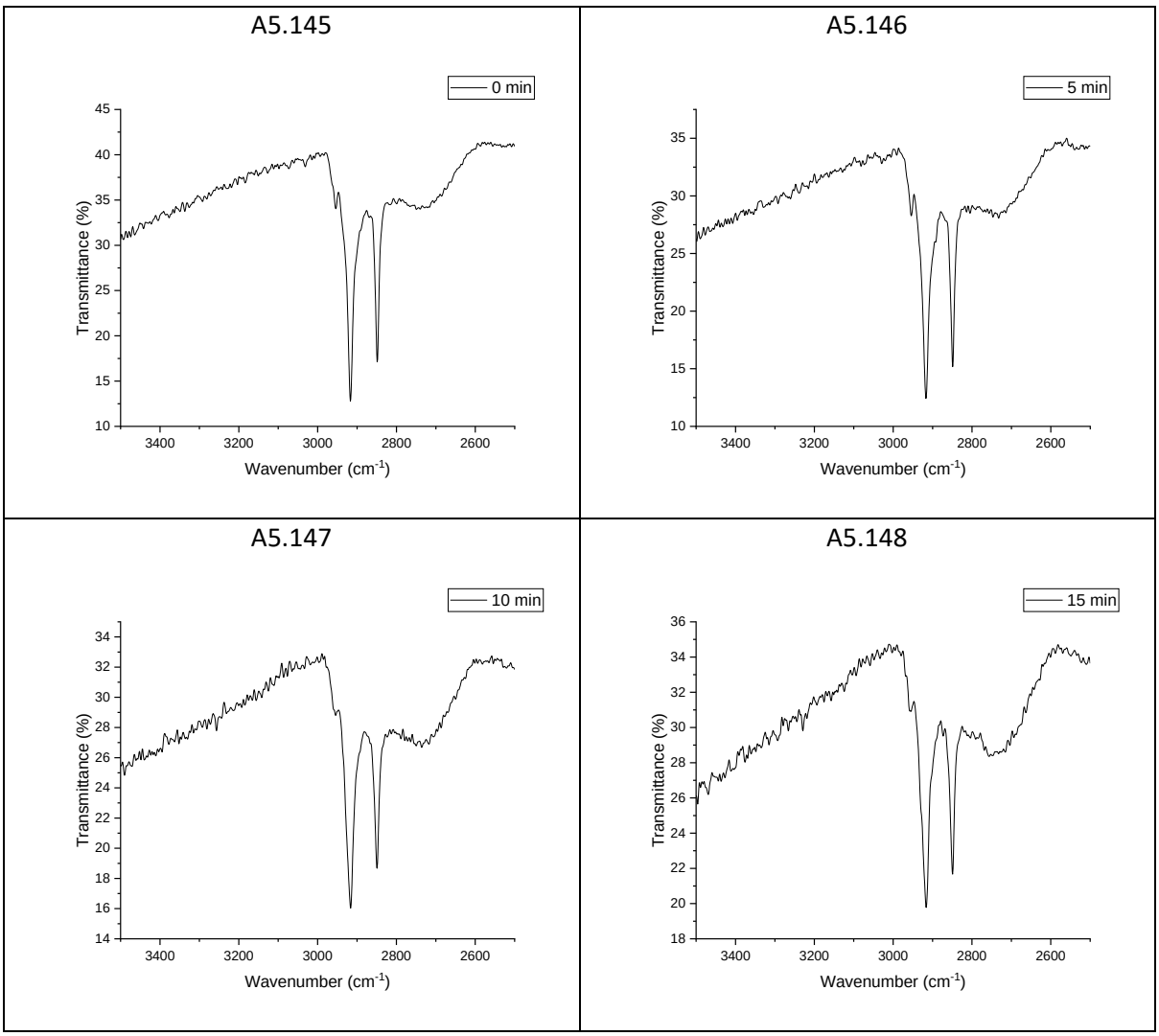

A5.149

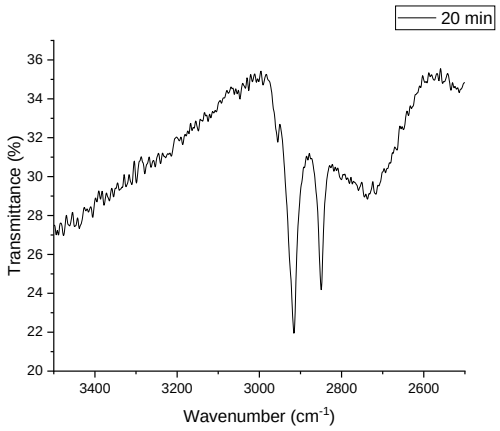

A5.150

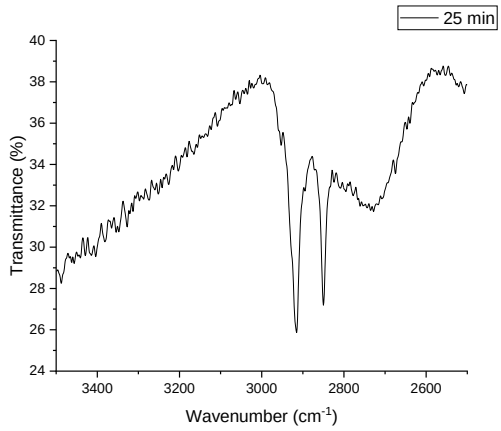

A5.151

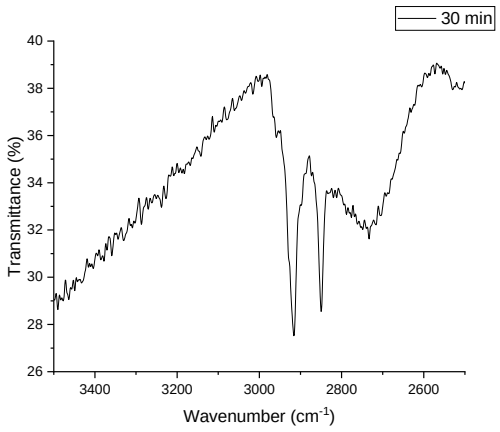

A5.152

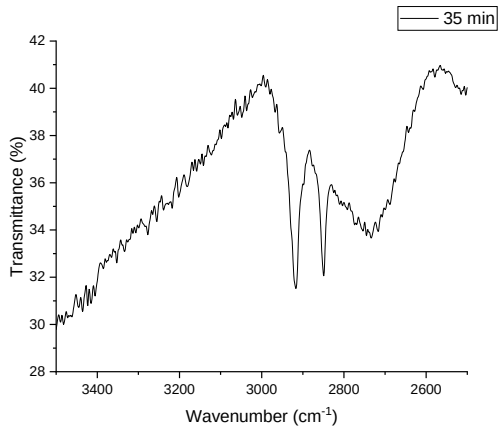

A5.153

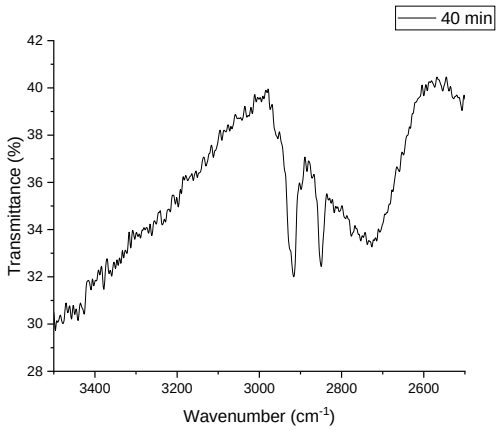

A: 5.18 DRIFT spectra of stearic acid on a 2.5 wt% Cu-doped *meso*-TiO_2 film prepared at 500 rpm

These FTIR spectra show the C-H stretch of stearic acid that was used during photocatalytic testing to monitor the progress of the reaction with exposure to UV light. The total irradiation time is listed on each graph.

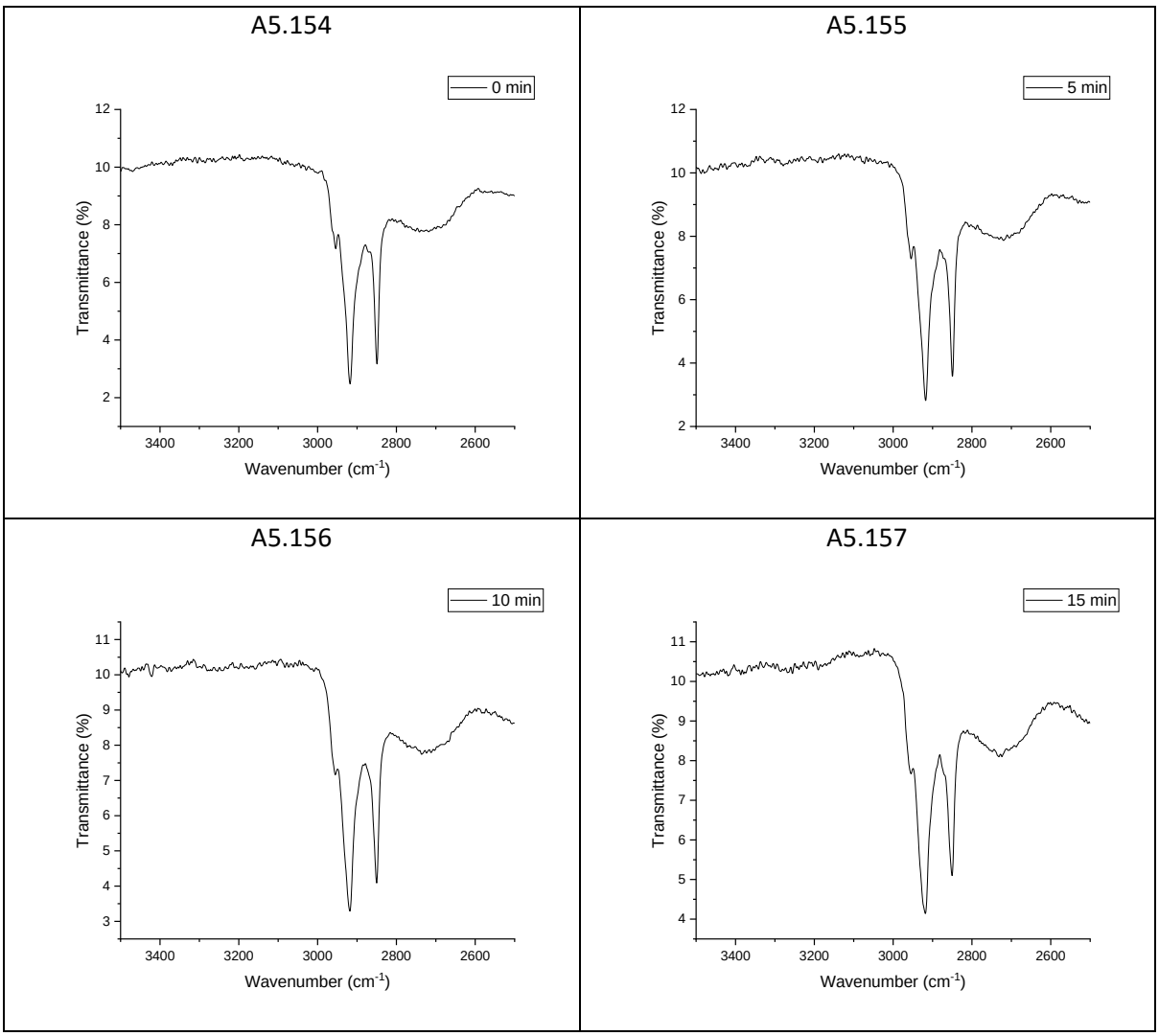

A5.158

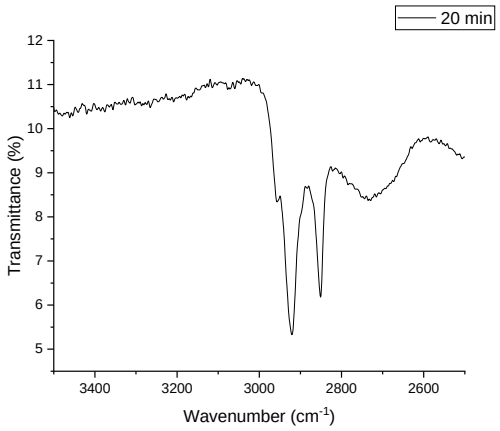

A5.159

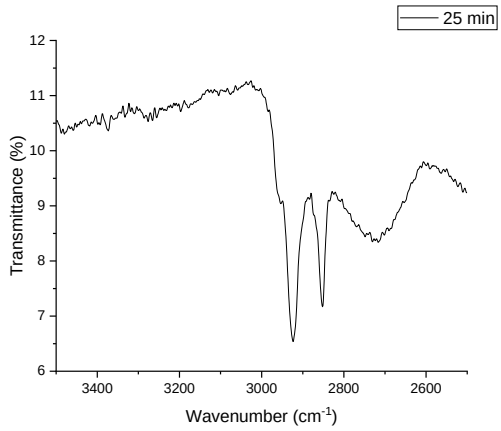

A5.160

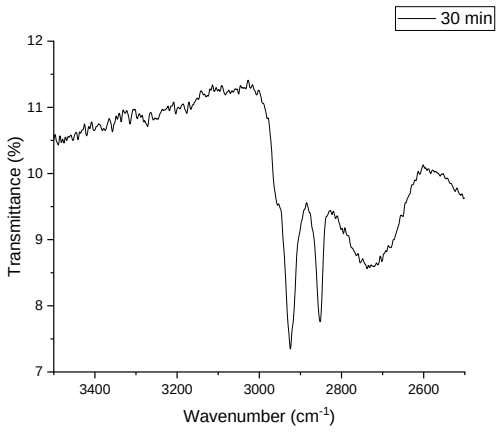

A5.161

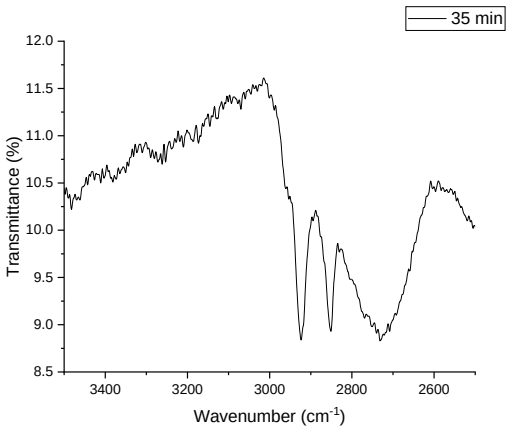

A5.162

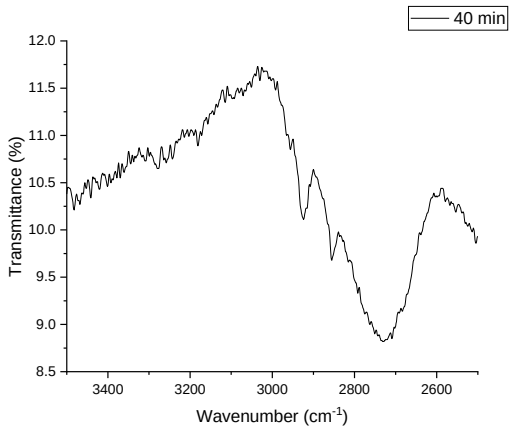

A: 5.19 DRIFT spectra of stearic acid on a 2.5 wt% Cu-doped *meso*-TiO_2 film prepared at 1000 rpm

These FTIR spectra show the C-H stretch of stearic acid that was used during photocatalytic testing to monitor the progress of the reaction with exposure to UV light. The total irradiation time is listed on each graph.

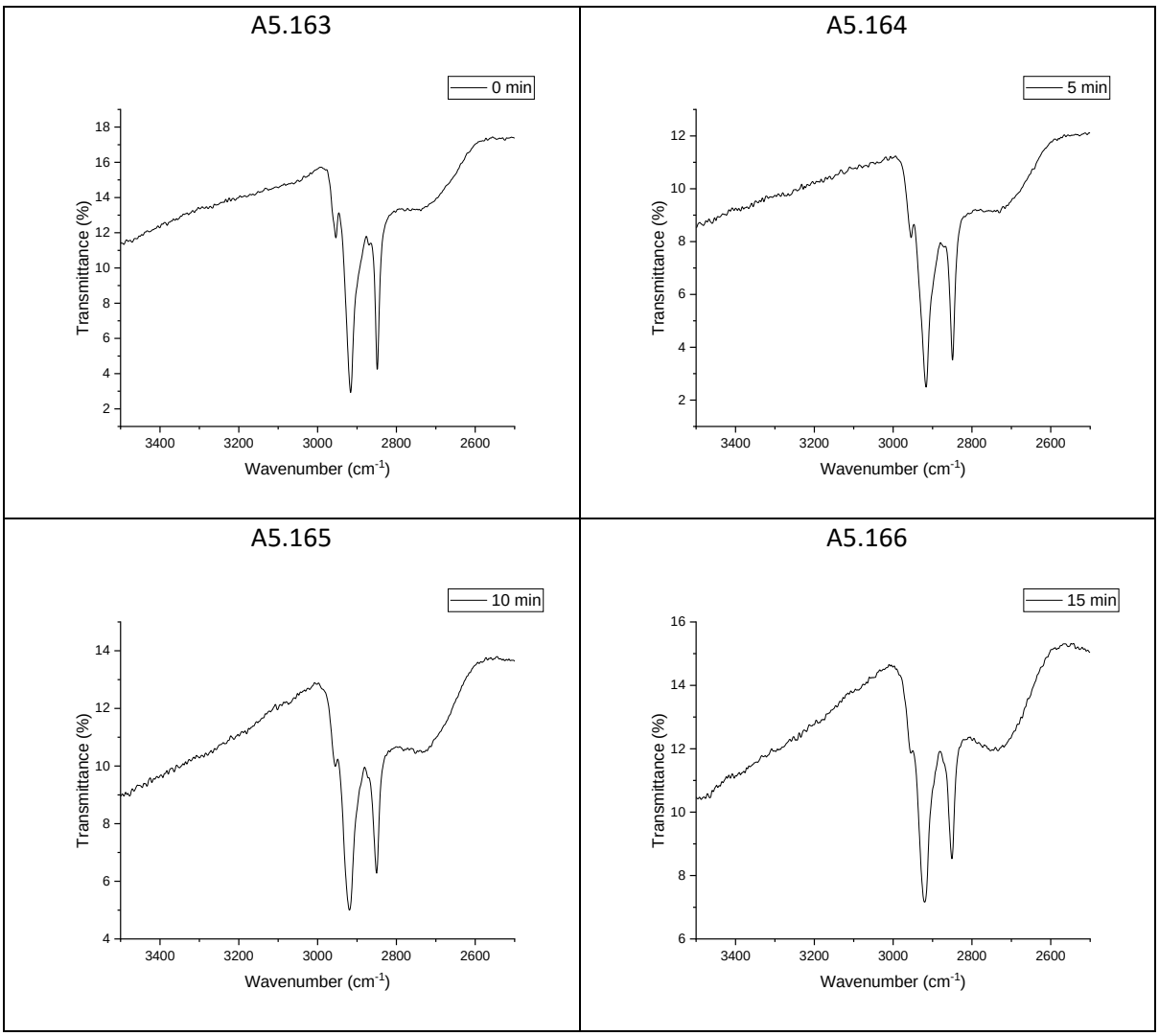

A5.167

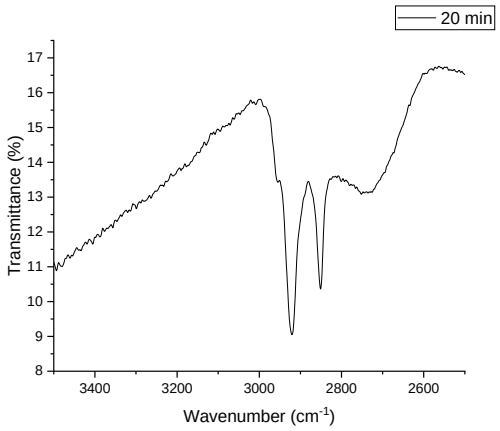

A5.168

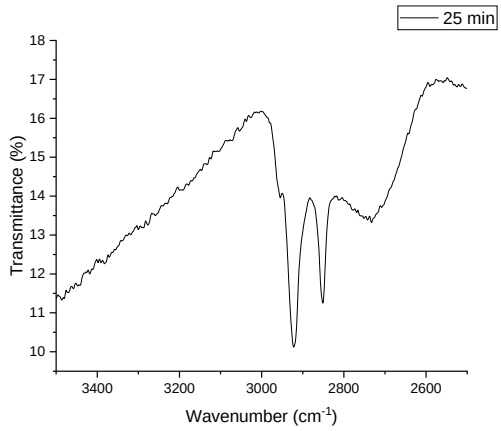

A5.169

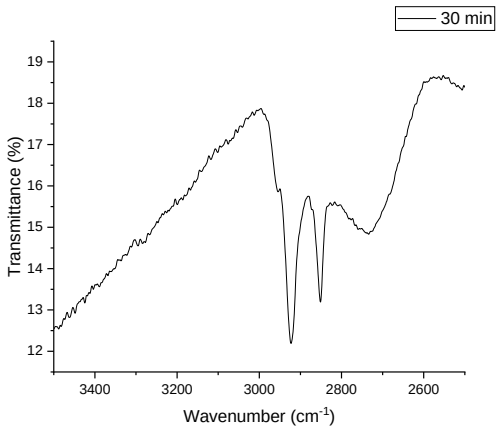

A5.170

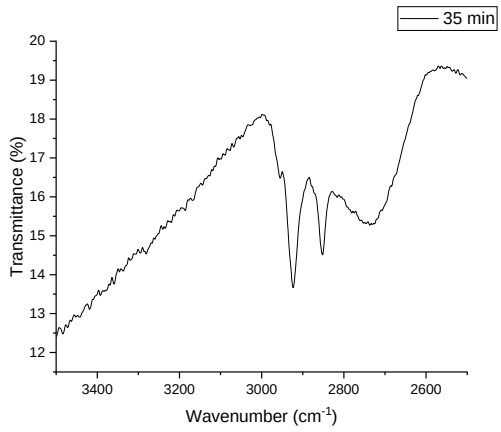

A5.171

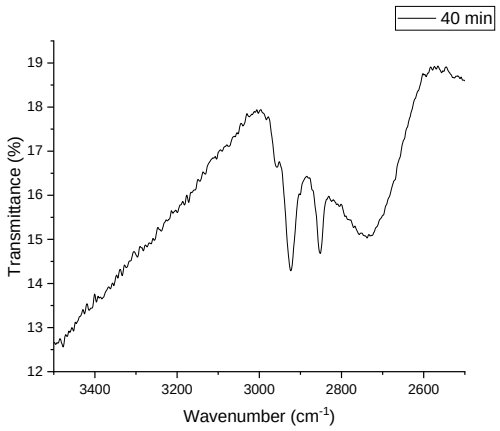

A: 5.20 DRIFT spectra of stearic acid on a 2.5 wt% Cu-doped *meso*-TiO_2 film prepared at 2000 rpm

These FTIR spectra show the C-H stretch of stearic acid that was used during photocatalytic testing to monitor the progress of the reaction with exposure to UV light. The total irradiation time is listed on each graph.

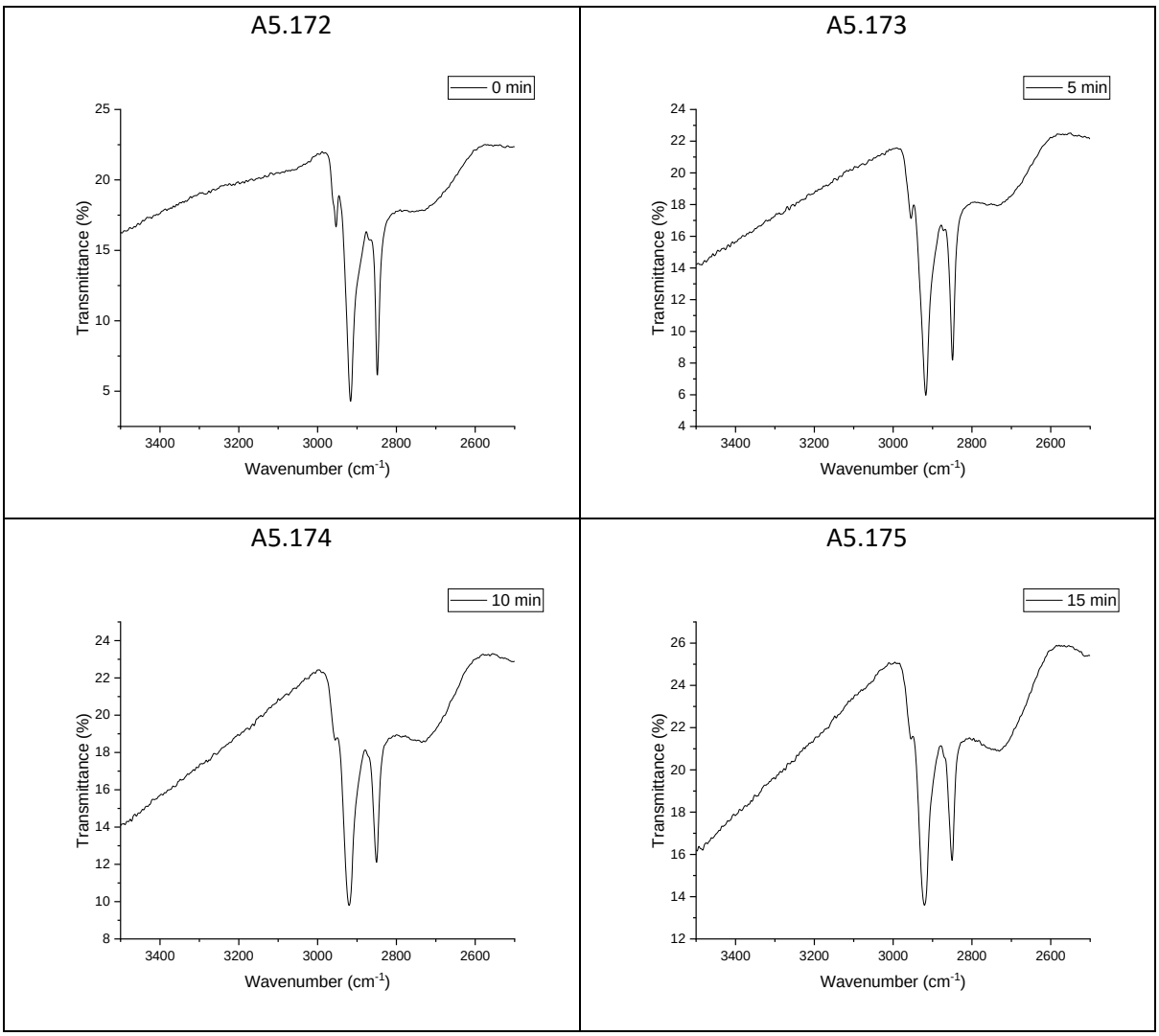

A5.176

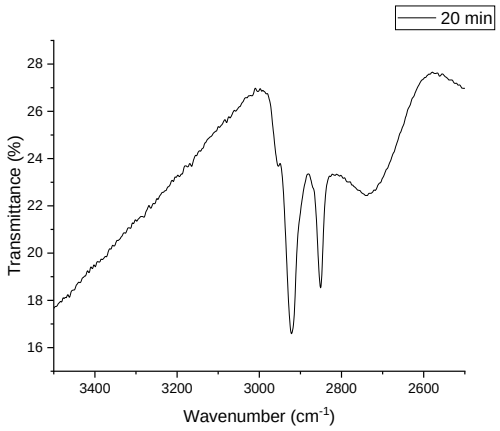

A5.177

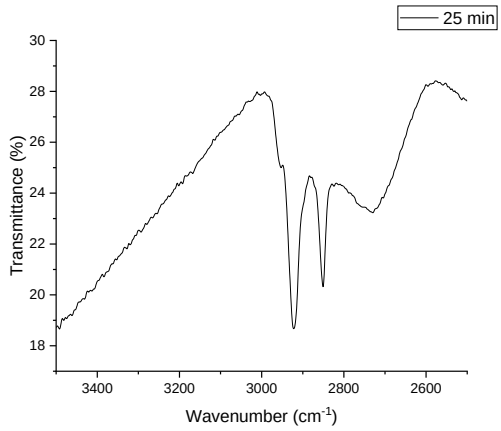

A5.178

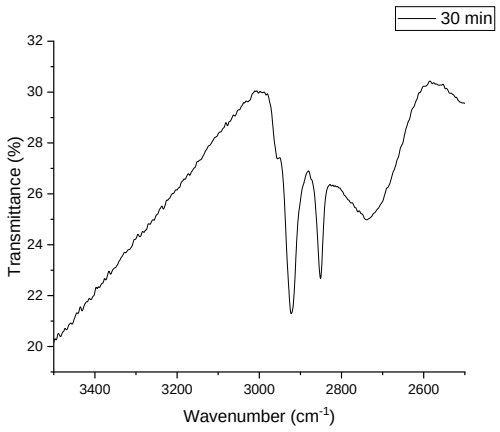

A5.179

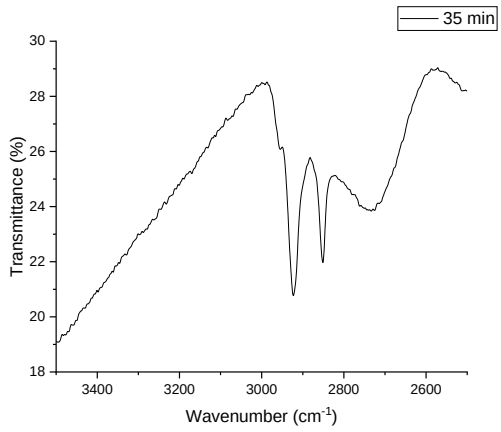

A5.180

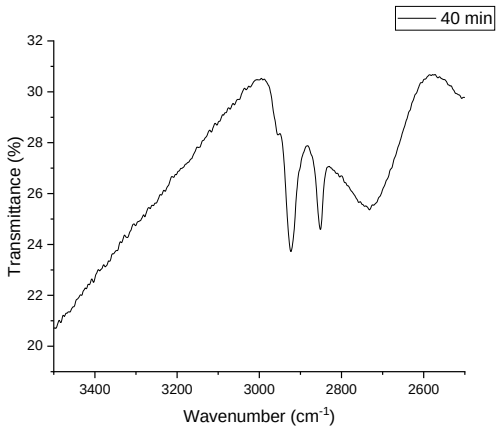

A: 5.21 DRIFT spectra of stearic acid on a 2.5 wt% Cu-doped *meso*-TiO_2 film prepared at 3000 rpm

These FTIR spectra show the C-H stretch of stearic acid that was used during photocatalytic testing to monitor the progress of the reaction with exposure to UV light. The total irradiation time is listed on each graph.

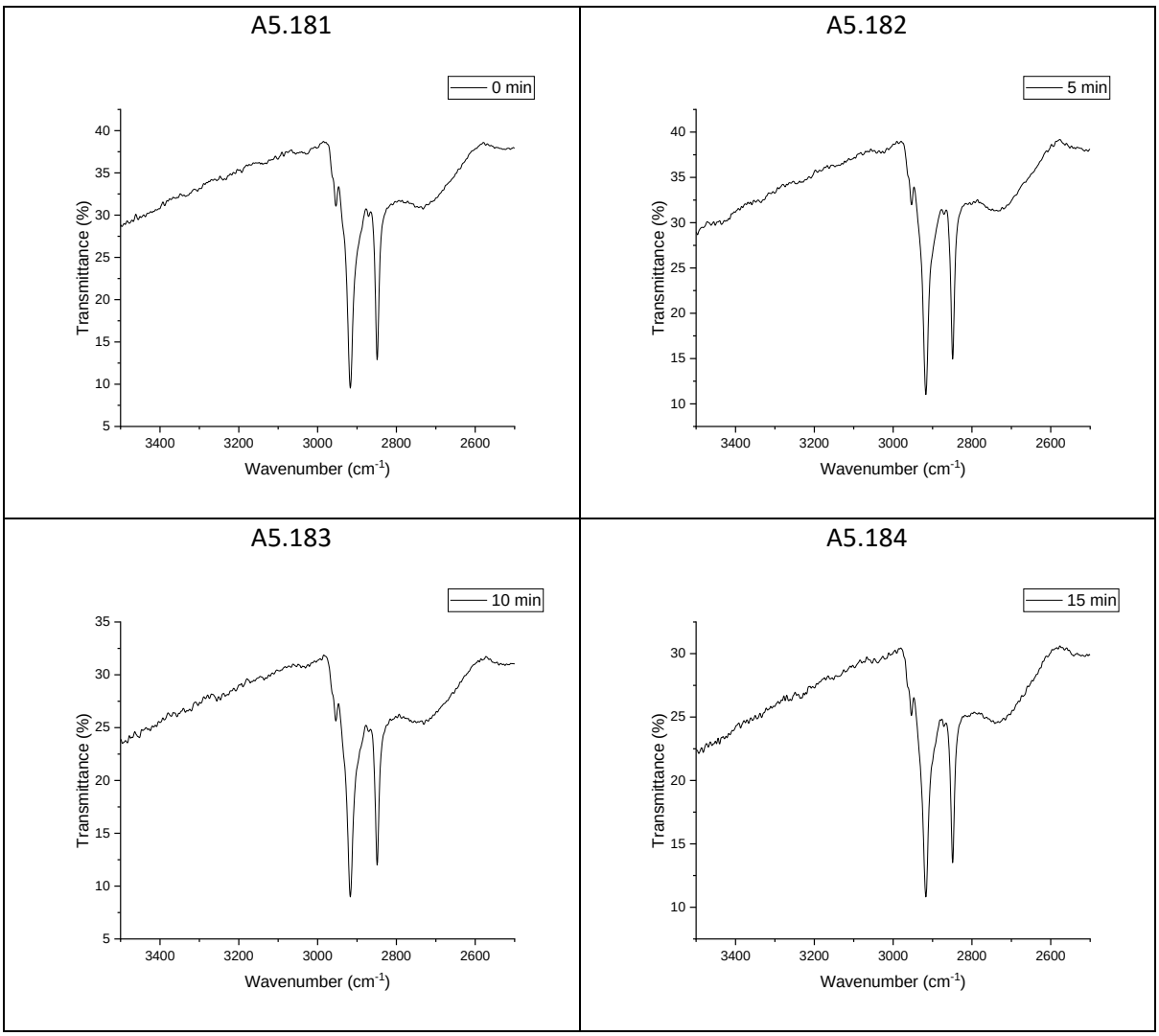

A5.185

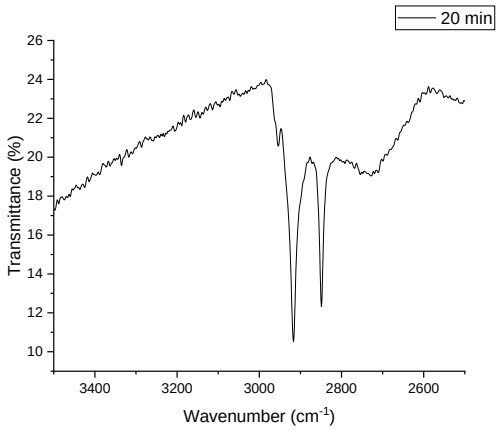

A5.186

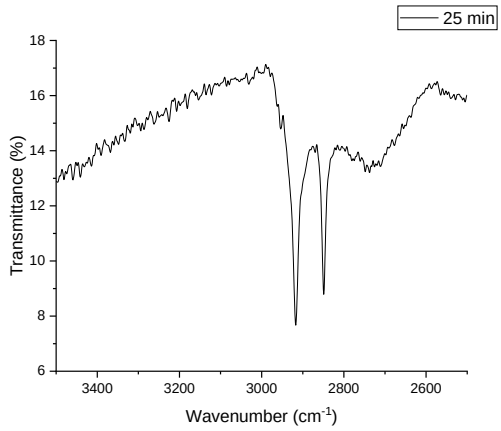

A5.187

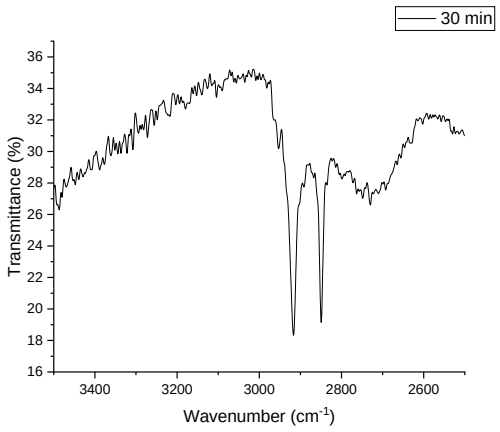

A5.188

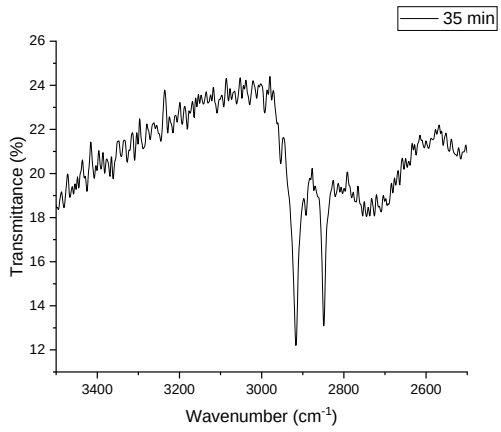

A5.189

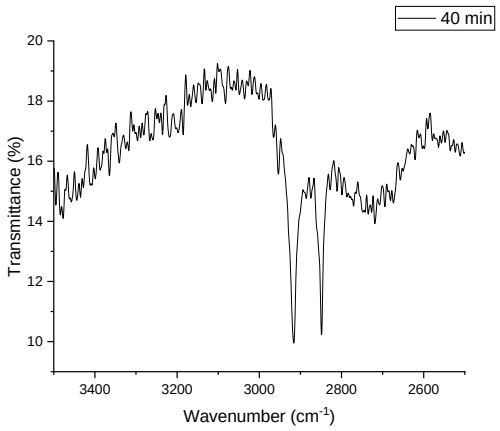

A: 5.22 DRIFT spectra of stearic acid on a 2.5 wt% Cu-doped *meso*-TiO_2 film prepared at 4000 rpm

These FTIR spectra show the C-H stretch of stearic acid that was used during photocatalytic testing to monitor the progress of the reaction with exposure to UV light. The total irradiation time is listed on each graph.

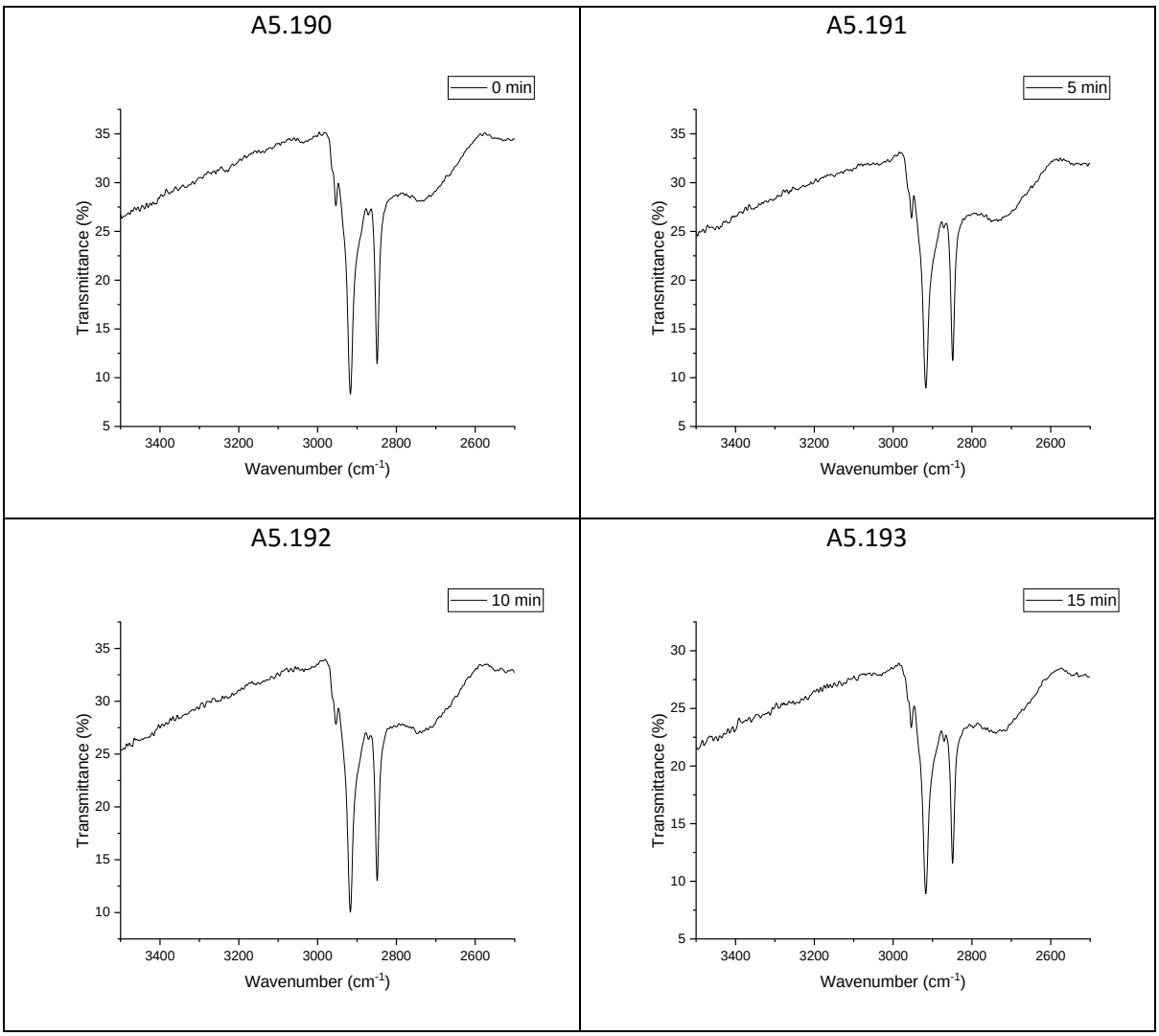

A5.194

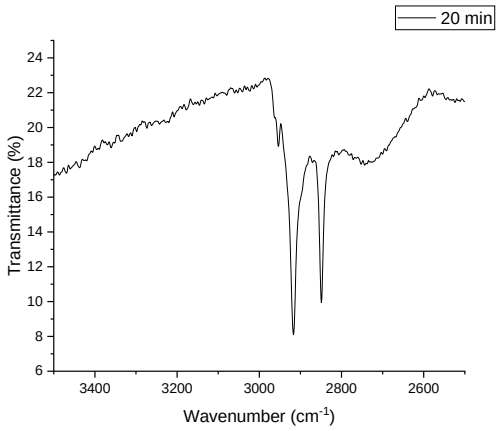

A5.195

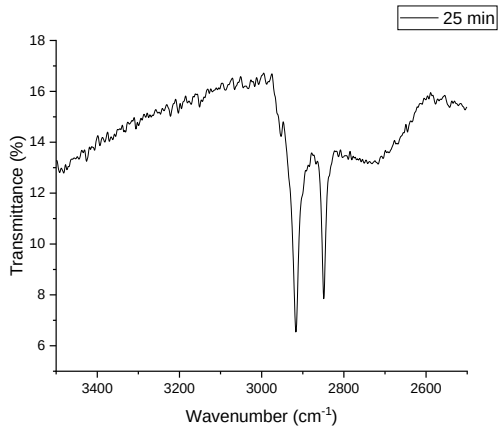

A5.196

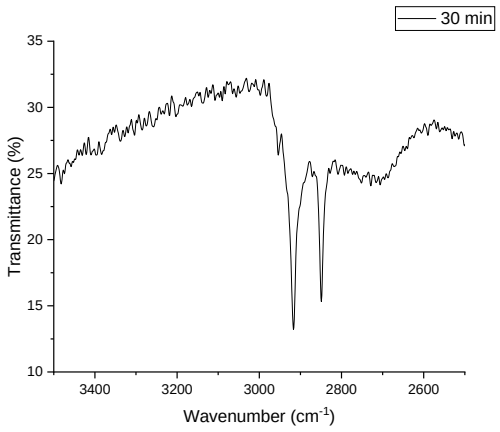

A5.197

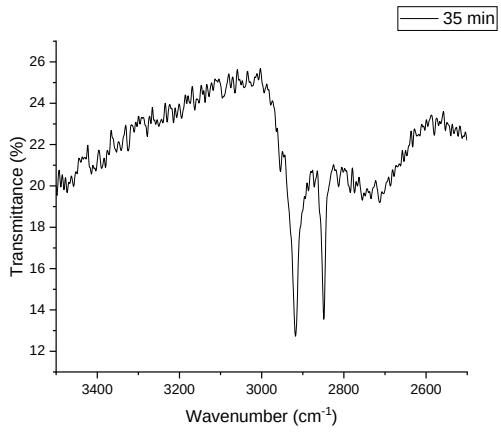

A5.198

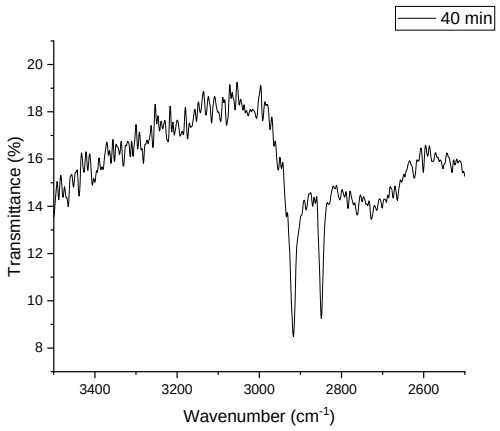

A: 5.23 DRIFT spectra of stearic acid on a 2.5 wt% Cu-doped *meso*-TiO_2 film prepared at 5000 rpm

These FTIR spectra show the C-H stretch of stearic acid that was used during photocatalytic testing to monitor the progress of the reaction with exposure to UV light. The total irradiation time is listed on each graph.

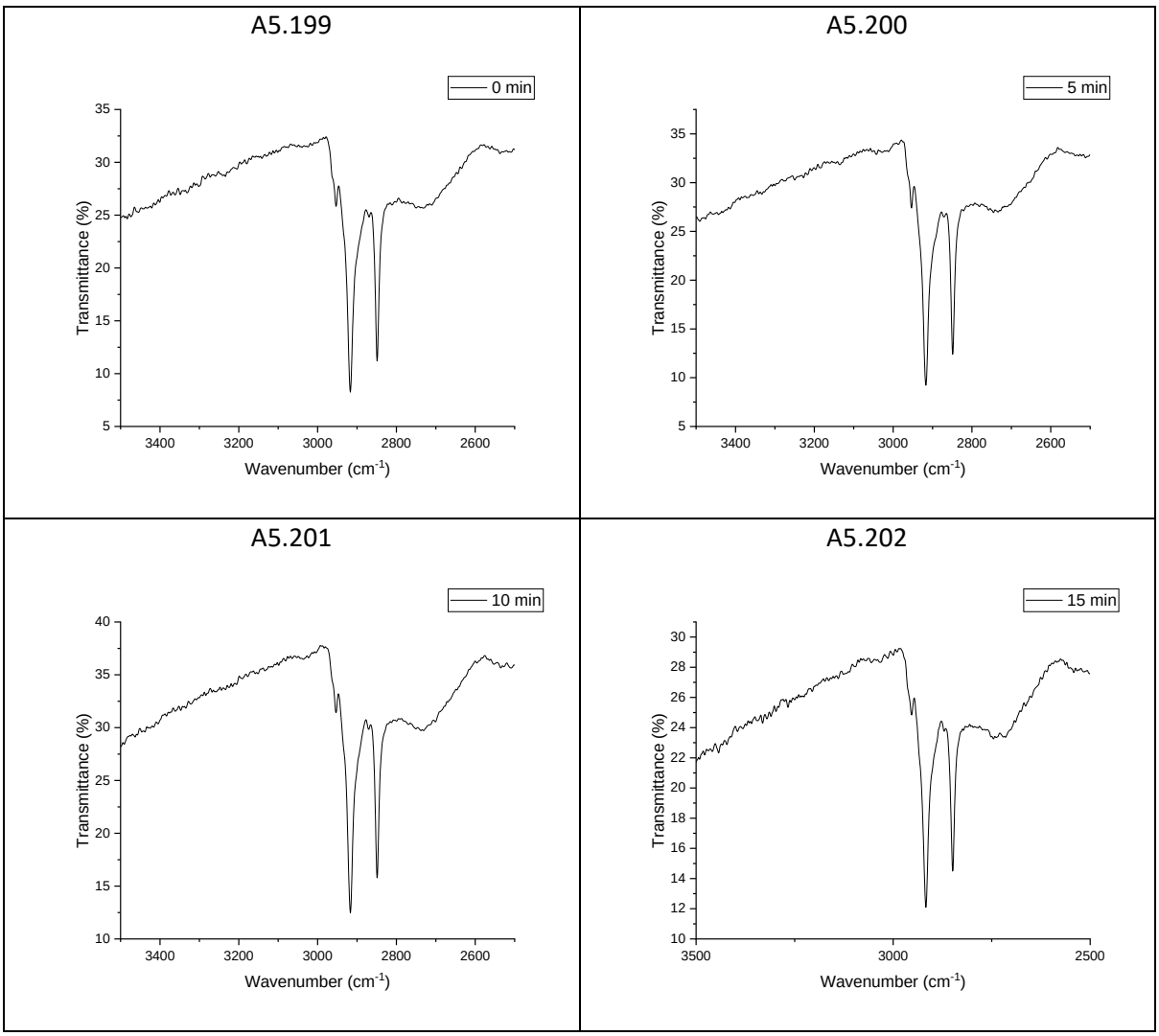

A5.203

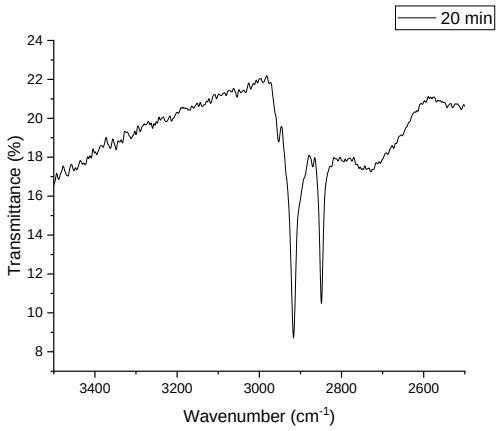

A5.204

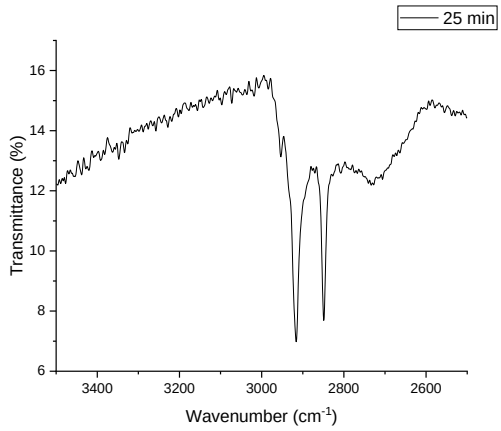

A5.205

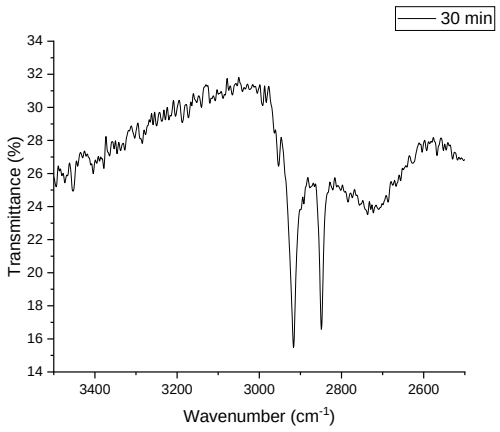

A5.206

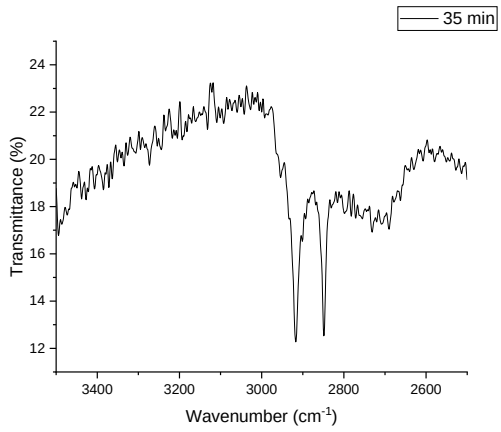

A5.207

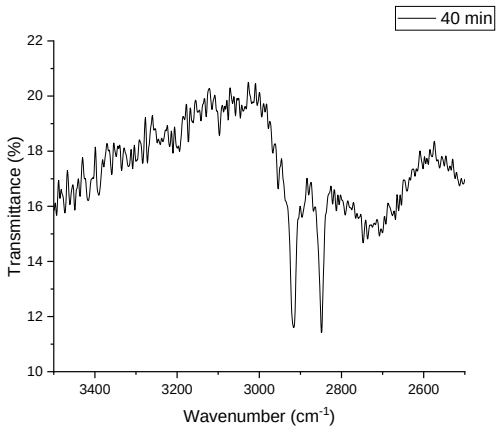

A: 5.24 DRIFT spectra of stearic acid on a 2.5 wt% Cu-doped *meso*-TiO_2 film prepared at 6000 rpm

These FTIR spectra show the C-H stretch of stearic acid that was used during photocatalytic testing to monitor the progress of the reaction with exposure to UV light. The total irradiation time is listed on each graph.

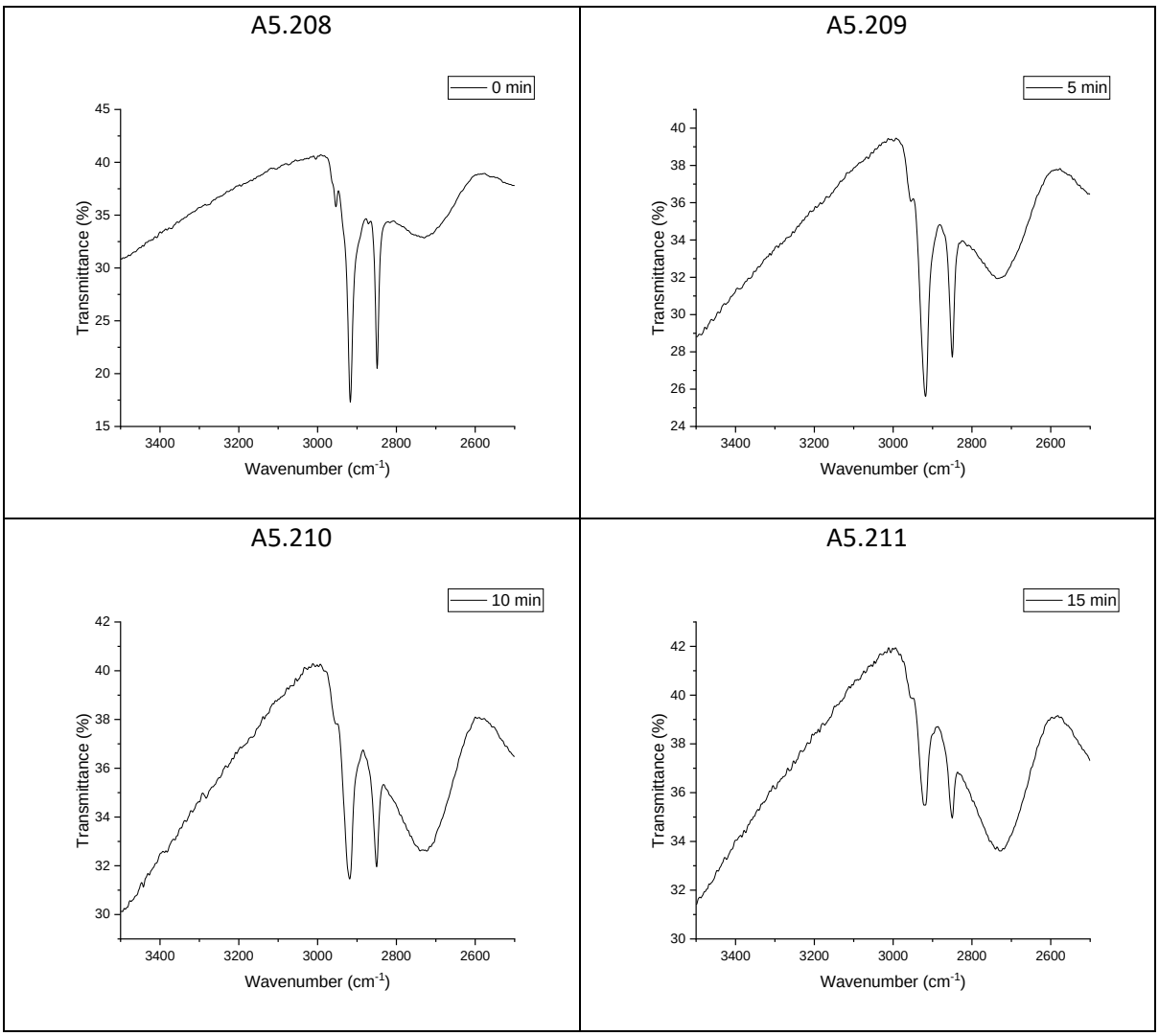

A5.212

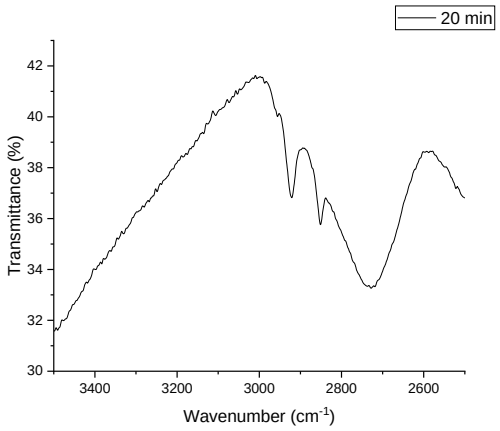

A5.213

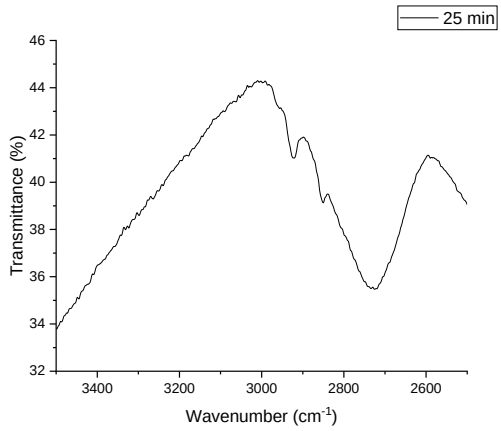

A5.214

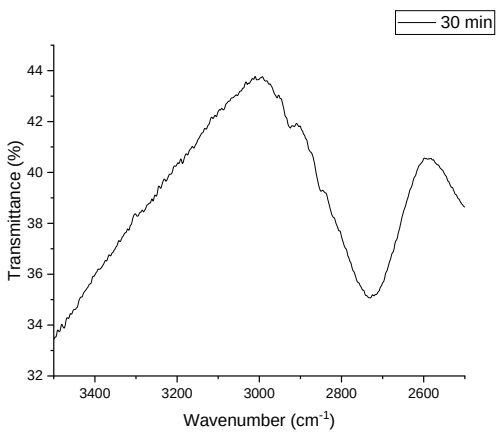

A5.215

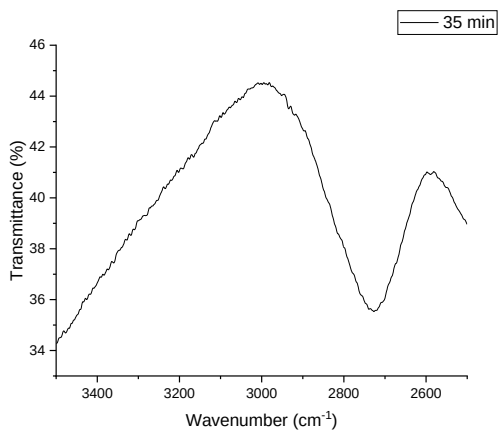

A5.216

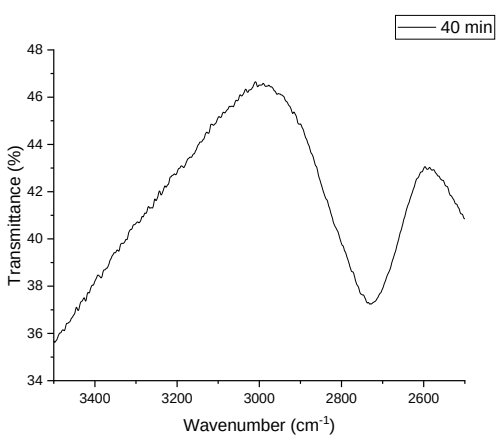

A: 5.25 DRIFT spectra of stearic acid on a 2.5 wt% Cu-doped *meso*-TiO_2 film prepared at 7000 rpm

These FTIR spectra show the C-H stretch of stearic acid that was used during photocatalytic testing to monitor the progress of the reaction with exposure to UV light. The total irradiation time is listed on each graph.

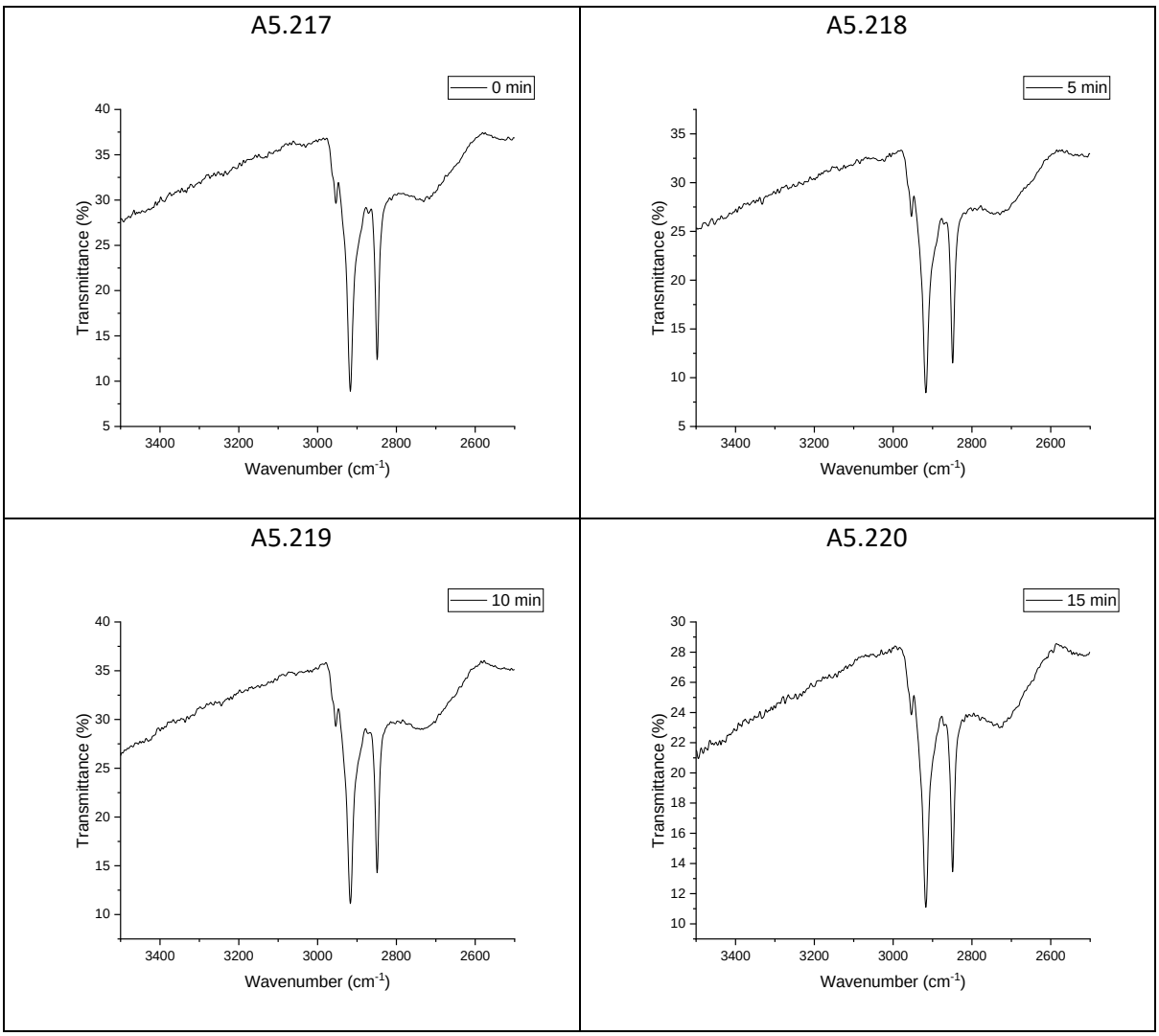

A5.221

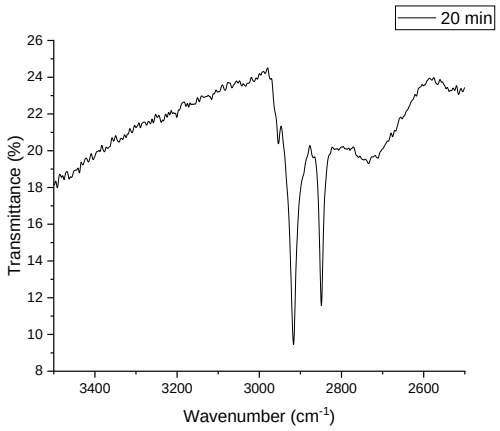

A5.222

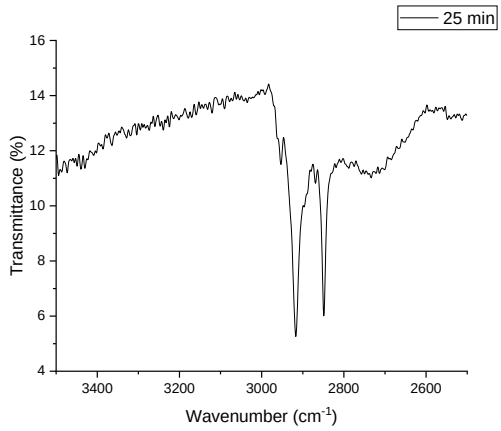

A5.223

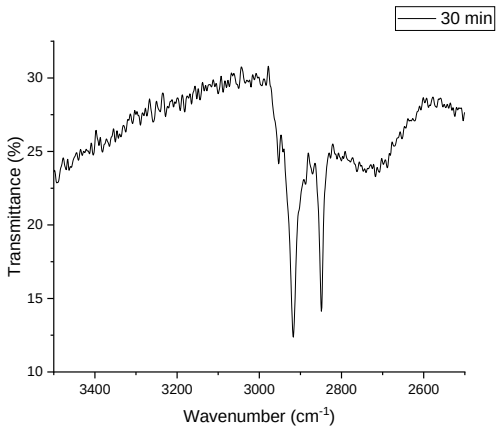

A5.224

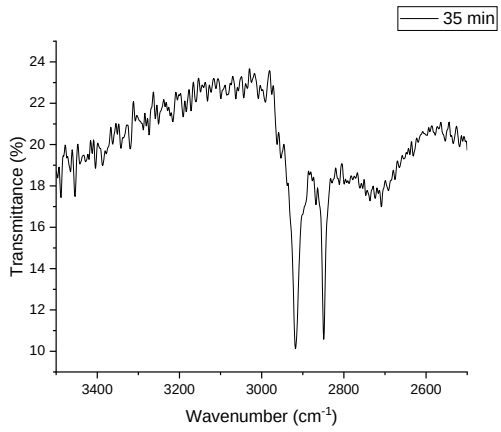

A5.225

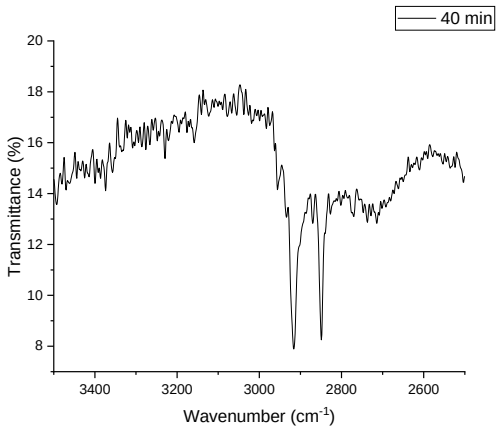

A: 5.26 DRIFT spectra of stearic acid on a 2.5 wt% Cu-doped meso-TiO2 film prepared at 8000 rpm

These FTIR spectra show the C-H stretch of stearic acid that was used during photocatalytic testing to monitor the progress of the reaction with exposure to UV light. The total irradiation time is listed on each graph.

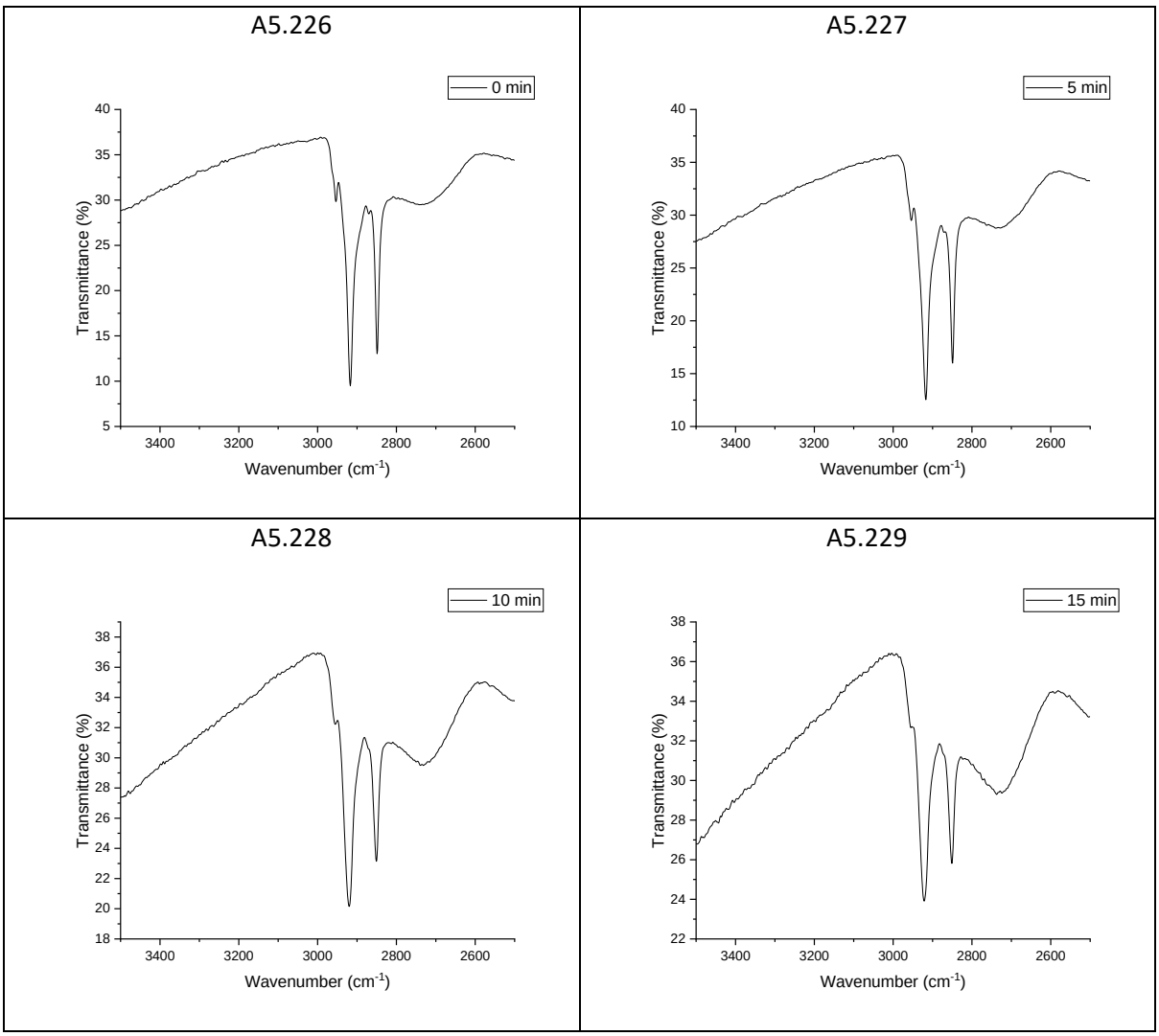

A5.230

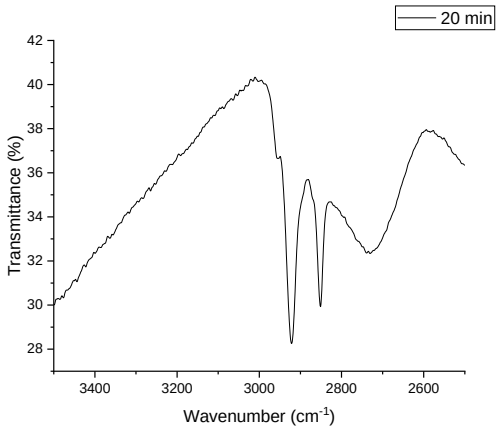

A5.231

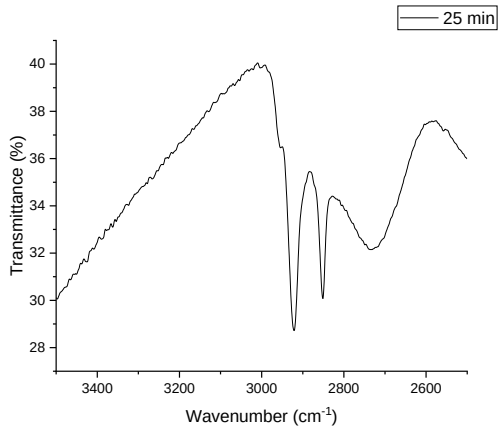

A5.232

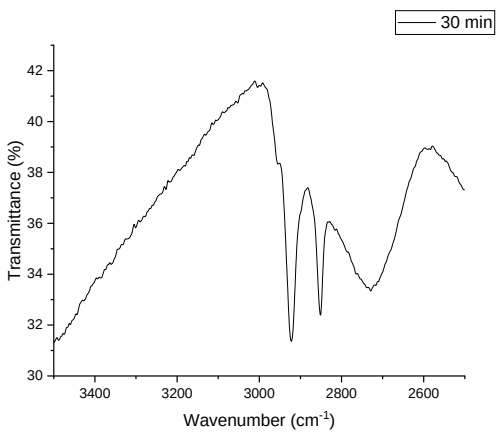

A5.233

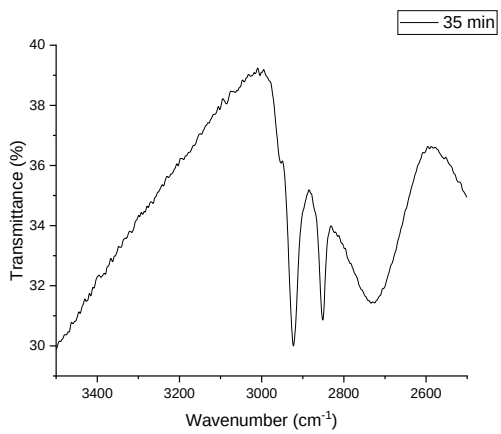

A5.234

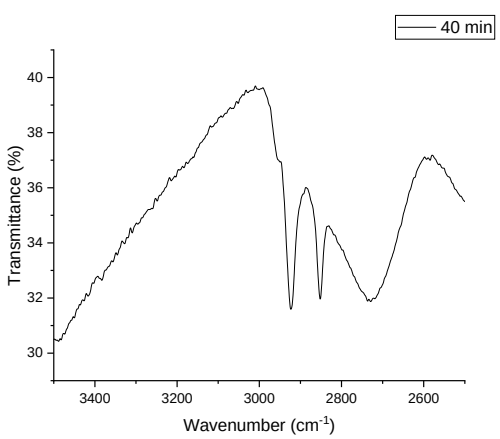

A: 5.27 DRIFT spectra of stearic acid on a 1 wt% Cu-doped *meso*-TiO_2 film prepared at 500 rpm

These FTIR spectra show the C-H stretch of stearic acid that was used during photocatalytic testing to monitor the progress of the reaction with exposure to UV light. The total irradiation time is listed on each graph.

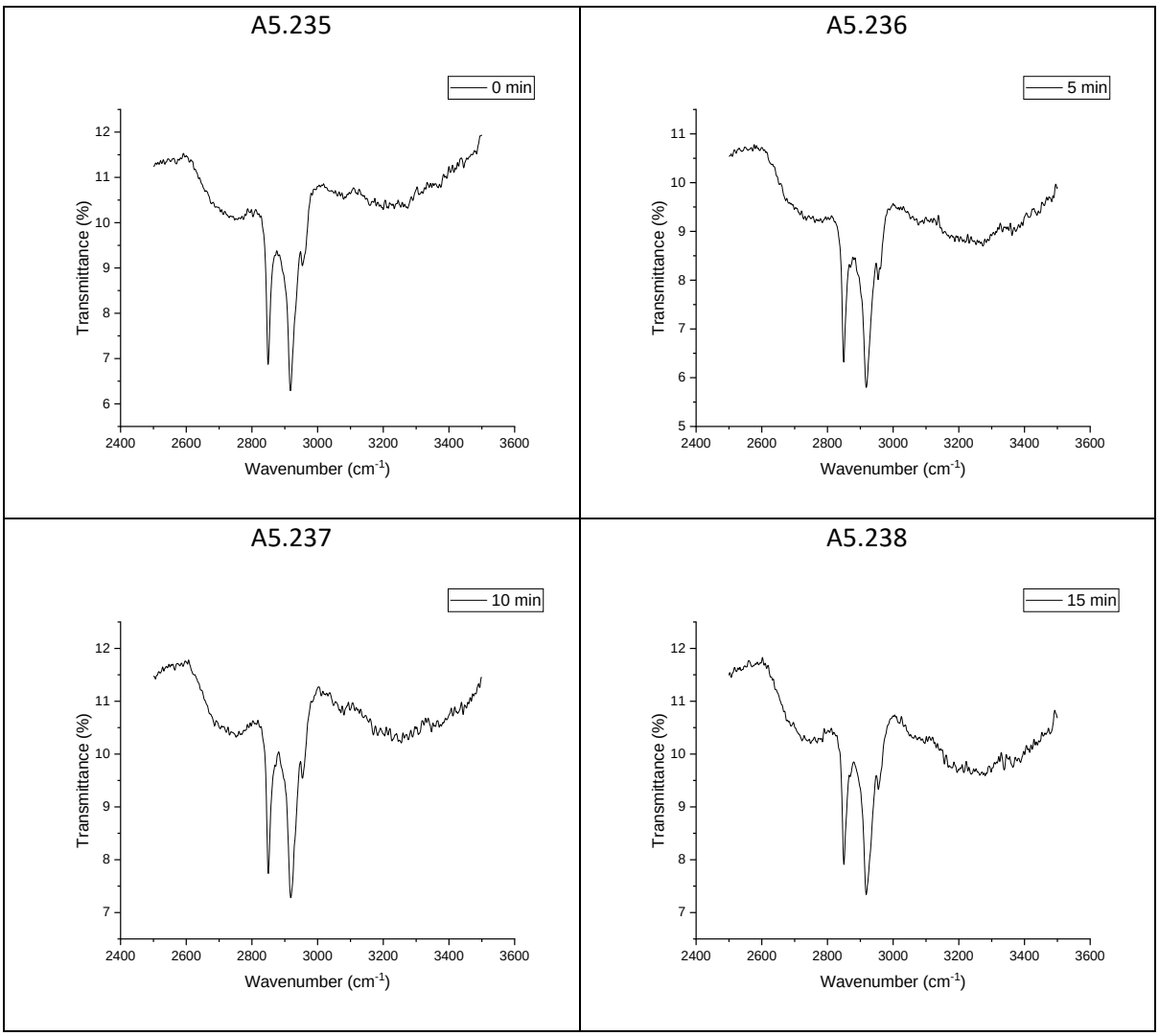

A5.239

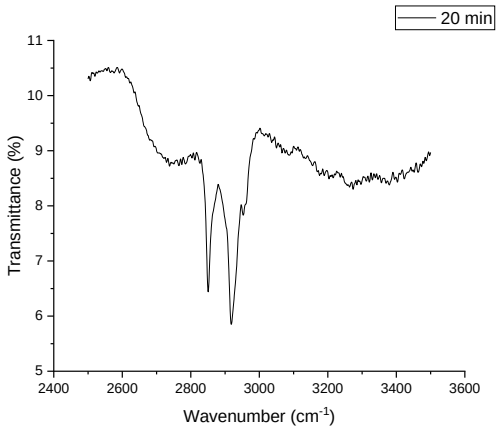

A5.240

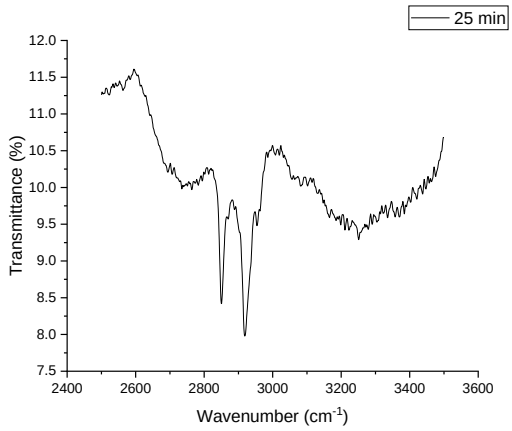

A5.241

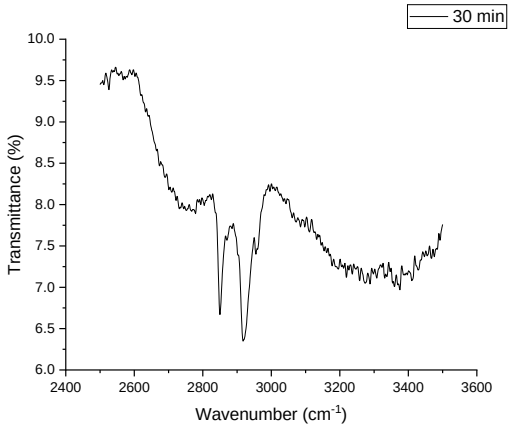

A5.242

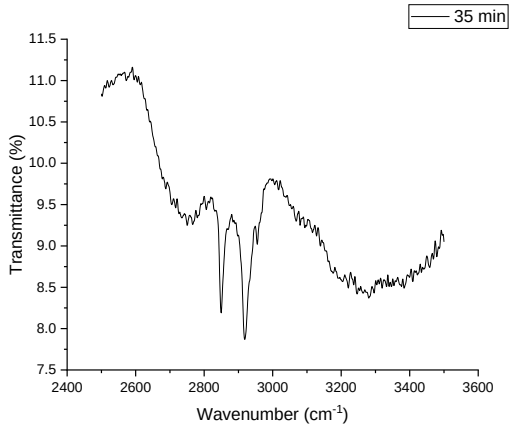

A5.243

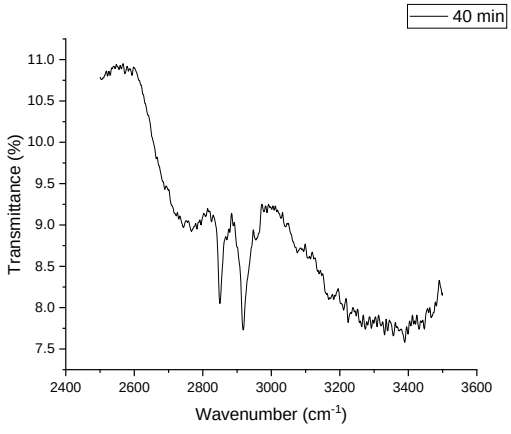

A: 5.28 DRIFT spectra of stearic acid on a 1 wt% Cu-doped *meso*-TiO_2 film prepared at 1000 rpm

These FTIR spectra show the C-H stretch of stearic acid that was used during photocatalytic testing to monitor the progress of the reaction with exposure to UV light. The total irradiation time is listed on each graph.

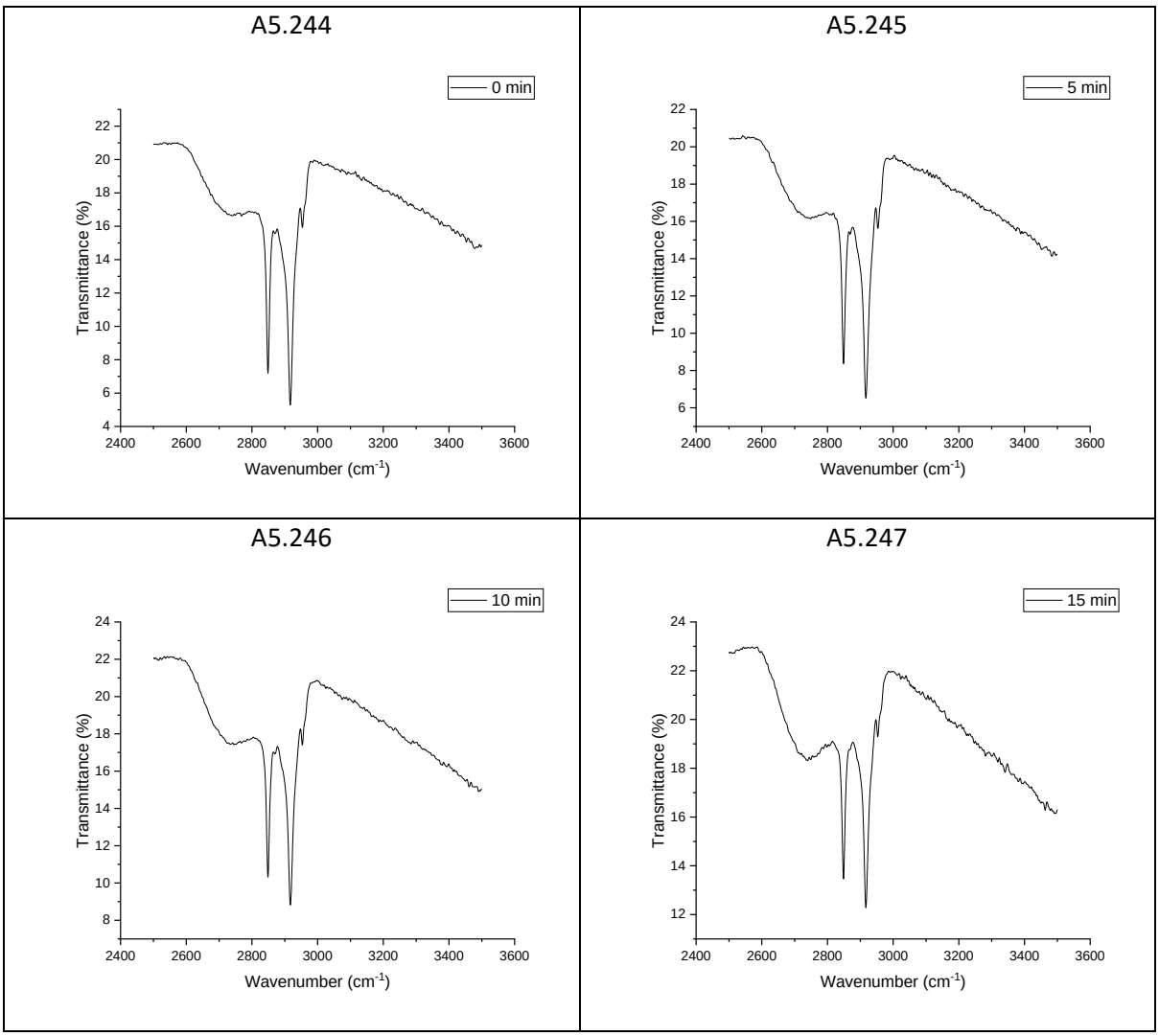

A5.248

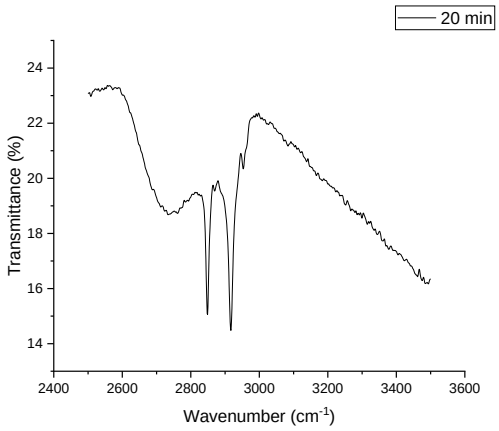

A5.249

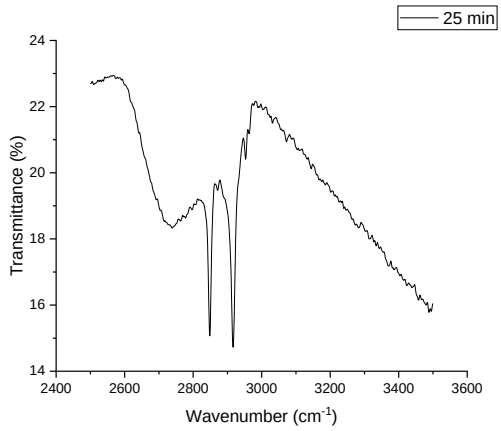

A5.250

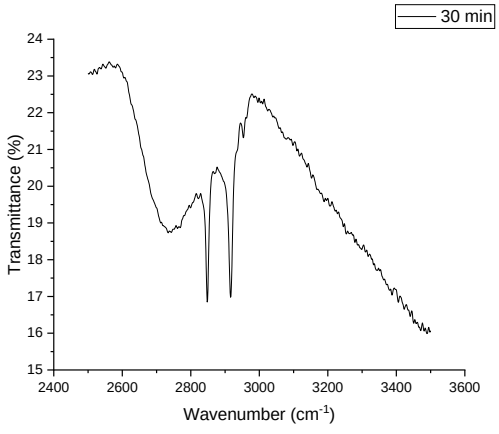

A5.251

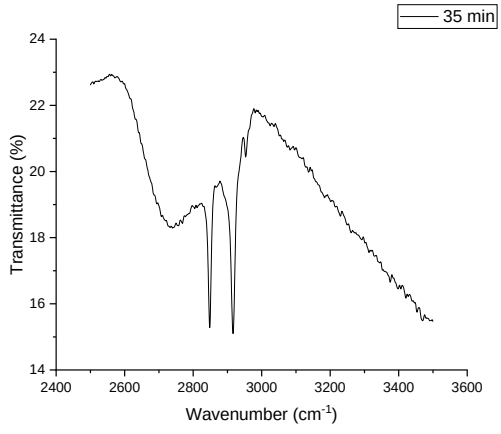

A5.252

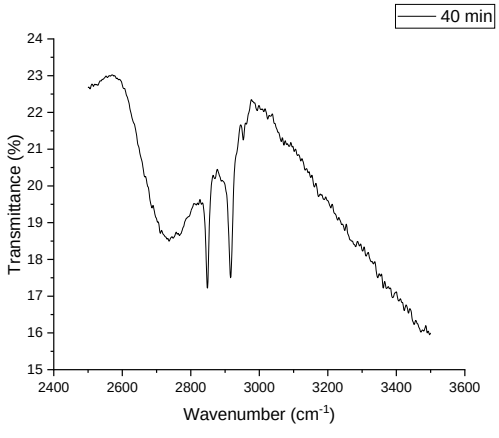

A: 5.29 DRIFT spectra of stearic acid on a 1 wt% Cu-doped *meso*-TiO_2 film prepared at 2000 rpm

These FTIR spectra show the C-H stretch of stearic acid that was used during photocatalytic testing to monitor the progress of the reaction with exposure to UV light. The total irradiation time is listed on each graph.

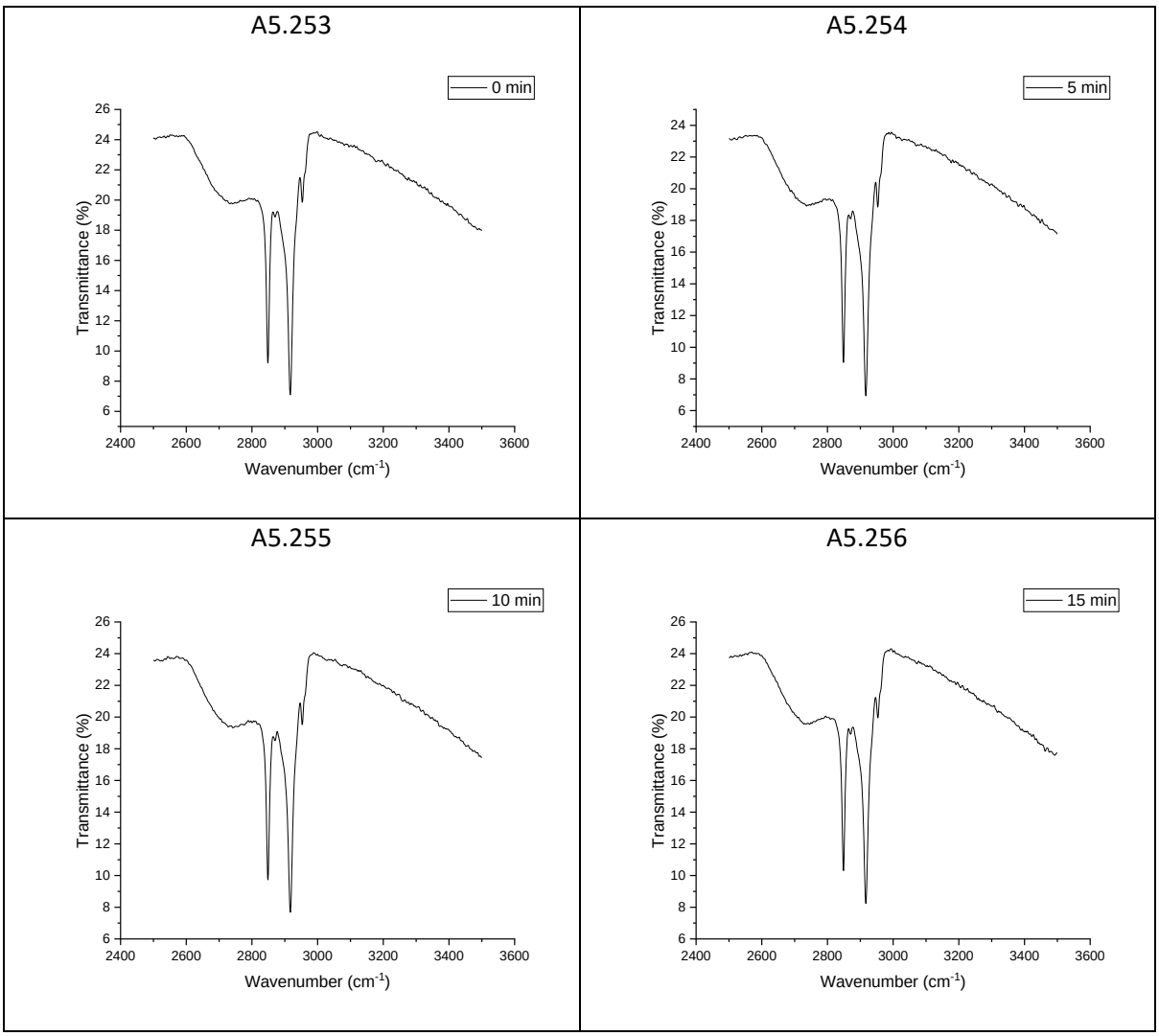

A5.257

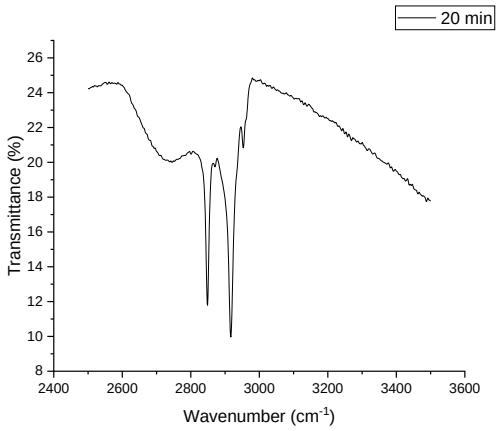

A5. A5.258

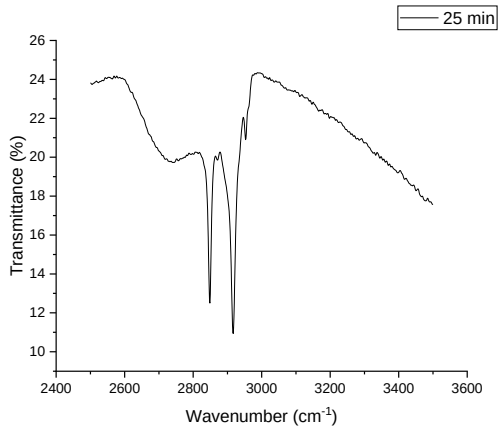

A5.259

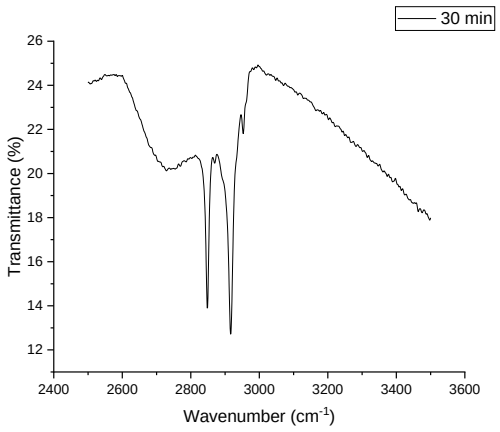

A5.260

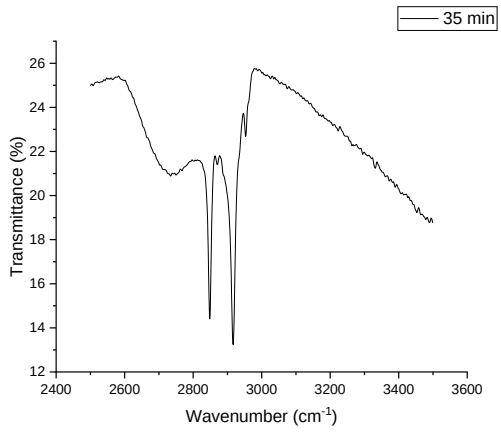

A5.261

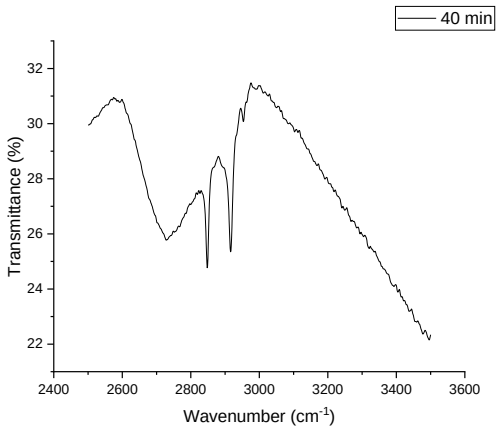

A: 5.30 DRIFT spectra of stearic acid on a 1 wt% Cu-doped *meso*-TiO_2 film prepared at 3000 rpm

These FTIR spectra show the C-H stretch of stearic acid that was used during photocatalytic testing to monitor the progress of the reaction with exposure to UV light. The total irradiation time is listed on each graph.

A5.262

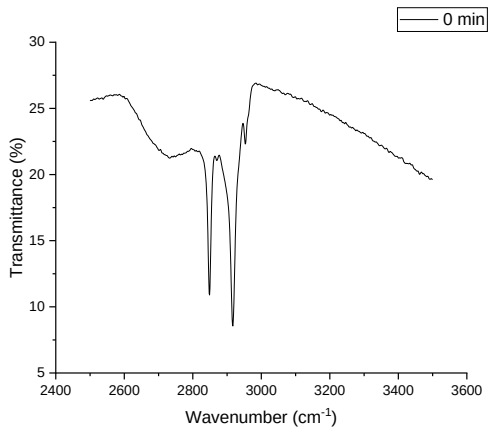

A5.263

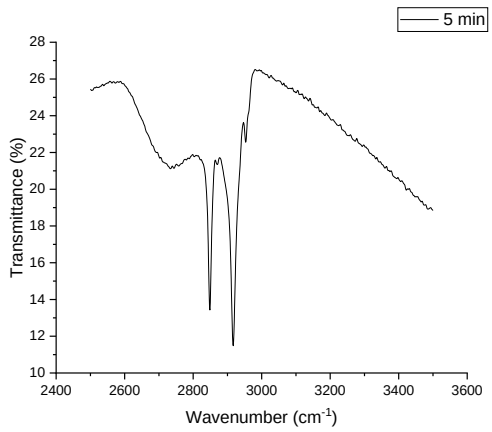

A5.264

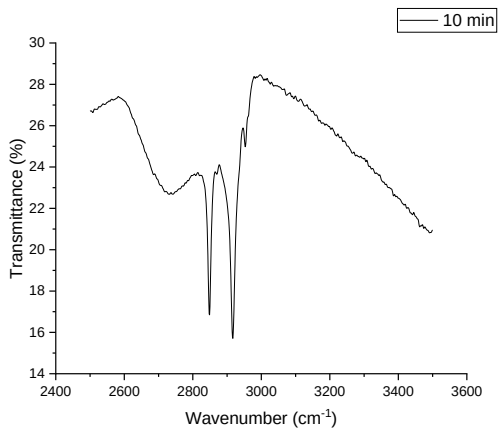

A5.265

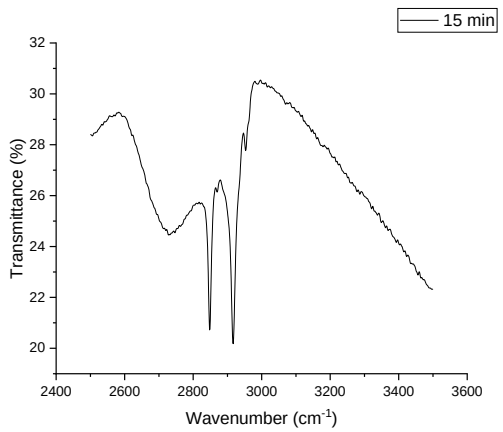

A5.266

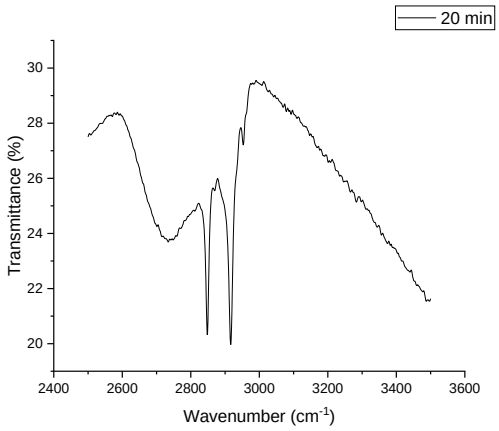

A5.267

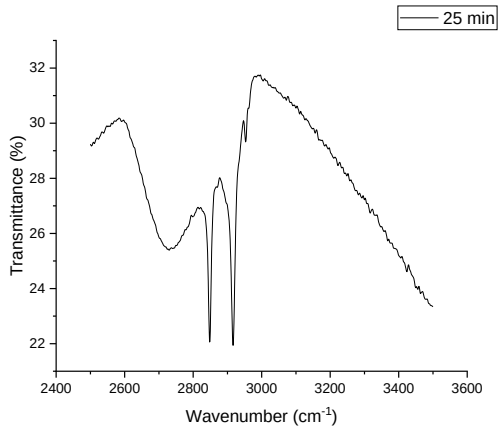

A5.268

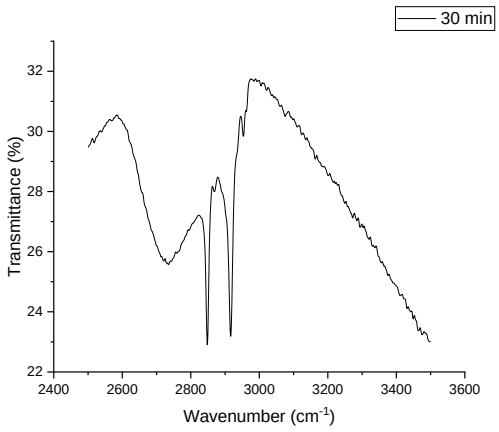

A5.269

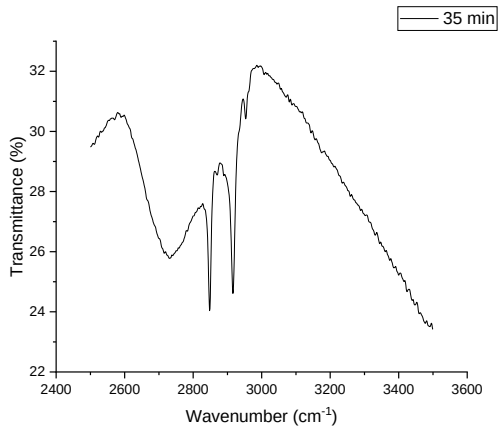

A5.270

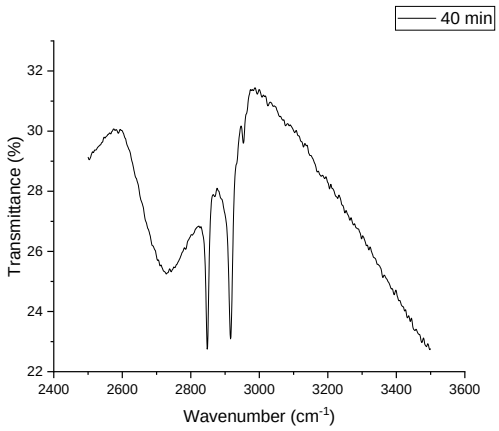

A: 5.31 DRIFT spectra of stearic acid on a 1 wt% Cu-doped *meso*-TiO_2 film prepared at 4000 rpm

These FTIR spectra show the C-H stretch of stearic acid that was used during photocatalytic testing to monitor the progress of the reaction with exposure to UV light. The total irradiation time is listed on each graph.

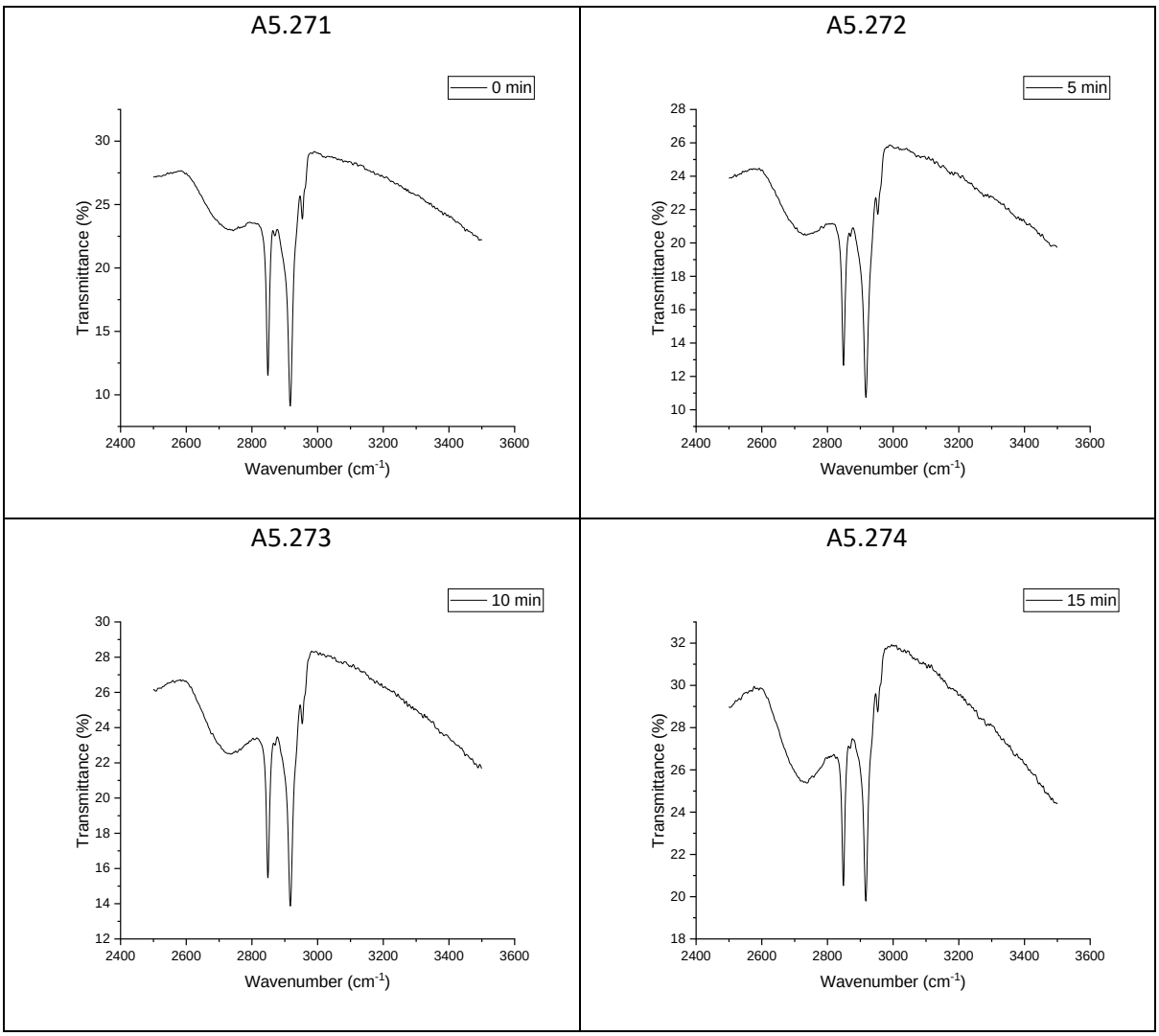

A5.275

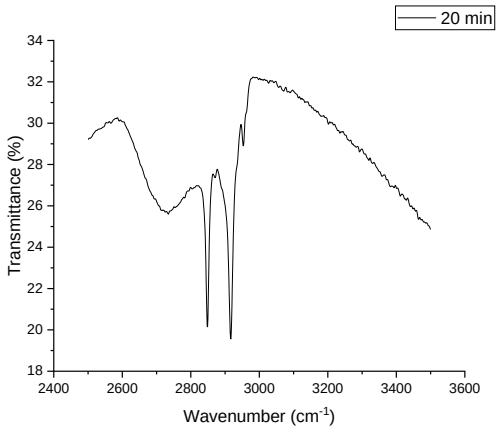

A5.276

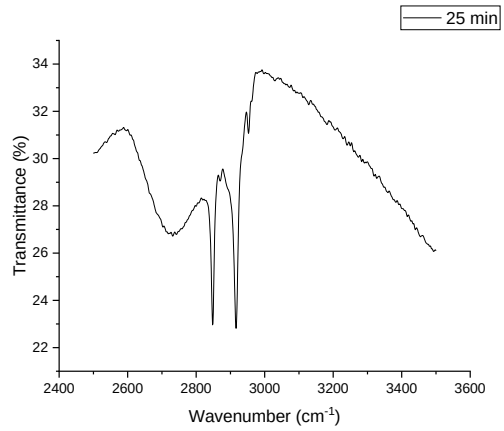

A5.277

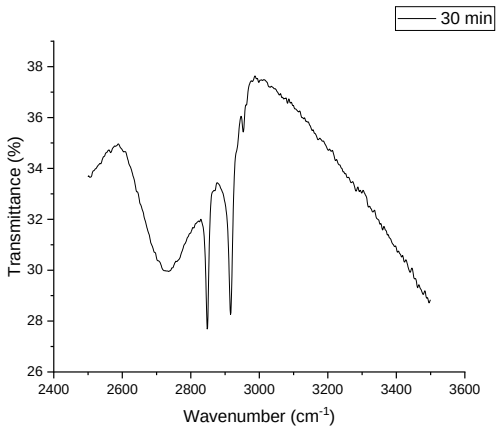

A5.278

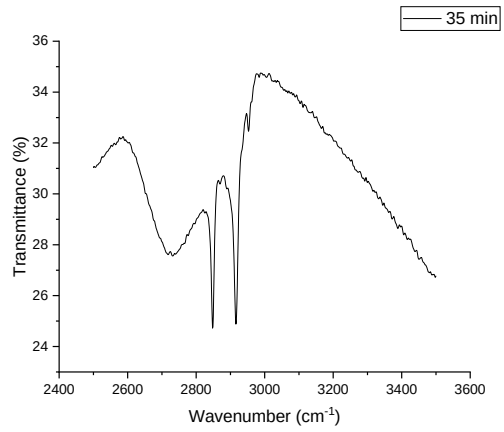

A5.279

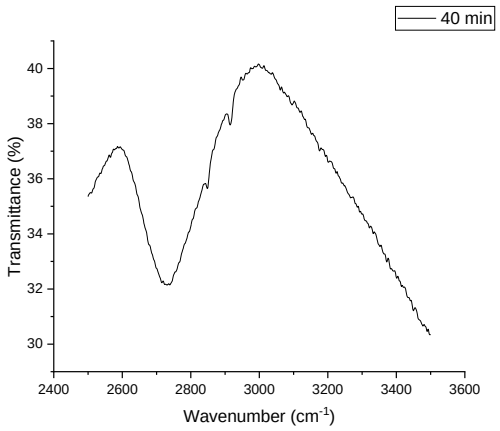

A: 5.32 DRIFT spectra of stearic acid on a 1 wt% Cu-doped *meso*-TiO_2 film prepared at 5000 rpm

These FTIR spectra show the C-H stretch of stearic acid that was used during photocatalytic testing to monitor the progress of the reaction with exposure to UV light. The total irradiation time is listed on each graph.

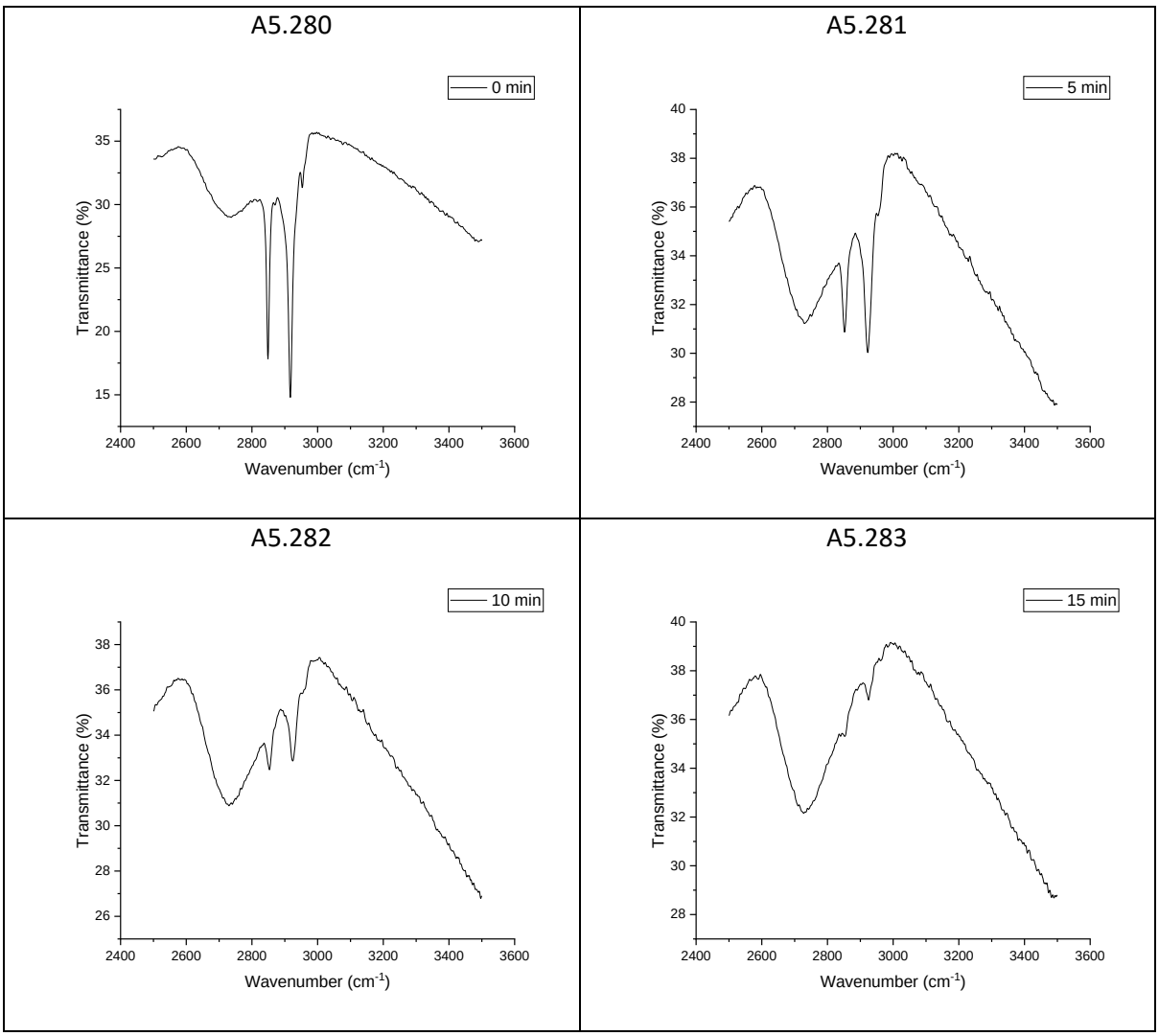

A5.284

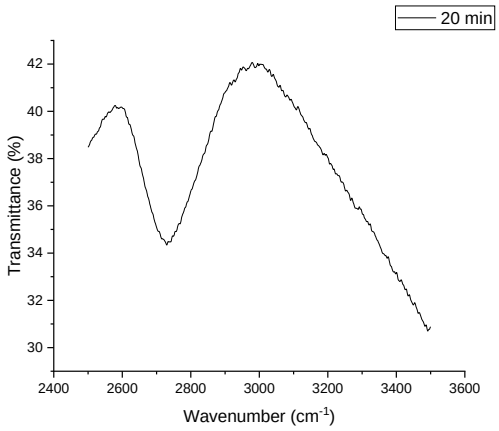

A5.285

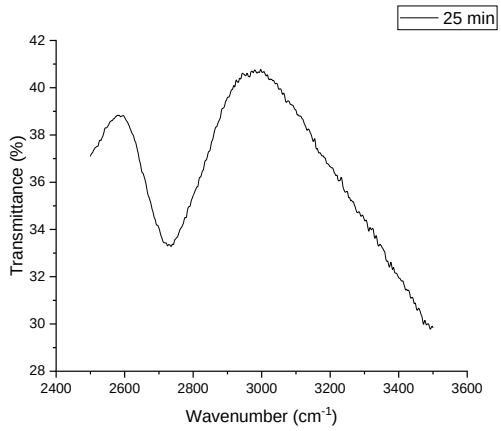

A5.286

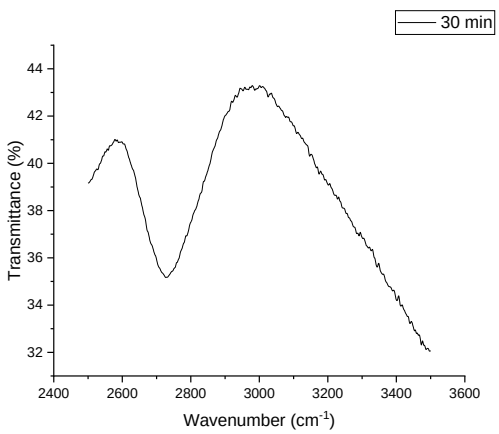

A5.287

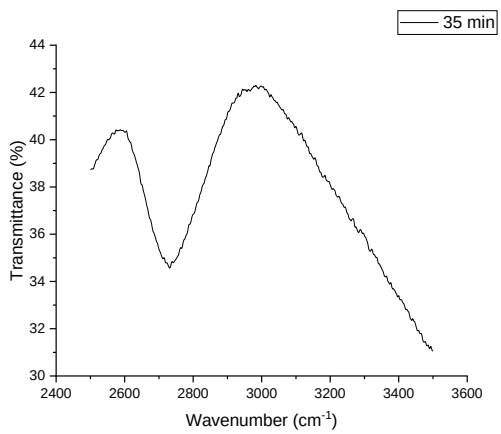

A5.288

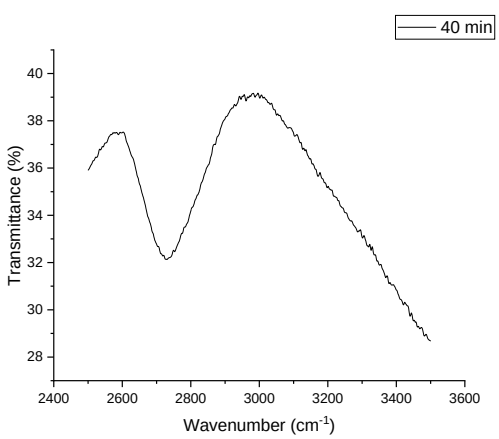

A: 5.33 DRIFT spectra of stearic acid on a 1 wt% Cu-doped *meso*-TiO_2 film prepared at 6000 rpm

These FTIR spectra show the C-H stretch of stearic acid that was used during photocatalytic testing to monitor the progress of the reaction with exposure to UV light. The total irradiation time is listed on each graph.

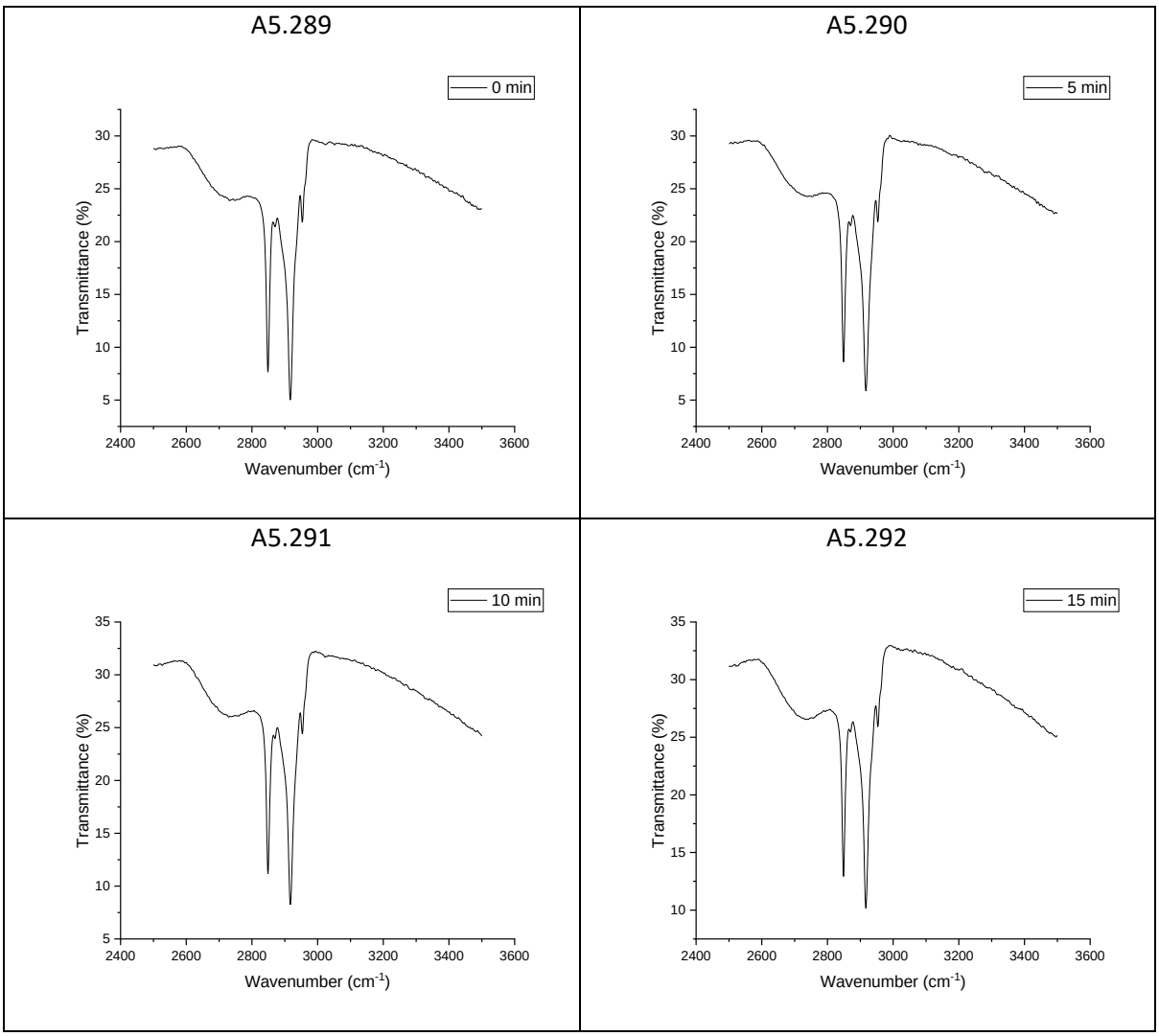

A5.293

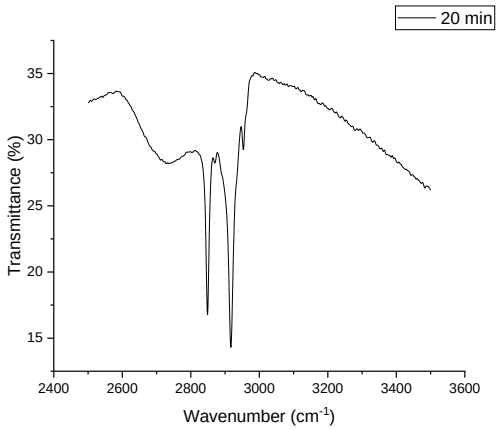

A5.294

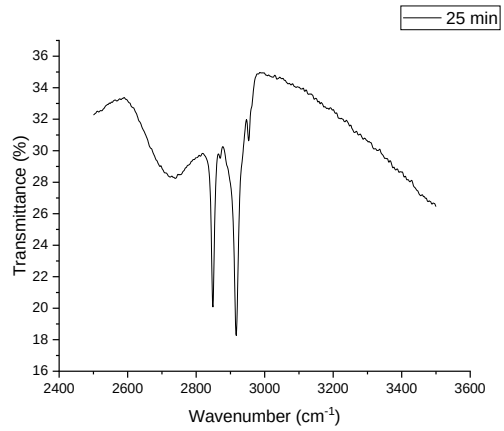

A5.295

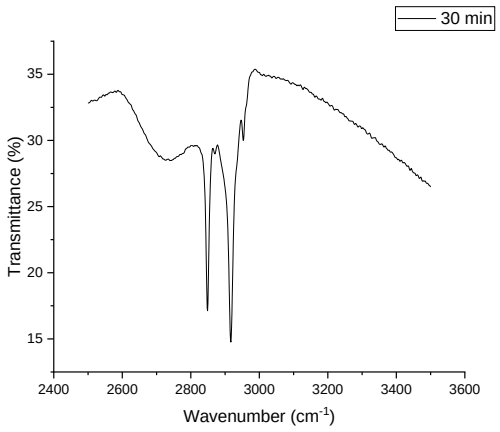

A5.296

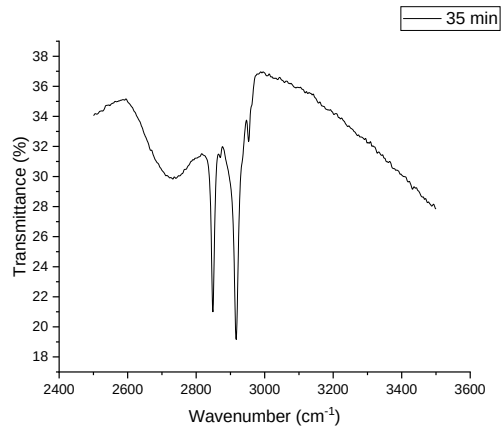

A5.297

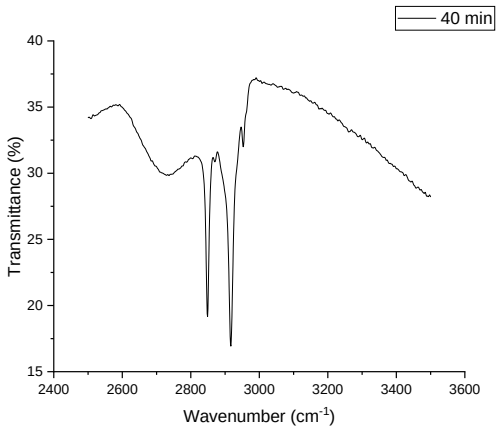

A: 5.34 DRIFT spectra of stearic acid on a 1 wt% Cu-doped *meso*-TiO_2 film prepared at 7000 rpm

These FTIR spectra show the C-H stretch of stearic acid that was used during photocatalytic testing to monitor the progress of the reaction with exposure to UV light. The total irradiation time is listed on each graph.

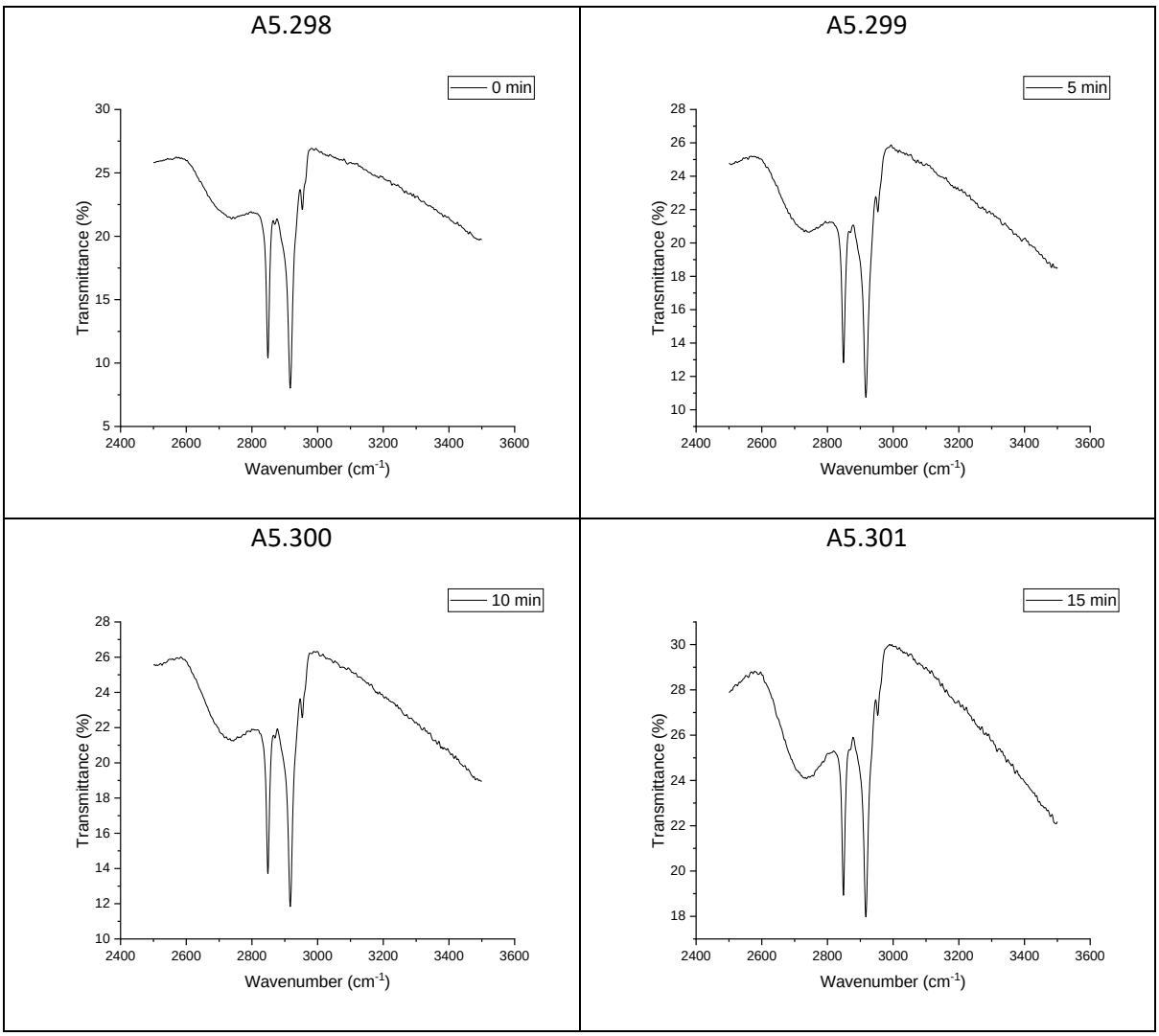

A5.302

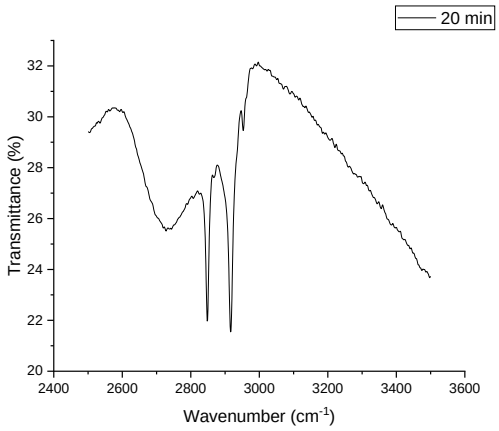

A5.303

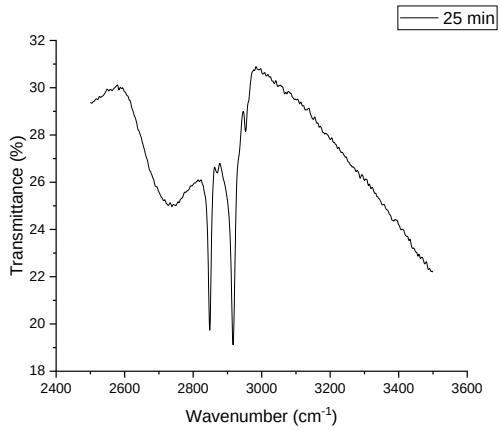

A5.304

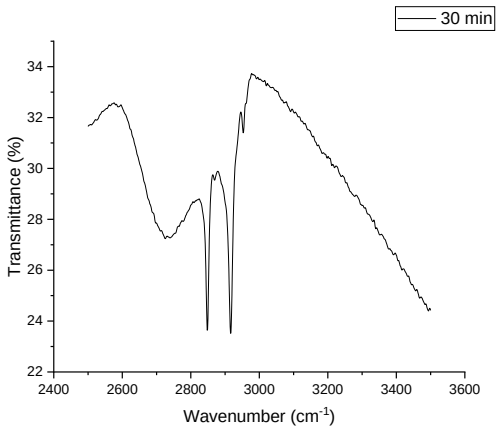

A5.305

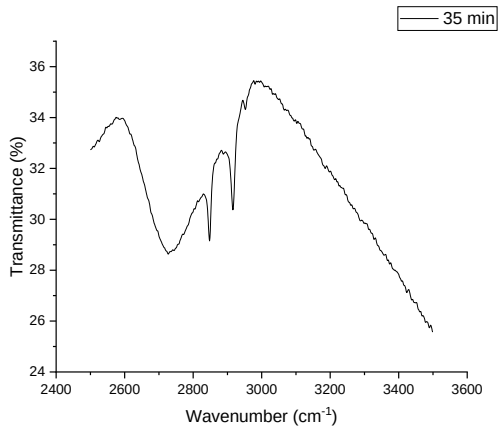

A5.306

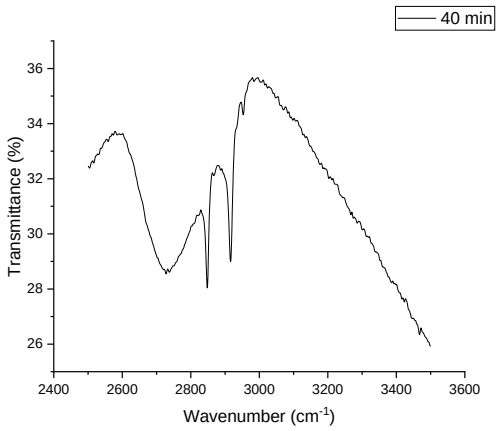

A: 5.35 DRIFT spectra of stearic acid on a 1 wt% Cu-doped *meso*-TiO_2 film prepared at 8000 rpm

These FTIR spectra show the C-H stretch of stearic acid that was used during photocatalytic testing to monitor the progress of the reaction with exposure to UV light. The total irradiation time is listed on each graph.

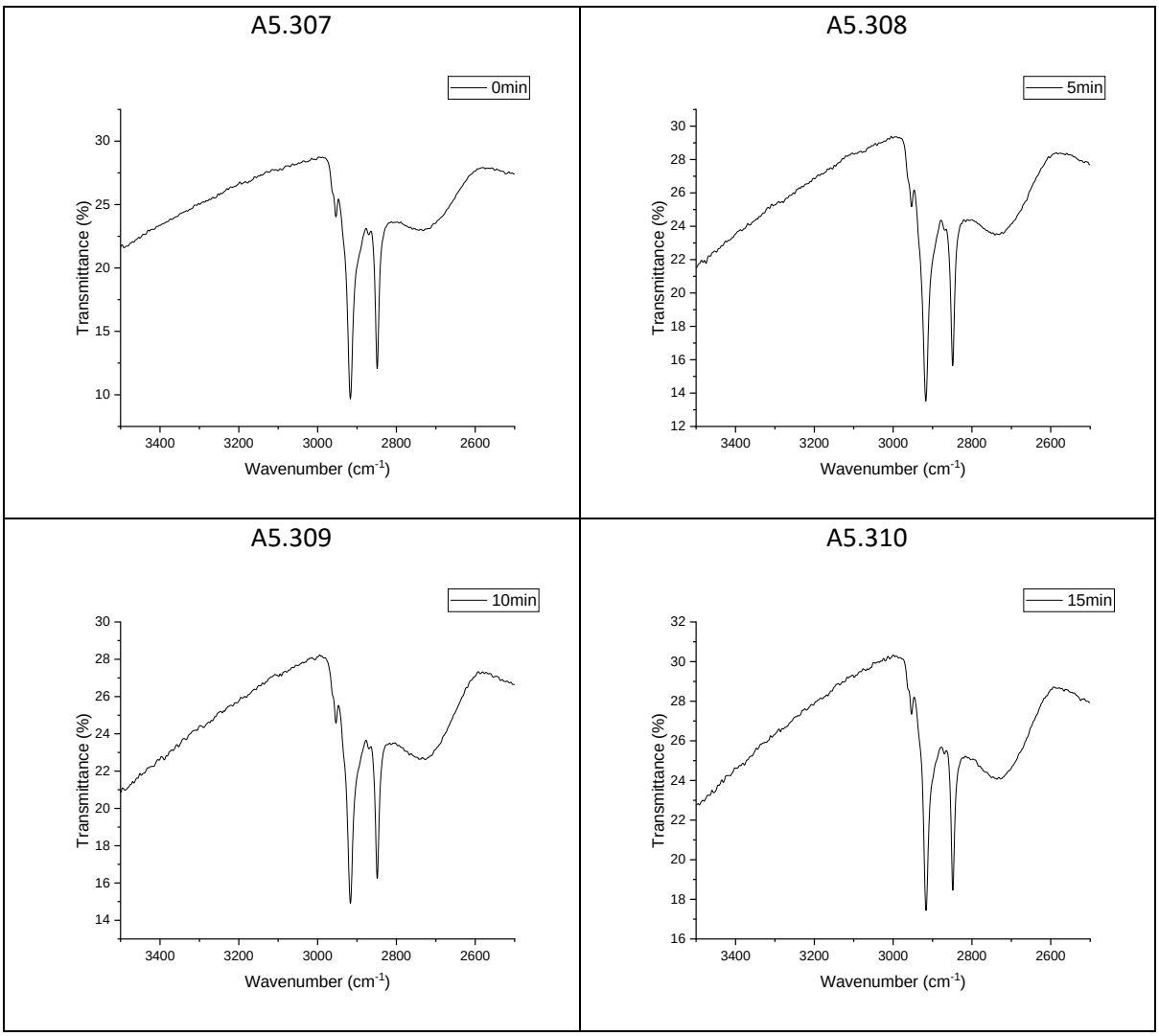

A5.311

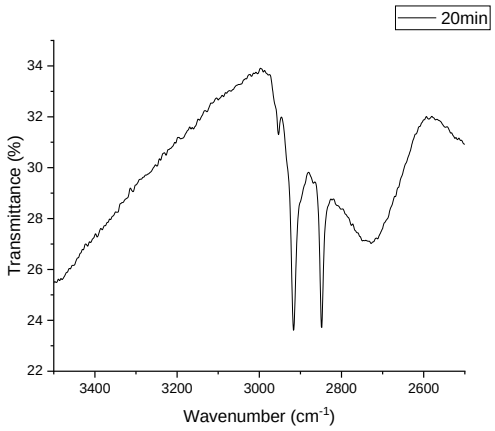

A5.312

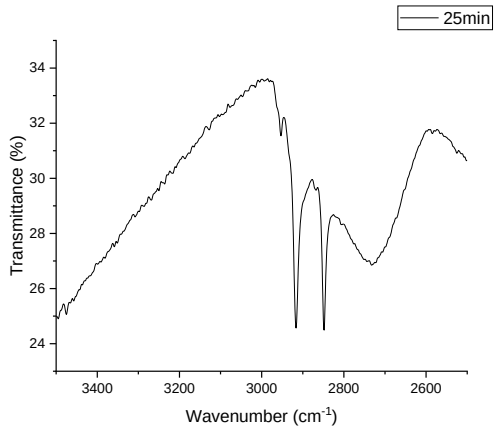

A5.313

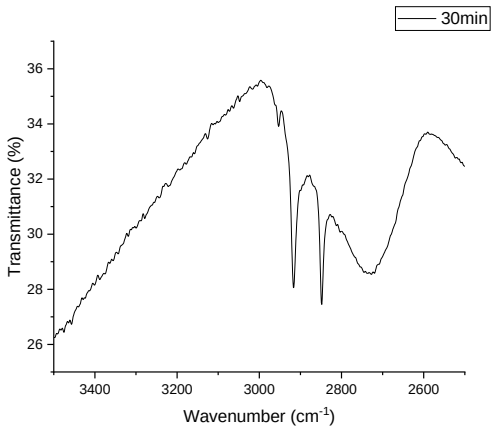

A5.314

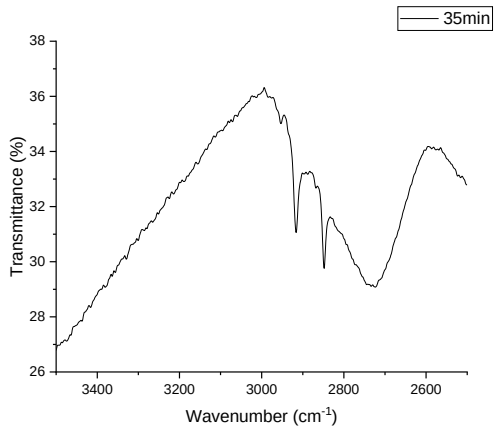

A5.315

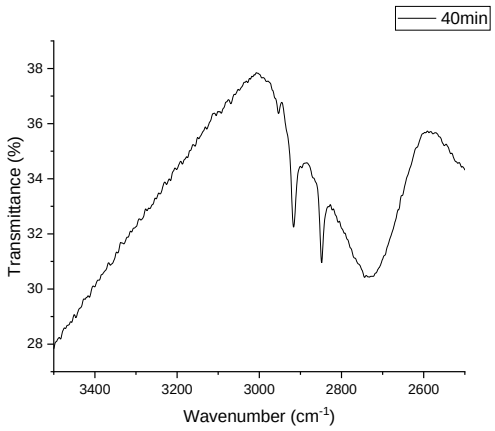

A: 5.36 DRIFT spectra of stearic acid on a 0.5 wt% Cu-doped *meso*-TiO_2 film prepared at 1000 rpm

These FTIR spectra show the C-H stretch of stearic acid that was used during photocatalytic testing to monitor the progress of the reaction with exposure to UV light. The total irradiation time is listed on each graph.

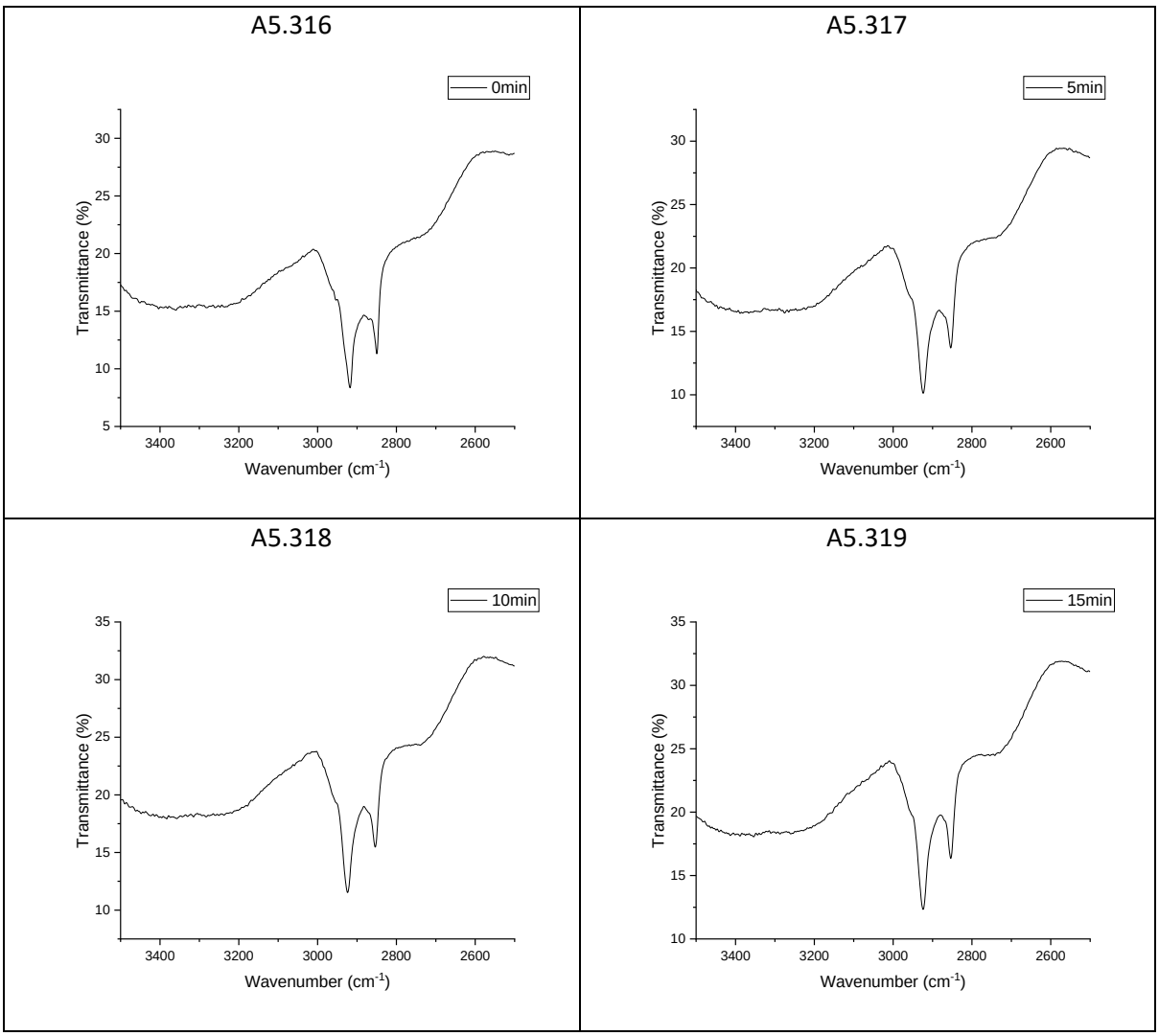

A5.320

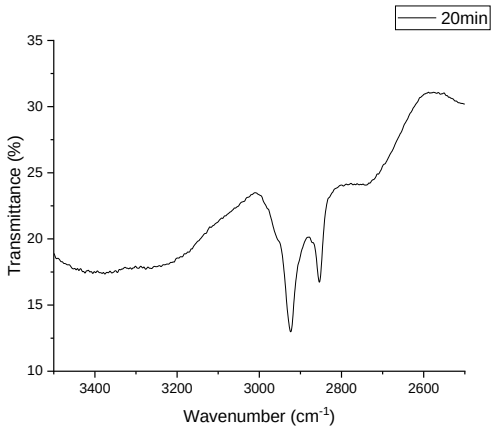

A5.321

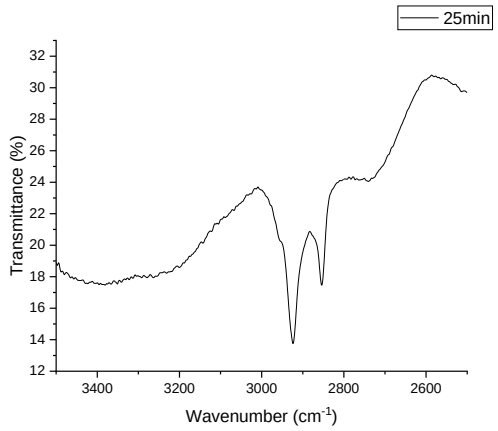

A5.322

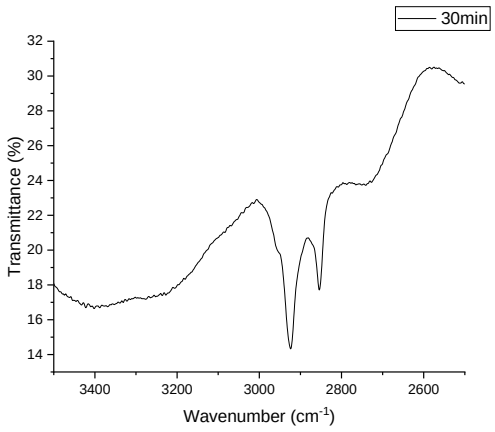

A5.323

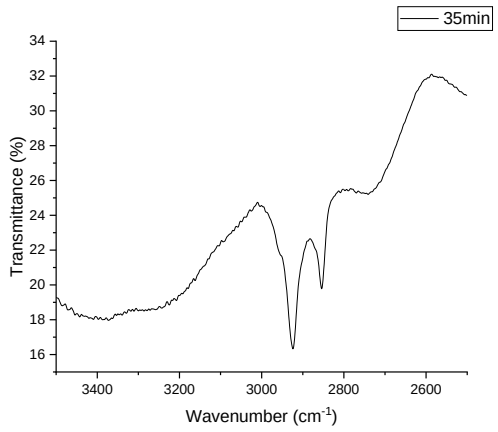

A5.324

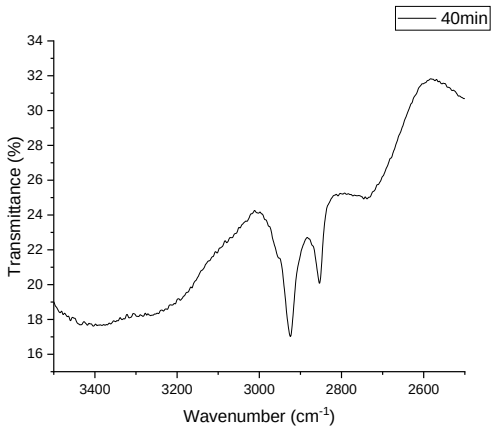

A: 5.37 DRIFT spectra of stearic acid on a 0.5 wt% Cu-doped *meso*-TiO_2 film prepared at 2000 rpm

These FTIR spectra show the C-H stretch of stearic acid that was used during photocatalytic testing to monitor the progress of the reaction with exposure to UV light. The total irradiation time is listed on each graph.

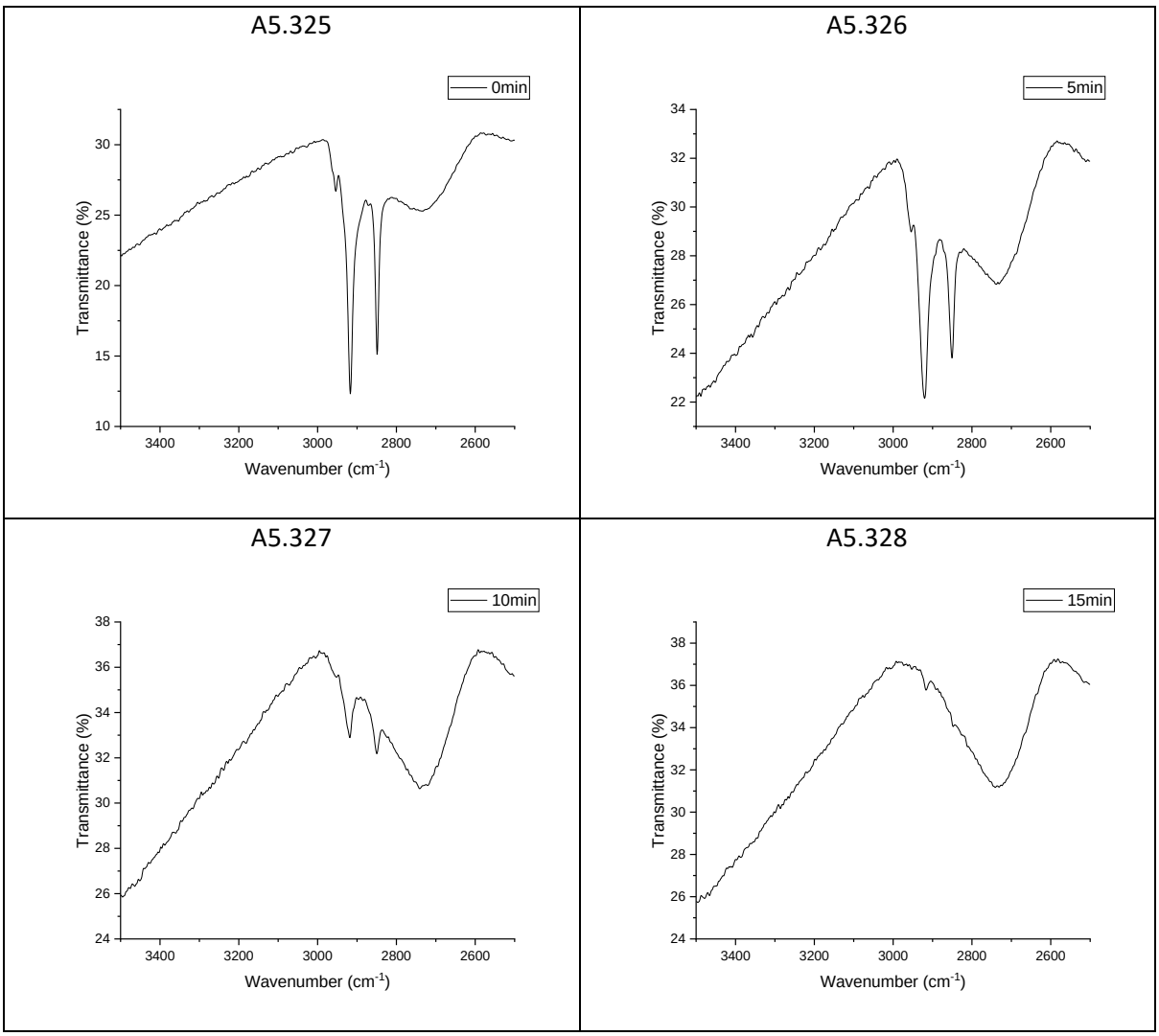

A5.329

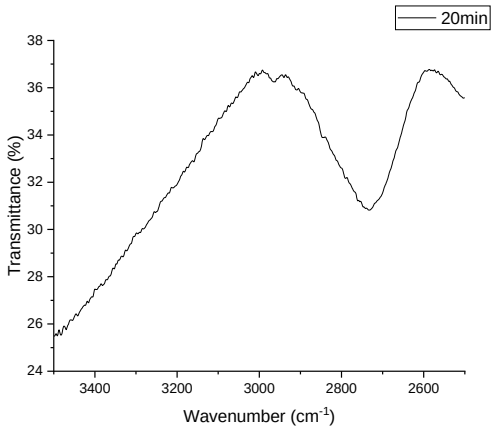

A5.330

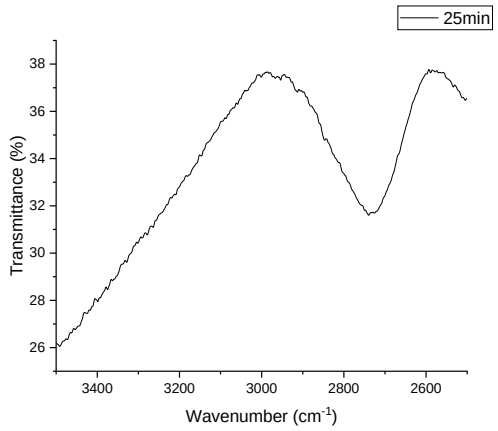

A5.331

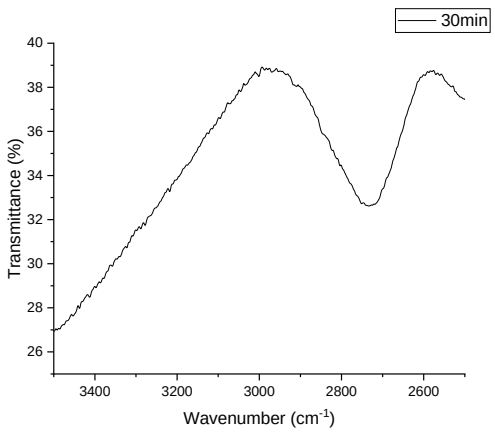

A5.332

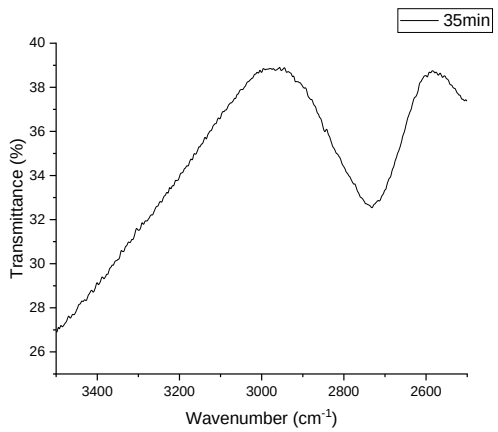

A5.333

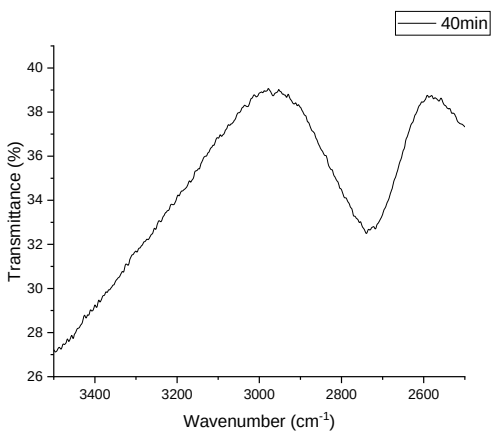

A: 5.38 DRIFT spectra of stearic acid on a 0.5 wt% Cu-doped *meso*-TiO_2 film prepared at 3000 rpm

These FTIR spectra show the C-H stretch of stearic acid that was used during photocatalytic testing to monitor the progress of the reaction with exposure to UV light. The total irradiation time is listed on each graph.

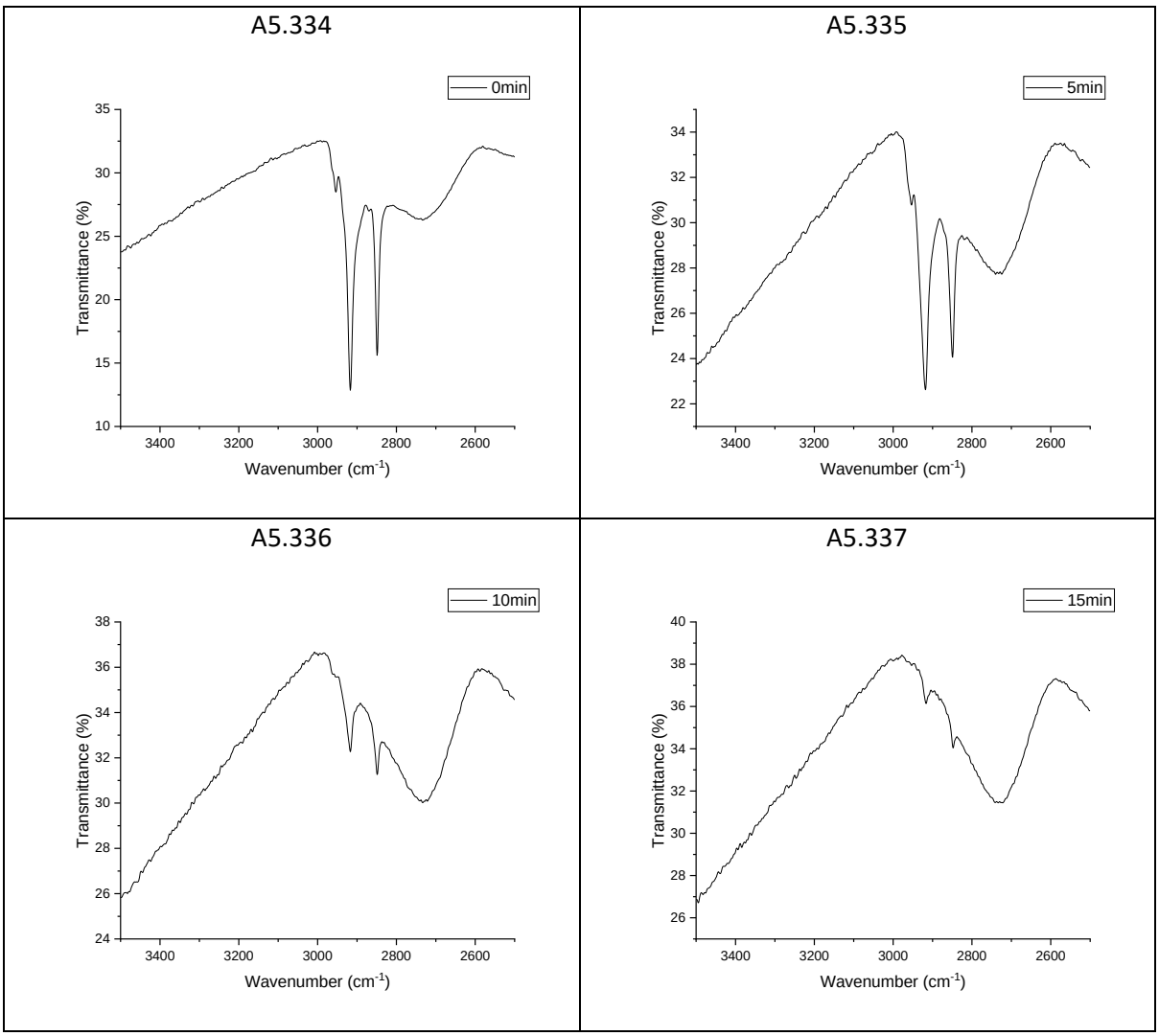

A5.338

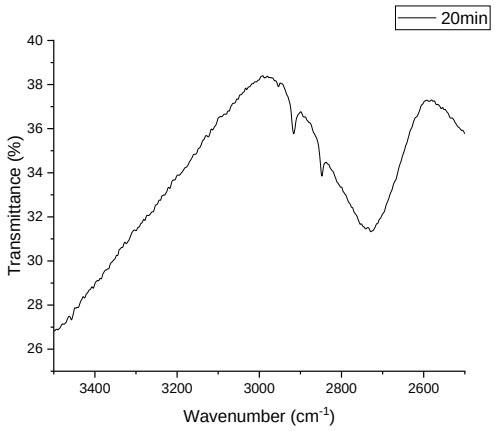

A5.339

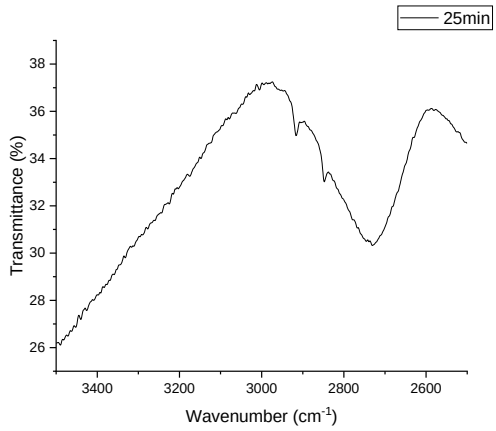

A5.340

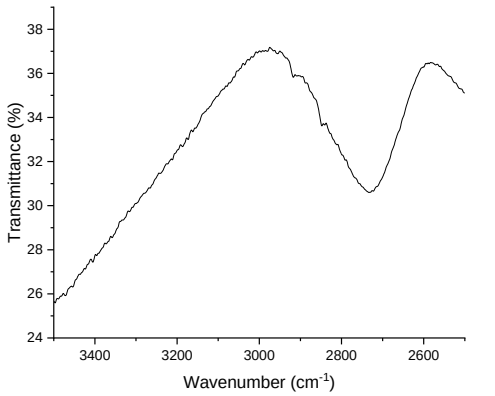

A5.341

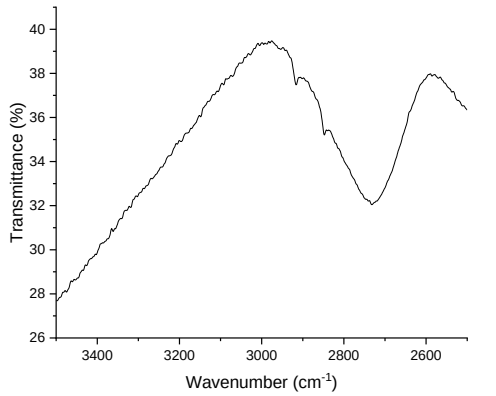

A5.342

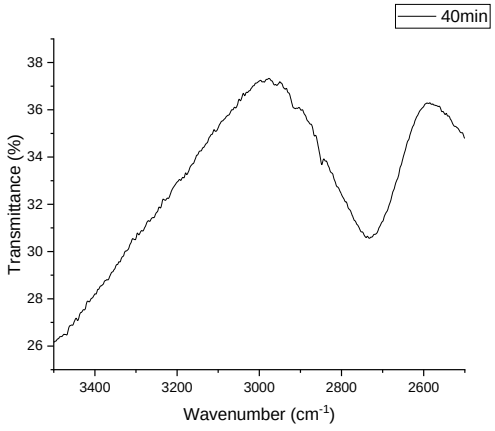

A: 5.39 DRIFT spectra of stearic acid on a 0.5 wt% Cu-doped *meso*-TiO_2 film prepared at 4000 rpm

These FTIR spectra show the C-H stretch of stearic acid that was used during photocatalytic testing to monitor the progress of the reaction with exposure to UV light. The total irradiation time is listed on each graph.

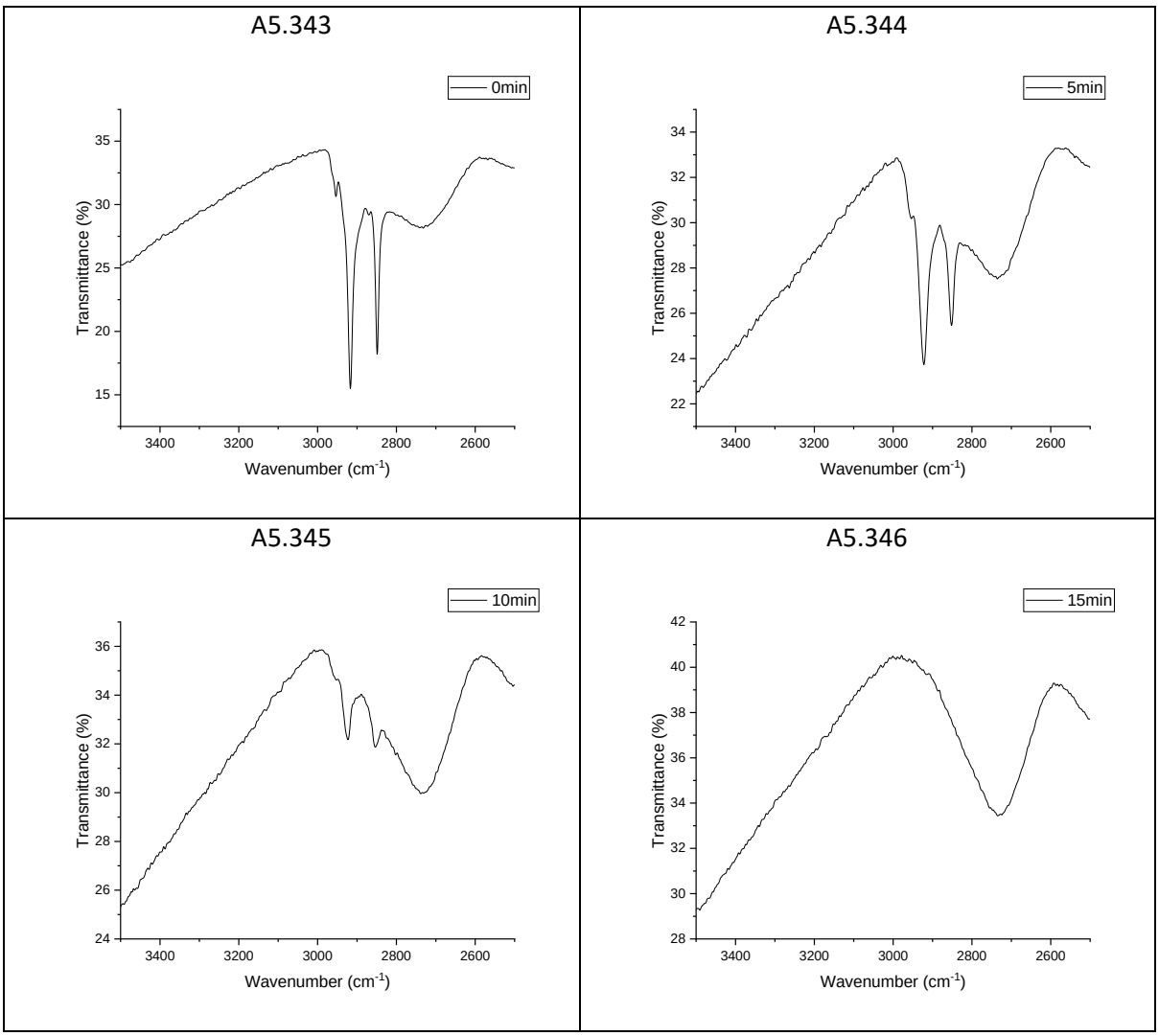

A5.347

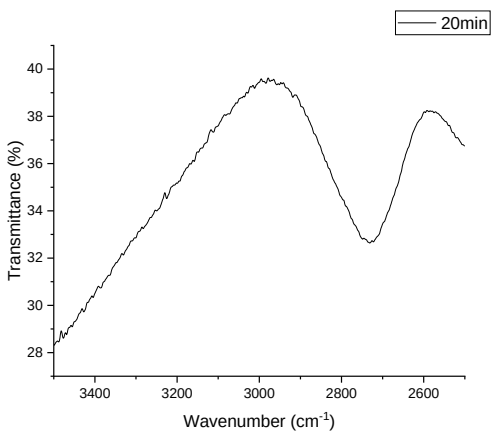
20min
Transmittance (%)
40
38
36
34
32
30
28
3400
3200
3000
2800
2600
Wavenumber (cm-1)

A5.348

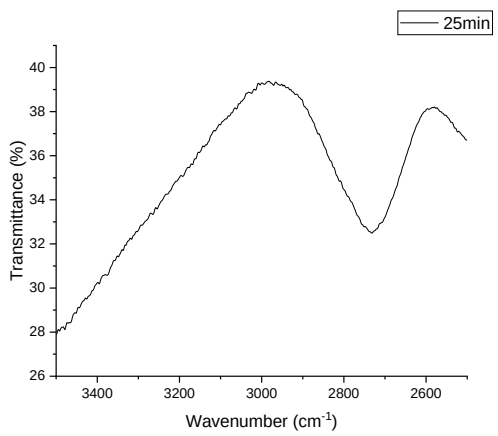
25min
Transmittance (%)
40
38
36
34
32
30
28
26
3400
3200
3000
2800
2600
Wavenumber (cm-1)

A: 5.40 DRIFT spectra of stearic acid on a 0.5 wt% Cu-doped *meso*-TiO_2 film prepared at 5000 rpm

These FTIR spectra show the C-H stretch of stearic acid that was used during photocatalytic testing to monitor the progress of the reaction with exposure to UV light. The total irradiation time is listed on each graph.

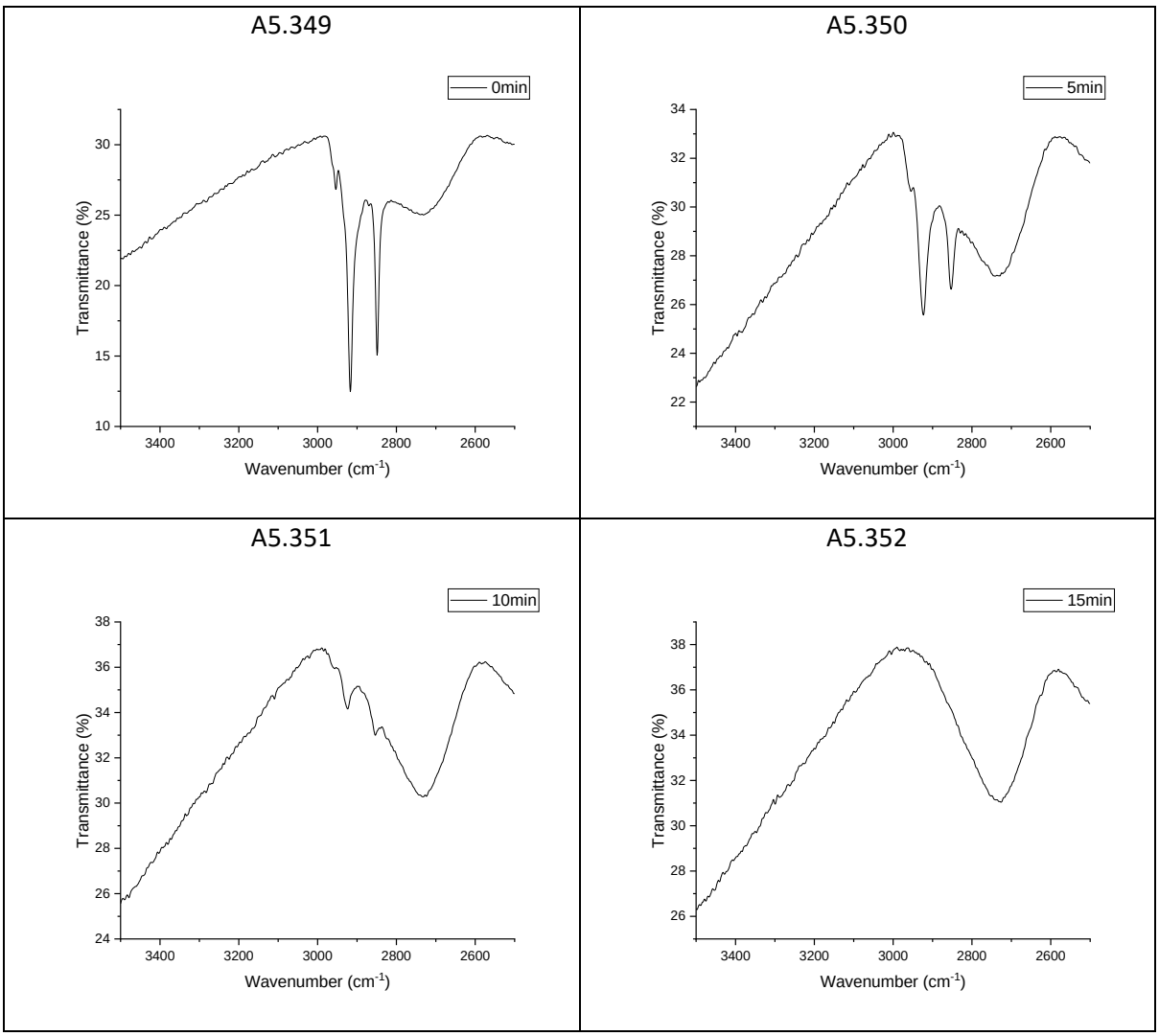

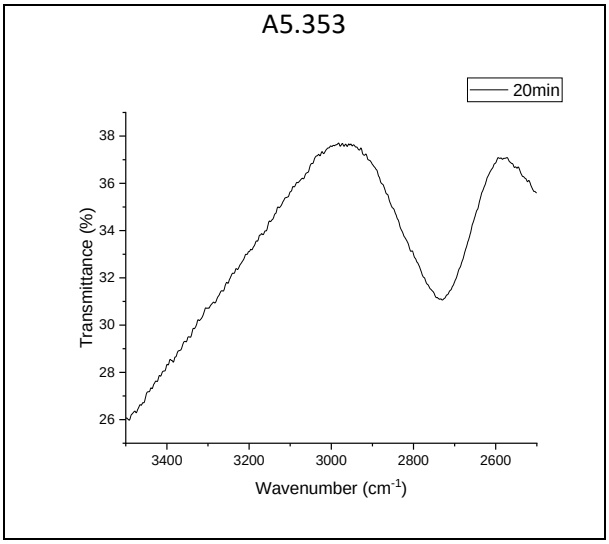
A5.353
20min
Transmittance (%)
38
36
34
32
30
28
26
3400
3200
3000
2800
2600
Wavenumber (cm-1)

A: 5.41 DRIFT spectra of stearic acid on a 0.5 wt% Cu-doped *meso*-TiO_2 film prepared at 6000 rpm

These FTIR spectra show the C-H stretch of stearic acid that was used during photocatalytic testing to monitor the progress of the reaction with exposure to UV light. The total irradiation time is listed on each graph.

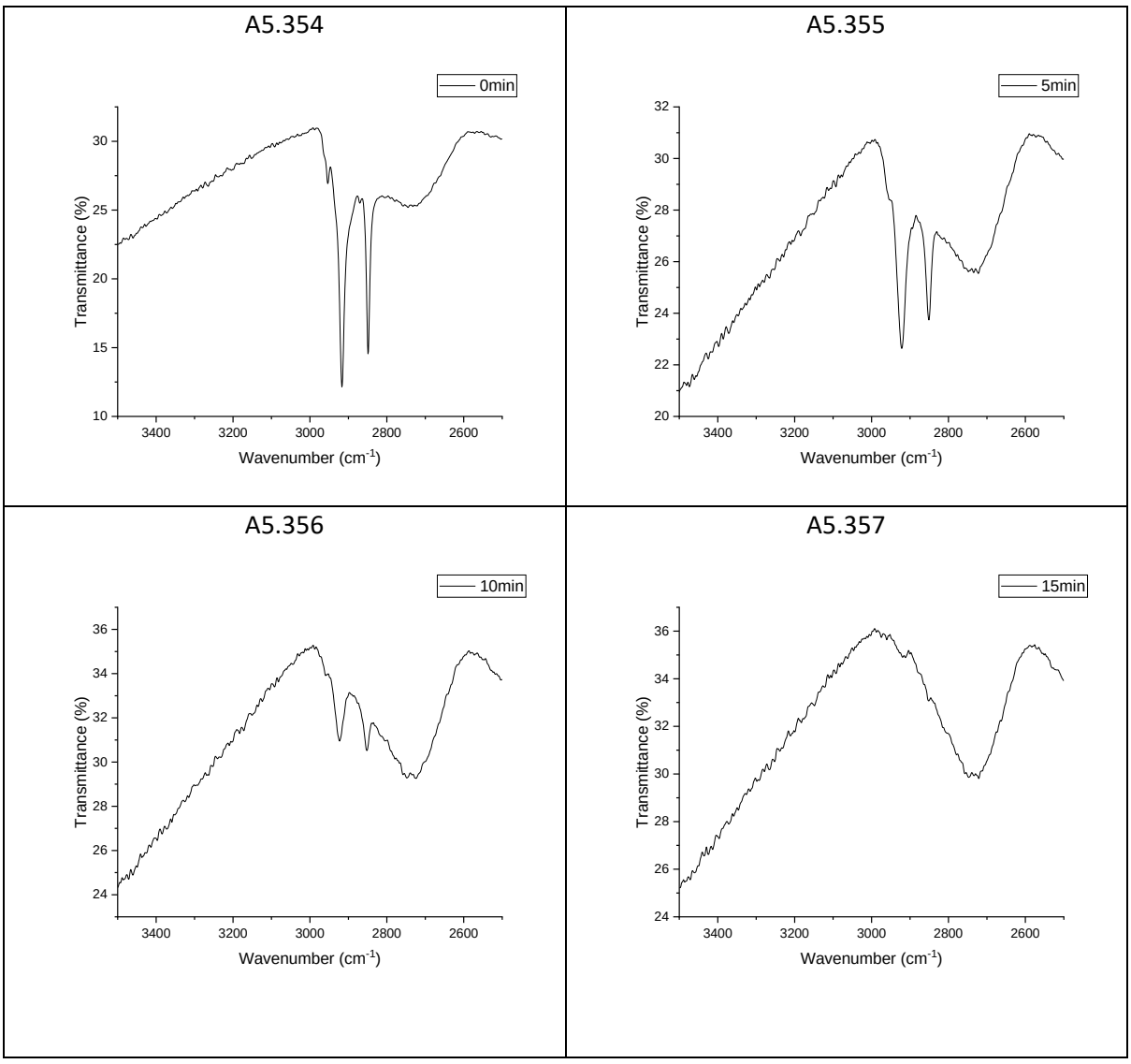

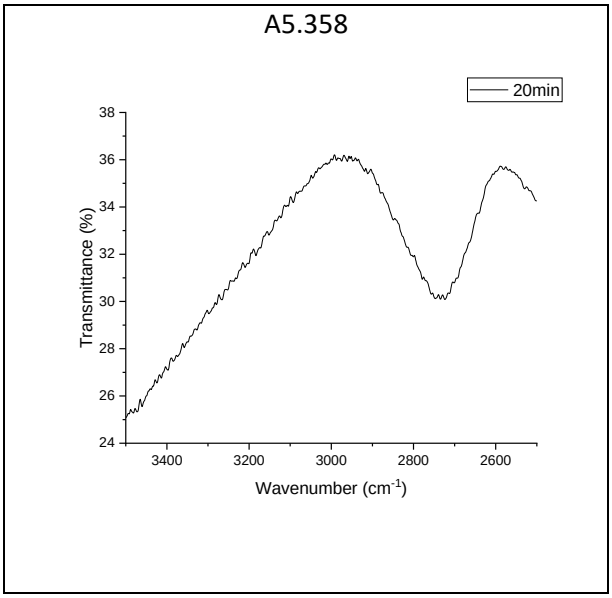
A5.358
20min
Transmittance (%)
38
36
34
32
30
28
26
24
3400
3200
3000
2800
2600
Wavenumber (cm-1)

A: 5.42 DRIFT spectra of stearic acid on a 0.5 wt% Cu-doped *meso*-TiO_2 film prepared at 7000 rpm

These FTIR spectra show the C-H stretch of stearic acid that was used during photocatalytic testing to monitor the progress of the reaction with exposure to UV light. The total irradiation time is listed on each graph.

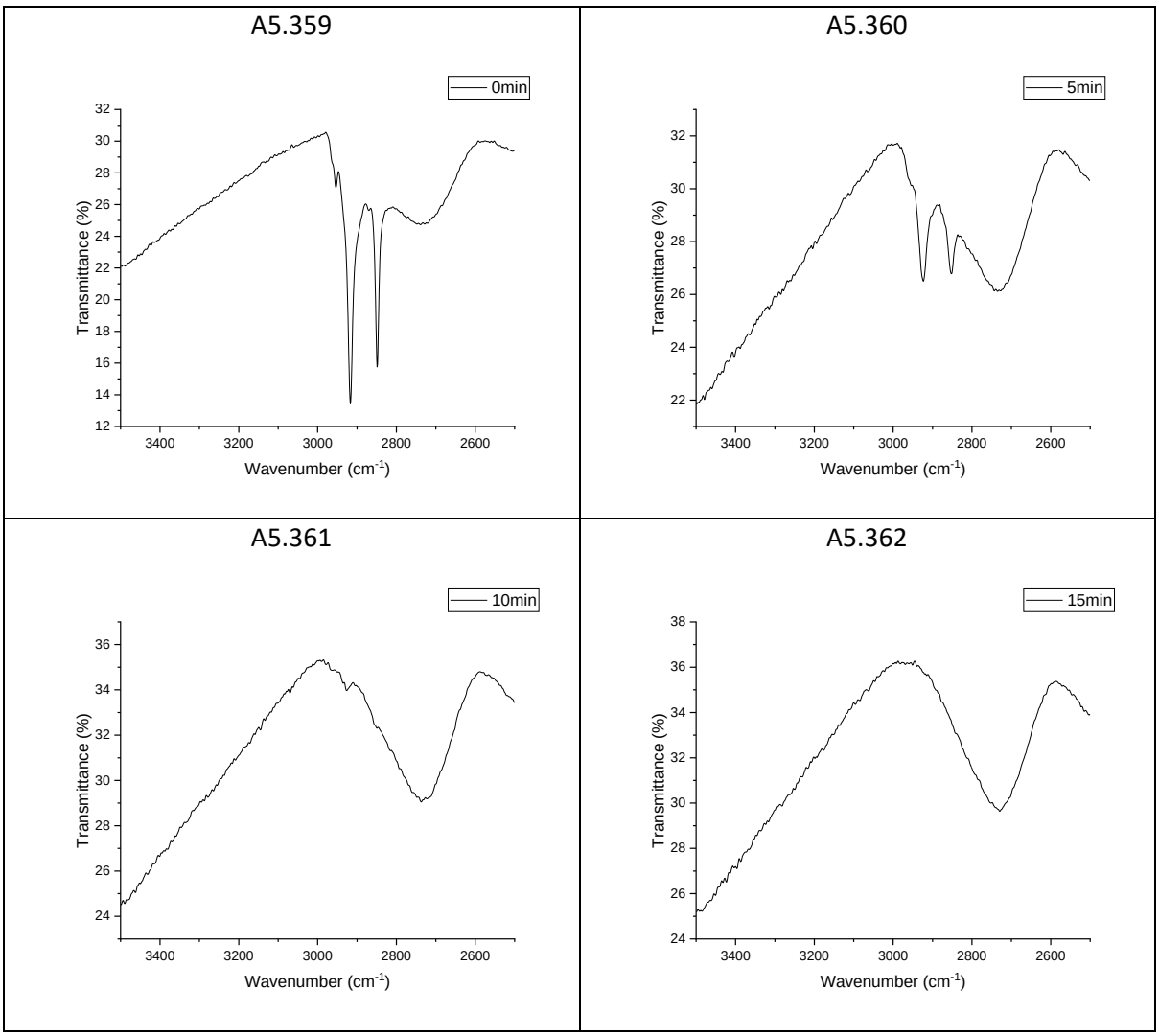

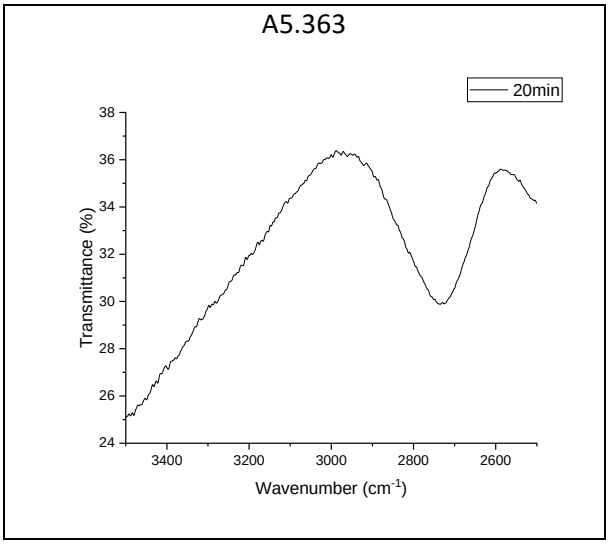
A5.363
20min
Transmittance (%)
38
36
34
32
30
28
26
24
3400
3200
3000
2800
2600
Wavenumber (cm-1)

A: 5.43 DRIFT spectra of stearic acid on a 0.5 wt% Cu-doped *meso*-TiO_2 film prepared at 8000 rpm

These FTIR spectra show the C-H stretch of stearic acid that was used during photocatalytic testing to monitor the progress of the reaction with exposure to UV light. The total irradiation time is listed on each graph.

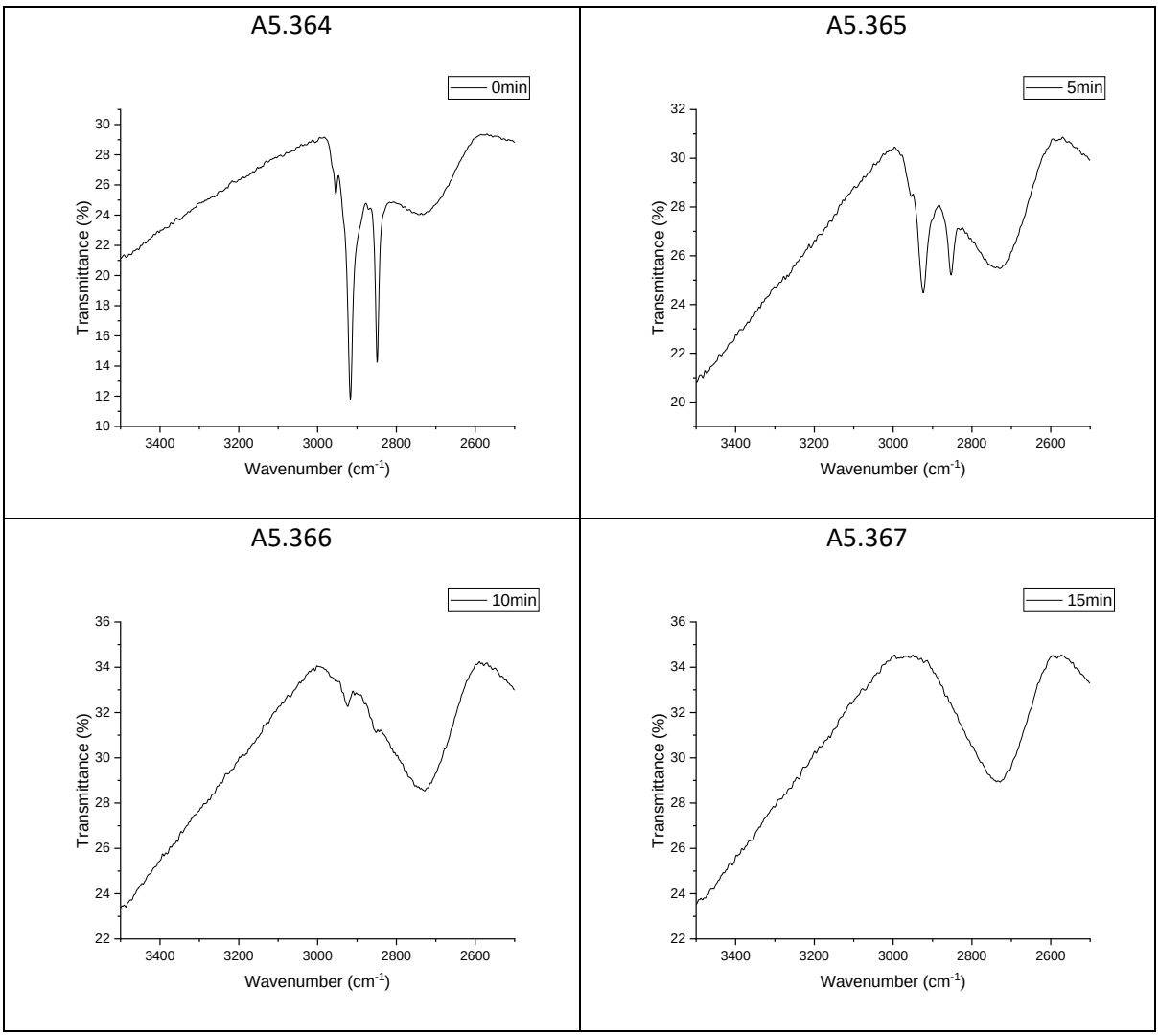

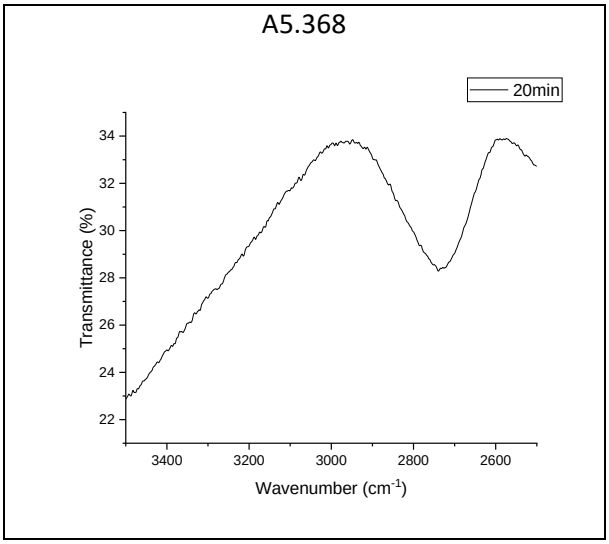
A5.368
20min
Transmittance (%)
34
32
30
28
26
24
22
3400
3200
3000
2800
2600
Wavenumber (cm-1)

A: 5.44 DRIFT spectra of stearic acid on a 0.1 wt% Cu-doped *meso*-TiO_2 film prepared at 500 rpm

These FTIR spectra show the C-H stretch of stearic acid that was used during photocatalytic testing to monitor the progress of the reaction with exposure to UV light. The total irradiation time is listed on each graph.

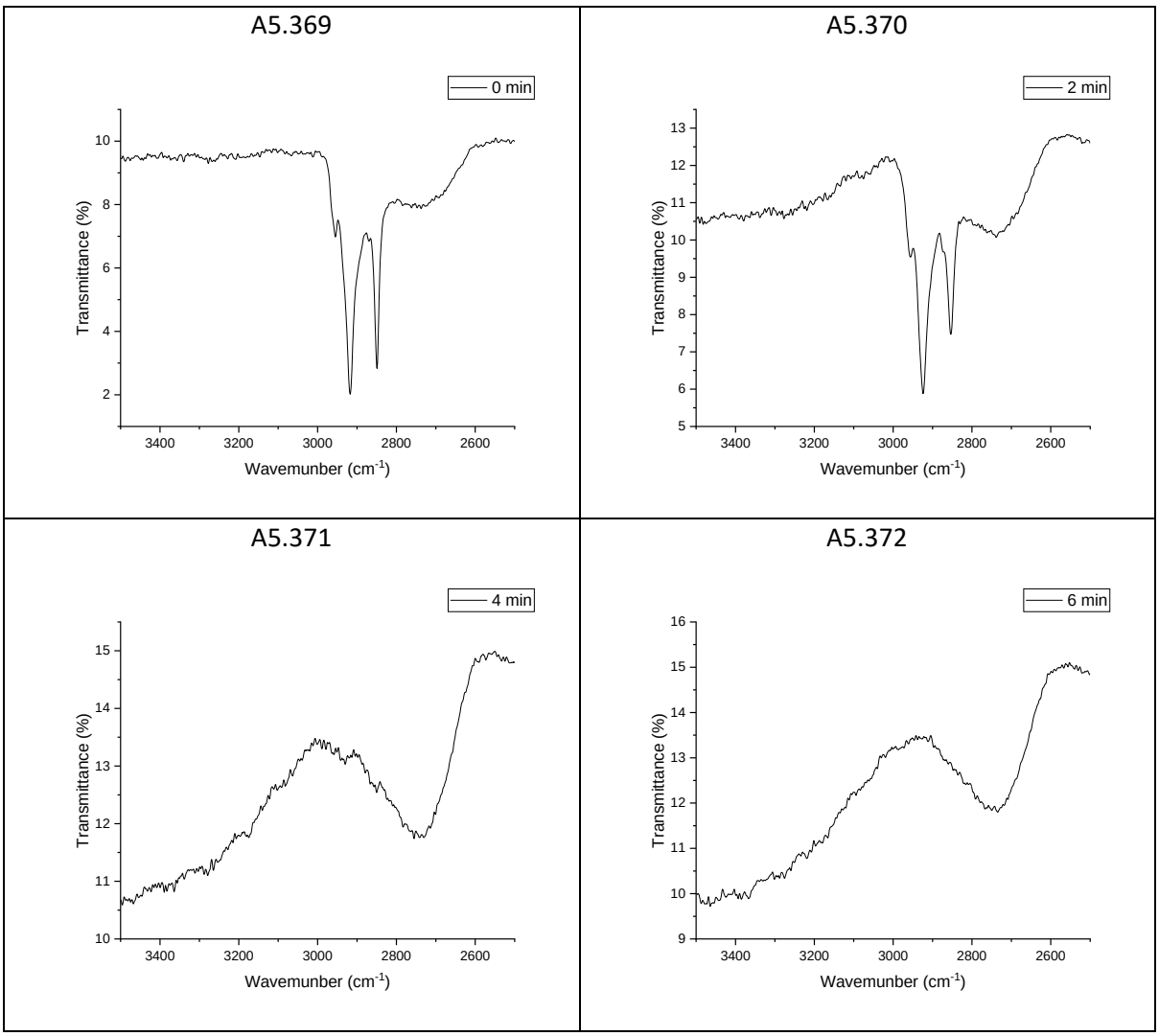

A5.373

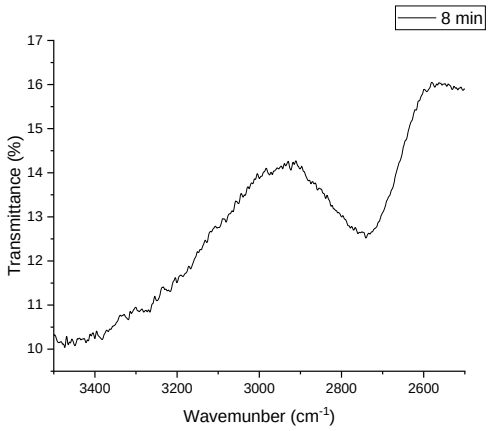
8 min
Transmittance (%)
Wavemunber (cm-1)

A5.374

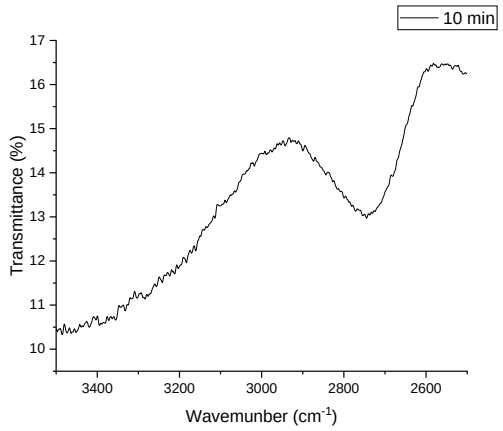
10 min
Transmittance (%)
Wavemunber (cm-1)

A: 5.45 DRIFT spectra of stearic acid on a 0.1 wt% Cu-doped *meso*-TiO_2 film prepared at 1000 rpm

These FTIR spectra show the C-H stretch of stearic acid that was used during photocatalytic testing to monitor the progress of the reaction with exposure to UV light. The total irradiation time is listed on each graph.

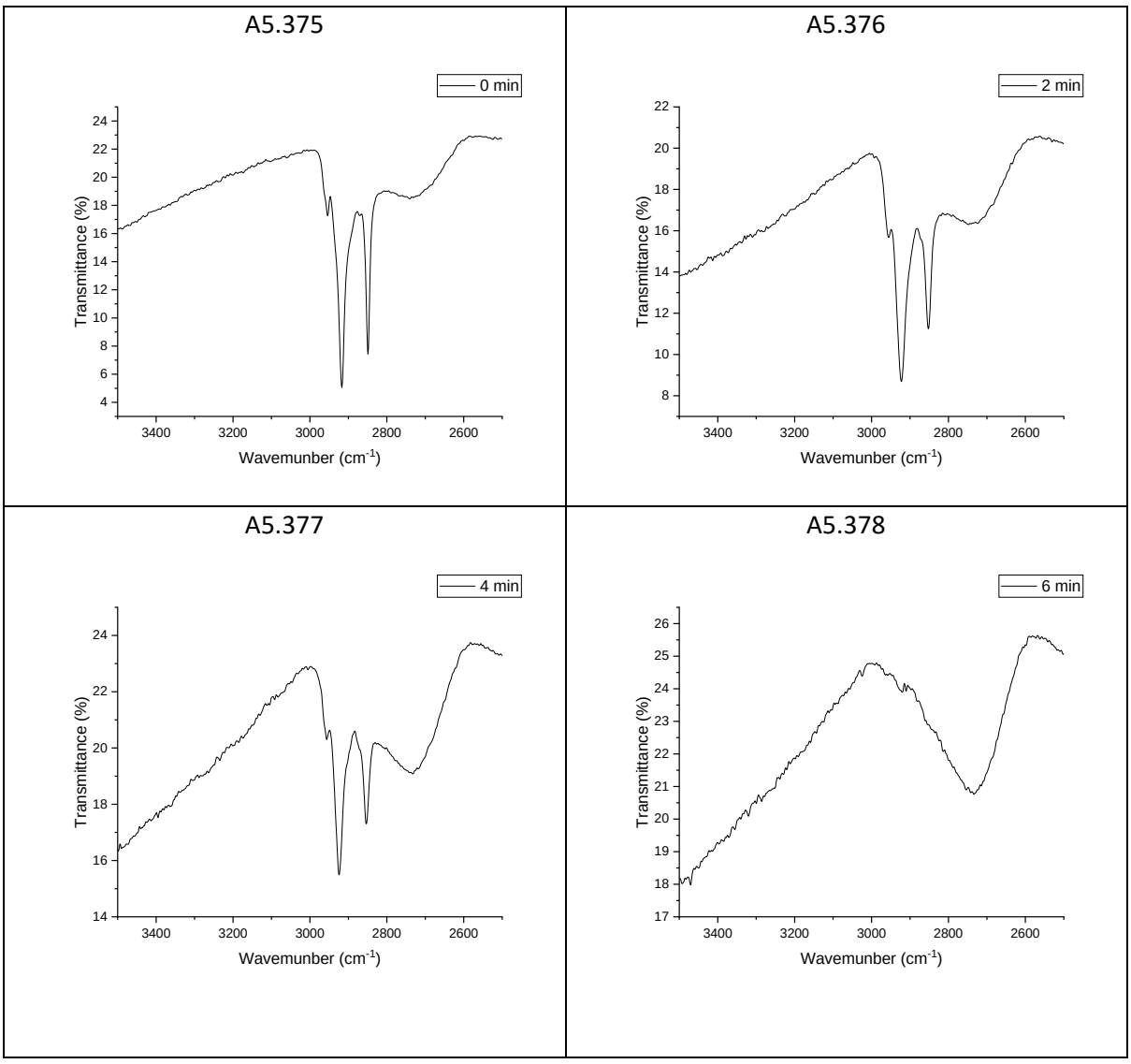

A5.379

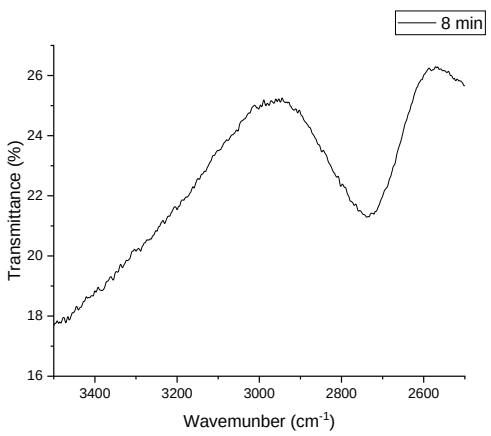
8 min
Transmittance (%)
26
24
22
20
18
16
3400
3200
3000
2800
2600
Wavemunber (cm-1)

A5.380

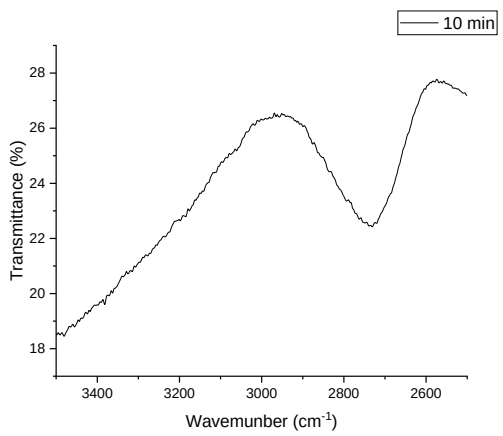
10 min
Transmittance (%)
28
26
24
22
20
18
3400
3200
3000
2800
2600
Wavemunber (cm-1)

A: 5.46 DRIFT spectra of stearic acid on a 0.1 wt% Cu-doped *meso*-TiO_2 film prepared at 2000 rpm

These FTIR spectra show the C-H stretch of stearic acid that was used during photocatalytic testing to monitor the progress of the reaction with exposure to UV light. The total irradiation time is listed on each graph.

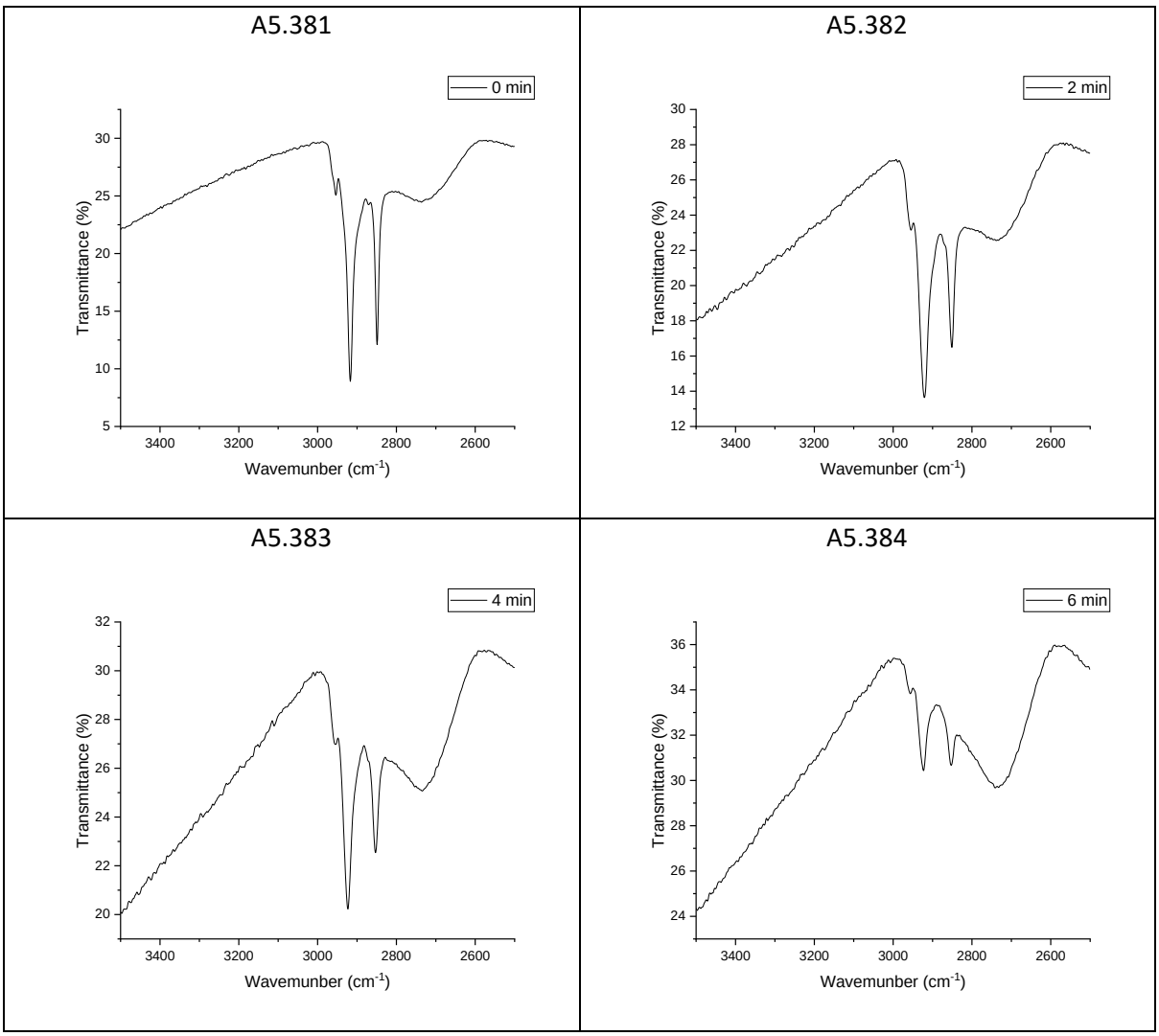

A5.385

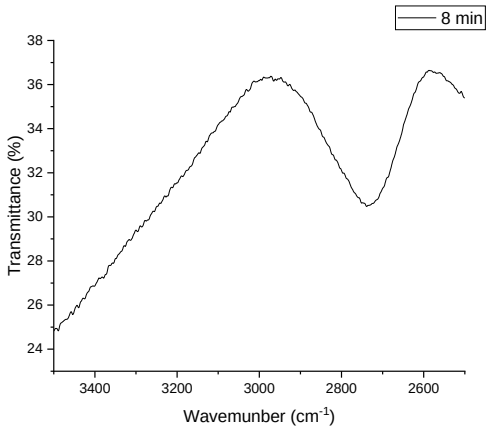
8 min
Transmittance (%)
38
36
34
32
30
28
26
24
3400
3200
3000
2800
2600
Wavemunber (cm-1)

A5.386

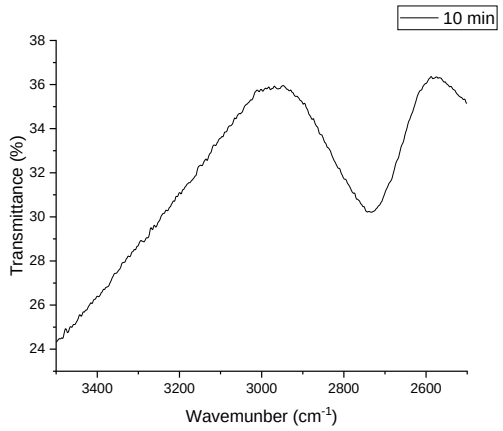
10 min
Transmittance (%)
38
36
34
32
30
28
26
24
3400
3200
3000
2800
2600
Wavemunber (cm-1)

A: 5.47 DRIFT spectra of stearic acid on a 0.1 wt% Cu-doped *meso*-TiO_2 film prepared at 3000 rpm

These FTIR spectra show the C-H stretch of stearic acid that was used during photocatalytic testing to monitor the progress of the reaction with exposure to UV light. The total irradiation time is listed on each graph.

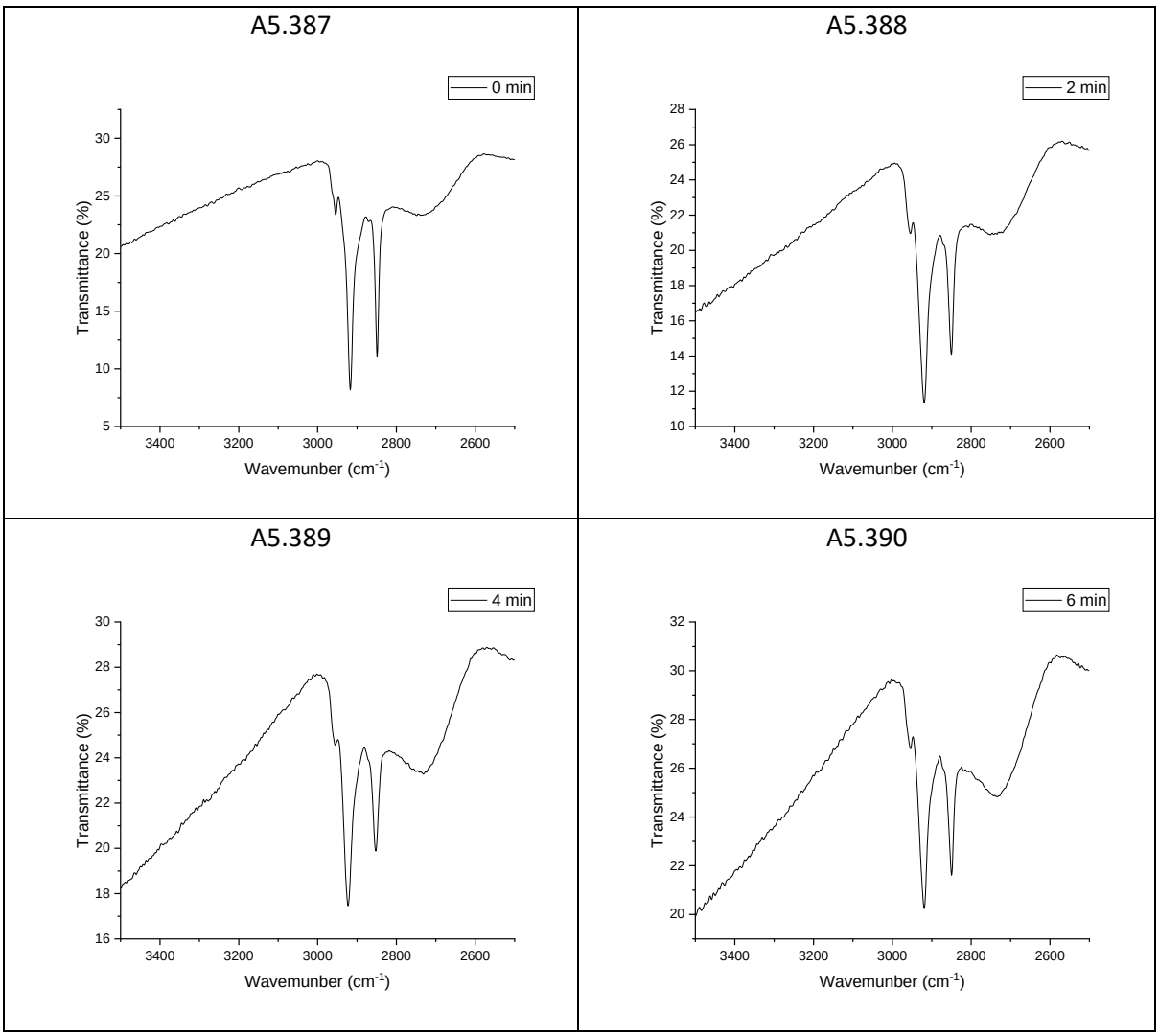

A5.391

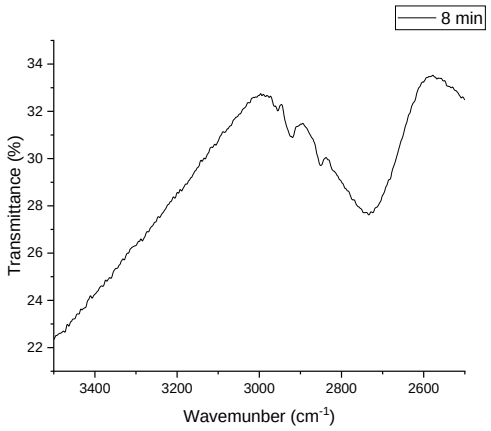

A5.392

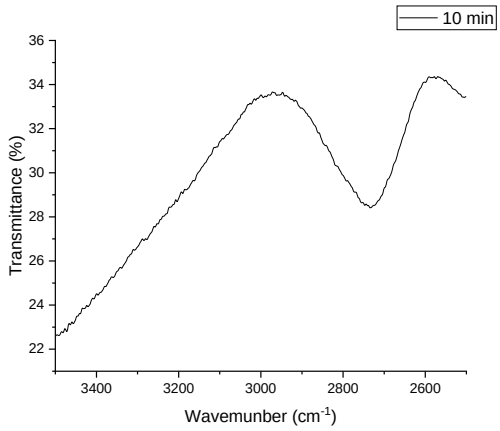

A5.393

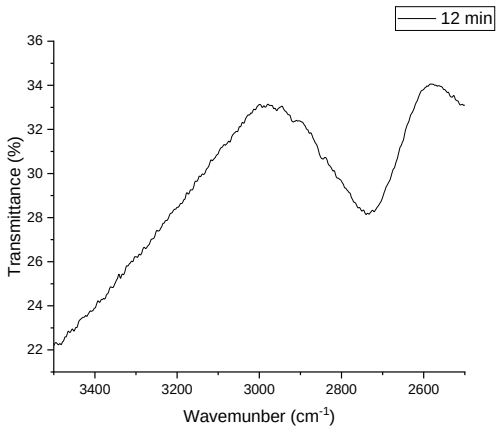

A: 5.48 DRIFT spectra of stearic acid on a 0.1 wt% Cu-doped *meso*-TiO_2 film prepared at 4000 rpm

These FTIR spectra show the C-H stretch of stearic acid that was used during photocatalytic testing to monitor the progress of the reaction with exposure to UV light. The total irradiation time is listed on each graph.

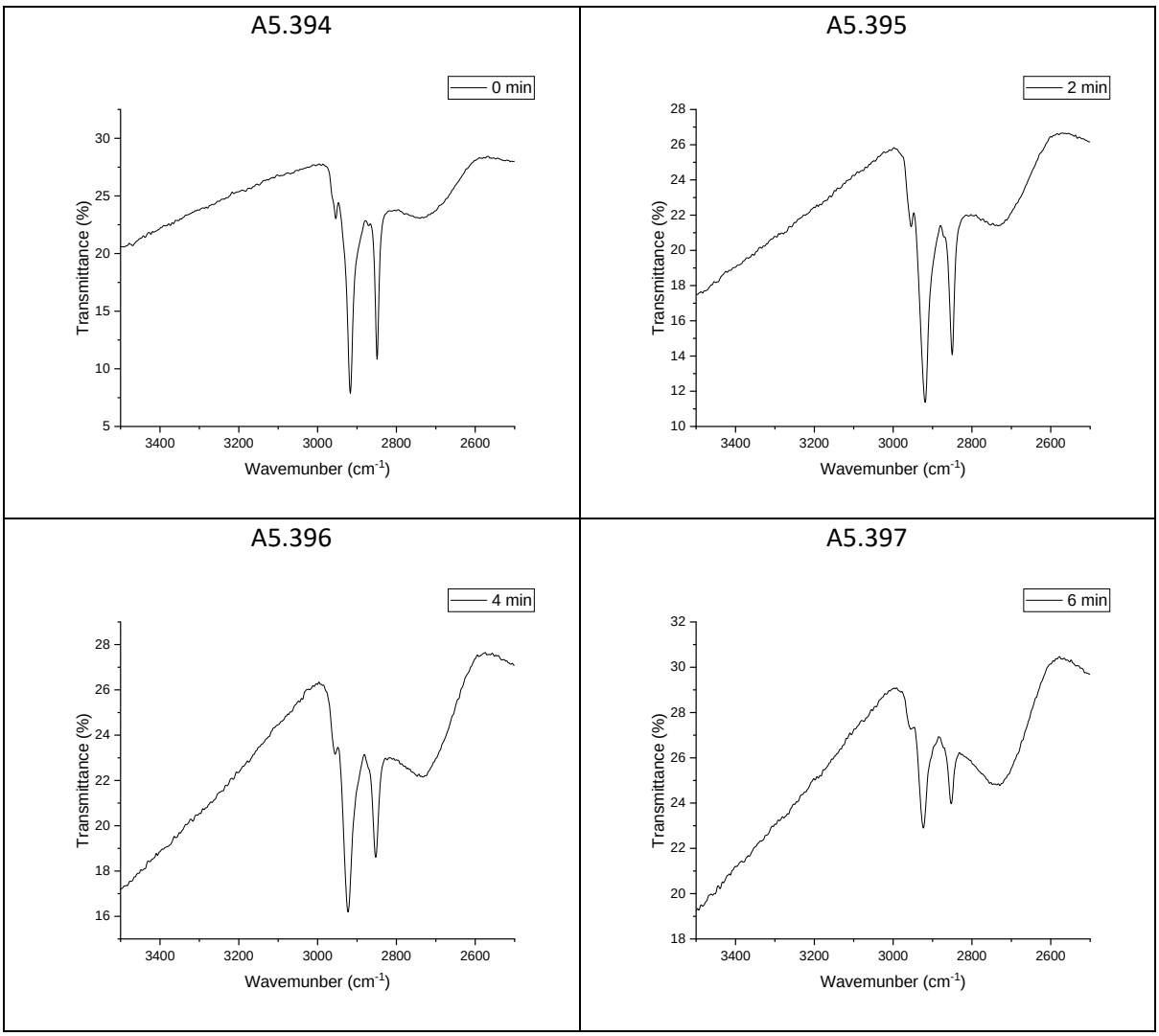

A5.398

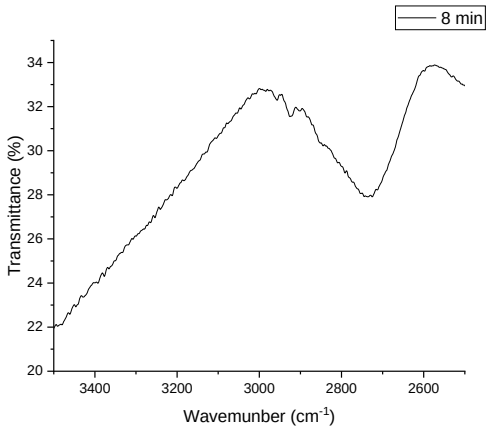

A5.399

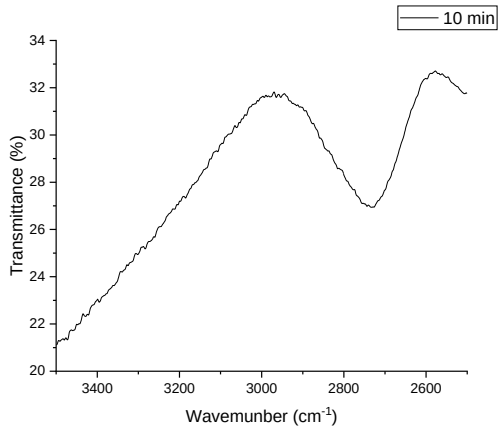

A5.400

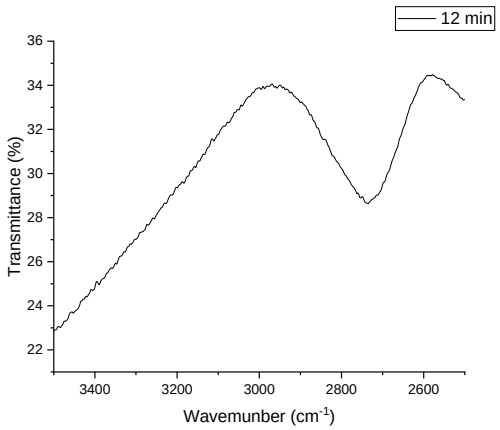

A: 5.49 DRIFT spectra of stearic acid on a 0.1 wt% Cu-doped *meso*-TiO_2 film prepared at 5000 rpm

These FTIR spectra show the C-H stretch of stearic acid that was used during photocatalytic testing to monitor the progress of the reaction with exposure to UV light. The total irradiation time is listed on each graph.

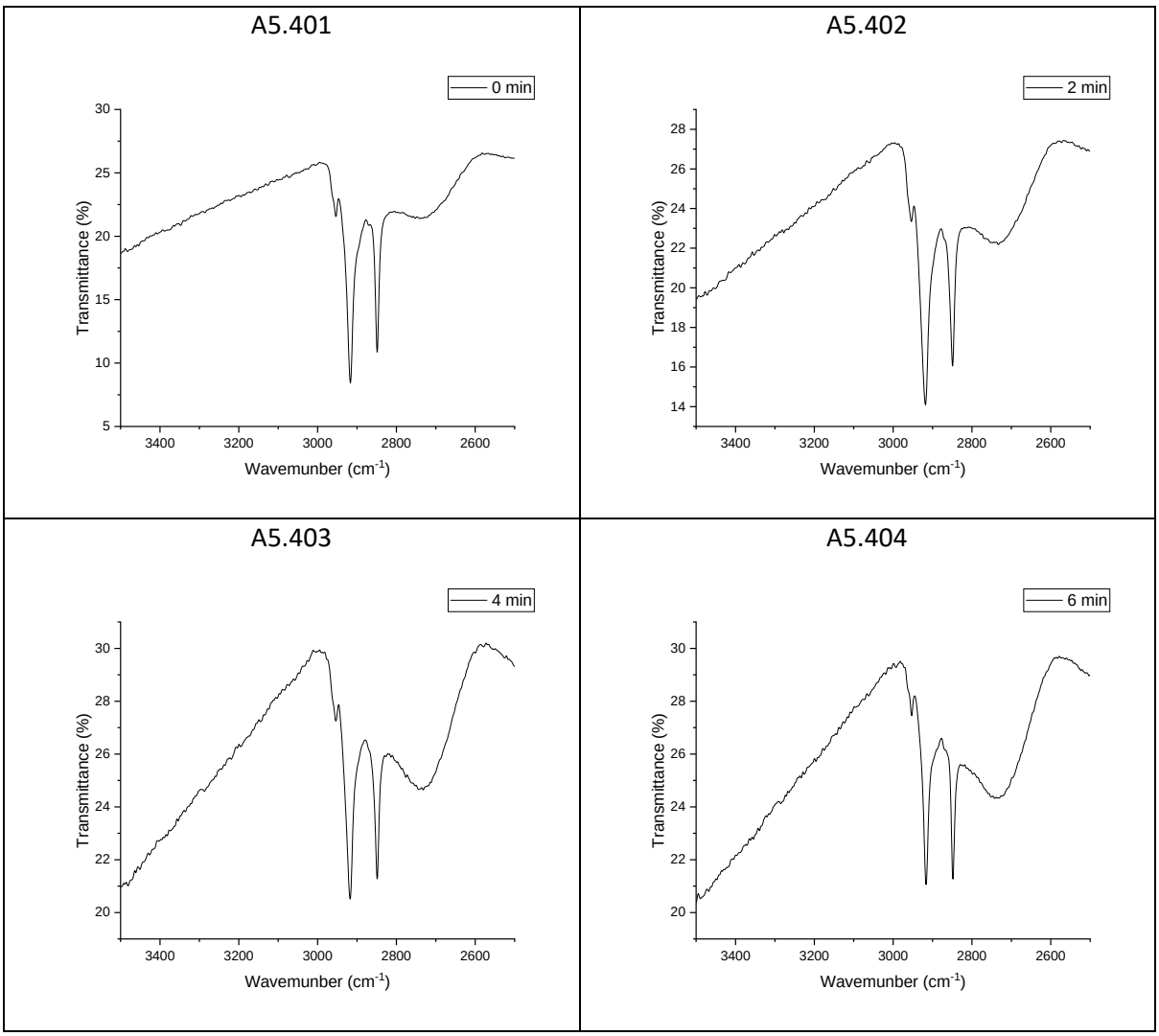

A5.405

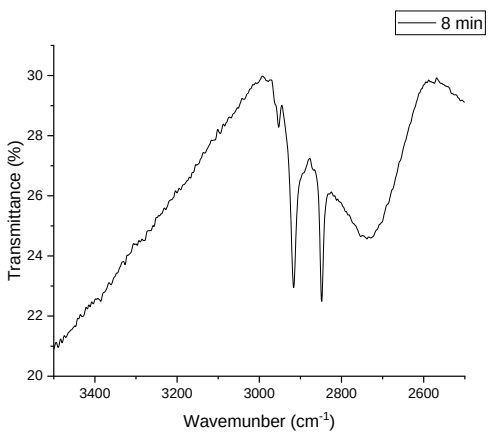

A5.406

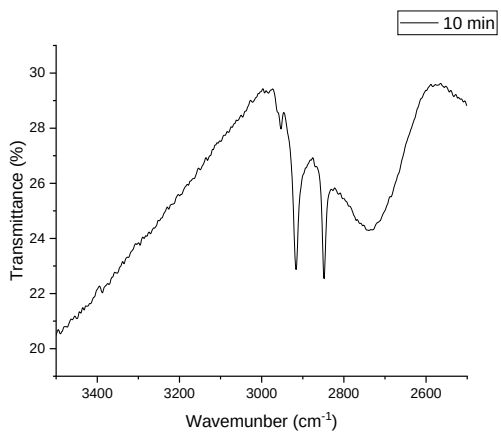

A5.407

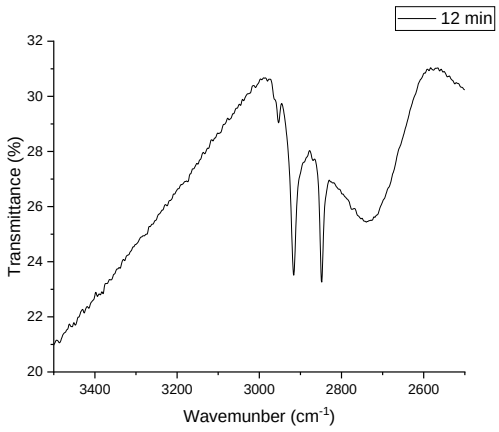

A5.408

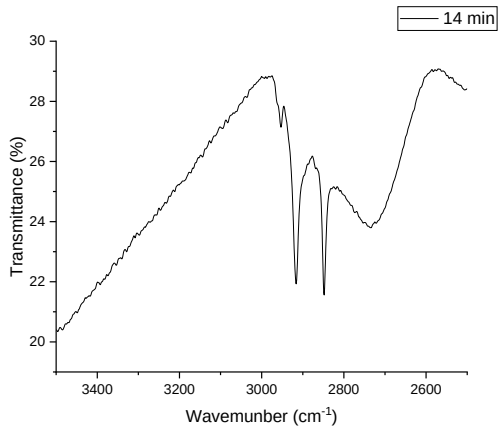

A5.409

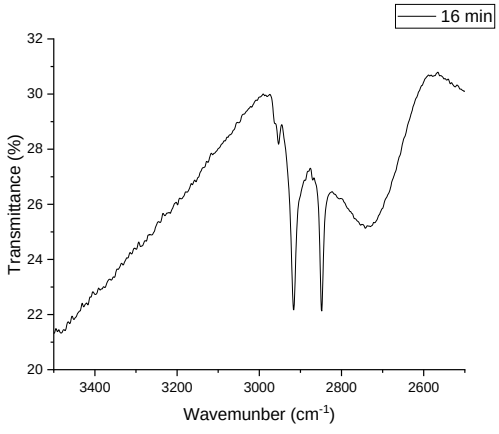

A: 5.50 DRIFT spectra of stearic acid on a 0.1 wt% Cu-doped *meso*-TiO_2 film prepared at 6000 rpm

These FTIR spectra show the C-H stretch of stearic acid that was used during photocatalytic testing to monitor the progress of the reaction with exposure to UV light. The total irradiation time is listed on each graph.

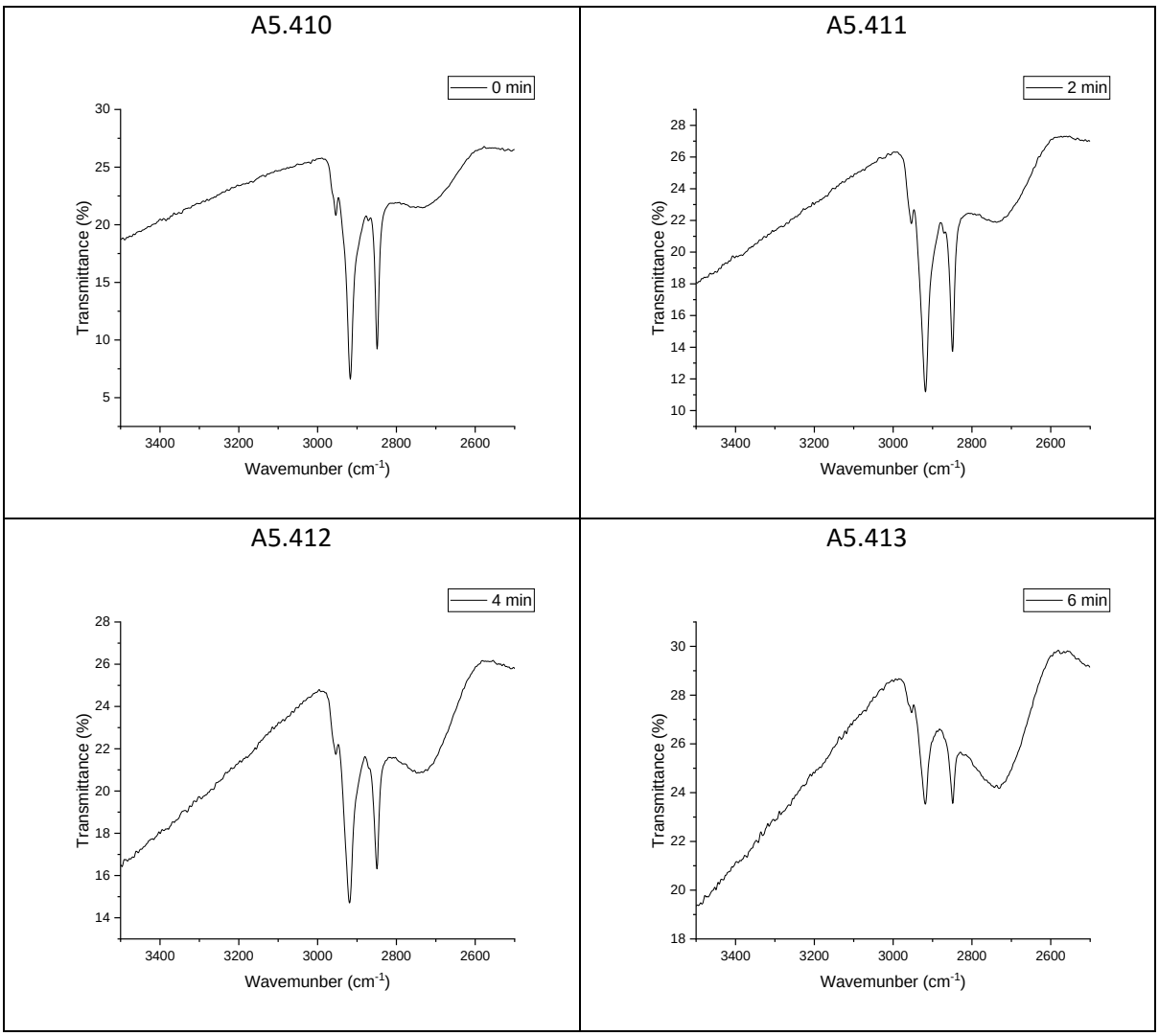

A5.414

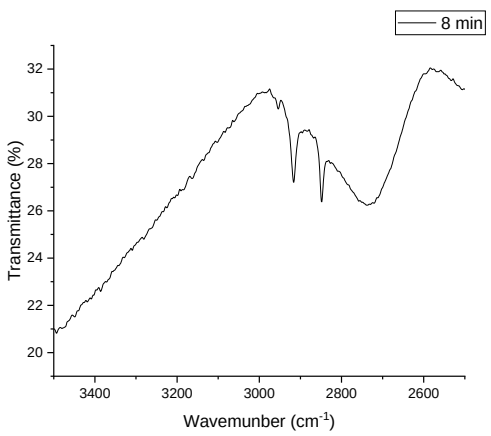

A5.415

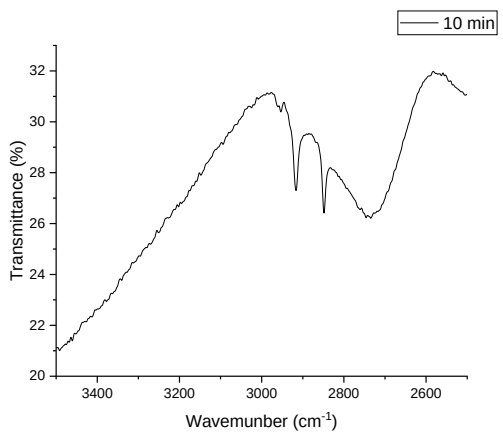

A5.416

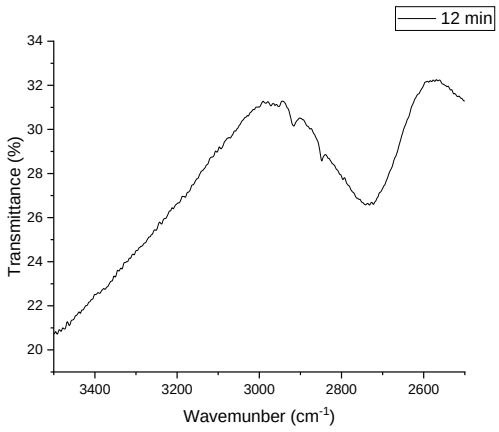

A5.417

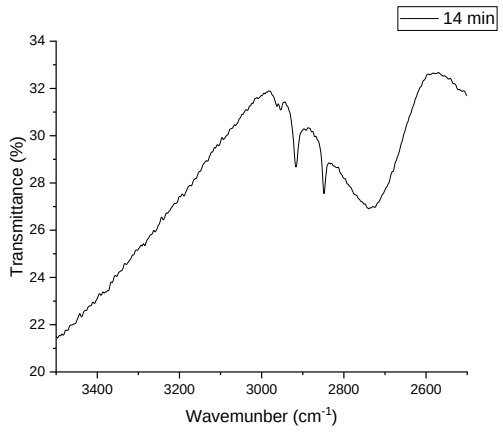

A5.418

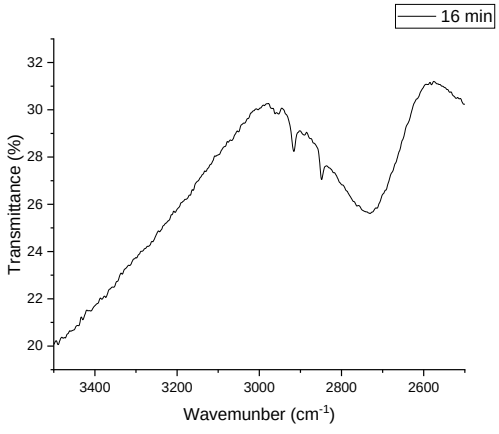

A: 5.51 DRIFT spectra of stearic acid on a 0.1 wt% Cu-doped *meso*-TiO_2 film prepared at 7000 rpm

These FTIR spectra show the C-H stretch of stearic acid that was used during photocatalytic testing to monitor the progress of the reaction with exposure to UV light. The total irradiation time is listed on each graph.

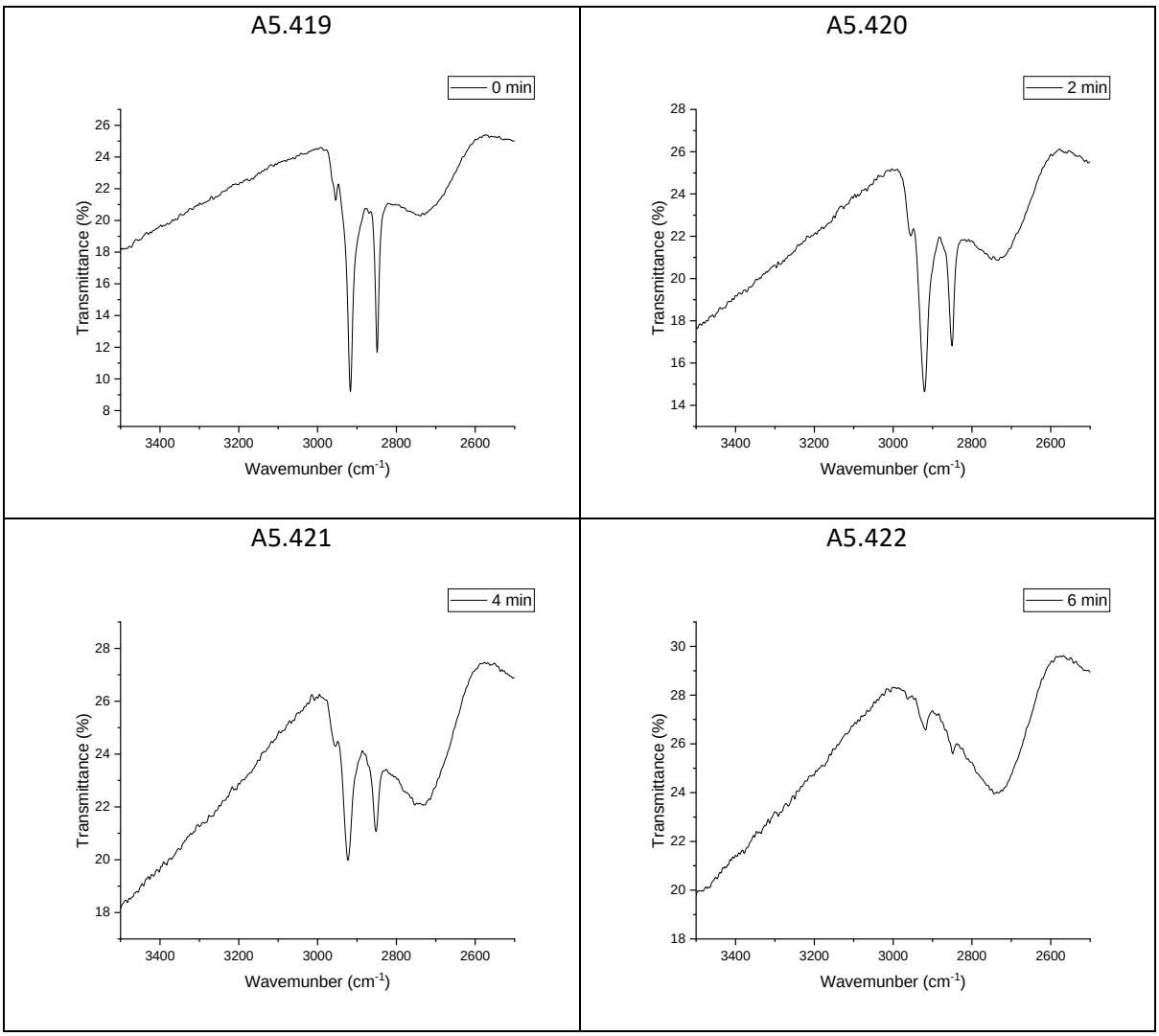

A5.423

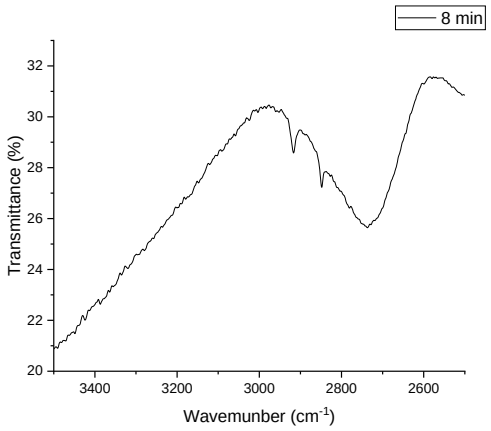

A5.424

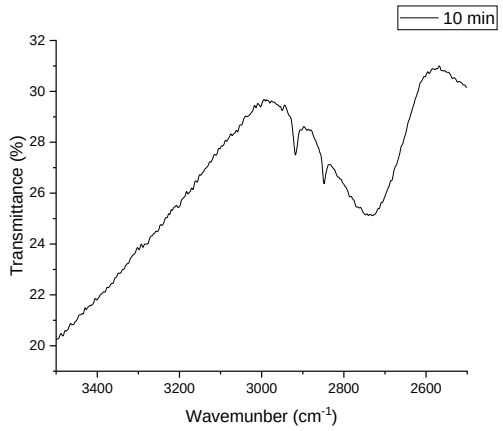

A5.425

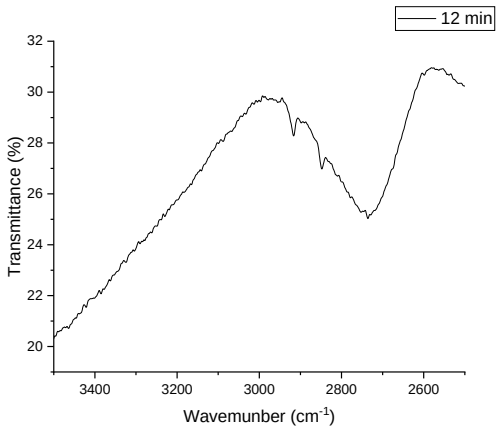

A5.426

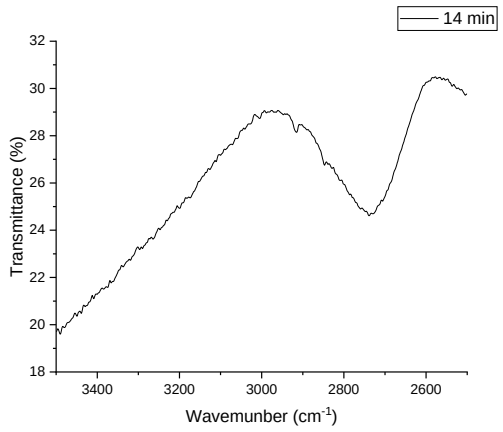

A5.427

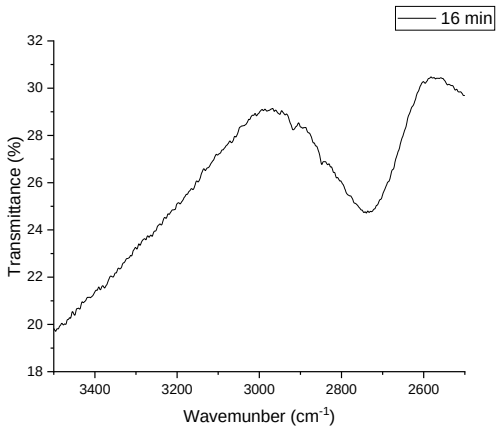

A: 5.52 DRIFT spectra of stearic acid on a 0.1 wt% Cu-doped *meso*-TiO_2 film prepared at 8000 rpm

These FTIR spectra show the C-H stretch of stearic acid that was used during photocatalytic testing to monitor the progress of the reaction with exposure to UV light. The total irradiation time is listed on each graph.

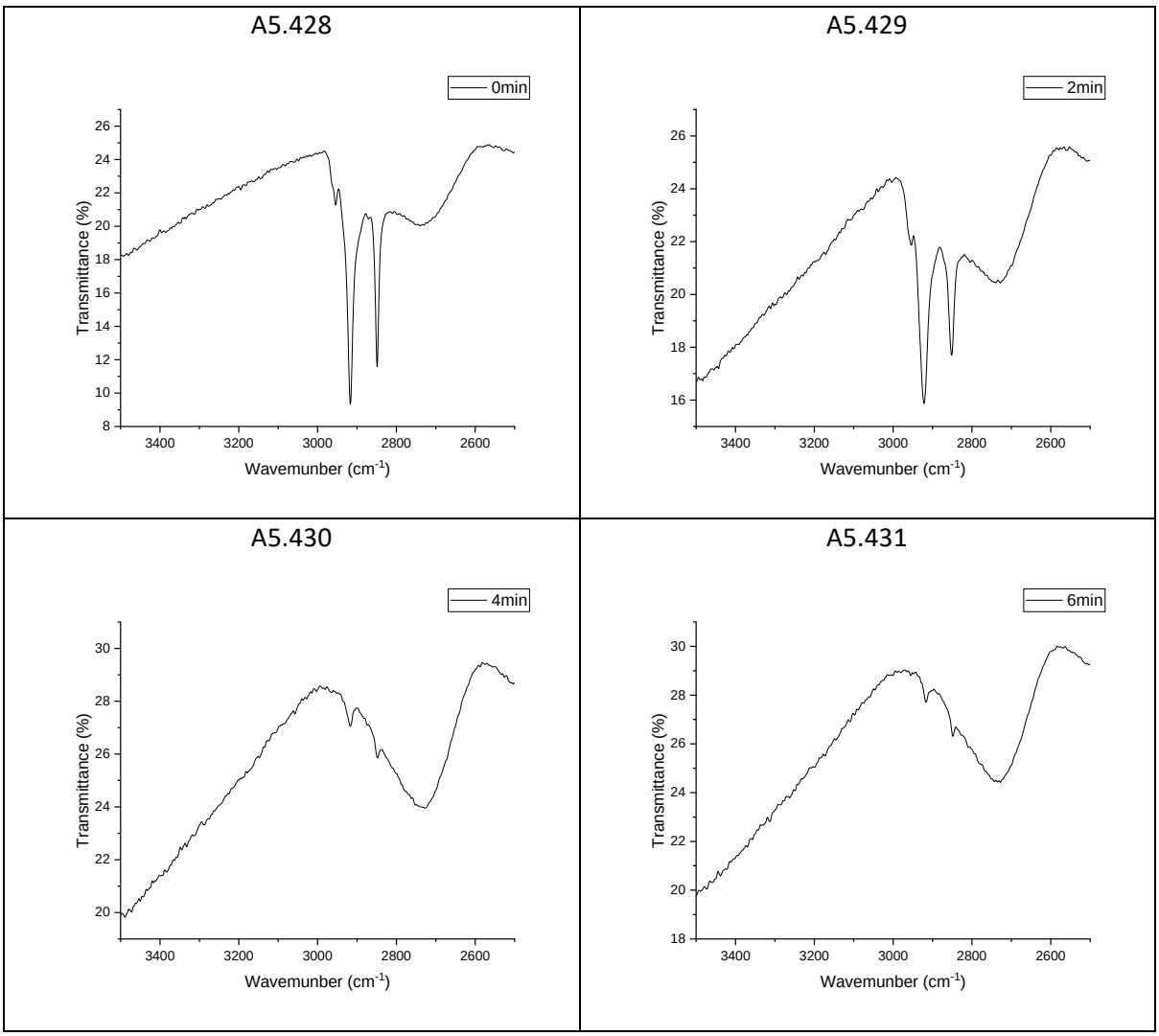

A5.432

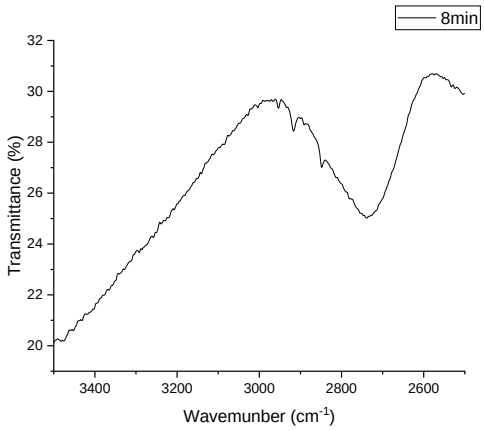

A5.433

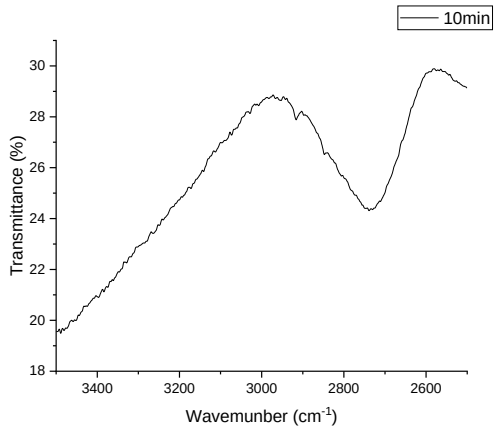

A5.434

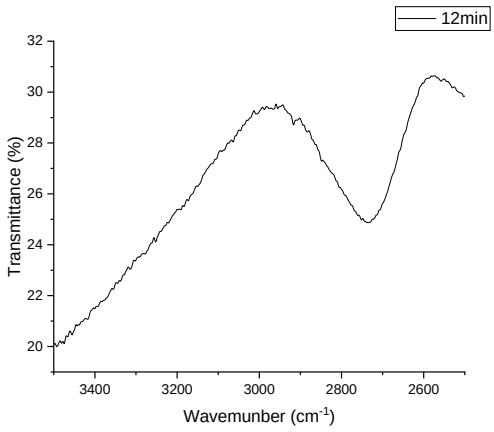

A5.435

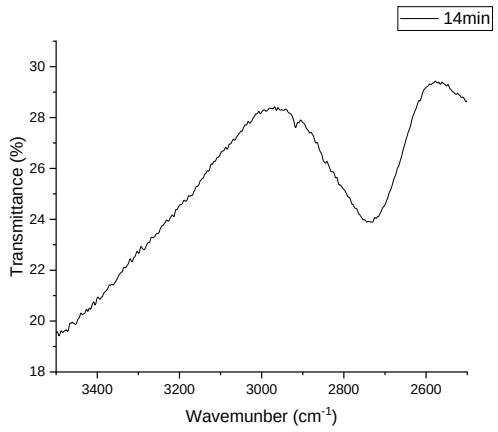

A5.436

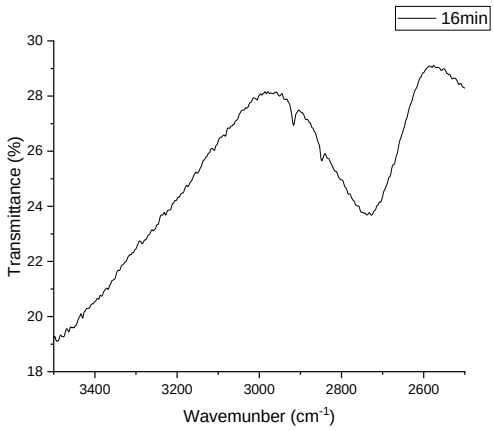

A5.437

FTIR of Stearic Acid on a 5 wt% Cu-doped *meso*-TiO_2 Film

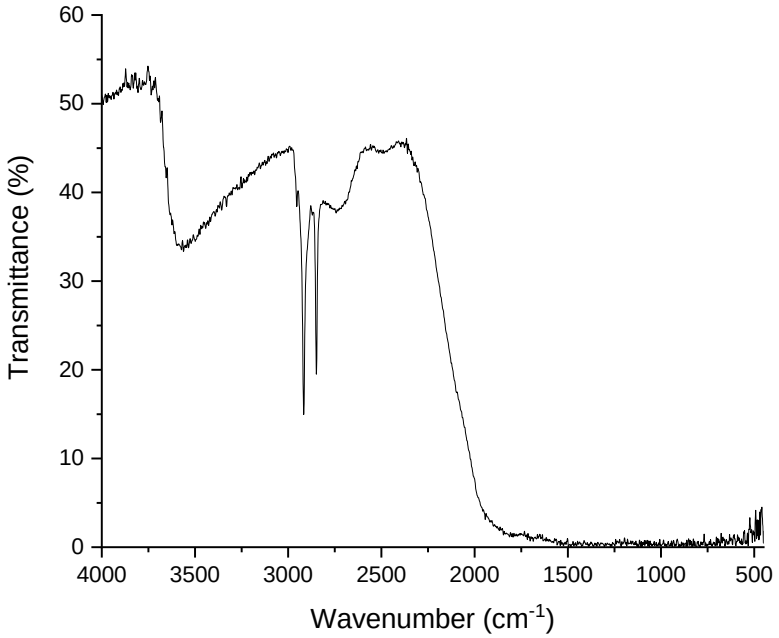

A5.438

FTIR of Stearic Acid on a 2.5 wt% Cu-doped *meso*-TiO_2 Film

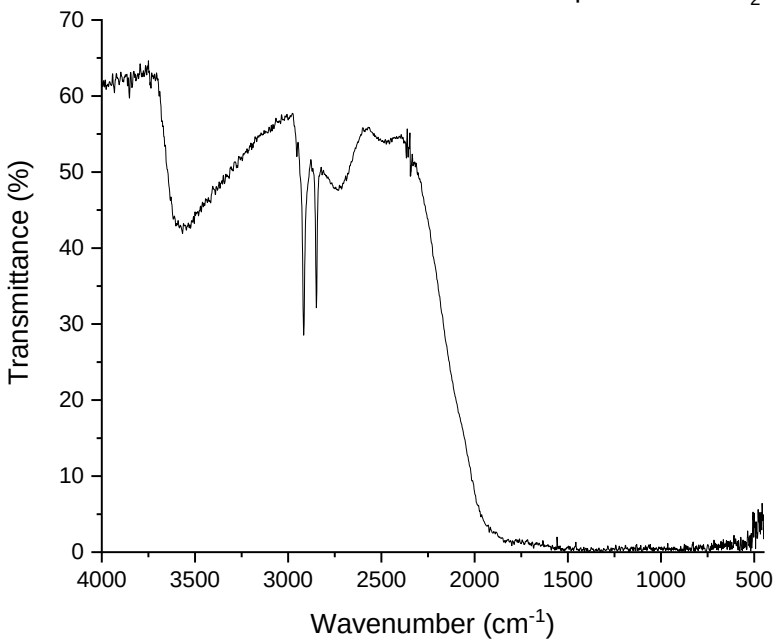

A5.439

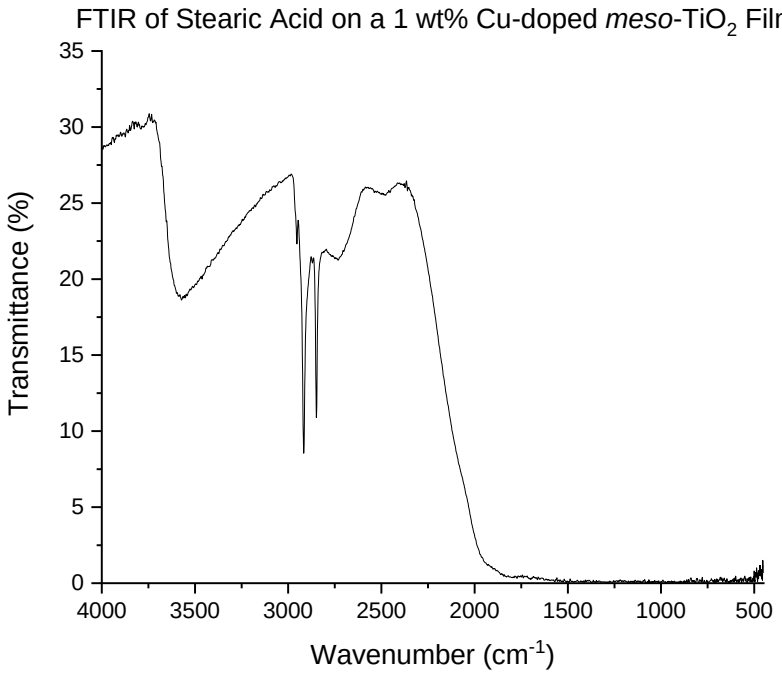
FTIR of Stearic Acid on a 1 wt% Cu-doped *meso*-TiO_2 Film
Transmittance (%)
Wavenumber (cm^{-1})
0
5
10
15
20
25
30
35
4000
3500
3000
2500
2000
1500
1000
500

A5.440

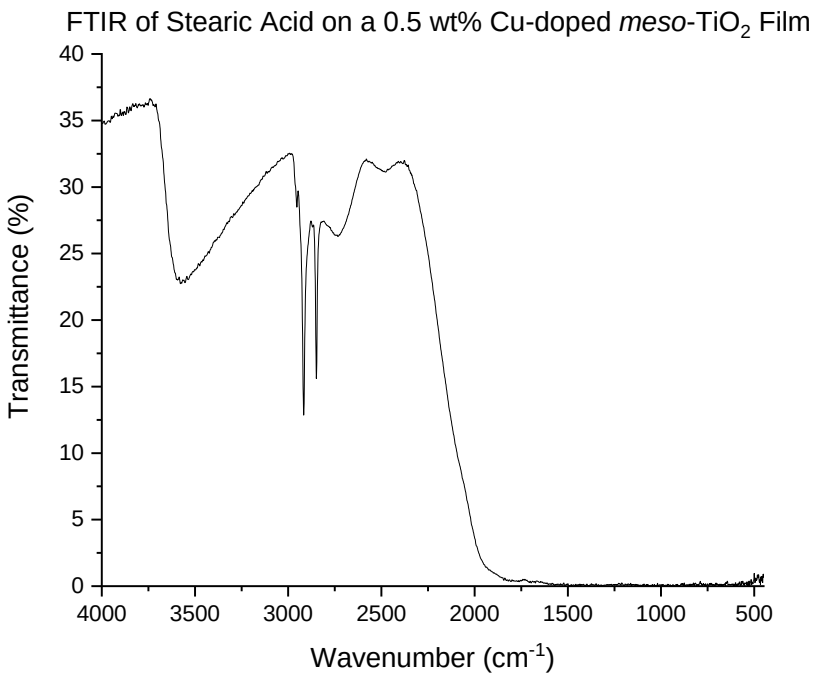
FTIR of Stearic Acid on a 0.5 wt% Cu-doped *meso*-TiO_2 Film
Transmittance (%)
Wavenumber (cm^{-1})
0
5
10
15
20
25
30
35
40
4000
3500
3000
2500
2000
1500
1000
500

A5.441

FTIR of Stearic Acid on a 0.1 wt% Cu-doped *meso*-TiO_2 Film

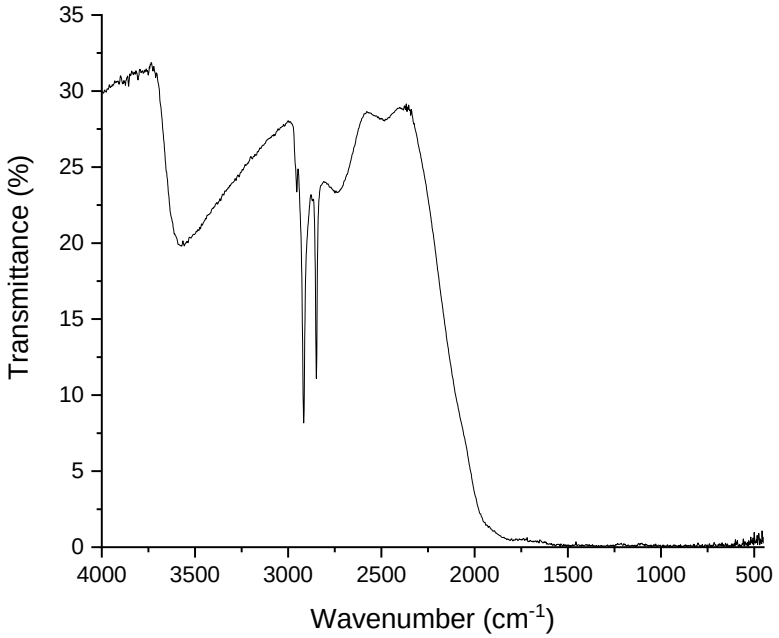

A5.442

FTIR of Stearic Acid on an Undoped *meso*-TiO_2 Film

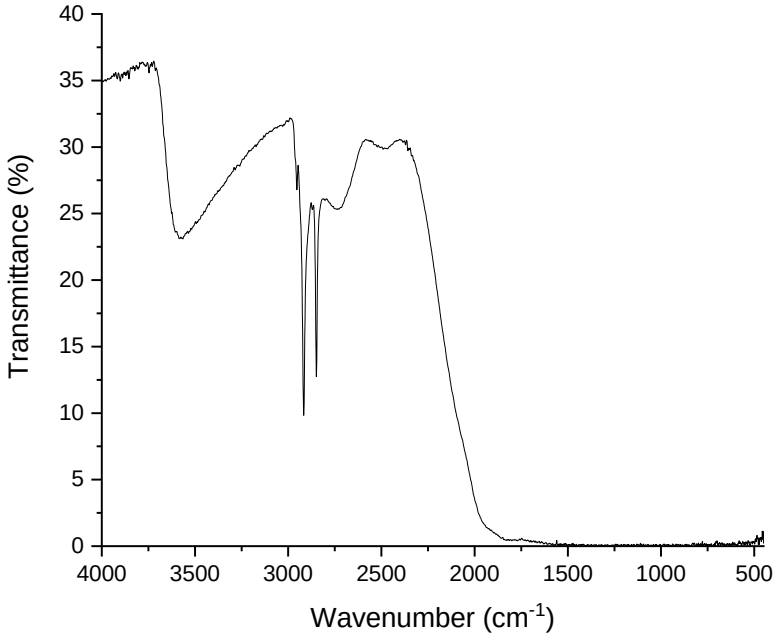

Appendix 6: FTIR Spectra of Polystyrene on Photocatalytic Films

A: 6.1 DRIFT spectra of polystyrene on a 0.1 wt% Cu-doped *meso*-TiO_2 film prepared at 1000 rpm

These FTIR spectra show the C-H stretches of polystyrene that was used during photocatalytic testing to monitor the progress of the reaction with exposure to UV light. The total irradiation time is listed on each graph.

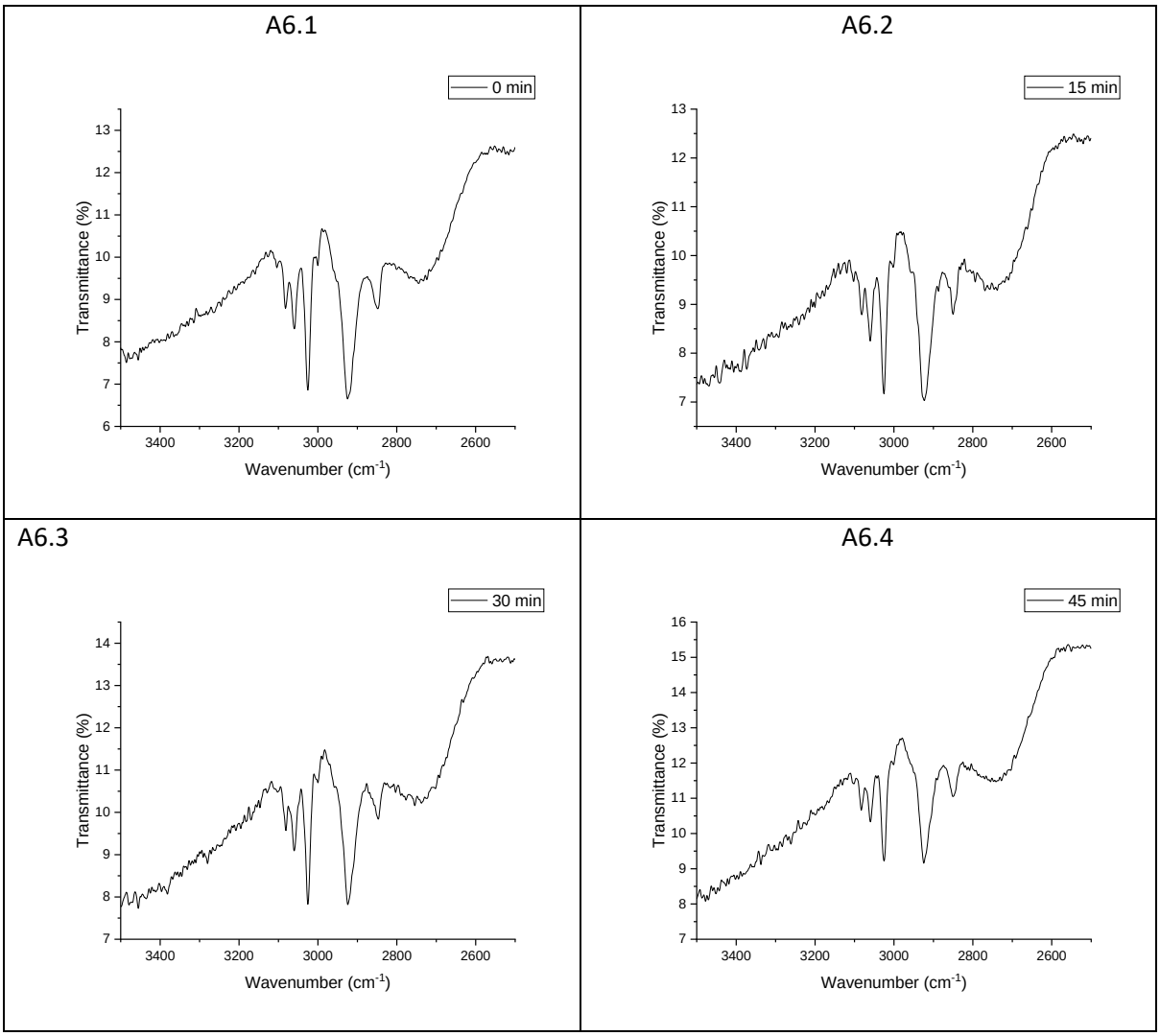

A6.5

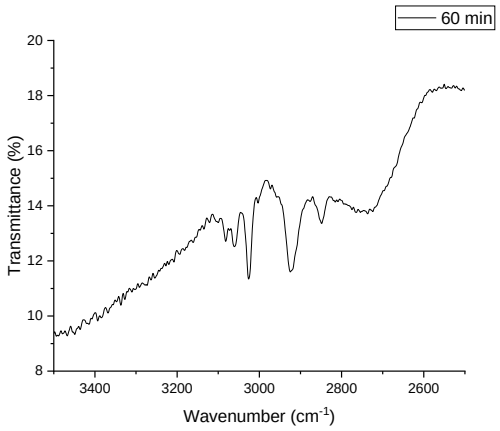

A6.6

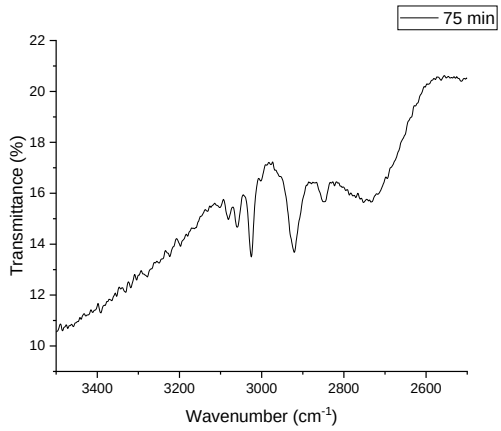

A6.7

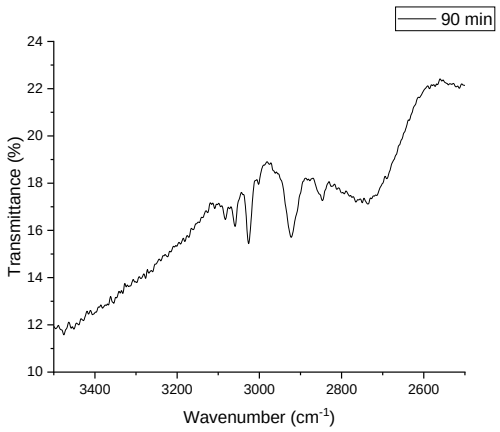

A6.8

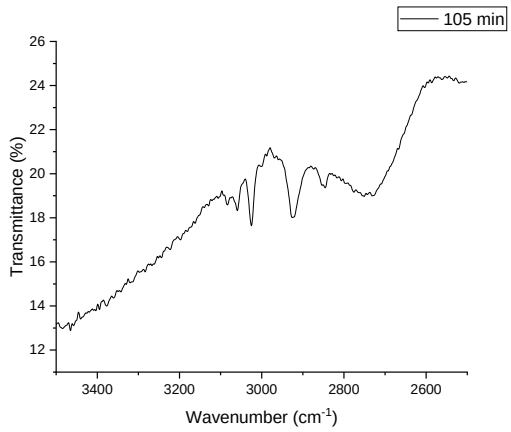

A6.9

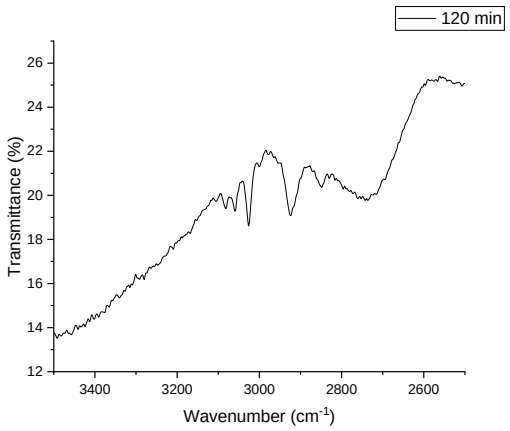

A6.10

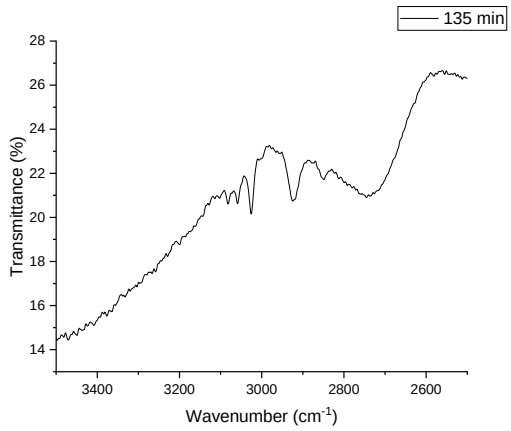

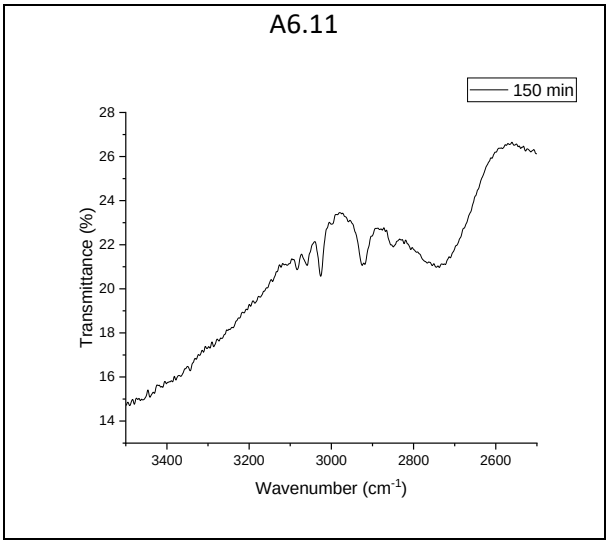
A6.11
150 min
Transmittance (%)
28
26
24
22
20
18
16
14
3400
3200
3000
2800
2600
Wavenumber (cm-1)

DRIFT spectra after subtraction of a baseline

A6.12

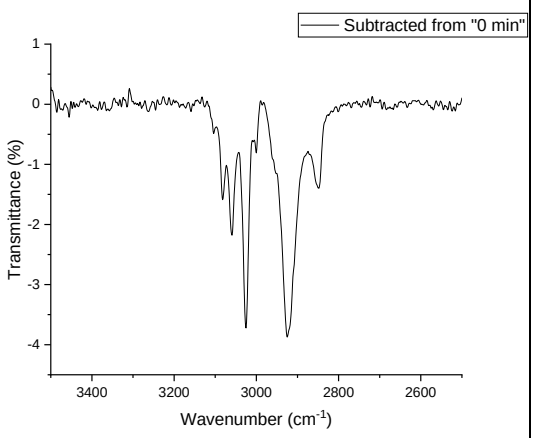

Total irradiation time: 0 min

A6.13

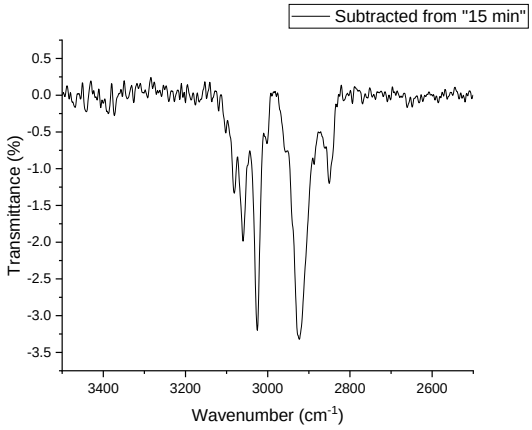

Total irradiation time: 15 min

A6.14

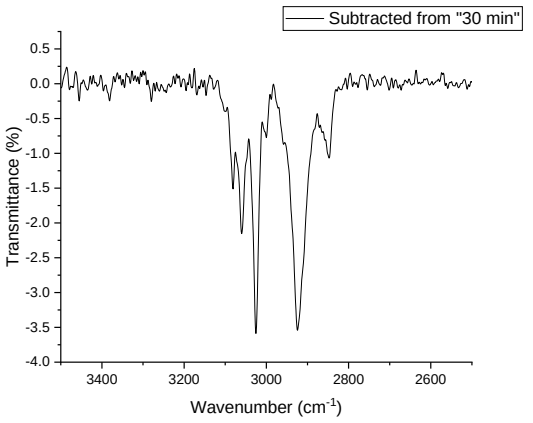

Total irradiation time: 30 min

A6.15

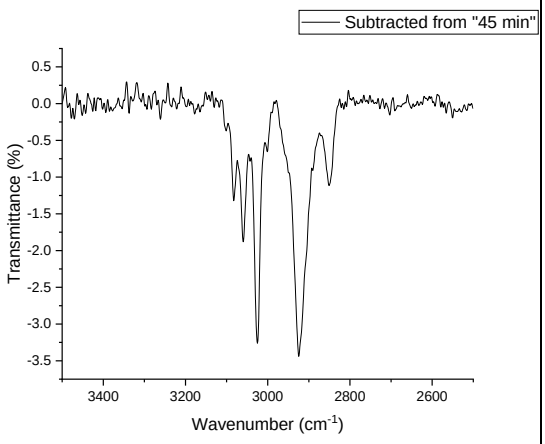

Total irradiation time: 45 min

A6.16

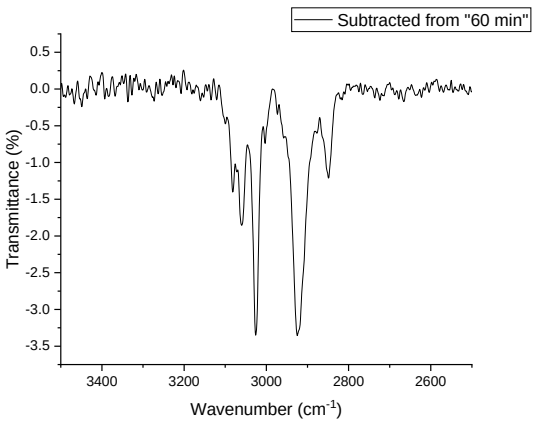

Total irradiation time: 60 min

A6.17

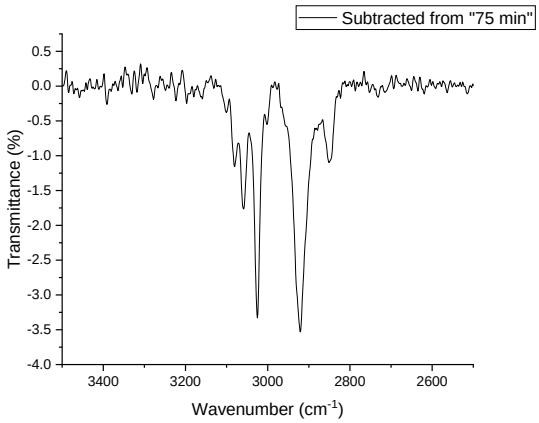

Total irradiation time: 75 min

A6.18

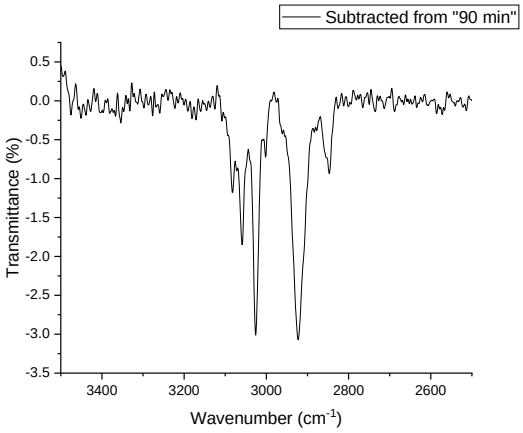

Total irradiation time: 90 min

A6.19

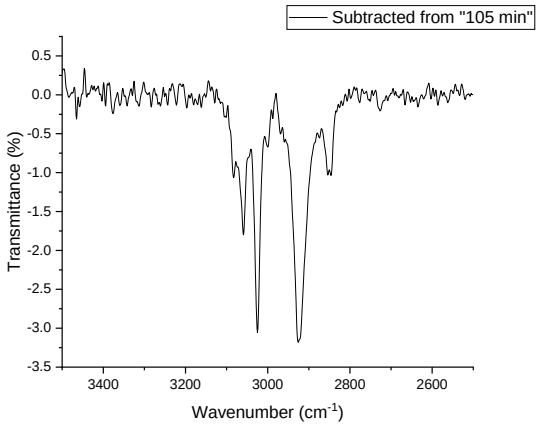

Total irradiation time: 105 min

A6.20

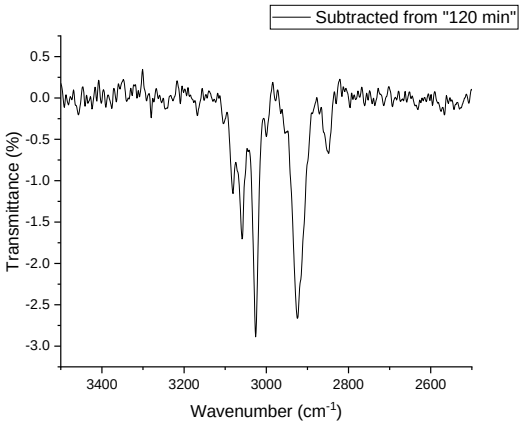

Total irradiation time: 120 min

A6.21

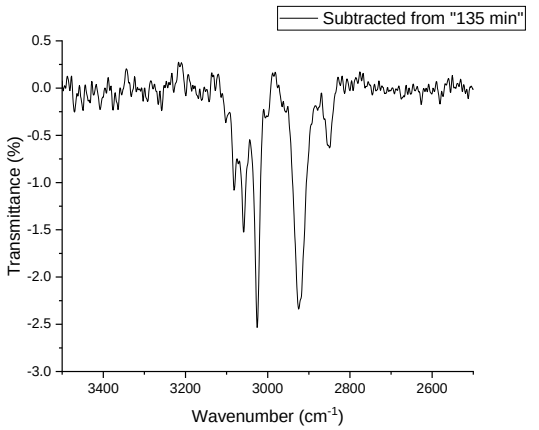

Total irradiation time: 135 min

A6.22

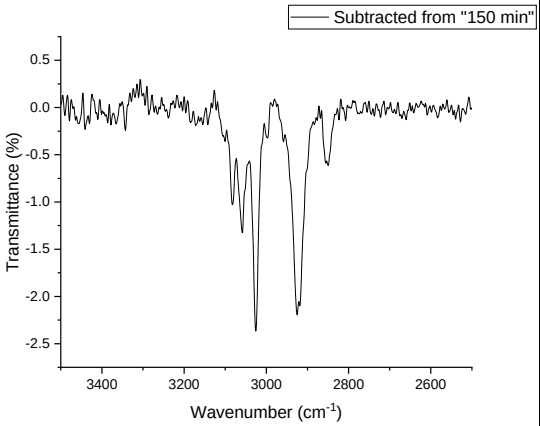

Total irradiation time: 150 min

A: 6.2 Curve fitting of DRIFT spectra after baseline subtraction

A6.23

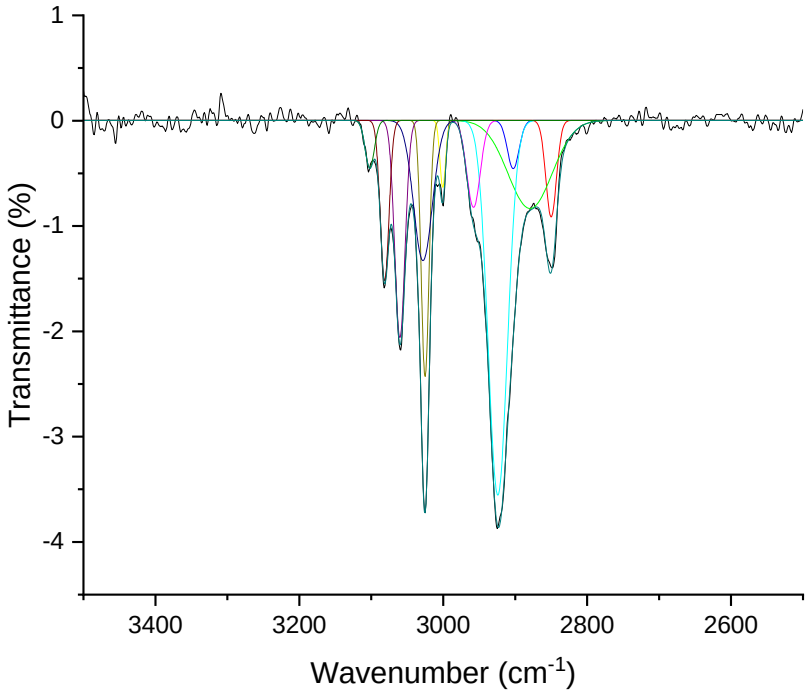

Total irradiation time: 0 min

A6.24

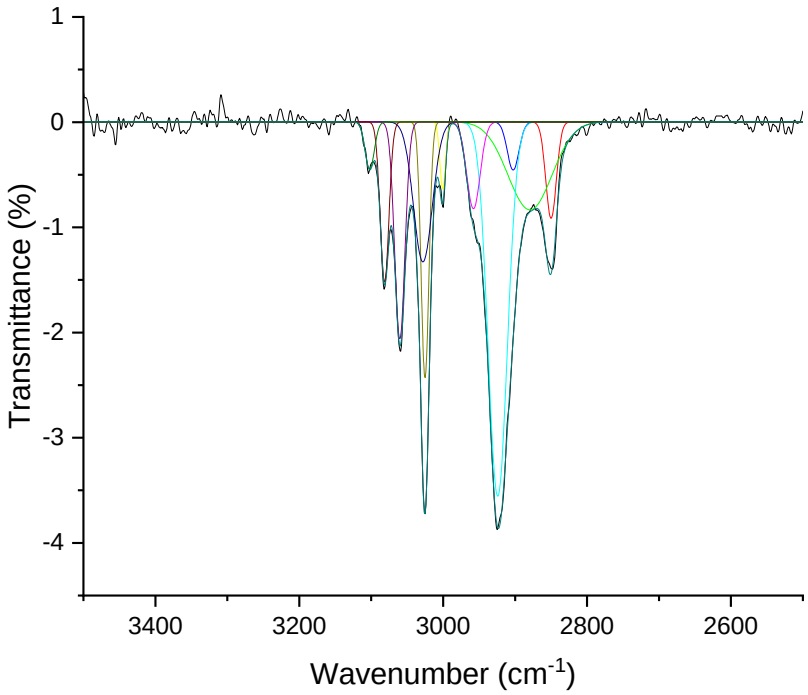

Total irradiation time: 15 min

A6.25

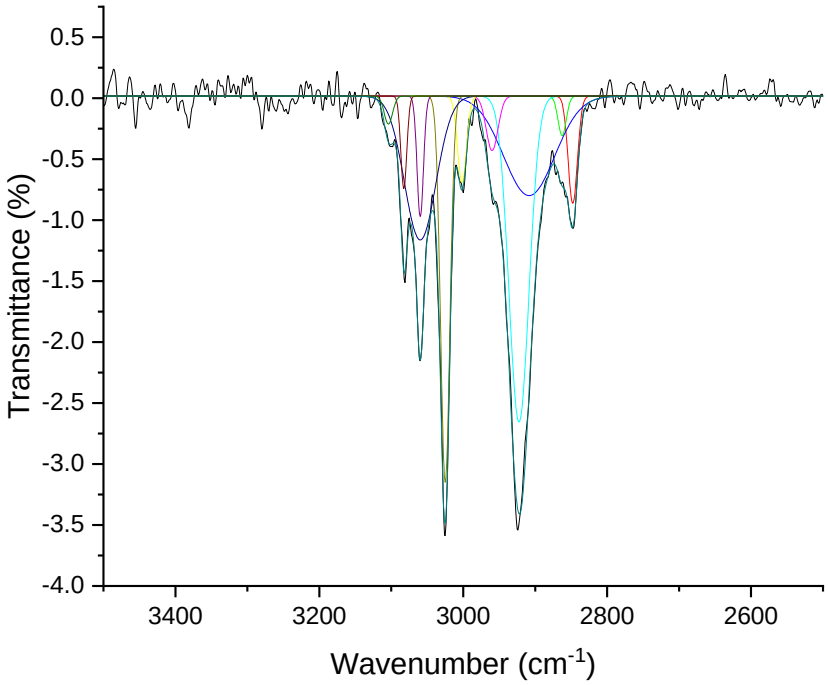

Total irradiation time: 30 min

A6.26

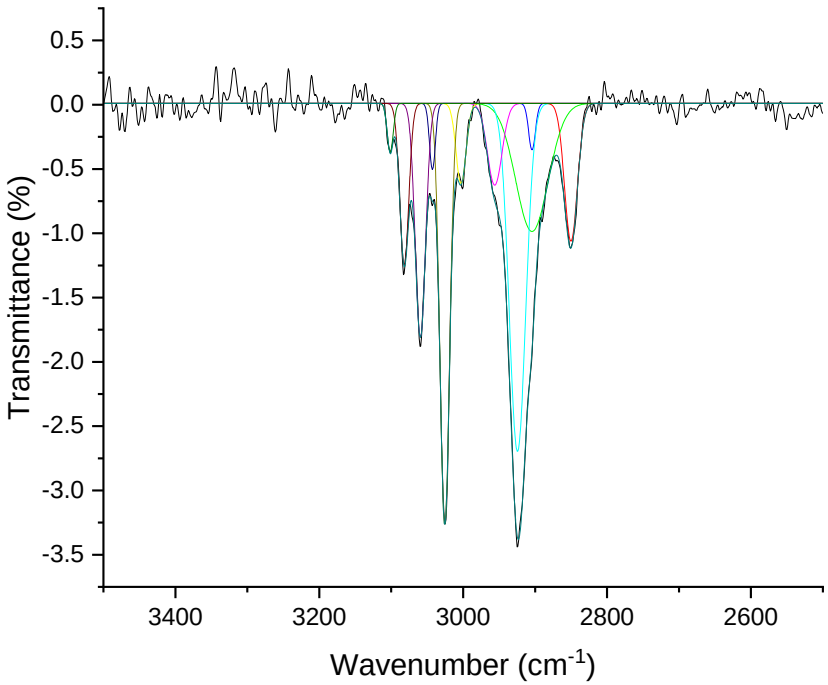

Total irradiation time: 45 min

A6.27

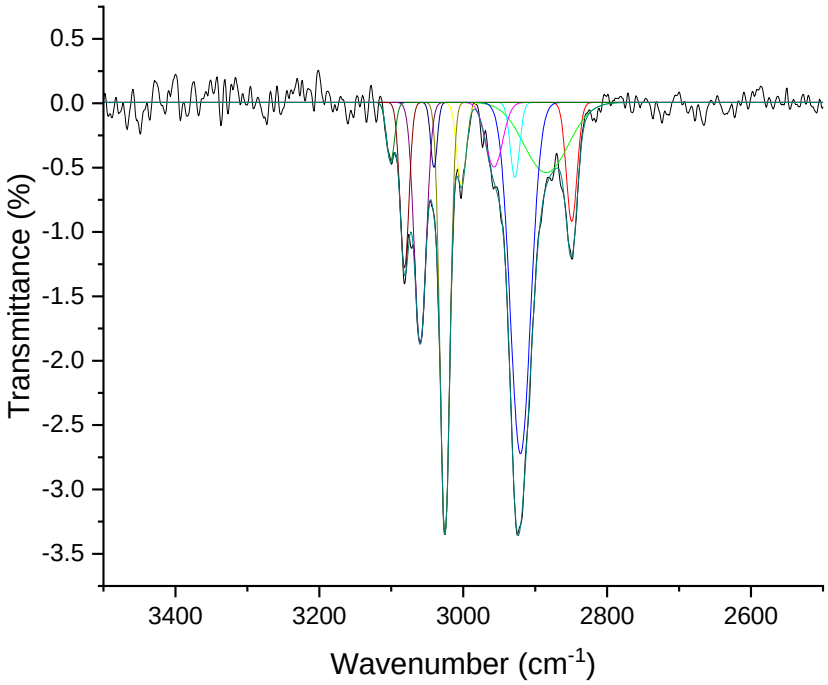

Total irradiation time: 60 min

A6.28

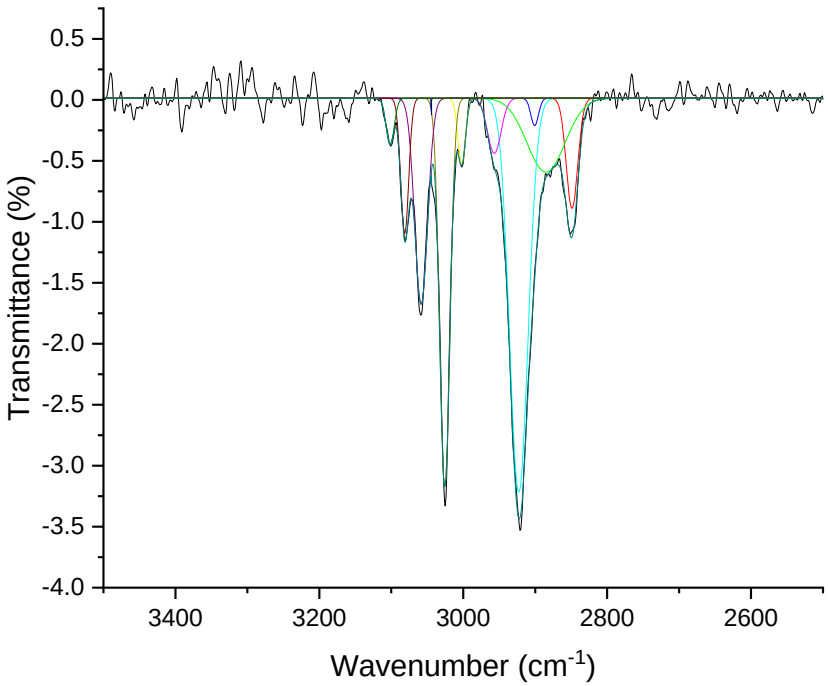

Total irradiation time: 75 min

A6.29

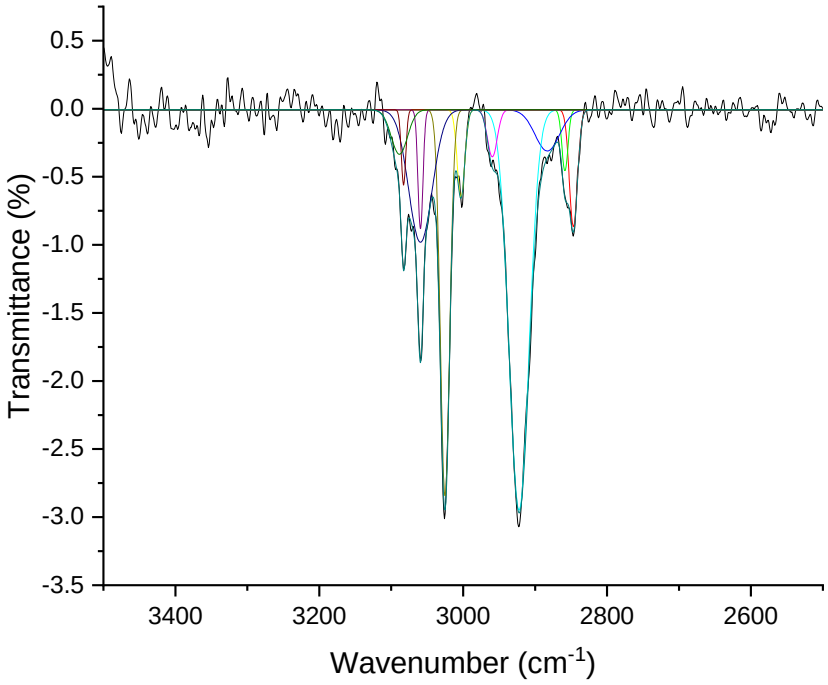

Total irradiation time: 90 min

A6.30

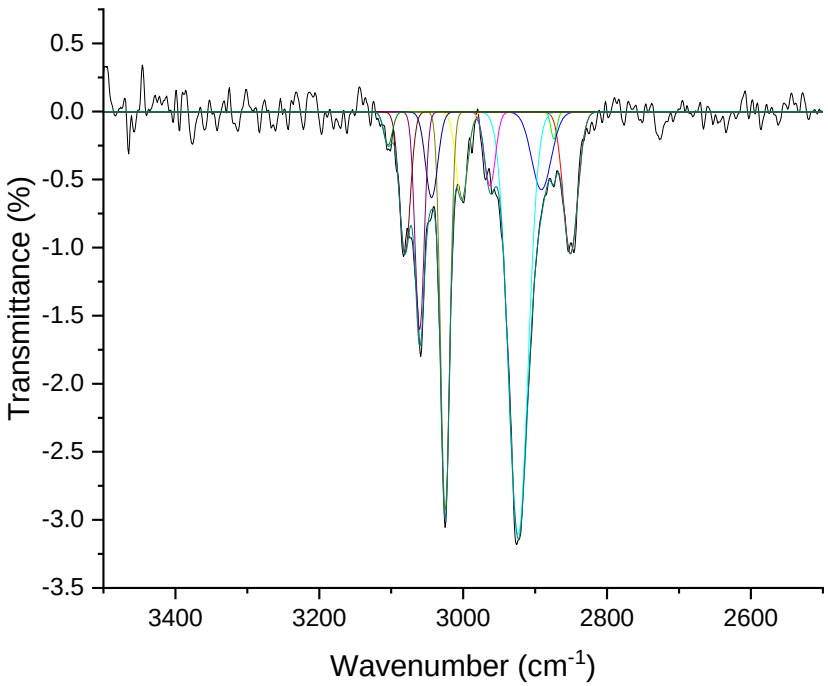

Total irradiation time: 105 min

A6.31

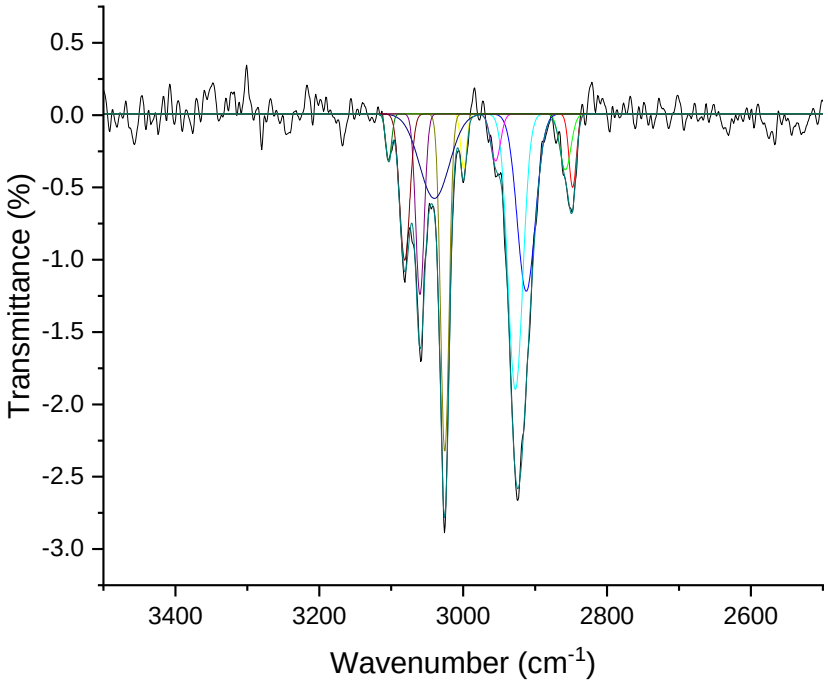

Total irradiation time: 120 min

A6.32

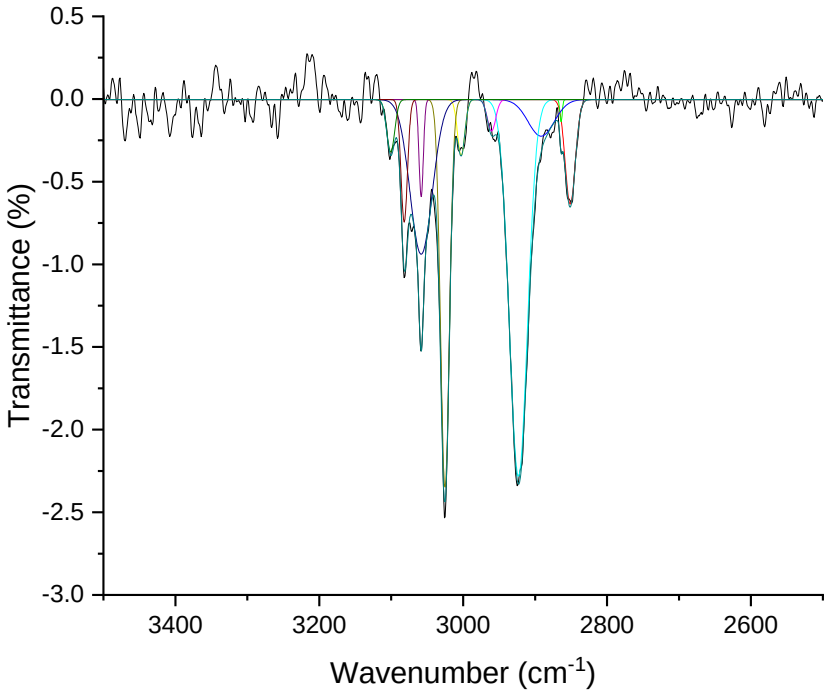

Total irradiation time: 135 min

A6.33

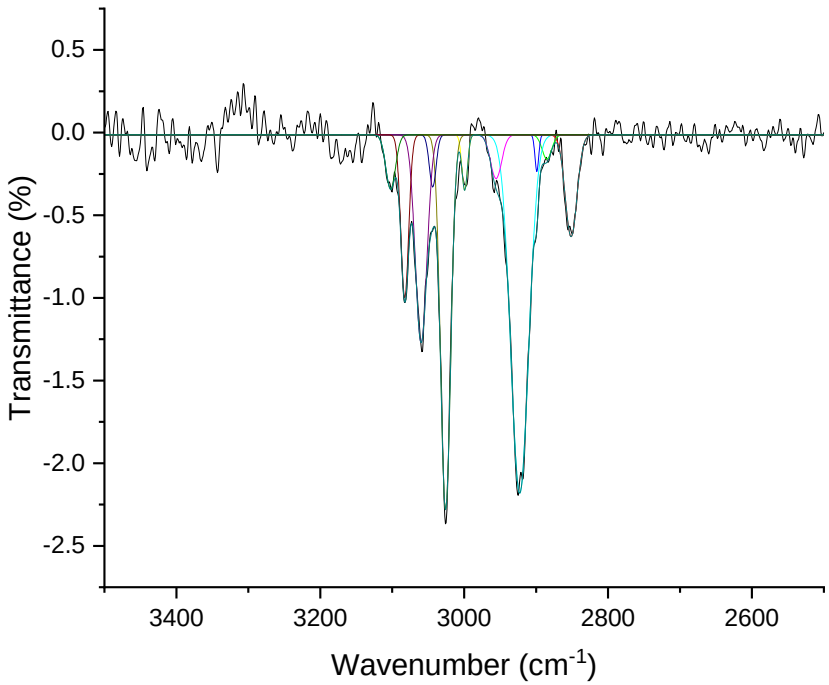

Total irradiation time: 150 min